Fracture Prediction in Metal Sheets

by

Young-Woong Lee

B.S. in Mechanical Engineering (1993)
Yonsei University, Republic of Korea
M.S. in Mechanical Engineering (1995)
Yonsei University, Republic of Korea

Submitted to the Department of Ocean Engineering
in partial fulfillment of the requirements for the degree of

Doctor of Philosophy in Applied Mechanics

at the

MASSACHUSETTS INSTITUTE OF TECHNOLOGY

February 2005

Author .....
Department of Ocean Engineering
December 6, 2004

Certified by .....
Tomasz Wierzbicki
Professor of Applied Mechanics
Thesis Supervisor

Accepted by .....
Michael S. Triantafyllou
Professor of Ocean Engineering
Chairman, Department Committee on Graduate Students

Fracture Prediction in Metal Sheets

by

Young-Woong Lee

Submitted to the Department of Ocean Engineering
in November 2004, in partial fulfillment of the requirements for the degree of
Doctor of Philosophy in Applied Mechanics

ABSTRACT

One of the most important failure modes of thin-walled structures is fracture. Fracture is predominantly tensile in nature and, in most part, is operated by the physical mechanisms of void nucleation, growth, and linkage. For ductile sheet, fracture is preceded by necking. Prediction of necking which limits sheet metal formability is well established and has been developed over the past several decades. However, an in-depth understanding of the mechanical process inside the neck leading to sheet metal fracture is lacking. This is true for both static and high intensity, short duration loads. Furthermore, there is an ever increasing need to raise the safety envelope of existing protective structures against localized extreme loading. The present thesis addresses four parts of the many outstanding issues in sheet metal fracture.

In the first part, the new Bao-Wierzbicki (BW) fracture criterion formulated in terms of the accumulated equivalent plastic strain with the stress triaxiality as a weighting function is considered. Using the equations of plane stress von-Mises plasticity and the strain-to-stress mapping procedure, the BW fracture criterion is transformed to the spaces of the principal tensile strains and stresses in a sheet and compared with experimental results for various materials. An extensive comparative study of the most widely used fracture criteria is then conducted. The applicability and expected errors of those criteria are investigated.

In the second part, calibration methods for the determination of the stress-strain curve after necking and critical damage parameters are discussed. Most importantly, a simple method of calibrating for fracture from a round or flat specimen tensile test is developed ans shown to be valid in a wide range of stress triaxiality.

In the third part, experimental, numerical, and analytical studies on the deformation and fracture of thin plates subjected to localized static and impulsive loadings are conducted. A new method of constructing a Fracture Forming Limit Diagram (FFLD), which is understood as the locus of fracture strain in the principal strain space, is proposed and confirmed by the classical problem of punch indentation in thin plates. Moreover, it is demonstrated that the present fracture criterion captures the formation and propagation of cracks in thin plates.

In the fourth part, extensive parametric studies on the transient responses and fracture of various core arrangements in sandwich structures under explosive loading are carried out. A new Blast Resistant Adaptive Sandwich (BRAS) structure is proposed, which substantially increases fracture resistance during static and dynamic loading events. In particular, the threshold impulse to initial fracture of the optimized BRAS is 1.8 times higher than the optimized conventional sandwich structure (USDH). Also the maximum reduction of the ruptured area with the optimized BRAS is 90%, as compared to the optimized USDH.

Thesis Supervisor: Tomasz Wierzbicki
Title: Professor of Applied Mechanics

This page intentionally left blank

Acknowledgement

First and foremost, I would like to express my heartfelt thanks to my advisor, Professor Tomasz Wierzbicki, for his guidance, support, encouragement and great vision during the last four years. I haven't met and won't meet such a wonderful person as an advisor throughout my life. I would also like to express my sincere appreciation to Professor Frank McClintock, Professor Raul Radovitzky, and Dr. David Burke for their time, effort, expert advice as members of my doctoral thesis committee and again to Professor Frank McClintock for his inspiring suggestions and encouraging feedbacks.

To my colleagues at the Impact and Crashworthiness Laboratory, Dr. Yingbin Bao, Dr. Dirk Mohr, Mr. Xiaoqing Teng, Ms. Li Zheng, Mr. Liang Xue, Mr. Yuanli Bai, and Mr. Carey Walters and others, thank you very much for all the great conversations and good times we've had. I wish all of you the best of luck in your future endeavors. Thanks are also extended to Ms. Sheila McNary for her assistance on administrative matters.

To my OE Korean colleagues, Dr. Wonjoon Cho, Dr. Yonhwan Kim, Dr. Heung-Soo Kim, Dr. Jay Auh, Dr. Sungjoon Kim, Dr. Kwanghee Ko, Mr. Sunwoong Lee, Mr. Kwanghyun Lee, and Mr. Hyunjo Kim, thank you very much all your help and advice. May success shine on you constantly.

To my wife, Joo-Hee, your love, support, and forbearance have been and will always be a source of inspiration to me. Thank you very much for all that you have done for me. Thank my amazing daughters, Jane and Hyein, for giving me new world and for delighting my life. My appreciation also goes out to my other family members for their great support at distance.

I greatly acknowledge the financial support for this work provided by the MURI project, under the sponshorship of ONR.

This page intentionally left blank

Contents

List of Figures

This page intentionally left blank

List of Tables

Nomenclature

Acronyms

BRAS	Blast Resistant Adaptive Sandwich
BW	Bao and Wierzbicki (fracture criterion)
C-L	Cockcroft-Latham (fracture criterion)
CTOD	Crack Tip Opening Displacement
FLD	Forming Limit Diagram
FFLD	Fracture Forming Limit Diagram
J-C	Johnson-Cook (fracture criterion)
USDH	Unidirectionally Stiffened Double Hull
W	Wilkins (fracture criterion in Chapter 2)

Symbols

A_0	Initial half width of clamped square plate
A_1	Half width of centrally loaded area of square plate
a	Equivalent strain to fracture in pure shear
a	Current radius at the minimum cross-section of tensile bar
a_0	Initial radius of tensile bar
a_f	Radius at the minimum cross-section of bar after fracture
b	Equivalent plastic strain to fracture in uniaxial tension
$c = \sqrt{\sigma_0 / \rho}$	Plastic transverse wave velocity
D_c	Critical damage value for ductile fracture
$\widetilde{D}_c$	Average value of critical damage
$\dot{E}$	Total rate of energy dissipated per petals
H	Distance between inner and outer hull (cell height or hull separation)
h	Current thickness of plate

h_o	Initial thickness of plate; Uniform thickness of sandwich panel (Chapters 8 and 9)
h_f	Thickness in the neck of plate after fracture; Thickness of face plates (Chapters 8 and 9)
h_w	Thickness of web
$\widetilde{h}_w = h_w / h_0$	Normalized thickness of web (Chapters 8 and 9)
$\widetilde{h}_f = h_f / h_0$	Normalized thickness of face plate (Chapter 8 and 9)
I	Total impulse imparted to plate
I_0	Impulse per unit area
$(I_0)_{cr}$	Critical impulse per unit area for ductile fracture
K	Strength coefficient of power law
L_l	Half width of centrally loaded area of sandwich panel (Chapters 8 and 9)
L_o	Initial gauge length for tensile specimen; Half width of sandwich panel (Chapters 8 and 9)
l_c	Crack length
l_i	Mesh size in the "i" direction ($i = x, y, z$)
M_0	Fully plastic bending moment per unit length
m^*	Mass per unit area
$\widetilde{m} = m^* / \rho L_0$	Dimensionless mass (mass per unit area normalized by ρL_0)
n	Hardening exponent of power law
p	Pressure load per unit area for dynamic loading
p_0	Amplitude of applied pressure
$(p_0)_{cr}$	Critical magnitude of applied pressure for ductile fracture
P	Force
P_u	Maximum force in the axial direction (tensile test)
q	Instantaneous crushing resistance of sandwich core (Chapter 8)
q_m	Mean crushing resistance of sandwich core (Chapter 8)
r	Current radial coordinates of circular plate
r_0	Misalignment of applied hemi-spherical punch with respect to the centere (Chapter 6)

r_c	Radial coordinates of outermost contact point (Chapter 6)
r_f	Critical radial coordinates to fracture (Chapter 6)
R	Radius of curvature of the neck surface of tensile bar
R_0	Initial half width or radius of clamped plate
R_1	Half width or radius of centrally loaded area
R_e	Effective deformation radisu
R_h	Radius of the hemi-spherical punch (Chapter 6)
R_i	Representative length in the "i" direction ($i = x, y, z$)
t	Time
t_o	Time duration of pressure
t_f	Duration of motion or time to reach peak central deflection of plates (Chapter 8)
t_{cb}	Response time of bottom face plate (Chapter 8)
u	Radial or horizontal displacement
$v = \partial W / \partial \tau$	Dimensionless transverse velocity of plate
$v_{0f} = I_0 / \rho h_f$	Initial transverse velocity of top face plate (Chapter 8)
$V = I_0 / cm^*$	Dimensionless impulse
V_{cr}^b	Critical dimensionless impulse to initial fracture of bottom plate
V_{cr}^s	Critical dimensionless impulse to capping failure of single plate
w	Transverse displacement
w_o	Transverse displacement of middle point
w_d	Post-necking width in the central region of specimen
$\widetilde{w}_o$	Ratio of central deflection of square plate to that of circular plate
W	Dimensionless plate deflection defined by $W = w / R_0$ or w / A_0; Spacing between webs (Chapters 8 and 9)
x	Current horizontal coordinates of plate
y	Current longitudinal coordinates of plate
z	Current transverse coordinates of plate
α	Principal strain ratio $d\varepsilon_2 / d\varepsilon_1$

β	Principal stress ratio σ_2 / σ_1
δ	Axial extension (tensile test); Punch penetration
δ_c	Critical indentation at which sharp increase of crushing force occurs (Chapter 8)
δ_f	Critical displacement or penetration to fracture
$\bar{\delta} = \delta_t / h$	Dimensionless crack tip opening displacement
ε_{1f}	Major principal strain to fracture
ε_{2f}	Minor principal strain to fracture
ε_{1f}^{p}	The major principal strain to fracture in plane strain tension
ε_{1f}^{s}	The major principal strain to fracture in pure shear
$\tilde{\varepsilon}_{1f}^{I}; \tilde{\varepsilon}_{2f}^{I}; \tilde{\varepsilon}_{3f}^{I}$	Dimensionless principal strains to fracture in the branch I
$\tilde{\varepsilon}_{1f}^{III}; \tilde{\varepsilon}_{2f}^{III}$	Dimensionless principal strains to fracture in the branch III
$\bar{\varepsilon}$	Equivalent plastic strain
$\bar{\varepsilon}_f$	Equivalent plastic strain to fracture
ϕ	Angle of localized necking to the tensile axis
γ	Principal stress ratio σ_3 / σ_1
$\eta = h_0^i / h_0$	Dimensionless thickness of i^{th} local element (thickness imperfection, Chapter 6)
η_0	Dimensionless area of applied pressure loading
η_{cb}	Dimensionless ruptured area of bottom face plate
μ	Friction coefficient
θ	Inclination angle of a web with respect to transverse axis (Chapters 8 and 9)
θ_p	Central angle of petal
φ	Bending moment amplification factor
ρ	Actual mass density of plate
σ_0	Material average plastic flow stress
σ_m	Hydrostatic mean stress
σ_y	Material yield stress

σ_{1f}^{0}	Uniaxial stress to fracture
$\bar{\sigma}$	Von Mises equivalent stress
$\sigma_m / \bar{\sigma}$	Stress triaxiality
$\Delta(\sigma_m / \bar{\sigma})$	Relative increase of stress triaxiality over uniaxial tension in the case of round tensile specimen
$(\sigma_m / \bar{\sigma})_{av}$	Average stress triaxiality defined by $\left(\frac{\sigma_m}{\bar{\sigma}}\right)_{av} = \frac{1}{\bar{\varepsilon}_f}\int_0^{\bar{\varepsilon}_f}\frac{\sigma_m}{\bar{\sigma}}d\bar{\varepsilon}$
$(\sigma_m / \bar{\sigma})_{av}^{0}$	Average stress triaxiality in uniaxial tension
τ	Dimensionless time defined by $\tau = ct / R_0$ or ct / A_0
τ_H	Dimensionless time defined by $\tau_H = v_{of} t / H$ (Chapter 8)
$\tau_{\max}$	Maximum shear stress
Ω	Section parameter depending on the types of core structures (Chapters 8 and 9)
ξ	Dimensionless radial (circular) or horizontal (square) coordinates
ξ_0	Dimensionless radius (circular) or half width (square) of centrally loaded area
$\xi_c = l_c / R_0$	Dimensionless crack length in the circular plate under impulsive loading
$\xi_e = r_0 / R_0$	Dimensionless misalignment of punch (eccentricity imperfection, Chapter 6)
$\xi_f = r_f / R_0$	Dimensionless radial coordinate to fracture
$\xi_l = l_x / h_0$	Dimensionless mesh size in the tensile loading direction (tensile test)
ψ_c	Indenter wrapping angle at the outermost contact point (Chapter 6)
$\psi_{c,f}$	Critical wrapping angle to fracture (Chapter 6)
ζ	Dimensionless longitudinal coordinate

Subscripts

1,2,3	Principal directions
d;l;f	Onset of diffuse necking; localized necking; crack formation

Subscripts for α,β, and $\sigma_m / \bar{\sigma}$ in the case of flat tensile specimen (Chapter 3)

A; B; C	Pre-necking; Diffuse necking ~ Localized necking; Localized necking ~ Crack formation

Subscripts for α, β, and $\sigma_m / \bar{\sigma}$ in the case of round tensile specimen (Chapter 3)

A; B Pre-necking; Post-necking

Chapter 1

Introduction

1.1 Motivation

Sheet metal parts are used in many man-made structures, such as ships, planes, cars, and buildings. They form the backbone of most structures and therefore they should be designed for a set of failure modes that govern their structural reliability. Failure of sheet metal parts under accidental loadings can lead to the catastrophic collapse of individual components or whole structures, resulting in gross losses of life and property (see Figs. 1.1 and 1.2). A common characteristic of those failure mechanisms in sheet metal structures with increasing plastic deformation is necking followed by ductile fracture. Strain localization phenomena in the form of necking is thus an important mechanism that precedes fracture. Under increasing loading, materials reach a high strain at which fracture occurs in a rather sudden manner. The ductile fracture is predominantly tensile in nature and is operated by the physical mechanisms of nucleation, growth, and coalescence of microscopic voids. Since the ground-breaking work of McClintock (1968) who performed the first theoretical analysis of hole growth, various types of engineering fracture criteria to predict fracture in uncracked bodies have been developed. However, despite some initial progress with these fracture models in the 1970s and 1980s, rapid progress in industrial applications was impaired by a number of factors. These included the high complexity of the process of failure, the absence of elaborate computational methodologies capable of modeling crack formation and

propagation with reasonable computational times and high accuracy, and the lack of a well established calibration procedure. The term "calibration" means the determination of the critical parameters associated with the postulated fracture criterion. In the last few years several exciting developments have taken place and have opened up the possibilities of realistic prediction of fracture in a broad class of materials, structures, and loading conditions. In particular, based on extensive numerical and experimental frameworks with well defined calibration procedures, Bao and Wierzbicki (2004a/b) (hereafter, referred to as BW) developed an empirical fracture locus where the accumulated equivalent plastic strain to fracture with the average stress triaxiality during the test as a weighting function is formulated. As compared to similar fracture criteria proposed by many authors in the past, one of the new aspects of the BW criterion is that the fracture locus is not be described by one smooth monotonic function but rather consists of three distinct branches for low, intermediate and high stress triaxialities (up to 0.67 for plane stress). Still, several issues of the proposed BW and other fracture models, such as the simplification of the calibration procedure, the unique identification of critical damage parameters, verification and validation through analytical, numerical, and experimental investigations of real practical problems, and key benchmarks for comparison with other common fracture criteria, need to be addressed. These topics are extensively discussed in the present thesis.

Sheet metal parts are produced in large quantities using rolling, stamping, and other high volume production techniques. In the sheet metal forming industry, failure is generally considered as the onset of tensile flow localization, or necking, which limits the amount of deformation a part can sustain. The art of sheet metal forming is to devise processes in which the required shapes can be achieved without fracture. The behavior of sheet metals in press forming has long been investigated from various points of view and the topic has already well been established over the past several decades (see for example Marciniak and Duncan, 1993). However, most of the important contributions made earlier by many others cannot be directly applied to predict the formation of cracks in metal working processes since they were primarily focused on necking only, which sets up a limit for formability. Depending on the materials, the magnitude of necking and fracture strains could be far apart and corresponding loci in the principal membrane strain space are in fact represented by different functions. Besides, several aspects of fracture in the metal forming process remain to be solved. Furthermore, an in-depth understanding of the underlying mechanics of sheet metal failure under high intensity and short duration loads is lacking.

Due to military, civilian, and environmental concerns, there are ever increasing needs and legislative requirements to raise the safety envelope of existing protective structures against localized extreme loading. Such applications include armor penetration, aircraft hardening, advanced ship hulls, nuclear pressure vessels, containment cracks for radioactive materials, and others. In particular, a ship hull made of sheet metal is an essential component for the survivability of the ship as was recently experienced with the USS *Cole*, where the 12.2m by 12.2m hole was driven in the portside of the ship as a result of an explosion (Fig. 1.2). This example emphasizes the importance of a rigorous design of hull panel that should withstand various weapon treats. Although the characteristics of traditional hull structures have been studied extensively, no simple and reliable methods exist in the open literature to predict and assess the fracture damage of a hull panel under localized blast loading. Moreover, developing a new concept of structure is imperative to improve the fracture resistance of existing hulls and other protective structures subjected to explosive loading.

(a) Aircraft explosion, UK
(http://www.aviationpics.de)

(b) Train collision, UK, 2001
(http://www.lubbockonline.com/gallery)

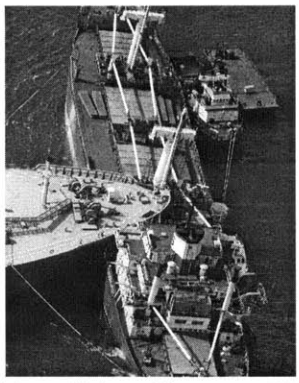

(c) Ship collision, Singapore, 2003
(http://www.cargolaw.com)

(d) Anti-tank mine blast, Bosnia, 1997

(e) Automotive collision
(http://www.nhtsa.dot.gov)

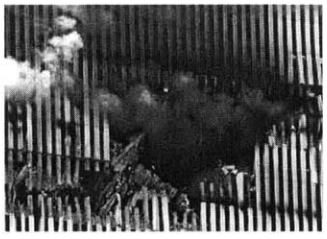

(f) World trade center, USA, 2001
(http://www.airdisaster.com)

Fig. 1.1 Real world examples of fracture in various structural applications of sheet metals

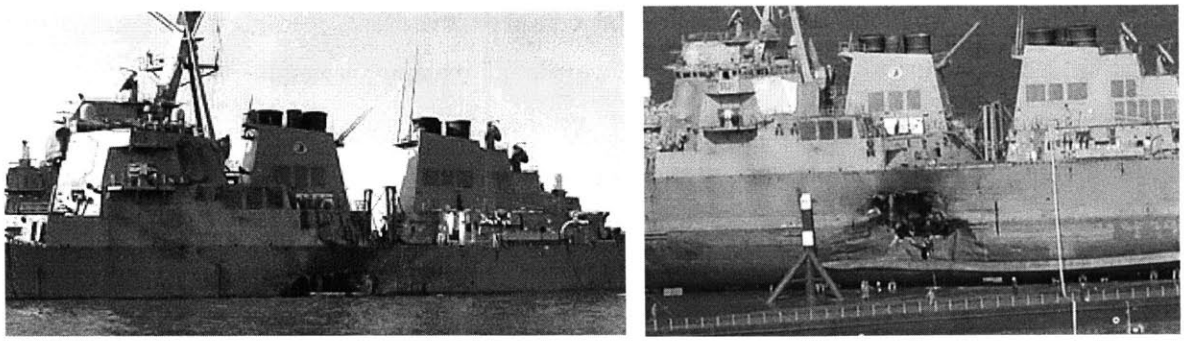

(a) above waterline damage (b) port side damage

Fig. 1.2 USS *Cole* (DDG 67) after an explosion on October 12, 2000, which left a 12.2m by 12.2m hole in the port side of the Norfolk, Virginia-based destroyer (U.S. Navy photos; *http://www.chinfo.navy.mil/navpalib/news/news_stories/cole-shippix.html*)

1.2 Research objective

The ultimate goal of the present research is to predict sheet metal fracture under localized extreme loading (see Fig. 1.3), and then to develop the adaptive sandwich structural system most resistant to fracture and overall damage (see Fig. 1.4).

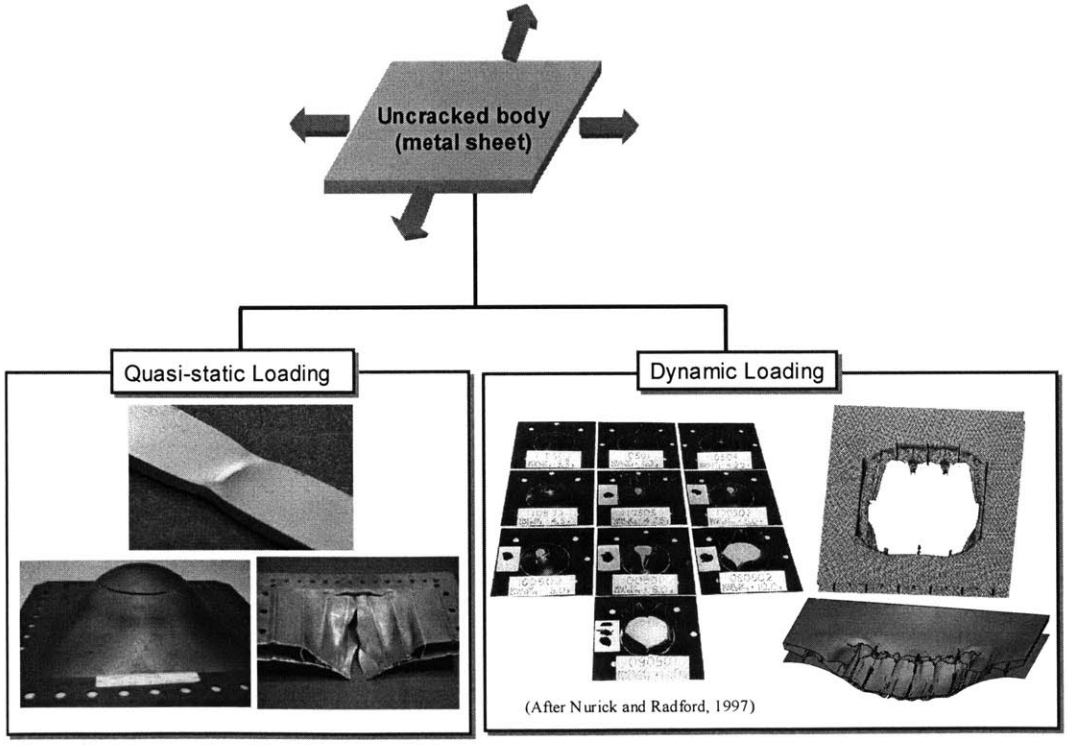

Fig. 1.3 Prediction on various features of sheet metal fracture under localized extreme loading

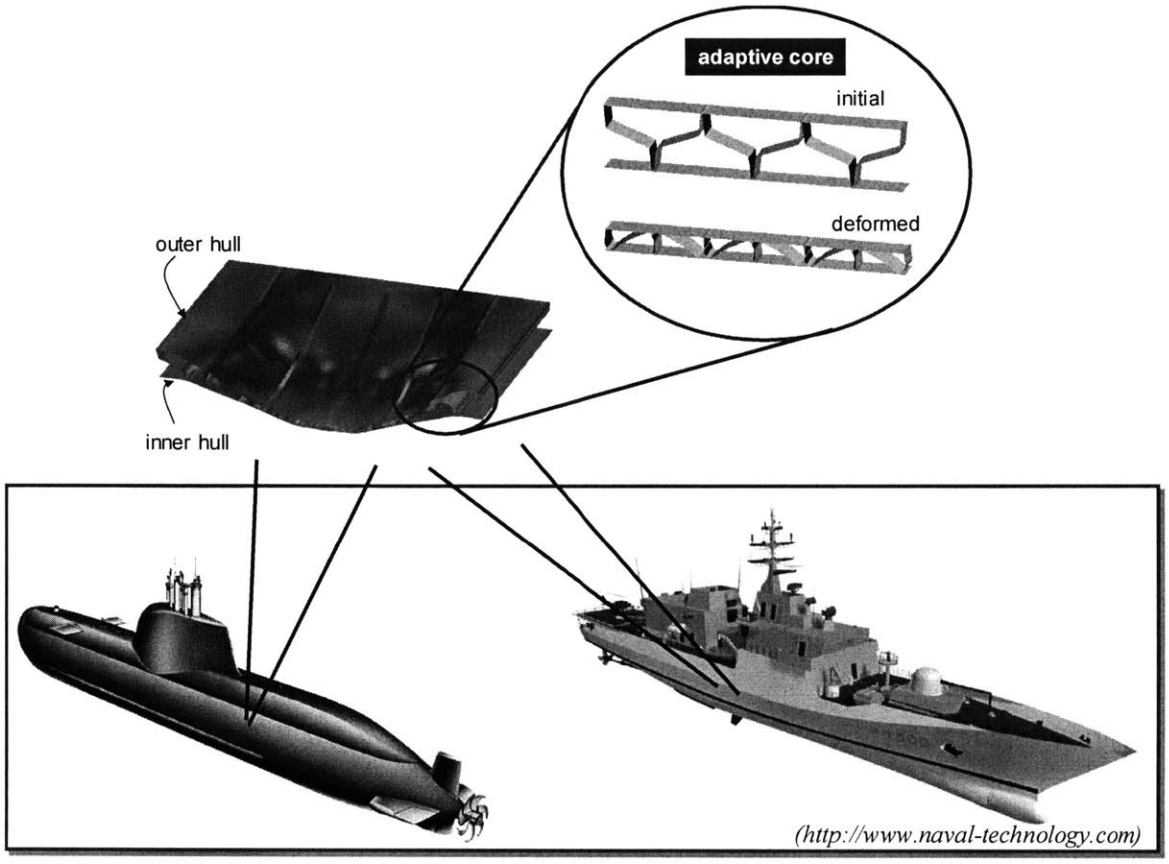

Fig. 1.4 Hierarchical concept of the proposed Blast Resistant Adaptive Sandwich (BRAS) structure. Note that the submarine and battleship pictures were taken from the website (*http:// www.naval-technology.com*).

A number of new contributions are made in this study:

- Based on a plane stress assumption, a stain-to-stress space mapping procedure, which enables the fracture criteria formulated in the strain space to be transformed into the stress space and vice versa, is proposed. Employing the mapping procedure, an extensive comparative study of the most common fracture criteria is carried out. The applicability and expected errors of those fracture criteria are investigated.
- Analytical approximations are developed to predict fracture of flat and round tensile specimens. Most importantly, a new "quick calibration" method is developed to simplify the existing calibration procedure and facilitate fracture prediction in many industrial processes.
- The current status in computational fracture methods are described

- A computational study involving the effect of mesh size on the formation and propagation of cracks in flat tensile specimen is carried out. Two approaches are developed to remove the mesh sensitivity in the computational framework.
- An analytical model of deformation and fracture in a single plate under static punch indentation is developed. Analytical approximations are validated by numerical simulations and physical testing. The computational method of constructing a Fracture Forming Limit Diagram (FFLD) is proposed.
- A connection between crack formation and propagation is thoroughly investigated by three case studies at the specimen and component levels.
- An analytical and numerical investigation is conducted to study the deformation and fracture of thin single plates subjected to localized impulsive loading. The effect of various spatial and temporal distributions of applied dynamic loading are quantitatively assessed based on the results of numerical and analytical solutions.
- An extensive parametric study on the transient responses and fracture of sandwich structures with various core arrangements is carried out. Finally, the new concept of a "Blast Resistant Adaptive Sandwich" structure is developed to minimize the fracture damage of double hulls under impulsive loading.

1.3 Overview of the thesis

The present thesis consists of ten clearly defined and interrelated chapters, as schematically illustrated in Fig. 1.5. Parallel analytical and numerical solutions are obtained and a thorough comparison with experimental results on several typical structures and loading conditions is conducted. Furthermore, an in-depth understanding of deformation and fracture behavior in metal sheets under localized loading is achieved. Based on this knowledge, a new structural configuration is developed to increase the safety envelope of existing protective structures against fracture. The work within each of the chapters is briefly described in the following.

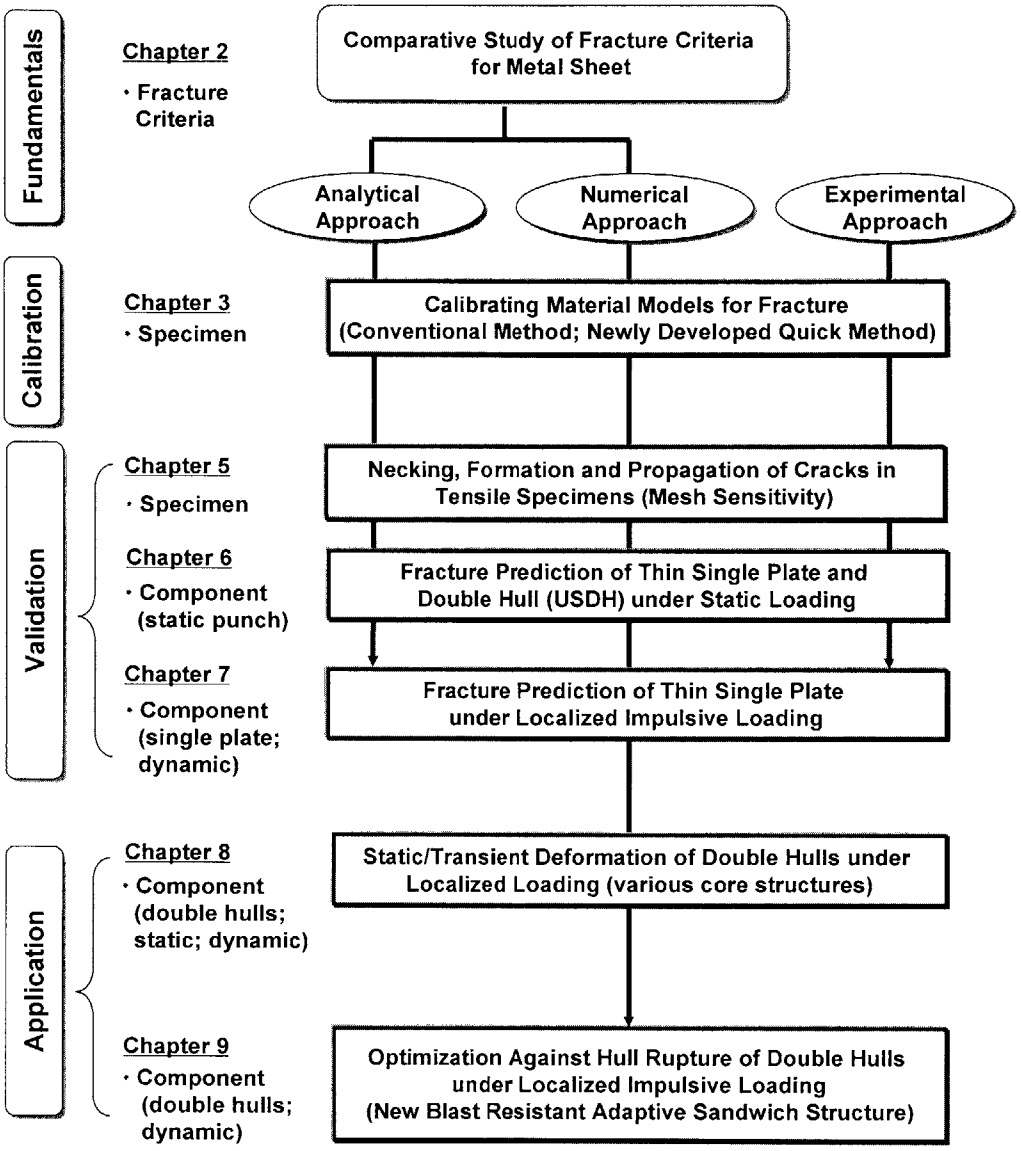

Fig. 1.5 Schematic diagram showing the systematic approach covering the broad ranges of sheet metal failure

The first introductory chapter gives motivation, defines objective, and presents an overview of the thesis. In Chapter 2, the most widely used fracture criteria in engineering applications are reviewed. Under the condition of static loading, all those criteria formulated in the general 3-D case are specified for the plane stress condition utilizing the strain-to-stress mapping procedure proposed in this thesis. Special attention is paid to demonstrate the applicability of the BW fracture locus,

constructed in terms of invariant of the stress and strain tensors, to other types of material. An extensive comparative study of seven fracture criteria is then carried out. All these criteria are constructed and compared in the space of principal strains, principal stresses, and in the mixed space of equivalent strain and stress triaxiality.

Chapter 3 presents two calibration methods of the BW fracture criterion. One of the most important and most often misunderstood procedures in industrial applications of fracture criteria is the calibration of material and fracture models. In the first part of Chapter 3, a conventional calibration method for the BW criterion, where the critical parameters are obtained by the fitting procedure that requires the combined testing and numerical simulation, is reviewed and its deficiencies are pointed out. Then, in the second part of Chapter 3, a much simpler calibration method that bypasses a need for numerical simulation and extensive testing is proposed and its accuracy is validated.

Chapter 4 provides a concise review on the current status of computational methodologies in the simulation of fracture process. Recent advances in computational mechanics to ensure that the physical mechanisms of fracture are incorporated into the numerical codes have allowed for the investigation of a wider spectrum of fracture behavior than was previously possible. These include element removal, node release, adaptive mesh refinement, moving mesh, and enrichment techniques. The applicability and deficiencies of the above methods are discussed. A possibility for the improvement of these methods is also presented. Finally, an overview of the computational approach to fracture used in this thesis is introduced.

Chapter 5 presents comprehensive numerical and experimental analyses of necking, crack formation, and subsequent crack propagation in a uniaxial tensile test of a flat specimen. Furthermore, Chapter 5 primarily deals with one of the most important issues encountered in current computational methods, that is, the mesh size dependence. The effect of mesh size on tensile behaviors involving necking and fracture of specimens is thoroughly investigated by numerical simulations and rigorous parallel comparisons with experimental results. Then, two promising approaches are proposed to remove the possible mesh dependence and to obtain reliable results.

One of the main objectives of Chapter 6 is to validate the BW fracture criterion at the component level. Two component studies are carried out: a clamped thin single plate and clamped stiffened sandwich plates subjected to static punch indentation. In the first component study of Chapter 6, the response of the thin single plate is investigated experimentally, numerically, and analytically to determine the crack formation. Based on the calibration of the material model, and

calculated distributions and histories of stress and strain, the various responses including the global punch force-penetration, the deflection profiles, the critical locations and penetration to fracture are predicted analytically and numerically within 5-10% accuracy for three different punch radii. Analytical approximations are derived by taking into account a variable stress ratio and varying stress triaxiality. Moreover, by changing the friction coefficient between punch and plate, the locus of the principal strain to fracture (i.e. FFLD) is constructed numerically, which can replace the time-consuming conventional experimental technique. In the second component study of Chapter 6, experimental and numerical analyses of the formation and subsequent propagation of circumferential and radial cracks are presented with particular focus on the local stress and strain states ahead of the crack tip.

In Chapter 7, a comprehensive analysis of deformation and fracture of thin single plates subjected to localized impulsive loading is presented. Chapter 7 gives a detailed description of the three stages of dynamic response - i.e. dishing (bulging of plate without fracture), discing (onset of circumferential crack) and petalling (propagation of radial crack with rotation of plate). In the first part of Chapter 7 (dishing), the transient response of the plates is investigated analytically and numerically. Two existing analytical solutions of the problem are reviewed and the accuracy of those solutions are discussed based on the comparison with numerical and experimental results. Several new aspects of the transient response of plates, not previously reported are identified and discussed. In particular, a parametric study on the dynamically loaded plates with various spatial and temporal distributions of dynamic pressure is conducted. Furthermore, a comparison between the responses of circular and square plates is also presented.

In the second part of Chapter 7, the onset of circumferential cracks (discing) and the subsequent propagation of radial cracks (petalling) of thin circular plates under central impulsive loading are predicted analytically and numerically for a range of intensity of applied impulse and various radii of loaded area. A thorough numerical investigation of the strain, stress, and resulting cumulated damage at the critical locations of fracture is conducted. The previous analytical solution of the petalling problem is compared with the present numerical results.

Chapter 8 presents the numerical investigation of the static and transient responses of sandwich panels with various core arrangements. A new concept of an adaptive and reconfigurable structural component, here called a Blast Resistant Adaptive Sandwich (BRAS) structure, is introduced to achieve a substantial improvement of resistance to explosive loading. The relation between static crush resistance and energy absorption characteristics of the BRAS is discussed. The effect of

various core configurations on the crush resistance is then quantified. Comparative and parametric studies on the transient responses including energy absorption capability with particular focus on the partition of energy between face cover plates and core, deflection, and response time of various types of sandwich structures under localized impulsive loading are carried out.

In Chapter 9, an extensive parametric study is presented to determine an optimal configuration of sandwich structure to explosive loading. The optimization formulation is constructed for the minimum fractured area of inner hull (bottom face plate) with the constraints of component weight. Normalized geometrical variables are introduced in the formulation. Based on the extensive parametric study, optimal configurations that have a consistent deformation and fracture modes for a wide range of intensity of impulsive loading and a specified weight are proposed in the cases of the conventional and BRAS structures. It is shown that the optimized BRAS is superior to other conventional types of core structures. In particular, the resistance to the localized impulsive loading in terms of an increased threshold impulse to initial fracture as well as a substantial reduction of the cracked area is much higher for BRAS than for other core structures.

Finally, a summary of the main results is presented in Chapter 10. Recommendations for future research are also provided.

Chapter 2

Fracture Criteria for Metal Sheet

2.1 Introduction

Various approaches to model ductile crack formation in structural metals have been proposed in the past. Most of the promising approaches belong to the class of the so-called local fracture models, which are based on early analyses of the growth of a single void in an infinite elastic-plastic solid by McClintock (1968) and Rice and Tracey (1969). Over the last two decades, these local fracture models have enjoyed increasing interest and importance for industrial applications. As compared to the classical fracture mechanics, the advantage of the models is that the determination of the critical damage/fracture function is only material and not geometry dependent. These local fracture models can be further classified into two groups: coupled and uncoupled models. The first group includes the porous plasticity model in which an interaction between internal damage and flow behavior of the material is taken into account by a porous sensitivity yield function. The model was first proposed by Gurson (1977) and extended by Tvergaard and Needleman (1984). Other similar models were also proposed by Rousselier (1987) based on thermodynamic considerations. In the second group of fracture models, the damage does not change the constitutive equation. These models are formulated in terms of accumulated plastic strain with various stress triaxiality weighting functions, McClintock (1968), Rice and Tracey (1969), Hancock and Mackenzie (1976), Norris et al. (1978), and Oyane et al. (1980). Recently, Bao and Wierzbicki (2004a/b) determined the weighting

function in a wide range of stress triaxiality from eleven different types of tests on Al 2024-T351 specimens.

In this thesis, the condition for fracture is assumed to be identical to the newly developed and constructed empirical Bao-Wierzbicki (hereafter, referred to as BW; Wierzbicki et al., 2002; Bao and Wierzbicki, 2004a/b) fracture criterion. In Section 2.2, the BW fracture criterion originally formulated in terms of the accumulated equivalent plastic strain with the stress triaxiality as a weighting function is presented. Using equations of plane stress von-Mises plasticity, the above fracture criterion is transformed to the space of the principal strains to fracture and compared with experimental results for various materials. In Section 2.3, a thorough comparison of the BW criterion with other widely used fracture models is presented.

2.2 Presentation of Bao-Wierzbicki (BW) fracture criterion

2.2.1 Representation in the space of the average stress triaxiality and the equivalent plastic strain to fracture $((\sigma_m/\bar{\sigma})_{av},\ \bar{\varepsilon}_f)$

In the BW fracture criterion, it is assumed that fracture initiates at the critical point of structure when the accumulated equivalent plastic strain $\bar{\varepsilon}$ with a suitable weighting function reaches a critical value according to

$$D=\int_{\bar{\varepsilon}_1}^{\bar{\varepsilon}_2} f\left(\frac{\sigma_m}{\bar{\sigma}},\dot{\bar{\varepsilon}},T\right)d\bar{\varepsilon} \tag{2.1}$$

where D is the so-called "damage indicator"; $\bar{\varepsilon}_1$ is the magnitude of equivalent strain when the damage starts to accumulate and $\bar{\varepsilon}_2$ is the current intensity of strain; f is a weighting function depending on the stress triaxiality defined as the ratio of the hydrostatic mean stress σ_m to the von Mises equivalent stress $\bar{\sigma}$, the strain rate, and temperature. When the upper limit of the integral attains the critical fracture strain of the material, $\bar{\varepsilon}_2=\bar{\varepsilon}_f$, the damage indicator reaches a critical value $D=D_c$. In the class of problems considered in this thesis, the loading path is confined only to a relatively narrow range of the stress triaxiality where a monotonic increase of the stress triaxiality as a function of the equivalent strain is observed. Under this condition, it is assumed that the damage

is accumulated right from the beginning of loading, $\bar{\varepsilon}_1 = 0$. Under more complex loading history, it is necessary to consider a variable lower limit of the integral. This problem is discussed by Wierzbicki and Bao (2004). In the case of quasi-static test at room temperature, Eq. (2.1) can be further reduces to

$$D_c = \int_0^{\bar{\varepsilon}_f} g\left(\frac{\sigma_m}{\bar{\sigma}}\right) d\bar{\varepsilon} \tag{2.2}$$

The shape of fracture envelope for 2024-T351 aluminum alloy, controlled by Eq. (2.2), is shown in Fig. 2.1(a) with the equivalent strain as the vertical axis and the average stress triaxiality as horizontal axis. In general, $\sigma_m / \bar{\sigma}$ varies during the deformation process. Therefore, a concept of average stress triaxiality is introduced, defined by

$$\left(\frac{\sigma_m}{\bar{\sigma}}\right)_{av} = \frac{1}{\bar{\varepsilon}_f} \int_0^{\bar{\varepsilon}_f} \frac{\sigma_m}{\bar{\sigma}} d\bar{\varepsilon} \tag{2.3}$$

Note that the locus shown in Fig. 2.1(a) is based on quasi-static tests and parallel numerical simulations on eleven different types of Al 2024-T351 specimens shown in Fig. 2.1(b), Bao and Wierzbicki (2004a). They determined the weighting function in the wide range of stress triaxiality ($-1/3 \le \sigma_m / \bar{\sigma} \le 1.0$) from three groups of tests on specimens with various shapes. Interesting aspect of the fracture envelope shown in Fig. 2.1(a) is that it is composed of three distinct branches. The branch for stress triaxialities larger than 1/3 corresponds to fracture controlled by the mechanism of void nucleation, growth, and coalescence (branch I). Tensile tests on smooth and notched specimens (see specimens No. 9 ~ 11 in Fig. 2.1(b)) were used in this branch. The second branch obtained from compression tests on short cylinders (see specimens No. 1 ~ 5 in Fig. 2.1(b)) describes the so-called shear decohesion fracture under negative stress triaxiality (branch III). Finally, there is a third regime (branch II) in which fracture is a combination of the two simple modes describes above. Pure shearing and combined loading tests were used to determine fracture locus in branch II (see specimens No. 6 ~ 8 in Fig. 2.1(b)).

In the range of stress triaxiality (branch I, $\sigma_m / \bar{\sigma} \ge 1/3$) the weight function can be assumed as a linear function of its argument (Bao and Wierzbicki, 2004a). Therefore, Eq. (2.2) may be reduced to

$$D_c = \int_0^{\bar{\varepsilon}_f} \frac{\sigma_m}{\bar{\sigma}} d\bar{\varepsilon} \tag{2.4}$$

By introducing the average stress triaxiality defined by Eq. (2.3), the fracture criterion in the branch I (i.e. Eq. (2.4)) can be rewritten as

$$\left(\frac{\sigma_m}{\bar{\sigma}}\right)_{av} \bar{\varepsilon}_f = D_c \tag{2.5}$$

The three branches shown in Fig. 2.1(a) can be further approximated by the following analytical functions for a wide range of materials, Bao et al. (2004c)

$$\bar{\varepsilon}_f = \begin{cases} \infty, & (\sigma_m/\bar{\sigma})_{av} \le -\dfrac{1}{3} \\ \dfrac{\mathbf{a}}{1+3(\sigma_m/\bar{\sigma})_{av}}, & -\dfrac{1}{3} < (\sigma_m/\bar{\sigma})_{av} \le 0 \\ \dfrac{\mathbf{b}-\mathbf{a}}{\left[(\sigma_m/\bar{\sigma})^0_{av}\right]^2}\left[(\sigma_m/\bar{\sigma})_{av}\right]^2 + \mathbf{a}, & 0 \le (\sigma_m/\bar{\sigma})_{av} \le (\sigma_m/\bar{\sigma})^0_{av} \\ \dfrac{\mathbf{b}(\sigma_m/\bar{\sigma})^0_{av}}{(\sigma_m/\bar{\sigma})_{av}}, & (\sigma_m/\bar{\sigma})^0_{av} \le (\sigma_m/\bar{\sigma})_{av} \end{cases} \tag{2.6}$$

The coordinate of the intersection point of the branches II and III is $(0, \mathbf{a})$, where $\mathbf{a}$ is critical fracture strain in pure shear, $(\sigma_m/\bar{\sigma})_{av} = 0.0$. The intersection point of the branches I and II is $((\sigma_m/\bar{\sigma})^0_{av}, \mathbf{b})$, where $(\sigma_m/\bar{\sigma})^0_{av}$ and $\mathbf{b}$ are average stress triaxiality and critical fracture strain in uniaxial tension, respectively. Then, two parameters $(\mathbf{a}, \mathbf{b})$ define fully the fracture envelope in the present formulation.

2.2.2 Theoretical determination of BW fracture locus for plane stress

2.2.2.1 Relations between stress and strain in general 3-D plasticity

It is assumed that the material, experiencing general plastic flow $(\sigma_{ij}, \varepsilon_{ij})$, follows the Mises yield criterion and associated flow rule:

$$\bar{\sigma} = \frac{1}{\sqrt{2}}\left[(\sigma_1-\sigma_2)^2 + (\sigma_2-\sigma_3)^2 + (\sigma_3-\sigma_1)^2\right]^{\frac{1}{2}} \tag{2.7}$$

$$d\varepsilon_{ij} = d\lambda \frac{\partial \bar{\sigma}}{\partial \sigma_{ij}} \tag{2.8}$$

where σ_1, σ_2 and σ_3 are the principal stresses; $d\varepsilon_{ij}$ the plastic strain increment; $d\lambda$ the constant whose magnitude depends on the amount of deformation. It is further assumed that the material strain hardens isotropically according to the power law

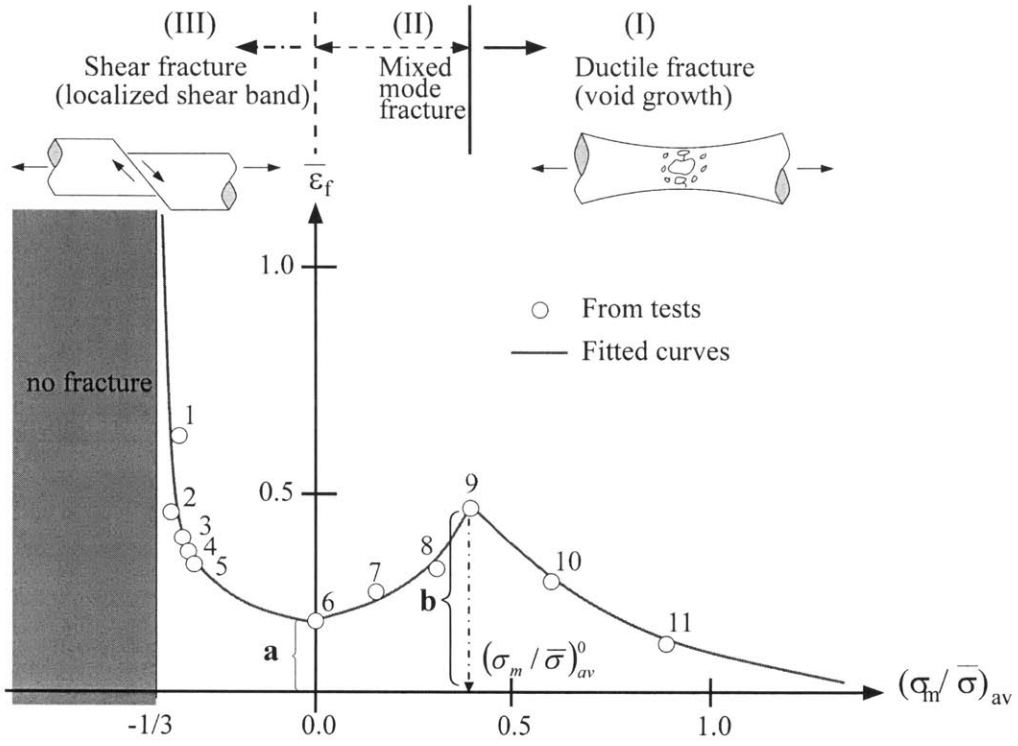

(a)

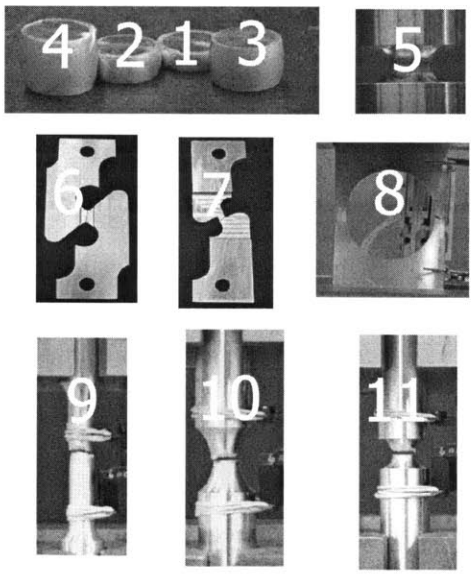

(b)

Fig. 2.1 (a) Bao-Wierzbicki (BW) fracture envelope for Al 2024-T351 constructed in the plane of equivalent plastic strain to fracture $\bar{\varepsilon}_f$ and average stress triaxiality $(\sigma_m/\bar{\sigma})_{av}$; (b) Eleven different types of specimens for the determination of the fracture envelope of Al 2024-T351 (after Bao and Wierzbicki (2004a), with permission)

$$\bar{\sigma} = K\bar{\varepsilon}^{n} \tag{2.9}$$

where K and n are the strength coefficient and the hardening exponent of the material, respectively. The increment of equivalent plastic strain is defined in terms of principal strain components:

$$d\bar{\varepsilon} = \sqrt{\frac{2}{3}}\left(d\varepsilon_1^2 + d\varepsilon_2^2 + d\varepsilon_3^2\right)^{\frac{1}{2}} \tag{2.10}$$

For an incompressible solid, the principal components of an increment of strain can be written as

$$d\varepsilon_1 : d\varepsilon_2 : d\varepsilon_3 = 1 : \alpha : -(1+\alpha) \tag{2.11}$$

where α is the principal strain rate ratio $\alpha \equiv \dot{\varepsilon}_2 / \dot{\varepsilon}_1 = d\varepsilon_2 / d\varepsilon_1$.

The following ratios of principal stresses are defined:

$$\beta \equiv \frac{\sigma_2}{\sigma_1}, \quad \gamma \equiv \frac{\sigma_3}{\sigma_1} \tag{2.12}$$

For instance, under the assumption of the Mises flow rule, the strain ratio α is linked to the above stress ratios by

$$\alpha = \frac{2\beta - \gamma - 1}{2 - \beta - \gamma} \tag{2.13}$$

Applying Eqns. (2.11) and (2.13) to (2.10) leads to another expression for the increment of equivalent plastic strain:

$$d\bar{\varepsilon} = \frac{2}{\sqrt{3}}\left(1 + \alpha + \alpha^2\right)^{\frac{1}{2}} d\varepsilon_1 = \frac{2\sqrt{1+\beta^2+\gamma^2-\beta-\gamma-\beta\gamma}}{2-\beta-\gamma} d\varepsilon_1 \tag{2.14}$$

Using Eqns. (2.7) and (2.12), the hydrostatic mean stress σ_m and effective stress $\bar{\sigma}$ can be expressed in terms of β, γ, and the principal stress σ_1 :

$$\sigma_m = \frac{\sigma_1 + \sigma_2 + \sigma_3}{3} = \frac{\sigma_1}{3}(1 + \beta + \gamma) \tag{2.15}$$

$$\bar{\sigma} = \frac{\sigma_1}{\sqrt{2}}\sqrt{(1-\beta)^2 + (\beta-\gamma)^2 + (\gamma-1)^2} \tag{2.16}$$

Thus, the stress triaxiality expressed in terms of the stress ratios is

$$\frac{\sigma_m}{\bar{\sigma}} = \frac{1}{3}\frac{1+\beta+\gamma}{\sqrt{1+\beta^2+\gamma^2-\beta-\gamma-\beta\gamma}} \tag{2.17}$$

2.2.2.2 Transformation of plasticity equation for plane stress

Plane stress implies that the sheet is deformed by the membrane stresses, transmitted through the sheet with the through-thickness stress being negligible (i.e. $\sigma_3 = 0, \gamma = 0$). The advantage of working with plane stress is that there is one-to-one mapping from the stress to the strain space. Therefore, the fracture criteria formulated in the stress space can be compared with those expressed in the strain space and vice versa. All components of the strain and stress tensors as well as the equivalent strain, equivalent stress and the hydrostatic stress can be determined from the known form of the power hardening law (i.e. $\bar{\sigma} = K\bar{\varepsilon}^n$) and the principal strain rate ratio α or stress ratio β.

In particular, the normalized principal stresses and the hydrostatic stress are expressed in terms of α by

$$\sigma_1 = \frac{2}{\sqrt{3}}\bar{\sigma}\frac{1+\frac{\alpha}{2}}{\sqrt{1+\alpha+\alpha^2}} \tag{2.18}$$

$$\sigma_2 = \frac{2}{\sqrt{3}}\bar{\sigma}\frac{\alpha+\frac{1}{2}}{\sqrt{1+\alpha+\alpha^2}} \tag{2.19}$$

$$\frac{\sigma_m}{\bar{\sigma}} = \frac{1}{\sqrt{3}}\frac{\alpha+1}{\sqrt{1+\alpha+\alpha^2}} \tag{2.20}$$

where α is equal to $(2\beta-1)/(2-\beta)$ by substituting $\gamma = 0$ into Eq. (2.13).

Assuming proportional loading and using Eq. (2.14), the above system could be easily inverted so that components of the principal strains could be found according to.

$$\varepsilon_1 = \frac{\bar{\varepsilon}}{\frac{2}{\sqrt{3}}\sqrt{1+\alpha+\alpha^2}} \tag{2.21}$$

$$\varepsilon_2 = \alpha\varepsilon_1 \tag{2.22}$$

where $\bar{\varepsilon}$ can be related to $\bar{\sigma}$ through the hardening power law. The above procedure of transformation is schematically illustrated in Fig. 2.2.

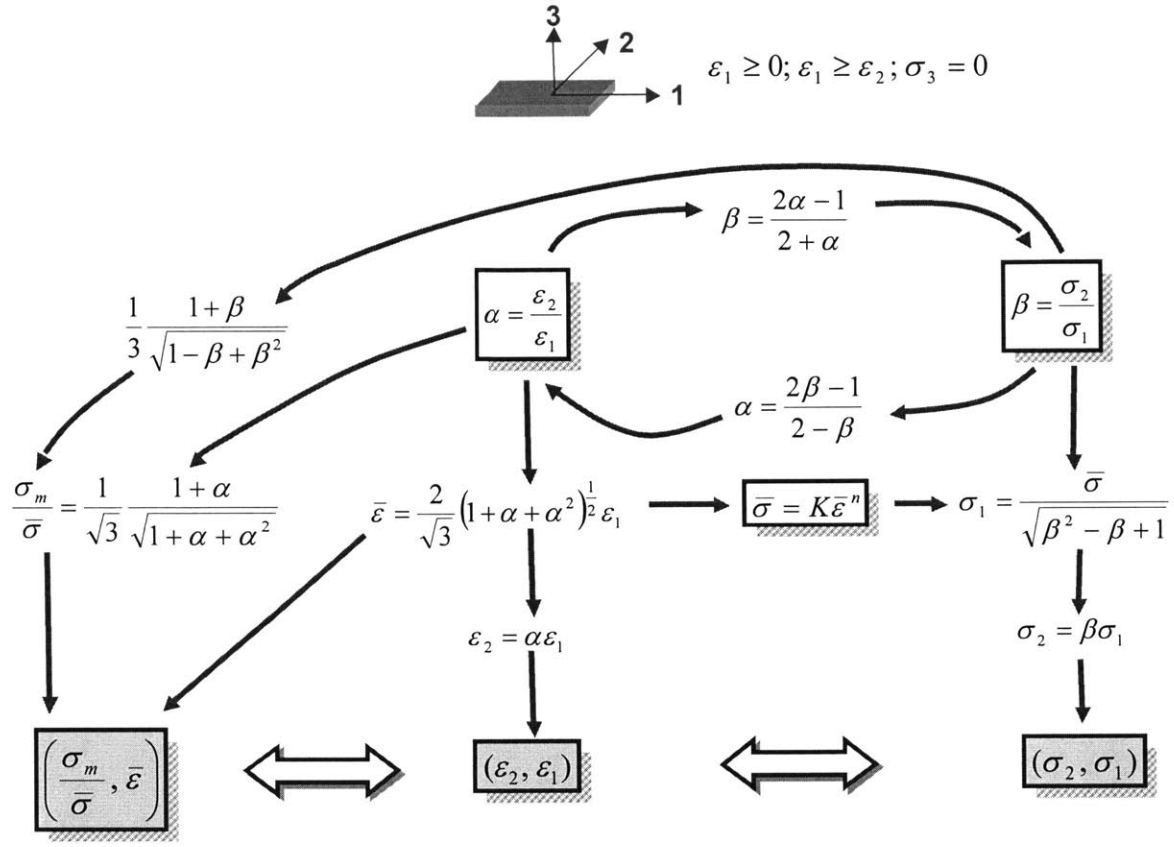

Fig. 2.2 Schematic diagram showing transformation between three different spaces: mixed space of equivalent strain and stress triaxilaity; principal strains; principal stress

2.2.2.3 Representation in the space of the principal strains to fracture $(\varepsilon_{1f},\ \varepsilon_{2f})$

Using the assumption of plane stress plasticity and the mapping scheme presented in previous Section 2.2.2.2, the BW fracture locus originally represented in the space of equivalent strain to fracture and stress triaxiality is transformed into the space of principal strains to fracture, as schematically shown in Fig. 2.3.

Specification of BW fracture criterion for plane stress (branch I) In the range of stress triaxiality (branch I, $\sigma_m / \bar{\sigma} \geq 1/3$), the postulated ductile fracture criterion is defined by Eq. (2.4).

Expressing $\sigma_m / \bar{\sigma}$ in terms of the strain ratio α (Eq. (2.20)) and $d\bar{\varepsilon}$ in terms of the strain ratio α and $d\varepsilon_1$ (Eq. (2.14)), Eq. (2.4) becomes

$$D_c = \int_0^{\bar{\varepsilon}_f} \frac{\sigma_m}{\bar{\sigma}} d\bar{\varepsilon} = \int_0^{\varepsilon_{1f}} \frac{2}{3}(1+\alpha) d\varepsilon_1 \tag{2.23}$$

It was shown by Atkins (1985) that all criteria of the form $\int(\mathbf{A} + \mathbf{B}\alpha)d\varepsilon_1$, where **A** and **B** are constant, are path independent (see Chapter 5 of Atkins (1985) for a discussion and worked examples). Integrating Eq. (2.23) with the assumption of proportional loading path, i.e. $\alpha = const$, takes the form

$$D_c = \frac{2}{3}(1+\alpha)\varepsilon_{1f} \tag{2.24}$$

By replacing α by $\varepsilon_{2f} / \varepsilon_{1f}$, the fracture locus in the space of principal strains to fracture is given by

$$\varepsilon_{1f} + \varepsilon_{2f} = -\varepsilon_{3f} = \frac{3}{2} D_c \tag{2.25}$$

which is so-called Fracture Forming Limit Diagram (FFLD).

In sheet metal forming industry, failure is often understood as onset of necking. The Forming Limit Diagram (FLD) determines a locus of principal membrane strains in a sheet under which the process of localized neck is initiated. On continuing loading, plastic deformations are localized inside the neck and the associated local strains can often reach high values before fracture occurs. A combination of local strains inside the neck at the point of through thickness fracture is understood as a FFLD. The existence of FFLD, which is different from FLD, was first observed by Embury and LeRoy (1977) and LeRoy et al. (1981). Later on, the FFLD was analytically constructed by Atkins (1985, 1996a), Dyrli HK (1999), and Lee and Wierzbicki (2003). A schematic illustration of the FLD and FFLD is shown in Fig. 2.3. The FLD is shown by thin dotted line, while the FFLD is displayed by thicker full line. It should be mentioned that the FFLD corresponds exactly to one branch of the BW criterion (branch I in Fig. 2.1(a)) in the case of plane stress condition, as schematically illustrated in Fig. 2.4.

According to Eq. (2.25), fracture occurs when the through-thickness strain reaches a critical value $3D_c / 2$. It is convenient to introduce the following dimensionless quantities

$$\tilde{\varepsilon}_{1f}^{I} = \frac{\varepsilon_{1f}}{\varepsilon_{1f}^{p}}, \quad \tilde{\varepsilon}_{2f}^{I} = \frac{\varepsilon_{2f}}{\varepsilon_{1f}^{p}}, \quad \tilde{\varepsilon}_{3f}^{I} = \frac{\varepsilon_{3f}}{\varepsilon_{1f}^{p}} \tag{2.26}$$

where $\varepsilon_{1f}^{p} = 3D_c / 2$ corresponds to the major principal strain to fracture in the case of plane strain tension ($\varepsilon_2 = 0$). In terms of the above quantities, the fracture locus, Eq. (2.25), takes the form

$$\widetilde{\varepsilon}_{1f}^{I} + \widetilde{\varepsilon}_{2f}^{I} = -\widetilde{\varepsilon}_{3f}^{I} = 1 \tag{2.27}$$

The prediction of the fracture locus (Eq. (2.27)) has been verified by classical punch indentation tests into thin single plate and stiffened double plates in Chapter 6. As shown in Fig. 2.5, the analytically predicted fracture locus from Eq. (2.27) is compared with numerically and experimentally obtained loci for eleven different materials. For a comparison purpose, the normalized form of FFLD is presented in Fig. 2.5 so that all curves pass through the same reference point on the $\widetilde{\varepsilon}_1^{I}$ axis. One can see that the fracture locus (Eq. (2.27)), which is a 45^0 line from left to right on equal-scaled axes, is in good agreement with all measured loci for different materials.

Specification of BW fracture criterion for plane stress (branch III) The BW fracture locus in the range between pure shear and uniaxial compression (branch III, $-1/3 \le \sigma_m / \bar{\sigma} \le 0$) can be approximated by a straight line with $\tan^{-1}(-1/2)$ in the space of principal strain to fracture (see solid line with symbol ' | ' in Fig. 2.3) and equal to

$$\varepsilon_{1f} + \frac{1}{2}\varepsilon_{2f} = C \tag{2.28}$$

where C is a constant depending on materials. The above locus given by Eq. (2.28) is of the same form as the empirical locus suggested by Kudo and Aoi (1967) and the well-known Cockroft-Latham criterion (1968) for onset of cracking in bulk forming operations. In the present representation of the BW fracture locus, the constant C is determined from the pure shear deformation ($\alpha = -1$) and given by

$$C = \frac{\sqrt{3}}{4}\mathbf{a} = \frac{1}{2}\varepsilon_{1f}^{s} \tag{2.29}$$

where $\varepsilon_{1f}^{s} = \frac{\sqrt{3}}{2}\mathbf{a}$ is the magnitude of the major principal strain to fracture in the case of pure shear, see Fig. 2.3. By introducing following dimensionless quantities,

$$\widetilde{\varepsilon}_{1f}^{III} = \frac{\varepsilon_{1f}}{\varepsilon_{1f}^{s}}, \quad \widetilde{\varepsilon}_{2f}^{III} = \frac{\varepsilon_{2f}}{\varepsilon_{1f}^{s}} \tag{2.30}$$

the fracture locus given by Eqns. (2.28) and (2.29) can be rewritten as

$$\tilde{\varepsilon}_{1f}^{III} + \frac{1}{2}\tilde{\varepsilon}_{2f}^{III} = \frac{1}{2} \tag{2.31}$$

In Fig. 2.6, the normalized fracture locus (Eq. (2.31)) is compared with experimentally obtained loci for five different materials by different authors. The locus (Eq. (2.31)) is seen to be an accurate representation for a number of different materials in the range between pure shear and compression.

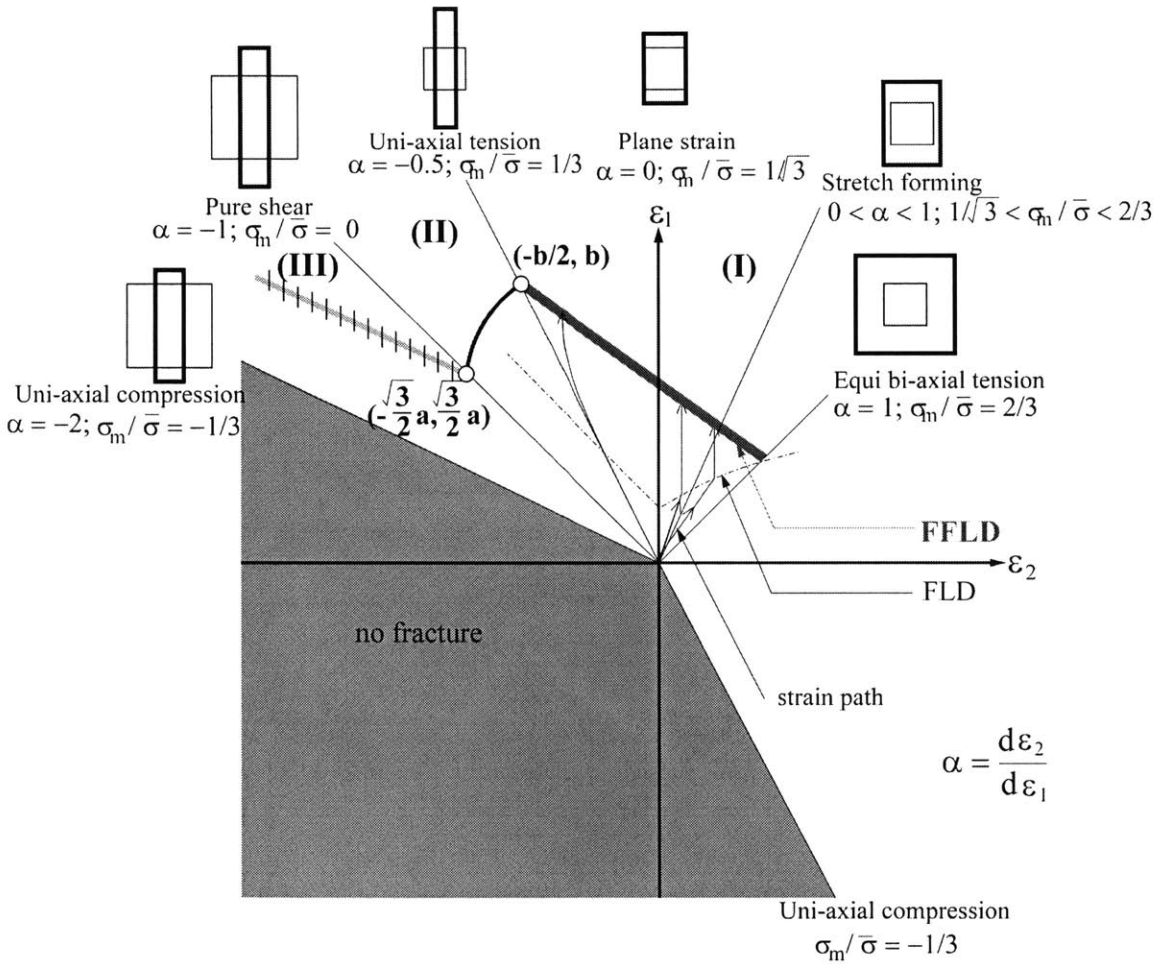

Fig. 2.3 The BW fracture locus shown in Fig. 2.1(a) transformed into the space of the principal strains to fracture. Note that α denotes the in-plane principal strain rate ratio $\alpha \equiv \dot{\varepsilon}_2 / \dot{\varepsilon}_1 = d\varepsilon_2 / d\varepsilon_1$.

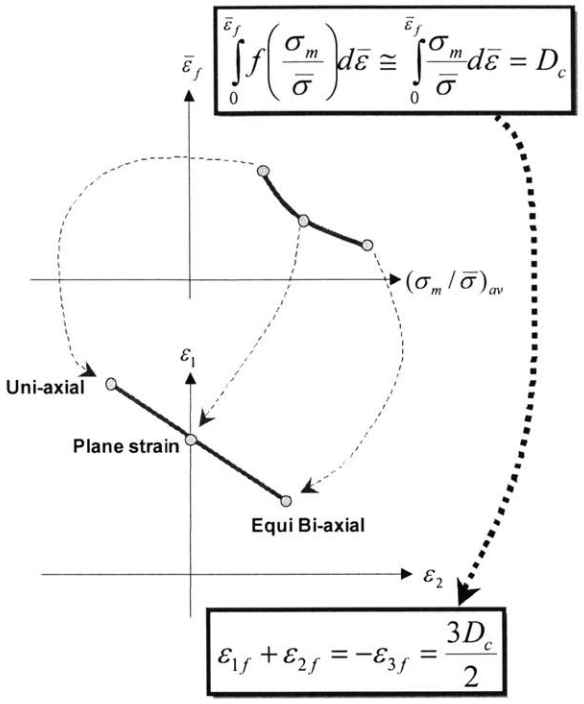

Fig. 2.4 Transformation of the BW fracture locus into the space of principal strains (branch I)

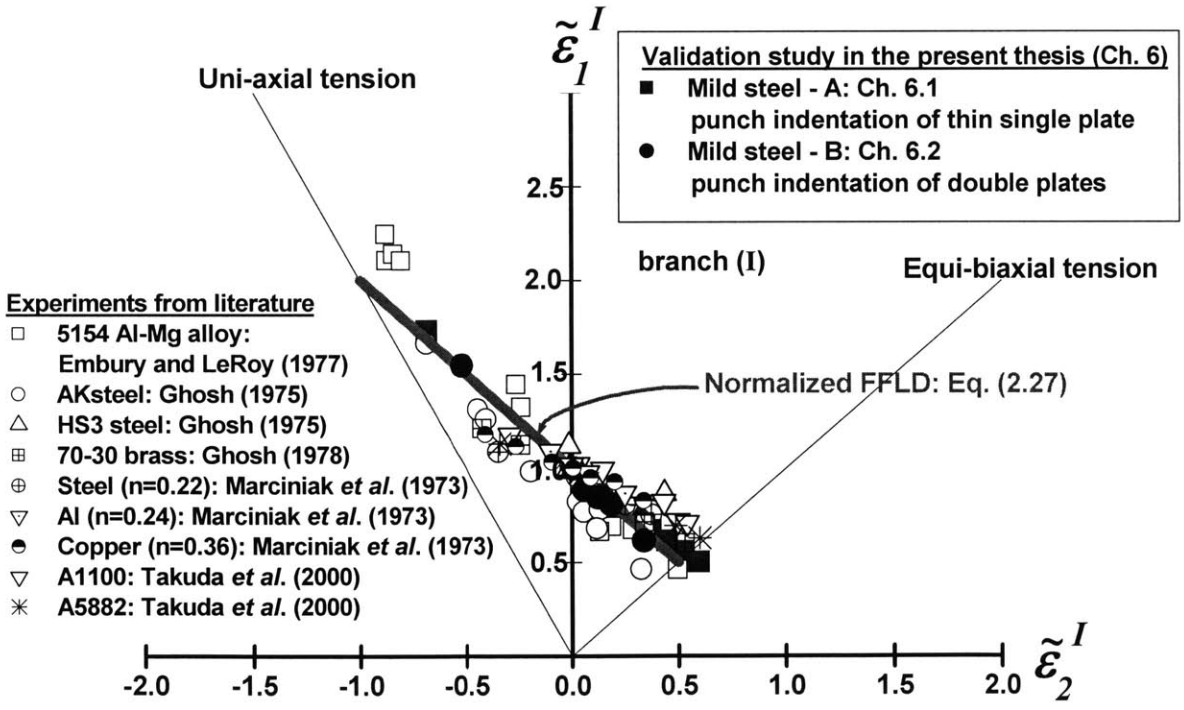

Fig. 2.5 Normalized FFLDs for eleven different materials in classical punch indentation problems. Note that all curves are made to pass through the same point ($\tilde{\varepsilon}_2^I = 0,\ \tilde{\varepsilon}_1^I = 1.0$) on the $\tilde{\varepsilon}_1^I$ axis.

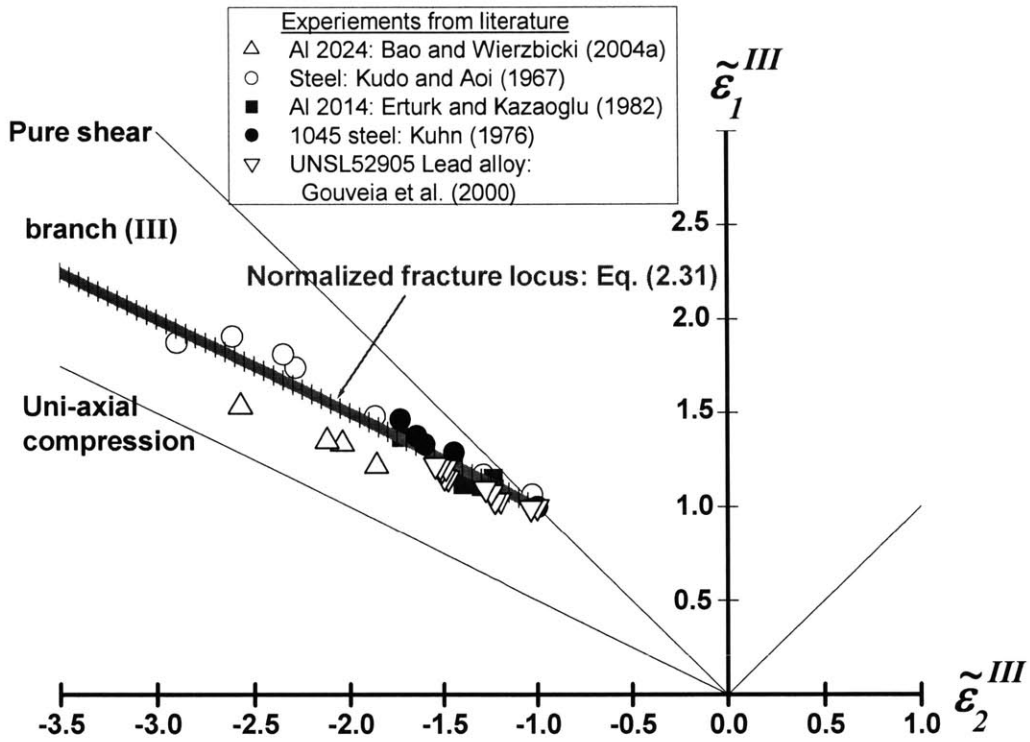

Fig. 2.6 Normalized fracture loci for five different materials in upsetting tests. Note that all curves are made to pass through the same point ($\tilde{\varepsilon}_2^{III} = -1.0$, $\tilde{\varepsilon}_1^{III} = 1.0$) and the data for Al 2014 and 1045 steel are taken from Ref. (Atkins, 1985).

2.3 Comparative study of seven fracture criteria

The objective of this section is to present an assessment of the accuracy of those local fracture criteria (uncoupled models) that are widely used in engineering applications. For a full comparative study of the fracture criteria, the reader is also referred to the work by Bao et al. (2004c). As a reference, taken is the newly constructed empirical Bao-Wierzbicki (BW) fracture criterion. This criterion is compared with the maximum shear stress, the Cockcroft-Latham (C-L), and the Wilkins (W) models. Additionally, the constant equivalent strain criterion, the Johnson-Cook (J-C) fracture model, and the Fracture Forming Limit Diagram (FFLD) are included in the present evaluation. Under the condition of quasi-static loading, all criteria are formulated in the general 3-D case for the power law hardening materials and then are specified for the plane stress condition. Fracture loci for all above cases were constructed in the space of principal strain, principal stress, and in the mixed

space of the equivalent strain and the stress triaxiality. Interesting observations are made regarding the range of applicability and expected errors of some of the most common fracture criteria.

2.3.1 Presentation of seven fracture criteria

Criterion I, Bao-Wierzbicki Model A detail description on the BW fracture criterion is already presented in Section 2.2. The BW fracture criterion for general case of 3-D continuum is given by Eq. (2.2) and the fracture locus for Al 2024-T351 obtained through an extensive experimental program is presented in Fig. 2.1 in the space of the effective strain and the average stress triaxiality. The BW fracture criterion is taken as a bench mark result here mainly because this criterion has been calibrated most extensively. Other criteria have not been calibrated in such a comprehensive way.

Criterion II, Maximum Shear Stress Fracture is governed by the condition

$$\tau_{\max} = (\tau_{\max})_f \tag{2.32}$$

where $\tau_{\max} = \max(\frac{\sigma_1 - \sigma_2}{2}, \frac{\sigma_1 - \sigma_3}{2}, \frac{\sigma_2 - \sigma_3}{2})$, and σ_1, σ_2 and σ_3 are the principal stresses. Qualitatively, Eq. (2.32) is similar to the familiar Tresca yield condition. However, the critical shear fracture stress $(\tau_{\max})_f$ is not the same as the shear flow stress of the material.

Criterion III, Cockcroft-Latham Cockcroft-Latham (1968) proposed the energetical fracture criterion which states that fracture depends on the integrated principal tensile stress. Thus, for a given material, this criterion suggests that fracture occurs when integral of tensile stress reaches a critical value according to

$$\int_0^{\bar{\varepsilon}_f} \sigma_1 d\bar{\varepsilon} = (W_{cr})_f \tag{2.33}$$

where $(W_{cr})_f$ is the critical specific 'plastic work'.

Criterion IV, Wilkins (W) Model The approach to fracture which conceptually is similar to the empirical BW fracture locus has been proposed much earlier by Wilkins (1980). It is postulated that fracture occurs when the following integral exceeds a critical value D_c^* over a critical dimension R_c.

$$D^* = \int_0^{\bar{\varepsilon}_f} \frac{1}{(1 - a_w \sigma_m)^{\lambda_w}} (2 - A_w)^{\mu_w} d\bar{\varepsilon} \tag{2.34}$$

where $A_w = \max(\frac{S_2}{S_1}, \frac{S_2}{S_3})$, $S_1 > S_2 > S_3$ are principal stress deviators, and a_w, λ_w and μ_w are material constants. These constants as well as the critical parameters D_c^* and R_c should be determined from suitably designed calibration tests.

Criterion V, Johnson-Cook (J-C) Fracture Criterion Johnson and Cook (1985) postulated that the critical equivalent fracture strain is a function of stress triaxiality, strain rate and temperature. However, the stain rate and temperature are considered to be the secondary effect on fracture as compared to that of the stress triaxiality. Here a special case of J-C model is considered in which the effects of stain rate and temperature are dropped.

$$\bar{\varepsilon}_f = C_1 + C_2 \exp(C_3 \frac{\sigma_m}{\bar{\sigma}}) \tag{2.35}$$

There are three material constants in the above model that should be determined from tests. It should be mentioned that Johnson and Cook gave a table of materiel fracture data for a number of structural materials. However, the constants C_1, C_2 and C_3 were determined from tests with high stress triaxiality. Therefore, Eq. (2.35) may not describe correctly fracture behavior for zero or negative stress triaxialities. Furthermore, the J-C fracture criterion does not tell how to deal with the situation when the stress triaxiality is not constant but changes in the loading process.

Criterion VI, Constant Equivalent Strain Fracture Criterion This is a special case of Criterion I, in which the weighting function g in Eq. (2.2) is assumed to be constant. Accordingly, fracture would occur when the equivalent plastic strain reaches a critical value,

$$\bar{\varepsilon} = \bar{\varepsilon}_f \tag{2.36}$$

Criterion VII, Fracture Forming Limit Diagram (FFLD) A plot of the major and minor strains at the point of through thickness fracture in the principal strain space constitutes a FFLD and the equation for the FFLD is given by Eq. (2.25). Moreover, the notion of Forming Limit Diagram (FLD), which is the locus of principal strains that can be sustained by sheet materials prior to the onset of localized necking, is introduced here because it have been observed that the W fracture

criterion in the range of high stress triaxiality is closer to the Forming Limit Diagram (FLD) rather than to the Fracture Forming Limit Diagram (FFLD).

The concept of FLD is firstly introduced by Keeler and Backofen (1964) and Goodwin (1968) to determine the amount of deformation a material can withstand prior to necking. Using the flow theory of plasticity, Hill (1952) developed a general criterion for localized necking in thin sheets under plane stress condition. His theory predicts that localized necking occurs along a direction of zero extension and is restricted to negative minor strain value. Stören and Rice (1975) used a bifurcation analysis to predict the FLD that arises from a vertex on the yield surface by imposing force equilibrium between the necked and non-necked region of metal.

Defining the ratio of the increment of principal strains as $\alpha = d\varepsilon_2 / d\varepsilon_1$, the FLD consist of two branches depending on the range of α. Thus,

$$(\varepsilon_1)_{neck} = \varepsilon_{1n} = \frac{n}{1+\alpha} \qquad \text{for } \alpha \in (-\frac{1}{2}, 0) \tag{2.37}$$

$$\varepsilon_{1n} = \frac{3\alpha^2 + n(2+\alpha)^2}{2(2+\alpha)(1+\alpha+\alpha^2)} \qquad \text{for } \alpha \in (0,1) \tag{2.38}$$

where n is the hardening exponent. Assuming linear strain paths where the ratio between the major and minor principal strains is constant throughout the deformation process (i.e. $\alpha = const.$), the second principal strain is simply $\varepsilon_{2n} = \alpha\varepsilon_{1n}$. Equation (2.37) is due to Hill (1952), while Eq. (2.38) was derived by Stören and Rice (1975). An illustration of the FLD and FFLD for a particular case of a mild steel is shown in Fig. 2.7. The material is characterized by the hardening exponent $n = 0.2$ and the damage parameter $D_c = 0.35$ where D_c is defined by Eq. (2.2). The FLD is shown by the thin solid line, while the FFLD is displayed by the thick solid line.

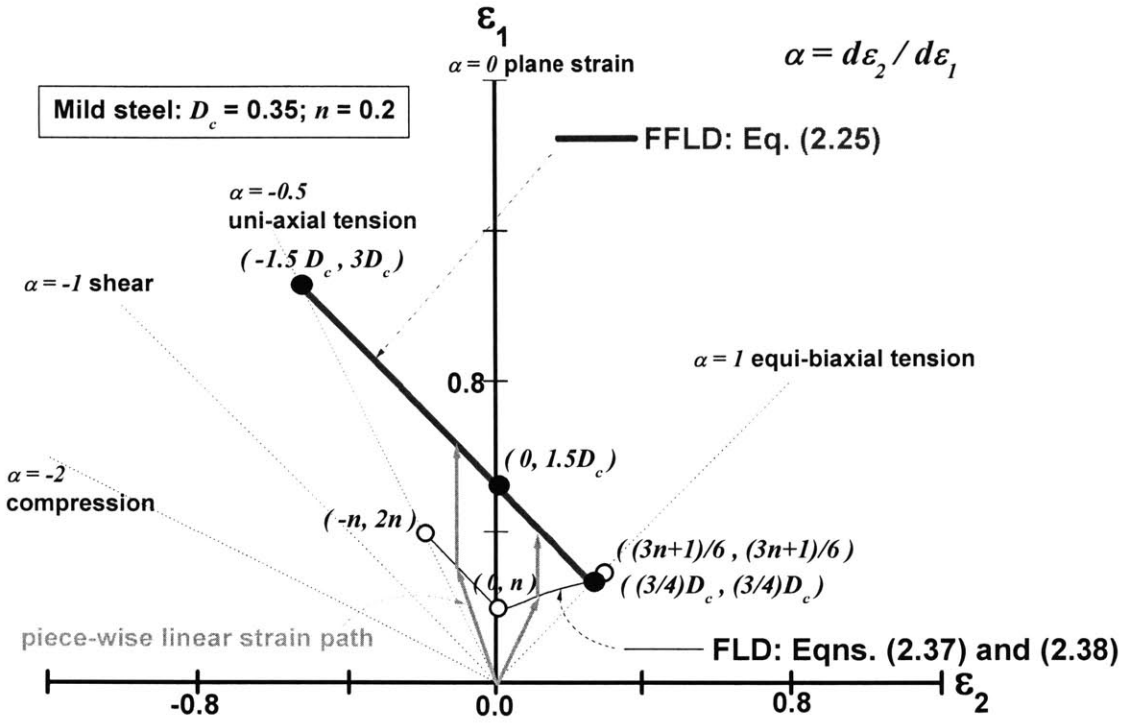

Fig. 2.7 Comparison of FFLD and FLD for a mild steel

2.3.2 Calibration of fracture model

In the present comparative study, 2024-T351 aluminum alloy is considered since this material has been calibrated for a wide range of stress triaxiality of practical importance.

Calibration of BW model for fracture A total of eleven different tests illustrated in Fig. 2.1(b) on 2024-T351 aluminum alloy were performed by Bao (2003) in a universal test machine to find the relation between the equivalent strain to crack formation and the magnitude of the stress triaxiality. The tests are covering a relatively wide range of the stress triaxiality from -0.33 to 1.0. Note that the test points denoted by open circle in Fig. 2.1(a) were obtained through phenomenological fitting procedure that requires a hybrid methodology of combined testing and numerical simulation. More detail information on this conventional and the newly developed calibration methods is presented in Chapter 3.

Calibration of Maximum Shear Stress fracture model There is only one fracture parameter in this model, which is the maximum shear stress at fracture $(\tau_{\max})_f$. This quantity can be determined from the calculated final values of the three principal stresses at the point of fracture, according to Eq (2.32). For example, calibration can be done from the uniaxial tensile test or any other test. Furthermore, it is not important if fracture occurs before or after necking because in each case the principal stresses at point of fracture can be easily calculated. Specifically, in the case of Al 2024-T351, the calibration parameter obtained from uniaxial tensile test on unnotched specimen was found to be $(\tau_{\max})_f = 770$ MPa.

Calibration of Cockcroft-Latham model for fracture In a similar manner to the case of maximum shear stress model, Cockcroft-Latham criterion requires only a single test for calibration, for example either tension or shear. In the present study, the calibration constant $(W_{cr})_f$ is obtained from pure shear test.

Calibration of W model for fracture Due to the presence of two weighting terms and two exponents in Eq. (2.34), the calibration process of the W is much more difficult than that in the case of other simple empirical fracture criteria (eg. Cockcroft and Latham (1968), Clift et al. (1990), Brozzo et al. (1972), and Rice and Tracey (1969)). The best way to calibrate the W model is to perform tests such that only one weighting term is operating at a time. A complete calibration procedure for the W model is presented by Bao et al. (2004c). As a final result, the calibrated parameters for the W model are given in Table 2.1.

Table 2.1 Calibrated parameters of the W model for Al 2024-T351 (taken from Bao et al., 2004c)

a_w [(GPa)$^{-1}$]	λ_w	μ_w	D_c^*	R_c [mm]
1.2	2.15	2.18	0.93	0.2-1

Calibration of Johnson-Cook model for fracture The constants C_1, C_2 and C_3 for 2024-T351 aluminum alloy determined by Johnson and Holmquist (1989) are $C_1 = 0.13$, $C_2 = 0.13$ and $C_3 = -1.5$. It should be noted that three constants determined were obtained from tests with

relatively high stress triaxiality. In addition, recall that the point representing shear experiments (corresponding to zero stress triaxiality) was found to be far away from a smooth monotonic fracture locus and was ignored by Johnson and Cook (1985) in their calibration for a mild steel.

Calibration of Critical Equivalent Strain fracture model The corresponding fracture locus is represented by a horizontal line in the $(\bar{\varepsilon}_f, (\sigma_m/\bar{\sigma})_{av})$ space. In the present comparative study, the magnitude of critical equivalent fracture strain is determined from the requirement that coordinates of the constant and variable fracture loci intersect at plane strain tension. This corresponds to stress triaxiality equal to $\sigma_m/\bar{\sigma} = 1/\sqrt{3} = 0.58$. Such a normalization gives the best possible approximation of the real fracture locus by the constant fracture locus in the range of stress triaxiality of the considered problem in this thesis. It should be noted that traditionally, the calibration of the constant strain fracture locus is made on the basis of the tensile tests on unnotched specimens. The corresponding magnitude of the fracture strain is much higher leading to a poor approximation in the spaces of principal stresses or strains. This point will be further discussed in the subsequent sections. Depending on the ductility of the material, the corresponding average stress triaxiality could be anywhere between 0.33 and 0.5. In the case of 2024-T351 aluminum alloy, it was found that the coordinates of the fracture points are $\mathbf{b} = \bar{\varepsilon}_f = 0.45$ and $(\sigma_m/\bar{\sigma})_{av} = 0.4$.

An alternative way of finding the constant critical fracture strain would be to average the empirically determined BW fracture locus. The calculated average equivalent plastic fracture strain is 0.34. This fracture condition is represented in Fig. 2.8 as a thick horizontal line. A comparison of three methods of calibrating of equivalent strain fracture model is also shown in Fig. 2.8.

Calibration for FLD and FFLD The formation of localized necking does not mean crack formation. The FLD is included here only for comparison purpose. The only material constant needed to construct FLD is the hardening exponent n. Note that in sheets, necking and fracture are the failure modes corresponding to high stress triaxiality larger than 1/3. The fracture inside the neck in the space of principal strain is given by Eq. (2.25). The calibration constant is identical to the one discussed in conjunction with the calibration of BW criterion and is equal to $D_c = 0.18$ for 2024-T351 aluminum alloy.

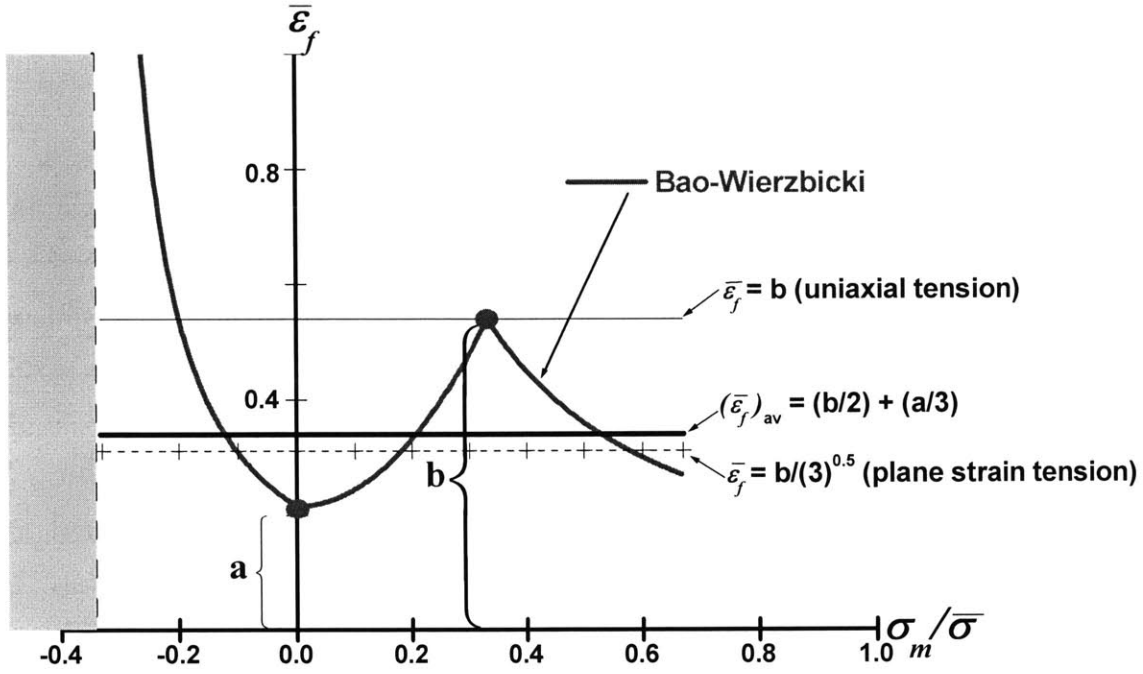

Fig. 2.8 A comparison of three methods of calibrating of the constant equivalent strain fracture model

2.3.3 Specification of fracture criteria for plane stress

In Section 2.3.1, the formulations for seven different fracture criteria are presented in the general case of 3-D continuum. Considerable simplifications of the forms of those criteria are obtained in the special case of plane stress. It is recalled that the plane stress is defined by the condition of vanishing of one principal stress component, say $\sigma_3 = 0$. For example, in thin sheets, this is a through thickness stress, while in upsetting tests, this is the radial stress at the outer surface of barreled cylinders.

For the purpose of the present comparative study, further simplifications are introduced:

- The first one is to propose a simple analytical representation of the BW criterion. As given by Eq. (2.6), the fracture locus is represented by three branches in the space of equivalent strain and average stress triaxiality. It was further assumed that average stress triaxiality in uniaxial tension is $(\sigma_m/\bar{\sigma})^0_{av} = 1/3$, which leads to the intersection point of the branches I and II is (1/3, **b**).

Accordingly, by substituting $(\sigma_m/\bar{\sigma})_{av}^{0} = 1/3$ into Eq. (2.6), the simplified BW fracture locus becomes

$$\bar{\varepsilon}_f = \begin{cases} \infty, & (\sigma_m/\bar{\sigma}) \le -\dfrac{1}{3} \\ \dfrac{\mathbf{a}}{1+3(\sigma_m/\bar{\sigma})}, & -\dfrac{1}{3} < (\sigma_m/\bar{\sigma}) \le 0 \\ 9(\mathbf{b}-\mathbf{a})(\sigma_m/\bar{\sigma})^2 + \mathbf{a}, & 0 \le (\sigma_m/\bar{\sigma}) \le \dfrac{1}{3} \\ \dfrac{\mathbf{b}}{3(\sigma_m/\bar{\sigma})}, & \dfrac{1}{3} \le (\sigma_m/\bar{\sigma}) \le \dfrac{2}{3} \end{cases} \tag{2.39}$$

where **a** is the magnitude of critical fracture strain in shear.

- The second simplification is that the intersection point of the central and right branches is moved slightly to the left and up from the experimentally determined locus shown in Fig. 2.1(a). This was done in order for the BW and W criteria to pass through the same point with coordinates (1/3, **b**), where **b**=0.54. Consequently, the intersection point (0, **a**), where **a** = 0.21, is also moved vertically to keep the same relative magnitude as **a/b** = 0.4 shown in Fig. 2.1(a).
- At the same time, the calibration constants of the FFLD, the maximum shear stress and the Wilkins models were also adjusted so that all the respective fracture loci will pass through the same points with coordinates (1/3, **b**). Physically, it requires that fracture in uniaxial tension (at $\sigma_m/\bar{\sigma} = 1/3$) will occur under the same stresses and strains for those fracture criteria.
- The constitutive relationship imposed for the material model is governed by power law relation (i.e. $\bar{\sigma} = K\bar{\varepsilon}^{n}$).
- The stress or strain components keep constant ratios (proportional loading).

Representation of fracture criteria in three different spaces Various authors in the past used different representations of their respective fracture criteria in different spaces. Fracture loci corresponding to all seven fracture criteria defined in the present study will be represented in three different spaces: space of the equivalent plastic strain to fracture and the average stress triaxiality ($(\sigma_m/\bar{\sigma})$, $\bar{\varepsilon}_f$); space of the principal strains ($\varepsilon_{2f}, \varepsilon_{1f}$); space of the principal stresses (σ_{2f}, σ_{1f}).

As shown in Fig. 2.2, the advantage of working with plane stress conditions is that there is a unique transformation from one space to the other. Therefore, a criterion formulated in one space can be represented in another space. For example, the fracture condition governed by the Cockcroft-

Latham (C-L) fracture criterion can be transformed to the two other spaces and compared with fracture criteria which originally have been formulated in one of the remaining spaces. In the following, the transformation procedure is described for the case of C-L criterion. The calibration parameter for the C-L model is determined from the condition of pure shear (i.e. α = -1). By substituting α = -1 into Eq. (2.18) together with the assumed power law relation ($\bar{\sigma} = K\bar{\varepsilon}^n$), the principal stress σ_1 becomes

$$\sigma_1 = \frac{K\bar{\varepsilon}^n}{\sqrt{3}} \tag{2.40}$$

Applying Eq. (2.40) to (2.33) and integrating, the critical specific 'plastic work' $(W_{cr})_f$ takes the form

$$(W_{cr})_f = \frac{1}{\sqrt{3}} \frac{K}{n+1} \mathbf{a}^{n+1} \tag{2.41}$$

where **a** is magnitude of critical fracture strain in pure shear. Consequently, the C-L fracture criterion can be expressed by

$$\int_0^{\bar{\varepsilon}_f} \sigma_1 d\bar{\varepsilon} = \frac{1}{\sqrt{3}} \frac{K}{n+1} \mathbf{a}^{n+1} \tag{2.42}$$

Using Eq. (2.18) and $\bar{\sigma} = K\bar{\varepsilon}^n$, the left hand side of Eq. (2.42) is then

$$\int_0^{\bar{\varepsilon}_f} \sigma_1 d\bar{\varepsilon} = \frac{2+\alpha}{\sqrt{3}\sqrt{1+\alpha+\alpha^2}} \frac{K}{n+1} \bar{\varepsilon}_f^{n+1} \tag{2.43}$$

Equating Eq. (2.42) with (2.43), the equivalent strain to fracture corresponding to the C-L model is represented in terms of strain ratio α according to

$$\bar{\varepsilon}_f = \mathbf{a} \left(\frac{\sqrt{1+\alpha+\alpha^2}}{2+\alpha} \right)^{\frac{1}{n+1}} \tag{2.44}$$

Referring to Eq. (2.20), the stress triaxiality $(\sigma_m / \bar{\sigma})$ can be determined from the strain ratio α.

From Eqns. (2.21), (2.22), and (2.44), the components of principal strains to fracture are

$$\begin{Bmatrix} \varepsilon_{1f} = \mathbf{a} \left(\frac{\sqrt{1+\alpha+\alpha^2}}{2+\alpha} \right)^{\frac{1}{n+1}} \frac{\sqrt{3}}{2\sqrt{1+\alpha+\alpha^2}} \\ \varepsilon_{2f} = \alpha \varepsilon_{1f} \end{Bmatrix} \tag{2.45}$$

Using Eqns. (2.18), (2.19), and (2.44) with the power law relation ($\bar{\sigma} = K\bar{\varepsilon}^n$), the C-L fracture criterion can be represented in the space of principal stress according to

$$\left\{\begin{array}{l} \sigma_{1f} = \dfrac{\sigma_{1f}^0}{2}\left(\dfrac{2+\alpha}{\sqrt{1+\alpha+\alpha^2}}\right)^{\frac{1}{n+1}} \\ \sigma_{2f} = \dfrac{1+2\alpha}{2+\alpha}\sigma_{1f} \end{array}\right\} \tag{2.46}$$

where $\sigma_{1f}^0 = K\mathbf{a}^n(1/\sqrt{3})^{\frac{n}{n+1}}$ is the final value of uniaxial stress to fracture for the case of C-L model.

Likewise, the BW and W model could be transformed to the space of principal stresses or principal strains. It is relatively straightforward to represent the fracture locus of any of the seven criteria in three different spaces using transformation equations presented in Section 2.2.2.2. The equations describing various fracture loci, expressed in terms of the strain rate ratio α, are given in the Appendix A. It should be noted that depending on particular criteria there will be several ranges of α and therefore several branches of the fracture envelope. For example, the BW fracture envelope consists of three branches while in the case W model, there are four branches. Both the maximum shear stress and the FLD consist of two branches. The remaining criteria that are J-C, FFLD, C-L, and the constant equivalent strain are represented by a single curve in all three spaces. The comparative study of prediction of various criteria is presented in the next section.

2.3.4 Comparison in the ($\sigma_m/\bar{\sigma}$, $\bar{\varepsilon}_f$) space

Comparison of seven fracture criteria in the space of the equivalent plastic strain to fracture and the stress triaxiality for Al 2024-T351 is shown in Fig. 2.9. Note that the range of stress triaxialities considered in this comparative study is from -1/3 to 2/3. The low limit of -1/3 corresponds to the so-called cut-off value for negative triaxiality discovered by Bao and Wierzbicki (2004a). At the same time, the upper limit of 2/3 is the maximum value of stress triaxiality that could be obtained in plane stress. The relative position of various lines in Fig. 2.9 depends on the range of the stress triaxiality parameter. Therefore, the discussion is divided into three ranges.

High stress triaxiality $(1/3 < \sigma_m/\bar{\sigma} < 2/3)$ The J-C (line with open square) and BW (thick full line) models are the only two empirically determined criteria. In Fig. 2.9, Johnson and Holmquist's data (1988) for 2024-T351 aluminum alloy was taken to construct the fracture envelope of the J-C model. Even though, the J-C and BW models were obtained apparently for the same aluminum alloy, the corresponding lines are far apart. Note that J-C did not test the material for small stress triaxiality but simply extrapolated the curve fitted from high stress triaxiality to the left. Besides, the calibration by Johnson and Holmquist (1988) was performed some 20 years ago, so it is possible that the 2024-T351 aluminum alloy was in fact not the same as the one testes recently by Bao and Wierzbicki (2004a).

The second observation is that FFLD fracture locus (line with filled triangle) is represented by the same line as the BW locus in the range between uniaxial and equi-biaxial tension $(1/3 < \sigma_m/\bar{\sigma} < 2/3)$. Traditionally, the FFLD criterion is represented in the space of principal strains. It was shown by Embury and LeRoy (1977) on the basis of tests that the locus of principal strains corresponding to fracture of sheets follow a straight line. It was later proved by Atkins (1985) that there is a path independent transformation of this straight line into the $(\sigma_m/\bar{\sigma}, \bar{\varepsilon}_f)$ space. The transformed curve is given by Eq. $(2.39)_4$, which is exactly of one branch of the BW criterion.

As mentioned earlier, the FLD (line with filled square) defines localized necking rather than fracture. It is included for the present comparative study simply because the corresponding line is similar in shape to the W curve (solid line). Moreover, the FLD is almost identical in shape and magnitude to the maximum shear stress fracture criterion (line with open circle) in the case of biaxial tension $(1/\sqrt{3} < \sigma_m/\bar{\sigma} < 2/3)$. The magnitude of the constant equivalent fracture strain $\bar{\varepsilon}_f = 0.31$ was calibrated from the plane strain test. Finally, the C-L criterion (line with open triangle) follows the generally diminishing trend but falls far below all other fracture criteria.

Intermediate stress triaxiality $(0 < \sigma_m/\bar{\sigma} < 1/3)$ The first observation is that the range of intermediate stress triaxiality is seldom encountered in sheet metal forming problems because the corresponding stress state has one large compressive stress component, which may lead to winkling. Therefore, lines corresponding to FLD and FFLD are not drawn in that range. It is seen from Fig. 2.9 that fracture loci corresponding to the BW, W and the maximum shear stress criteria are very

close to each other. At the same time, the lines corresponding to J-C, the constant equivalent strain and the C-L criterion are lying far apart. Qualitatively, the J-C and C-L models are different from the true trend of experimentally determined BW fracture locus which is of rising shape with increasing stress triaxiality.

Negative stress triaxiality $(-1/3 < \sigma_m / \bar{\sigma} < 0)$ It can be observed that the BW, C-L, and W criteria appear to be close to each other. However, there is a vertical asymptote at the value of $\sigma_m / \bar{\sigma} = -1/3$ in the BW and C-L criteria (the fracture strain goes to infinity). At the same time, the W criterion gives a finite value of the strain to fracture $\bar{\varepsilon}_f = 2.65\mathbf{b} = 1.43$. The maximum shear stress criterion captures to certain extent the trend of the experimental points but at $\sigma_m / \bar{\sigma} = -1/3$ also predicts $\bar{\varepsilon}_f = \mathbf{b} = 0.54$. The J-C criterion does not correspond to reality in any way. The term "reality" means here the empirically determined fracture locus which was fit by the full line in Figs. 2.9-2.11. The J-C criterion involves three material constants (C_1, C_2 and C_3). By suitable choice of those constants, one can get a better approximation of the empirical locus either in the range of high stress triaxiality or in the range of negative stress triaxiality, but never in both ranges at the same time. Finally, the constant equivalent strain criterion gives very unrealistic prediction of ductile fracture.

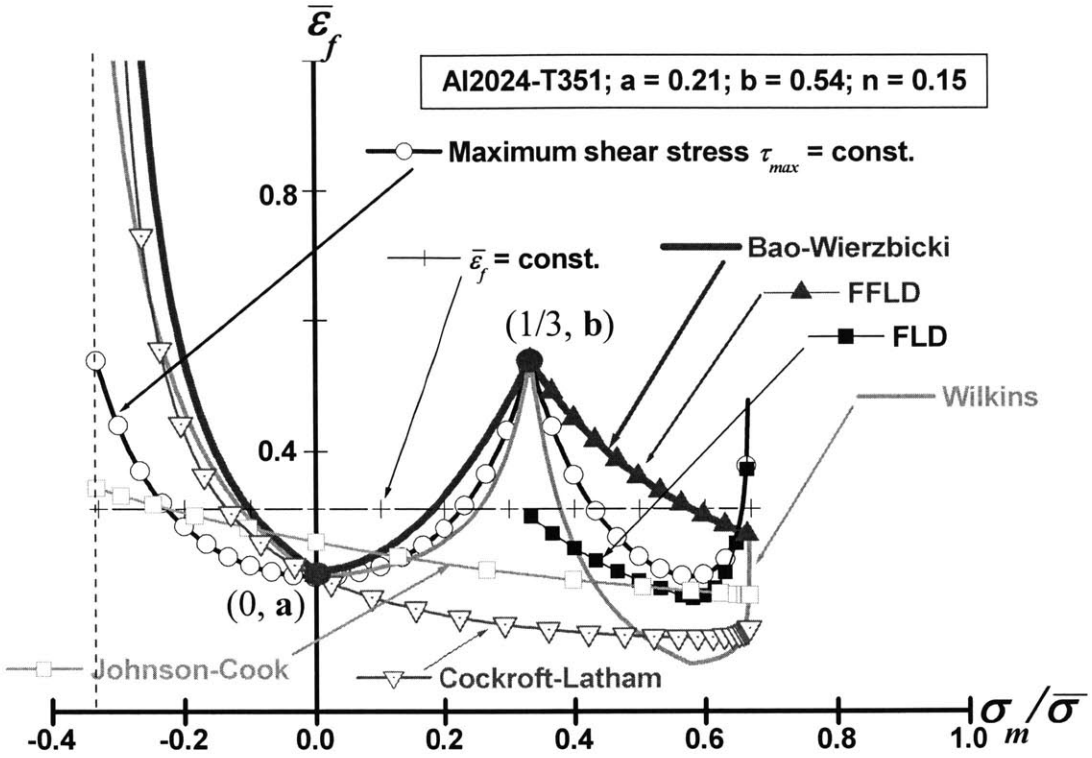

Fig. 2.9 Comparison of seven fracture criteria in the space of the equivalent plastic strain to fracture and the stress triaxiality. Note that the FLD (denoted by line with filled square) is included in this figure for comparison purpose.

2.3.5 Comparison in the (ε_{1f}, ε_{2f}) space

In this section, the fracture loci represented in the space of the equivalent plastic strain and stress triaxiality are transformed into the space of principal strains to fracture. The parameter of this transformation is the strain rate ratio α. The plane of two principal strains has traditionally been used in sheet metal industry to represent necking conditions. As shown in Fig. 2.7, for any given initial strain path, the material forms a neck which continues to deform by an approximately plane strain path up to fracture. Thus, a second envelope (FFLD) can be added to the diagram representing a principal strain to fracture. This FFLD is attained by a combined path involving proportional loading (α = constant) up to the localized necking followed by transverse plane strain deformation

($\alpha = 0$) up to fracture. Using the above piece-wise linear trajectory of the strain rate ratio shown in Fig. 2.7, the integration involved in the BW fracture criterion, Eq. $(2.39)_4$ can be easily performed and the final result is given by Eq. (2.25). Physical interpretation of this criterion is that the through thickness strain at fracture is constant and equal to $-\varepsilon_{3f} = 3D_c/2$ for all combination of the strain rate ratio α. An illustration of the above transformation process is shown in Fig. 2.4. In view of the above transformation, the lines in Fig. 2.10 corresponding to BW and FFLD fracture criteria are identical.

As to the FLD, two sets of curves given by Eqns. (2.37) and (2.38) are used. Overall, none of the six fracture criteria are following the BW empirical fracture locus in the entire range of the minor principal strain ε_2. However, in the range between uniaxial tension ($\alpha = -0.5$) and shear ($\alpha = -1$), the W and the maximum shear stress criteria are very close to the BW prediction. In the range between uniaxial tension ($\alpha = -0.5$) and equi-biaxial tension ($\alpha = 1$), the curve corresponding to W fracture locus is much lower than the BW and FFLD lines. The J-C as well as the constant equivalent strain fracture criteria, when properly scaled can indeed be close to the BW line in the range between plane strain ($\alpha = 0$) and equi-biaxial tension ($\alpha = 1$). This explains a relative success in using those criteria to predict tensile fracture of thin sheets. The prediction of J-C and the constant equivalent strain fracture criteria rapidly deteriorate as one move away from plane strain into negative value of the parameter α covering uniaxial tension, shear all the way to unaixal compression ($\alpha = -2$). The maximum shear stress criterion, while giving errors in some ranges of the parameter α, follow in general the trend of the empirical fracture locus. Finally, the C-L criterion compares well with the empirical BWfracture locus in the range between pure shear ($\alpha = -1$) and uniaxial compression ($\alpha = -2$).

It can be concluded that representation of fracture loci in the space of principal strains is very instructive because they emphasize difference between various criteria that might be hidden in the ($\sigma_m/\bar{\sigma}$, $\bar{\varepsilon}_f$) space and especially in the space of principal stresses.

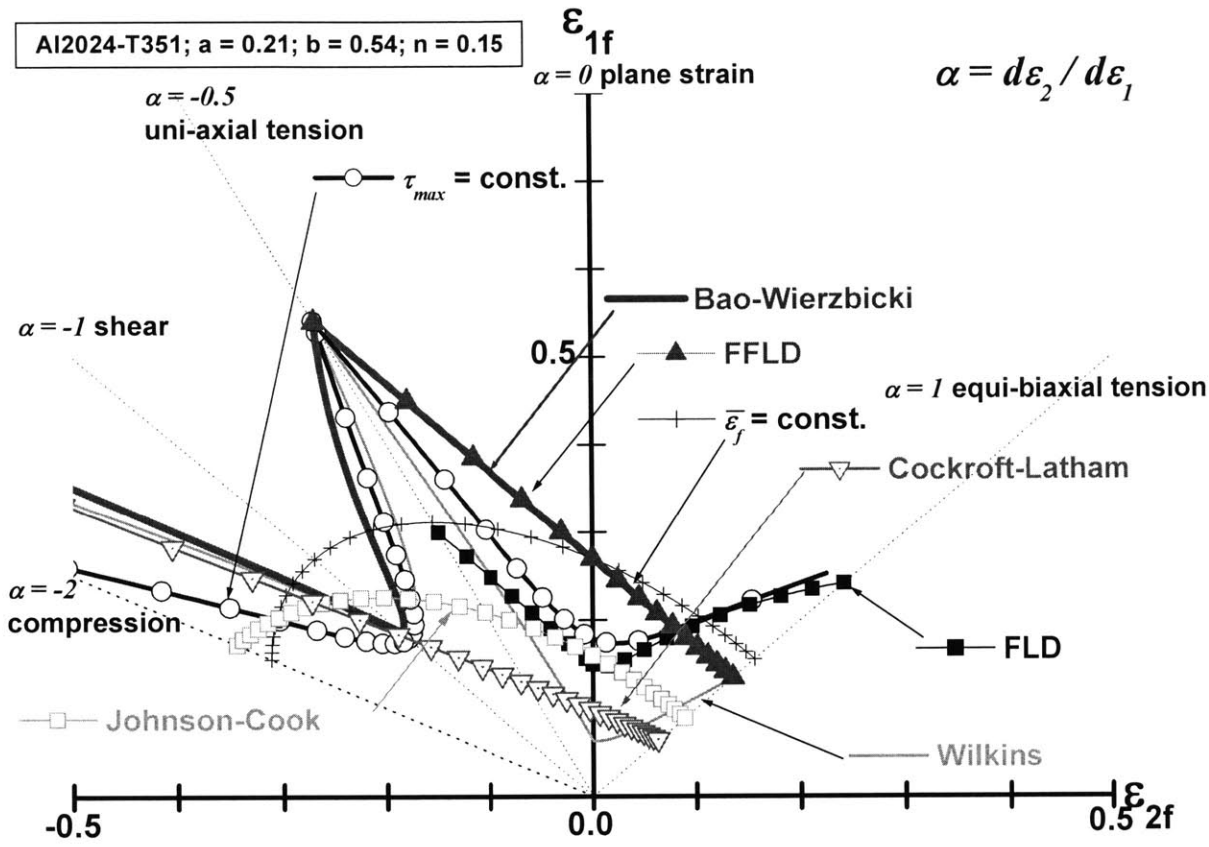

Fig. 2.10 Comparison of seven fracture criteria in the space of the principal strain to fracture. Note that the FLD (denoted by line with filled square) is included in this figure for comparison purpose.

2.3.6 Comparison in the $(\sigma_{1f}/\sigma_{1f}^{0}, \sigma_{2f}/\sigma_{2f}^{0})$ space

Traditionally, the space of principal stresses is used to formulate fracture for brittle materials. However, in the case of plane stress, fracture loci for ductile material expressed in the strain or mixed space could also be represented in the stress space. This is illustrated in Fig. 2.11. It can be seen that curves corresponding to almost all approaches for fracture fall within a relative narrow band. The lower and upper bounds for the above mentioned band are set up by the "von Mises" and "Tresca" failure conditions. In the present fracture study, the Tresca hexagon and the von Mises ellipse should be identified as combination of principal stresses corresponding to fracture rather first

yield. Note that nondimensional stresses are used in Fig. 2.11, where both principal stresses were normalized with respect to uniaxial fracture stress σ_{1f}^{0}. There are two noticeable departures from the above mentioned narrow band in the first positive quadrant. The lines corresponding to J-C and W criteria lie considerably below. Another distinguished feature of Fig. 2.11 is that the BW and C-L fracture loci in the second quadrant (tension-compression) are represented by a concave curve with a horizontal asymptote. This is a consequence of the presence of the vertical asymptote in the ($\sigma_m / \bar{\sigma}$, $\bar{\varepsilon}_f$) space.

The conclusion drawn from present section is that the representation of the fracture locus in the space of principal stresses is deceiving because differences between most of the criteria partially disappear when in fact they exist. It should be noted that the hardening exponent for Al 2024-T351 is relative small ($n = 0.15$) and the stress-strain curve is rather flat. In consequence, large differences in strain correspond to small differences in stresses.

The idea of transforming limit state condition from one space to the other has been around in the sheet metal forming community. In an effort to remove the path dependence in FLD, Stoughton (2000) and Stoughton and Zhu (2004) transformed the forming limit diagram to the space of principal stresses. By doing so, the path dependence was almost eliminated and several alternative FLDs collapse approximately to a single curve.

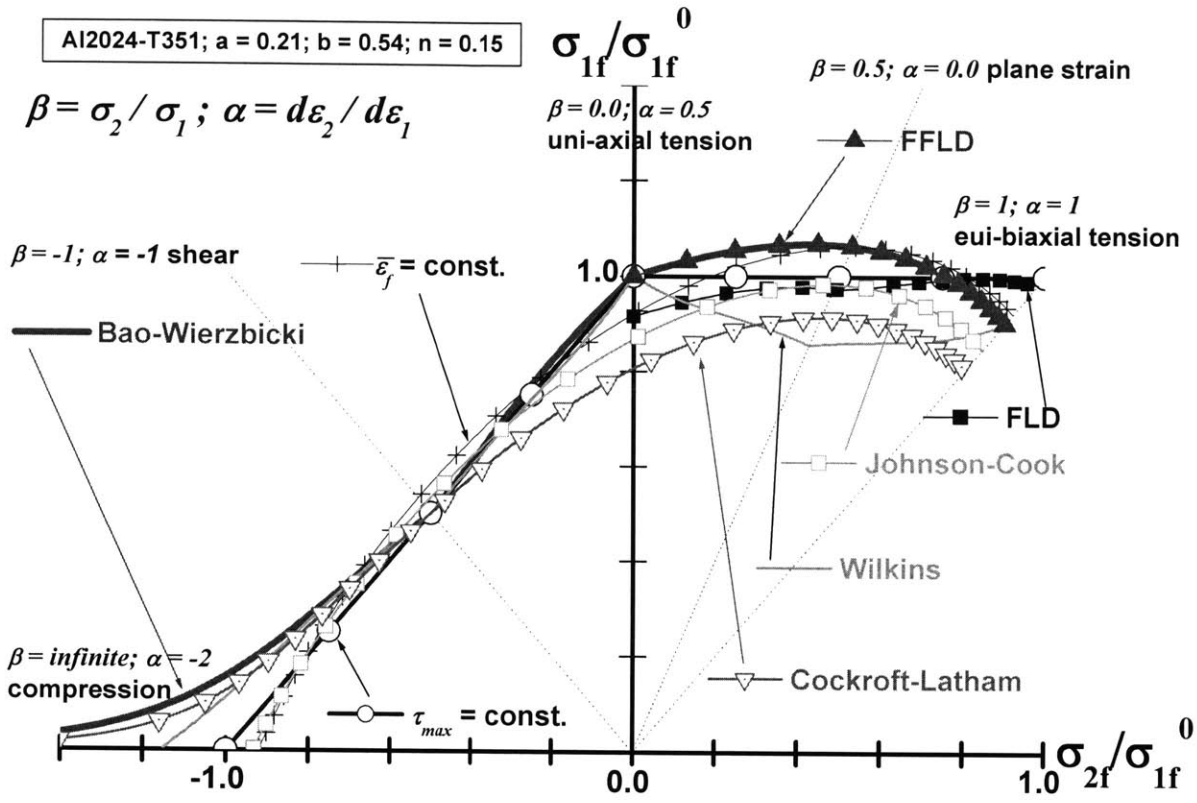

Fig. 2.11 Comparison of seven fracture criteria in the space of principal stresses. Note that axes are normalized by uniaxial stress to fracture σ_{1f}^0 and the FLD (denoted by line with filled square) is included in this figure for comparison purpose.

2.4 Relation between ductile crack formation and propagation

The BW fracture locus constructed in Fig. 2.1 (a) applies strictly to the prediction of the onset of fracture of uncracked bodies. In the present thesis, it was further assumed that the ductile crack propagation is, essentially, a process of continuous re-initiation ahead of the crack, so that the same micro-structural events occur in front of the crack tip of a previously existing crack as in the region of a flawless body in which the crack initiates (Atkins, 1985, 1996b). In the present research, the validity of the above hypothesis on possible connection between crack formation and propagation is

confirmed through three case studies at the specimen and component levels shown in Fig. 2.12 (see Chapters 5, 6, and 7).

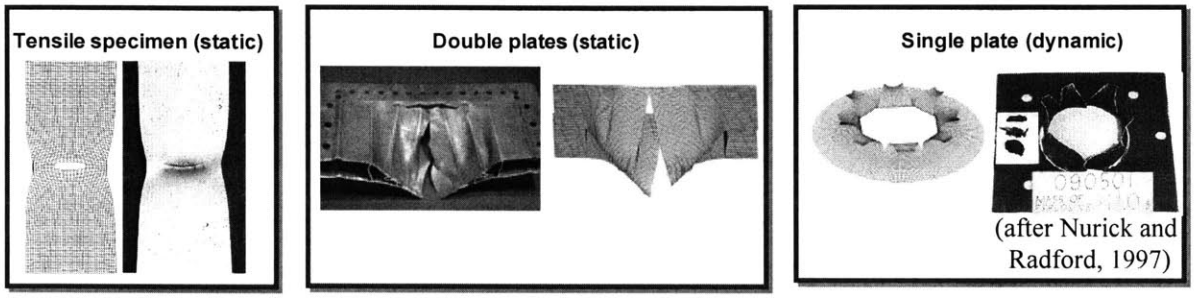

Fig. 2.12 Three case studies confirming the hypothesis on the possible relationship between ductile crack formation and propagation

2.5 Strain rate and temperature dependence of fracture criterion

The effect of possible strain rate and temperature dependence of the fracture criterion was not considered in the present thesis. However, it was recently shown by Borvik et al. (1999, 2001, 2003) and Hopperstad et al. (2003) that the effect of strain rate and temperature on the fracture strain are much smaller than that of stress triaxiality for Weldox 460E steel, see Fig. 2.13. Similar observations were also made for other materials, Johnson and Cook (1985), Johnson and Holmquist (1989), and Lesuer (2000). In the problem of projectile impact studied by Borvik et al (1999, 2001, 2003) and Hopperstad et al. (2003), plastic deformations are highly localized. This give rises to a substantial adiabatic heating. By contrast, in the pressure loading problems considered in Chapters 7, 8, and 9, there are no such large gradient of strain and adiabatic shear band are less likely to occur. Therefore, the fracture strain was assumed to be a unique function of stress triaxiality in the present thesis. However, the accuracy of this assumption might be different depending on the material. Further research is needed for various types of materials to confirm the above statement.

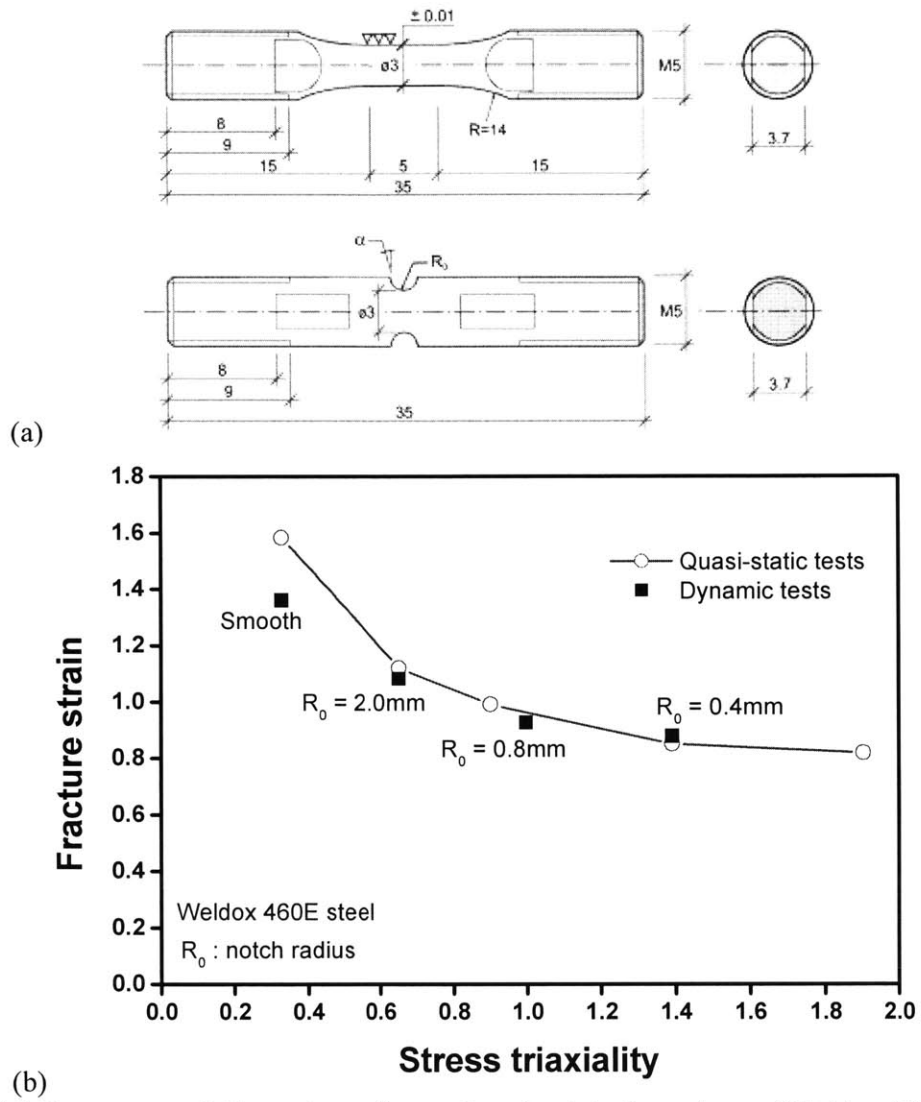

Fig. 2.13 (a) Geometry and dimensions of smooth and notched specimens (Weldox 460E steel) for high rate tests in the Split Hopkins Bar (in mm); (b) Fracture strain versus stress triaxiality (based on initial geometry) (taken from Hopperstad et sl., 2003)

2.6 Conclusion

- It was shown that in the ranges of high and negative stress triaxialities, the relevant branches of Bao-Wierzbicki (BW) fracture locus can be uniquely transformed as straight lines in the space of principal strains. Furthermore, it was demonstrated that these lines accurately represent experimental fracture points obtained for various materials by different authors. Therefore, it is

believed that the shape of the BW fracture locus constructed either in the space of the equivalent strain and the stress triaxiality or in the space of principal strains is sufficiently accurate.

- Through a comparative study of the seven fracture criteria, it was found that in the range of high stress triaxiality ($\sigma_m / \bar{\sigma} > 1/3$) the BW and the FFLD criteria give identical and accurate results. In the intermediate range of stress triaxiality ($0 < \sigma_m / \bar{\sigma} < 1/3$), the BW, the W, and the maximum shear stress follow closely the experimental points. Finally, in the range of negative stress triaxiality ($\sigma_m / \bar{\sigma} < 0$), the C-L and the BW fracture envelopes capture best the process of crack formation.
- The FFLD represented by a straight line in the space of principal strains follows very closely the experimental fracture locus. It is recommended to use the FFLD for sheets in the range between uniaxial tension and equi-biaxial tension.
- The C-L criterion, which gives 2:1 strain pairs in the tension-compression quadrant of the principal strains, is the closest to the empirically determined BW fracture locus in the range of negative stress triaxiality. However, the monotonic decreasing trend of this criterion for the range of intermediate stress triaxiality is different from the experimentally obtained one that is of rising shape with increasing stress triaxiality.
- The fracture locus predicted by the W model follows a general trend of test points, especially in the range of low and negative stress triaxiality. However, major differences exist in the range between uniaxial and equi-biaxial tension ($1/3 < \sigma_m / \bar{\sigma} < 2/3$). The corresponding locus of W model is similar in shape to the FLD, which is the onset of localized necking, rather than fracture.
- The maximum shear stress failure criterion captures the general trend of the experimental points, especially in the range of intermediate stress triaxiality ($0 < \sigma_m / \bar{\sigma} < 1/3$). Moreover, the advantage of this criterion requires only a single test for calibration, for example either tension or shear. Hence, the maximum shear stress fracture criterion could be utilized in the development procedure of the quick calibration, which is presented in Chapter 3.3.
- The J-C criterion can get a good approximation of the BW locus either in the range of high stress triaxiality or in the range of negative stress triaxiality, but never in both ranges at the same time.

- The constant equivalent strain fracture criterion may give a good prediction of ductile fracture in the narrow range between plane strain and equi-biaxial tension ($1/\sqrt{3} < \sigma_m / \bar{\sigma} < 2/3$). Outside this range, it leads to large, unacceptable errors.
- The representation of the fracture locus in the space of principal stresses is not informative since differences between most of the criteria partially disappear when in fact they exist.

Chapter 3
Calibration of Material and Fracture Models

3.1 Introduction

One of the largest obstacles for a wide-spread use of various engineering type fracture criteria in industry is a poorly understood and presented calibration procedure. This is true for the porous plasticity fracture model, damage mechanics approach as well as empirical formulations. Furthermore, the application of those models to practical problems proceeds very slowly. The primary reason is that the identification of the material parameters associated with the fracture criteria is complex and difficult to perform. For example, up to nine parameters, which are strongly coupled, needed to be determined for a single material in the application of the porous plasticity model (Gurson, 1977; Tvergaard and Needleman, 1984). The empirical fracture models have usually the least number of free parameters and functions. Still, the empirical models also require detail numerical simulations in addition to extensive and expensive material tests themselves, which might be discouraging for engineers. Furthermore, the numerical simulations using non-linear finite element methods may introduce an inherent mesh dependence (Needleman, 1988; Needleman and Tvergaard, 1994; Skallerud and Zhang, 1999). Therefore, the need of simplifying calibration

procedure with an acceptable level of accuracy is obvious for engineering type of fracture criteria in industrial applications.

The objective of this study is to propose a new calibration method that eliminates a need for the numerical simulation and determine all relevant fracture parameters in terms of the measurable quantities. The newly developed and constructed empirical Bao-Wierzbicki (Wierzbicki et al., 2002; Bao and Wierzbicki, 2004a/b) fracture criterion is taken as reference for the present calibration method. In Section 3.2, a conventional calibration procedure for the determination of critical damage parameters is presented and its deficiency is also pointed out. In Section 3.3, a simple method of calibrating for fracture from round or flat specimen of tensile test is developed valid in the range of high stress triaxiality. Furthermore, a new approach to construct the BW fracture locus is presented based on the hypothesis of maximum shear stress fracture in the range of intermediate stress triaxiality.

3.2 Conventional calibration method

The "conventional" calibration procedure was developed over the past few years in the Impact and Crashworthiness Lab. at MIT (Bao, 2003). The word "conventional" is used to distinguish between the time consuming and expensive method and the "quick" calibration method, which was developed in this thesis. In the conventional method, the damage parameters – i.e. stress triaxiality, equivalent plastic strain, and critical damage value as well as an accurate representation of the true stress-strain curve - were obtained by tracing the experimental load-displacement curve using parallel finite element calculations of uniaxial tensile test on standard specimen. This fitting procedure is, indeed, a hybrid methodology of combined testing and numerical simulation. As an example, calibration from unnotched flat tensile specimen for A710 steel material is presented in this section.

3.2.1 Calibration for plasticity

A tensile test was performed on a flat, dog-bone specimen with initial cross section $A_0 = 12.5 \times 2.04 mm^2$. The gauge length of the extensometer was $L_0 = 25.4 mm$. Figure 3.1 shows

the experimentally obtained necking and fracture patterns of the specimen. The experiment was stopped at the time when the crack length reaches approximately half of the initial width of the specimen. One can clearly see that both diffuse and localized neckings were developed prior to fracture. The fracture started at the center of the specimen and subsequent cracks propagated in a direction perpendicular to the tensile axis - i.e. $\phi \approx 90^{o}$. For the fracture prediction of material with high ductility, an accurate stress-strain curve of the material is needed. A load-displacement curve obtained from the universal MTS testing machine is shown in Fig. 3.2 by the thicker solid line. The stress state is uniform up to the point of maximum load ($P_u = 16784N$) which occurs at a displacement equal to $\delta_d = 3.12mm$ (see open circle in Fig. 3.2). In this range, the true stress-strain curve could be obtained rather easily by dividing the force and corresponding displacement by the reference values and by applying a correction between the engineering and the true stress and strain measures. After the peak load, the true stress-strain curve can only be obtained by trial-and-error so that the measured global load-displacement relation matches that obtained from a large elastic-plastic finite element method.

In the numerical implementation of the present trial-and-error method, the explicit finite element code *PAM-CRASH* was used and eight-node solid elements were employed to model the flat specimen. The specimen was modeled with 10 and 20 elements through the thickness and the width, as shown in Fig. 3.3. The displacement and rotation of nodes on the lower end parts of the specimen were fixed. The upper end parts of the specimen were assumed to move with a prescribed velocity. The ramping time was 0.001sec, and a constant velocity was 200mm/sec. The dynamic effect was avoided by reducing the mass density of the model by the factor of 1000.

The numerically obtained load-displacement responses with the initial stress-strain curve and the actual one from the trial-and-error method are shown in Fig. 3.2. Furthermore, the corresponding true stress and strain curves calculated in the above way are shown in Fig. 3.4. Note that the initial stress-strain curve was composed of the experimentally measured portion (before diffuse necking) and the power law portion after necking. As may be seen in Fig. 3.2, an excellent correlation was achieved by the simulation with the actual stress-strain curve. Therefore, the actual stress-strain curve, shown in Fig. 3.4 by thicker solid line, was used as material input data in all numerical simulations to predict fracture. It should be noted that small changes in the true stress-strain curve after diffuse necking may in fact produce large difference in the prediction of fracture. Moreover, the effort for obtaining the actual stress-strain relation measured by the number of iteration highly

depends on material as well as the shape of tensile specimens. For the A710 steel material and specimen considered in this section, six iterations were performed to obtain the actual stress-strain curve.

In Fig. 3.5, close-ups of the deformed specimen geometries obtained from numerical simulation are plotted by contour of equivalent plastic strain. After the onset of diffuse necking, two crossing localized neckings with an inclined angle $\phi = 65^o$ were observed (see Fig. 3.5(a)). As the two crossing necks saturated, the first fracture occurred at the center of the specimen (see Fig. 3.5(b)), which agrees with the experimental observation.

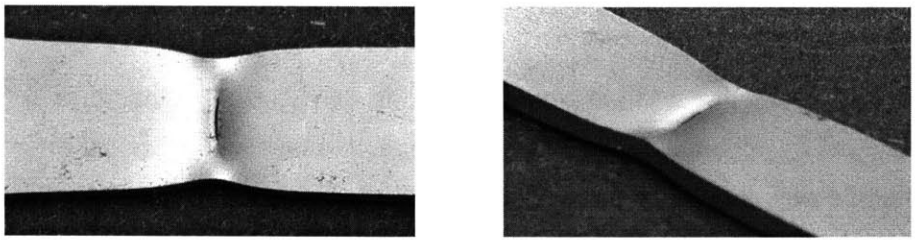

(a) top view (b) 3D view

Fig. 3.1 Experimentally obtained necking and fracture in a flat steel specimen (initial gauge length $L_0 = 25.4mm$; initial width $w_0 = 12.5mm$; initial thickness $h_0 = 2.04mm$)

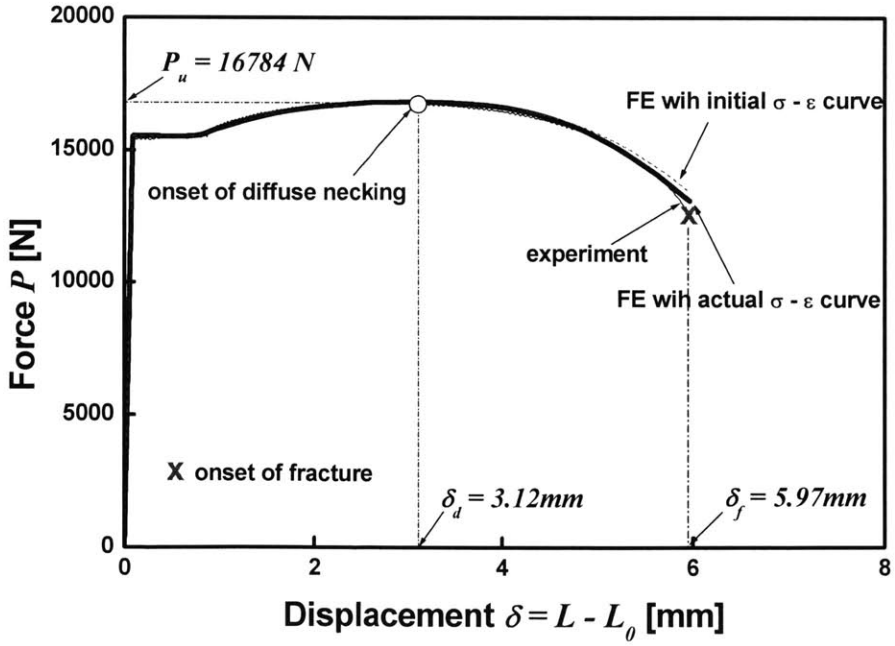

Fig. 3.2 Experimentally and numerically obtained force-displacement responses of a steel flat specimen

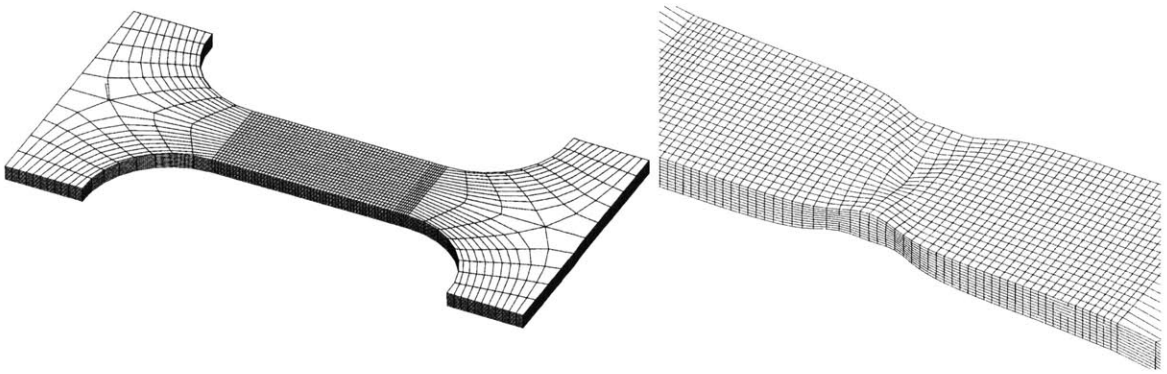

Fig. 3.3 FE models of the flat tensile specimen; initial FE model (left); closed-up view of deformation in the central region right before the formation of crack (right)

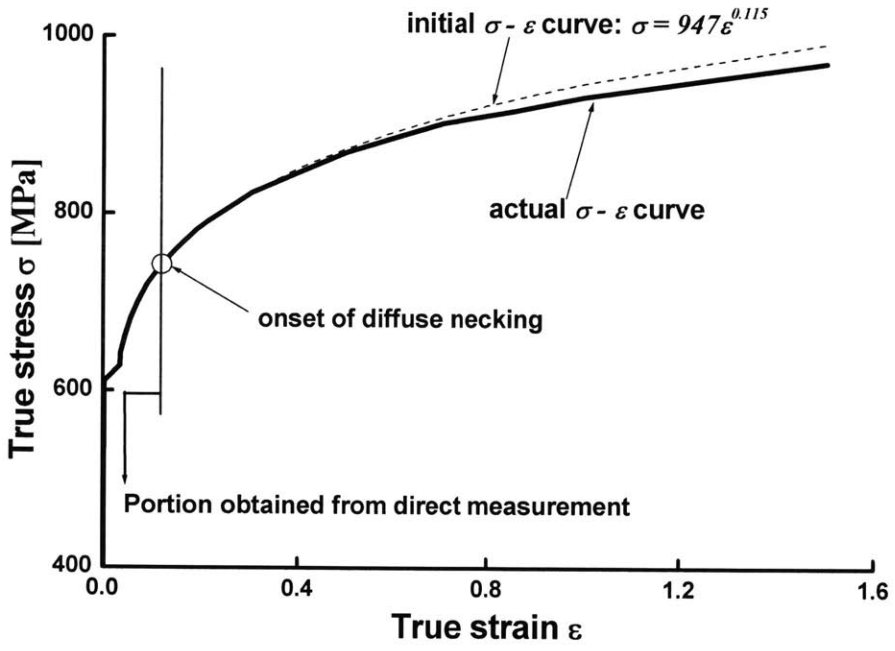

Fig. 3.4 Initially assumed and finally obtained true stress-strain curves for a steel

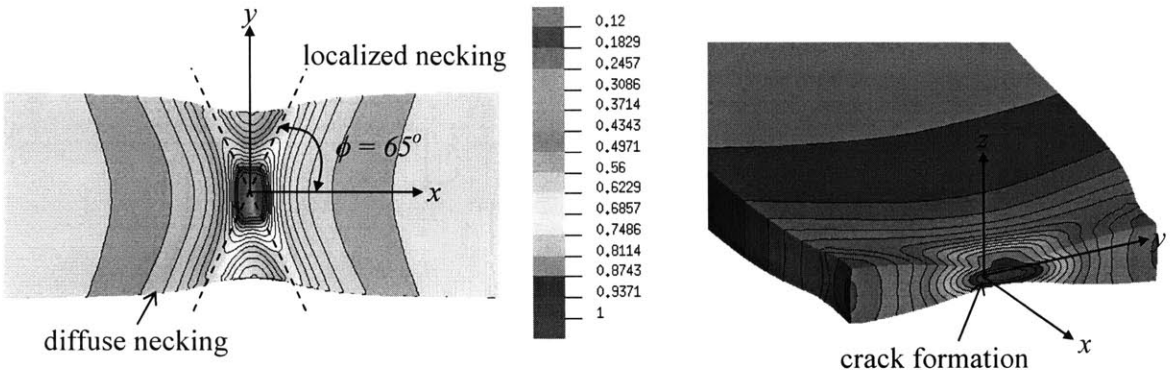

(a) top view (b) 3D view (cut through view of center)

Fig. 3.5 Numerically predicted deformation mode of a flat tensile specimen right before the fracture initiation (color coded equivalent strain contour)

3.2.2 Evaluation of critical damage parameters for fracture

In order to calibrate the postualted fracture criterion i.e. that is to find the critical damage value of material D_c in Eq. (2.4), the histories of the accumulated equivalent plastic strain and the stress triaxiality during deformation at the potential fracture point are obtained by numerical simulation. Specifically, plots of the equivalent strain and stress triaxiality versus cross-head displacement were constructed. Shown in Fig. 3.6 is history of equivalent strain at the center of specimen. From that figure, it is possible to determine the magnitude of equivalent strain at fracture $(\mathbf{b} = \bar{\varepsilon}_f = 1.01)$ because the displacement to fracture $(\delta_f = 5.97mm)$ is known from test. There is a visible change in the rate of growth of strain at the initiation point of the diffuse necking (δ_d = *3.12mm*). Note that the onset of diffuse neck formation on the force-displacement diagram (Fig. 3.2) corresponds to the maximum force. This is indicated by open circle in Fig. 3.2.

The history of triaxilaty function with an equivalent strain as an independent variable is shown in Fig. 3.7. The area under those curves over the range from zero to the maximum equivalent strain to fracture represent the magnitude of calibration constant D_c. It is seen that most of the "damage" in the center of the specimen is produced after formation of the localized neck. The complete procedure of convention calibration method is schematically illustrated in Fig. 3.8.

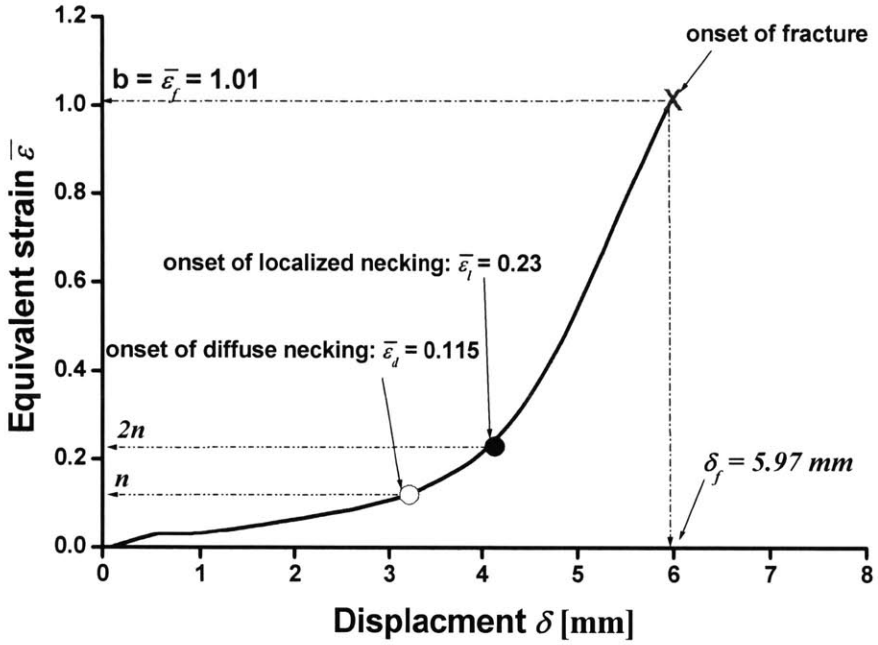

Fig. 3.6 Growth of the equivalent strain at the critical point of crack formation (strain hardening exponent $n = 0.115$)

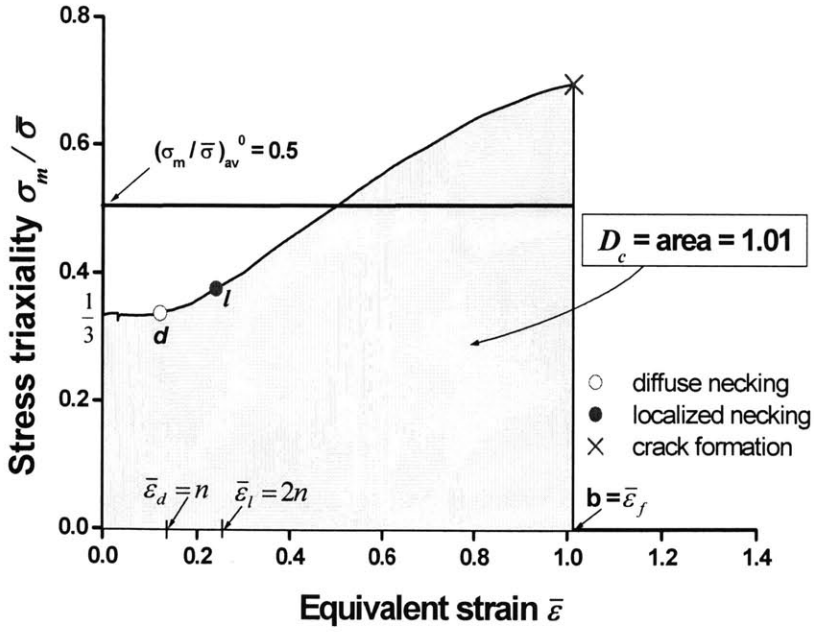

Fig. 3.7 Evolution of stress triaxiality at the critical point of crack formation (strain hardening exponent $n = 0.115$)

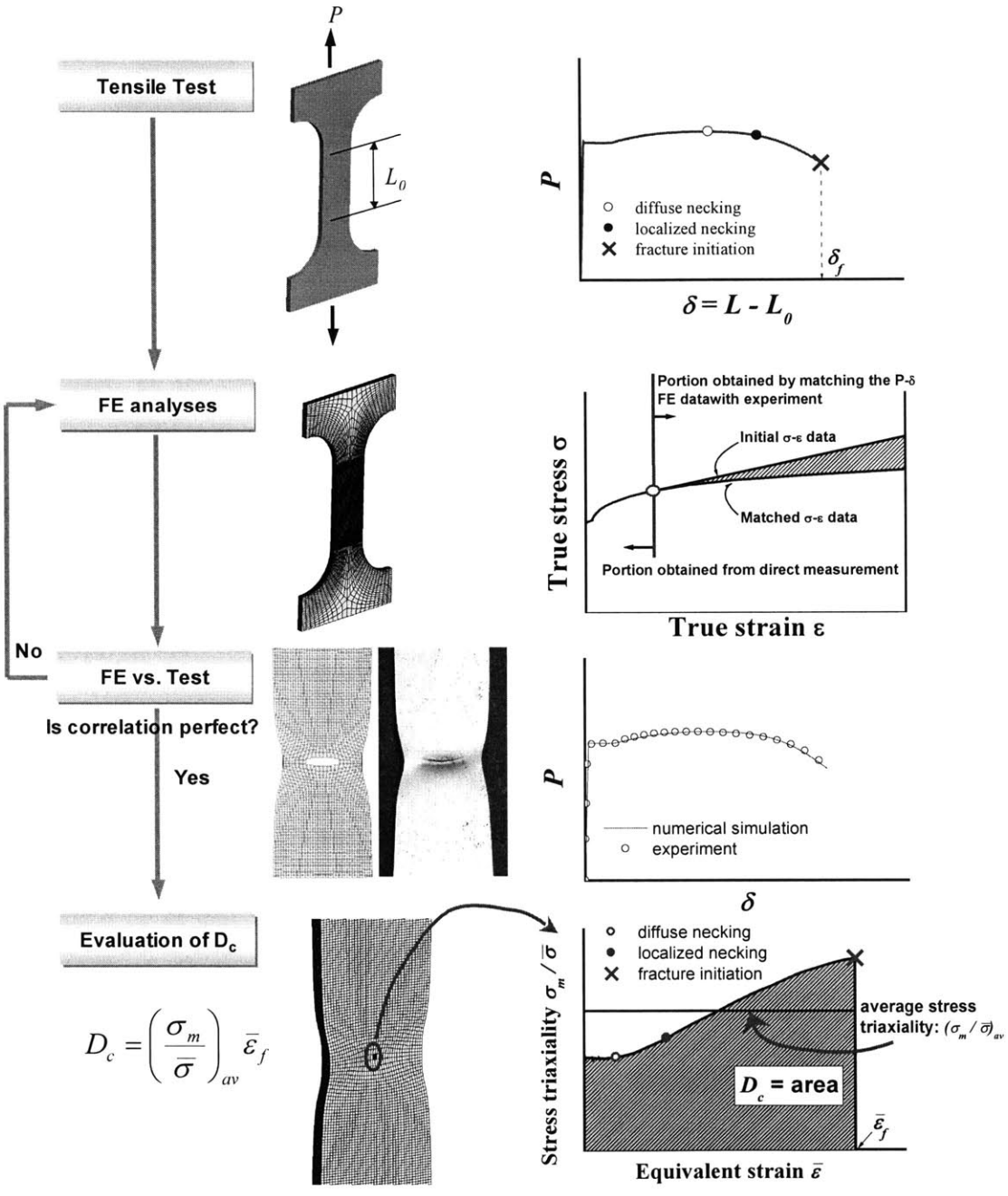

Fig. 3.8 Schematic illustration of the conventional calibration procedure

3.2.3 Shortcoming of the conventional calibration method

As shown in Fig. 3.8, the conventional method is a time consuming procedure that may be difficult to perform in the industrial environment. Besides, when using the conventional method, it appeared that the finite element solutions of post-localization responses suffer from an unwanted effect of mesh size, which is difficult to remove. Its effect depends on the material and geometries. For example, the magnitude of critical damage value D_c of A710 steel was shown to be a decreasing function of the normalized mesh size, see Fig. 3.9. A full study on the mesh size effect on the formation and propagation of cracks is presented in Chapter 5.

A simplified procedure is proposed to eliminate a need for the numerical simulation and determine all relevant fracture parameters in terms of the measurable quantities. Those measurable quantities are hardening exponent (n) and the relative area reduction inside the neck at the instant of fracture. The procedure is conceptually simple but involves many transformation and algebraic manipulations, as discussed in next Section 3.3.

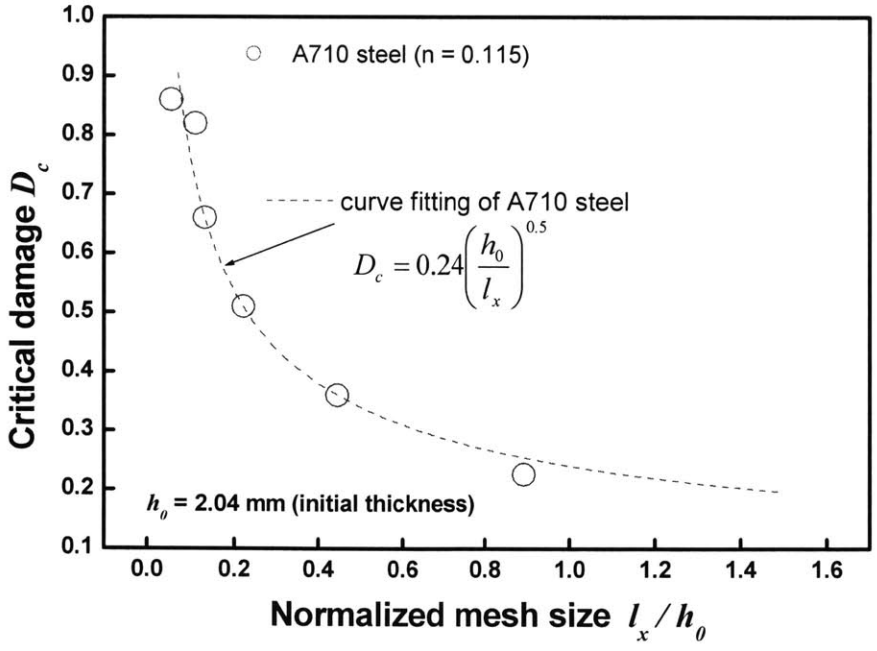

Fig. 3.9 Plots of critical damage value D_c as a function of normalized mesh size l_x / h_0 in the tensile loading direction for A710 steel material (conventional calibration method)

3.3 Quick fracture calibration for industrial use

In this section, a much simpler calibration method that bypasses a need for numerical modeling and simulations is proposed. This new approach is based on approximate closed form solutions for triaxiality in the critical locations as a function of the equivalent strain. Two types of specimens most commonly used in all testing labs are considered. In the flat dog-bone specimen which satisfies plane stress condition, three phases are taken into account that is pre-necking, diffuse necking, and localized necking. Fracture occurs within the localized neck under the transverse plane strain condition. In round specimen, the state of stress is axi-symmetric and fracture occurs in the middle of neck. In both cases the critical damage parameters associated with the BW fracture criterion are determined in terms of the exponent of a power stress strain law and the strain to fracture. Both parameters are directly measurable from single tensile test on the unnotched specimen where the true strain to fracture can be calculated from the measured final area reduction. Furthermore, a new approach for the construction of fracture envelope in a wide range of stress triaxiality is proposed.

3.3.1 Calibration from flat tensile specimens

Consider a tensile test of a flat sheet with a gauge section of initial length L_0, thickness h_0, and width w_0, respectively. The specimen is subjected to an axial tensile load P as shown in Fig. 3.10. A set of typical plots of global tensile load-axial displacement and histories of local stress and strain at the center of the specimen is schematically illustrated in Fig. 3.11. The deformation and the fracture of the flat tensile specimen can be divided into three distinct phases. Up to the load maximum, point d with symbol (○), deformation is uniform and the stress state is uniaxial (see phase A in Fig. 3.11(a)). After the load maximum which is the onset of diffuse necking, the stress state throughout the gauge section is no longer uniaxial or uniform. From this point on, a plastic deformation localizes in the zone of the diffuse necking until a localized neck develops (phase B). After the onset of the localized necking (point l with symbol(●)), the local stress, strain, and resulting accumulated damage suddenly increases in the center of the specimen. As the load drops, a crack initiates from the center and propagates at an inclined angle ϕ to the loading axis (phase C).

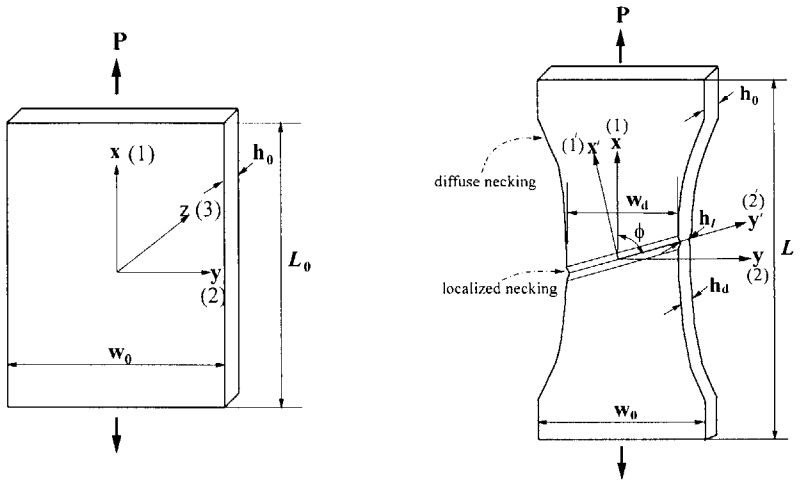

(a) initial (b) after necking

Fig. 3.10 Initial and deformed geometry of the uniaxial tensile deformation of a flat sheet

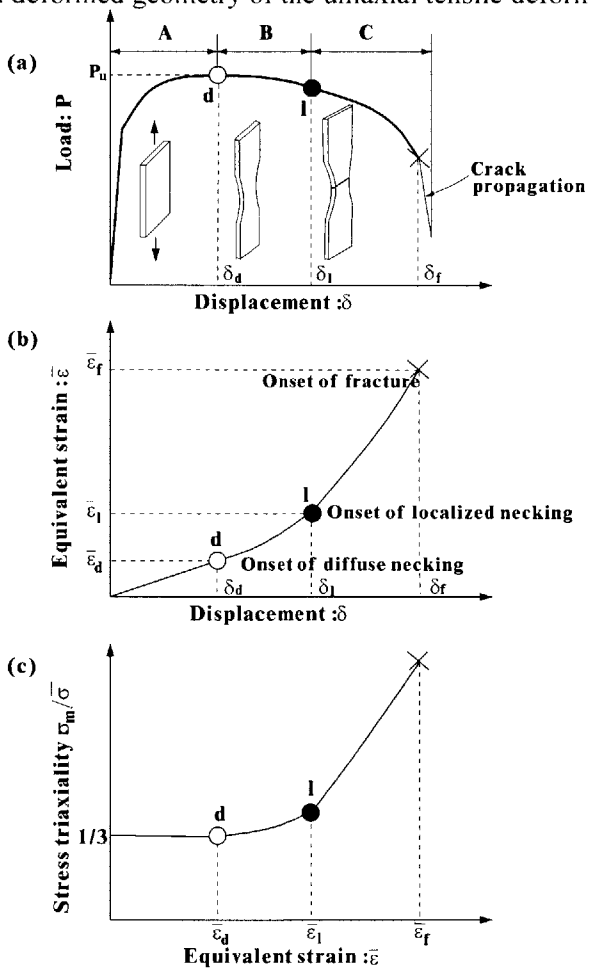

Fig. 3.11 Schematic diagrams of various responses for flat tensile specimens: (a) load-displacement, (b) equivalent plastic strain at the center of the specimen – displacement, and (c) stress triaxiality at the center of the specimen – equivalent plastic strain.

3.3.1.1 Theoretical prediction of necking in flat tensile specimen

An important mechanism that precipitates ductile fracture in a sheet metal is the onset of plastic instability in the form of necking prior to ductile fracture. The analysis for necking under the assumption of plane stress (i.e. $\sigma_3 = 0, \gamma = 0$) was performed by Hill (1952) and McClintock and Zheng (1993). It was further assumed that the material strain hardens isotropically according to the power law

$$\bar{\sigma} = K\bar{\varepsilon}^n \tag{3.1}$$

where K and n are the strength coefficient and the hardening exponent of the material, respectively. The condition for a diffuse necking which extends along the sheet by a distance of the order of the width w_0, due to Considere (1885) states

$$\frac{1}{\bar{\sigma}}\frac{d\bar{\sigma}}{d\bar{\varepsilon}} = 1 \tag{3.2}$$

The quantity on the left hand side is the non-dimensional strain hardening which is equal to $n/\bar{\varepsilon}$ under the assumption of power law hardening. Assuming a proportional loading up to the current state with constant strain ratio, the strain increments can in fact be expressed in terms of total strains. Referring to Eqns. (2.14) and (3.2), the corresponding equivalent and axial strains in the diffuse necking phase of the uniaxial tensile test ($\alpha = -0.5$) are

$$\bar{\varepsilon}_d = \varepsilon_{1d} = n \tag{3.3}$$

If the strain is further increased, localized necking may occur within a distance along the sheet that is of the order of the sheet thickness, as shown in Fig. 3.10(b). Hill (1952) postulated that the local through-thickness neck develops when the deformation-induced hardening associated with stress is balanced by the geometrical softening within the neck – i.e. thinning. In a biaxial stress state, the onset of localized necking is possible along a characteristic line of zero extension in the plane of the sheet ($\varepsilon_{y'} = \varepsilon_{2'} = 0$, Fig. 3.10(b)) and the angle of inclination of the neck to the direction of tensile axis being $\phi = \tan^{-1}\sqrt{(-1/\alpha)}$. The above postulate leads to the following condition for localized necking

$$\frac{d\sigma_1}{\sigma_1} = \frac{d\sigma_2}{\sigma_2} = d\varepsilon_1 + d\varepsilon_2 \tag{3.4}$$

From Eq. (2.7) with the assumption of plane stress (i.e. $\sigma_3 = 0$), the increment of the yield function becomes

$$d\bar{\sigma} = \frac{\partial \bar{\sigma}}{\partial \sigma_1} d\sigma_1 + \frac{\partial \bar{\sigma}}{\partial \sigma_2} d\sigma_2 \tag{3.5}$$

Substituting the condition for localized necking, Eq. (3.4), into Eq. (3.5) and invoking Eq. (2.8) gives the following relation:

$$d\bar{\sigma} = \left(\frac{\partial \bar{\sigma}}{\partial \sigma_1} + \frac{\partial \bar{\sigma}}{\partial \sigma_2} \right) \bar{\sigma} d\bar{\varepsilon} \tag{3.6}$$

From Eq. (2.7) with $\sigma_3 = 0$,

$$\left\{ \begin{array}{l} \dfrac{\partial \bar{\sigma}}{\partial \sigma_1} = \dfrac{2\sigma_1 - \sigma_2}{2\sqrt{\sigma_1^2 - \sigma_1\sigma_2 + \sigma_2^2}} \\ \dfrac{\partial \bar{\sigma}}{\partial \sigma_2} = \dfrac{2\sigma_2 - \sigma_1}{2\sqrt{\sigma_1^2 - \sigma_1\sigma_2 + \sigma_2^2}} \end{array} \right\} \tag{3.7}$$

Introducing the principal stress ratio $\beta \equiv \sigma_2 / \sigma_1$, the condition for localized necking, Eq. (3.6), becomes

$$\frac{1}{\bar{\sigma}} \frac{d\bar{\sigma}}{d\bar{\varepsilon}} = \frac{1+\beta}{2\sqrt{1-\beta+\beta^2}} \tag{3.8}$$

The corresponding equivalent strain is then

$$\bar{\varepsilon}_l = \frac{2n\sqrt{1-\beta+\beta^2}}{1+\beta} = \frac{2n\sqrt{1+\alpha+\alpha^2}}{\sqrt{3}(1+\alpha)} \tag{3.9}$$

In the uniaxial tensile test ($\beta = 0, \alpha = -0.5$), the equivalent and axial strains at the region of localized necking are

$$\bar{\varepsilon}_l = \varepsilon_{1l} = 2n \tag{3.10}$$

and $\phi = \tan^{-1}\sqrt{2} = 54.7^o$.

Once localized neck forms, all the plastic strain is confined to the necking region. Finally, the growing strain in the band of localized neck is accompanied by a process of growth and coalescence of internal voids, leading to a fracture in the specimen. Hence, local stress and strain states at the critical location should be further investigated for fracture prediction. This will be treated in the subsequent section.

3.3.1.2 Analytical approximation of damage parameters in flat tensile specimen

Critical damage value in terms of equivalent strain and hardening exponent As already shown in Fig. 3.11, three phases are distinguished in the tensile test of flat specimen: phase A, phase B, and phase C. In the present analytical approximation on the critical damage value D_c calibrated from flat specimen, the variation in thickness of sheet is necessarily assumed to be small enough so that plane stress condition (i.e. $\sigma_3 = 0, \gamma = 0$) apply. Accordingly, substituting $\gamma = 0$ into Eqns. (2.13) and (2.17), the stress triaxiality in the case of plane stress is expressed in terms of strain ratio α or stress ratio β:

$$\frac{\sigma_m}{\bar{\sigma}} = \frac{1}{3}\frac{1+\beta}{\sqrt{1-\beta+\beta^2}} = \frac{1}{\sqrt{3}}\frac{1+\alpha}{\sqrt{1+\alpha+\alpha^2}} \tag{3.11}$$

Expressing $\sigma_m / \bar{\sigma}$ in terms of the strain ratio α (Eq. (3.11)) and $d\bar{\varepsilon}$ in terms of the strain ratio α and $d\varepsilon_1$ (Eq. (2.14)), the critical damage value D_c defined by Eq. (2.4) becomes

$$D_c = \int_0^{\bar{\varepsilon}_f} \frac{\sigma_m}{\bar{\sigma}} d\bar{\varepsilon} = \int_0^{\varepsilon_{1f}} \frac{2}{3}(1+\alpha) d\varepsilon_1 \tag{3.12}$$

In the uniaxial tensile test of sheet metal, diffuse and localized neckings occur before fracture (see Fig. 3.11). Hence the integration is performed in three different phases so that

$$D_c = \int_0^{\varepsilon_{1d}} \frac{2}{3}(1+\alpha_A) d\varepsilon_1 + \int_{\varepsilon_{1d}}^{\varepsilon_{1l}} \frac{2}{3}(1+\alpha_B) d\varepsilon_1 + \int_{\varepsilon_{1l}}^{\varepsilon_{1f}} \frac{2}{3}(1+\alpha_C) d\varepsilon_1 \tag{3.13}$$

where α_A, α_B, and α_C are the strain ratios in phases A, B, and C, respectively. Once necks form, the strain path is far more complex than that which prevailed up to necking. Hence, slight complications arise in the above calculation. In the plastic forming of crack-free sheet metal, experiments show that localized necks are perpendicular to the major in-plane strain ε_1 and that they grow as plane strain necks, since minor in-plane strain ε_2 remains constant and $d\varepsilon_2 = 0$ (Embury and LeRoy, 1977; Marciniak, 1978; Atkins, 1996). Here, the following assumptions about the strain paths during neck and crack formations are further made: (1) strain paths are piece-wisely linear, that is, strain ratios are constant for each phase; (2) stress and strain states are uniform up to the onset of localized necking - i.e. $\alpha_A = \alpha_B = 0.5$; (3) both plane stress and transverse plane strain deformation ($\alpha_C = 0$) is assumed after the onset of localized necking. This form of strain path is analogous to that formed in a sheet metal forming (Embury and LeRoy, 1977; Atkins, 1996; Lee

and Wierzbicki, 2003). Figures 3.12 and 3.13, respectively, show the postulated strain and stress paths at the center of the flat specimens from the beginning to the instant of fracture. The evolution of stress triaxiality corresponding to the assumed loading path is shown in Fig. 3.14 as a function of equivalent strain. Using the above piece-wise linear loading trajectory in the space of principal strains together with the axial strains to the neckings for the power law material (Eqns. (3.3) and (3.10)), Eq. (3.13) takes the form

$$D_c = \frac{2}{3}\left(\varepsilon_{1f} - n\right) \tag{3.14}$$

Using Eq. (2.14) with the assumed strain paths, the relation between the accumulated equivalent and the axial strains to fracture can be obtained by

$$\int_0^{\bar{\varepsilon}_f} d\bar{\varepsilon} = \int_0^{\varepsilon_{1u}} d\varepsilon_1 + \int_{\varepsilon_{1u}}^{\varepsilon_{1f}} \frac{2}{\sqrt{3}} d\varepsilon_1 \tag{3.15}$$

since $\alpha_A = \alpha_B = 0.5$ up to the point of localized necking and $\alpha_C = 0.0$ after the localized necking. Then, Eq. (3.15) becomes

$$\bar{\varepsilon}_f = \frac{2}{\sqrt{3}}\varepsilon_{1f} - \frac{2n}{\sqrt{3}}\left(2 - \sqrt{3}\right) \tag{3.16}$$

Solving Eq. (3.16) for ε_{1f} and substituting it into Eq. (3.14), an expression for the critical damage value in terms of equivalent strain to fracture $\bar{\varepsilon}_f$ and hardening exponent n is obtained

$$D_c = \frac{1}{\sqrt{3}}\bar{\varepsilon}_f - \frac{2n}{3}(\sqrt{3} - 1) \tag{3.17}$$

Critical damage parameters in terms of measurable quantities Using the condition of the diffuse necking (Eq. (3.3)) and the transformation from engineering to true stress-strain measures, the hardening exponent n of the power law can be determined by

$$n = \ln\left(1 + \frac{\delta_u}{L_0}\right) \tag{3.18}$$

where δ_u is the magnitude of displacement corresponding to the maximum load P_u in tensile load-displacement curve (see Fig. 3.11(a)); L_0 is an initial gauge length of tensile specimen. For the case of round tensile bars, the equivalent strain to fracture $\bar{\varepsilon}_f = \ln(A_0 / A_f)$ can be conveniently obtained by measuring the initial (A_0) and reduced (A_f) sectional area in the neck after fracture. On the other

hand, it is difficult to calculate or measure the true area of thin specimens with rectangular cross-section, which is not only a function of loading, but also depends on section's aspect ratio and plastic hardening. An approximate relation between the area reduction of minimum cross-section and the measured thickness reduction is proposed by Zhang et al. (1999) based on extensive 3-D numerical study on flat tensile specimens. However, as stated by Zhang et al. (1999), the validity of the proposed relation is only restricted to the phase B shown in Fig. 3.11(a) (i.e. diffuse necking to localized necking).

In the present study, the relation between three important damage parameters describing fracture (i.e. average stress triaxiality, equivalent plastic strain to fracture, and critical damage value) and measured thickness reduction and hardening exponent is proposed for the case of flat specimen. According to the FFLD defined by Eq. (2.25), the critical damage value can be also obtained from the constant thickness strain to fracture and given by

$$D_c = \frac{2}{3}\ln\frac{h_0}{h_f} \tag{3.19}$$

where h_0 and h_f are respectively, the initial and reduced thickness inside the neck of flat specimen after fracture, see inserted figure in Fig. 3.15. Eq. (3.19) indicates that the cumulated damage is a linear function of thickness strain to fracture, $-\varepsilon_{3f} = \ln(h_0 / h_f)$, with constant amplitude of 2/3. The above relationship between D_c and $-\varepsilon_{3f}$ is compared in Fig. 3.15 with finite element results for various range of thickness strain. Note that the right hand side of Eq. (3.19) is used as horizontal axis in Fig. 3.15. The thickness h_0 and h_f are taken from the numerical simulations, as shown in Fig. 3.15. One can see that the agreement between numerical results and present predictions from Eq. (3.19) is within 10%.

By equating Eq. (3.17) with Eq. (3.19), the magnitude of the equivalent strain to fracture in uniaxial tension $\mathbf{b} = \bar{\varepsilon}_f$ can be expressed in terms of thickness strain and exponent n

$$\mathbf{b} = \bar{\varepsilon}_f = \frac{2}{\sqrt{3}}\ln\frac{h_0}{h_f} + \frac{2n}{\sqrt{3}}\left(\sqrt{3}-1\right) \tag{3.20}$$

In view of Eq. (2.5), the average stress triaxiality in uniaxial tension $(\sigma_m / \bar{\sigma})^0_{av} = D_c / \mathbf{b}$ is

$$\left(\frac{\sigma_m}{\bar{\sigma}}\right)^0_{av} = \frac{1}{\sqrt{3}} - \frac{2n}{3\bar{\varepsilon}_f}(\sqrt{3}-1) \tag{3.21}$$

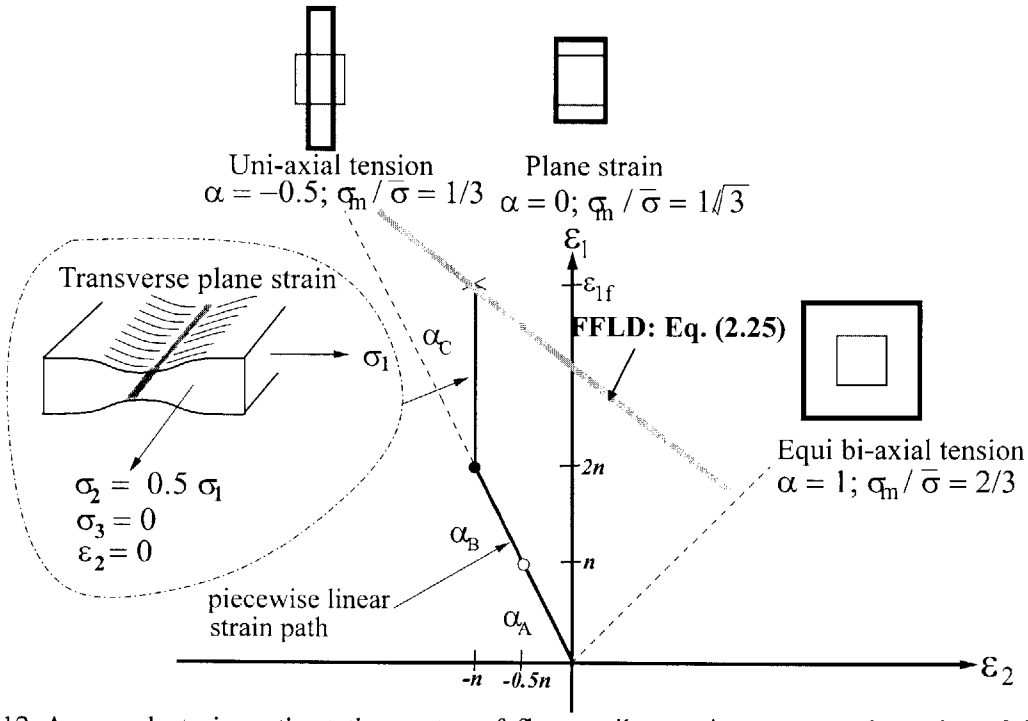

Fig. 3.12 Assumed strain path at the center of flat tensile specimen up to the point of fracture initiation. A plane strain tension ($\alpha_C = 0$) deformation is assumed after the onset of localized necking.

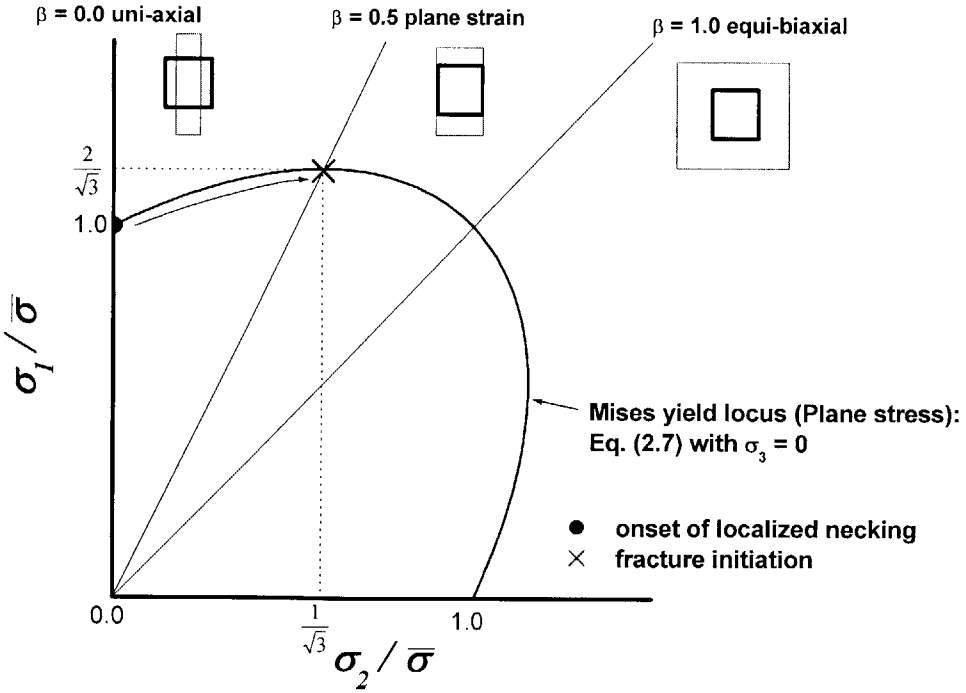

Fig. 3.13 Change of stress ratio from uniaxial to plane strain state after the onset of localized necking under plane stress condition

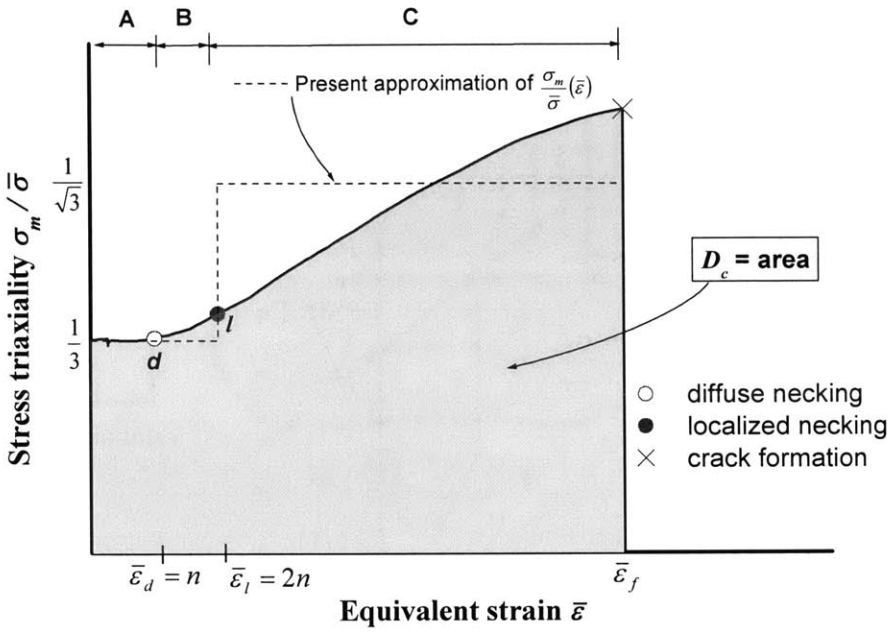

Fig. 3.14 Assumed evolution of stress triaxiality at the center of flat tensile specimen up to the point of crack formation. A plane strain tension, $(\sigma_m / \bar{\sigma})_C = 1/\sqrt{3}$, deformation is assumed after the onset of localized necking.

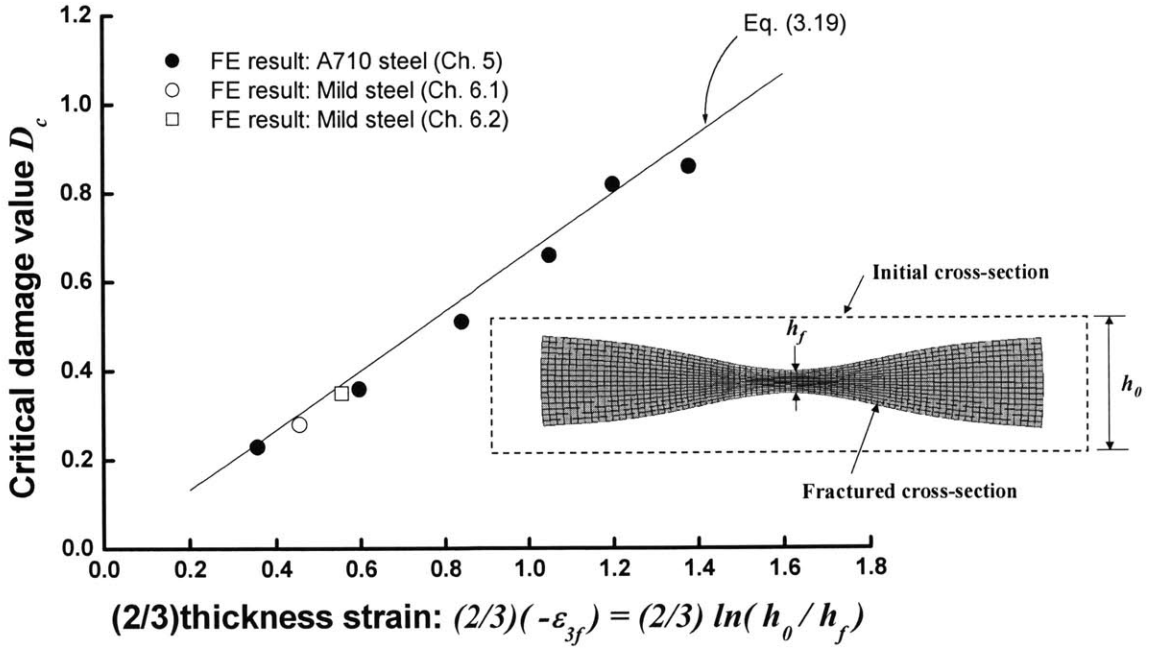

Fig. 3.15 Comparison of the critical damage value obtained from analytical approximation (Eq. (3.19)) with that from numerical simulation

3.3.2 Calibration from round tensile specimens

Similar information can also be obtained from the analysis of round specimen which develops only diffuse neck prior to fracture. The plane stress approximation is no longer valid and instead a suitably modified Bridgman analysis for axi-symmetric rod is proposed in this section.

3.3.2.1 Stress triaxiality in the neck of round tensile specimen

Consider a round bar of the initial radius a_0 subjected to an extension, see Fig. 3.16. In Fig. 3.16, $\sigma_z, \sigma_r, \sigma_\theta$ denote the axial, radial, and circumferential stresses, which are also principal stresses, a is the current radius of the minimum section and R is the radius of curvature of the neck surface. Figure 3.17 schematically illustrates various responses of the cylindrical tensile specimen including global tensile load-axial displacement plot as well as histories of local stress and strain at the center of the specimen ($r = z = 0$). Typically, two phases are distinguished in the tensile test: pre-necking (phase A) and post-necking (phase B). The cylindrical specimen begins to neck when the load attains a maximum. After the diffuse neck has formed, the stress distribution in the bar is no longer uniform and the state of stress is 3-dimensional, as shown in Fig. 3.17(c). Because of rotational symmetry, $\sigma_r = \sigma_\theta$ at the center of the specimen ($r = z = 0$). This leads to the following relation between the principal stress ratios

$$\beta = \gamma, \quad (r = z = 0) \tag{3.22}$$

Consequently, the strain ratio defined by Eq. (2.13) is always constant during the whole process of deformation, $\alpha = -0.5$, see also Fig. 3.17(d). By substituting $\beta = \gamma$ into Eq. (2.17), the stress triaxiality at the center of round tensile bar is uniquely determined by stress ratio β or γ:

$$\frac{\sigma_m}{\bar{\sigma}} = \frac{1}{3}\frac{1+2\beta}{\sqrt{1-2\beta+\beta^2}} \tag{3.23}$$

where the stress ratio $\beta \equiv \sigma_r / \sigma_z = \sigma_2 / \sigma_1$ can be expressed into two distinct phases (see Fig. 3.17(e)) according to

$$\beta = \begin{cases} \beta_A = 0, & \text{phase A } (0 \le \bar{\varepsilon} < n) \\ \beta_B > 0, & \text{phase B } (n \le \bar{\varepsilon} \le \bar{\varepsilon}_f) \end{cases} \tag{3.24}$$

Furthermore, the evolving stress triaxiality can be distinguished by the pre and post-necking phases:

$$\frac{\sigma_m}{\bar{\sigma}} = \begin{cases} \left(\frac{\sigma_m}{\bar{\sigma}}\right)_A = \frac{1}{3}, & \text{phase A } (0 \le \bar{\varepsilon} < n) \\ \left(\frac{\sigma_m}{\bar{\sigma}}\right)_B = \frac{1}{3} + \Delta\frac{\sigma_m}{\bar{\sigma}}, & \text{phase B } (n \le \bar{\varepsilon} \le \bar{\varepsilon}_f) \end{cases} \tag{3.25}$$

where $\Delta\sigma_m / \bar{\sigma}$ denotes the relative increase of stress triaxiality with respect to the uniaxial tension deformation $(\sigma_m / \bar{\sigma} = 1/3)$ in the post-necking stage.

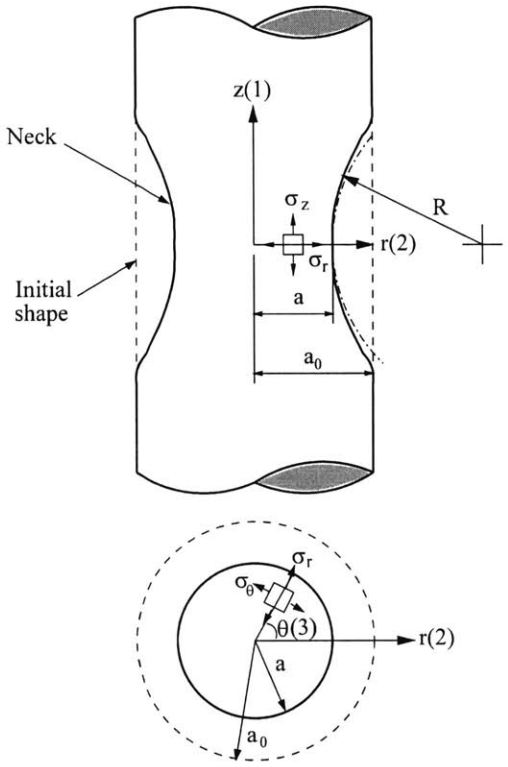

Fig. 3.16 The idealized shape of the neck in a smooth round tensile specimen showing the cylindrical coordinate system *(r, θ, z)* and the neck geometry parameters *(a, R)*

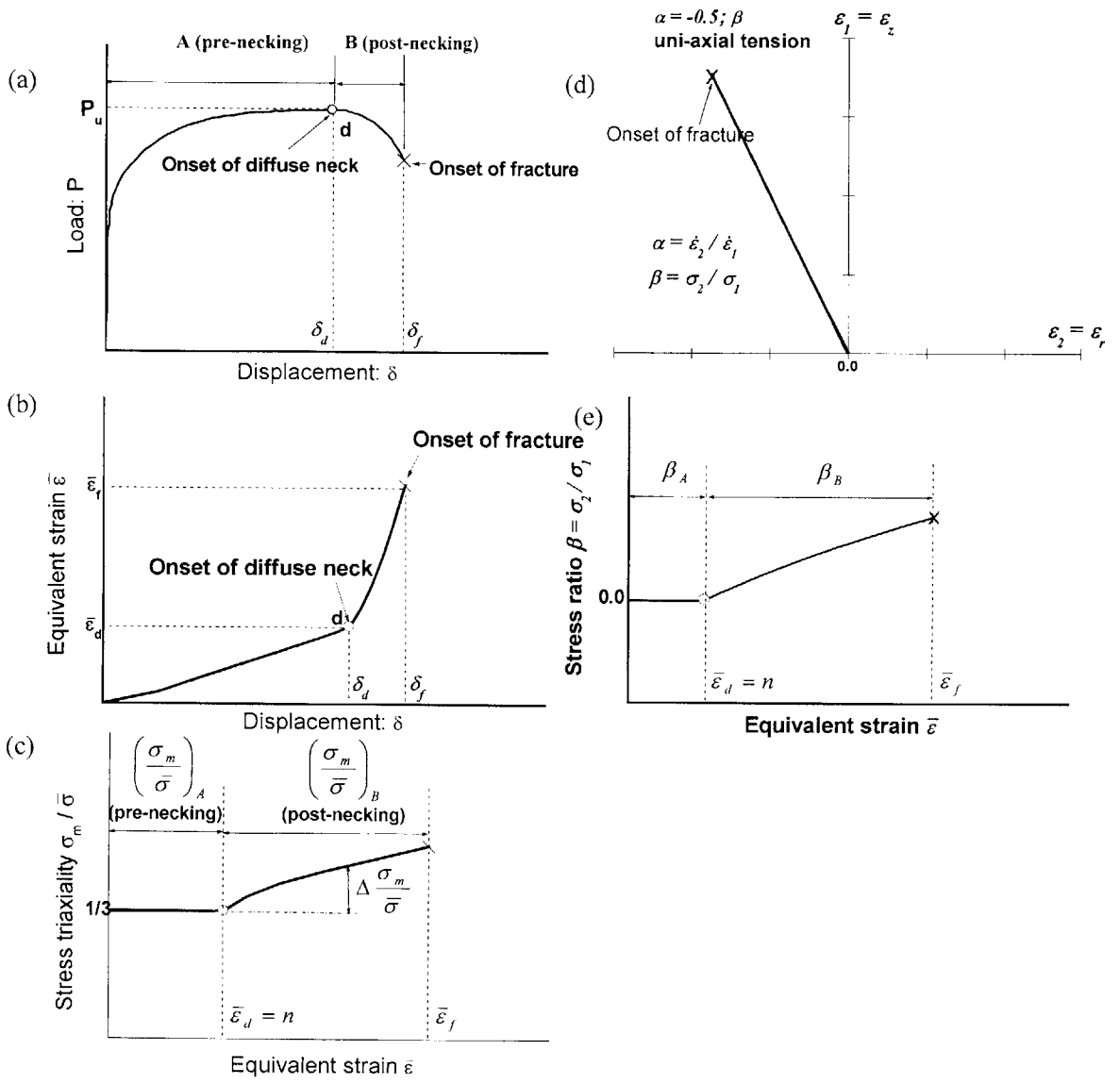

Fig. 3.17 Schematic diagrams of various responses for smooth round tensile specimens: (a) load-displacement; (b) equivalent plastic strain at the centre of the specimen – displacement; (c) stress triaxiality at the centre of the specimen – equivalent plastic strain; (d) constant path of axial and radial strains during deformation; (e) change of stress ratio $\beta \equiv \sigma_2 / \sigma_1 = \sigma_r / \sigma_z$ after the onset of diffuse necking

Stress triaxiality in terms of neck geometry parameters Bridgman (1944, 1952) proposed the approximate analysis of the local stress and strain in the plane of symmetry of the neck, which is based on the assumption that material elements are deformed uniformly over the minimum neck

section, thus giving a constant axial strain ($\varepsilon_z = \varepsilon_1 = \text{constant}$) across the neck. From this basic assumption and the postulate that the local curvature of the neck profile is constant, Bridgman derived the stress-filed equations for the minimum neck section (see Fig. 3.16) in terms of the profile radius R and the radius of minimum cross section a:

$$\frac{\sigma_z}{\bar{\sigma}} = 1 + \ln\left(\frac{a^2 + 2aR - r^2}{2aR}\right) \tag{3.26}$$

$$\frac{\sigma_r}{\bar{\sigma}} = \frac{\sigma_\theta}{\bar{\sigma}} = \frac{\sigma_z}{\bar{\sigma}} - 1 = \ln\left(\frac{a^2 + 2aR - r^2}{2aR}\right) \tag{3.27}$$

The post-necking stress triaxilaity $(\sigma_m / \bar{\sigma})_B$ in the mostly stresses point of the bar ($r = z = 0$) can be calculated from Eqns. (3.26) and (3.27)

$$\left(\frac{\sigma_m}{\bar{\sigma}}\right)_B = \frac{1}{3} + \ln\left(1 + \frac{a}{2R}\right) \tag{3.28}$$

Several authors in the past studied the correctness of Bridgman approximate solution, see for example Needleman (1972), Clausing (1970), and Norris et al. (1978). Recently, Wierzbicki and Bao (2004) performed a detail finite element analysis for all parameters inside the neck including the neck geometry ratio (a/R) and stress triaxiality as a function of equivalent strain. The simulation was carried out by means of *ABAQUS/Explicit* with 1778 axi-symmetric elements for 1045 steel bar. The finite element results showed that the Bridgman analysis gives a qualitatively correct approximation to the distribution of stain and stress across the neck. However, it was also shown that the stress triaxiality at the center of the neck from Bridgman's solution (Eq. (3.28)) underestimates the numerically obtained value and leads to a large, up to 30% error, with increasing neck geometry ratio (a/R), Wierzbicki and Bao, (2004). According to Wierzbicki and Bao (2004), the dependence of the stress triaxiality on the parameter a/R can be fit by the same function as in the Bridgman formula but with larger amplitude of the second term (i.e. $\Delta\sigma_m / \bar{\sigma}$)

$$\left(\frac{\sigma_m}{\bar{\sigma}}\right)_B = \frac{1}{3} + \sqrt{2}\ln\left(1 + \frac{a}{2R}\right) \tag{3.29}$$

Stress triaxiality in terms of post-necking strain The difficult part in the application of the stress triaxiality given by Eq. (3.28) or (3.29) is the determination of the neck geometry parameter a/R, which involves a measurement of the root radius R of the formed neck at each stage, in addition to the radius of the minimum section. These quantities are difficult to measure during a test. Therefore,

Bridgman presented an empirical expression for the neck geometry parameter (as stated by Hill, 1948)

$$\frac{a}{R} = \sqrt{\bar{\varepsilon} - n} \tag{3.30}$$

which indicates that the neck geometry ratio is primarily function of the reduction in area ($\bar{\varepsilon} = \ln(A_0 / A)$) and incipient diffuse necking strain ($\bar{\varepsilon}_d = n$). The $\bar{\varepsilon} - n$ is so-called post-necking strain. The above equation has now been examined for 1045 steel bar and compared with numerical results in Fig. 3.18. As can be seen in this figure, the empirical relation given by Eq. (3.30) reveals up to 93% error, as compared to more exact numerical simulation results.

In the present paper, the evolving neck geometry is better fitted by the following analytical function, which leads to a maximum 10% error

$$\frac{a}{R} = 0.68(\bar{\varepsilon} - n)^{0.8} \tag{3.31}$$

By using the second term of Eq. (3.29) together with Eq. (3.31), a closed form solution for the variation in the stress triaxiality at the center of neck, as a tension deformation proceeds, can be obtained and this has the form:

$$\Delta \frac{\sigma_m}{\bar{\sigma}} = \sqrt{2} \ln\left[1 + 0.34(\bar{\varepsilon} - n)^{0.8}\right] \tag{3.32}$$

The above Eq. (3.32) can be further approximated by more simple form

$$\Delta \frac{\sigma_m}{\bar{\sigma}} = 0.4(\bar{\varepsilon} - n)^{0.8} \tag{3.33}$$

For the case of Bridgman analysis, Eqns. (3.28) and (3.30) give

$$\Delta \frac{\sigma_m}{\bar{\sigma}} = \ln\left[1 + \frac{1}{2}\sqrt{\bar{\varepsilon} - n}\right] \tag{3.34}$$

The analytically approximated $\Delta\sigma_m / \bar{\sigma}$ from Eqns. (3.33) and (3.34) are compared with numerically obtained results for two different types of material in Fig. 3.19. The accuracy of the present approximation (Eq. (3.33)) has been proved.

By substituting Eq. (3.33) into Eq. (3.25), the closed form solution for the stress triaxiality at the center of round tensile specimen during the whole process of deformation becomes

$$\frac{\sigma_m}{\bar{\sigma}} = \begin{cases} \left(\frac{\sigma_m}{\bar{\sigma}}\right)_A = \frac{1}{3}, & \text{phase A } (0 \le \bar{\varepsilon} < n) \\ \left(\frac{\sigma_m}{\bar{\sigma}}\right)_B = \frac{1}{3} + 0.4(\bar{\varepsilon} - n)^{0.8}, & \text{phase B } (n \le \bar{\varepsilon} \le \bar{\varepsilon}_f) \end{cases} \tag{3.35}$$

The evolution of $\sigma_m / \bar{\sigma}$ with the equivalent strain predicted by Eq. (3.35) is shown in Fig. 3.20 along with numerical results from Wierzbicki and Bao (2004). Good correlation between two predictions can be observed.

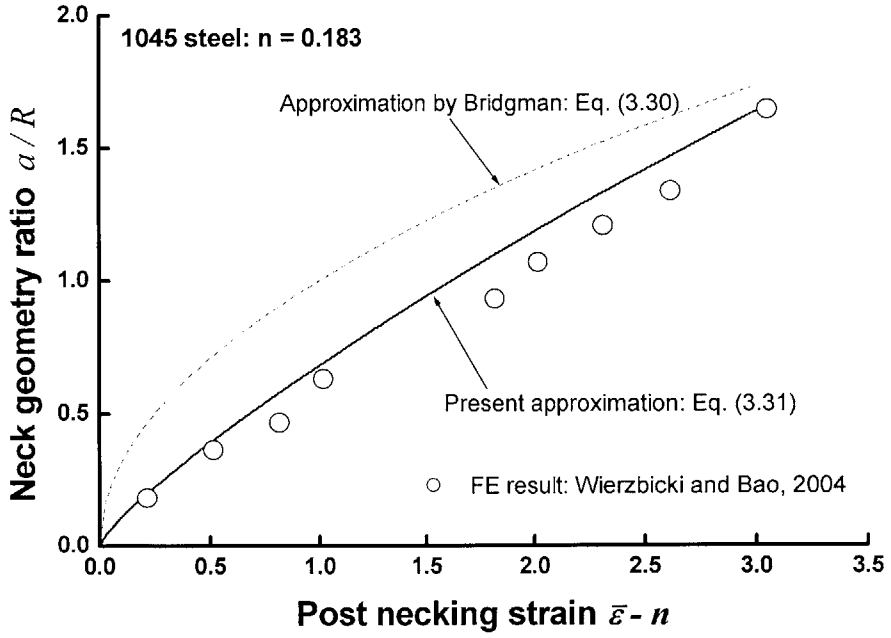

Fig.3.18 Neck geometry ratio (a/R) versus post necking strain for 1045 steel bar

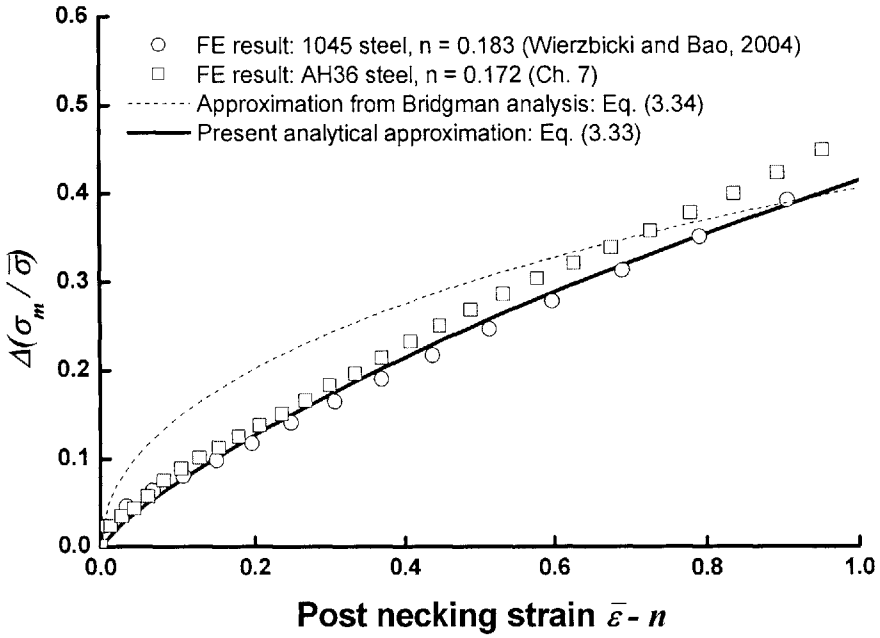

Fig. 3.19 Relative increase of stress triaxiality $\Delta\sigma_m/\bar{\sigma}$ versus post necking strain

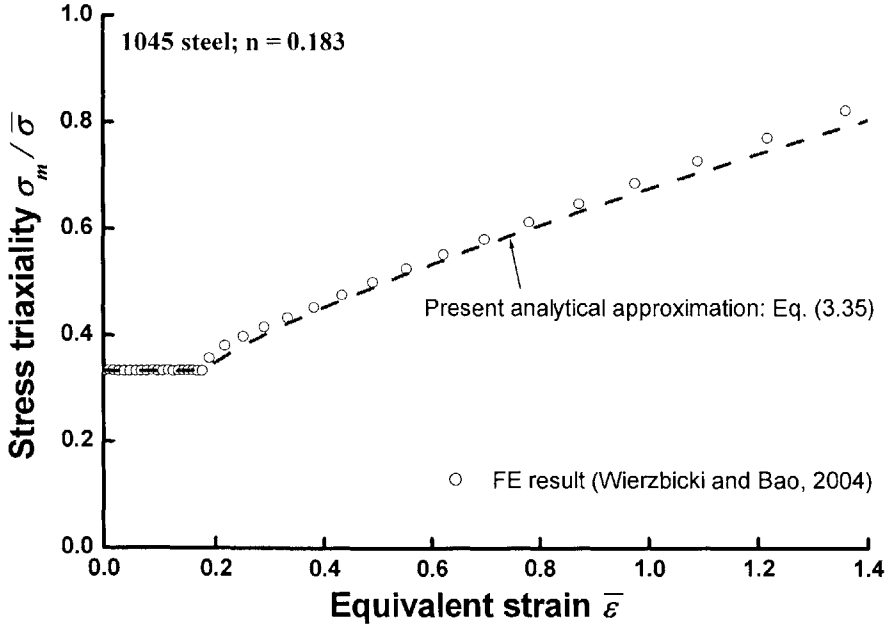

Fig. 3.20 Evolution of stress triaxiality at the center of round specimen as a function of equivalent strain obtained from numerical and present analytical results

3.3.2.2 Analytical approximation of damage parameters in round tensile specimen

In the uniaxial tensile test of round bar, the integration of Eq. (2.4) could be performed along the pre and post necking phases so that

$$D_c = \int_0^n \left(\frac{\sigma_m}{\bar{\sigma}}\right)_A d\bar{\varepsilon} + \int_n^{\bar{\varepsilon}_f} \left(\frac{\sigma_m}{\bar{\sigma}}\right)_B d\bar{\varepsilon} \tag{3.36}$$

Substituting Eq. (3.35) into the integrand of Eq. (3.36) leads to the following final expression for the critical damage value

$$D_c = \frac{\bar{\varepsilon}_f}{3} + 0.22(\bar{\varepsilon}_f - n)^{1.8} \tag{3.37}$$

The constant strain ratio (α = -0.5) at the center of round bar gives

$$\mathbf{b} = \bar{\varepsilon}_f = \varepsilon_{1f} = 2\ln\frac{a_0}{a_f} \tag{3.38}$$

where a_0 is the initial radius and a_f is the reduced radius of the minimum section after fracture. Then, average stress triaxiality is

$$\left(\frac{\sigma_m}{\bar{\sigma}}\right)_{av}^{0} = \frac{1}{3} + \frac{0.22}{\bar{\varepsilon}_f}(\bar{\varepsilon}_f - n)^{1.8} \tag{3.39}$$

This completes the calibration process (determination of the equivalent strain to fracture $\mathbf{b} = \bar{\varepsilon}_f$, average stress triaxiality $(\sigma_m/\bar{\sigma})_{av}^{0}$, and critical damage value D_c in uniaxial tension) in the range of high stress triaxiality ($\sigma_m/\bar{\sigma} > 1/3$). Besides the above three parameters, the position of the remaining branches of the BW fracture locus depends on the parameter **a**, according to Eq. (2.6). Note that the parameter **a** denotes the magnitude of critical fracture strain in pure shear (i.e. $\mathbf{a} = \bar{\varepsilon}_f(\sigma_m/\bar{\sigma} = 0 \; or \; \alpha = -1)$). The determination of the **a** is discussed in next Section.

3.3.3 Calibration from shear tests

The parameter (**a**) can be obtained either from the shear test, which is difficult to perform, or more conveniently, from the hypothesis of the maximum shear stress fracture condition: $\tau_{max} = (\tau_{max})_f$, where $\tau_{max} = \max[(\sigma_1 - \sigma_2)/2, (\sigma_1 - \sigma_3)/2, (\sigma_2 - \sigma_3)/2]$. From the comparative study of the seven fracture criteria presented in Chapter 2.3, it was found that the maximum shear

stress criterion is very close to the empirically determined BW fracture locus in the intermediate range of stress triaxiality (branch II, $0 \le \sigma_m / \bar{\sigma} \le 1/3$). This can be clearly observed from Figs. 3.21 and 3.22 where those two fracture criteria are compared in the space of the principal stress and in the mixed space of the equivalent strain and the stress triaxiality, resectively. In order to calculate the parameter **a**, the following assumptions are introduced: (1) material follows the special case of plane stress Mises plasticity ($\gamma = 0$); (2) the constitutive relationship imposed for the material model is governed by power law relation (i.e. $\bar{\sigma} = K\bar{\varepsilon}^n$); (3) the stress or strain components keep constant ratios (proportional loading); (4) the calibration constant for the maximum shear stress criterion $(\tau_{\max})_f$ is determined from the calculated final value of uniaxial stress to fracture σ_{1f}^0, which leads to $(\tau_{\max})_f = \sigma_{1f}^0 / 2$.

Based on the above assumptions, the maximum shear stress fracture criterion is represented in the space of principal stress (see dashed line in Fig. 3.21):

$$\sigma_{1f} = \begin{cases} \sigma_{1f}^0, & branch\ I(-1/2 < \alpha \le 1;\ 1/3 < \sigma_m / \bar{\sigma} \le 2/3) \\ \sigma_{1f}^0 \dfrac{2+\alpha}{1-\alpha}, & branch\ II(-1 \le \alpha \le -1/2;\ 0 \le \sigma_m / \bar{\sigma} \le 1/3) \\ \sigma_{1f}^0 \dfrac{2+\alpha}{1-\alpha}, & branch\ III(-2 \le \alpha < -1/2;\ -1/3 \le \sigma_m / \bar{\sigma} < 1/3) \end{cases} \tag{3.40}$$

Referring to Eq. (3.11), the stress triaxiality $\sigma_m / \bar{\sigma}$ can be determined from the strain ratio α. From Eqns. (2.13) and (2.16) with the plane stress condition ($\gamma = 0$), an alternative form for the principal stress σ_1 is available

$$\sigma_1 = \bar{\sigma} \frac{2+\alpha}{\sqrt{3}\sqrt{1+\alpha+\alpha^2}} \tag{3.41}$$

Substituting Eq. (3.40) into Eq. (3.41), the effective stress to fracture can be described as shown below

$$\bar{\sigma}_f = \begin{cases} \sigma_{1f}^0 \dfrac{\sqrt{3}\sqrt{1+\alpha+\alpha^2}}{1-\alpha}, & branch\ I(-1/2 < \alpha \le 1) \\ \sigma_{1f}^0 \dfrac{\sqrt{3}\sqrt{1+\alpha+\alpha^2}}{2+\alpha}, & branch\ II(-1 \le \alpha \le -1/2) \\ \sigma_{1f}^0 \dfrac{\sqrt{3}\sqrt{1+\alpha+\alpha^2}}{2+\alpha}, & branch\ III(-2 \le \alpha < -1/2) \end{cases} \tag{3.42}$$

From the assumed power law relation, the effective strain to fracture is

$$\bar{\varepsilon}_f = \left(\frac{\bar{\sigma}_f}{K} \right)^{\frac{1}{n}} \tag{3.43}$$

Eq. (3.43) gives an alternative expression for the critical strain to fracture in uniaxial tension (**b**), which corresponds to σ_{1f}^0

$$\mathbf{b} = \bar{\varepsilon}_f = \left(\frac{\sigma_{1f}^0}{K} \right)^{\frac{1}{n}} \tag{3.44}$$

Applying Eqns. (3.42) and (3.44) to (3.43), the equivalent strain to fracture can be expressed for a wide range of strain ratio or stress triaxiality:

$$\bar{\varepsilon}_f = \begin{cases} \mathbf{b}\left(\dfrac{\sqrt{3}\sqrt{1+\alpha+\alpha^2}}{2+\alpha} \right)^{\frac{1}{n}}, & branch\ I(-1/2 < \alpha \le 1) \\ \mathbf{b}\left(\dfrac{\sqrt{3}\sqrt{1+\alpha+\alpha^2}}{1-\alpha} \right)^{\frac{1}{n}}, & branch\ II(-1 \le \alpha \le 1) \\ \mathbf{b}\left(\dfrac{\sqrt{3}\sqrt{1+\alpha+\alpha^2}}{1-\alpha} \right)^{\frac{1}{n}}, & branch\ III(-2 \le \alpha < -1) \end{cases} \tag{3.45}$$

The fracture envelope given by Eq. (3.45) is shown as dashed line in Fig. 3.22. Substituting $\alpha = -1$ into the second equation of Eq. (3.45) yieds the critical fracture strain in pure shear ($\mathbf{a} = \bar{\varepsilon}_f(\alpha = -1)$):

$$\mathbf{a} = \mathbf{b}\left(\frac{\sqrt{3}}{2} \right)^{\frac{1}{n}} \tag{3.46}$$

which indicates that the parameter **a** is related to the fracture strain in uniaxial tension (**b**) and hardening exponent (n). The above relationship between **a** and **b**, which is a unique function of exponent n, is plotted for a wide range of n in Fig. 3.23. As can be seen from this figure, the range of the relative magnitude of the fracture strains is $0.25 < \mathbf{a/b} < 0.7$ for most ductile metals ($0.1 < n < 0.4$). For example of 2024-T351 aluminum, the hardening exponent $n = 0.15$ and $\mathbf{b} = 0.43$, which are obtained from Eqns. (3.18) and (3.38), respectively. Eq. (3.46) gives $\mathbf{a} = 0.165$ while the magnitude

of the shear fracture strain obtained from test (Bao and Wierzbicki, 2004a) was equal to $\bar{\varepsilon}_f = 0.181$. The error of present quick calibration method is less than 10%, see also inserted table in Fig. 3.24.

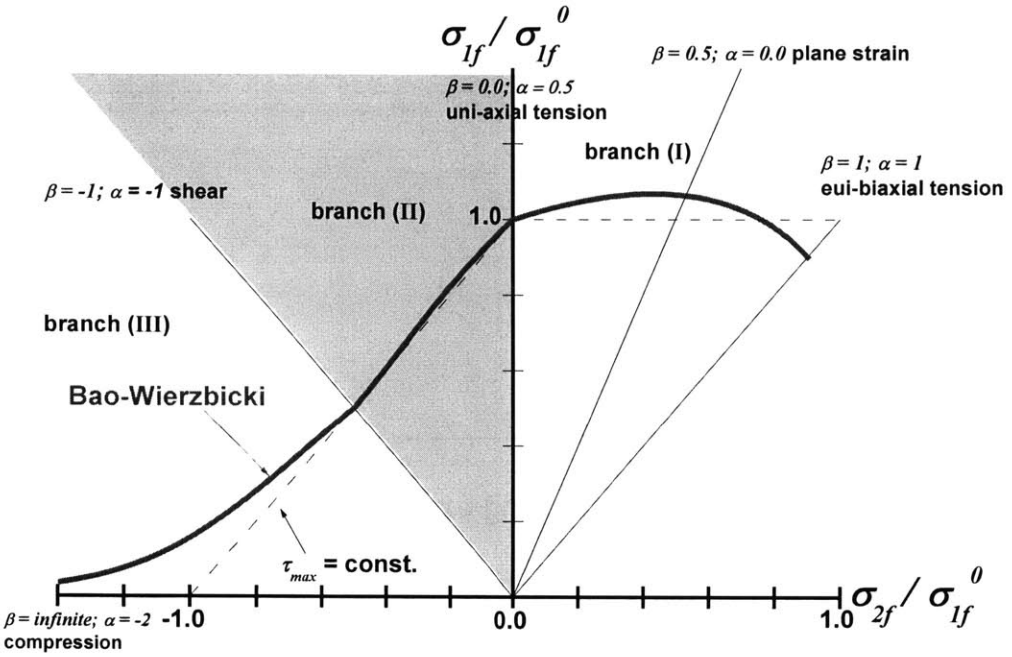

Fig. 3.21 Schematic diagram showing the failure envelopes for the BW criterion (thick full line) and the maximum shear stress criterion (dashed line) in the space of principal stress. Note that the axes are normalized by uniaxial stress to fracture σ_{1f}^{0}.

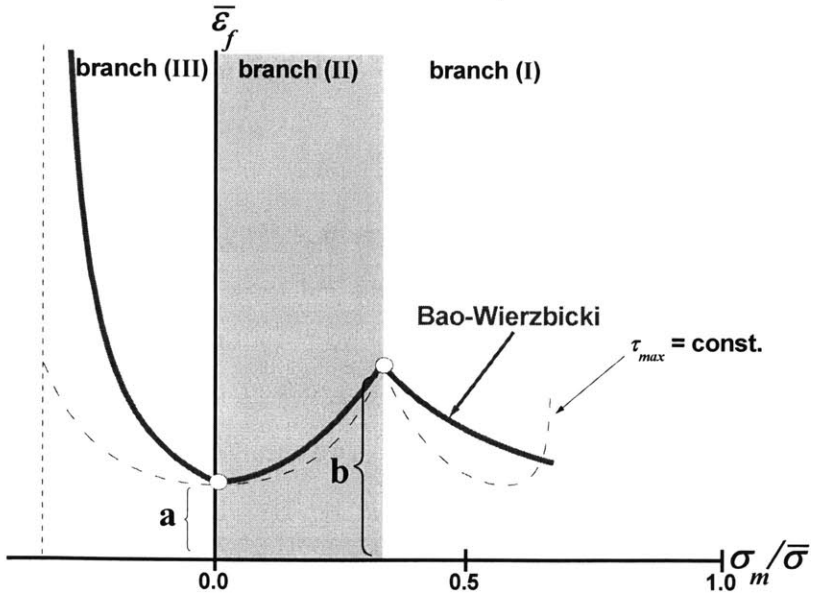

Fig. 3.22 Schematic diagram showing the failure envelopes for the BW criterion (thick full line) and the maximum shear stress criterion (dashed line) in the space of equivalent fracture strain and stress triaxiality

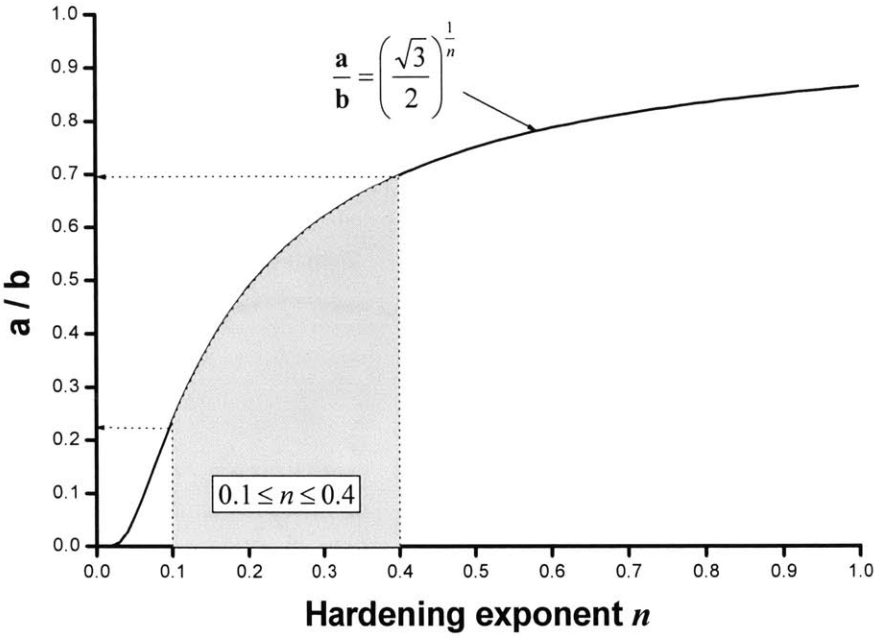

Fig. 3.23 Relative magnitude of fracture strains (**a/b**) versus hardening exponent (n)

3.3.4 Validation of quick calibration method

3.3.4.1 Critical damage parameters of five different materials in the range of high stress triaxiality

In the range of high stress triaxiality ($\sigma_m / \overline{\sigma} > 1/3$), a comparison between the experimentally and numerically found critical damage parameters and those obtained from the present quick calibration method is given in Tables 3.1 and 3.2. Except for the case of Al 2024-T351 where the experimental data of a_f is available, the thickness h_f and the radius a_f were numerically measured in other cases shown in Tables 3.1 and 3.2. It can be clearly confirmed that the present quick calibration method provides an accurate prediction for all three important damage parameters (strain to fracture, average stress triaxiality, and critical damage value of material) within 10% error range.

Table 3.1 Comparison of the critical damage parameters for three different materials obtained from the two different methods of calibration (flat tensile specimens)

Type of material	Measured parameters			$\mathbf{b} = \bar{\varepsilon}_f$		$(\sigma_m / \bar{\sigma})^0_{av}$		$D_c = \mathbf{b}(\sigma_m / \bar{\sigma})^0_{av}$		
	n	h_0 (mm)	h_f (mm)	**Quick Eq. 3.20**	Conv.	**Quick Eq.3.21**	Conv.	**Quick Eq.3.19**	Conv.	Error (%)
A710 steel	0.12	2.0	0.86	**1.08**	1.0[1]	**0.52**	0.51[1]	**0.56**	0.51[1]	9.8
Mild steel-A	0.2	0.75	0.43	**0.81**	0.84[2]	**0.45**	0.42[2]	**0.37**	0.35[2]	5.7
Mild steel-B	0.22	1.42	0.91	**0.72**	0.8[3]	**0.40**	0.34[3]	**0.29**	0.27[3]	7.4

Note: [1] taken from Ch. 5; [2] taken from Ch. 6.2; [3] taken from Ch. 6.1; Conv. (Conventional method)

Table 3.2 Comparison of the critical damage parameters for two different materials obtained from the two different methods of calibration (smooth round tensile specimens)

Type of material	Measured parameters			$\mathbf{b} = \bar{\varepsilon}_f$		$(\sigma_m / \bar{\sigma})^0_{av}$		$D_c = \mathbf{b}(\sigma_m / \bar{\sigma})^0_{av}$		
	n	a_0 (mm)	a_f (mm)	**Quick Eq.3.38**	Conv.	**Quick Eq.3.39**	Conv.	**Quick Eq.3.37**	Conv.	Error (%)
2024-T351 aluminum	0.15	8.94	7.2	**0.43**	0.45[1]	**0.4**	0.4[1]	**0.17**	0.18[1]	5.6
AH36 steel	0.17	3.18	2.58	**0.42**	0.43[2]	**0.38**	0.4[2]	**0.16**	0.17[2]	5.8

Note: [1] taken from Bao and Wierzbicki (2004a); [2] taken from Ch. 7; Conv. (Conventional method)

3.3.4.2 Fracture locus of Al 2024-T351 for a wide range of stress triaxiality

To validate the present quick calibration method over wide range of stress triaxiality, in particular, Al 2024-T351 was taken as benchmark material here because the fracture locus for this material has been obtained through an extensive experimental process, Bao and Wierzbicki (2004a). Figure 3.24 compares the complete (denoted by open circle), empirically found (dashed line) BW fracture locus and one obtained from quick calibration method (thicker full line). As can be seen in this figure, the simplicity and accuracy of the present rapid calibration for fracture is apparent.

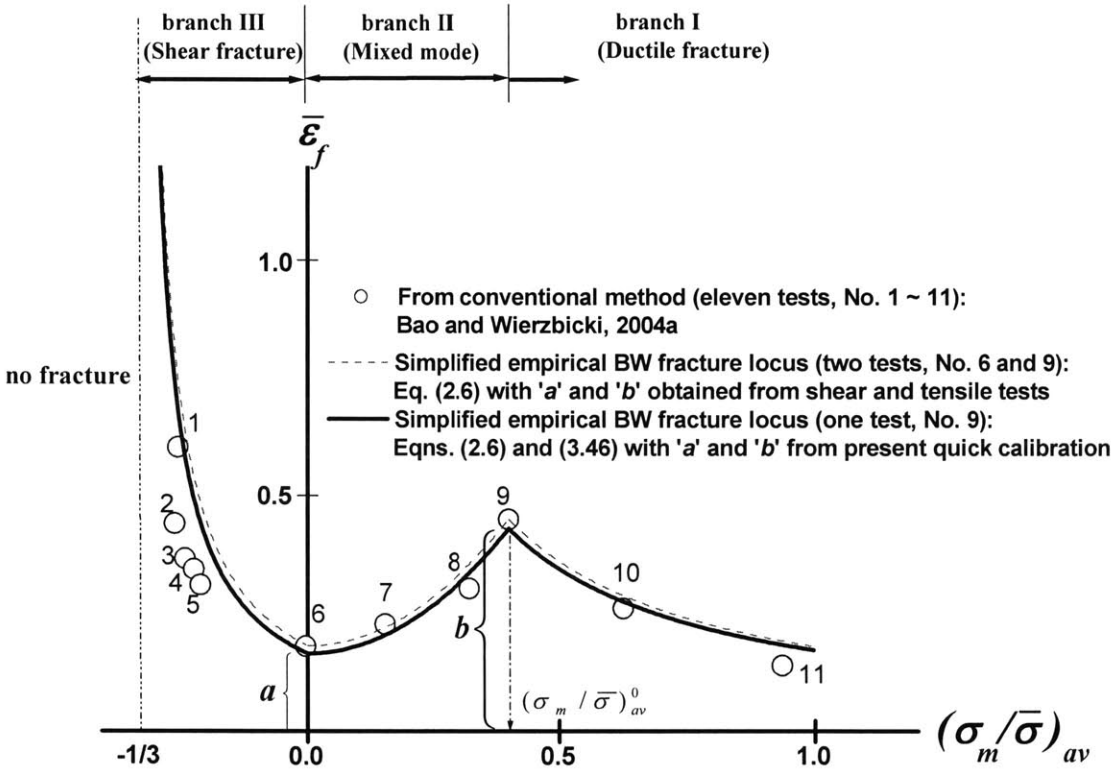

Calibration method	Type of line	n	a	b	$(\sigma_m/\bar{\sigma})^0_{av}$
Conventional	dashed	0.15[1]	0.181[1]	0.45[1]	0.4[1]
Quick	**full**	**0.15 (Eq. (3.18))**	**0.165 (Eq. (3.46))**	**0.43 (Eq. (3.38))**	**0.4 (Eq. (3.39))**

Note: [1] taken from Bao and Wierzbicki (2004a)

Fig. 3.24 Fracture envelope for Al 2024-T351 constructed in the plane of equivalent plastic strain to fracture $\bar{\varepsilon}_f$ and average stress triaxiality $(\sigma_m/\bar{\sigma})_{av}$

3.4 Conclusion

The main points of the conventional calibration method can be summarized as follows:

- The procedure of the conventional method includes two parts. In the first, an accurate (or actual) stress-strain curve of the considered material is determined by tracing the experimental tensile loading-displacement curve using parallel finite element calculations. The stress-strain curve is considered actual only if the numerical simulation using this curve can accurately represent the experimental loading-displacement response. In the second, the key critical damage parameters associated with the fracture criterion (i.e. stress triaxiality, equivalent plastic strain, and critical damage value D_c) are obtained by the above simulation with the actual stress-strain curve.
- However, the "conventional" calibration procedure is complex and difficult to perform in industrial environments. Furthermore, there is still unsolved problem may exist with respect to the uniqueness of the parameters, especially due to the inherent mesh dependence of finite element analysis.

The main points of the newly developed quick calibration method are:

- Four stages were distinguished in the tensile test of flat specimen: uniform extension, diffuse necking, localized necking, crack formation. Assuming piece-wise linear loading paths together with transverse plane strain beyond the localized necking, approximate solutions for the critical damage parameters (Eqns. 3.19 ~ 3.20) were developed in terms of measurable quantities: hardening exponent (n) and the relative thickness reduction inside the neck.
- Using a suitably modified Bridgman analysis for the post-necking stage of axi-symmetric rod, closed form solutions associated with the BW fracture criterion (Eqns. 3.37 ~ 3.39) were proposed for the case of round tensile specimen.
- The critical fracture strain in pure shear (i.e. **a**) was calculated from the hypothesis of the maximum shear stress fracture criterion, which uniquely relates the parameter **a** with the fracture strain in uniaxial tension (**b**) and hardening exponent n (Eq. (3.46)).
- The prediction of the newly developed calibration method has been verified for five different materials. The agreement between conventional methods and present predictions was always within 10%. Therefore, the quick calibration method will greatly simplify the existing calibration procedure and facilitate fracture prediction in many industrial processes.

This page intentionally left blank

Chapter 4
Computational Methods for Fracture Prediction

4.1 State-of-the-Art

A fundamental difficulty in the computational simulation of discrete fracture process is the requirement that the spatial discretization accommodate the changing topology of the domain. Over the past few decades, many numerical methods have been proposed to get accurate and reliable simulations of crack advance in arbitrary domains. These methods can be classified into two groups: standard FEM and extended FEM (see Table 4.1). The first group is based on a continuous regular displacement field ($\mathbf{u}_{cont}$). In this standard displacement-based approximation, element removal or node release (element split) approach is used to model crack propagation. Moreover, remeshing techniques, which model a discontinuity by modifying the mesh topology to explicitly capture a discontinuity, are employed in conjunction with the element removal or node release approach. In the second group (extended FEM), using the partition of unity property of finite element shape functions identified by Babuska and Melenk (1997), the standard displacement-based approximation is enriched by incorporating discontinuous fields ($\mathbf{u}_{discont}$). A key feature of this method is the possibility of extending crack during the calculation in an arbitrary direction, independent of the

structure of the underlying finite element mesh. A short summary of each method shown in Table 4.1 is given in the following subsections.

Table 4.1 Summary of computational methods for fracture prediction (i.e. numerical representation of discontinuities)

	Standard FEM	**Extended FEM**
Displacement field formulation	$\mathbf{u} = \mathbf{u}_{cont}$	$\mathbf{u} = \mathbf{u}_{cont} + \mathbf{u}_{discont}$
Simulation of crack propagation (new surface formulation)	• Element removal • Node release • Remeshing	• Enrichment techniques • Moving mesh technique

Note: $\mathbf{u}$ is the displacement field in the domain; $\mathbf{u}_{cont}$ is the continuous regular displacement field; $\mathbf{u}_{discont}$ is the discontinuous displacement filed which contains local enrichment functions.

4.1.1 Element removal

The element removal procedure is the most common and popular method to simulate fracture due to its convenience and efficiency in terms of implementation and calculation. When scalar parameters such as equivalent plastic strain or an accumulated damage reach a prescribed critical value at a given integration point, the associated element is removed during the calculation. The failed element completely loses its ability to carry load while its mass is conserved or not conserved (see for example *PAM-CRASH*, 2003). In this way, the formation of new free surface is approximately modeled in the computational setting. The element removal method also gives fairly accurate results provided that it is properly used with small element sizes and correct fracture models. Furthermore, it does not require the user to specify the crack path prior to analysis.

The drawback of this method is that dense mesh configuration must be used to accurately simulate crack propagation. If this option is used to for large elements with coarse mesh size in the process of crack growth, then the crack tip is artificially blunted. The resulting stress triaxiality and equivalent strain ahead of crack tip would very much depend on the geometry near the crack tip.

Consequently, the artificially blunted crack leads to an error in the predictive capability of this method.

4.1.2 Node release (element split)

Several commercial FE codes provide a node release option (often referred to as an element split) where the element boundaries split apart when a certain force or element strain is exceed the specified critical value (see for example "Constrained Tie Break" and "Constrained Tied Nodes to Failure" options in *LS-DYNA*, 2003). Accordingly, fracture may be simulated without the loss of any element information. This method generally work by assuming the crack path. Early finite element work focused on the node release approach to model crack propagation (Keegstra et al., 1978; Yagawa et al., 1977). When the crack path is known in advance from experiments, accurate predictions can be obtained by this approach (Rankin et al., 1993). However, fracture is limited to a predefined crack path, which is a clear limitation of this method. In fact, since the constraints in the form of tied nodes are aligned with the element boundaries, the orientation of cracks is restricted to a limited number of predefined angles.

Recently, a thorough comparative study on the shell element removal and splitting was conducted by Hagbart (2004) for the problems of Mode I tearing and plate cutting (see Fig. 4.1). He showed that both fracture approaches behave well for smaller element sizes and produce a difference in global force-displacement response as well as local stress and strain fileds for the cases of larger element sizes.

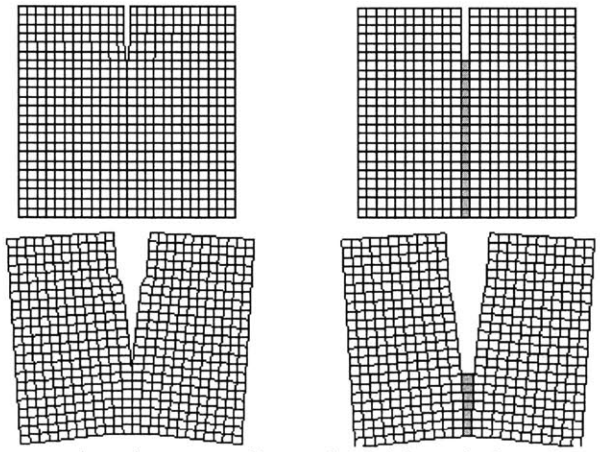

Fig. 4.1 Comparison between the element split method (a) and the element removal method (b) (after Hagbart, 2004)

4.1.3 Remeshing (adaptive mesh refinement)

Modeling arbitrary crack paths requires that the discretization be redesigned during the simulations to the locally needed levels. One possibility is to employ an adaptive scheme to reconstruct and locally refine the mesh to accommodate each increment of crack propagation. The benefits of such scheme not only reside in the achievement of homogeneous levels of solution accuracy, but in particular also in a higher solution efficiency, since the model is continually kept at a state of refinement for constant local accuracy. In general, the remeshing scheme incorporates an error indicator to guide the refinement procedure. The error indicator to be used depends on the nature of the problem considered. For thin shell non-linear transient simulations, a choice may be made among the following indicators: gradients of membrane stresses or energy; hourglass energy; interelemental angles. The first two choices are based on considerations of local energy densities and the last indicator is a purely geometrical measure that regards the changes in angles between the thin shell finite element domain surfaces. The shortcoming of the remeshing technique is the additional effort associated with continuous remeshing in order to update the mesh to match the geometry of the discontinuity.

In spite of its complexity, remeshing is a widely used techniques for meshes consisting of triangular or quadrilateral elements, e.g. in simulations of sheet metal forming processes (see Cheng, 1988; Cheng and Kikuchi, 1986; Dyduch et al., 1992; Marusich and Ortiz, 1995) and localization problems (see Ortiz and Quigley, 1991; Lee and Bathe, 1994). In the present thesis, the remeshing technique is also employed in conjunction with the element removal for the petalling problem of single circular plate and the results are compared with those of fixed mesh configurations (see Chapter 7.3.5).

4.1.4 Enrichment techniques

Several new finite element techniques have been developed to represent the true discrete character of fracture, while allowing for an arbitrary direction of crack propagation, not hampered by the initial mesh design. These include the element-free Galerkin (EFG) method developed by Belytschko and coworkers (Belytschko et al., 1994, 1995a/b), a moving mesh technique (Rashid,

1998), and enrichment techniques for finite elements based on a partition of unity shape functions (Moes et al., 1999; Daux et al., 2000; Belytschko et al., 2001; Moes and Belytschko, 2002; Wells and Sluys, 2001; Borst, 2003; Remmers et al., 2003). In particular, the EFG method has been shown to offer many attractive features in the crack propagation analysis. However, it appears to be less robust than traditional finite element methods, it is computationally more demanding and the implementation in three dimensions appears to be less straightforward, according to Borst (2003). A short summary of the moving mesh technique is given in next Section 4.1.5. The enrichment techniques are moderate extension to existing standard displacement based methods which capture discontinuities using the local enrichment functions in conjunction with additional degree of freedom. In particular, discontinuous shape functions are used with the magnitude of displacement jump represented by extra nodal degree of freedom at existing nodes. The enrichment method permits crack formation and discontinuous crack growth to be modeled, irrespective of the structure of the finite element mesh.

In general, the formulation associated with the enrichment method begins by considering the kinematics of a body crossed by a displacement jump. The finite element formulation is developed by considering the interpolation of the displacement filed and then inserting the discontinuous displacement field into the virtual work equation. Here, as an illustration, a short description on the enrichment method is presented with the underlying kinematic relations and finite element formulation. A complete description is given by Wells and Sluys (2001), Remmers et al. (2003), and others.

Kinematic relations Consider the body Π ($\Pi = \Pi^+ \cup \Pi^-$) with boundary Γ, as shown in Fig. 4.2. The displacement $\mathbf{u}$ can be decomposed into two parts: a continuous and a discontinuous part

$$\mathbf{u}(\mathbf{x}, t) = \hat{\mathbf{u}}(\mathbf{x}, t) + H_{\Gamma_d}(\mathbf{x})\tilde{\mathbf{u}}(\mathbf{x}, t) \tag{4.1}$$

where $\hat{\mathbf{u}}$ and $\tilde{\mathbf{u}}$ are continuous functions on Π; $\mathbf{x}$ denotes the position of material point; t is time; H_{Γ_d} is Heaviside step function centered on the discontinuity Γ_d, defined as

$$H_{\Gamma_d}(\mathbf{x}) = \begin{cases} 0 & if\ \mathbf{x} \in \Pi^- \\ 1 & if\ \mathbf{x} \in \Pi^+ \end{cases} \tag{4.2}$$

Note that various types of step function can be used in the formulation of displacement field, Eq. (4.1) (see for example Moes et al., 1999).

The strain field can be found by taking the derivative of the displacement field, Eq. (4.1)

$$\varepsilon(\mathbf{x},t) = \nabla^s \hat{\mathbf{u}}(\mathbf{x},t) + H_{\Gamma_d}(\mathbf{x})\nabla^s \tilde{\mathbf{u}}(\mathbf{x},t) \tag{4.3}$$

where a subscript s denotes the symmetric part of a differential operator based on the assumption of infinitely small deformation. Note that at the discontinuities Γ_d, the strains are not defined. There, the magnitude of displacement jump

$$\mathbf{v}(\mathbf{x},t) = \tilde{\mathbf{u}}(\mathbf{x},t) \qquad \mathbf{x} \ on \ \Gamma_d \tag{4.4}$$

is the relevant kinematic quantity.

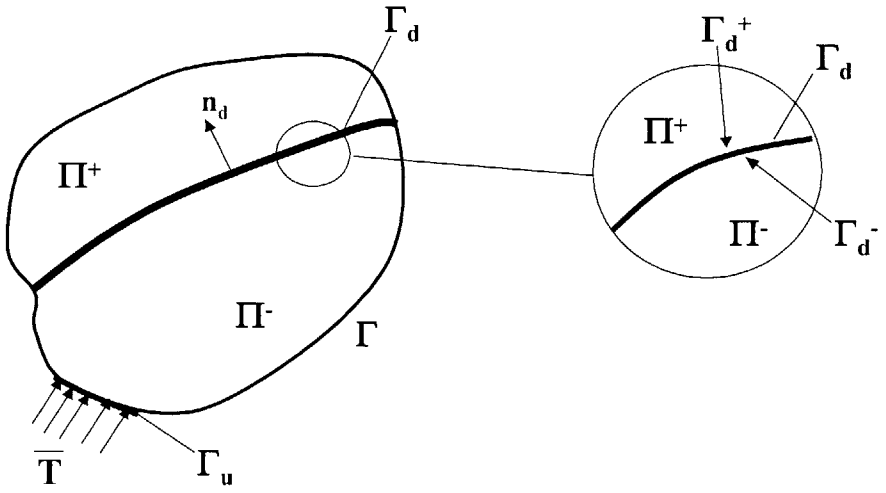

Fig. 4.2 Body Π crossed by a discontinuity Γ (after Wells and Sluys, 2001)

Finite element formulation For the finite element formulation, most of the enrichment methods have employed the partition of unity property of shape functions (Melenk and Babuska, 1997), which allows the local enrichment functions to be easily incorporated into a finite element approximation. A collection of functions Φ_i, associated with node i $(1 \le i \le m)$ form a partition of unity if

$$\sum_{i=1}^{m} \Phi_i = 1 \tag{4.5}$$

For any set of functions that satisfy Eq. (4.5), a filed **u** can be interpolated as follows

$$\mathbf{u}(\mathbf{x},t)=\sum_{i=1}^{m}\Phi_i(\mathbf{x})\left[\hat{d}_i(t)+\sum_{j=1}^{k}\gamma_j(\mathbf{x})\tilde{d}_{ij}(t)\right] \tag{4.6}$$

with $\hat{d}_i(t)$ the regular nodal degree of freedom, $\gamma_j(\mathbf{x})$ the enhanced basis with k terms, and $\tilde{d}_{ij}(t)$ the additional degree of freedom at node i, representing the amplitude of the jth basis term γ_j. The displacement fields $H_{\Gamma_d}\tilde{\mathbf{u}}$ can be considered as enhanced basis fields. By replacing γ_j by the corresponding Heaviside function H_{Γ_d}, the displacement field in Eq. (4.1) can be expressed in the following discrete form

$$\mathbf{u}=\mathbf{N}\hat{\mathbf{d}}+H_{\Gamma_d}\mathbf{N}\tilde{\mathbf{d}} \tag{4.7}$$

where the vector $\hat{\mathbf{d}}$ contains the regular nodal degrees of freedom of the element and $\tilde{\mathbf{d}}$ contains all additional nodal degrees of freedom associated with discontinuity Γ_d. The matrix $\mathbf{N}$ contains the conventional element shape functions. The discrete strain field in terms of nodal displacements can be written as

$$\boldsymbol{\varepsilon}=\nabla^{s}\mathbf{u}=\mathbf{B}\hat{\mathbf{d}}+H_{\Gamma_d}\mathbf{B}\tilde{\mathbf{d}} \tag{4.8}$$

where $\mathbf{B} = \mathbf{LN}$ contains the spatial derivative of the element shape functions. $\mathbf{L}$ is a differential operator matrix. Finally, the discrete displacement jump at discontinuity Γ_d (Eq. (4.4)) is equal to

$$\mathbf{v}=\mathbf{N}\tilde{\mathbf{d}} \tag{4.9}$$

The numerical development now follows standard ways by inserting above discrete fields into the virtual work equation.

Most of the enrichment methods have incorporated a cohesive zone (or decohering zone) model to simulate fracture. A complete derivation on how the cohesive zone model can be implemented within the enrichment methodology has been given by Wells and Sluys (2001) and later by Moes and Belytschko (2002). The effectiveness of the enrichment method in terms of predicting arbitrary crack propagation and removing mesh dependence has been demonstrated by many authors (see for example Moes and Belytschko, 2002; Wells and Sluys, 2001; Borst, 2003; Remmers et al., 2003). However, most of the validation examples taken in the above references has been confined to situations that are essentially heterogeneous quasi-brittle materials, such as concrete, under planar static loading. Furthermore, these examples have not been conclusively corroborated by detailed experiments. The ability of this method to capture the failure mechanisms in ductile materials under static and dynamic loading conditions has yet to be established.

4.1.5 Moving mesh technique

A moving mesh technique (or referred to as "arbitrary local mesh refinement" method) was proposed by Rashid (1998) in order to provide a consistent spatial resolution in the vicinity of an advancing crack tip, and to accommodate new free surfaces with minimal additional computational expense. In the methodology of moving mesh approach, the exclusion region (hereafter, referred to as ER) formulation, proposed by Rashid (1997), was adopted. The ER formulation is a general theoretical framework for the treatment of fracture under arbitrary material response. It involves identification of a small material neighborhood that contains the separation front.

In the moving mesh method, two distinct meshes are employed: one that surrounds the advancing crack front and moves with it, and the other that fills the entire domain. As illustrated in Fig. 4.3, the background mesh denotes the discretization of the body without crack. The crack is represented by new-free-surface curve, which is defined arbitrarily and independently of the background mesh. The final ingredient in the discretization is the patch mesh, which, in two dimensions, is a circular disc composed of annular rings of elements. The patch mesh is centered at the tip of the crack, and moves with it as the crack advances.

As a demonstration example, Fig. 4.4 shows the predicted crack path in a cracked rectangular plate containing an off-center circular hole loaded by uniform normal traction along the top and bottom edges. The crack tip was treated using a numerical implementation of the ER theory.

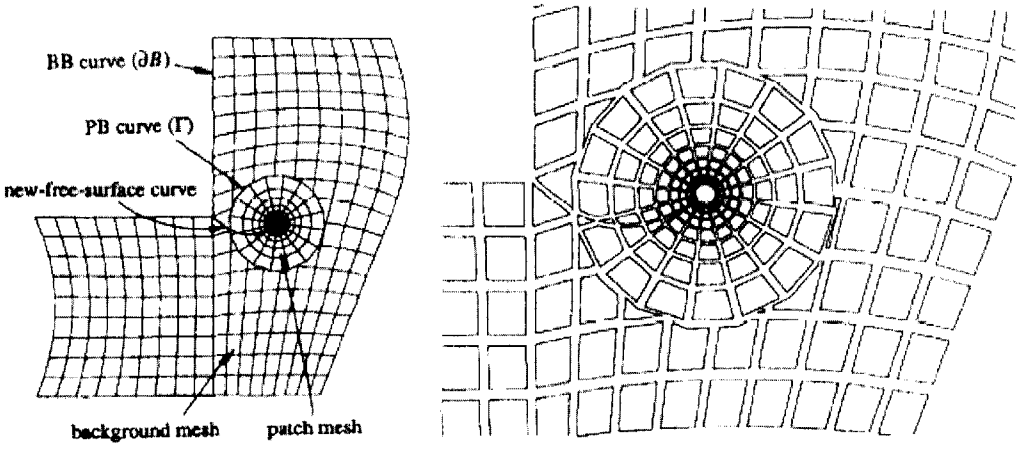

Fig. 4.3 Typical finite element discretization for the moving mesh method with background-boundary, patch-boundary, and new free surface curves identified (left); and detail of the patch mesh (right) (taken from Rashid, 1998)

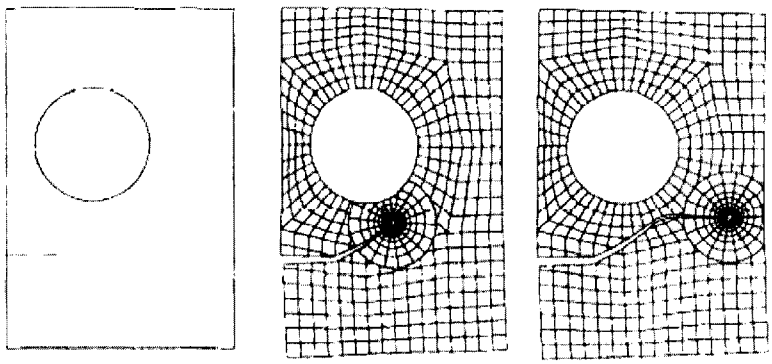

Fig. 4.4 Crack extension in a planar domain with an off-center hole subject to uniform normal traction on the top and bottom edges: initial crack (left); intermediate deformed mesh (center); and final deformed mesh (right) (taken from Rashid, 1998)

4.1.6 Discussion

It is worth noting that no distinction between crack formation and propagation is made in the computational methods summarized in the previous sections, that is, fracture emerges as a natural outcome of the deformation process, without introducing an additional failure criterion for crack propagation. However, to the best of author's knowledge, a thorough investigation on the states of critical parameters associated with the postulated fracture criteria during the process of crack propagation is scarce in the literature. Therefore, this topic is extensively discussed in the present thesis to confirm the above assumption (see Chapters 5.3, 6.2, and 7.3).

As mentioned earlier, an attractive aspect of the extended FEM is to allow crack propagation to be represented independently of the mesh structure and size, and so remeshing is not necessary to mode crack growth. However, above advantages have been mostly demonstrated by the limited cases that are linear elastic material, infinitesimal deformation, planar geometry, and static loading, as schematically shown in Fig. 4.5. This is true for both enrichment and moving mesh techniques. Further investigation incorporating rigorous comparison with experimental results should be performed to confirm the capability of these methods in large deformation problems. Moreover, depending on the material and loading conditions, the extended FEM itself may suffer possible mesh size sensitivity in the prediction of post-localization responses since it is essentially identical to the standard FEM up to the stage of crack formation. The only difference between two methods

exists in the crack propagation process, see Fig. 4.5. Note that the standard FEM is considered in this thesis. Two possible ways to avoid the problem of mesh sensitivity in the numerical solution are presented in Chapter 5.

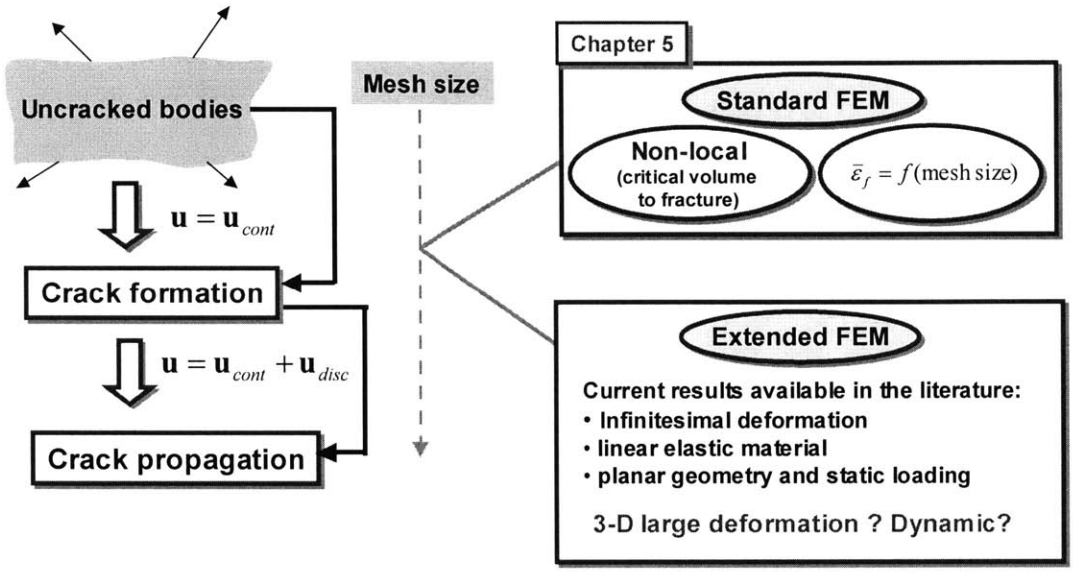

Fig. 4.5 Summary of the remedies to remove mesh dependence and provide reliable prediction in current computational methods for fracture

4.2 Present FE approach to fracture

Figure 4.6 summarizes the fracture criteria provided by the leading commercial FE codes that are considered in this thesis. As can be seen, the Johnson-Cook (JC) facture criterion is implemented in both *ABAQUS* and *LS-DYNA3D*. *PAM-CRASH* has recently incorporated the Wilkins (W) criterion in the library of material models. Those criteria (JC and W) include the effect of stress triaxiality. However, no clear calibration procedure exists especially in the W model and therefore it is difficult to use it in practical simulation. Moreover, according to the comparative study presented in Chapter 2.3, it appears that the W and the JC criteria are able to capture qualitatively the trend of fracture strain as a function of stress triaxiality. However, it was also shown that there are large

difference in the magnitude of fracture strain between those two criteria and the empirically determined Bao-Wierzbicki (BW) model, see Fig. 2.9.

The general formulation of the Bao-Wierzbicki fracture criterion (Eq. (2.1)) has been already implemented into *ABAQUS* by the developer of this code in an alternative form, according to

$$\int_0^{\bar{\varepsilon}} \frac{1}{\bar{\varepsilon}_f\left(\frac{\sigma_m}{\bar{\sigma}}, \dot{\bar{\varepsilon}}, T\right)} d\bar{\varepsilon} = 1 \tag{4.10}$$

where $1/\bar{\varepsilon}_f$ is a weighting function dependent on current values of the stress triaxiality, strain rate, and temperature. As mentioned in Chapter 2.5, the effect of possible strain rate and temperature dependence on the fracture criterion is not taken into account and therefore, the fracture strain is assumed to be a unique function of stress triaxiality in the present thesis. Consequently, the Eq. (4.10) may be reduced to

$$\int_0^{\bar{\varepsilon}} \frac{1}{\bar{\varepsilon}_f\left(\frac{\sigma_m}{\bar{\sigma}}\right)} d\bar{\varepsilon} = 1 \tag{4.11}$$

In addition to the JC and W criteria, *PAM-CRASH* and *LS-DYNA3D* have the most widely used option where fracture is predicted based on the criterion of a constant strain or stress reaching a critical value specified by the user. In the numerical simulations using *PAM-CRASH* and *LS-DYNA3D* reported in this thesis, a constant equivalent plastic strain weighted by average stress triaxiality was used and defined as

$$\bar{\varepsilon}_f = \frac{D_c}{\left(\frac{\sigma_m}{\bar{\sigma}}\right)_{av}} \tag{4.12}$$

which is an alternative expression of the criterion given by Eq. (2.4). In Eq. (4.12), D_c is the critical damage value of material and the average stress triaxiality is defined by $\left(\frac{\sigma_m}{\bar{\sigma}}\right)_{av} = \frac{1}{\bar{\varepsilon}_f}\int_0^{\bar{\varepsilon}_f} \frac{\sigma_m}{\bar{\sigma}} d\bar{\varepsilon}$.

As schematically shown in Fig. 4.7, above the two different approaches (Eqns. (4.11) and (4.12)) are considered in the present thesis. Most of the numerical results are obtained by *PAM-CRASH*. For the specific cases, additional runs are also made using *ABAQUS* and *LS-DYNA3D* to compare the predictions. It will be demonstrated later on that the constant strain to fracture (Eq. (4.12)) may provide a good prediction of ductile fracture in the class of problem where the average stress triaxiality (Eq. (2.3)) of the critical locations is confined in a narrow range (see Chapters 5.3,

6.2, 7.3, and 9.3). In the present thesis, the crack formation and subsequent propagation are simulated by the element removal option in conjunction with the postulated fracture criterion (Eq. (4.11) or (4.12)). To ensure a reliable simulation accuracy, sufficiently small mesh sizes (i.e. $0.1h <$ mesh size $< h$, where h is the thickness of plate) are used in all numerical simulations presented in this thesis. Furthermore, separate mesh sensitivity studies are also conducted for each material of the problem considered.

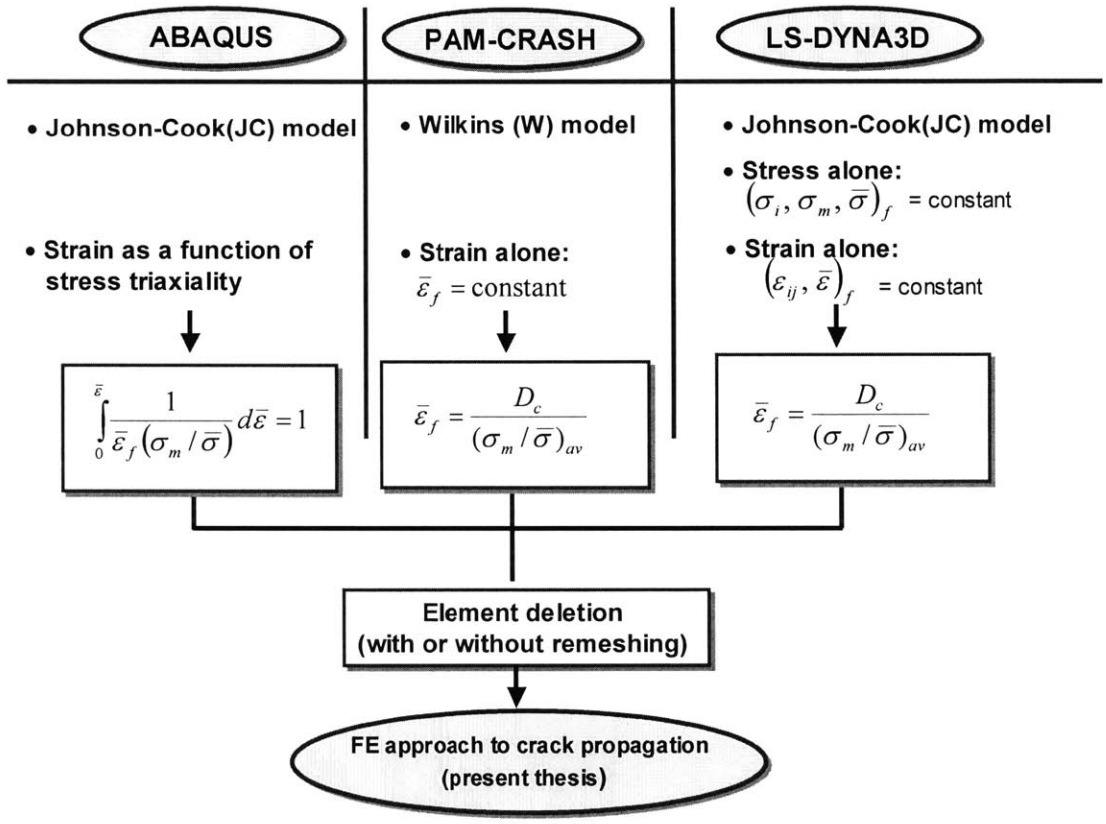

Fig. 4.6 Summary of the fracture criteria implemented in the commercial FE codes and the approach to crack propagation employed in this thesis

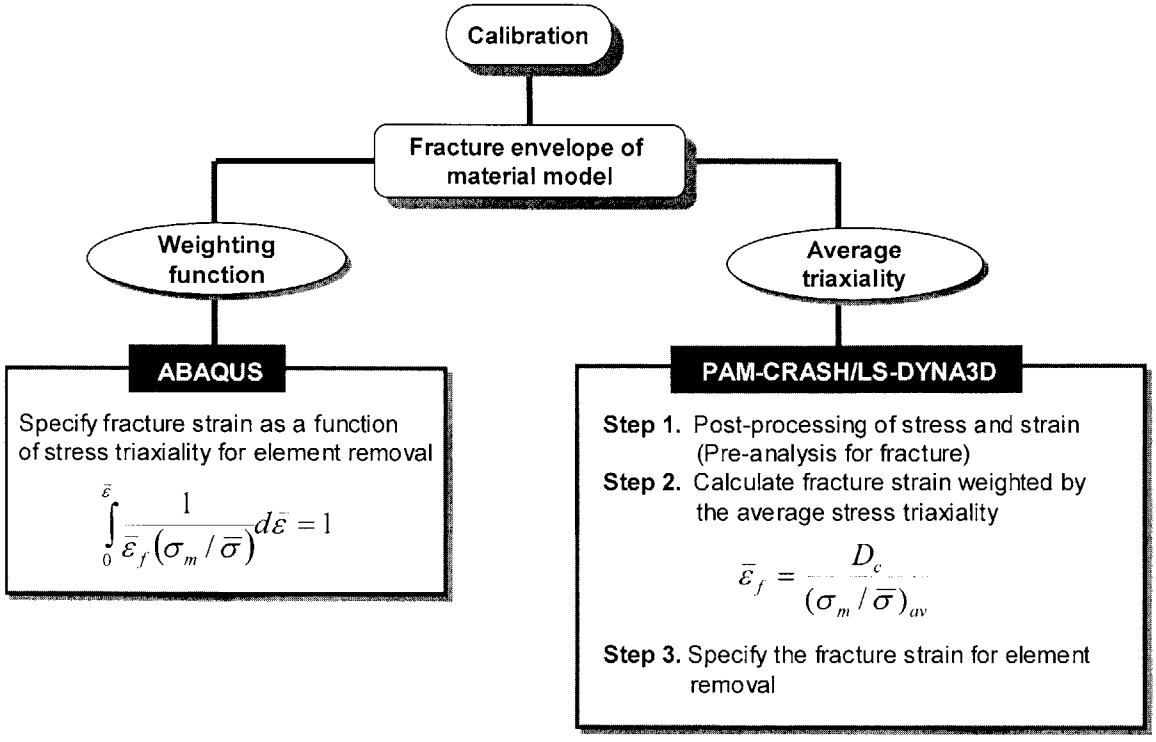

Fig. 4.7 Schematic diagram showing the fracture criterion implemented into the commercial FE codes in the present thesis

This page intentionally left blank

Chapter 5

Effect of Mesh Size on Formation and Propagation of Cracks in Flat Tensile Specimens

5.1 Introduction

As mentioned earlier in Chapter 2, the so-called local fracture models can be classified into two groups: coupled (e.g. Gurson, 1977) and uncoupled (e.g. Rice and Tracey, 1969) models. Non linear Finite Element (FE) methods have been extensively used with some of the local fracture models. The first group (couple model) requires specific material subroutines for performing the FE analysis, as the evolution of the damage affects the yield behavior. On the other hand, the second group (uncoupled model) is based on a subsequent evaluation of stress and strain fields obtained in a conventional elastic-plastic FE analysis. However, when using the local approach to failure, it appeared that the FE solutions of post-localization responses suffer from a mesh sensitivity effect for both groups of models. This effect of mesh depends both on the material and geometry of specimen (Needleman (1988), Needleman and Tvergaard (1994), and Skallerud and Zhang (1999)). Many alternative ways have been suggested to remove the mesh dependence and obtain the physical reliability of the results. One of the most successful approaches is the nonlocal damage formulation

where delocalization is related to the damage mechanism. The concept of the nonlocal approach was first proposed by Pijauder-Cabot and Bazant (1987). Based on this idea, a nonlocal version of the Gurson constitutive relation was developed by Leblond et al. (1994). From the comparison between cell model computation and nonlocal version of the modified Gurson model, Tvergaard and Needleman (1997) found that plastic flow localization and the slope of the stress-strain curve in the post-localization range are affected by the value of specified material length in the nonlocal model. The idea of nonlocal technique was also introduced in the second group of local fracture models (uncoupled models) by Wilkins et al. (1980) and Giavanola and Kirkpatrick (1998), but the effect of material length scale on the accumulated damage was not quantified in their studies.

Useful information on crack formation in a metal sheet is obtained from tensile test specimen with a rectangular cross-section. An important mechanism that precipitates ductile fracture in a sheet metal is the onset of plastic instability in the form of necking prior to ductile crack formation. Therefore, necking and post-necking of the tensile specimen have been investigated by many researchers. In the theoretical analysis of necking, Hill (1952) considered localized necking as a problem of plane stress characteristic theory and showed that localized necking will occur at an inclined angle from the tensile axis. In a much more recent development, Hill's analysis was reviewed and extended by McClintock and Zheng (1993). In the numerical analysis of necking, full 3-D finite element analysis on the post-necking behavior of the specimen was performed by Tvergaard (1993). Based on an enhanced 2-D plane stress finite element model where the thickness effect is taken into account by an incorporated length scale, Mikkelsen (1997, 1999) predicted the development of the post-necking zone. The formation of slanted fracture under plane strain conditions was studied by Besson et al. (2003), where the Gurson and Rousselier constitutive models were used and the role of mesh design (element size, element aspect ratio, and symmetry) was investigated. What has been lacking in the above numerical studies is that no rigorous comparison with experimental results was made. Further investigation should be performed to confirm the accuracy of the numerical analysis.

The objective of this study is to predict all main features of tensile test on a flat specimen from necking to final crack propagation. The accumulated plastic strain with stress triaxiality as a weighting function is introduced as a local ductile fracture criterion in the full 3-D finite element analysis. Furthermore, the global load-displacement responses as well as the onset and extension of the fracture obtained from numerical simulations are thoroughly compared with experimental results. This chapter is constructed in the following way. In Section 5.2, extensive numerical studies

involving the effect of mesh symmetry and mesh size on the crack formation are discussed. Furthermore, the representative length scale is incorporated into the integral formulation of damage to remove the mesh dependence and its effect on the critical damage parameters is also investigated. Section 5.3 presents the evolution of stress, strain, and resulting damage at the critical locations of fracture during crack propagation with particular focus on the relation between the crack formation and subsequent crack propagation.

5.2 Finite Element (FE) simulation of tensile necking and crack formation

For the finite element analysis, the geometrical model was created using the mesh generator program *HyperMesh*. The explicit non-linear finite element code *PAM-CRASH* was used to calculate the quasi-static process of a uniaxial tensile test. A710 steel material with relatively high ductility is considered in this study. A detail calibration procedure for the plasticity and damage parameters of the A710 steel is given in Chapter 3.2. In order to capture successfully the thinning and the localized deformation of the flat specimen characterized by high ductility, a solid element discretization was used. The eight-node solid element with one point integration and stiffness based hourglass control was employed. To investigate mesh sensitivity on the key parameters for fracture prediction, such as equivalent strain $\bar{\varepsilon}_f$, stress triaxiality $\sigma_m / \bar{\sigma}$, and critical damage value D_c, four different mesh configurations were considered. The corresponding initial meshes are shown in Fig. 5.1 together with the deformed meshes at the point of crack formation. The numerical values of mesh sizes and aspect ratio are summarized in Table 5.1. Recently, Besson et al. (2003) showed that the elements dimension in the loading direction should be proportional to the dissipated energy during the fracture process, whereas the dimension perpendicular to the loading direction is important to reproducing the gradients of stress and strain fields accurately. Therefore, using a constant aspect ratio of initial mesh is essential for the evaluation of mesh sensitivity. In the present study, the initial aspect ratio of an in-plane element (size in the direction of the width / size in the direction of the tensile loading) was chosen to be 1.38.

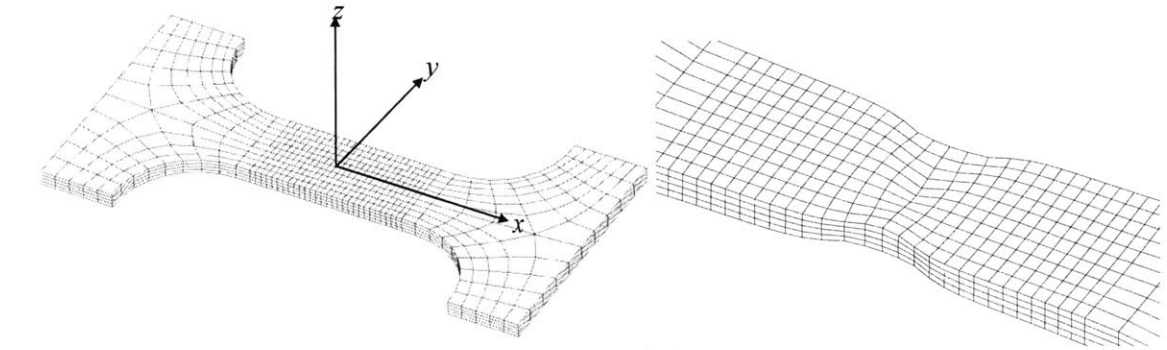

(a) Mesh-1

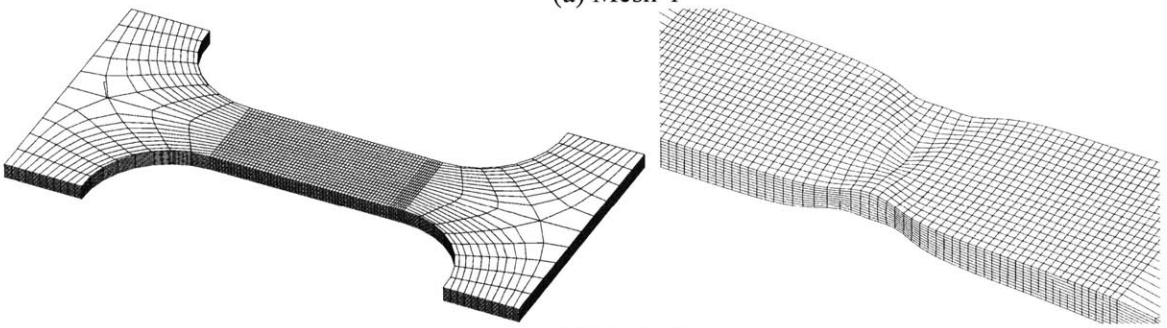

(b) Mesh-2

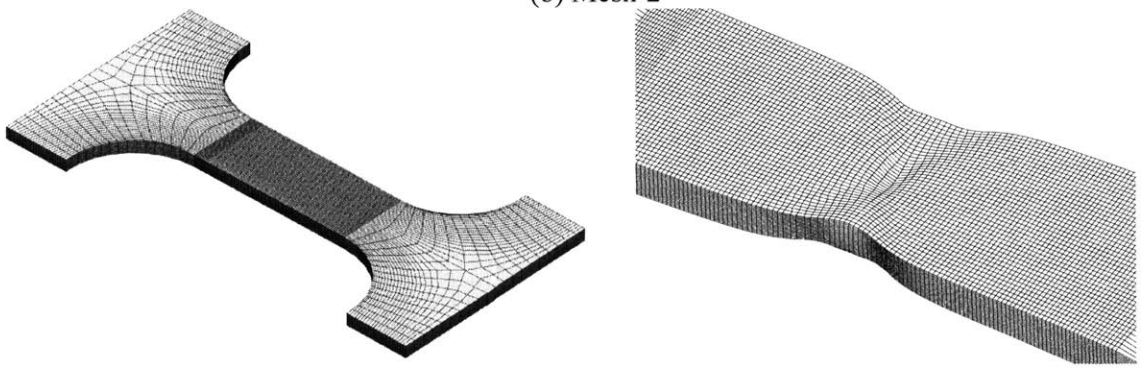

(c) Mesh-3

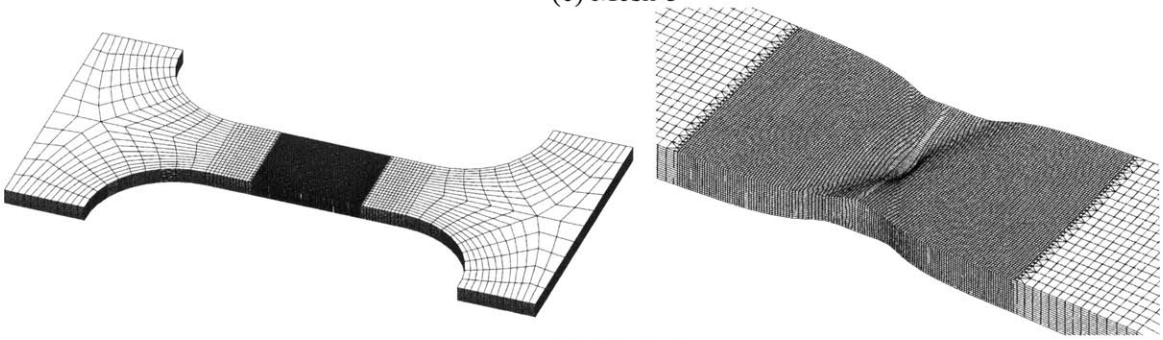

(d) Mesh-4

Fig. 5.1 FE models of the flat specimen with different mesh size; initial FE model(left); Closed-up view of deformation in the central region right before the fracture initiation(right)

Table 5.1 Summary of mesh size in the central gauge region of the specimen. Note, that l_x, l_y, and l_z are the size of solid elements corresponding to the loading direction, the width, and the thickness of tensile test specimen in the central gauge region, respectively. ξ_l indicates dimensionless mesh size in the tensile loading direction where l_x is divided by the initial thickness h_0 of the tensile specimen ($h_0 = 2.04$mm).

Type of mesh	Total number of elements (1/2 model)	Mesh size in mm			Aspect ratio of in-plane mesh l_y / l_x	Normalized mesh size $\xi_l = l_x / h_0$
		l_x	l_y	l_z		
Mesh-1	961	0.907	1.250	0.50	1.38	0.446
Mesh-2	8301	0.454	0.625	0.20	1.38	0.223
Mesh-3	66401	0.227	0.313	0.10	1.38	0.111
Mesh-4	97601	0.114	0.156	0.14	1.38	0.056

5.2.1 Mesh symmetry

For computational efficiency, a symmetric model is generally preferred and used for numerical simulation. However, in the case of a highly ductile material, a symmetric model may cause differences in the local stress and strain states due to the imposed constraints when compared to a full model. Simulated load-displacement plots involving a quarter, half, and full specimen are compared in Fig. 5.2 together with the deformed meshes. Shown in Figs. 5.3 and 5.4 are histories of equivalent strain and stress triaxiality at the center of the specimen for three different mesh symmetries used. It can be observed from all of the above figures that meshing a quarter of the specimen leads to a slightly higher force level, equivalent strain, and accumulated damage than in the case of a half or full specimen. It is further observed that the difference between half and full models is almost zero, which means that there is full symmetry through the thickness of the specimen. Therefore, the half model was used in all following simulations.

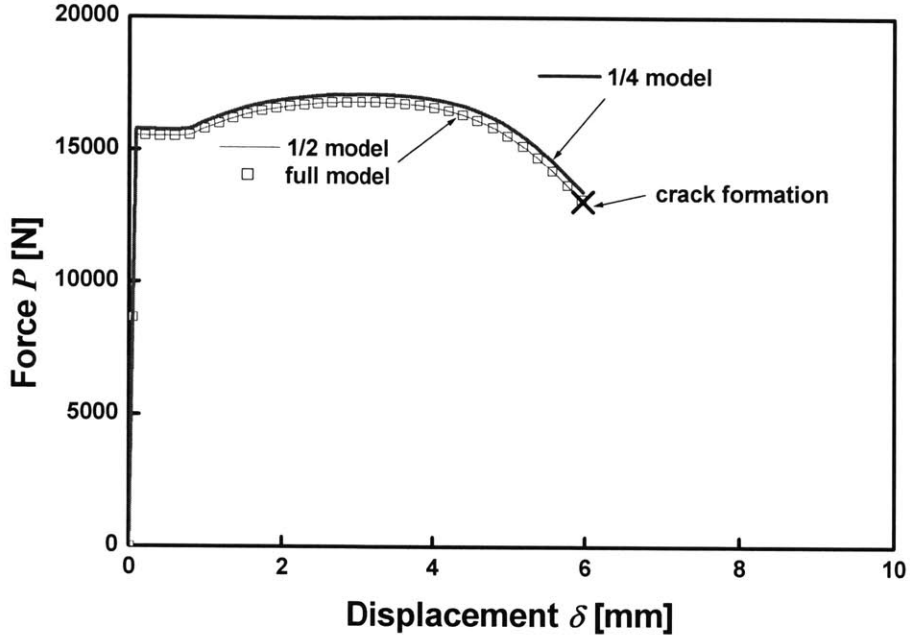

(a) load-displacement

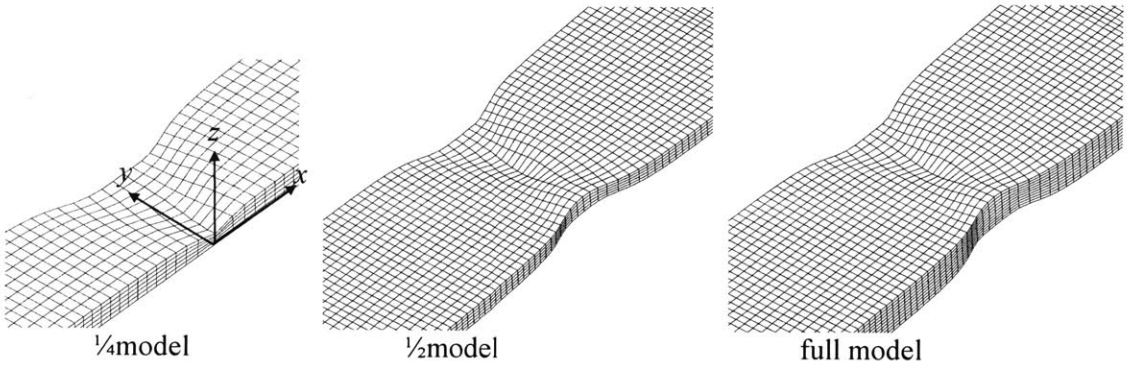

(b) deformed meshes

Fig. 5.2 Effect of mesh symmetry on the responses of the flat specimen: (a) global load-displacement, (b) deformed meshes at the point of fracture (Mesh-2 is used).

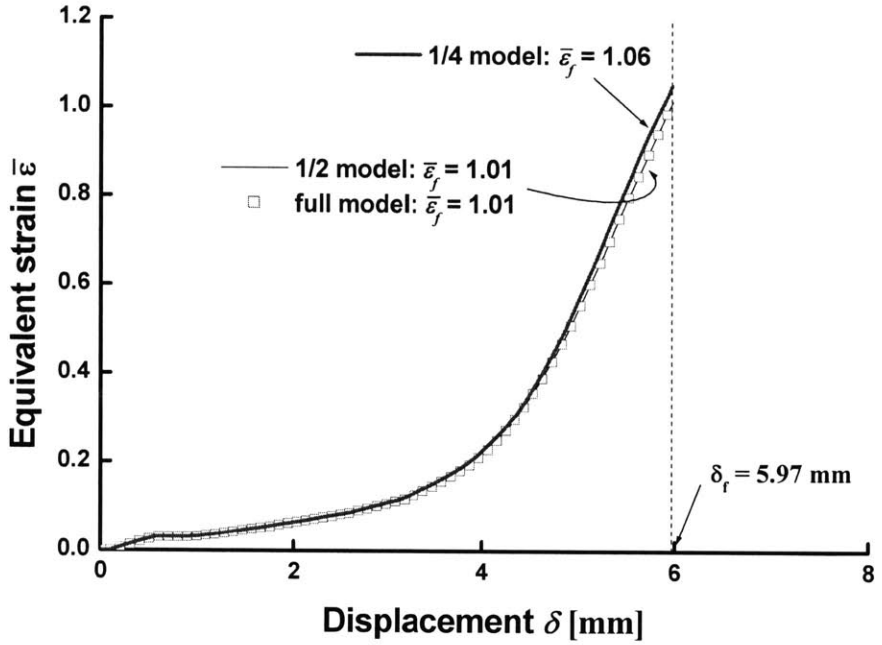

Fig. 5.3 Growth of the equivalent strain at the fracture location using three different types of mesh symmetry (Mesh-2)

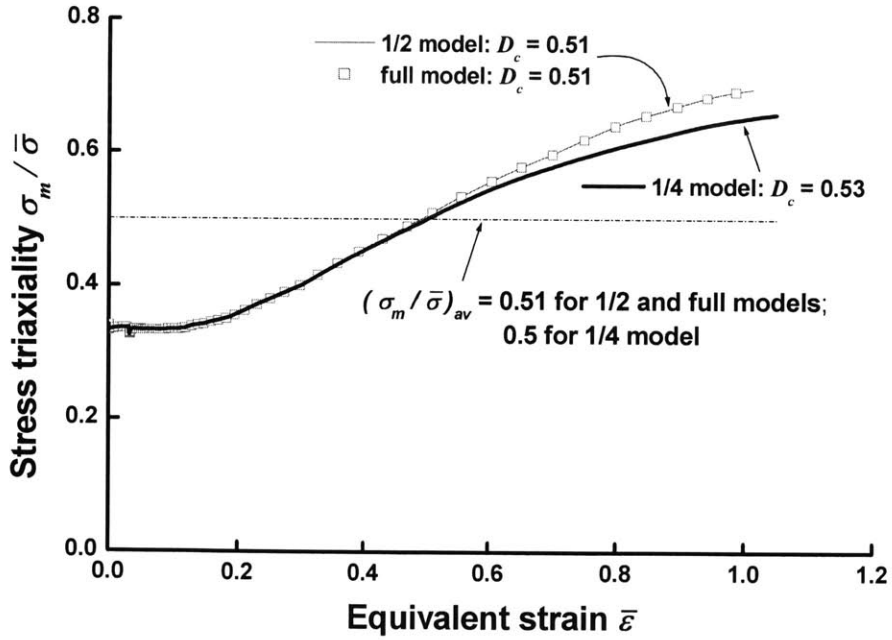

Fig. 5.4 Evolution of stress triaxiality as a function of equivalent strain with three different mesh symmetry (Mesh-2)

5.2.2 Effect of mesh size on crack formation

Figure 5.5 shows the numerically obtained load-displacement plots with four different mesh configurations. The close-ups of the post localization portions of the curves are also included in this figure. After localized necking, it is observed that finer meshes result in a faster drop in load. The total load is a global property and thus does not change much from one mesh to the other. The history plots of the equivalent strain and the stress triaxiality at the center of the specimen are shown in Figs. 5.6 and 5.7, respectively. It can be inferred from those two figures that the curves obtained for different mesh sizes coincide until the development of diffuse necking marked with symbol (○). Once diffuse necking forms, there is a slight change in the rate of growth of strain and triaxiality. In addition, the curves obtained from a relatively coarse mesh (Mesh-1) are different from than the other three with different mesh configurations. As the deformation continues, a large increase in the rate of growth of strain and triaxiality can be observed at the onset of localized necking (●). Note that the equivalent strains to the formation of diffuse and localized necking, predicted by Eqns. (3.3) and (3.10), agree well with the numerical results, as shown in Fig. 5.6. After the localized necking, the strain and the triaxiality show strong dependence of mesh size. The final equivalent strain to fracture increases with finer meshes, see Fig. 5.6. However, it should be mentioned that the stress triaxiality obtained by the Mesh-4 configuration (see thicker solid line in Fig. 5.7) shows a maximum value of $\sigma_m / \bar{\sigma} = 0.84$ at displacement $\delta = 5.78mm$ and later on decreases to the value of $\sigma_m / \bar{\sigma} = 0.77$ at $\delta_f = 5.97mm$. This indicates that the drop of stress triaxiality coupled with the increase in plastic strain will lead to a small increase in the resulting damage. It can be further observed from Fig. 5.8 that numerical predictions show a strong thickness reduction and thereby high σ_3 is developed with finer mesh sizes - i.e. plane stress condition $(\sigma_3 = 0)$ is no longer met beyond the localized necking point.

Shown in Fig. 5.9 is the variation of the equivalent strain to fracture $\bar{\varepsilon}_f$, average stress triaxiality $(\sigma_m / \bar{\sigma})_{av}$, and critical damage value D_c with various mesh sizes in the loading direction l_x. As can be seen, $\bar{\varepsilon}_f$ increases with decreasing mesh size, whereas $(\sigma_m / \bar{\sigma})_{av}$ defined by Eq. (2.3) increases until $l_x = 0.23mm$ and then decreases. Therefore it is obvious that D_c defined by Eq. (2.4) will increase only slightly for mesh sizes finer than $l_x = 0.23mm$. In the present study, a mesh finer than Mesh-4 $(l_x = 0.11mm)$, was not tested due to the limitation of computational time. However, it

can be expected that there may be a unique value of D_c for the present material with high ductility. Even though the convergence of D_c would be achieved, a mesh size with microstructurally-based length scales, namely the average spacing of void nucleating particles, is not practical for the fracture prediction in geometrically similar structures of much larger sizes. Clearly, an alternative approach is required to evaluate D_c for the present material. This will be discussed in following section.

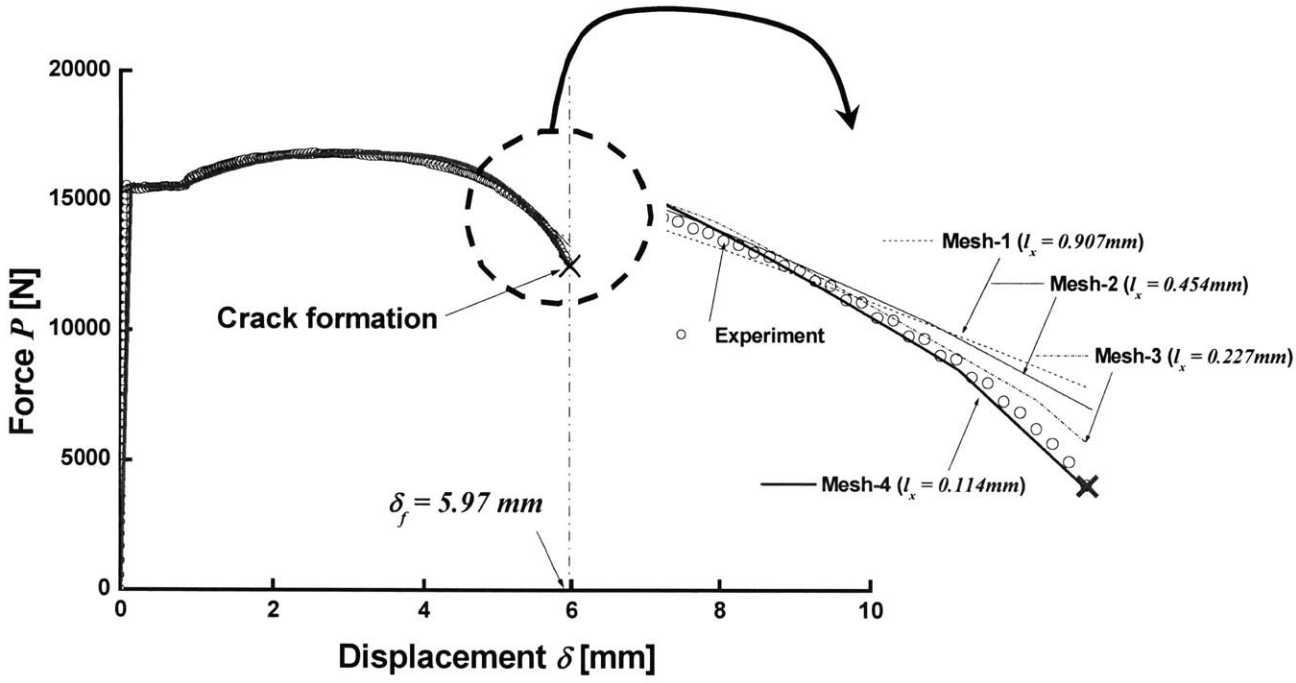

Fig. 5.5 Effect of mesh size on the load-displacement response. After the localized necking, the enlarged plots of the load-displacement are also included in the right side.

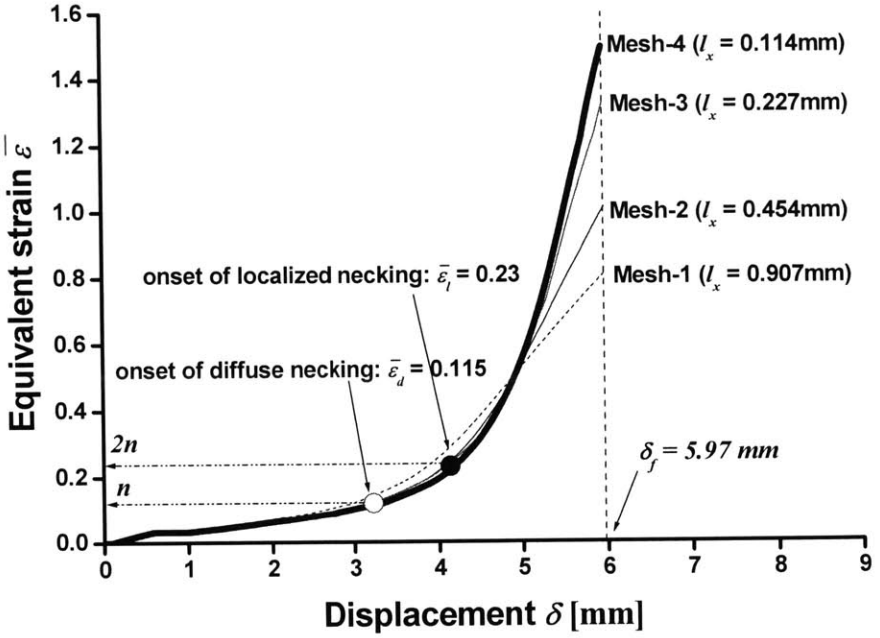

Fig. 5.6 Growth of the equivalent strain at the fracture location using four different mesh size (strain hardening exponent $n = 0.115$)

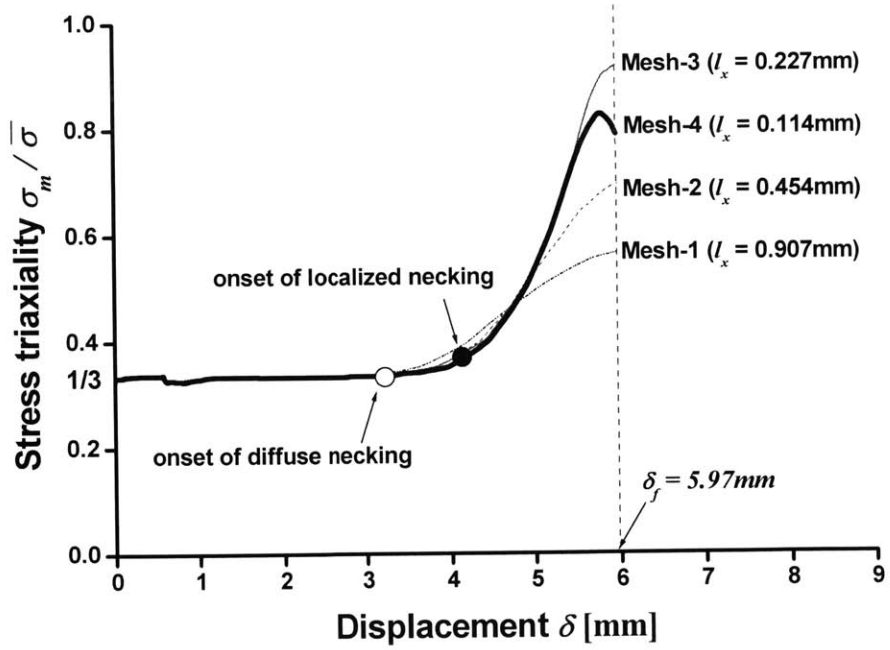

Fig. 5.7 Evolution of stress triaxiality at the fracture location with four different mesh configurations (strain hardening exponent $n = 0.115$)

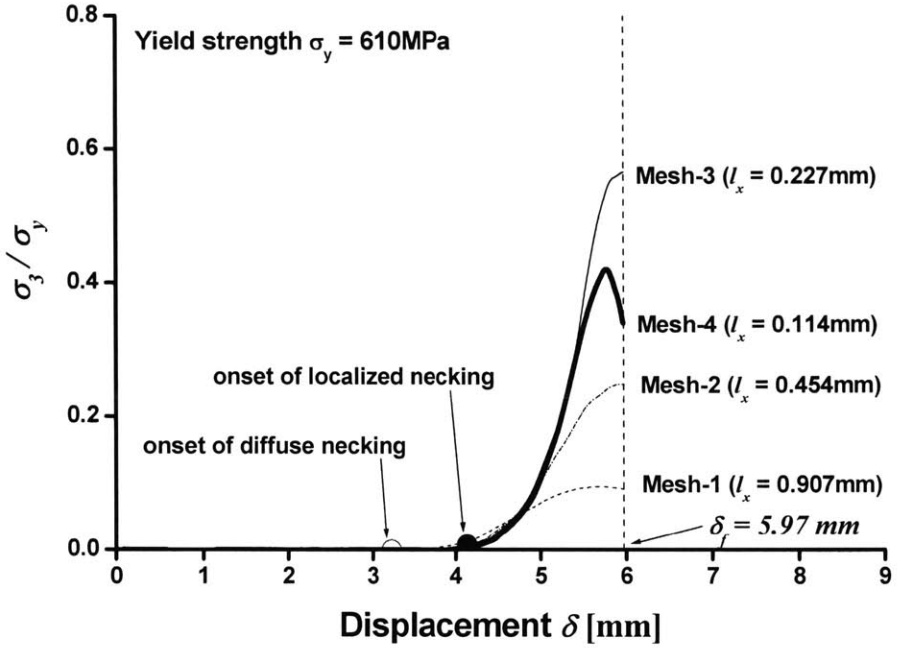

Fig. 5.8 Evolution of stress component through the direction of thickness (σ_3) with four different mesh configurations

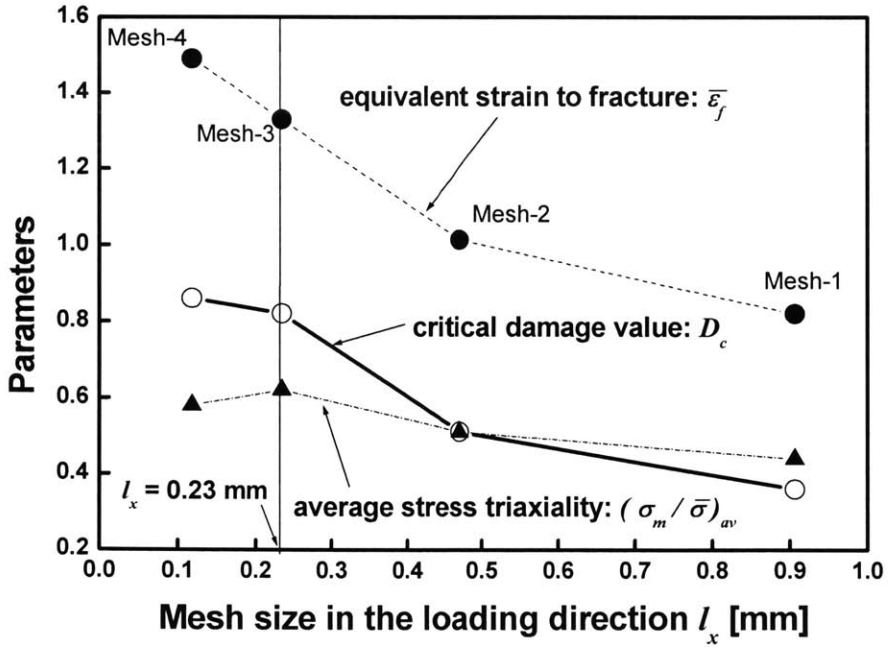

Fig. 5.9 Effect of mesh size on the resulting equivalent strain to fracture, average stress triaxiality (Eq. (2.3)), and critical damage value (Eq. (2.4))

5.2.3 Average value of critical damage $\widetilde{D}_c$ and a practical approach

One possible way of removing mesh sensitivity is to introduce the concept of a critical volume or representative length scale in which the average value of critical damage is calculated over the specified critical volume in the vicinity of the point of consideration. Similar approaches have been suggested earlier in the literatures – e.g. Wilkins et al. (1980) and Giovanola and Kirkpatrick (1998). Let V_R be the characteristic volume. Then the average value of critical damage is defined as

$$\widetilde{D}_c = \frac{1}{V_R} \int D_c(x, y, z) dx dy dz \tag{5.1}$$

From three additional runs where only the mesh sizes through thickness direction (l_z) were changed, it was found that the effect of l_z is negligible when compared to the effect of in-plane elements. Therefore, Eq. (5.1) reduces to

$$\widetilde{D}_c = \frac{1}{A_R} \int D_c(x, y) dx dy \approx \frac{1}{A_R} \sum_{i=1}^{N_r} D_c^i A_i \tag{5.2}$$

where A_i, and D_c^i are the area and the critical damage value of the i^{th} element. With the specific aspect ratio of 1.38 for the present FE models, the representative area A_R can be expressed by the one-dimensional length in the tensile loading direction R_x:

$$A_R = R_x R_y = 1.38 R_x^2 \tag{5.3}$$

Note that R_x can be associated with a microstructural dimension, such as the size and the spacing of the void, provided that the critical length is known for the material. Since the localization was concentrated in the exact center of the specimen, the calculation of $\widetilde{D}_c$ was restricted to the central zone, as defined in Fig. 5.10. The profiles of damage in the tensile axis, function $D(x/R_x)$ are plotted in Fig. 5.11 for three different mesh sizes at the point of crack formation. An arbitrarily chosen length scale was used in this plot because the characteristic length of the present material was not known. For example, $R_x = 0.907mm$ was chosen to be equal to the element size of Mesh-1. It can be seen that accumulated damage is localized in the narrow zone of the center as the mesh is refined. However, $\widetilde{D}_c$ averaged over the representative length is exactly same for each of the different mesh sizes and the corresponding numerical value is indicated by the thicker line in Fig. 5.11. It is further shown in Fig. 5.12 that strong mesh dependence of the present material is greatly

reduced leading to results which converge to a unique solution by the proposed averaging approach. However, it should be pointed out that the value of $\widetilde{D}_c$ is also dependent on the specified length scale, as shown in Fig. 5.13, which emphasizes importance of introducing physical realistic length scale. The dependence of $\widetilde{D}_c$ on the R_x in the present material can be represented by fitting the numerically obtained data for a wide range of R_x and the expression is

$$\widetilde{D}_c = 0.34(R_x)^{-0.5} \tag{5.4}$$

To the author's knowledge, thorough experimental and numerical studies that would provide this material length have not been published. Furthermore, simulation of large component structures made of the present material is not feasible using a mesh size that is of the order of a microstructural dimension. Therefore, from an engineering point of view, a way to remedy the mesh dependence and ensure transferability from small laboratory specimens to structures over a wide range of sizes is to use the finite element model with the same mesh densities for all geometrically similar structures - i.e., the absolute size of elements increases as the structures dimension increases, but the total number of elements used is the same (Giovanola and Kirkpatrick, 1998; Simonsen et al. 2000, 2004). This can be achieved by keeping the normalized mesh size of the finite element model constant. In Fig. 5.14, the variation of the damage parameters - $\bar{\varepsilon}_f$, $(\sigma_m / \bar{\sigma})_{av}$, and D_c - with various mesh sizes presented earlier in Fig. 5.9 is re-plotted as a function of dimensionless mesh size ξ_l, defined as

$$\xi_l = \frac{l_x}{h_0} \tag{5.5}$$

where l_x is the size of solid element in the tensile loading direction and h_0 is the initial thickness of the tensile specimen. As compared to Fig. 5.9, results from two additional mesh sizes (l_x = 0.27 and 1.8mm) are included in Fig. 5.14. For the simulation of larger structures, ξ_l can be regarded as the ratio of the mesh size in the critical region to the thickness of the structures. Using curve fitting of the numerical results shown in Fig. 5.14, the relationship between the parameters and the ξ_l in the present material can be described by

$$D_c = 0.24\xi_l^{-0.5}, \quad 0.06 \le \xi_l \le 1.0 \tag{5.6}$$

$$(\sigma_m / \bar{\sigma})_{av} = 0.36\xi_l^{-0.2}, \quad 0.06 \le \xi_l \le 1.0 \tag{5.7}$$

$$\bar{\varepsilon}_f = 0.65\xi_l^{-0.3}, \quad 0.06 \le \xi_l \le 1.0 \tag{5.8}$$

However, one should be careful when using the normalized mesh size (ξ_l) under similar geometric and loading conditions. To successfully capture necking and fracture, the maximum value of ξ_l should be defined. Over this limit, the mesh is too coarse to predict the ductile crack growth. In the present material, the corresponding scale is 0.223 denoted by the dash-dotted line in Fig. 5.14. This scale is based on the Mesh-2 configuration. Further research is needed to validate the above approach.

The above Eq.(5.8) compares favorably to a similar equation derived by Simonsen and Törnqvist (2004) from Mode I fracture test of a large pre-notched panels:

$$\bar{\varepsilon}_f = 0.5\xi_l^{-0.4} \tag{5.9}$$

However, the Eq. (5.9) was derived for mild steel, while Eq. (5.8) applies to A710 steel. It is interesting to note that the equations relating the critical value of constant fracture strain as a function of mesh size, derived from small scale specimens and large scale panels are very close to each other even though the material is different (see Fig. 5.15).

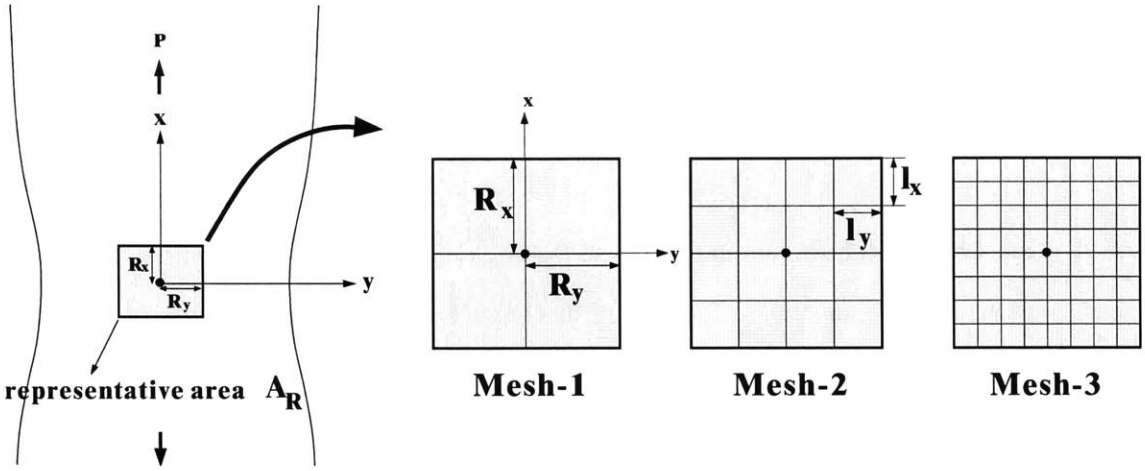

Fig. 5.10 Representative area with various mesh sizes for the evaluation of average damage value (middle layer: z = 0)

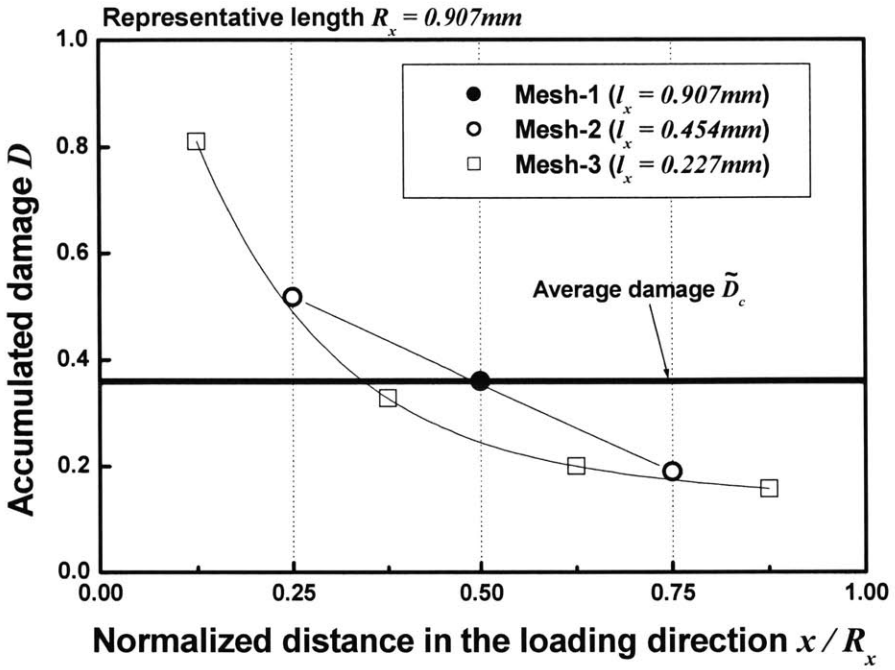

Fig. 5.11 Distribution of accumulated damage versus normalized distance in the loading direction at the point of fracture initiation $\delta_f = 5.97mm$; Considered representative dimension R_x = 0.907mm is equal to the mesh size of Mesh-1.

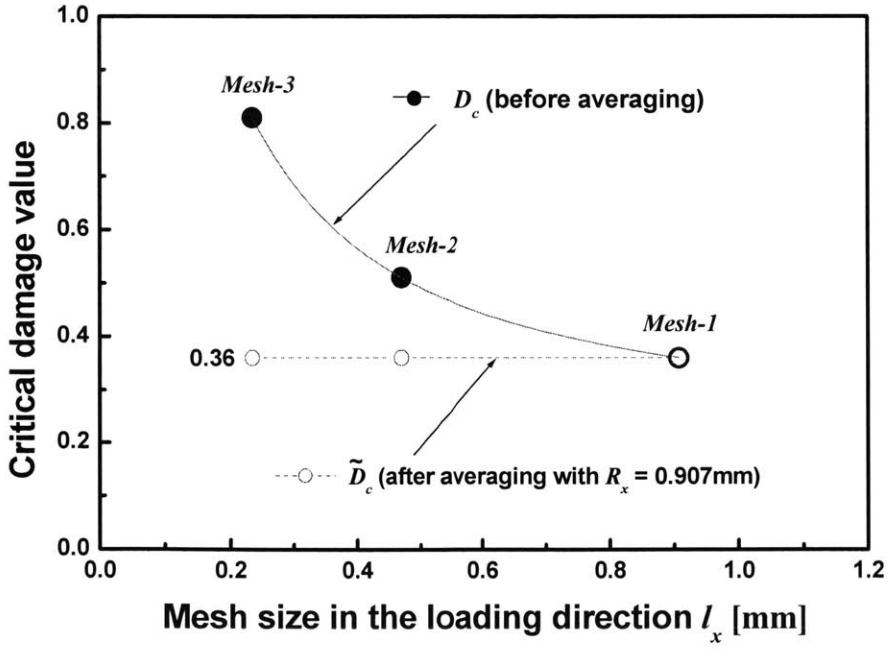

Fig. 5.12 Variation of critical damage value with three different mesh sizes in the loading direction; Considered representative dimension R_x = 0.907mm is equal to the mesh size of Mesh-1.

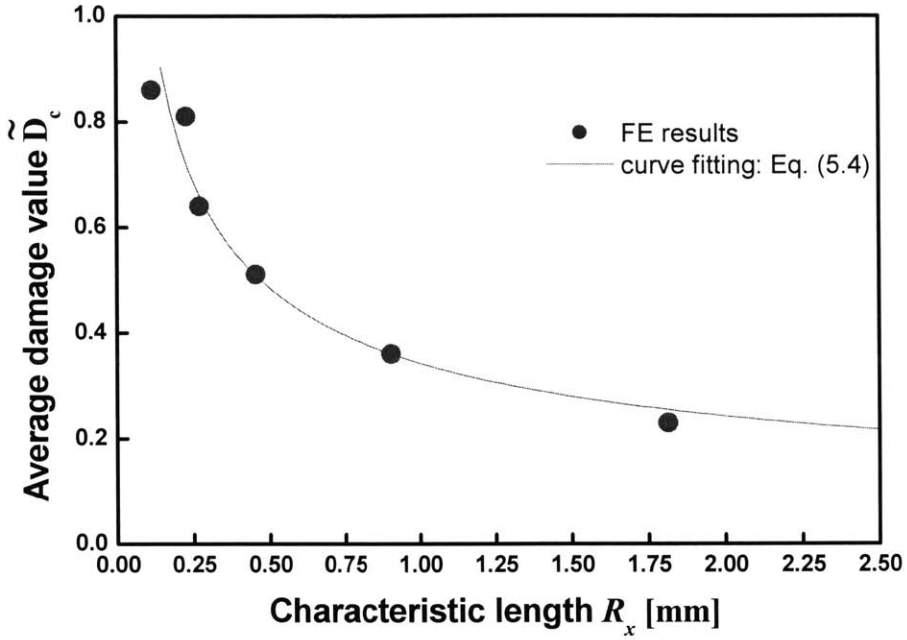

Fig. 5.13 Plot of average damage value as a function of characteristic length in the tensile loading direction

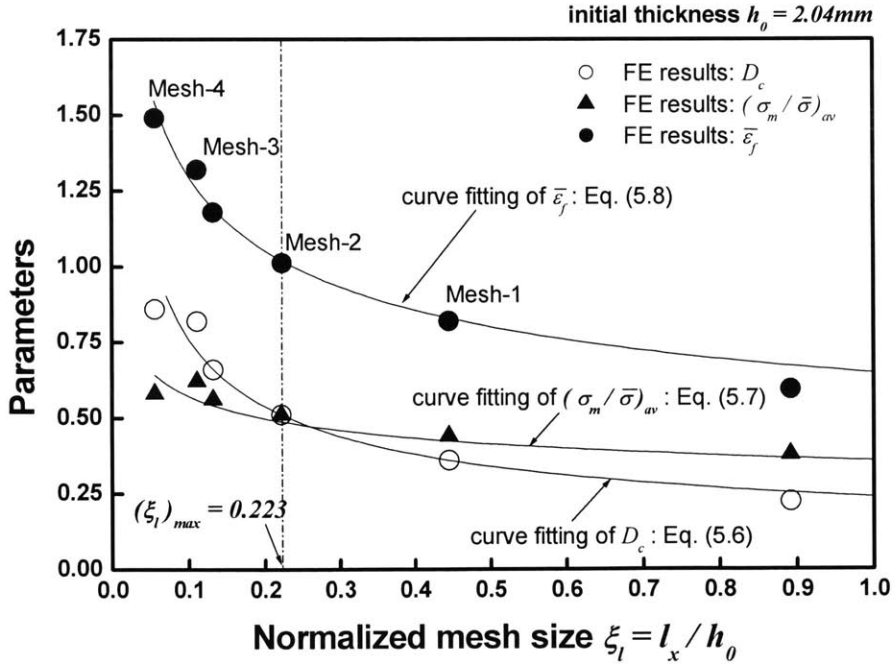

Fig. 5.14 Plots of critical damage value D_c, average stress triaxiality $(\sigma_m / \bar{\sigma})_{av}$, and equivalent strain to fracture $\bar{\varepsilon}_f$ as a function of normalized mesh size $\xi = l_x / h_0$ in the tensile loading direction (initial thickness $h_0 = 2.04$mm)

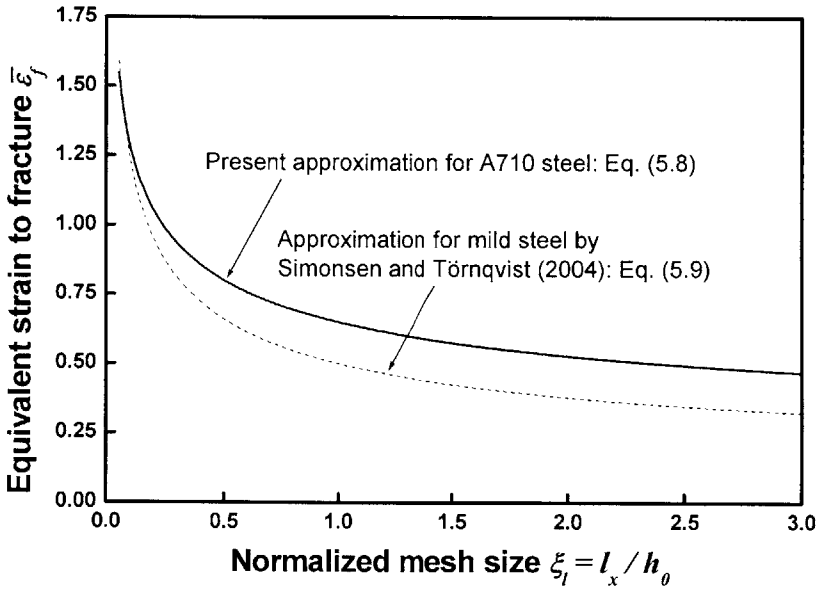

Fig. 5.15 Critical strain to fracture versus dimensionless mesh size curve for the present A710 steel material compared with the predictions of Simonsen and Törnqvist (2004) for mild steel

5.3 Analysis of crack propagation

As pointed out in Chapter 2.4, the BW fracture criterion given by Eq. (2.4) or (2.5) applies strictly to the prediction of the onset of fracture of uncracked bodies. In the present study, it was further assumed that ductile crack propagation may be viewed as a process of continuous re-initiation along the path of cracking (Atkins, 1985, 1996), as also stated in Chapter 2.4. It was found that the average stress triaxiality (defined by Eq. (2.3)) in the potential fracture point of the present problem is approximately constant during the crack propagation, see Fig. 5.19. Hence, according to Eq. (2.5), the equivalent strain is a good measure for the prediction of crack formation and propagation in the present problem. For the finite element predictions, the elements with an equivalent strain larger than the specified fracture strain from Eq. (5.8) were deleted at the point of crack formation.

5.3.1. Load-displacement response

The experimental load-displacement curve showing crack formation and subsequent crack propagation is compared to those from numerical simulations for three different mesh configurations

in Fig. 5.16. The vertical and horizontal axes in this figure are normalized by the maximum load ($P_u = 16784N$) and displacement to crack formation ($\delta_f = 5.971mm$), respectively. It is seen that the prediction with Mesh-3 configuration is in good agreement with the experiment throughout the whole process of tensile test. On the other hand, Mesh-2 follows the experiment up to the normalized displacement $\delta / \delta_f = 1.02$ and then deviates from the test. It can be further observed that Mesh-1 is too coarse to capture the localization of crack growth. Hence, for the present material, at least 10 elements over the half-width are required. The 3-D and the cross-sectional views of the deformed shapes from the crack formation to final stages of crack propagation are shown in Fig. 5.17. The considered FE model was Mesh-3. As clearly shown in Fig. 5.17(b), the crack exhibits a tunneling effect, where it grows faster in the center of the specimen due to the higher stress triaxiality. The first fracture is initiated at the center of the specimen, $(x, y, z) = (0, 0, 0)$, and then cracks propagate towards the vertical (through-thickness) direction (z) and the direction perpendicular (y) to tensile axis. The final length of crack extension at the point at which the virtual test was stopped is about half of the width of the specimen, which is similar to the experimental observation, see Fig. 5.18.

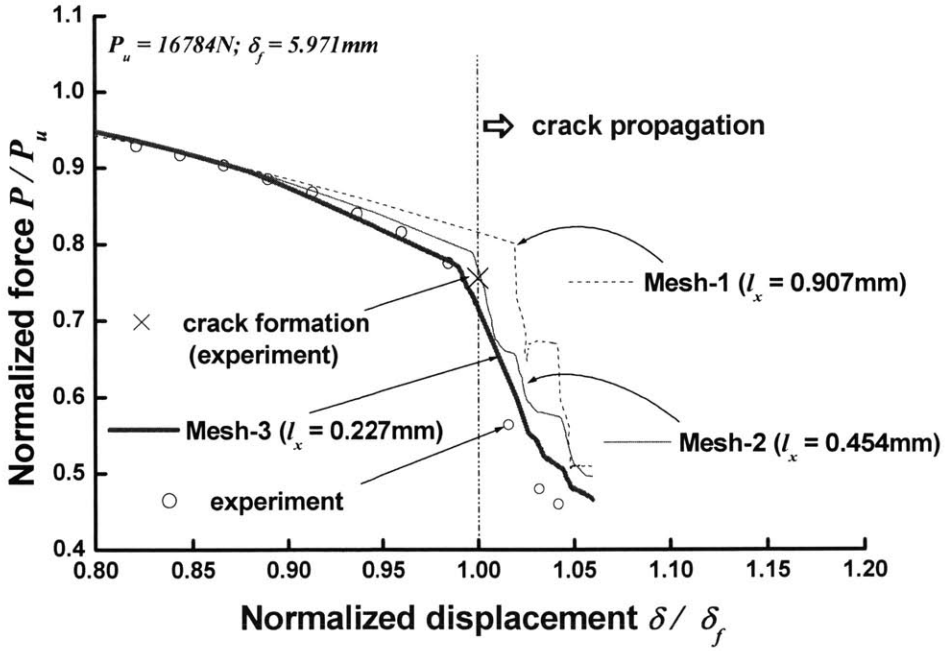

Fig. 5.16 Close-ups of the normalized load-displacement curve showing the fracture initiation and the subsequent crack propagation for different mesh sizes

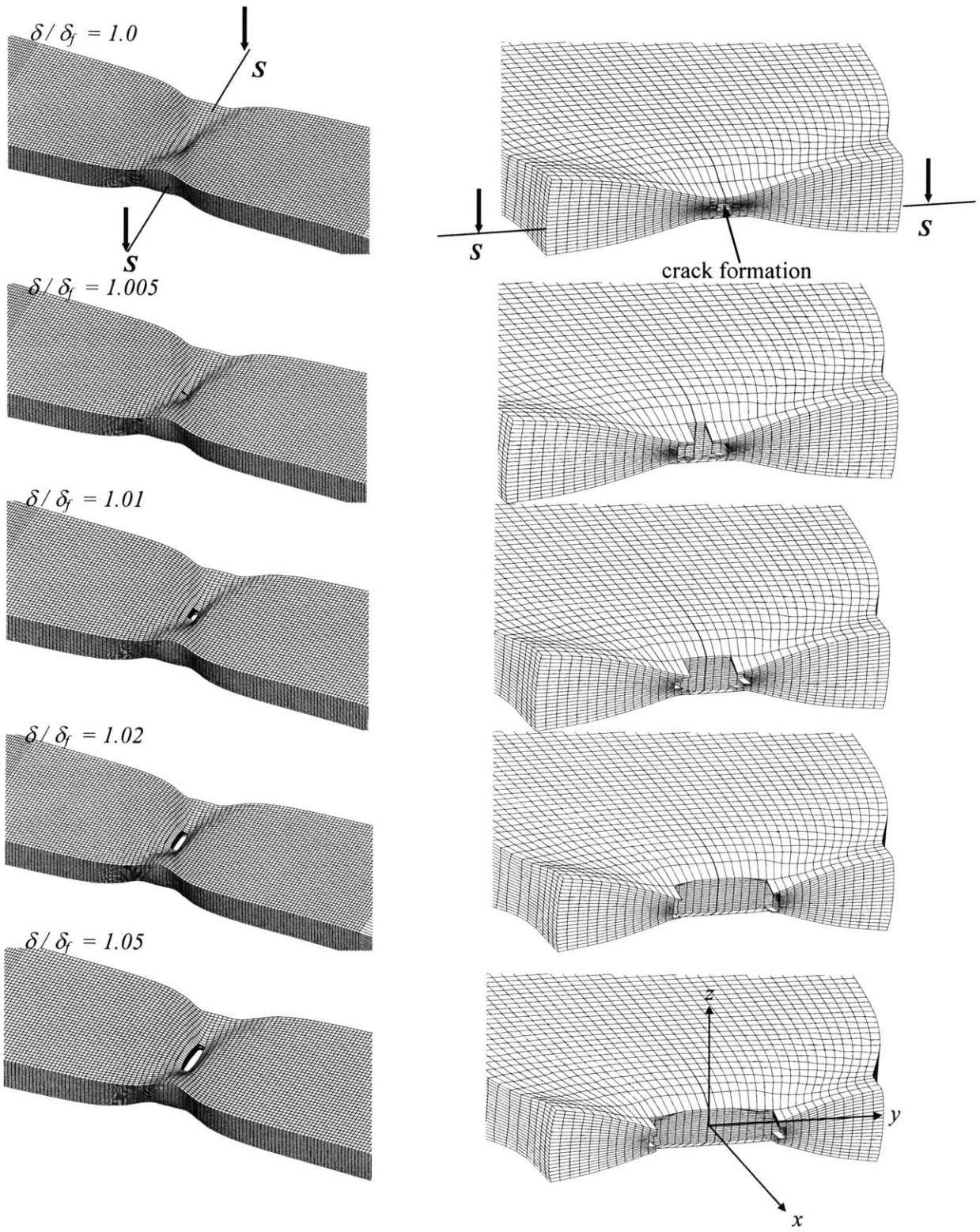

(a) 3D view in the central gauge region (b) cut through view of section S-S

Fig. 5.17 Sequence of fracture pattern from the point of fracture initiation to the subsequent crack propagation. Considered FE model is Mesh-3.

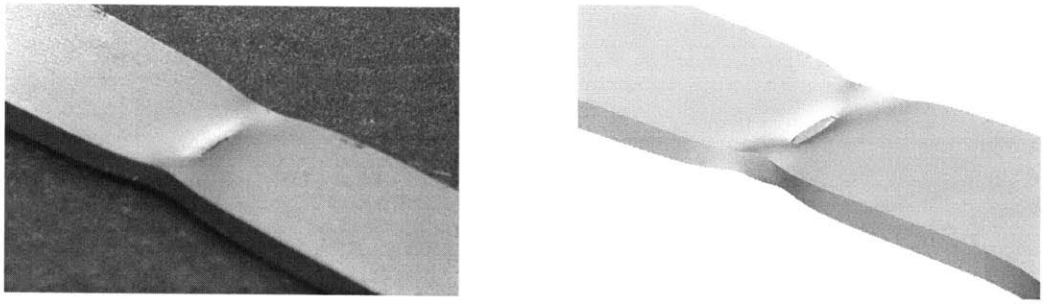

(a) experiment (b) simulation (*PAM-CRASH*)

Fig. 5.18 Comparison of experimentally and numerically obtained necking and fracture in a flat tensile specimen

5.3.2 Evolution of stress and strain fields

The histories of stress, strain, and the resulting damage at the various locations of potential fracture elements (see Fig. 5.19) were explored during the crack propagation. All the results reported in the following are obtained from the middle layer (z = 0) of Mesh-2 configuration, unless otherwise stated. Note that fracture occurred in elements C_0, C_1, C_2, and C_3 defined in Fig. 5.19. Figure 5.20 shows the stress triaxiality versus normalized displacement at the locations, as defined in Fig. 5.19. Since the deformation is approximately symmetric in the loading direction, the results of elements a_i are not included in this figure. It is seen that the stress triaxialities in all cases are almost constant and the same up to the instant at which localized necking starts. Once neck forms, stress triaxialities in the elements along the crack path (denoted by C_i) increases with the progression of deformation. The triaxiality of the central element C_0 growths faster than the neighboring elements C_1, C_2 *etc*. By contrast, stress triaxialities in the neighboring elements of the crack path (denoted by b_i) decreases. The triaxiality of element C_0 corresponding to the crack formation of the uncracked specimen shows a smooth increase with displacement. On the other hand, once fracture occurs, there are significant variations in stress triaxiality for other elements. This can be explained by the fact that the first crack formation in element C_0 introduces redistribution of stresses and large stress gradients around the crack path. Furthermore, the stress triaxiality in the elements ahead of a propagating crack (C_1, C_2, C_3, and C_4) increases steeply after the onset of fracture. This provides a sufficient stress elevation for ductile crack growth. In Fig. 5.20, also the average stress triaxiality

defined by Eq. (2.3) - i.e. $\left(\frac{\sigma_m}{\bar{\sigma}}\right)_{av} = \frac{1}{\bar{\varepsilon}_f}\int_0^{\bar{\varepsilon}_f}\frac{\sigma_m}{\bar{\sigma}}d\bar{\varepsilon}$ - is included. One can see that the difference in the average stress triaxiality $(\sigma_m / \bar{\sigma})_{av}$ between crack formation (element C_0) and propagation (elements C_1, C_2, and C_3) is very small. This clearly confirms the correctness of Eq. (2.5) for the fracture prediction. Thus, recalling from Eqns. (5.6) and (5.8), the equivalent strain to fracture, $\bar{\varepsilon}_f = 1.02$, for the critical damage value of Mesh-2 ($\xi_l = 0.223$), $D_c = 0.51$, can be also used for the prediction of crack propagation. Shown in Fig. 5.21 and 5.22 are histories of the equivalent strain and damage at the above locations. Note that the vertical axis in Fig. 5.22 indicates a dimensionless parameter where the accumulated damage during the deformation is normalized by the critical damage value. It is seen that element C_0 first reaches the critical strain and damage to fracture. Then elements C_1, C_2, and C_3 sequentially reach the critical value with the progression of displacement. We can also observe that the strain and damage of element C_4 are below the critical value - i.e. crack growth comes to the end near the normalized distance from the center, $y / w_d = 0.4$.

The profiles of stress triaxiality ahead of the crack tip are shown in Fig. 5.23 for five different stages of deformation. At the point of crack formation ($\delta / \delta_f = 1.0$), the stress state shows smooth distribution from the center to the free end of the specimen. It can be seen that there is sharp increase of triaxiality in front of the crack tip as the crack advances. However, the stress peak starts to slightly decrease after a displacement of $\delta / \delta_f = 1.02$, and appears to saturate around a certain level. These results are consistent with earlier finding that the process of crack initiation, initial growth, and quasi-static extension are different. Figure 5.24 shows that the above variation of stress triaxiality is strongly influenced by the hydrostatic stress component, whereas the effective stress remains nearly constant. The spatial distributions of plastic strain and damage in front of the crack tip are shown in Figs. 5.25 and 5.26, respectively. The spatial distribution of the completely damaged zone corresponds to the propagation of the crack. Those two figures clearly show that cracks propagate from the center of the specimen to the normal of the tensile direction. Furthermore, it is worth noting that the profiles of normalized damage during the crack propagation stage and the length of crack extension in the case of Mesh-3 (Fig. 5.27) are similar to those for the case of Mesh-2 (Fig. 5.26). From Eq. (5.8), the critical strain to fracture $\bar{\varepsilon}_f = 1.3$ was calculated and used to simulate fracture in Mesh-3 where the normalized mesh size $\xi_l = 0.111$. The above result indicates that what primarily depends on the mesh size is the onset of crack formation while the distribution of

normalized damage ahead of the crack tip and fracture pattern during the crack propagation are not mesh sensitive provided that the strain-to-fracture, which is function of mesh size in the present material, is properly defined by Eq. (5.8).

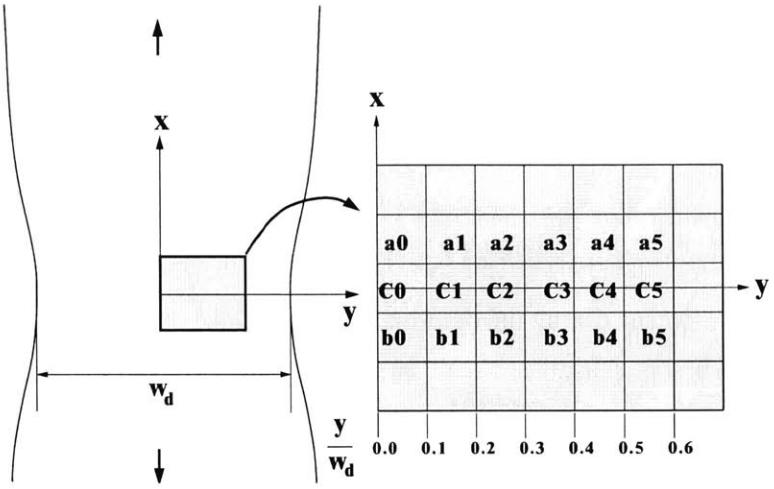

Fig. 5.19 Location of measurement for strain, stress, and damage along the crack propagation (middle layer: z = 0)

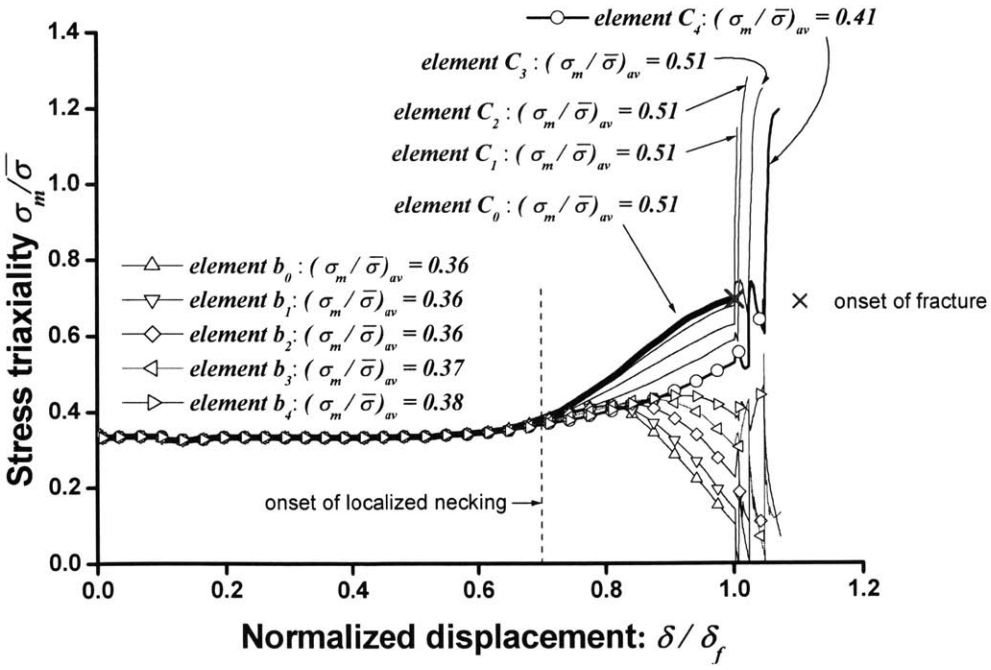

Fig. 5.20 Evolution of stress triaxiality at the critical locations of potential fracture. Note that Mesh-2 is considered and the average stress triaxiality is defined by $\left(\frac{\sigma_m}{\bar{\sigma}}\right)_{av} = \frac{1}{\bar{\varepsilon}_f}\int_0^{\bar{\varepsilon}_f}\frac{\sigma_m}{\bar{\sigma}}d\bar{\varepsilon}$.

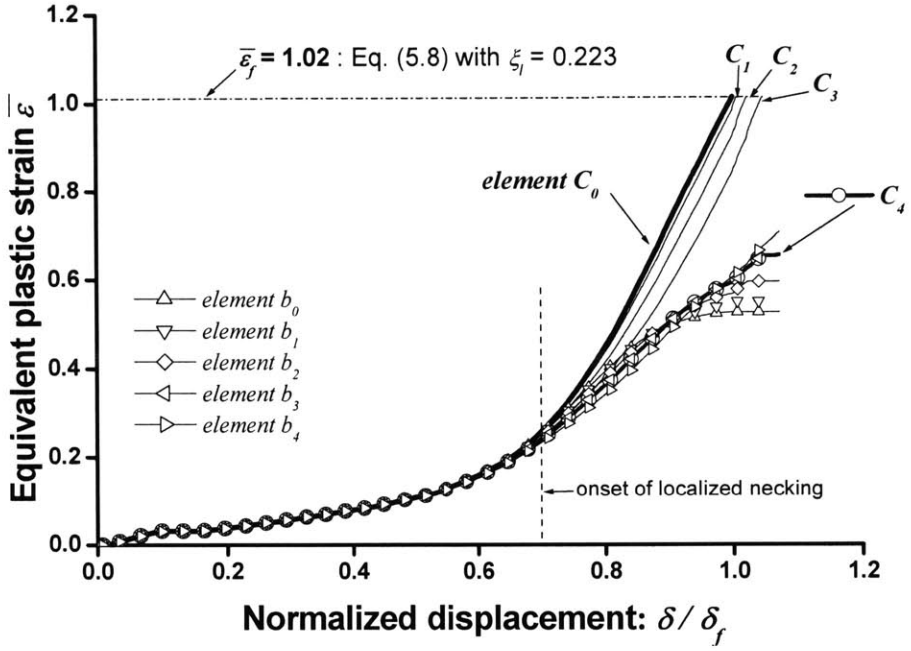

Fig. 5.21 Evolution of equivalent plastic strain at the critical locations of potential fracture. Mesh-2 is considered.

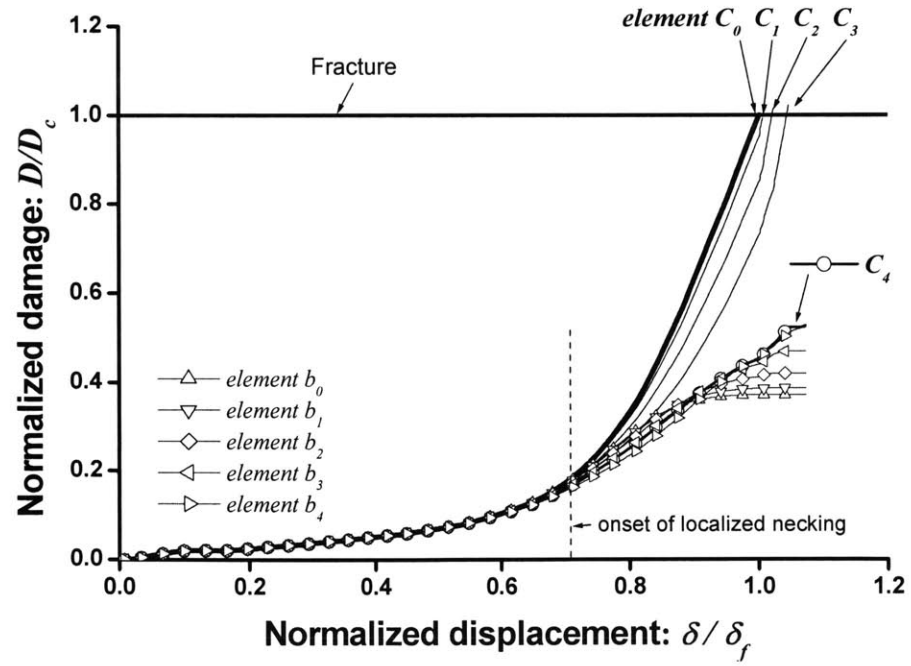

Fig. 5.22 Evolution of accumulated equivalent plastic strain and damage at the critical locations of potential fracture. Mesh-2 is considered ($D_c = 0.51$).

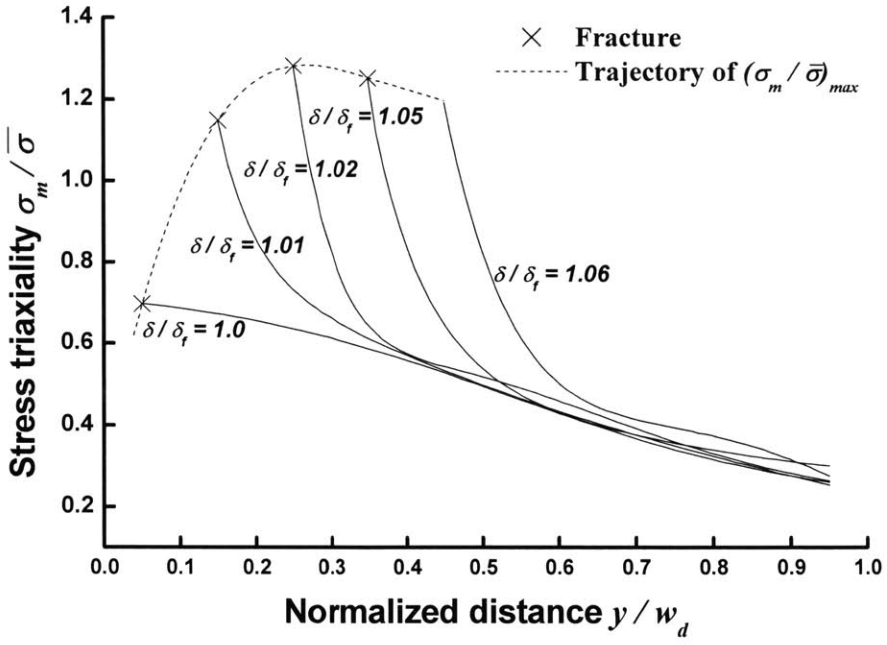

Fig. 5.23 Distribution of the stress triaxiality ahead of crack tip during the crack propagation. Mesh-2 is considered ($z = 0$; $x = 0$).

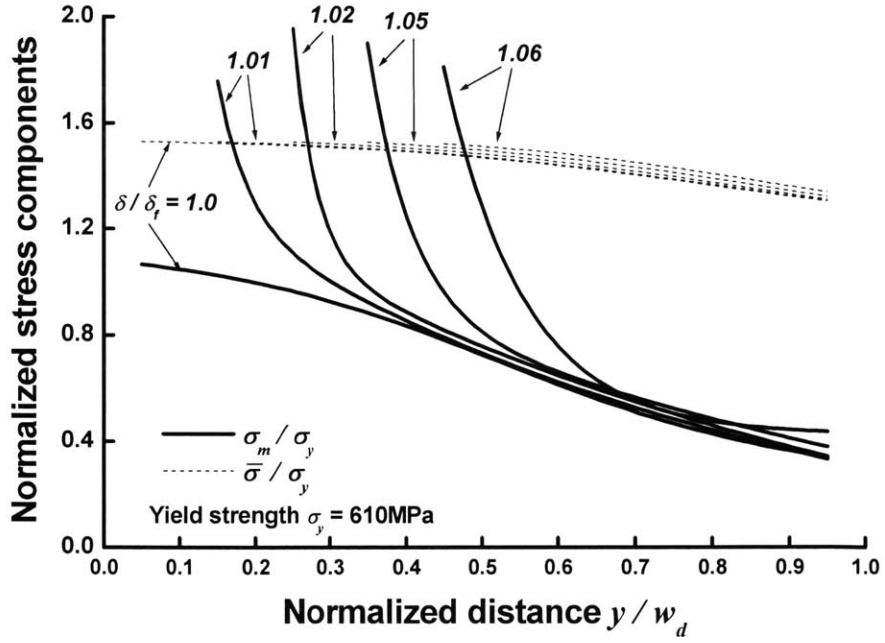

Fig. 5.24 Distribution of the hydrostatic stress σ_m and von-Mises equivalent stress $\bar{\sigma}$ ahead of crack tip during the crack propagation. Mesh-2 is considered ($z = 0$; $x = 0$).

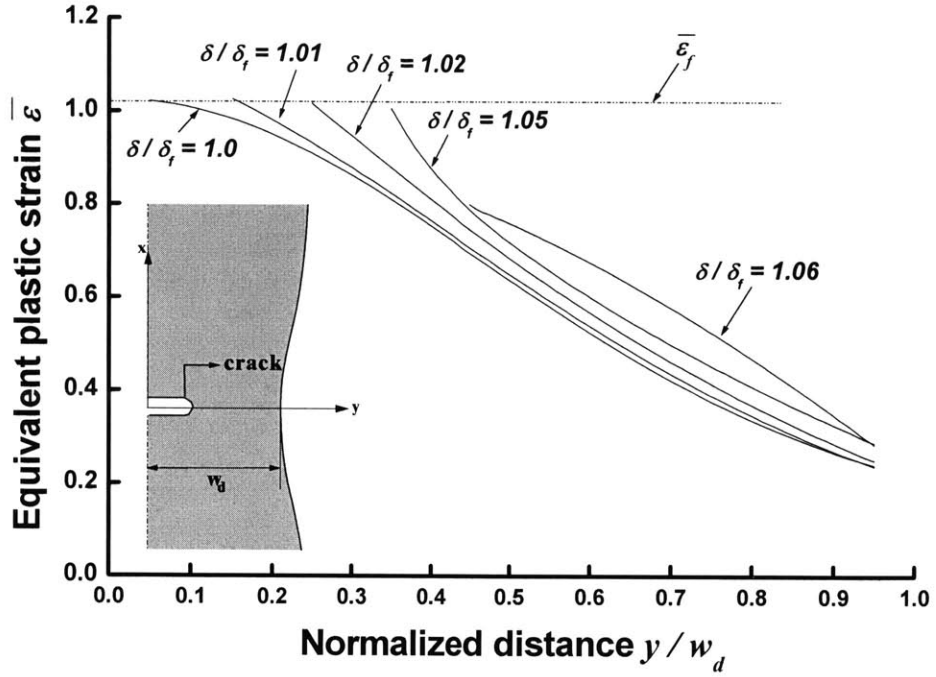

Fig. 5.25 Distribution of the equivalent plastic strain in front of crack tip during the crack propagation. Mesh-2 is considered ($z = 0$; $x = 0$).

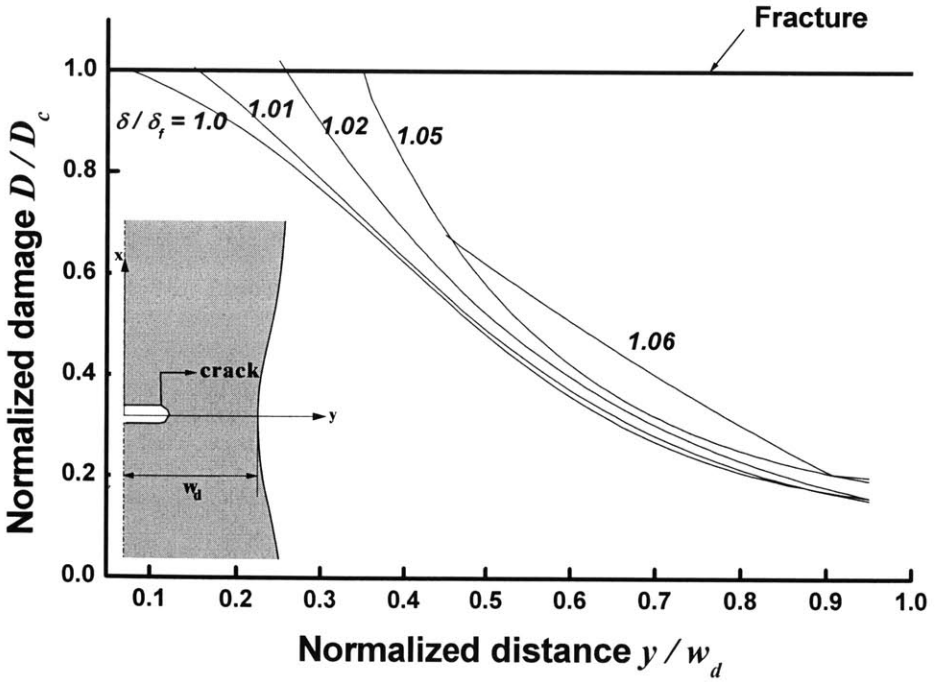

Fig. 5.26 Distribution of the normalized damage in front of crack tip during the crack propagation. Mesh-2 is considered ($z = 0$; $x = 0$; $D_c = 0.51$).

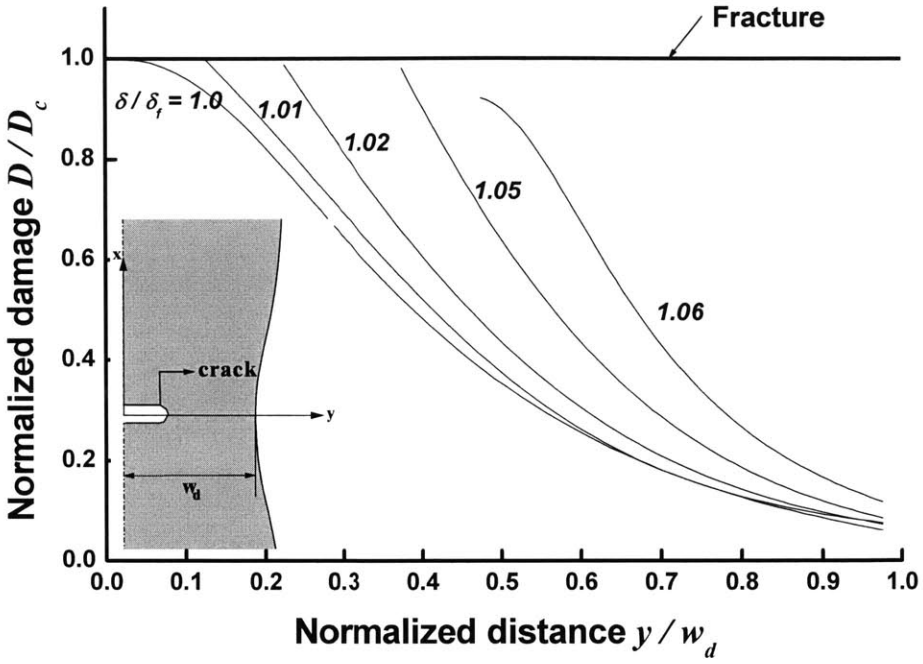

Fig. 5.27 Distribution of the normalized damage ahead of the crack tip during the crack propagation. Mesh-3 is considered ($z = 0$; $x = 0$; $D_c = 0.81$).

5.4 Conclusion

In this chapter, the formation and propagation of a crack in flat tensile specimen has been predicted by the BW fracture criterion. The main points of the present study can be summarized as follows:

- It was found that meshing a quarter of the specimen produces higher force, strain, and damage than in the case of half or full specimens. For meaningful results at least 10 elements over the half-width of the specimen are required. A coarser mesh fails to predict the onset of fracture and crack growth in such a high ductile material. A typical mesh size dependence was further observed when varying the element size. While the equivalent strain is an ever increasing function, a decrease of stress triaxilaity is observed when using a certain level of refined element size. In the present material, the corresponding element size was 0.11mm, which is comparable to the order of microstructural dimension. This drop of triaxiality coupled with the

increase in plastic strain may indicate the existence of a unique value in the critical damage parameter for the present material.

- The concept of averaging damage over a representative length scale described in this study reveals that strong mesh dependence is greatly reduced, leading to result which converges to a unique value at the specified length scale. However, it was also shown that the average value is dependent on the length scale. For the practical prediction of fracture for larger structures, a relationship between the damage parameters and the normalized mesh size (Eqns. (5.6) ~ (5.8)) was constructed.
- The stress and strain states at the potential fracture sites were explored numerically during crack propagation. It was found that the average stress triaxiality $(\sigma_m / \overline{\sigma})_{av}$ along the crack path is nearly constant. This provides a reasonable assumption that ductile crack propagation is indeed a process of continuous re-initiation ahead of the crack for materials in which cracks are formulated by the process of void growth and coalescence. The various features of crack propagation including the global load-displacement, fracture pattern, and crack extension were well predicted by numerical simulations with fine mesh configurations. Furthermore, it was shown visually that simulations with the ductile fracture criterion are able to predict a tunneling effect. With respect to the mesh size dependence during the crack propagation, it was also observed that the distribution of normalized damage in front of the crack tip and final crack extension are not mesh sensitive, provided that the strain-to-fracture, which is function of mesh size in the considered material and defined by Eq. (5.8), is used.

This page intentionally left blank

Chapter 6

Fracture Prediction of Thin Plates under Static Punch Indentation

One of the main objectives of this chapter is to validate the present ductile fracture criterion at the component level. Two component studies are carried out: a thin plate and stiffened double plates indented by a rigid punch. We will show that using the local fracture criterion given by Eq. (2.4) one can accurately predict the location of the fracture, the extension of cracks, the fracture patterns, and the corresponding load-displacement curve.

6.1 Thin single plates under hemi-spherical punch indentation

6.1.1 Introduction

An experimental, numerical, and analytical investigation on the deformation and failure of clamped thin plates subjected to localized static punch loading is presented in Section 6.1. The immediate objective of this work is to determine the onset of fracture in a class of thin plates with three different thicknesses and three sizes of a hemi-spherical punch. The point of departure is a postulated local fracture criterion formulated in terms of the accumulated plastic strain with various

stress triaxiality weighting functions, as discussed by Bao and Wierzbicki (2004a/b). Similar fracture criteria were postulated earlier by others, see for example McClintock (1968), Rice and Tracey (1969), and Hancock and Mackenzie (1976). The fracture criterion is first calibrated from uniaxial tensile test and then applied to predict formation of a circumferential crack in a plate punch stretching operation. A good agreement between the results of tests and finite element simulations provides an important validation of the fracture criterion at the component level.

Punch indentation of thin sheets is a well established technique to determine the Forming Limit Diagram (FLD). In the sheet metal forming industry, failure is understood as a formation of a localized neck under plane stress state. In order to cover the range of strain increments in the tension-tension and tension-compression quadrants, different blankholder forces or different radii of cut-outs were applied in punch-stretch experiments, Keeler (1963). Since the ground-breaking work by Hill (1948, 1952), various methods were used to construct FLD from theoretical considerations, Swift (1952), Stören and Rice (1975), and Marciniak and Kuczynski (1967). It is well known that friction changes the state of stress and strain in sheets and thereby affect formation of neck and fracture, Ferron and Zeghloul (1993) and Marciniak and Duncan (1992). Friction is difficult to control in tests but is relatively easy to model in finite element simulation. In this study the process of punch indentation is simulated using *PAM-CRASH* and *LS-DYNA3D* over a wide range of friction coefficient $\mu = 0$ to 1. In each case the onset of a circumferential crack is determined and the locus of fracture points in the space of principal strains is interpreted as a Fracture Forming Limit Diagram (FFLD). Ferron and Zeghloul (1993) used the variable friction coefficient as a calibration method to generate FFLD from the energetical criterion of Cockcroft and Latham (1968). In the present section a similar approach is taken using commercial codes as a convenient tool. It was found that changing friction coefficient from the keyboard is much easier than to construct several models with different cut-outs. It should be mentioned that numerical tools in conjunction with Marciniak and Kuczynski necking criterion were recently used by Butuc et al. (2002) to construct FLD taking into account linear and complex strain paths as well as different yield functions and associated hardening laws. The fracture limit of anisotropic metal sheets was investigated by Tang et al. (1999) where the state of anisotropic damage was taken into account.

Parallel to numerical studies, interest in the analytical predictions of deformation and fracture of plates under a spherical punch was renewed over the past few years (Wang et al., 1998; Chakrabarty, 1970, 1999; Kaminishi, 1992; Simonsen and Lauridsen, 2000). Simple solutions of the resistance of thin plates prior to fracture was derived by Wang et al. (1998) assuming an idealized rigid-plastic

material and deformation. Chakrabarty (1970, 1999) developed the analytical solution for the stretch forming over a hemispherical punch with the assumption of a balanced biaxial state of stress throughout the deforming surface. The onset of fracture of thin plates was determined by Kaminishi (1992), where the localized necking condition was employed. Based on a global instability criterion taking into account both the change of geometric and material stiffness during the indentation process, Simonsen and Lauridsen (2000) derived analytical solutions for the force-displacement behavior of a plastic membrane up to failure and the solution was correlated with tests. In this Section 6.1, an approximate closed-form solution is derived for the formation of circumferential crack. In particular, an expression for the critical punch displacement to fracture was derived in terms of the critical damage value of material, plate radius, and punch radius. This expression is more exact than a similar result derived earlier by Simonsen and Lauridsen (2000) using the global instability approach.

In the present study, the accumulated plastic strain with the stress triaxiality as a weighting function is introduced as a local ductile fracture criterion in the finite element analysis and analytical approximation. The global punch force-indentation responses as well as the onset of fracture obtained from the numerical and analytical solutions are thoroughly compared with experimental results. This Section 6.1 is organized as follows. Analytical approximations on the deformation and onset of fracture are presented in Section 6.1.2, along with the postulated ductile fracture criterion. In Section 6.1.3, the fracture criterion is calibrated by finite element simulations of uniaxial tensile tests for the considered mild steel material. In Section 6.1.4, experimental and numerical procedures on the punch indentation are explained. Section 6.1.5 presents the frictional effect on the strain and stress states at the critical locations of fracture with particular focus on the construction of FFLD. Furthermore, the numerically obtained history and profiles of stress, strain, and resulting damage are included and compared with the analytical approximation. The global punch force-indentation responses and fracture patterns of the plates are presented in Section 6.1.6. Finally, the effect of punch radii on the onset of fracture is investigated in Section 6.1.7 with focus on the validation of analytical approximation.

6.1.2 Analytical approximation

Consider a clamped thin circular plate subjected to lateral indentation by a hemi-spherical rigid punch, as shown in Fig. 6.1. The radius of the clamped plate, the punch radius, and the initial thickness of the plate are denoted respectively by R_0, R_b, and h_0. Let h denote the current thickness of the plate at a distance r from the plate center. The total punch penetration is denoted by δ and the corresponding punch force by P. The plate is clamped at the outer radius so that $w(R_0) = 0$, where w is the transverse deflection of the plate. Because of the loading is axi-symmetric, it is assumed that the plate response is also axi-symmetric so that the transverse deflection is only a function of current plate radius r.

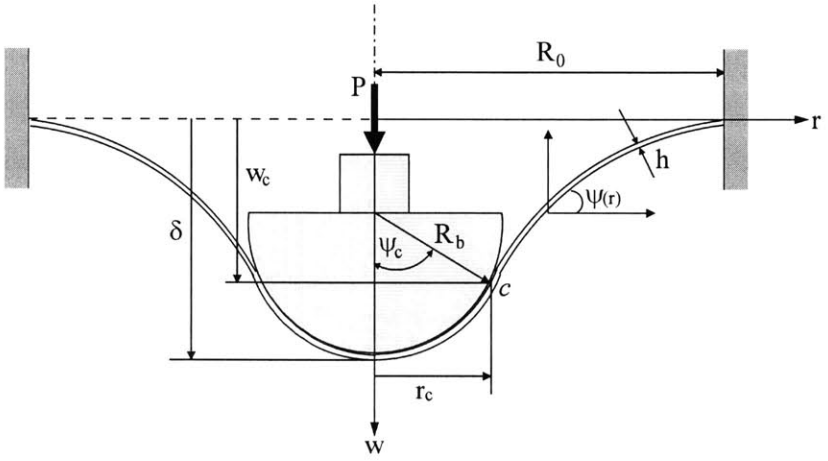

Fig. 6.1 Geometry of a clamped thin plate loaded quasi-statically by a hemispherical punch

The main objective of present study is to predict the onset of fracture. It is known from many earlier publications (see for example Simonsen and Lauridsen, 2000) that fracture occurs when the deflections are an order of magnitude larger than the plate thickness. In the range of large deflections, the bending resistance can be neglected and the plate response is governed by the membrane response. There are two components of the membrane forces (per unit length) in the present axi-symmetric problems. The radial membrane force $N_r = \sigma_r h$ and the circumferential membrane force $N_\theta = \sigma_\theta h$. The generalized components of strain tensors, associated with the

above stresses are the radial strain ε_r and the circumferential strain ε_θ. These are defined in polar coordinate systems by

$$\varepsilon_r = \frac{1}{2}\left(\frac{\partial w}{\partial r}\right)^2 + \left(\frac{\partial u}{\partial r}\right) \tag{6.1}$$

$$\varepsilon_\theta = \frac{u}{r} \tag{6.2}$$

Many authors in the past including Refs. (Wang et al., 1998; Simonsen and Lauridsen, 2000) introduced the further simplification that the in-plane displacement u is zero. In order to obtain a mathematically tractable system of equations, it is assumed here that $u = 0$ and consequently $\varepsilon_\theta = 0$. The validity of this assumption will be discussed in conjunction with the analytical and numerical solutions later in Section 6.1.7.

6.1.2.1 Force–penetration

Over the region of contact between plate and a hemi-spherical punch of radius R_b, the equation of normal equilibrium is

$$\frac{N_\theta}{R_b} + \frac{N_r}{R_b} = p, \quad r \in (0, r_c) \tag{6.3}$$

where p is the normal force per unit surface area applied by the punch. Recall that from condition of symmetry, the radial membrane force N_r and the resulting shear force $N_r \sin\psi_c$ (ψ_c is the angle from the center of the punch to the outermost contact point c between the plate and the punch) around the point c are independent of the circumferential coordinate. Using the vertical equilibrium of this point, the total punch force P is given by

$$P = 2\pi r_c N_r \sin\psi_c \tag{6.4}$$

where $r_c = R_b \sin\psi_c$. The radial stress σ_r or the radial membrane force N_r has so far not been specified. We introduced here the concept of a limited interaction curve so that the radial component of the stress tensor is assumed to be equal to the uniaxial stress. It is further assumed that the material of plate follows a power-hardening law.

$$\sigma_r = K\varepsilon_r^n \tag{6.5}$$

where K and n are strength coefficient and work hardening exponent of the material. With the assumption of $u = 0$ and geometrical relation, the expression for radial membrane force becomes

$$N_r = K\left(\frac{1}{2}\tan^2\psi\right)^n h_0 \cos\psi \tag{6.6}$$

Substituting Eq. (6.6) into Eq. (6.4), the total punch force P can be rewritten as

$$P(\psi_c) = 2\pi K h_0 R_b \left(\frac{1}{2}\tan^2\psi_c\right)^n \cos\psi_c \sin^2\psi_c \tag{6.7}$$

In the region of outside the contact, $r \in (r_c, R_0)$, the constant pressure is zero and Eq. (6.3) takes the form

$$\frac{N_\theta}{R_\theta} + \frac{N_r}{R_r} = 0, \quad r \in (r_c, R_0) \tag{6.8}$$

where the circumferential and radial curvatures are $1/R_\theta = \sin\psi / r$ and $1/R_r = (d\psi/dr)\cos\psi$, respectively. Therefore, the equation of normal equilibrium becomes

$$\frac{\sigma_\theta}{r}\sin\psi + \frac{d\psi}{dr}\sigma_r \cos\psi = 0, \quad r \in (r_c, R_0) \tag{6.9}$$

Let β denote the ratio of circumferential stress to radial stress and the above expression becomes

$$\beta(r) = \frac{\sigma_\theta}{\sigma_r} = -r\frac{d\psi}{dr}\cot\psi, \quad r \in (r_c, R_0) \tag{6.10}$$

Using the von Mises plane stress yield condition – i.e. $\bar{\sigma} = \sqrt{\sigma_r^2 - \sigma_r\sigma_\theta + \sigma_\theta^2}$, one can show that the stress triaxiality, defined as the ratio of the hydrostatic mean stress σ_m to the von Mises equivalent stress $\bar{\sigma}$, can be expressed either in terms of β or α,

$$\frac{\sigma_m}{\bar{\sigma}}(r) = \frac{1}{3}\frac{1+\beta}{\sqrt{1+\beta^2-\beta}} = \frac{1}{\sqrt{3}}\frac{1+\alpha}{\sqrt{1+\alpha^2+\alpha}} \tag{6.11}$$

where α is the strain rate ratio $\dot{\varepsilon}_\theta / \dot{\varepsilon}_r$, equal to $(2\beta - 1)/(2 - \beta)$ with the assumption of isotropy in the plane of the sheet. Since $\sigma_r = \sigma_\theta$ at the center $(r = 0)$, while $u = 0$ at the clamped edge $(r = R_0)$, the boundary conditions for the stress and strain rate ratios are

$$\begin{aligned} &\alpha(0) = \beta(0) = 1.0 \\ &\alpha(R_0) = 0, \beta(R_0) = 0.5 \end{aligned} \tag{6.12}$$

From the results of numerical simulation, Fig. 6.11, the profile of strain ratio is proposed in a form so that both boundary conditions satisfy as well as the loading trajectory around the area of potential fracture is well approximated. The postulated strain ratio is

$$\alpha(r) = 1 - \sqrt{(r / R_0)} \tag{6.13}$$

Hence, the corresponding stress ratio throughout the deforming surface can be approximated as

$$\beta(r) = \frac{2\alpha + 1}{2 + \alpha} = \frac{3 - 2\sqrt{(r / R_0)}}{3 - \sqrt{(r / R_0)}} \tag{6.14}$$

It should be mentioned that the proportional loading path is assumed from Eq. (6.13) on. It can be inferred from Figs. 6.14, 6.17, and 6.18 that this assumption does not introduce a substantial error in the analytical solution since the change in the $\beta, \alpha,$ and $\sigma_m / \bar{\sigma}$ at the potential locations of fracture is narrow during the deformation process. Furthermore, it was shown by Atkins (1985) that some forms of the fracture criterion, $\int f(\sigma_m / \bar{\sigma}) d\bar{\varepsilon}$, the integral is path independent. Based on the above observations, $\beta, \alpha,$ and $\sigma_m / \bar{\sigma}$ can be assumed to be a function of space coordinate (r) rather than functions of both r and time. The validity of above approximation is examined in Section 6.1.5 by comparing with the numerical results shown in Figs. 6.17 and 6.18.

It is convenient to introduce the following dimensionless quantities

$$\xi = \frac{r}{R_0}, \quad \xi_0 = \frac{R_b}{R_0}, \quad \xi_c = \frac{r_c}{R_0} = \xi_0 \sin\psi_c \tag{6.15}$$

In terms of the above quantities the normal equilibrium equations of the problem, Eq. (6.10) can be rewritten as

$$\cot\psi d\psi = \frac{2\sqrt{\xi} - 3}{3 - \sqrt{\xi}} \frac{d\xi}{\xi}, \quad \xi \in (\xi_c, 1) \tag{6.16}$$

The integration of the above equation results in

$$\psi(\xi, \psi_c) = \frac{\xi_c^2 (3 - \sqrt{\xi_c})^2}{\xi_0 (3 - \sqrt{\xi})\xi}, \quad \xi \in (\xi_c, 1) \tag{6.17}$$

Furthermore, a solution for transverse deflection $w(\xi, \psi_c)$ is determined by integrating the slope

$$w(\xi, \psi_c) = R_0 \int_{\xi}^{1} \tan\psi(\xi, \psi_c) d\xi, \quad \xi \in (\xi_c, 1) \tag{6.18}$$

where $\psi(\xi,\psi_c)$ is given by Eg. (6.17). In dimensionless form the resulting transverse deflection over the region of outside the contact is

$$\frac{w(\xi)}{R_0}=\frac{2\xi_c^2(3-\sqrt{\xi_c})^2}{\xi_0}\left[\frac{1-\sqrt{\xi}}{6(3-\sqrt{\xi})}-\frac{1}{9}\ln\left(\frac{2\sqrt{\xi}}{3-\sqrt{\xi}}\right)+\frac{2\xi_c^4(3-\sqrt{\xi_c})^4(1-\sqrt{\xi})}{9\xi_0^2(3-\sqrt{\xi})^6\xi^{2.5}}\right],\ \xi\in(\xi_c,1) \tag{6.19}$$

The maximum indentation of the tip δ is the sum of the height of the sphere from the center to point c and the plate displacement at c, $w_c(\psi_c)$ obtained from Eq. (6.19) by setting $\xi=\xi_c$

$$\frac{\delta(\psi_c)}{R_0}=\frac{\xi_0\psi_c^2}{2}+\frac{2\xi_c^2(3-\sqrt{\xi_c})^2}{\xi_0}\left[\frac{1-\sqrt{\xi_c}}{6(3-\sqrt{\xi_c})}-\frac{1}{9}\ln\left(\frac{2\sqrt{\xi_c}}{3-\sqrt{\xi_c}}\right)+\frac{2\xi_c^{1.5}(1-\sqrt{\xi_c})}{9\xi_0^2(3-\sqrt{\xi})^2}\right] \tag{6.20}$$

Finally, the punch force-penetration relation is given parametrically through a series of wrapping angles, ψ_c by Eqns. (6.7) and (6.20).

6.1.2.2 Crack formation

In the present punch indentation problem, the stress triaxiality is changing in a relatively narrow range $(1/3\le\sigma_m/\bar{\sigma}\le 2/3)$ and is always positive. Under this condition, it is assumed that the damage is accumulated right from the beginning of the loading. Note that the same assumption is consistently used in the calibration from uniaxial tensile tests. Accordingly, the condition for fracture was assumed to be controlled by Eq. (2.4). By introducing a concept of the average stress triaxiality during the deformation i.e. $\left(\frac{\sigma_m}{\bar{\sigma}}\right)_{av}=\frac{1}{\bar{\varepsilon}_f}\int_0^{\bar{\varepsilon}_f}\frac{\sigma_m}{\bar{\sigma}}d\bar{\varepsilon}$, an alternative expression for the fracture criterion is

$$\bar{\varepsilon}_f=\frac{D_c}{(\sigma_m/\bar{\sigma})_{av}} \tag{6.21}$$

As shown in Fig. 6.2 where the shape of fracture envelope controlled by Eq. (6.21) is schematically illustrated, the material ductility, as measured by the equivalent strain to fracture, decreases with the stress triaxiality in the range of stress triaxiality $(1/3\le\sigma_m/\bar{\sigma}\le 2/3)$. In sheet metal deformation of plates with clamped boundary conditions, the stress state (σ_1,σ_2) always stay in the first tension-tension quadrant. The corresponding stress triaxiality remains in the range between 1/3 (uniaxial tension) and 2/3 (equi-biaxial tension). The dependence of equivalent fracture strain on the average

stress triaxiality given by Eq.(6.21) is plotted in Fig. 6.2 as a full line. For example, in uniaxial tension, $(\sigma_m / \bar{\sigma})_{av} = 1/3$ and from Eq. (6.21) $\bar{\varepsilon}_f = 3D_c$.

The maximum radial strain in the plate occurs at point *c* (see Fig. 6.1) with $\varepsilon_{r,\max} = (1/2)\tan^2 \psi_c$. Under the assumption of plane stress and $u = 0$, the maximum equivalent strain is given by

$$\bar{\varepsilon}_{\max} = \frac{2}{\sqrt{3}} \varepsilon_{r,\max} = \frac{1}{\sqrt{3}} \tan^2 \psi_c \tag{6.22}$$

Thus, Eqns (6.21) and (6.22) with $\bar{\varepsilon}_{\max} = \bar{\varepsilon}_f$ give the approximated wrapping angle $\psi_c = \psi_{c,f}$ at fracture

$$\psi_{c,f} \approx \left(\frac{\sqrt{3} D_c}{(\sigma_m / \bar{\sigma})_{av}} \right)^{1/2} \tag{6.23}$$

From material calibration explained in next Section 6.1.3, the critical value of damage parameter is $D_c = 0.27$ and average stress triaxiality in the punch indentation $(\sigma_m / \bar{\sigma})_{av} = 0.6$ (see Fig. 6.14). Substituting the above values into Eq. (6.23), the critical wrapping angle becomes $\psi_{c,f} = 0.88$ or 50^0.

The normalized penetration to fracture δ_f / R_0 can be obtained from Eq. (6.20) by setting $\psi_c = \psi_{c,f}$.

$$\frac{\delta_f}{R_0} = f(\psi_{c,f}, \xi_0) \tag{6.24}$$

Referring to Eq. (6.23), it can be further assumed that $\psi_{c,f}$ is primarily dependent on D_c since the average stress triaxiality is almost constant in the present problem. For a given D_c, the critical penetration to fracture becomes functions of ξ_0 only. In order to be more general, we are developing of the relationship for δ_f / R_0 in the following form

$$\frac{\delta_f}{R_0} = a_1 D_c^{a_2} \xi_0^{a_3} \tag{6.25}$$

The constants a_1, a_2, and a_3 were determined by curve fitting of prediction of Eq. (6.20) for a wide range of ξ_0. Final expression for the normalized penetration to fracture is

$$\frac{\delta_f}{R_0} = \sqrt{2D_c}\, \xi_0^{0.38} \tag{6.26}$$

The proposed solution is within 5% of the experimental and numerical results for normalized punch radii $0.1 < \xi_0 < 0.75$, as shown in Fig. 6.28. The result is correct for this particular material for which calibration was made. It is believed to be also valid for other material characterized by similar ductility. It should be mentioned that similar equation derived by Simonsen and Lauridsen (2000) was based on the global stability condition and therefore did not include information about material ductility other than hardening exponent (n):

$$\frac{\delta_f}{R_0} = 1.41 n^{0.33} \xi_0^{0.52} \tag{6.27}$$

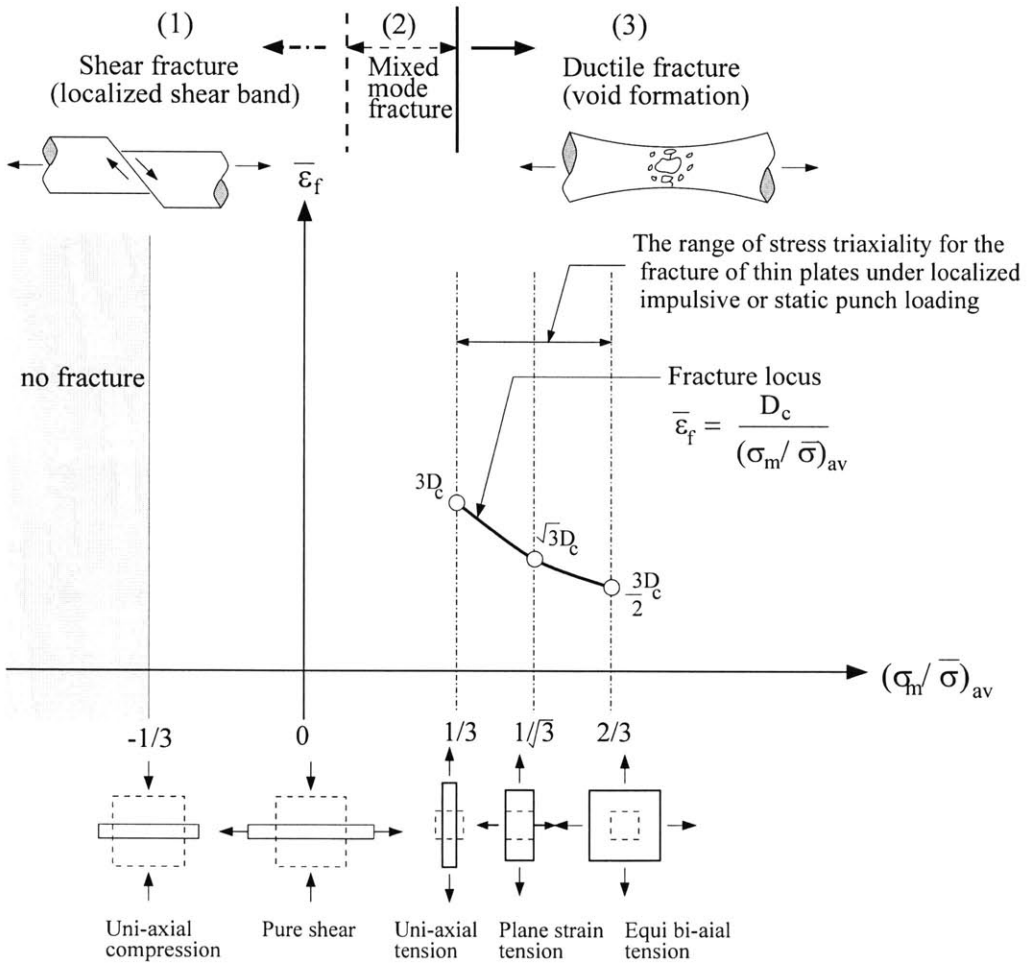

Fig. 6.2 A schematic diagram showing fracture envelope in the range of expected stress triaxiality for the present problem in the space of equivalent plastic strain to fracture $\bar{\varepsilon}_f$ and average stress triaxiality $(\sigma_m/\bar{\sigma})_{av}$ (branch I)

6.1.3 Calibration of material model (mild steel - A)

A general description on the calibration procedure to determine the actual stress-strain curve and critical damage parameters is presented in Chapter 3.2. In this section, the results for a mild steel - A, obtained from the conventional calibration method is summarized. Flat, dog-bone specimens were cut from the thin sheets to be tested. An experimentally obtained load displacement curve is shown in Fig. 6.3 by thick solid line. It should be mentioned that several tensile coupons were cut in two perpendicular directions but no appreciable differences were found between the corresponding tensile responses. In the numerical simulation of the tensile specimen, three different mesh configurations were employed to investigate the mesh sensitivity. The coarse mesh used 6 elements to the width. The medium mesh used 14 elements and the fine mesh 20 elements, see Fig. 6.5. The simulation results for three different mesh sizes are shown as thin lines in Fig. 6.3. The initial and actual stress-stain curve are depicted in Fig. 6.4 for the case of plate thickness h_0 = 1.4mm. The initial stress-strain curve could be approximated by the power law of the form $\sigma = K\varepsilon^n$. The best curve fitted was obtained using $K = 586MPa$ and $n = 0.22$ (see Table 6.1) and fitted power curve is shown as dotted line in Fig. 6.4.

Table 6.1 Summary of best curve fitting for the power law in three different thicknesses of plates

Plate thickness h_0	Strength coefficient K	Work hardening exponent n
0.9 mm	536 MPa	0.22
1.14 mm	586 MPa	0.22
1.40 mm	586 MPa	0.22

Figure 6.6 shows the history of equivalent strain at the critical point of fracture for three different meshes used. It can be observed that the difference between curves correspond to medium and smallest mesh is insignificant which means that solution is rapidly converging and there is a unique value of the equivalent strain to fracture for the mild steel - A. The history of triaxilaty function with an equivalent strain as an independent variable is shown in Fig. 6.7. The magnitudes of three critical damage parameters are summarized in Table 6.2 for three types of meshes.

Table 6.2 Configurations of the mesh used in the numerical simulation. Note that N is the number of shell elements in the width of tensile test specimen (h_0 = 1.4mm).

Mesh configuration	Number of elements N	Mesh size (mm)	Normalized mesh size (mesh size/ h_0)	$(\sigma_m / \bar{\sigma})^0_{av}$	$\mathbf{b} = \bar{\varepsilon}_f$	D_c
Coarse	6	2.10	1.5	0.34	0.71	0.241
Medium	14	0.90	0.64	0.34	0.80	0.270
Fine	20	0.63	0.45	0.34	0.81	0.276

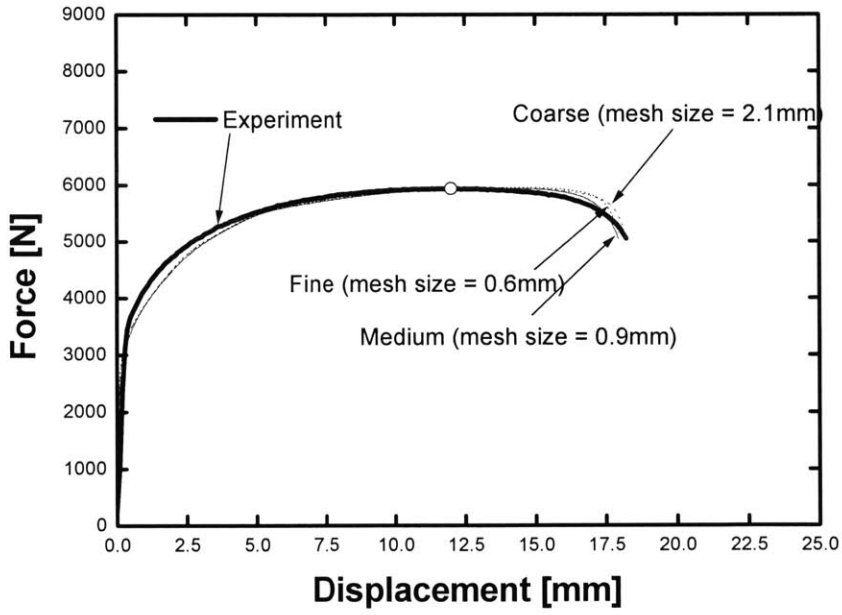

Fig. 6.3 Load displacement curve for the mild steel - A material used in the punch indentation test recorded from tensile test on flat dog bone coupons (h_0 = 1.4mm)

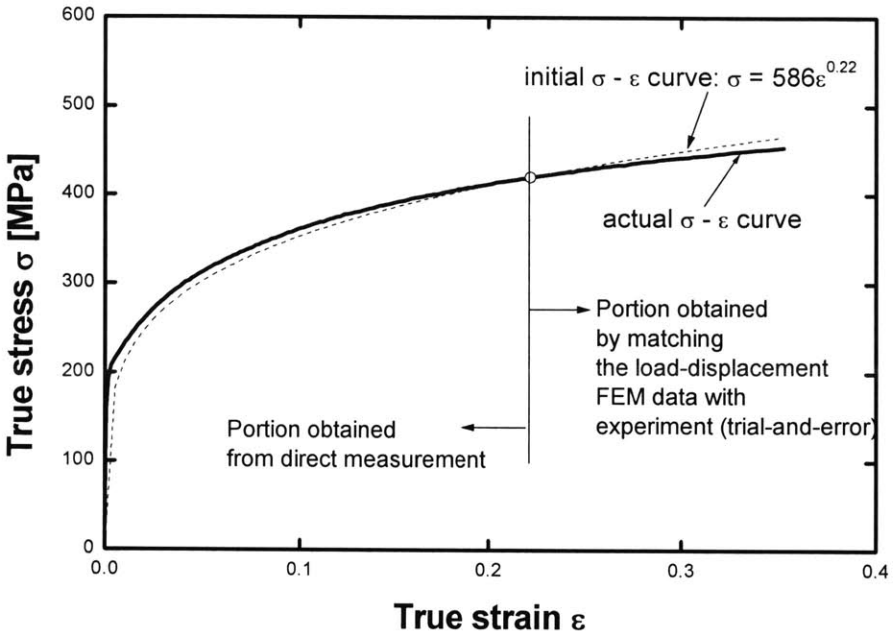

Fig. 6.4 Tensile stress-strain curves for the mild steel - A which was used in the punch indentation test (h_0 = 1.4mm)

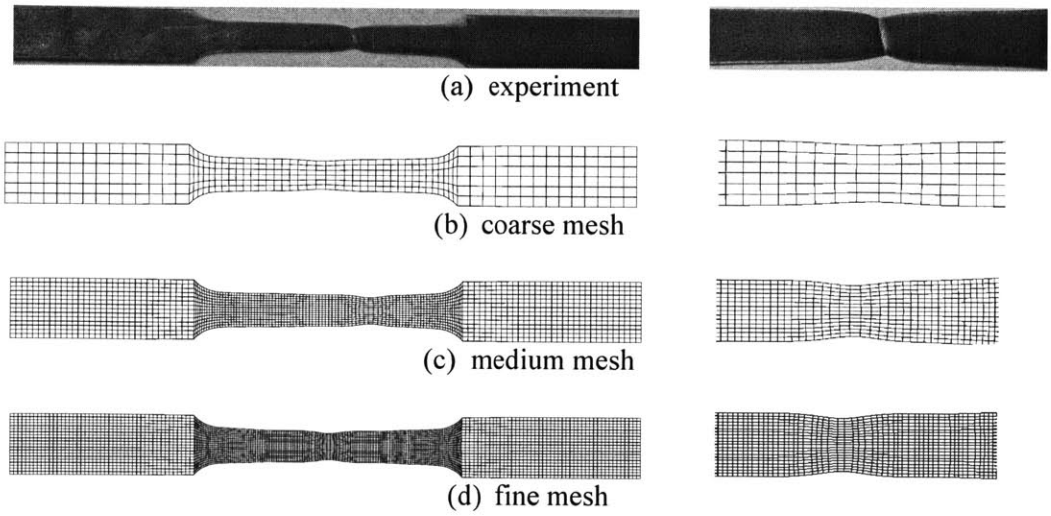

Fig. 6.5 Fracture of uniaxial tensile test and simulation with different mesh size (initial gauge length = 50.0mm, initial width = 12.5mm, initial thickness of specimen h_0 = 1.4mm)

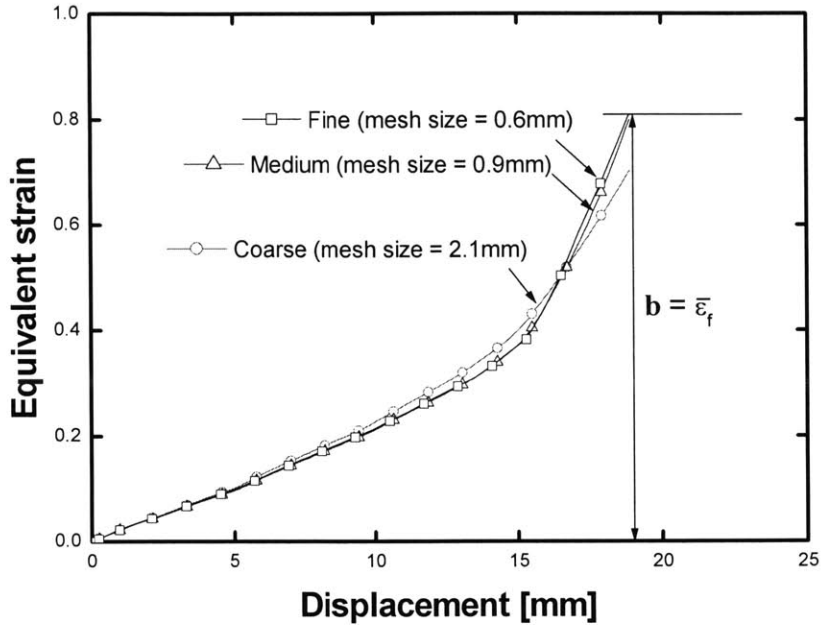

Fig. 6.6 Growth of the equivalent strain at the fracture location using different mesh size (h_0 = 1. 4mm)

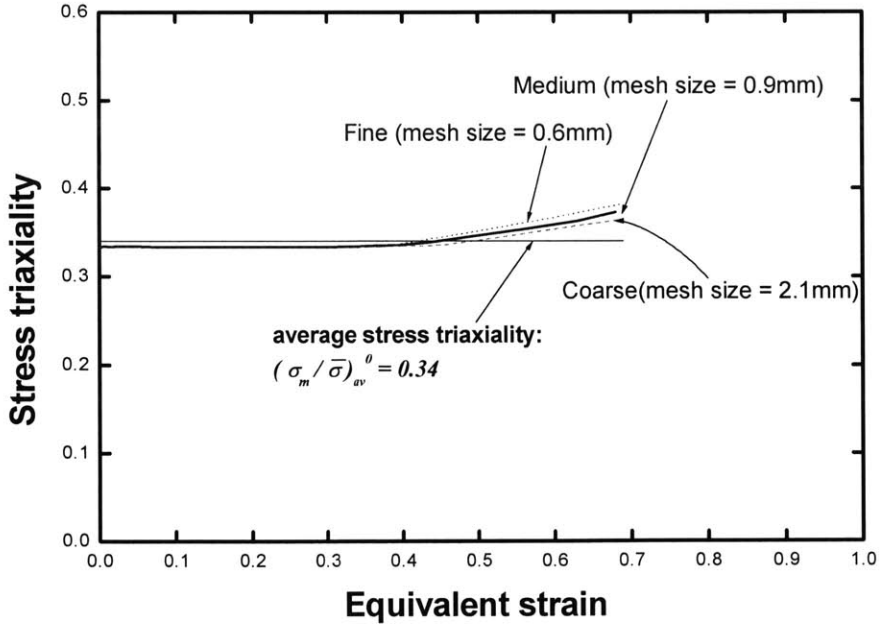

Fig. 6.7 Evolution of stress triaxiality with three different mesh configurations in the case of uniaxial tensile test

6.1.4 Experimental and numerical setup

6.1.4.1 Punch indentation test

In all tests the radius of a hemi-spherical punch was R_0 = 110mm. The thin mild steel square plates $(2R_0 \times 2R_0)$ were firmly clamped between two heavy rings and were loaded by a punch. Edge fixity is achieved through the use of serrated bolting ring mating surfaces in the 200 kN universal MTS testing machine, Fig. 6.8. Three combinations of punch radius and plate thickness were tested, as specified in Table 6.3. Note that the tests were performed by Woertz (2002).

Indenter speed was set at a baseline of 10 mm/min. Indentation was continued until the circumferential crack developed. The crack develops from axi-symmetric local neck but in most cases it went over approximately 180 degree and then deviated due to loss of symmetry. A photograph of the partially cracked plate is shown in Fig 6.23(a). The test was stopped at this instant at which radial cracks began to be formed.

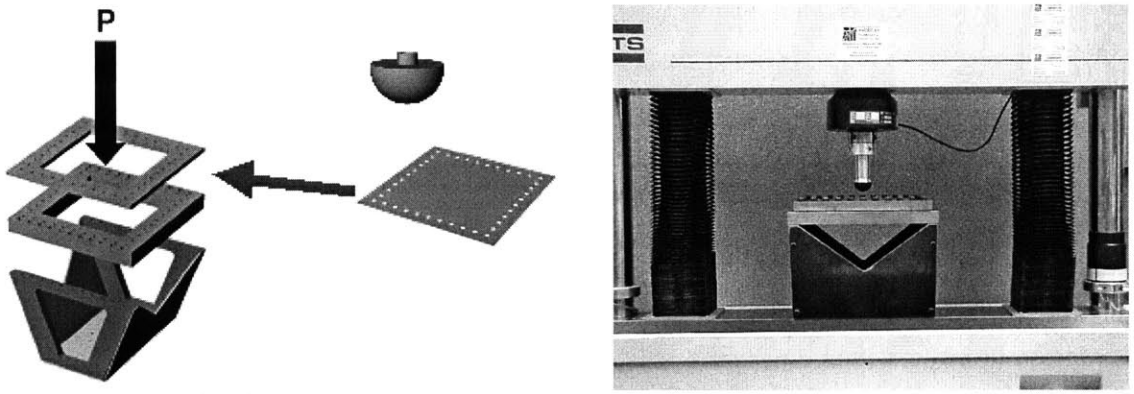

(a) schematic fixture (b) test photo

Fig. 6.8 Notional test fixture and completed design (after Woertz, 2002)

Table 6.3 Combination of punch radius (R_b) and plate thickness (h_0) in the tests and simulations

h_0 / R_b (ξ_0)	0.9mm	1.14mm	1.4mm
20mm (0.18)	•[1], ×[2]	×	×
50mm (0.45)	×	•, ×	×
75mm (0.68)	×	×	•, ×

•[1] : Test; ×[2] : Numerical analysis

6.1.4.2 Numerical analysis of punch indentation

The finite element model was created using the mesh generator program *HyperMesh* Version 6.0. The explicit non-linear finite element codes *PAM CRASH* (2003) and *LS-DYNA3D* (2003) were used to calculate the quasi-static process of uniaxial tensile and punch indentation test. The four-node Belytschko-Tsay shell element, with five integration points through the thickness and one integration point in the element plane, was employed. Because square plates have two axes of symmetry, a quarter model was considered. Most of the results were obtained using relatively fine mesh consisting of 12,100 elements (Medium mesh in Table 6.2). Five runs were also made using full model so that a partial failure could be predicted, which was observed in the experiment (see Figs. 6.22 and 6.23).

In the numerical simulation, the displacement and rotation of nodes corresponding to the clamped edges were fixed. The punch indenter was modeled by rigid wall with hemi-spherical shape and assumed to move with a downward velocity. The ramping time was 0.005 sec, and a constant velocity was 1000 mm/sec. The dynamic effect was avoided by reducing the mass density of the model by the factor of 1000. The relative motion of the plate in the radial direction with respect to the loading punch was simulated by a rigid wall-surface contact with a friction coefficient μ. We have found that structural response including fracture is very sensitive to the magnitude of friction coefficient. Therefore, numerical simulations were run over the entire range of the friction coefficient from $\mu = 0$ to 1.

6.1.5 Determination of Fracture Forming Limit Diagram (FFLD)

The combination of geometrical and frictional effect on the strain distribution during the punch indentation into circular plates and membranes was studied experimentally and numerically by various authors in the past (see for example Ferron and Zeghloul, 1993; Ghosh and Hecker, 1975; Knibloe and Wagoner, 1989). Of particular interest in these studies was spatial distribution of the components of the stress and strain tensors at various stages of the deformation process. It was found that a peak in radial strain develops during the punch penetration, plastic deformation localizes in the circumferential region and the strain localization leads to the development of a circumferential neck followed by a crack in the contact region between the plate and punch.

The effect of friction at the interfaces between the plate and punch indenters was included in our calculations and the results are shown in Fig. 6.9. Shown in Fig. 6.9 are the profiles of in-plane strain components under five different friction coefficients. Note that ξ indicates the normalized distance from the center of plate to the clamped end along the section ($y = 0;\ \theta = 0^0$). The radial and circumferential strains were respectively defined by Eqns. (6.1) and (6.2). It can be seen that the effect of friction evidently exists in constraining radial displacement u along the punch. Therefore, as μ increases, the circumferential strain decreases, while the concentration of radial strain increases. The peaks in the radial strain shown in Fig. 6.9 correspond to the edge of contact with the spherical indenter. The peaks in the circumferential strain are always in the center. The case of $\mu = 1.0$ i.e. corresponds to no sliding in the tangential direction to the punch and the circumferential strain becomes almost zero in this case. At the same time, there is sharp increase in the peak radial strain, which gives a more non-uniform distribution of the strain. Therefore, it can be concluded that the distribution and concentration of in-plane strain components is strongly influenced by μ for a given punch displacement. The above observations are quite consistent with the earlier results of Ferron and Zeghloul (1993). As shown in Fig. 6.10, it can be further observed that the location of the maximum of equivalent strain depends on the friction coefficient. For $\mu = 0$, the maximum is in the center of the plate, while it is in the outermost contact point c for larger friction. The profiles of strain ratio obtained from numerical simulation under various frictional coefficients are compared with that from analytical approximation (Eq. 6.13) in Fig. 6.11. It can be seen that both predictions exhibit complete biaxial condition around the plate center and change to plane strain state at the clamped end.

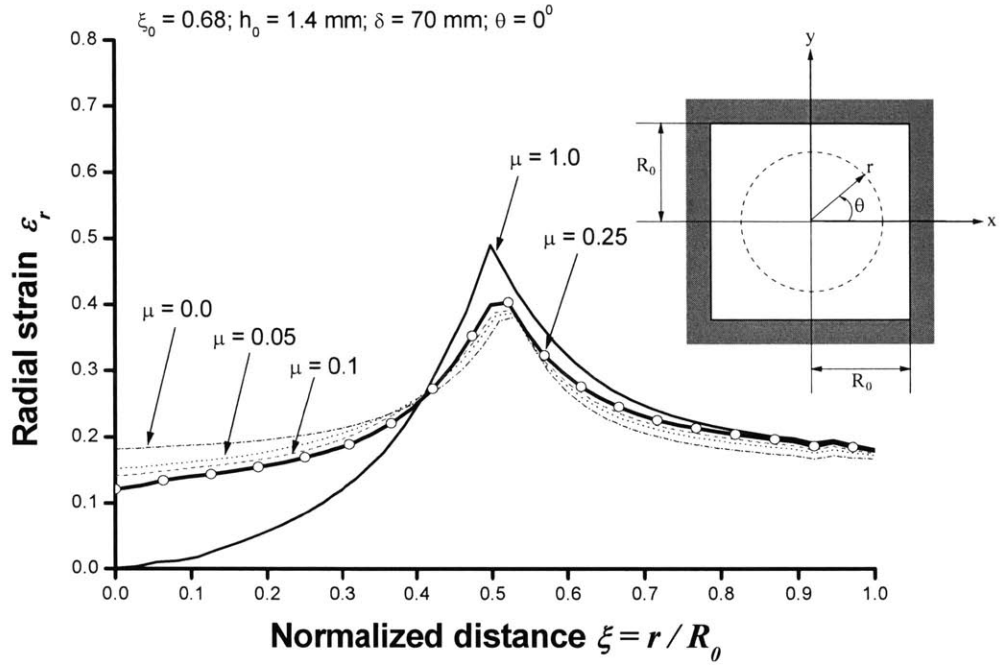

(a) radial strain distribution

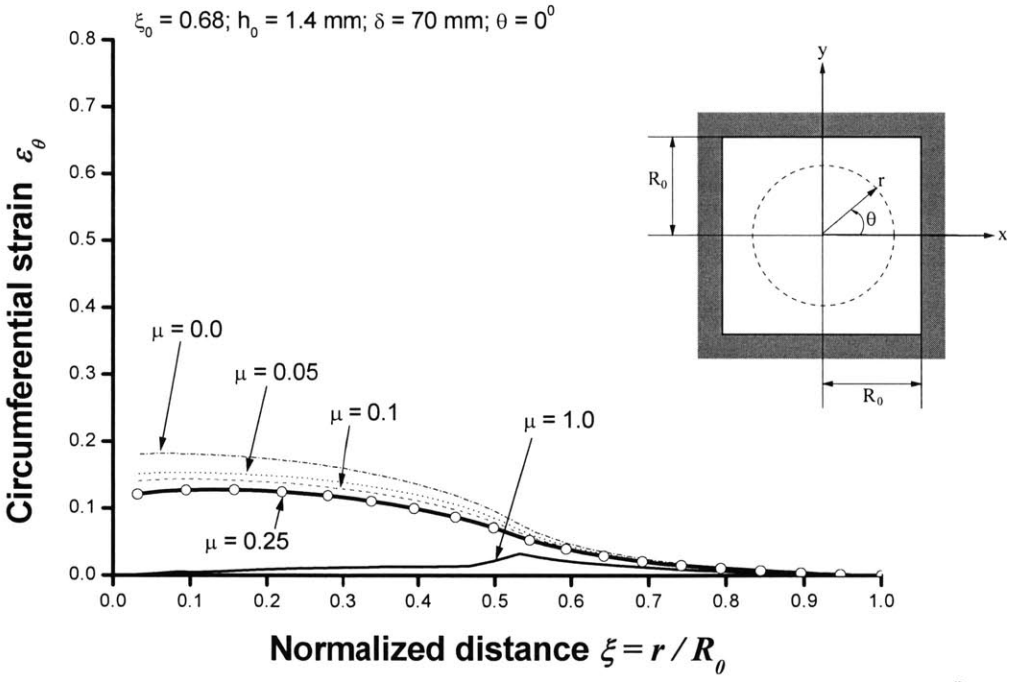

(b) circumferential distribution

Fig. 6.9 Effect of friction coefficient μ on the distribution of in-plane strain components from the center of plate to the clamped end at given punch displacement δ = 70mm. Note, that ξ indicates the normalized distance along the section ($y = 0;\ \theta = 0^0$) of the square plate considered in this study.

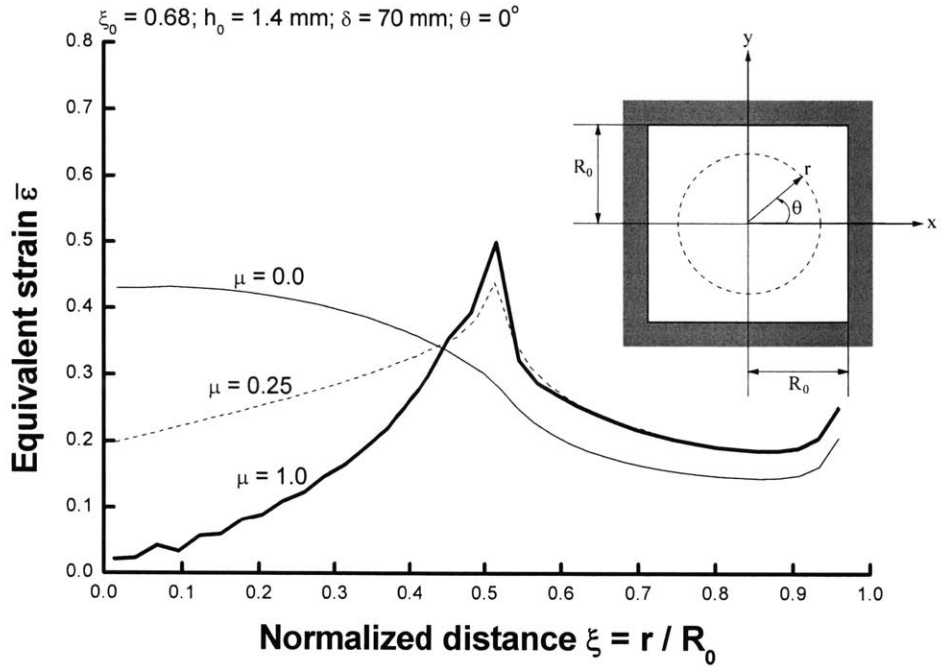

Fig. 6.10 Effect of friction coefficient μ on the distribution of equivalent strain ($\bar{\varepsilon}$) from the center of plate to the clamped end at given punch displacement δ = 70mm. Note, that ξ indicates the normalized distance along the section ($y = 0$; $\theta = 0^0$) of the square plate considered in this study.

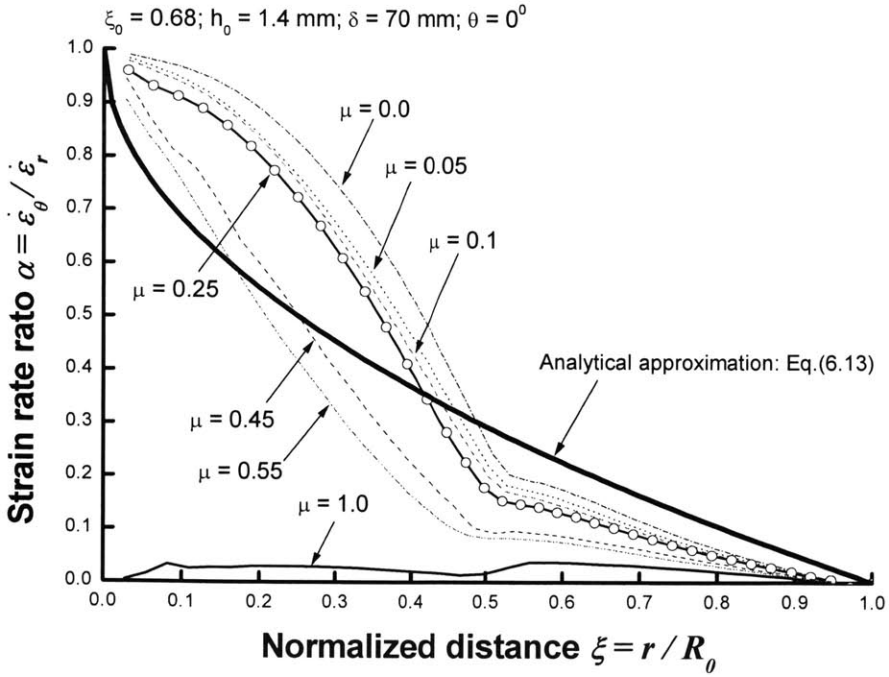

Fig. 6.11 Numerically obtained and analytically approximated profiles of strain ratio α at given punch displacement δ = 70mm ($\theta = 0^0$)

The calculated strain paths up to the fracture point from numerical simulation are shown in Fig. 12 for various friction coefficients. The axes are the in-plane major and minor strains, $\varepsilon_1 = \varepsilon_r$ and $\varepsilon_2 = \varepsilon_\theta$. The strains in this figure were obtained from the radial and circumferential strains at the critical locations of fracture for different friction coefficients. For a comparison purpose, the data for the uniaxial tension are also included in Fig. 6.12, together with the limit strains at necking. Based on a bifurcation analysis utilizing plastic deformation theory, Stören and Rice (1975) predicted the localized necking under biaxial stretching conditions i.e. for positive values of two principal strains. Accordingly, the limit strain, which is the largest strain developed in the neighborhood of a neck before failure, was shown to be

$$\varepsilon_1 = \varepsilon_r = \begin{cases} \dfrac{(2-\beta)[(2\beta-1)^2+3n]}{6(1-\beta+\beta^2)} = \dfrac{3\alpha^2+n(2+\alpha)^2}{2(2+\alpha)(1+\alpha+\alpha^2)}, & 0<\alpha\le 1 \\ n\left(\dfrac{2-\beta}{1+\beta}\right) = \dfrac{n}{1+\alpha}, & -\dfrac{1}{2}\le\alpha\le 0 \end{cases} \tag{6.28}$$

In the present numerical simulation, ductile fracture is controlled by Eq. (6.21). The locus of fracture points obtained from the best curve fitting of numerical result is marked with thick full line in Fig. 6.12. Equation $(6.28)_1$ is due to Stören and Rice (1975), while Eq. $(6.28)_2$ was derived by Hill (1952). It can be seen that the strain paths are close to equi-biaxial tension condition for small μ. As μ increases, the paths exhibit stretch forming and finally show plane strain path for the case of μ = 1.0. In the case of μ = 0.25, after the onset of strain localization indicated by solid circle, the strain path follows that $d\varepsilon_2 = 0$ and becomes parallel to ε_1 axis up to failure.

It should be noted that the present analysis was performed using shell element discretization. The element size was approximately half of plate thickness (see Medium mesh in Table 6.2). Therefore, the neck would be always confined only to one element. It can be seen from Fig. 6.12 that the radial strain at the point of localized neck was approximately 0.26. After necking, there was additional strain of 0.15 accumulated so that the total radial strain to fracture was 0.41 (for μ = 0.25).

The fracture strain can be clearly seen to be much higher than the limit (necking) strain, given by Eq. (6.28), except when μ = 0.0 and 0.05, for which both the conditions predict similar principal strains. This can be explained by the fact that the relatively uniform and smooth process of strain localization corresponding to μ = 0.0 and 0.05 (see Figs. 6.9 and 6.10) gives the good correlation between two cases in the vicinity of equi-biaxial tension only ($0.8 \le \alpha \le 1.0$). This coincidence of the limit strain with the fracture strain near equi-biaxial tension is consistent with the earlier

observation of Ferron and Zeghloul (1993) and the experimental results of Takuda et al. (2000) and Jain et al. (1999). However, it should be mentioned that this observation is only valid for those particular cases and may be dependent on materials.

The present FFLD obtained from numerical results shown in Fig. 6.12 compares, in fact, well with the fracture locus given by Eq. (2.25) which is a constant through-thickness strain at fracture of magnitude $3D_c/2$. In particular, Fig. 6.13 shows the process of through-thickness stain localization at the critical location (element C_1) for the case of large radius of punch ($\xi_0 = 0.68$) and friction coefficient μ = 0.25. It can be seen that the value of thickness strain at the point of fracture is $\varepsilon_{3f} = 0.41$ which agrees well with the magnitude of analytically derived thickness strain from Eq. (2.25) for $D_c = 0.27$. Furthermore, the shape of the FFLD shown in Fig. 6.12 is in good agreement with the experimentally measured loci by Embury and LeRoy (1977) for Al-Mg alloy and Takuda et al. (2000) for Al sheets.

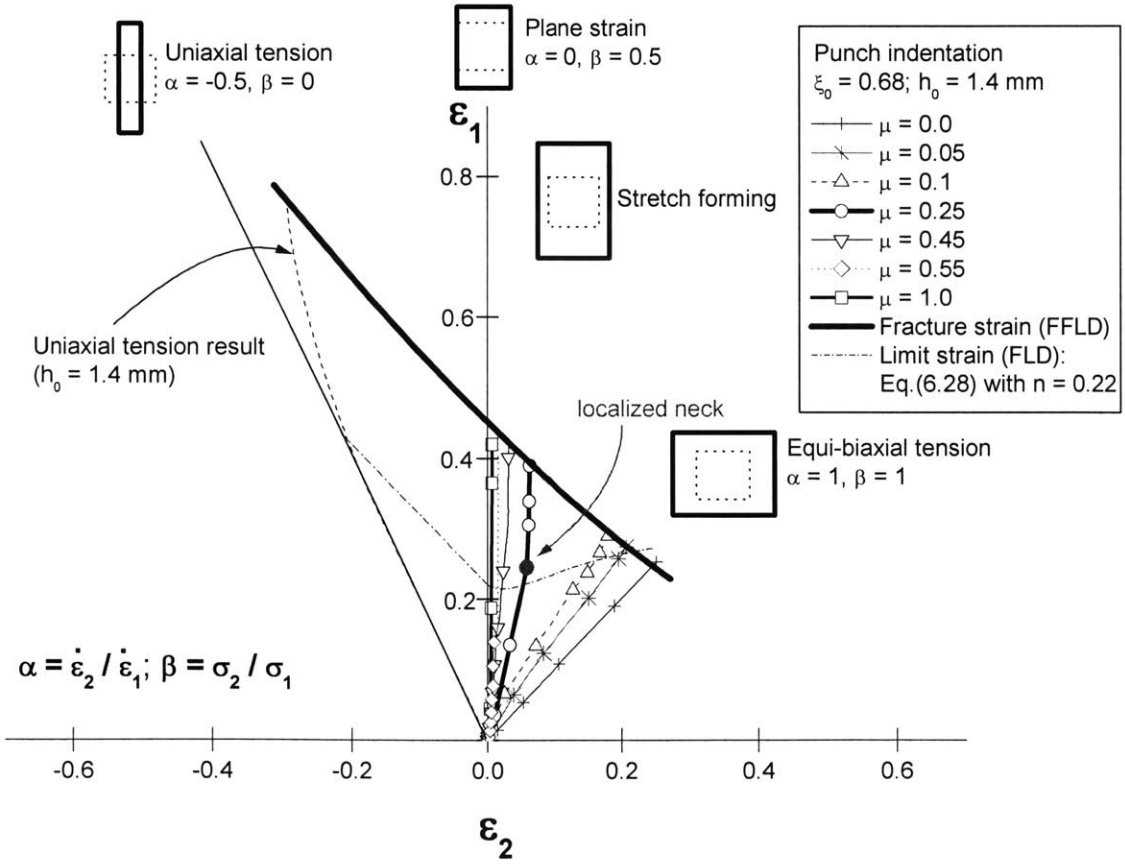

Fig. 6.12 Strain paths at the potential fracture point of punch indentation with different friction coefficients μ (strain path corresponding to the uniaxial tension is also included)

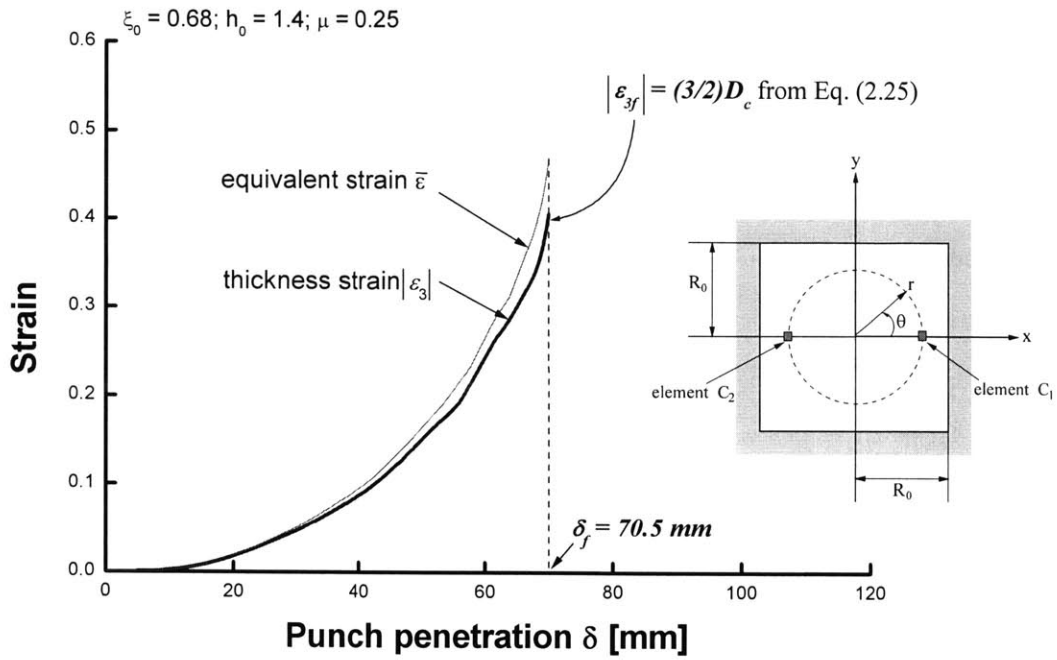

Fig. 6.13 Evolution of equivalent strain and thickness strain at the fracture point for – element C_1 ($\xi = 0.48, \theta = 0^0$) - for the case of $\xi_0 = 0.68$ and $\mu = 0.25$

The history of stress triaxiality versus equivalent strain is also shown in Fig. 6.14 with different friction coefficients. Even though there is some differences in the level of triaxiality for various friction coefficient, they are not very large and in all cases the triaxiality is of an order of 0.6. This corresponds to the neck and fracture formation in the stretch forming conditions.

The evolution of deflections of square plate and the corresponding equivalent plastic strain profiles, obtained from numerical simulation are shown respectively in Figs. 6.15 and 6.16. These results correspond to the punch radius R_b = 75mm and plate thickness h_0 = 1.4mm. Note that the friction coefficient μ used in simulation was 0.25. The trajectory of peak radial strain is also marked with symbol (····o····) in Fig. 6.15. As δ increases, the location of peak strain increases from the plate center towards the clamped end. After the punch displacement δ = 50mm, the peak strains migrate away from the punch. As mentioned earlier, the localized neck is initiated by change of stress or strain ratio at δ = 66mm. Finally this strain localization terminates by formation of circumferential crack. This result agrees with the concept of the so-called FFLD, developed by Embury and LeRoy (1977), LeRoy et al. (1981), and Atkins (1985, 1996).

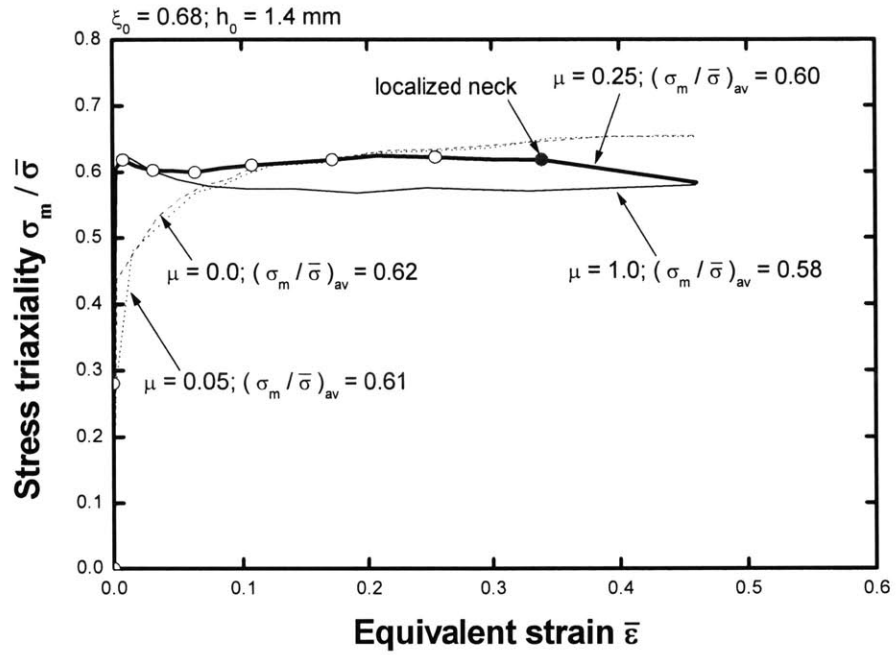

Fig. 6.14 Evolution of stress triaxiality at the potential fracture point with different friction coefficient μ ($\theta = 0^0$)

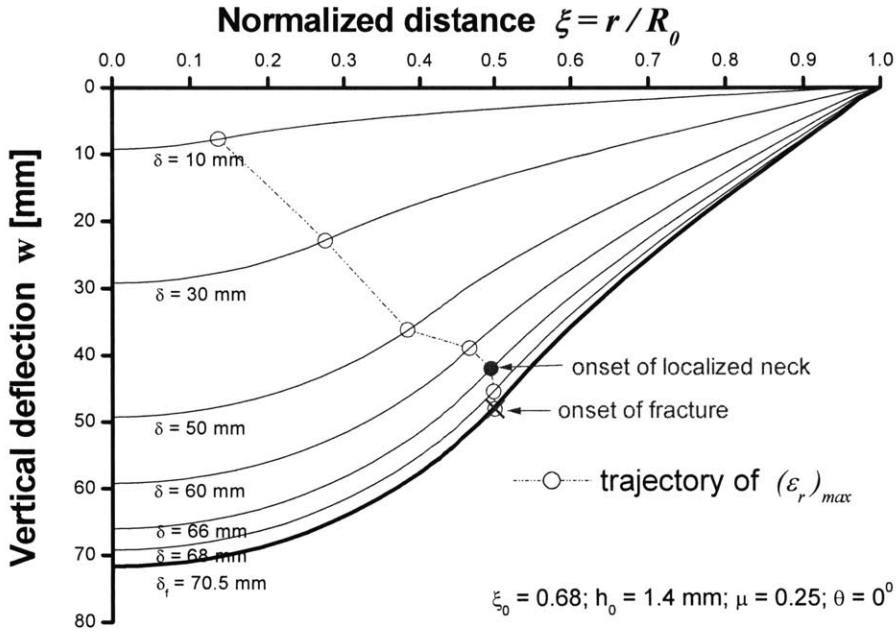

Fig. 6.15 Numerically obtained deflection profiles and trajectory of strain concentration of square plate under punch indentation (R_b = 75mm, h_0 = 1.4mm, μ = 0.25; $\theta = 0^0$)

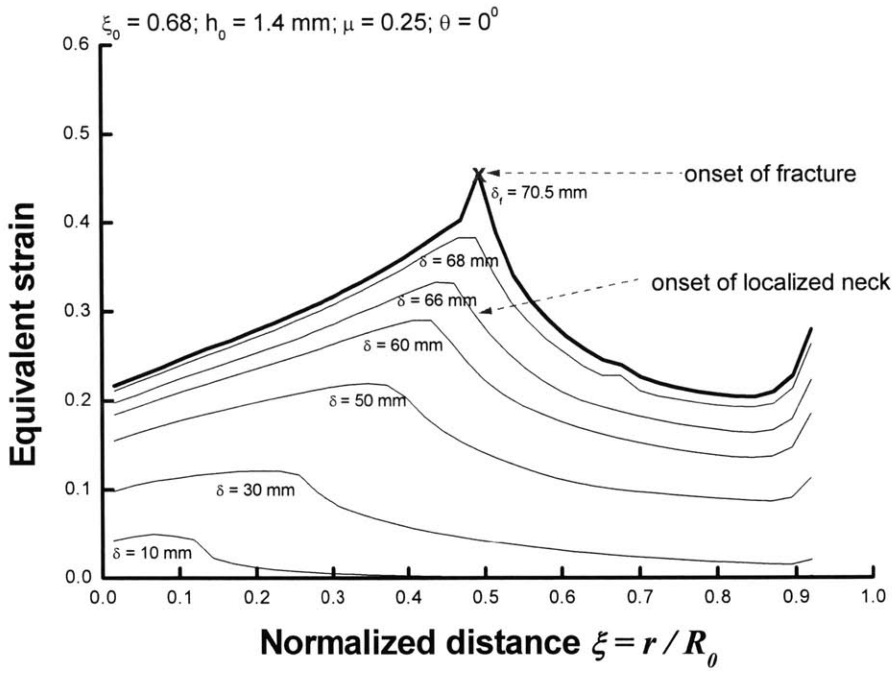

Fig. 6.16 Numerically obtained strain profiles of square plate under punch indentation (R_b = 75mm, h_0 = 1.4mm, μ = 0.25; $\theta = 0^0$)

The numerically obtained profiles of stress ratio and stress triaxiality are compared with those from analytical approximation in Figs. 6.17 and 6.18, respectively. Using Eqns. (6.11) and (6.14), the distribution of stress triaxiality from the center of plate to the clamped end can be approximated as

$$\frac{\sigma_m}{\bar{\sigma}} = \frac{1}{\sqrt{3}} \frac{2-\sqrt{\xi}}{3-3\sqrt{\xi}+\xi} \tag{6.29}$$

One can see that the stress state from numerical analysis satisfies the biaxial condition around the plate center and smoothly change to plane strain state at the clamped end. As shown in those two figures, the analytically assumed stress ratio β from Eq. (6.14) gives a good prediction of stress state especially in the vicinity of fracture location, ξ_f = 0.46~0.48.

Figure 6.19 shows the progression of damage as defined by Eq. (2.4) from the plate center to the clamped end. The damage in the element around ξ = 0.48 first reaches the critical value of D_c = 0.27 at the punch displacement δ = 71mm while other elements still have magnitudes of damage below

the critical value. This indicates that location of fracture initiation is $\xi_f = 0.48$ which agrees well with the experimentally measured value 0.46.

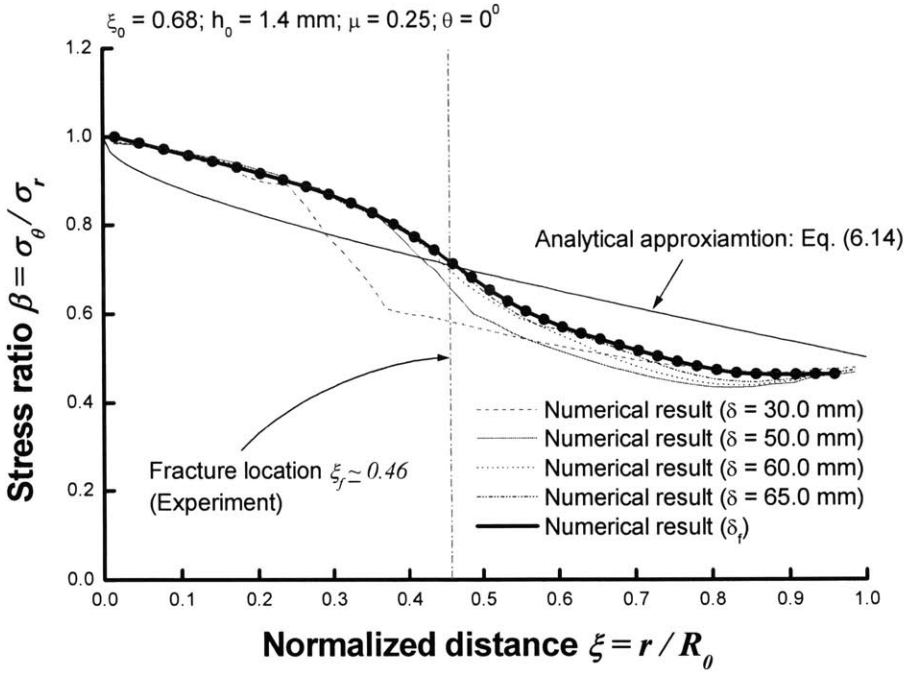

Fig. 6.17 Numerically obtained and analytically approximated profiles of stress ratio β
(R_b = 75mm, h_0 = 1.4mm, μ = 0.25; $\theta = 0^0$)

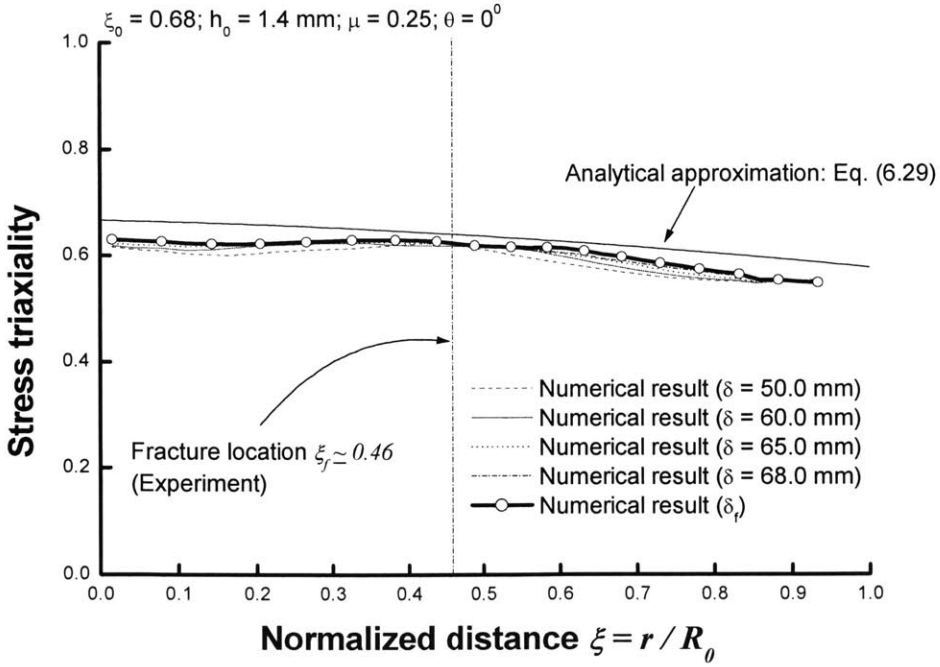

Fig. 6.18 Numerically obtained and analytically approximated profiles of stress triaxiality
(R_b = 75mm, h_0 = 1.4mm, μ = 0.25; $\theta = 0^0$)

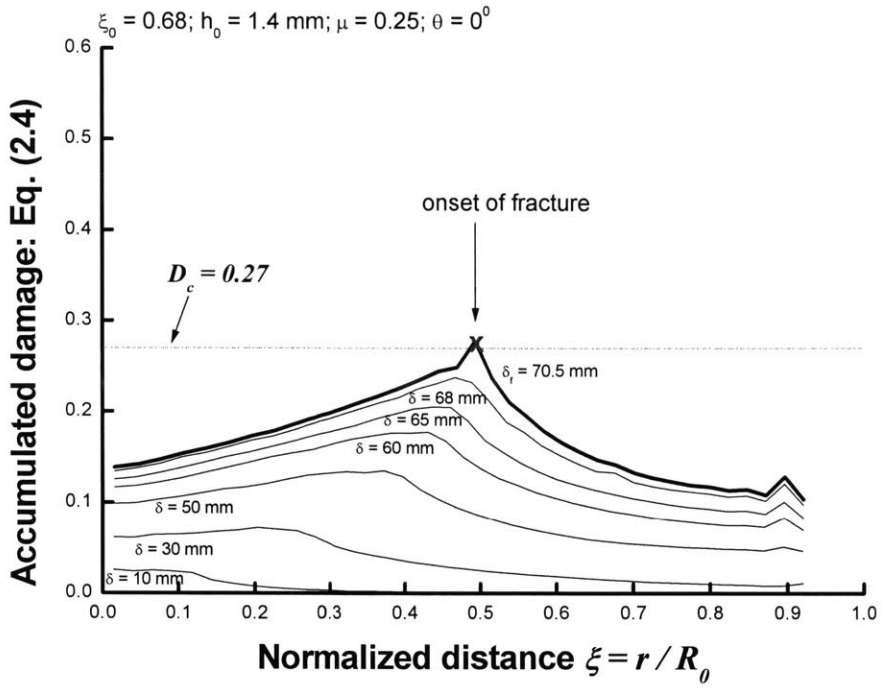

Fig. 6.19 Numerically obtained damage profiles of square plate under punch indentation (R_b = 75mm, h_0 = 1.4mm, μ = 0.25; $\theta = 0^0$)

6.1.6 Punch force-penetration response

The experimental punch force-penetration curves are compared with those from analytical approximation and numerical simulation for different set of test in Figs. 6.20, 6.21, and 6.22. The first fracture is clearly distinguished by a sudden drop in the force-penetration curves. The considered case here was stretch forming condition with friction coefficient μ = 0.25, average stress triaxiality $\left(\sigma_m / \bar{\sigma}\right)_{av} = 0.6$, and calibration constant D_c = 0.27. Since the stress triaxiality is almost constant for the case considered, then according to Eq. (6.21), the equivalent strain is a good measure of crack formation and critical strain to fracture $\bar{\varepsilon}_f = 0.45$. For the finite element predictions, the elements with an equivalent strain larger than the specified fracture strain were deleted at the instant point of crack formation. For the analytical prediction, the force-penetration curve was obtained by Eqns. (6.7) and (6.20). It is seen that the analytical solution presented here is in good agreement with the experiments when the exponent n = 0.22 determined from measured

stress strain curves and the critical wrapping angle $\psi_{c,f}$ = 0.88 from Eq. (6.23). Especially for normalized punch radii ξ_0 = 0.18 and 0.45, the analytical solution predicts well the force-penetration response up to the point of fracture. The finite element solutions obtained by *PAM-CRASH* and *LS-DYNA3D* are also shown in those figures and they too agree well with the experiments up to the point of fracture. Moreover, both commercial codes give almost same result in the force-displacement response over the entire range of deformation. To numerically predict the partial failure observed in the experiment, full finite element models with different types of imperfection were used. The results are shown in Figs. 6.22, 6.23 and 6.24 for the case of ξ_0 = *0.68*. Three configurations of imperfection were considered. First, the initial thickness of only one element (element C_2) was changed (the relative thickness of the local element is denoted by η in Fig. 6.22(b)). In the second configuration, an initial eccentricity of the applied punch (r_0) was assumed (see Fig. 6.22(c)). In the third configuration, both of the above imperfections were applied. As shown in Fig. 6.22(a), the effect of imperfections on the global punch force-penetration responses is negligible, while the resulting crack patterns are influenced by the applied imperfections in the finite element models (see Fig. 6.23).

The experimentally and numerically obtained circumferential cracks are compared visually in Fig. 6.23 for the large radius of punch indenter. As mentioned earlier, the crack develops from the axi-symmetric local neck formation and failure in the experiment is incomplete in the circumferential direction due to loss of symmetry. It is seen that the numerical simulations of full models with initial imperfections also predict the partial circular crack and formation of radial crack (see Figs 6.23(c), (d), and (e)). Figure 6.24 shows the histories of the equivalent strain at two potential locations of fracture (elements C_1 and C_2). It can be clearly seen that the equivalent strain of element C_2 is always less than its critical value ($\bar{\varepsilon}_f = 0.45$) for the cases of simulations where initial imperfections were applied. Finally, in terms of the location and pattern of fracture, the numerical simulations are shown to quite accurately predict the behavior of fracture in the thin plate under the punch indentation.

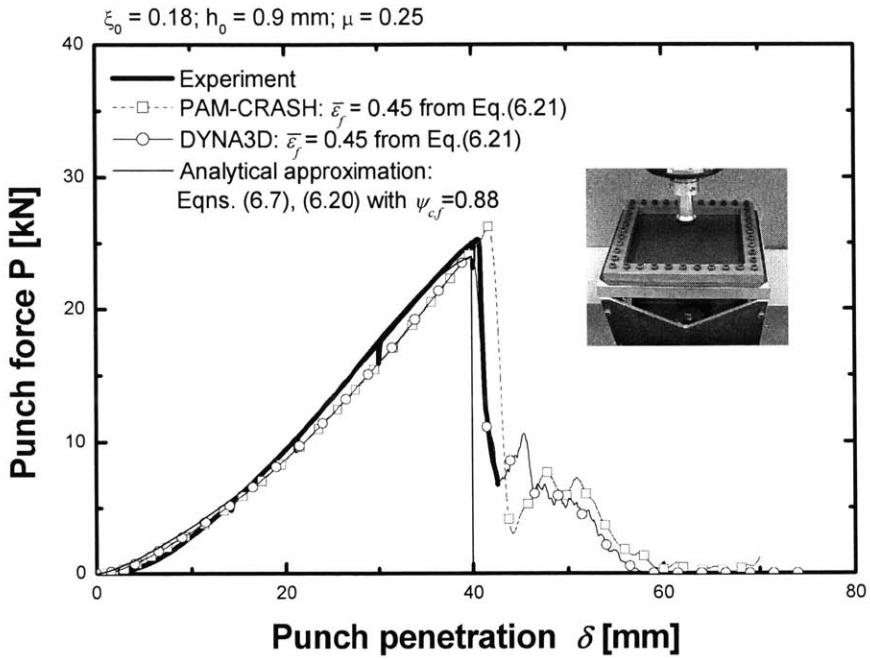

Fig. 6.20 Comparison of experimental, analytical and numerical force-penetration curves. Note, that the numerical results shown in this figure were obtained from the finite element model where a quarter model without imperfection ($\eta = 1.0;\ \xi_e = 0.0$) was applied. (R_b = 20mm, h_0 = 0.9mm, K = 536MPa, μ = 0.25)

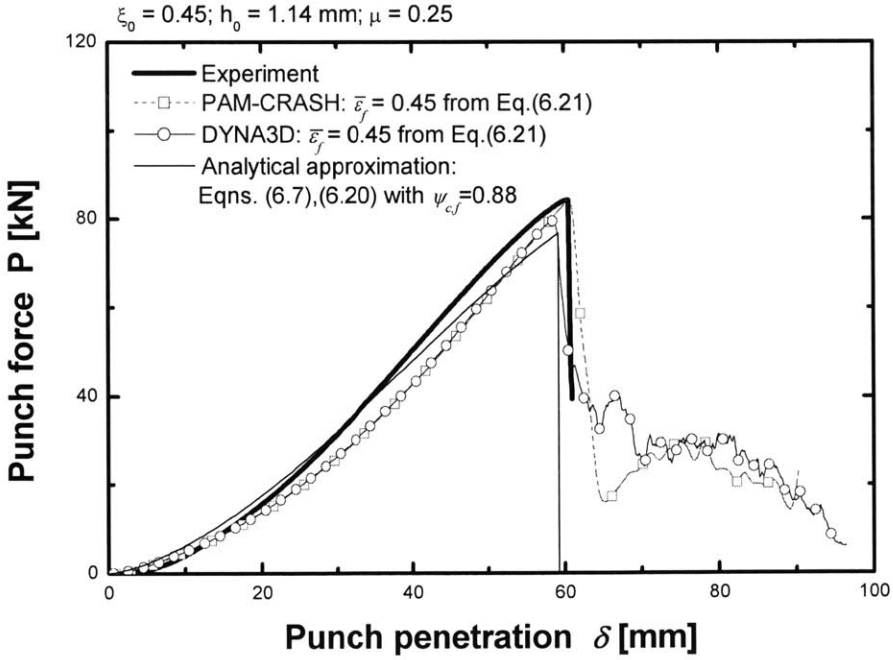

Fig. 6.21 Comparison of experimental, analytical and numerical force-penetration curves. Note, that the numerical results shown in this figure were obtained from the finite element model where a quarter model without imperfection ($\eta = 1.0;\ \xi_e = 0.0$) was applied. (R_b = 50mm, h_0 = 1.14mm, K = 586MPa, μ = 0.25)

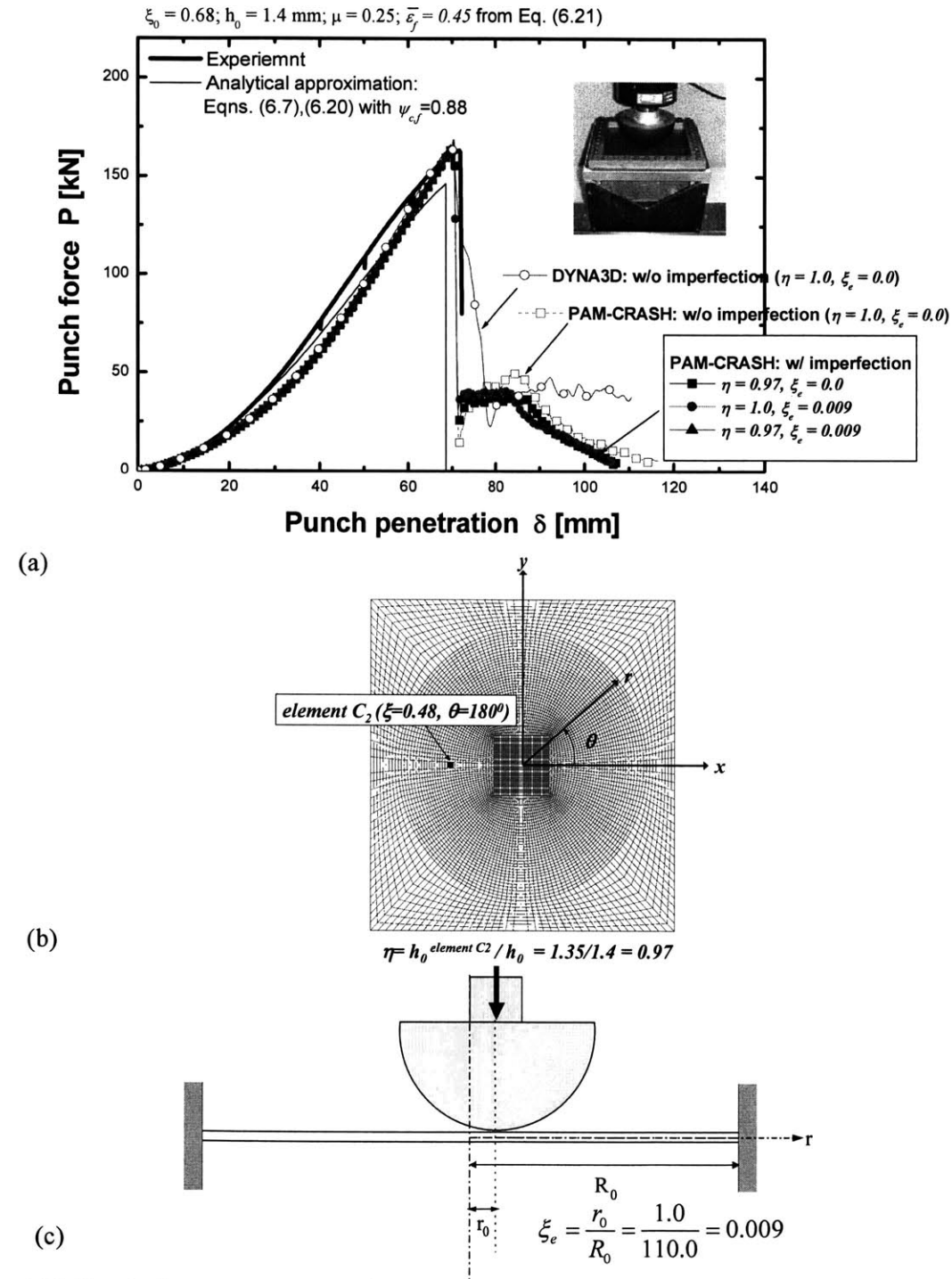

Fig. 6.22 Punch force responses and types of initial imperfection considered in simulations: (a) comparison of experimental, analytical and numerical force-penetration curves (R_b = 75mm, h_0 = 1.4mm, K = 586MPa, μ = 0.25); (b) thickness imperfection imposed on the element C_2 and the relative thickness of the element C_2 is denoted by η; (c) initial eccentricity of loading punch (r_0) and its normalized parameter is denoted by ξ_e.

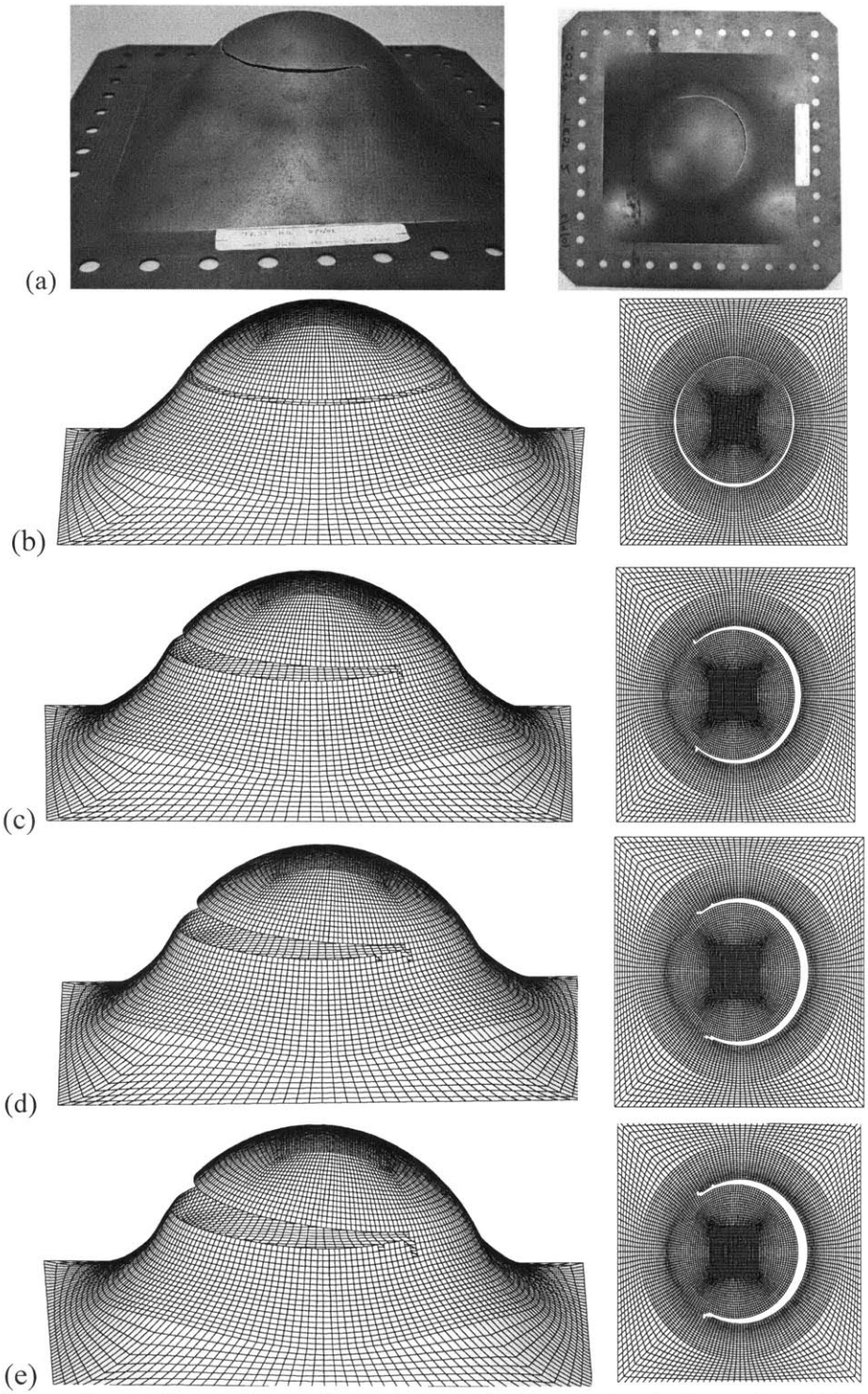

Fig. 6.23 Comparison of experimentally and numerically obtained circumferential crack (R_b = 75mm, h_0 = 1.4mm); (a) experiment; (b) PAM-CRASH (without imperfection: $\eta = 1.0;\ \xi_e = 0.0$); (c) PAM-CRASH (with imperfection: $\eta = 0.97;\ \xi_e = 0.0$); (d) PAM-CRASH (with imperfection: $\eta = 1.0;\ \xi_e = 0.009$); (e) PAM-CRASH (with imperfection: $\eta = 0.97;\ \xi_e = 0.009$)

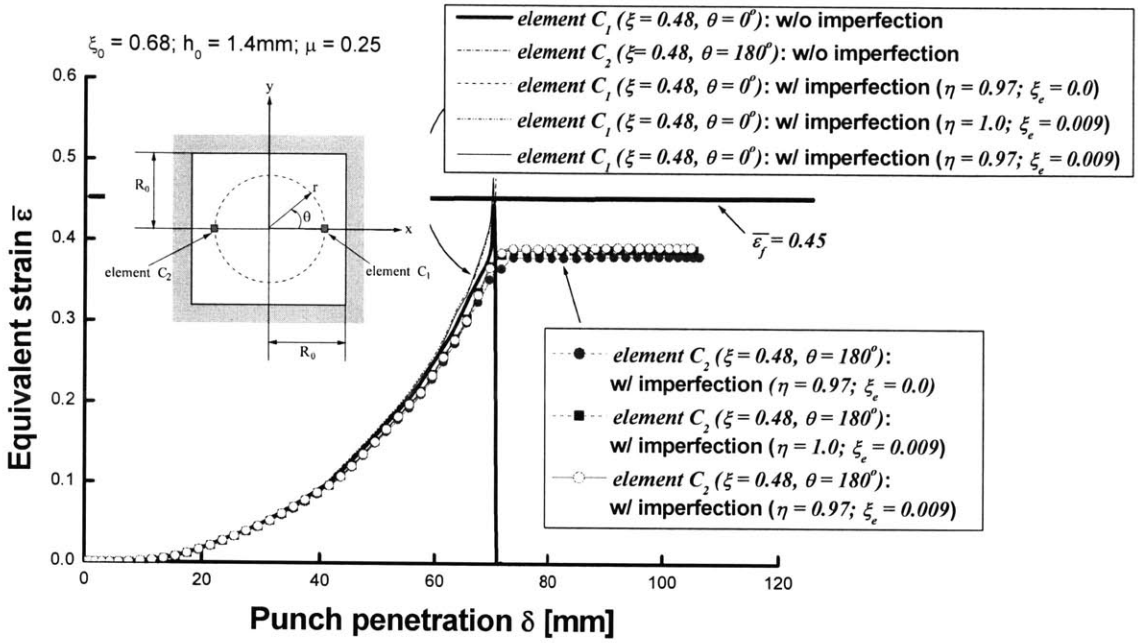

Fig. 6.24 Numerically obtainedd history plots of equivalent strain at two potential locations of fracture under different types of initial imperfections (R_b = 75mm, h_0 = 1. 4mm, μ = 0.25)

6.1.7 Effect of punch radius on fracture

The analytical and numerical deflection profiles at the point of fracture are compared in Fig. 6.25 for three different punch radii. The deflection was normalized by the plate radius, R_0. The analytical deflection profiles marked with dotted line in Fig. 6.25 was obtained from Eq. (6.19) for the outside of contact, $\xi_c \le \xi \le 1$. Over the region of contact, $0 \le \xi < \xi_c$, the wrapping angle $\psi = \xi / \xi_0$ was used. One can see that the correlation between the analytical predictions and the numerical results is excellent for both magnitude of maximum deflection and deformed shape.

Figure 6.26 shows the numerically and analytically obtained damage profiles at the crack formation with three different punch radii. It can be clearly seen that the critical distance from the plate center when the accumulated damage first reaches the critical value of D_c = 0.27 increases as ξ_0 increases. The corresponding locations of failure, denoted by $\xi_f = r_f / R_0$, are compared with experimentally measured data in Fig. 6.27. The numerically obtained location to failure is seen to agree well with the experiments in all three test configurations. On the other hand, the location from the analytical solution is higher than those of simulation and experiment for the larger punch radii.

The above difference can be explained by the neglect of the in-plane displacement u in the analytical solution, which is retarding the deformation around the contact point c.

The analytically obtained penetration to failure from Eq. (6.26) is compared with those from experiments and numerical simulation in Fig. 6.28 over the range of punch radius, $0.1 < \xi_0 < 0.75$. For a comparison purpose, prediction from Simonsen and Lauridsen (2000) is also included in this figure. One can see a good agreement between all cases. As compared to the present closed-form solution, the solution due to Simonsen and Lauridsen (2000) slightly overestimate the penetration to failure for the range of punch radii, $\xi_0 > 0.5$.

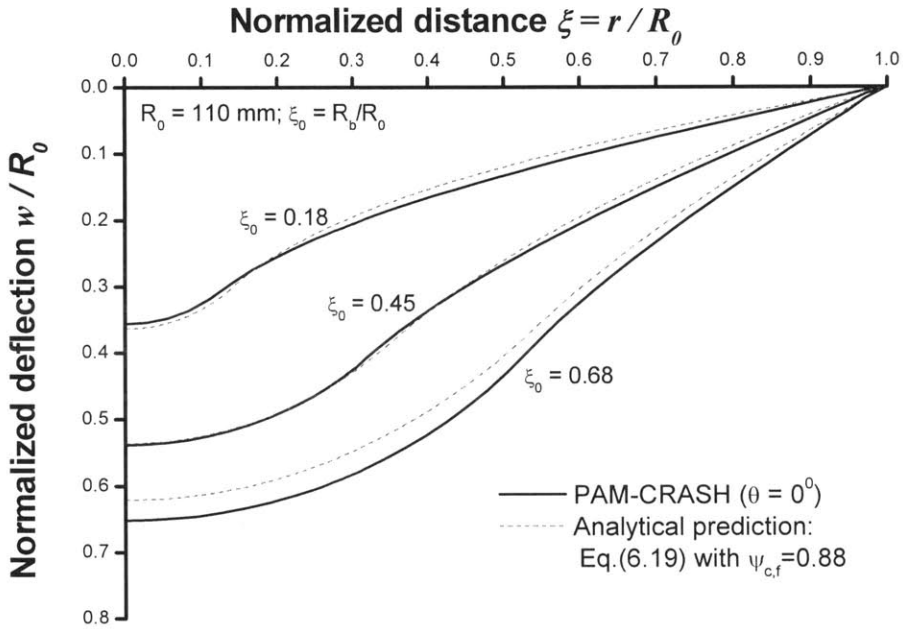

Fig. 6.25 Comparison of normalized deflection profiles at the crack formation between numerical and analytical predictions with three different values of ξ_0

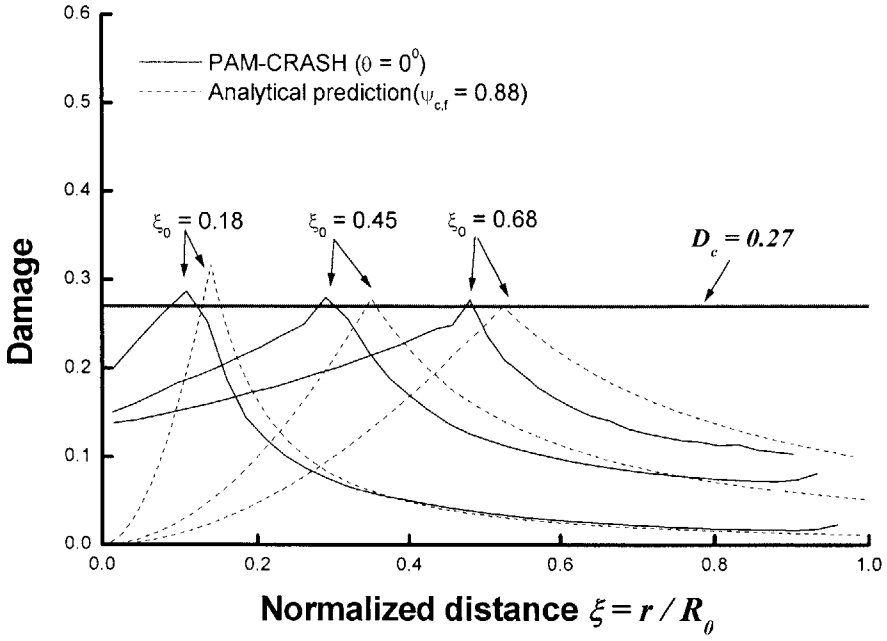

Fig. 6.26 Comparison of damage profiles at the crack formation between numerical and analytical predictions with three different values of ξ_0

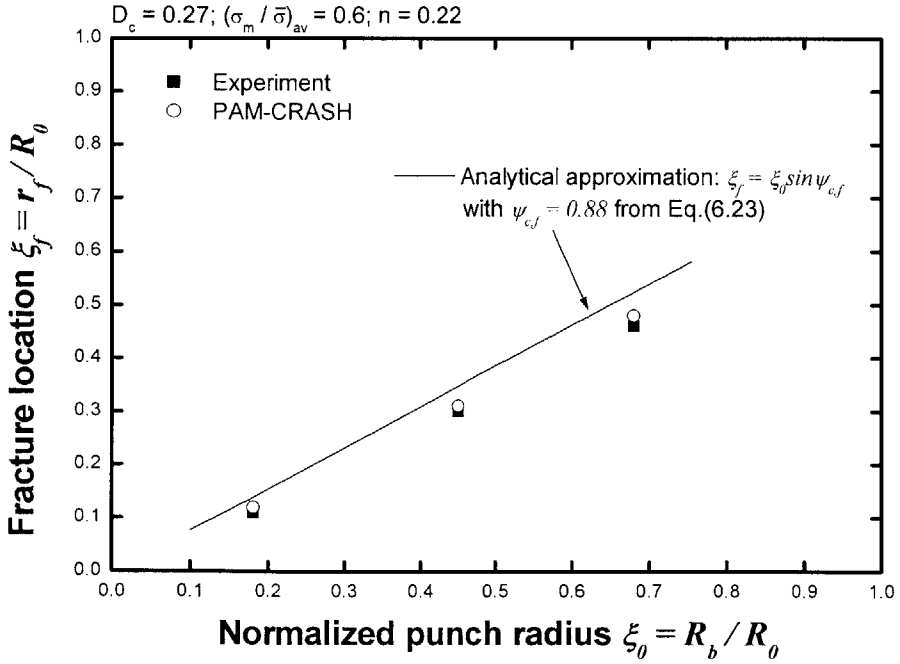

Fig. 6.27 Comparison of experimentally measured failure location ξ_f with those form numerical and analytical predictions as a function of normalized punch radius ξ_0

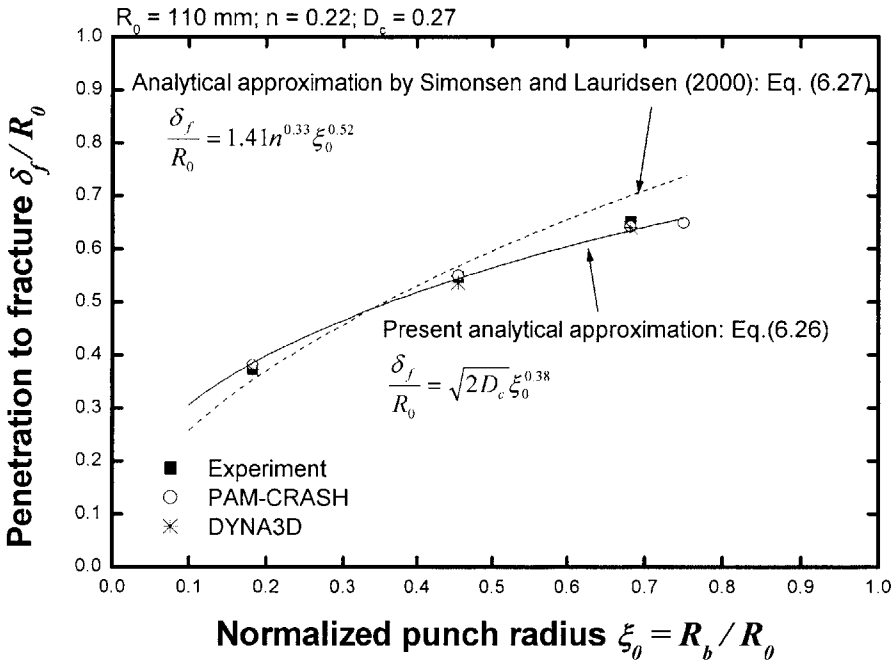

Fig. 6.28 Comparison of experimentally obtained critical penetration δ_f with those form numerical and analytical predictions as a function of normalized punch radius ξ_0

6.1.8 Summary of the results

- The deformation and fracture behavior of a thin, ductile metal plate statically loaded by a rigid sphere punch were investigated. It was shown that a peak in radial strain develops during the punch indentation and strain concentration terminates by circumferential crack in the contact between plate and punch. Moreover, the strain distributions along the plate were strongly influenced by the friction between the interfaces. Thus, strain paths and fracture strains at the potential fracture point were constructed numerically with different friction coefficients. A comparison between fracture strains and limit strains at necking was also made.
- A closed form solution for transverse deflections is derived by neglecting the radial displacement but taking into account a variable stress ratio and consequently the stress triaxiality. The plastic equivalent strain modified by the stress triaxiality was introduced as ductile fracture criterion. The present fracture criterion was calibrated by performing uniaxial tensile test with finite element calculation. Based on the calibration constant, the equivalent

strain to fracture, which is a function of the stress triaxilaity of the problem, was defined to predict analytically and numerically the onset of ductile fracture.

- It was shown that the analytically and numerically calculated responses up to the crack formation for three different combinations of punch radii and plate thickness appeared to be in a good agreement with the experiment. Furthermore, the analytically predicted transverse deflection profiles and location of failure were also shown to be in good accordance with the numerical results.
- Based on the postulated fracture criterion, the Fracture Forming Limit Diagram was constructed from numerical simulation, by changing the magnitude of the friction coefficient.

6.2 Unidirectionally Stiffened Double Hull (USDH) under conical punch indentation

Experimental and numerical study on the crack formation and subsequent crack propagation is presented for the case of stiffened double plates with clamped conditions under conical punch loading. The structure consists of two single plates and six longitudinal stiffeners connecting the inner and outer plates, see Fig. 6.29. This model is a typical segment of Unidirectionally Stiffened Double Hull (USDH) ship structure shown in Fig. 6.30. The USDH surface ship concept (Beach, 1991) consists of a twin skin structure which wraps around the bottom, the side shell, and across the main deck. The two skins are connected by longitudinal web girders forming a cellular structure as shown in Fig. 6.30.

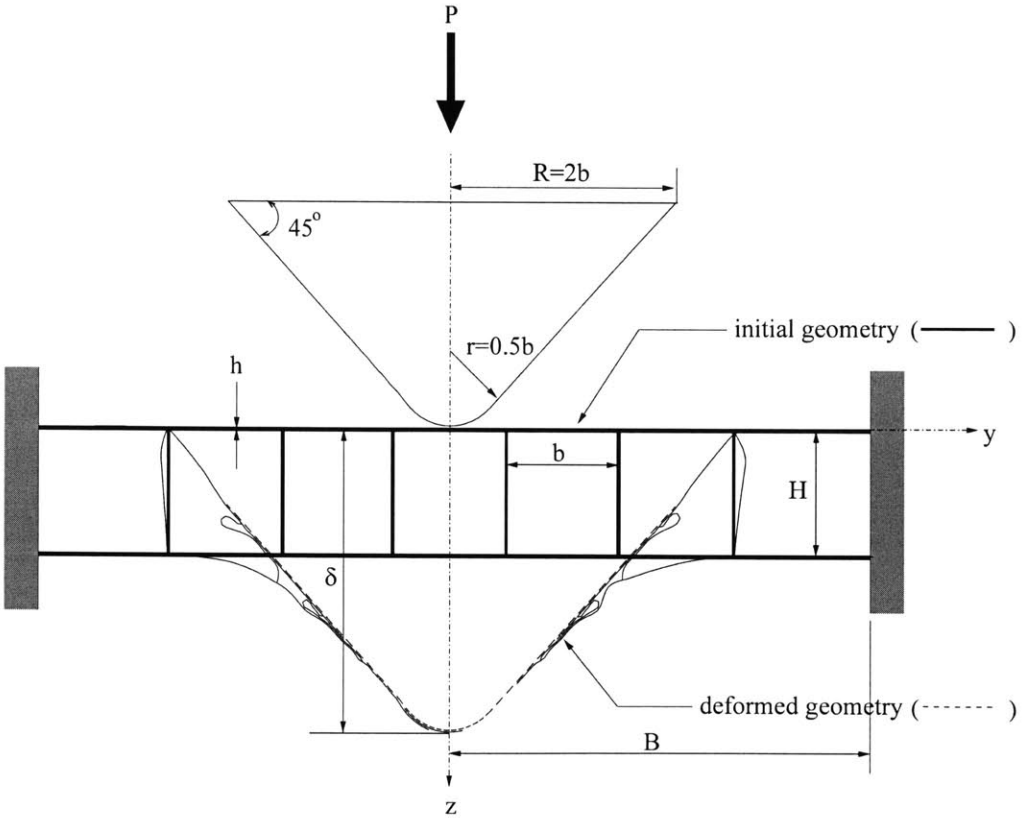

Fig. 6.29 Geometry of a clamped Unidirectionally Stiffened Double Hull (USDH) loaded quasi-statically by a conical punch with round nose. Note that the deformed shape is overlapped in the initial geometry; h = 0.75mm, b = 41.7mm, H = 41.7mm, B = 154.25mm, R = 83.4mm, r = 20.85mm

Fig. 6.30 Mid-body section of Unidirectionally Stiffened Double Hull (USDH) ship (after Beach, 1991)

6.2.1 Experimental and numerical setup

6.2.1.1 Experimental setup

A small scale experiment (approximately 1:50 scale of a typical USDH structure) was performed by Yahiaoui et al. (1994). Figure 6.31 shows schematically the set-up of the test. Clamped edges were chosen for the boundary conditions in the test. Due to the availability of equipment and the shape of the model, it was only possible to clamp three edges. However, the effect of this incomplete clamped condition was reduced by the choice of contact point. As indicated in Fig. 6.31, the point of contact between the punch and the plate was at an equal distance from the three clamped edges and far from the free edge. The draw beads were also provided to ensure full restrain from in-plane sliding.

The test pieces were made of mild steel - B 0.75 mm in thickness. The height of double hull (i.e. distance between inner and outer hull) was 41.7 mm and the spacing of web girders was 41.7 mm in longitudinal direction. The indenter, which was a rigid cone with slope of 45^0 and with a round off apex, was pushed downward and penetrated the double hull. The sectional dimensions of the double hull and indenter are shown in Fig. 6.29.

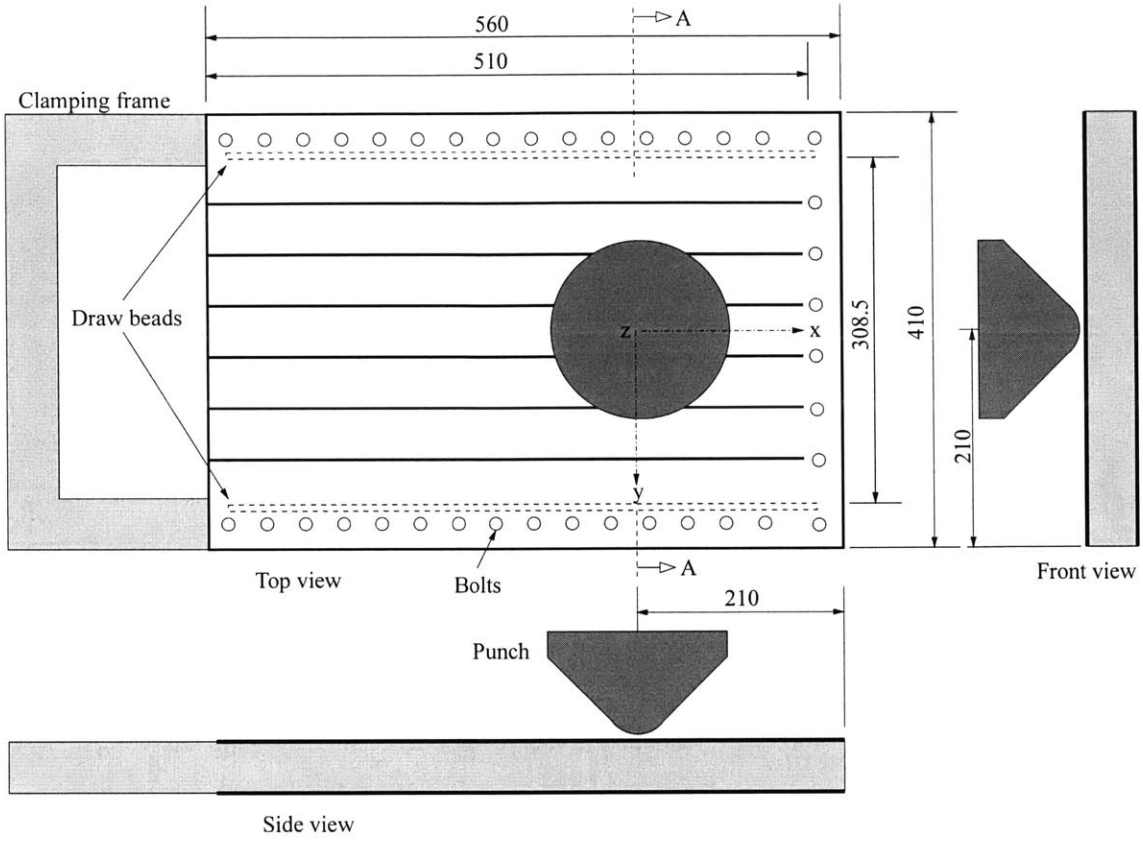

Fig. 6.31 Model and test arrangement used in the experiment of Yahiaoui et al. (1994) (in mm)

6.2.1.2 Finite Element (FE) analysis of punch indentation

FE model The finite element model of the double hull shown in Fig. 6.32 was created using the mesh generator program, *HyperMesh* Version 6.0. The explicit non-linear finite element code, *PAM-CRASH* Version 2G (2003) was utilized to simulate the deformation and fracture of double hull under punch indentation. The four-node Belytschko-Tsay shell element, with five integration points through thickness, one integration point in the element plane, finite membrane strain, arbitrarily large rotation, and stiffness based hourglass control, was employed. These shell elements have six degrees of freedom at each node (i.e. three displacement components and three global rotation components). The inner hull, outer hull, and longitudinal webs were constructed with the shell elements. The ratio of average element length to the plate thickness was 1.0, which provides 102,582

shell elements shown in Fig. 6.32. The virtual indenter was modeled with the same dimensions as the physical indenter used in the test. The indenter had a spherically shaped tip consisted of a 21.85 mm radius hemisphere. The tip was attached to a conical shell with a maximum radius 83.4 mm at the base. The indenter consisted of 1000 rigid elements. The displacement and rotation of nodes corresponding to the clamped edges were fixed. The highly improved self-contact option (contact algorithm #36 using "3D bucket" global search algorithm) provided by *PAM-CRASH* was used in the full model. Friction coefficient used in the contact option was $\mu = 0.2$.

Fracture In the present numerical simulation of punch indentation, ductile fracture was assumed to be controlled by Eq. (2.4) or Eq. (6.21). According to the calibration of material model presented in next Section 6.2.2, the critical damage value of the mild steel - B was $D_c = 0.35$. Furthermore, it was found that the average stress triaxiality in the potential fracture points of the present problem is approximately constant and equal to $(\sigma_m / \bar{\sigma})_{av} = 0.6$ throughout the whole process of deformation involving crack formation and subsequent crack propagation (see Figs 6.46 and 6.48). Therefore, referring to Eq. (6.21), the critical strain to fracture $\bar{\varepsilon}_f = 0.58$ was specified to simulate fracture. The element was removed from the set of active elements when it reached the specified equivalent strain to fracture. Note that no imperfection and fracture path were introduced in the calculations. Numerical simulations were carried out on a personal computer (2GHz Intel Pentium IV, 2 GBytes RAM) with 48 CPU hours.

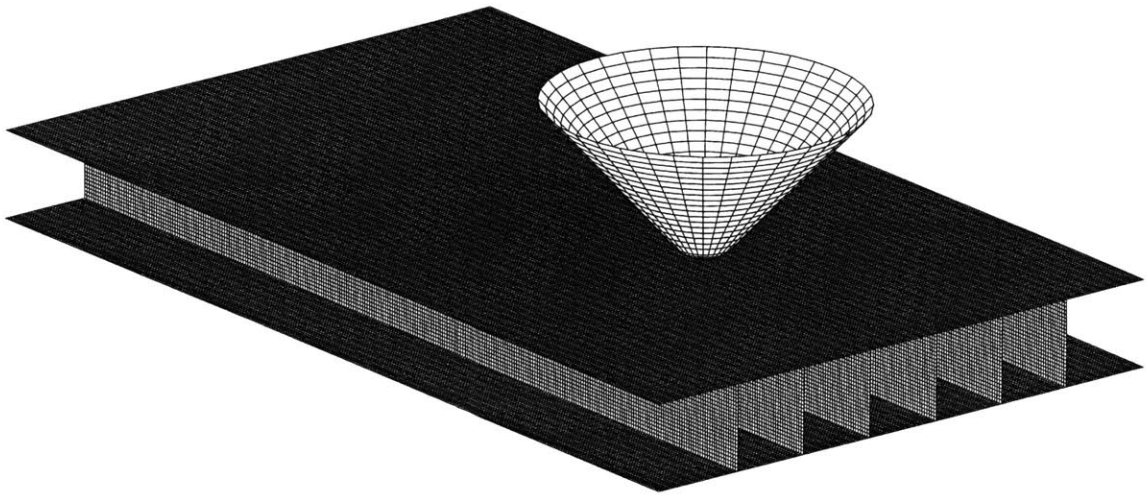

Fig. 6.32 Finite element model for the punch indentation test of USDH (102,582 shell elements; 1000 rigid elements)

6.2.2 Calibration of material model (mild steel - B)

Separate calibration for plasticity and fracture were performed for the mild steel - B. Flat tensile specimens shown in Fig. 6.33(a) were cut from the thin mild sheets to be tested. The specimens were modeled using four-node Belytschko-Tsay shell element as shown in Fig. 6.33(b). The specimens were modeled using 40 elements across the width, giving an element size of approximately 0.32 mm. As can be seen in Fig. 6.34, the correlation of the load-displacement response between tension test and numerical simulation is good. It should be mentioned that the trial-and-error method described in Chapter 3.2 was used to obtain the actual stress-strain curve of the considered material. The resulting actual stress-strain curve was taken as material input data in the numerical simulation shown in Fig. 6.34. The history plots of the equivalent strain and stress triaxiality at the center of specimen were shown in Figs. 6.35 and 6.36, respectively. Note that the specific points, such as the onset of necking and fracture, are marked with symbols in Figs. 6.34, 6.35, and 6.36. In Fig. 6.37, close-ups of the deformed specimen geometries obtained from numerical simulation are plotted with contour of equivalent plastic strain. It can be seen that numerical simulation successfully captured the whole features of tensile test on the flat specimen from necking to complete fracture.

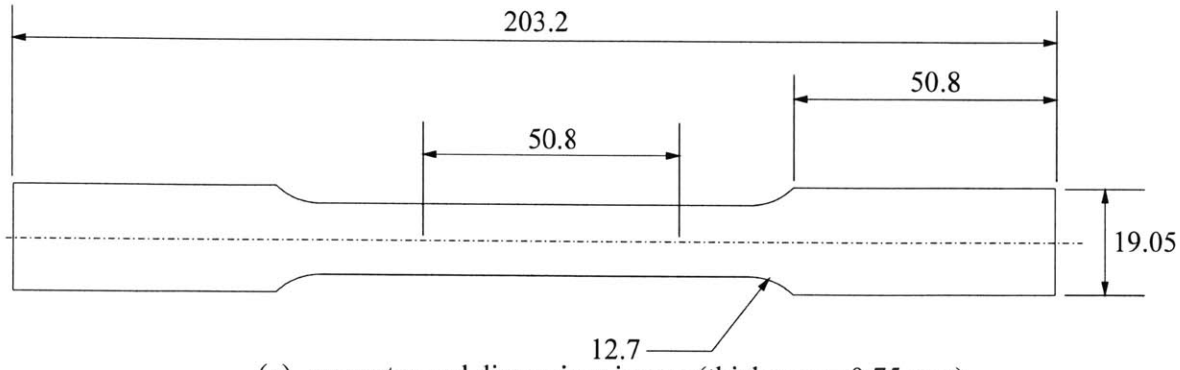

(a) geometry and dimensions in mm (thickness = 0.75 mm)

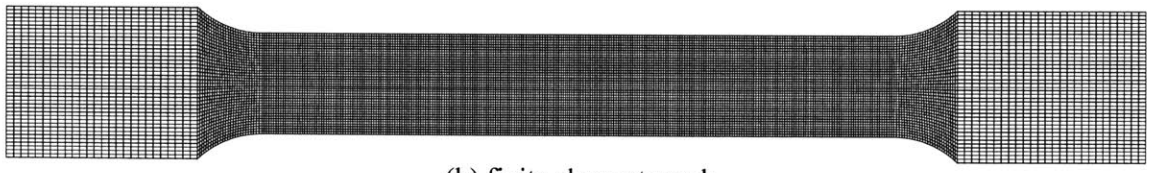

(b) finite element mesh

Fig. 6.33 Geometry, dimensions, and finite element mesh of flat specimen for uniaxial tension test of mild steel - B used in the punch indentation test

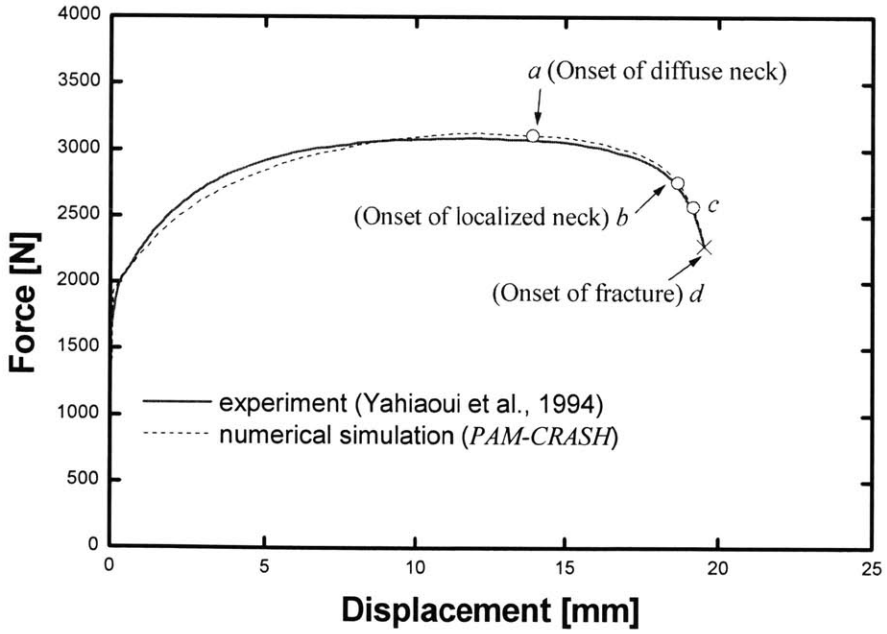

Fig. 6.34 Load displacement curve for the material used in the punch indentation recorded from tensile test on flat specimen (mild steel - B)

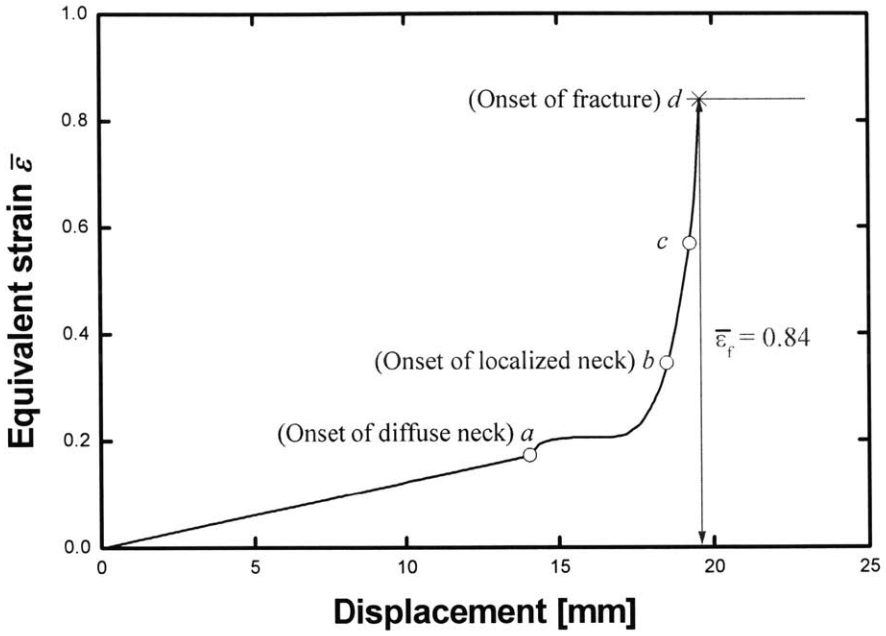

Fig. 6.35 Growth of the equivalent strain at the fracture location (center of specimen) of flat specimen (mild steel - B)

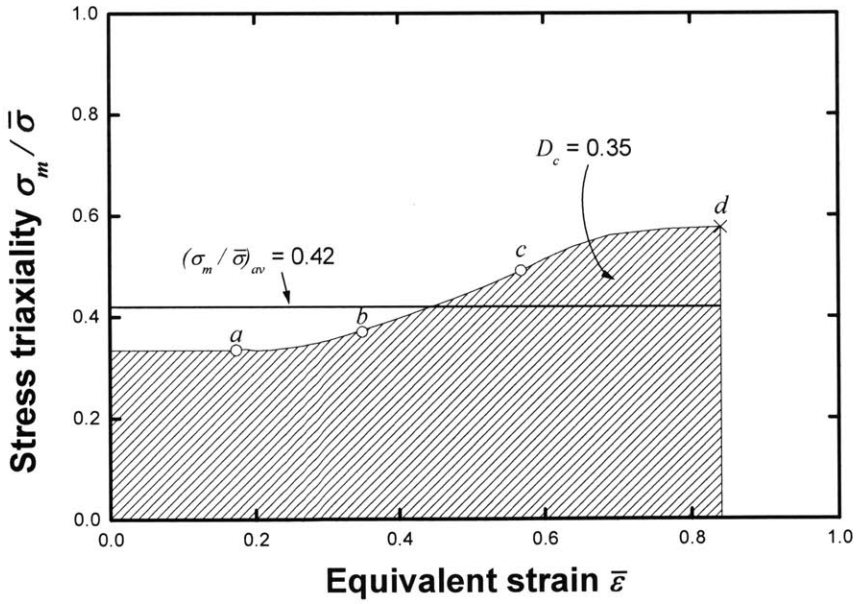

Fig. 6.36 Evolution of stress triaxiality $\sigma_m / \bar{\sigma}$ and equivalent strain $\bar{\varepsilon}$ in the uniaxial tension of flat specimen (mild steel - B)

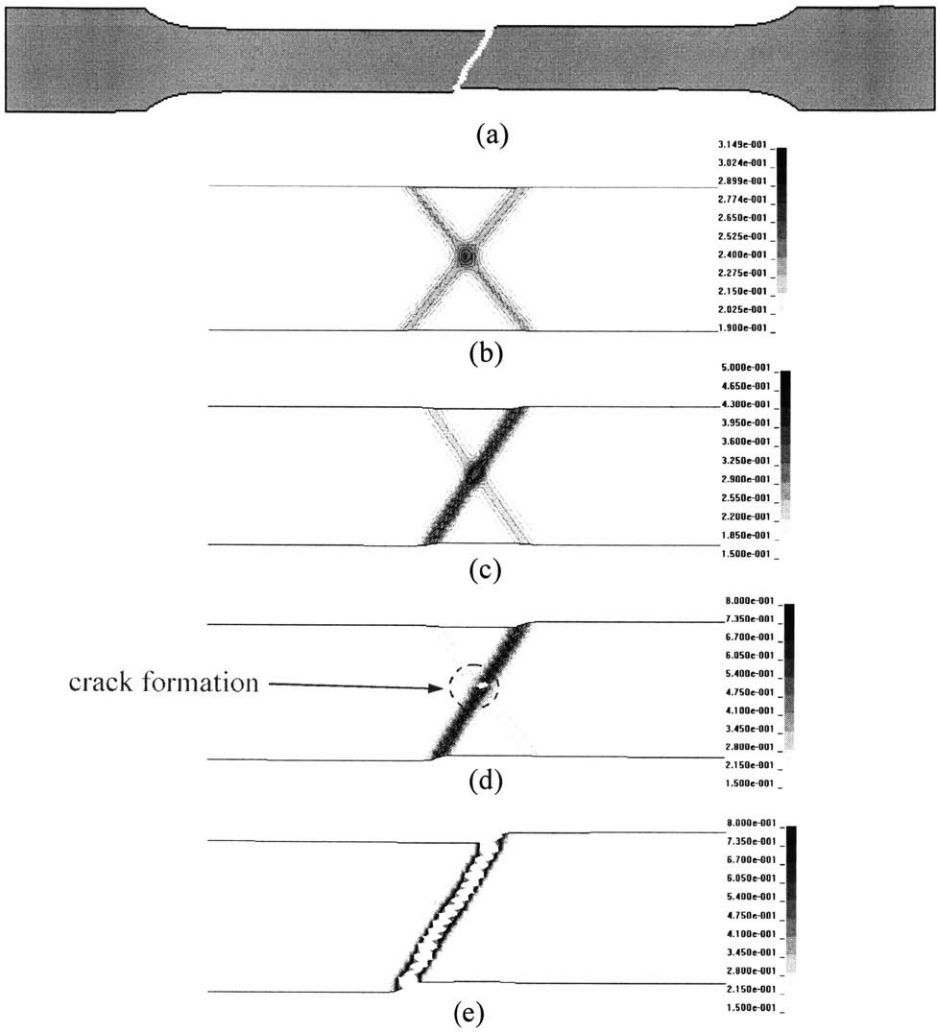

Fig. 6.37 Uniaxial tension simulation of flat specimen for the calibration of mild steel - B material used in the punch indentation test; (a) fracture pattern of flat specimen from numerical simulation; (b) equivalent strain contour in the gauge region (at point "b" in Figs. 6.34, 6.35, and 6.36); (c) equivalent strain contour in the gauge region (at point "c" in Figs. 6.34, 6.35, and 6.36); (d) equivalent strain contour in the gauge region (at point "d" in Figs. 6.34, 6.35, and 6.36); (e) equivalent strain contour in the gauge region (after point "d" in Figs. 6.34, 6.35, and 6.36)

6.2.3 Punch force-penetration response and fracture pattern

The results from the test and simulation are shown in Fig. 6.38, as the punch force-penetration curve. As can be seen in this figure, the finite element solution is in good agreement with the experiment throughout the whole stages of indentation. The numerically obtained cross-sectional views of the double hull are shown in Fig. 6.39 for three different values of normalized indentation, δ/H = 0.74, 1.65, and 2.6, where H is the height of the double hull. Furthermore, Fig. 6.40 compares visually final fracture pattern between the test and the simulation with various points of viewing direction. A detail description on the experimental punch force-penetration response was given by Thunes (1994). Based on his description on the test result together with the deformation and fracture patterns from the present numerical simulation, the following observations can be made, referring to points indicated on the curve shown in Fig. 6.38:

- Point '1'. First contact between indenter and outer hull (top face plate) occurs. Outer hull starts to deform between the first set of longitudinal girders.
- Point '2'. The cone touches the first set of longitudinal girders followed by progressive crushing of these girders. The deformation zone of outer hull plating extends over three cells.
- Point '3'. Fracture occurs in the outer hull between the first set of girders. The first crack develops at the side of the apex where the change in curvature is the highest and a peak in radial strain develops. The corresponding location of failure, denoted by $\xi_f = y_f / B$, is shown in Fig. 6.39(a) and equal to $\xi_f = 0.06$. From this point on, the crack propagates in the longitudinal direction and the load drops.
- Point '4'. Load starts to increase again. The outer hull has lost its membrane capacity, but the new areas of contact are activated.
- Point '5'. Load increases rapidly due to direct contact between indenter and inner hull. Inner hull deforms between the first set of girders.
- Point '6'. The indenter directly contacts with the second set of girders. The deformation zone of outer hull extends over five cells.
- Point '7'. The first set of girders is completely crushed. Inner hull starts to deform over three cells.
- Point '8'. Fracture occurs in the inner hull. Much like in the case of the outer hull, the crack formation is observed at the transition between constant slope and rounded off apex (see Fig.

6.39(b)). Cracks evolve in the longitudinal direction. Load drop is not as significant as for the fracture of outer hull.

- Point '9'. Experiment and numerical simulations are terminated. Indentation depth is 112 mm, which is about 2.4 times the height of the double hull.

In addition, the double hull experiences a rupture at the clamped edges for both cases of test and simulation, as shown in Fig. 6.40(d). From all above the results, it is clearly confirmed that the numerical simulation with the present fracture criterion accurately predicts not only crack formation but also crack propagation which is understood as a sequence of crack formation in both punch force-indentation response and fracture pattern. The histories and distributions of the critical damage parameters are presented in detail in subsequent sections.

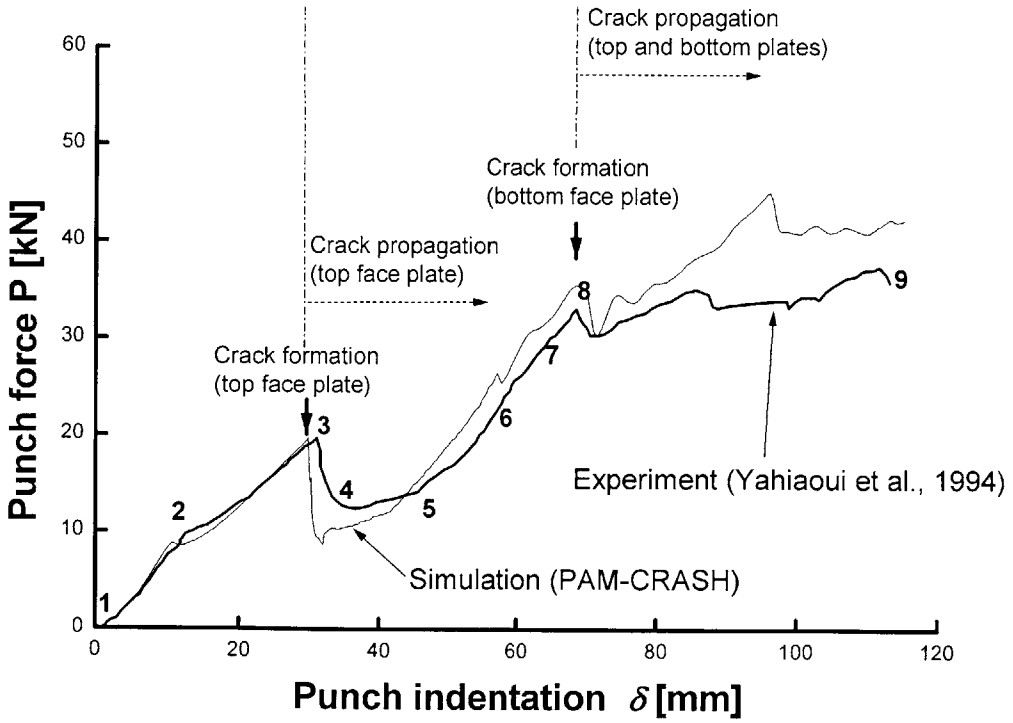

Fig. 6.38 Comparison of experimental and numerical punch force-indentation curves

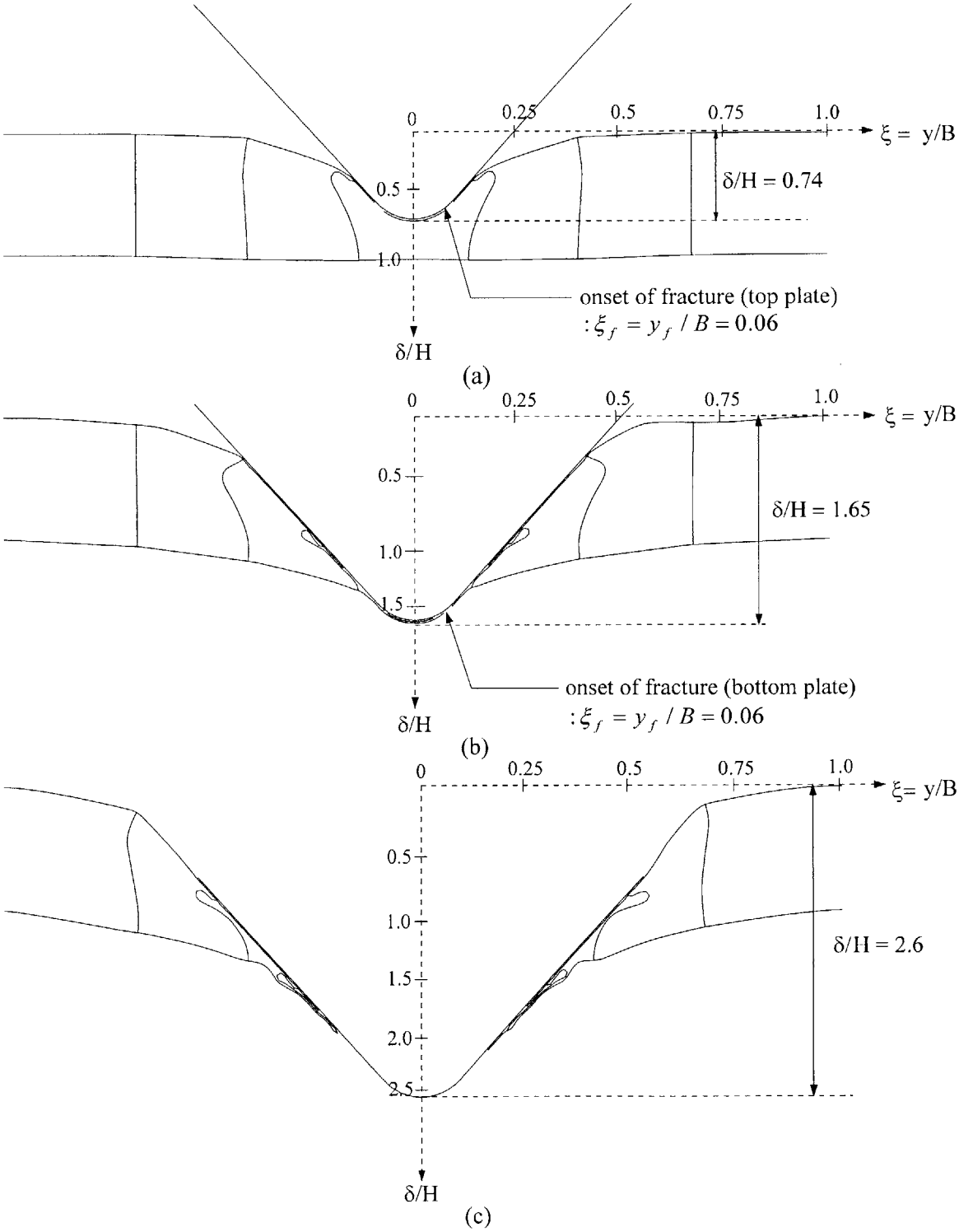

Fig. 6.39 Sectional view of deformed shape of double hull at three different values of punch indentation (H = 41.7mm; B = 41.7mm); (a) at δ = 31mm (point '3' in Fig. 6.38); (b) at δ = 69mm (point '8' in Fig. 6.38); (c) at δ = 108mm

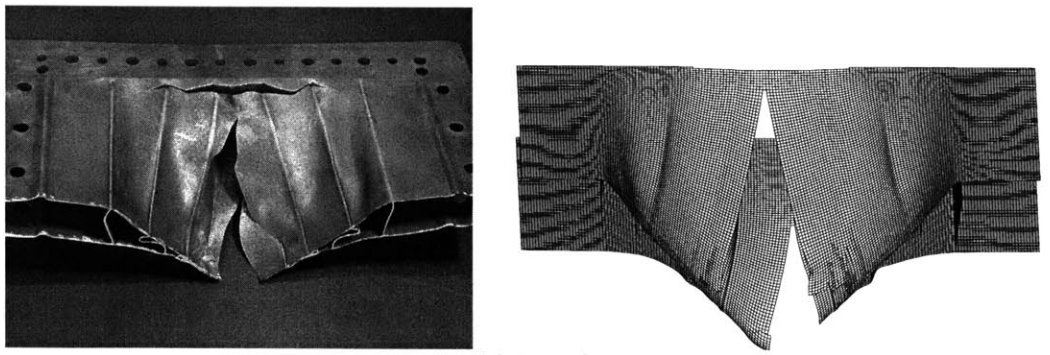

(a) 3-D view

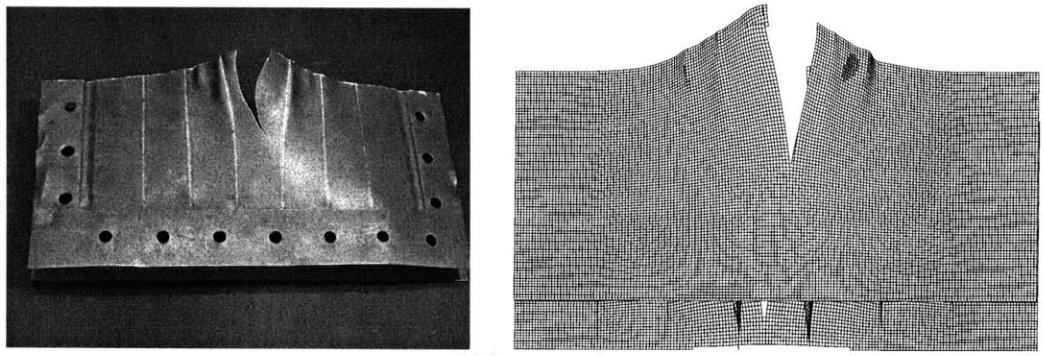

(b) bottom view

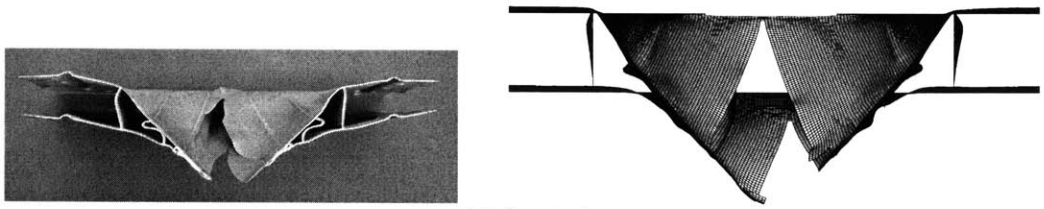

(c) front view

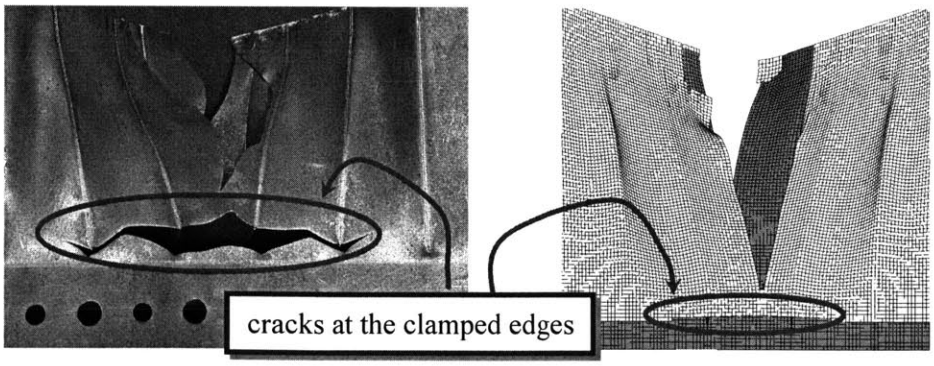

(d) top rear view

Fig. 6.40 Comparison of experimentally and numerically obtained fracture of double hull; experiment (left); numerical simulation (right)

6.2.4 Analysis of crack formation

The distributions of stress triaxiality and equivalent strain along the horizontal direction (y) are constructed at the point of crack formation in Figs 6.41 and 6.42, respectively. Note that the first cracks were observed at $\delta = 31$ mm and 69 mm in the outer and inner hulls, respectively (see Fig. 6.38). The corresponding 3-D fracture patterns are shown in Fig. 6.43. It can be seen from Fig. 6.41 that the stress state shows the equi-biaxial condition ($\sigma_m / \bar{\sigma} = 2/3$) around the plate center and plane strain deformation ($\sigma_m / \bar{\sigma} = 1/\sqrt{3}$) at the clamped edge. It can be further observed that there is rapid drop or increase of stress triaxiality in the plate junctions. The stress triaxiality at which fracture occurs (see symbol 'X' in Fig. 6.41) is of an order of 0.6. From Fig. 6.42 where the profiles of equivalent strain are shown from the plate center to the clamped end, it is seen that plastic deformation localizes at the side of apex of the indenter and in the plate junctions. The maximum peak strain develops at the contact point where the change in curvature is the highest (see symbol 'X' in Fig. 6.42). Note that this fracture point is indicated by $\xi_f = y/B = 0.06$ in Figs. 6.39(a) and 6.39(b). The above observations on the distributions of stress triaxiality and strain at the point of crack formation is quite consistent with the ones for the case of single plate presented earlier in Section 6.1.

Figure 6.44 shows the profiles of accumulated damage, as defined by Eq. (2.4), at the instant point of crack formation in both face plates. It can be clearly confirmed that the damage reaches the critical value of $D_c = 0.35$ (mild steel - B) around the normalized distance from the plate center ($\xi_f = y/B = 0.06$). Furthermore, the cumulated damages are mostly localized within the second set of girders ($0.0 < \xi < 0.4$). Beyond this region, there is no accumulated damage. This observation can be confirmed from Figs. 6.39(a) and 6.39(b) where the plastic deformations confined within the second set of girders are shown.

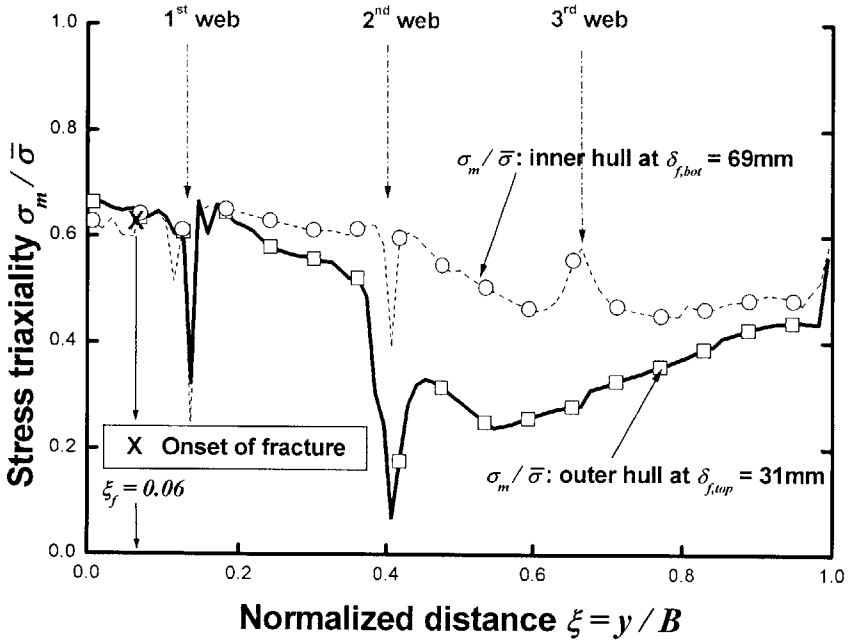

Fig. 6.41 Numerically obtained stress triaxiality profiles in the face plates of the USDH at the point of crack formation; outer hull (x = 0.0, y, z = 0.0); inner hull (x=0.0, y, z = H)

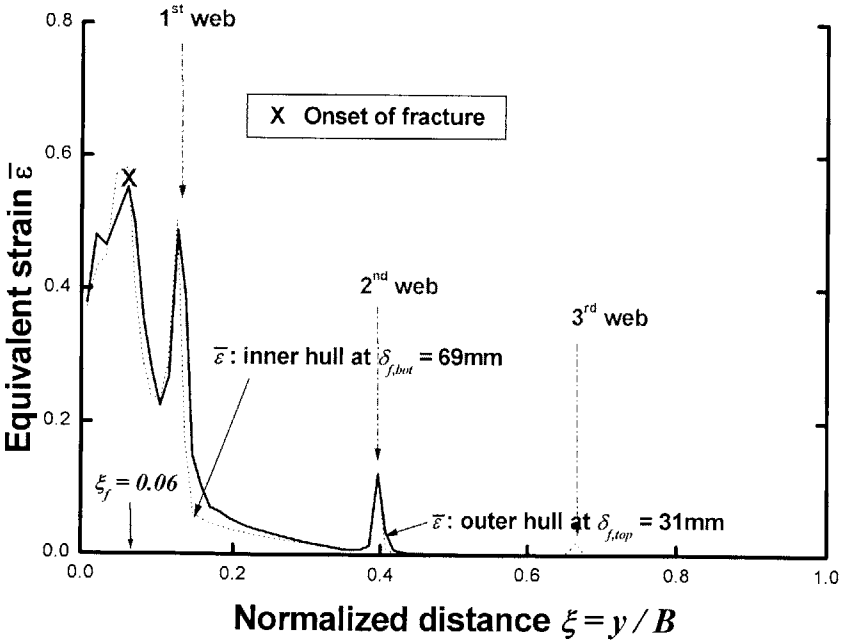

Fig. 6.42 Numerically obtained profiles of equivalent strain in the face plates of the USDH at the point of crack formation; outer hull (x = 0.0, y, z = 0.0); inner hull (x=0.0, y, z = H)

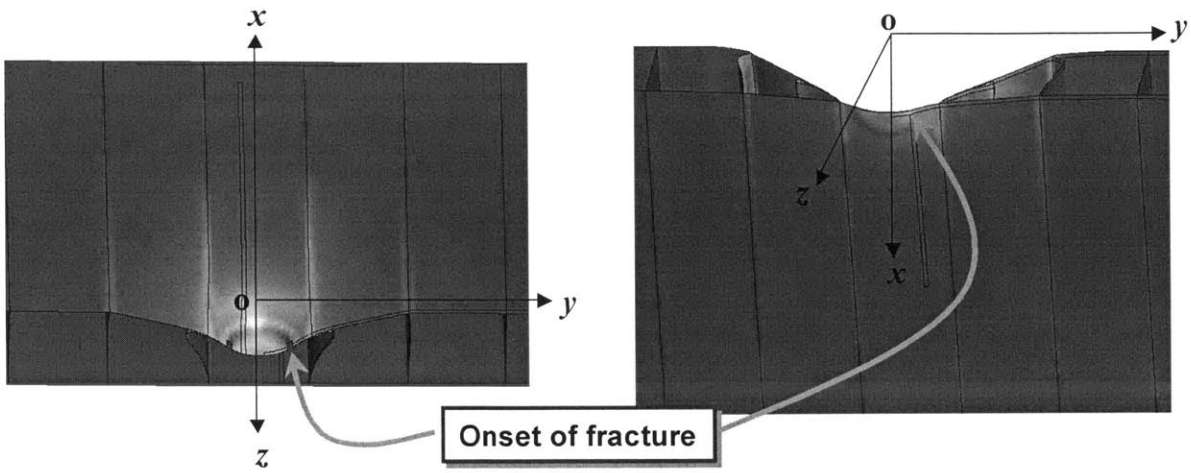

(a) outer hull (δ = 31mm) (b) inner hull (δ = 69mm)

Fig. 6.43 3-D deformed shapes of USDH at the point of crack formation

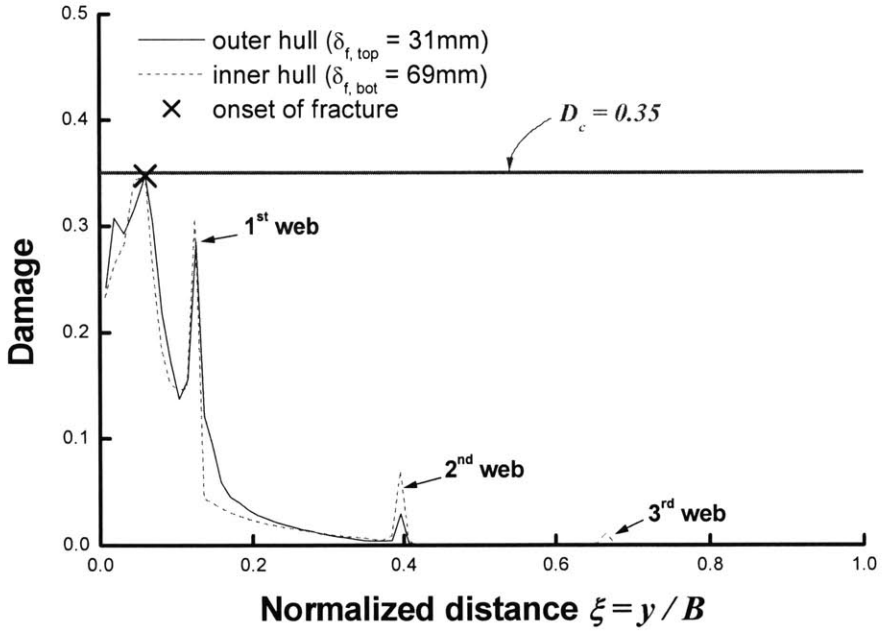

Fig. 6.44 Damage profiles of USDH at the point of crack formation

6.2.5 Analysis of crack propagation

The histories of critical damage parameters (i.e. strain, stress triaxiality, and resulting accumulated damage) at the various locations of potential fracture elements indicated in Figs. 6.45(b), 6.47(b), and 6.49(b) were obtained numerically during the whole indentation process.

6.2.5.1 Evolution of stress and strain fields

Outer hull (top face plate) The strain paths at the locations of outer hull, as defined in Fig. 6.45(b), are constructed in Fig. 6.45(a). The axes are the in-plane major and minor principal strains, $\varepsilon_1 = \max(\varepsilon_x, \varepsilon_y)$ and $\varepsilon_2 = \max(\varepsilon_x, \varepsilon_y)$. The fracture points of each element are denoted by symbol (X). Those fracture points are shown to be in good agreement with the analytically predicted FFLD from Eq. (2.25) for the critical damage value of $D_c = 0.35$. For a comparison purpose, the FLD given by Eq. (6.28) is also included in Fig. 6.45(a). As can be seen in this figure, the fracture process can be approximated by a combined path involving proportional straining up to instability followed by transverse plane strain deformation (i.e. $\alpha = 0; \sigma_m / \bar{\sigma} = 1/\sqrt{3}$).

Figure 6.46(a) shows the history of stress triaxiality versus indentation depth at the above locations. One can see that the stress triaxialities show smooth variation with the progression of indentation up to the point of crack formation at the element 'top_a' ($\delta = 31$ mm). From this point on, large variations of stress triaxialities are introduced. However, these significant variations are restricted to only the small regime of equivalent plastic strain ($\bar{\varepsilon} < 0.05$), as shown in Fig. 6.46(b). In Fig. 6.46, the average stress triaxiality defined by Eq. (2.3) is also included. It can be further observed that the difference in the magnitude of the average stress triaxiality between crack formation (element 'top_a') and propagation (other elements) is small and in all cases the average stress triaxiality is approximately equal to $(\sigma_m / \bar{\sigma})_{av} = 0.6$. Consequently, according to Eq. (6.21), the specified equivalent strain to fracture $\bar{\varepsilon}_f = 0.58$ for $D_c = 0.35$ can be also used to predict crack propagation. This observation is quite consistent with similar results obtained numerically for flat tensile specimen (see Chapter 5.3) and plates under localized impulsive loading (see Chapter 7.3).

Inner hull (bottom face plate) The in-plane principal strain paths at the critical locations of fracture are shown in Fig. 6.47. One can see from Fig. 6.47(a), the loci of those elements always stay in the first tension-tension quadrant. In a similar way to the case of outer hull, the initial loading paths can be approximated by linear strain ratio $\alpha = 0.2$ ($\sigma_m / \bar{\sigma} = 0.63$). Then, the final portion of all strain paths is parallel to the major strain axis whatever the original loading path. Accordingly, the orientation of neck and fracture coincides with the minor in-plane strain direction, in particular, longitudinal direction (x) for the present problem. The corresponding history plots of stress triaxialities are shown in Figs. 6.48(a) and 6.48(b) as functions of indentation depth and equivalent strain, respectively. As can be seen in Fig. 6.48(b), the variations in the stress triaxialities of those four elements are confined to very narrow range ($1/\sqrt{3} < \sigma_m / \bar{\sigma} < 0.63$). Consequently, the average stress triaxilaity, defined by Eq. (2.3), is almost constant for all cases.

Longitudinal web girder As shown in Fig. 6.49(a), the in-plane strain pairs of the elements in the longitudinal webs are within the range of fracture locus denoted by thick full line, which indicates no fracture in those locations. This observation agrees well with the experimental results, see the set of photos in Fig. 6.40. It is also interesting to note that the membrane principal strain states corresponding to the elements of the plate junctions (web1_a, web1_c, web2_a, web2_c) are located in the first tension-tension quadrant. On the other hand, the two strain paths taken from the elements at the center of the fold (web1_b, web2_b) are shown in the second tension-compression quadrant, see lines with filled symbols in Fig. 6.49(a). From Fig. 6.50, it can be further observed that the stress triaxialities at the plate junctions (e.g. web1_c, web1_a) mainly vary within the range between uniaxial (1/3) and equi-biaxial tension (2/3). The stress triaxialities of the wrinkling points (web1_b, web2_b), which is associated with compressive instability, have negative value and below the so-called cut-off value, $-1/3$, discovered by Bao and Wierzbicki (2004a). Based on the analysis of the results of upsetting tests, they found the limit value of the stress triaxiality below which fracture could never occur. Present findings clearly confirm the validity of the cut-off value.

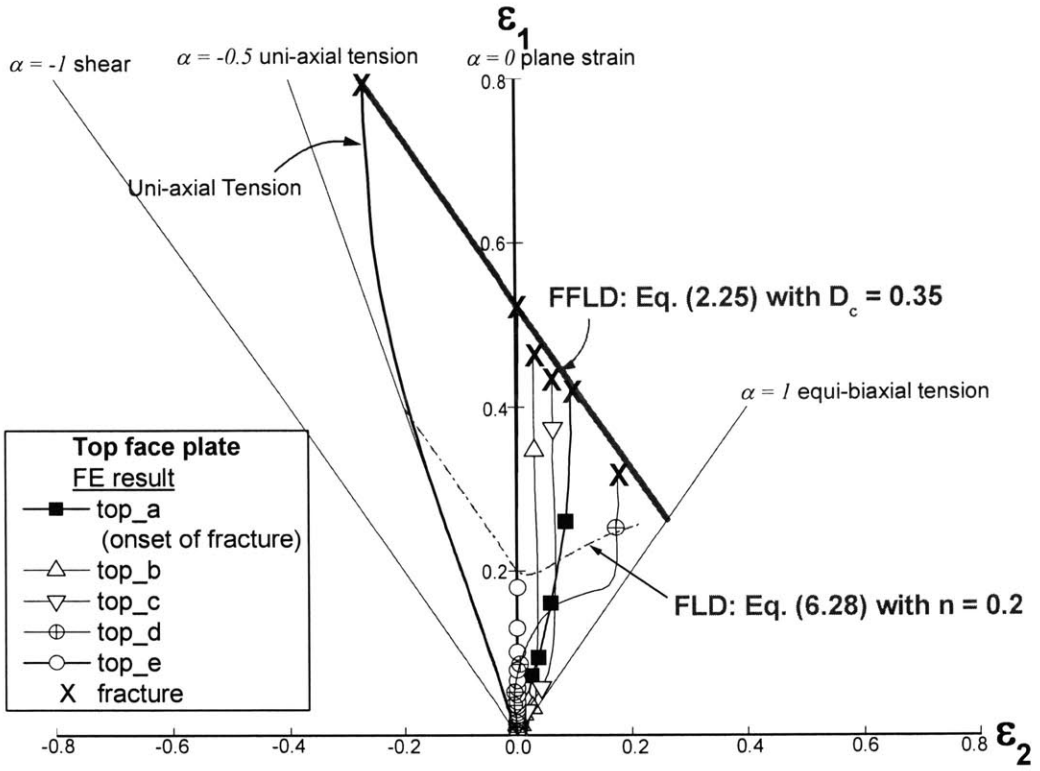

(a) strain paths at the potential fracture points of outer hull

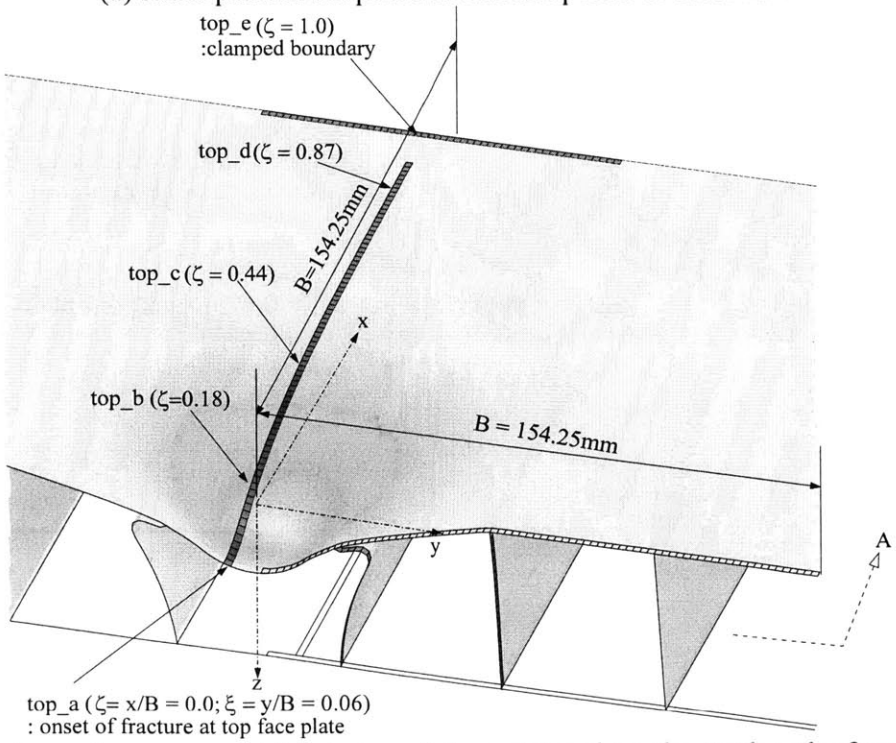

(b) locations of measurement for strain and stress states along the crack path of outer hull

Fig. 6.45 Numerically obtained FFLD of double hull (outer hull)

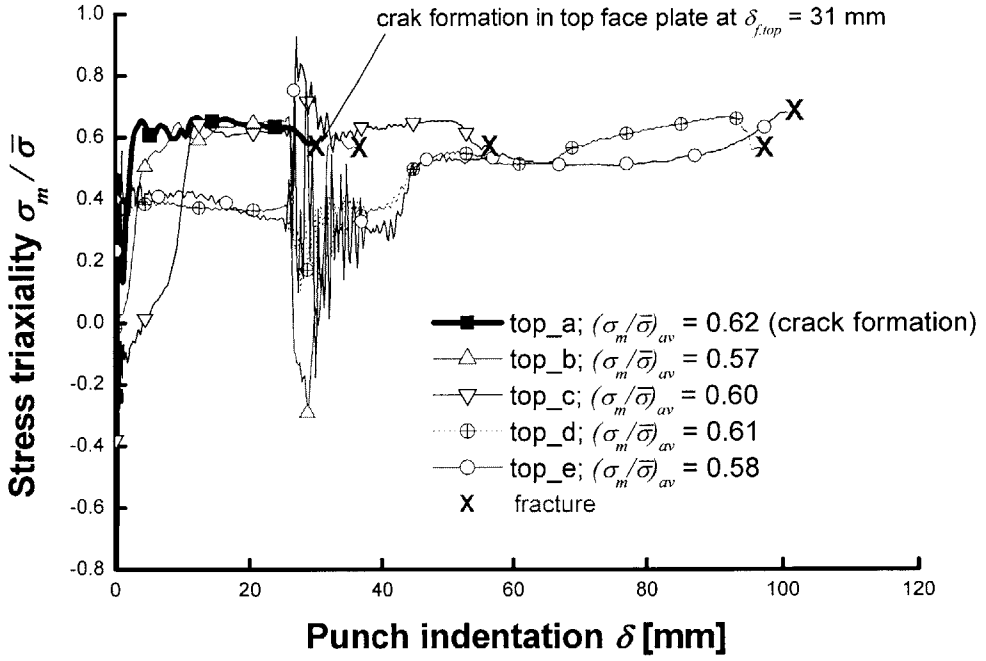

(a) stress triaxiality versus punch indentation

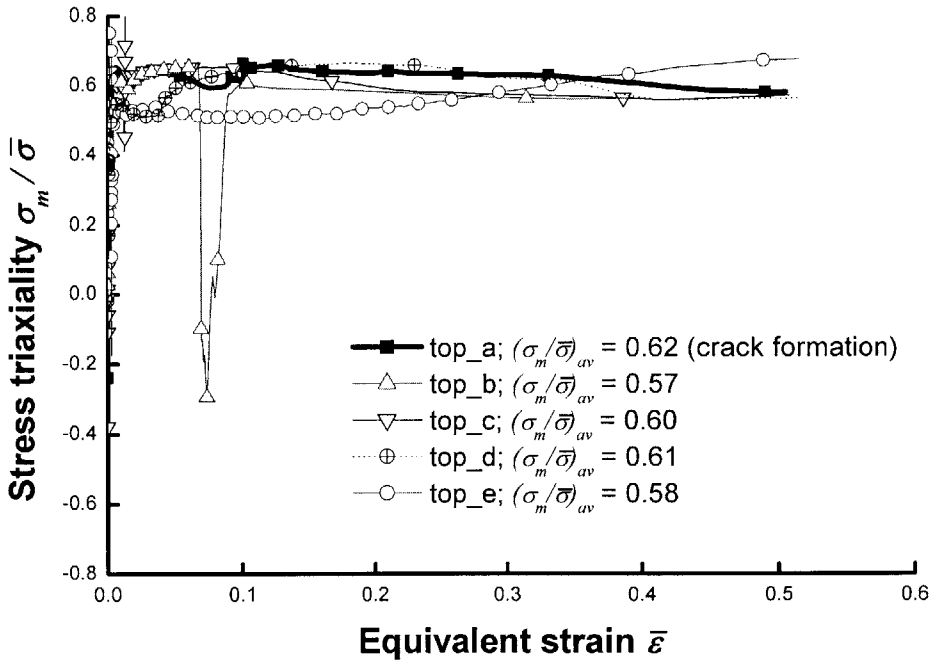

(b) stress triaxiality versus equivalent plastic strain

Fig. 6.46 Evolution of stress triaxiality at the potential fracture points along the crack path of top face plate (outer hull)

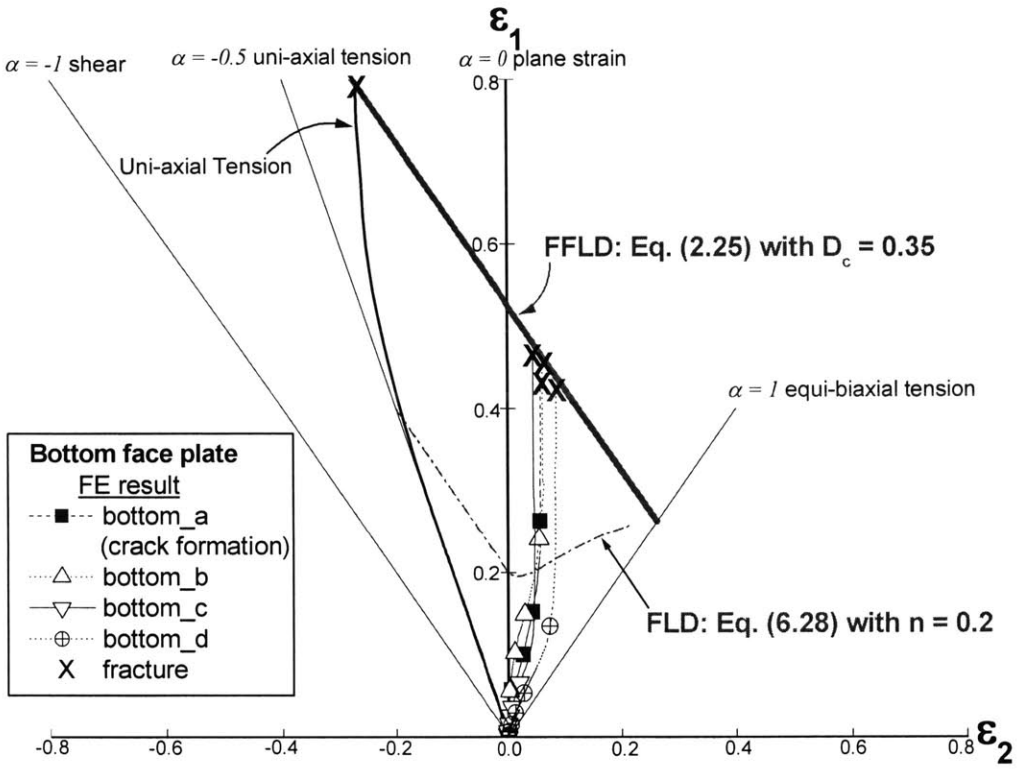

(a) strain paths at the potential fracture points of inner hull

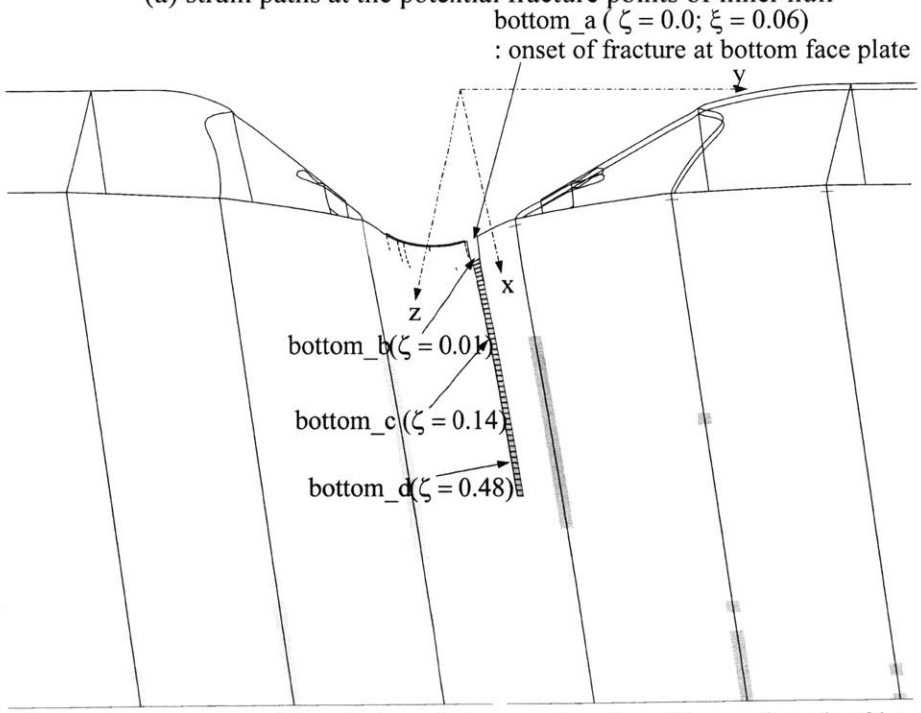

(b) locations of measurement for strain and stress states along the crack path of inner hull

Fig. 6.47 Numerically obtained FFLD of double hull (inner hull)

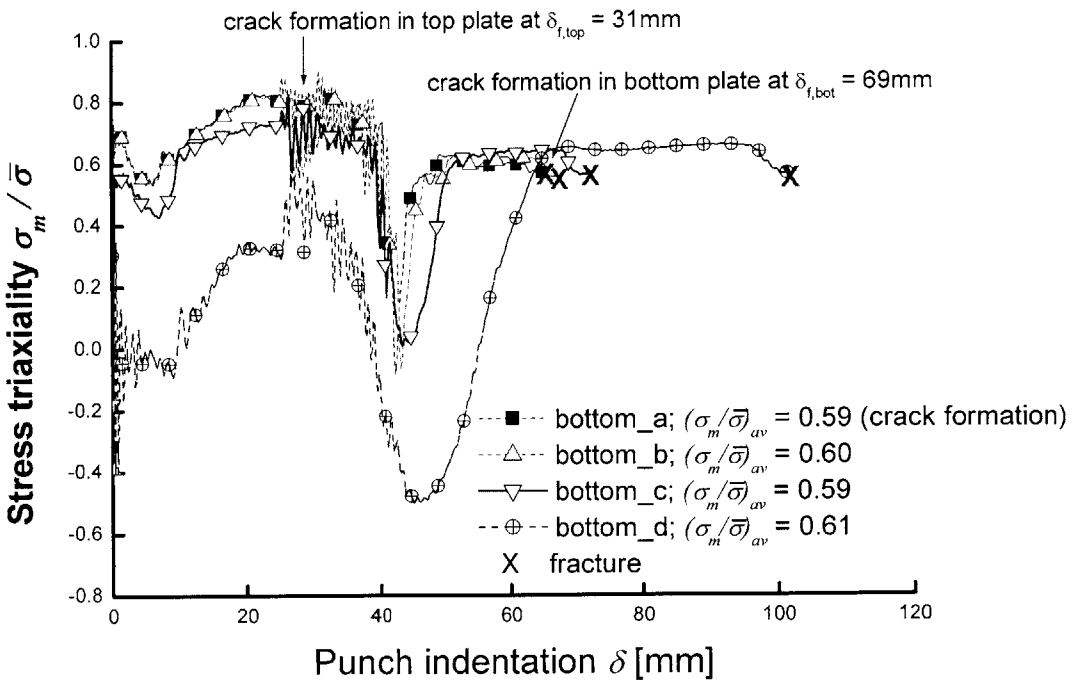

(a) stress triaxiality versus punch indentation

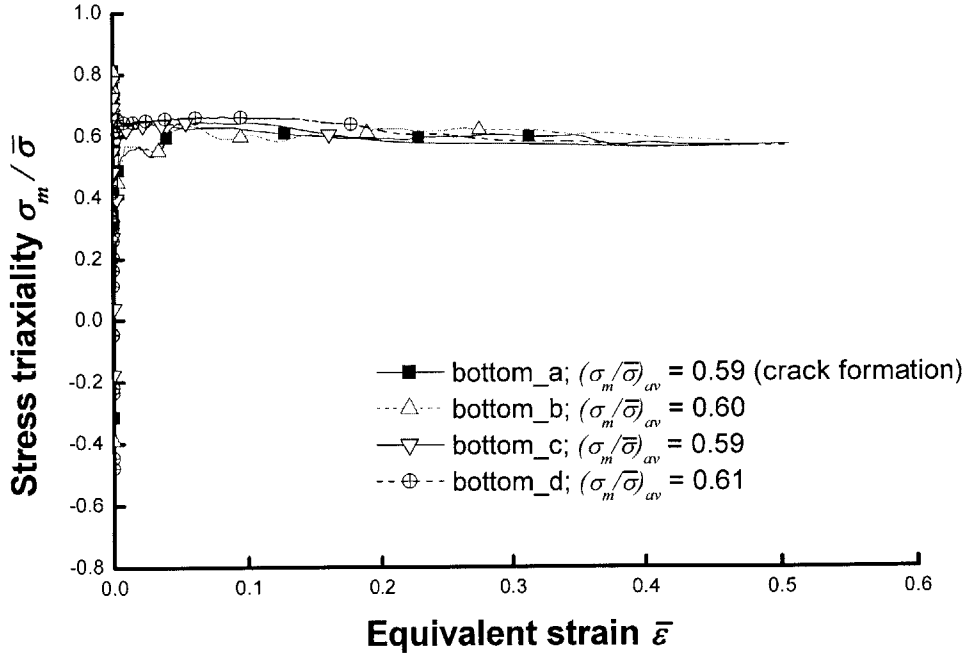

(b) stress triaxiality versus equivalent plastic strain

Fig. 6.48 Evolution of stress triaxiality at the potential fracture points along the crack path of bottom face plate (inner hull)

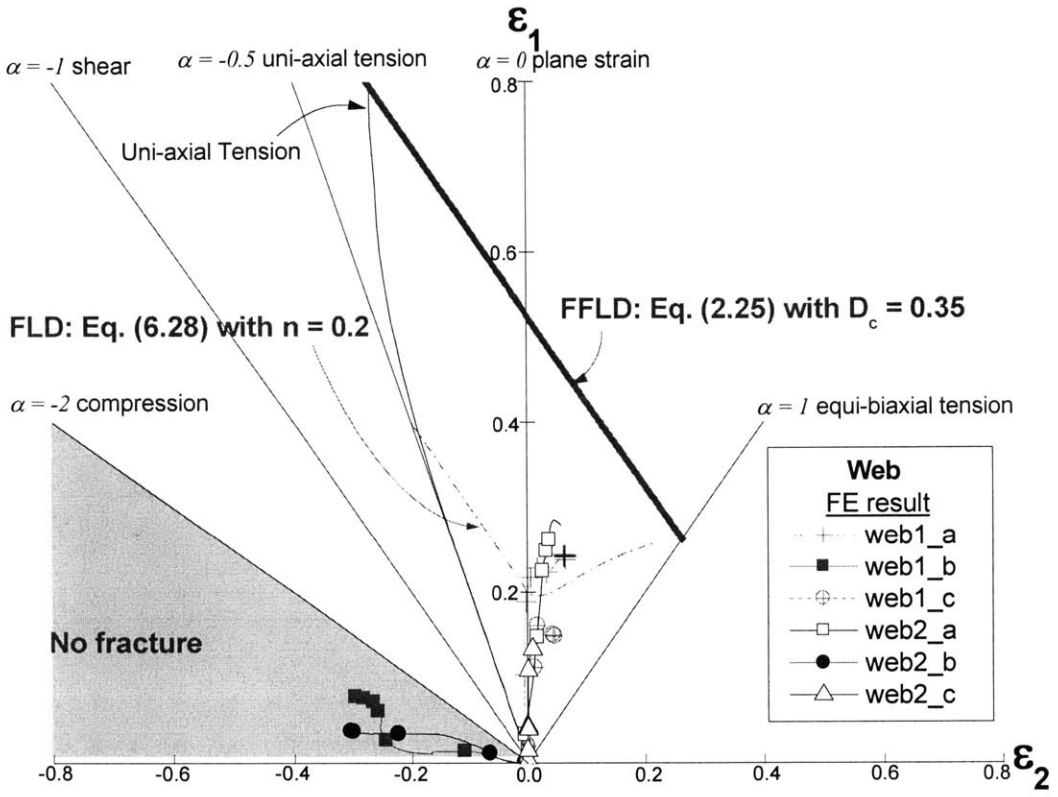

(a) strain paths at the potential fracture points of web girder

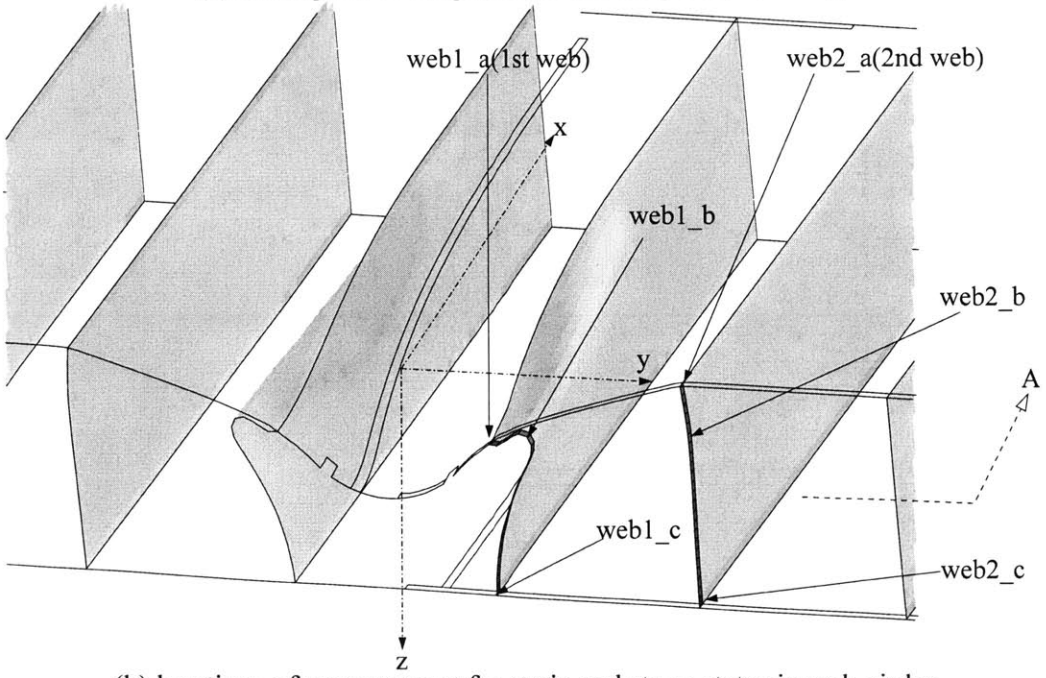

(b) locations of measurement for strain and stress states in web girder

Fig. 6.49 Numerically obtained FFLD of double hull (web girder)

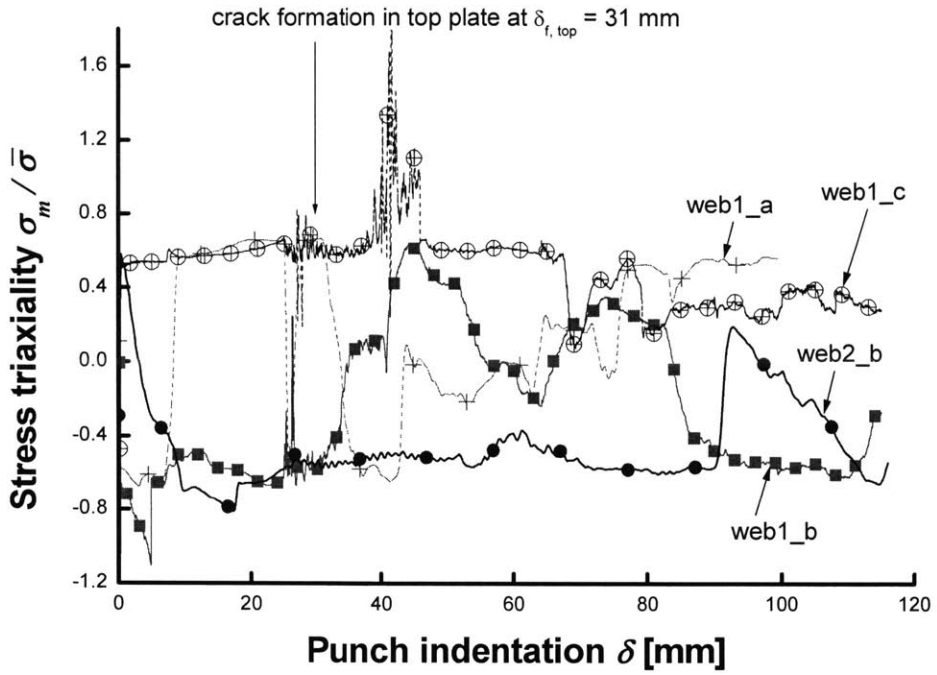

(a) stress triaxiality versus punch indentation

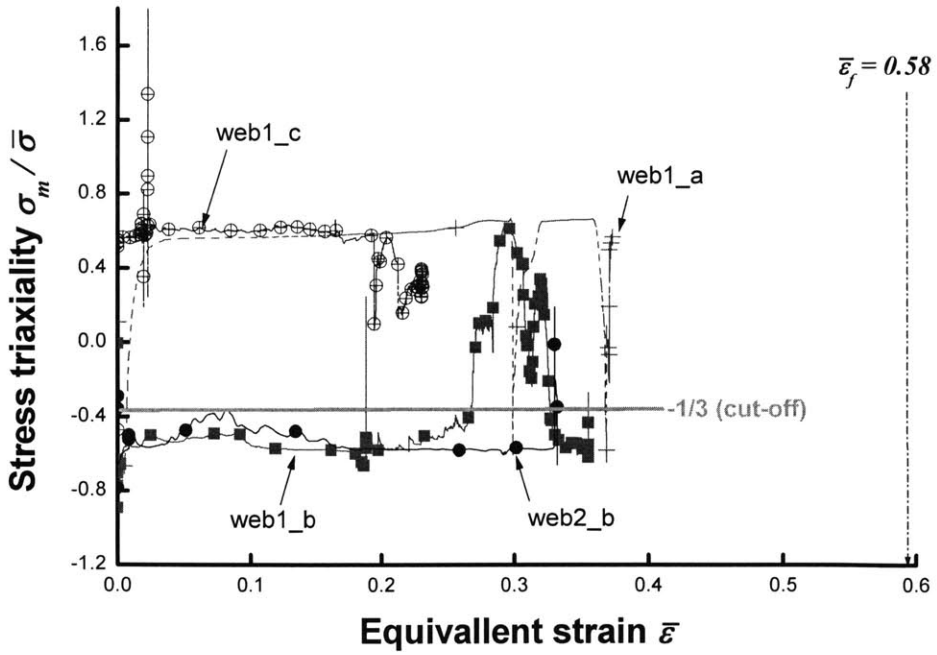

(b) stress triaxiality versus equivalent plastic strain

Fig. 6.50 Evolution of stress triaxiality at the potential fracture points along the crack path of web girder

6.2.5.2 History of accumulated damage

The plots of accumulated damage versus indentation depth at the critical locations of fracture are shown in Figs 6.51 and 6.52. Moreover, the sequence of the failure process is illustrated visually in Fig. 6.53. From all above the figures, it can be clearly seen that cracks propagate from the initial crack at the contact point between indenter and plate to the subsequent longitudinal cracks toward the clamped boundary of the double hull.

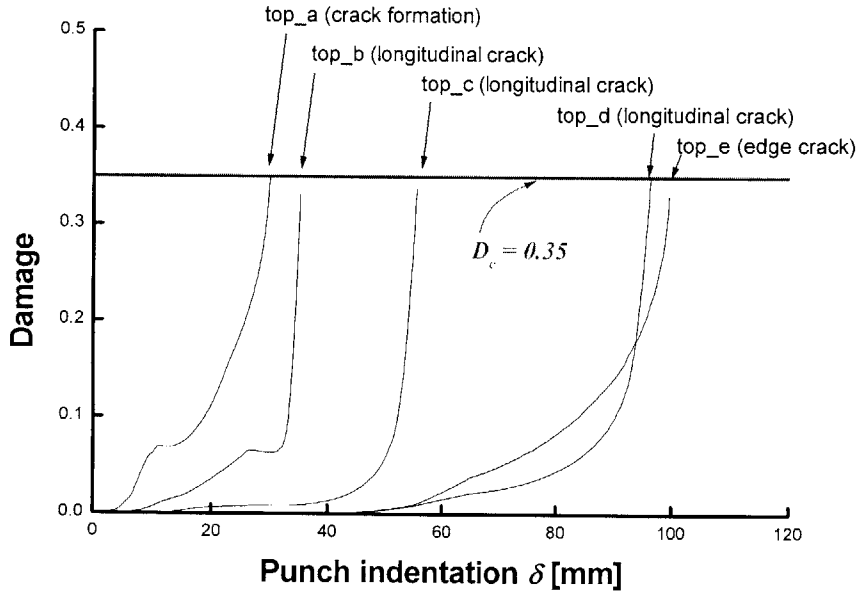

Fig. 6.51 Damage versus punch indentation at the fracture location along the crack path (outer hull)

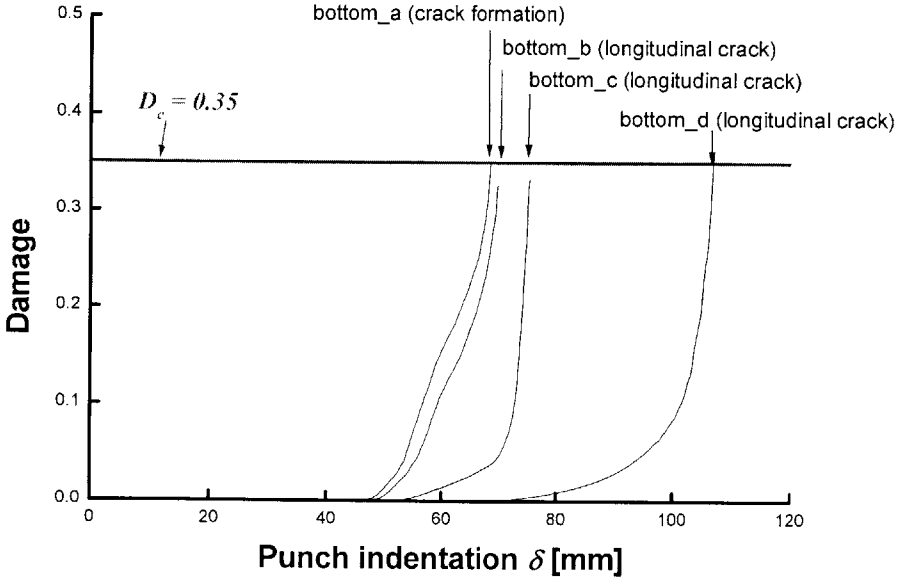

Fig. 6.52 Damage versus punch indentation at the fracture location along the crack path (inner hull)

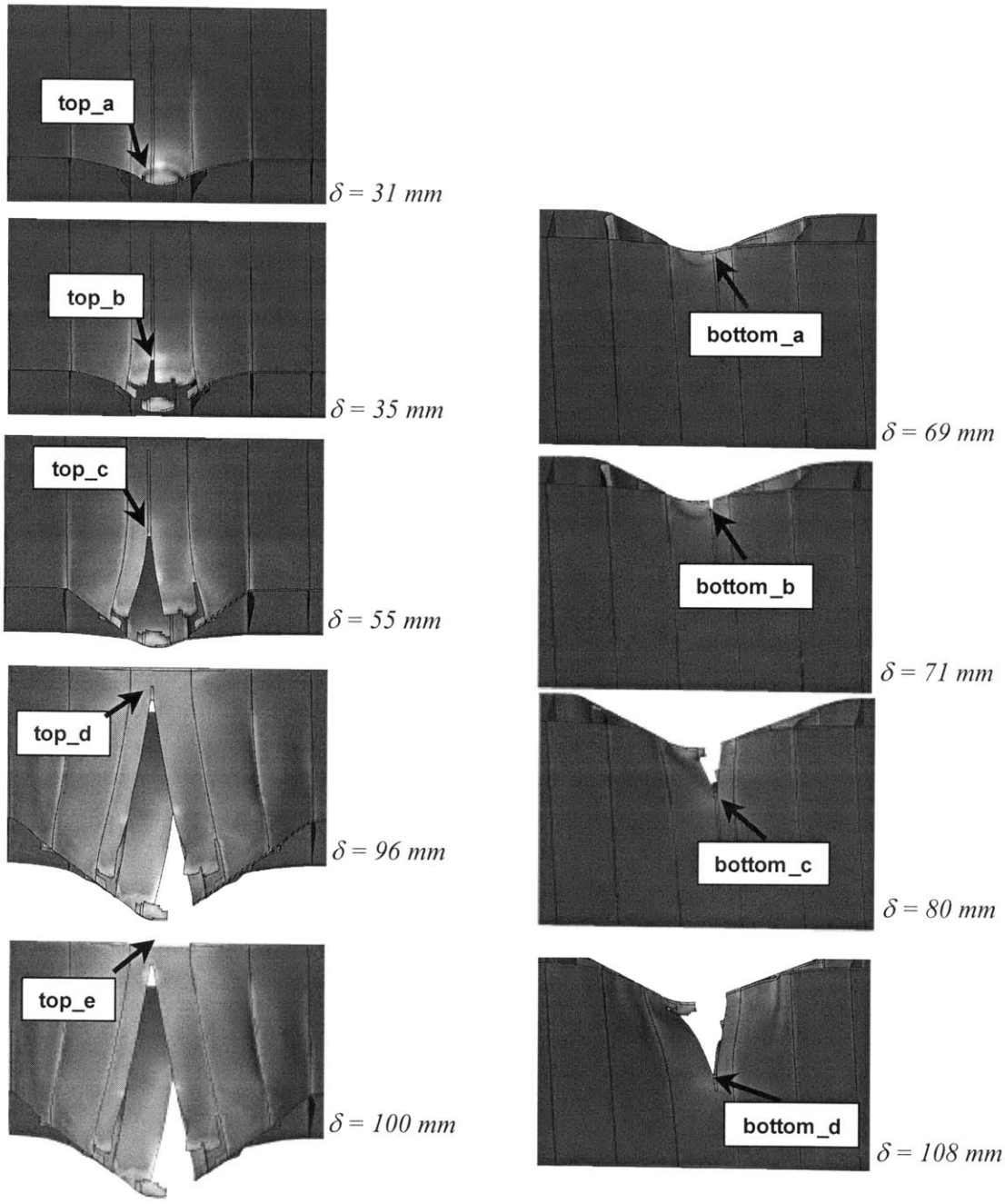

Fig. 6.53 Sequential fracture patterns of USDH under conical punch indentation; outer hull (left); inner hull (right)

6.2.6 Conclusion

- The present FE approach to crack formation and propagation (explained in Chapter 4.2) was applied to predict the fracture behavior of double hull structure in punch indentation test. Characteristics of the response of structural members were identified based on the results of test and numerical simulation. Primary damage mechanism consists of membrane stretching of face panel, crack formation, folding of longitudinal webs, crack propagation.
- In Chapter 2, it was shown that the fracture locus (FFLD) is actually represented by single straight line with negative slope (Eq. (2.25)). In this study, the position of this straight line for the considered mild steel - B was determined by the critical damage value D_c obtained from the conventional calibration procedure involving tensile test on flat specimen and parallel numerical simulation. Furthermore, it was demonstrated that the numerically obtained principal strain pairs at the site of cracking fall on well the FFLD (Eq. (2.25)).
- The local stress and strain conditions of material ahead of a propagating crack were shown to be similar to those which exist in loaded uncracked material prior to crack formation. For example, it was found that the difference of the average stress triaxiality between crack formation and propagation is very small and can be classified as near plane strain tension deformation (i.e. $(\sigma_m / \bar{\sigma})_{av} \approx 0.58 \sim 0.6$) for all the critical locations to fracture. Hence, the postulated fracture criterion can be reasonably applied to predict subsequent crack propagation in the present problem. This observation is quite consistent with the finding from the case of tensile specimen given in Chapter 5.

In summary, a good agreement between the results of test and finite element simulations provides an important validation of the fracture criterion at the component level. Therefore, the present approach can be used to predict the nature and extent of deformation and fracture for the USDH and other hull designs in this class. This topic is discussed in Chapter 9.

This page intentionally left blank

Chapter 7

Fracture Prediction of Thin Single Plates under Localized Impulsive Loading

7.1 Overview

A comprehensive analysis of deformation and fracture of thin plates subjected to localized impulsive loading is presented. A typical failure mode of thin clamped circular plates under localized explosive loading involves three stages with increasing intensity of applied loading. In the first dishing phase, the plate undergoes large inelastic deformation without fracture. This is followed by discing in which an initial circumferential crack detaches the circular cap from the plate. In the last petalling phase, observed under high intensity of impulsive loading, radial cracks propagate outward from the initial hole while the subsequent rotation of the plate segments leads to a number of petals. In the present Chapter, an analytical/numerical investigation on the deformation and failure of the plates is presented covering all the above stages of deformation with various radii of the centrally loaded area.

The objective of this study is to predict the transient response and fracture of thin plates to explosive loading with various spatial and temporal distributions, and intensity of applied impulse. For the dishing phase presented in Section 7.2, a primarily numerical investigation on the deformation of clamped thin plates under central impulse loading is presented for various radii of

the centrally loaded area. Section 7.2 is concerned with the final deflection profiles and strain distributions along the plate. In order to predict the onset of fracture and later on the propagation of crack, a precise determination of the deflection, strain, and stress fields is indeed necessary. For the discing and petalling phases presented in Section 7.3, the fracture criterion postulated by Bao and Wierzbcki (2004a/b) is first calibrated from uniaxial tensile tests and then applied to predict formation and propagation of cracks in the plates under localized high intensity loading. This is a new aspect of the problem because most of the relevant literature was concerned with the dishing phase without fracture.

7.2 Dishing

7.2.1 Introduction

Numerous papers were published on the deformation of thin plates to impulsive loading, which was uniformly distributed over the entire plate area. A review of the relevant literature was given by Jones (1968), and Nurick and Martin (1989a/b). Most of the experimental and analytical efforts were concerned with the relationship between the intensity of dynamic loading and the final permanent deflection of the plates. Tests on fully clamped circular plates under uniformly distributed impulses were reported by Bodner and Symonds (1979), Nurick and Martin (1989b), and Teeling-Smith and Nurick (1991). A more detail behavior at the boundary for the plate was studied experimentally and numerically by Nurick et al. (1996). Non-axisymmetric response of an impulsively loaded square plate was examined by Olson et al. (1993). Further tests to explore the failure modes of fully clamped square steel plate under uniformly distributed impulsive loadings were conducted by Nurick and Shave (1996). Experimental and numerical investigations on the transient responses of the square or rectangular plates to uniform blast loading were also carried out by several authors (Zhu, 1996; Rudrapatna et al., 1999; Ramajeyathilagam et al., 2000).

In the theoretical development of large deflection problem of thin plate, circular plate has been regarded as a prototype on which various modeling concepts could be conveniently "tested". To treat analytically the resulting discontinuous initial-boundary value problem of partially loaded membrane, several approximate methods were used. Duffey (1967) used a simplified energy method

for rigid-plastic material behavior and assumed several deformed shape profiles. Further step in developing approximate methods was taken by Symonds and Wierzbicki (1979), where the amplitude of the initial velocity field was obtained by minimizing the difference between the given initial velocity and that of the mode solution in a mean square sense. In a much more recent development, the momentum conservation approach and eigenvalue expansion method were used to derive an approximate solution for large transient deformations of plates subjected to central explosive loading, Wierzbicki and Nurick (1996). Wave form solution on the transient responses of circular membrane was proposed by Mihailescu-Suliciu and Wierzbicki (2003), where complete analysis of all possible waves was performed to solve the discontinuous initial-boundary value problem for the wave equation. They derived an analytical solution on the deflected shapes of membrane in terms of the magnitude of the applied impulse and a radius of centrally loaded area.

In Section 7.2, numerical simulations are performed with several radii of the centrally loaded area and the results are compared with experimental data (Teeling-Smith and Nurick, 1991; Wierzbicki and Nurick, 1996) and analytical predictions (Symonds and Wierzbicki, 1979; Mihailescu-Suliciu and Wierzbicki, 2002). Furthermore, an extensive parametric study on the transient responses of thin plates with various spatial and temporal distribution of dynamic pressure is conducted. The present thesis makes several new contributions to this largely researched area: (1) Various types of shape function are introduced into the mode solution (Symonds and Wierzbicki, 1979) and the accuracy of those assumed mode shapes in predicting the final deflection of plates is discussed. (2) Comparison of the present numerical results with the experimental results in literature is made. Furthermore, the analytical predictions (Symonds and Wierzbicki, 1979; Mihailescu-Suliciu and Wierzbicki, 2002) on the transient responses of thin plates under localized impulsive loading is verified by the present numerical simulations. (3) A comparison between the transient responses of circular and square plates is presented and difference of those plates is quantified. (4) The effect of various spatial and temporal distribution of dynamic pressure on the behavior of thin plates is investigated with particular focus on the deflection and local strain fields.

7.2.2 Formulation of the problem

Consider a clamped circular plate of a thickness h and radius R_0 under a uniform transeversal pressure $p(t)$ applied over a central region of the plate of radius R_1, $R_1 \leq R_0$. The plate is clamped at the outer radius so that $w(R_0) = 0$, where w is the transverse deflection of the plate. Because of the loading is axi-symmetric, it is assumed that the plate response is also axi-symmetric so that the transverse deflection is a function of the current plate radius of r and time t (see Fig. 7.1). It is further assumed that the material of plate is rigid-plastic, work hardening. It is possible to introduce the equivalent rigid-perfect plastic model of the material using the concept of the energy equivalent flow stress defined by

$$\sigma_0 = \frac{1}{\varepsilon_f} \int_0^{\varepsilon_f} \sigma(\varepsilon) d\varepsilon \tag{7.1}$$

where $\sigma(\varepsilon)$ is the input stress-strain curve and ε_f is the uniaxial fracture strain of the tensile specimen. For dynamic pressure loading, a notion of the total pulse per unit area I_0 is introduced according to

$$I_0 = \int_0^{t_0} p(t) dt \tag{7.2}$$

where t is current time and t_0 is duration of the pressure pulse. It was shown by many authors, for example Symonds and Wierzbicki (1979) that for short duration of pressure pulses such that occurs during explosive loading, the suddenly applied pressure is imparting to the plate an initial velocity v_0 which is related to the impulse I_0 by the momentum conservation equation.

$$I_0 = \rho h v_0 \tag{7.3}$$

In the case of rectangular pressure loading, the magnitude of impulse is equal to $I_0 = p_0 t_0$. Thus, the dynamic pressure loading problem is converted to the impulsive loading problem in the limiting case when $t_0 \to 0$.

$$\lim_{t_0 \to 0} t_0 p(t_0) = I_0 \tag{7.4}$$

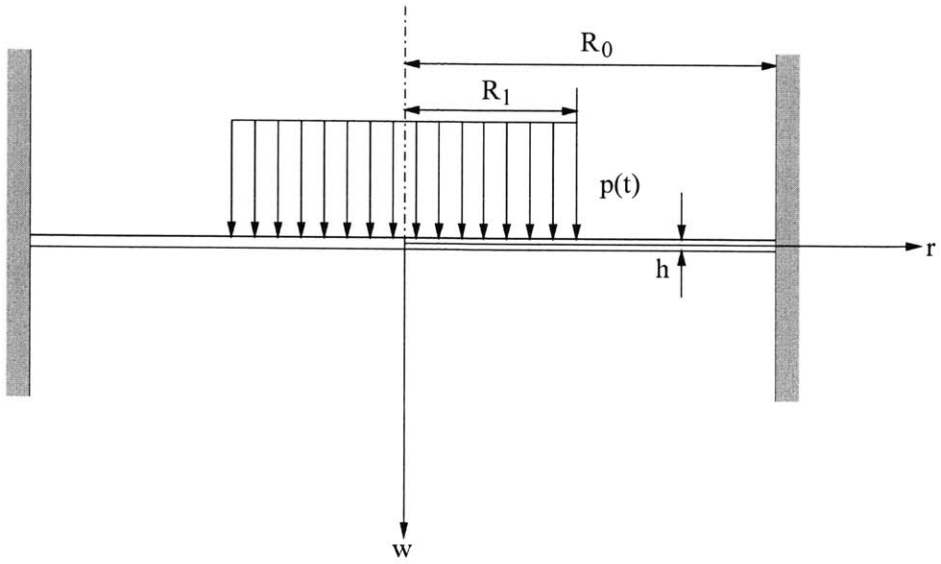

Fig. 7.1 Plate geometry and loading configuration

Several assumptions were made in order to reach a closed form solution. These assumptions are identical to those made in stretch forming of sheet metals, see Chapter 6.1.2. In particular, in the range of large deflection of interest here, the membrane forces (radial membrane force $N_r = \sigma_r h$ and circumferential membrane force $N_\theta = \sigma_\theta h$) induced by the change in geometry become significant. Therefore, plate bending was neglected in the present study. The components of the strain tensor, associated with the above stresses are the radial strain ε_r and the circumferential strain ε_θ. The following non-linear strain measures are used

$$\varepsilon_r = \frac{1}{2}\left(\frac{\partial w}{\partial r}\right)^2 + \left(\frac{\partial u}{\partial r}\right) \tag{7.5}$$

$$\varepsilon_\theta = \frac{u}{r} \tag{7.6}$$

Plate elements were further assumed to displaced only vertically (u = 0), and consequently $\varepsilon_\theta = 0$. The validity of this assumption will be discussed in conjunction with the wave-type solution and numerical solutions in the subsequent sections.

With the above assumption the equation of dynamic equilibrium take the form

$$\rho r \frac{\partial^2 w}{\partial t^2} = \frac{\partial}{\partial r}\left(\sigma_r r \frac{\partial w}{\partial r}\right) + rp(t) \tag{7.7}$$

This is the second order partial differential equation in space and time so that two boundary conditions are needed.

$$w(R_0, t) = 0, \quad t > 0 \tag{7.8}$$

$$\frac{\partial w(0, t)}{\partial r} = 0, \quad t > 0$$

Because of rotational symmetric, the slope of deflection curve should be zero at the center of plate. Also the deflection should be vanished at the clamped edge.

Two initial conditions are needed only for the case when the inertia term is retained in the dynamic equilibrium equation. The present study is concerned only with the explosive loading of plate idealized as an impulse loading. Thus, it is assumed that the plate is initially rest and that initial velocity is imparted to centrally loaded part of the plate. The initial conditions take therefore the following forms

$$w(r, 0) = 0, \quad r \in (0, R_0) \tag{7.9}$$

$$\frac{\partial w}{\partial t}(r, 0) = \left\{ \begin{array}{l} -\dfrac{I_0}{\rho h}, \quad r \in (0, R_1) \\ 0, \quad r \in (R_1, R_0) \end{array} \right\}$$

It is convenient to introduce the following dimensionless quantities

$$\xi = \frac{r}{R_0}, \quad \xi_0 = \frac{R_1}{R_0}, \quad \tau = \frac{ct}{R_0}, \quad c = \sqrt{\frac{\sigma_0}{\rho}}$$

$$W = \frac{w}{R_0}, \quad s = \frac{\sigma_r}{\sigma_0}, \quad V = \frac{I_0}{c\rho h} \tag{7.10}$$

$$\overline{\omega} = \frac{\partial W}{\partial \xi}, \quad v = \frac{\partial W}{\partial \tau}$$

In terms of the above quantities the initial-boundary value problem, Eqns. (7.7) ~ (7.9), can be reduced to two non-linear partial differential equations for v and $\overline{\omega}$.

$$\xi \frac{\partial v}{\partial \tau} = \frac{\partial}{\partial \xi}(\xi s \overline{\omega}), \quad \frac{\partial \overline{\omega}}{\partial \tau} = \frac{\partial v}{\partial \xi}$$

$$W(\xi, 0) = 0, \quad \xi \in (0, 1)$$

$$v(\xi, 0) = \left\{ \begin{array}{l} -V, \quad \xi \in (0, \xi_0) \\ 0, \quad \xi \in (\xi_0, 1) \end{array} \right\} \tag{7.11}$$

$$W(1, \tau) = 0, \quad \tau > 0$$

$$\overline{\omega}(0, \tau) = 0, \quad \tau > 0$$

7.2.3 Analytical solution of the impulsively loaded plate without fracture

7.2.3.1 Mode solution

Consider the case of an ideal impulse loading for which the pressure term is equal to zero and the effect of suddenly applied explosive pressure is introduced through the initial velocity according to Eg. (7.9). These results in a homogeneous partial differential equation

$$\rho r \frac{\partial^2 w}{\partial t^2} = \frac{\partial}{\partial r}\left(\sigma_r r \frac{\partial w}{\partial r}\right) \tag{7.12}$$

It was assumed that the radial stress σ_r is constant and equal to the uniaxial stress. With this additional assumption, $s = 1$ in Eq. (7.10), and the equation of the motion take the final form.

$$\xi \frac{\partial^2 W}{\partial \tau^2} = \frac{\partial}{\partial \xi}(\xi \overline{\omega}) \tag{7.13}$$

The general solution of the above equation can be written as sum of eigenfunctions $\phi_n(\lambda_n \xi)$ and time varying amplitudes $T_n(\lambda_n \tau)$

$$W(\xi, \tau) = \sum_{n=1}^{\infty} T_n(\lambda_n \tau)\phi_n(\lambda_n \xi) \tag{7.14}$$

where λ_n is an eigenvalue. Using the method of separation of variables, the eigenfunctions and amplitudes are expressed by a combination of Bessel and trigonometric functions, respectively

$$\phi_n(\lambda_n \xi) = J_0(\lambda_n \xi) + c_n Y_0(\lambda_n \xi) \tag{7.15}$$

$$T_n(\lambda_n \tau) = a_n \sin \lambda_n \tau + b_n \cos \lambda_n \tau \tag{7.16}$$

The first initial and the second boundary conditions $(7.11)_{2,5}$ implies that $c_n = b_n = 0$. The application of the first boundary condition $(7.11)_4$ gives the equation for eigenvalues $J_0(\lambda_n) = 0$. The eigenvalue of the fundamental mode is $\lambda_1 = 2.405$. The transient deflection profile of the membrane is

$$W(\xi, \tau) = \sum_{n=1}^{\infty} a_n \sin(\lambda_n \tau) J_0(\lambda_n \xi) \tag{7.17}$$

Following Martin and Symonds (1966), the approximate solution of the problem is obtained by taking the first term in (7.17), and described by

$$W(\xi, \tau) = a_1 \sin(\lambda_1 \tau) J_0(\lambda_1 \xi) \tag{7.18}$$

$$\dot{W}(\xi,\tau) = a_1\lambda_1 \cos(\lambda_1\tau)J_0(\lambda_1\xi) \tag{7.19}$$

where is a_1 an expansion coefficient and J_0 Bessel function of zero order. Initially, $t = 0$ the velocity filed is given by

$$\dot{W}(\xi,0) = a_1\lambda_1 J_0(\lambda_1\xi) \tag{7.20}$$

It can be seen that the above velocity field does not satisfy the second initial condition prescribed in the present impulsive loading (Eq. $(7.9)_2$ or $(7.11)_3$). However, according to Symonds and Wierzbicki (1979), the magnitude of the unknown integration constant a_1 can be determined using the concept of the minimization of the kinetic energy difference between the assumed and the prescribed initial velocity fields and the result is

$$a_1\lambda_1 = \frac{\int_0^1 v(\xi,0)J_0(\lambda_1\xi)\xi d\xi}{\int_0^1 J_0^2(\lambda_1\xi)\xi d\xi} \tag{7.21}$$

In addition to the present Bessel functions, several other deflection profiles have been introduced into Eq. (7.21) to get series of approximate solutions of the problem. The other shapes include the linear displacement and the exponential type of displacement shapes, defined in Fig. 7.2. A comparison of five different mode shapes is shown in Fig. 7.2. While it is understood that only one of those shapes indicated by thick full line satisfy exactly the dynamic equilibrium equation, other shapes corresponds better to the exact wave form and numerical solutions to be presented in subsequent section of this section. Therefore, the error minimization technique defined by Eq. (7.21) is also applied to those cases.

Of interest of this study is maximum permanent deflection of plate which occurs when the time variable amplitudes reach the maximum. This occurs at $\tilde{\tau} = \pi/(2\lambda_1)$. The corresponding maximum deflection of the plate is given by the following equation where the unknown amplitude is defined by Eq. (7.21).

$$W(\xi,\tilde{\tau}) = a_1 J_0(\lambda_1\xi) \tag{7.22}$$

In particular, the central deflection of the plate $W_{\max}(0) = a_1$. The normalized central deflection of the plate calculated using exact Bessel function shape and linear approximation are plotted in Fig. 7.3 as a function of the dimensionless loading radius, ξ_0. The full line in the same figure corresponds to the wave solution derived by Mihailescu-Suliciu and Wierzbicki (2002) and black

square are results of numerical analysis to be presented later on. It is seen that the curve corresponding to mode approximation gives rather good approximation to the more exact analytical and numerical solutions.

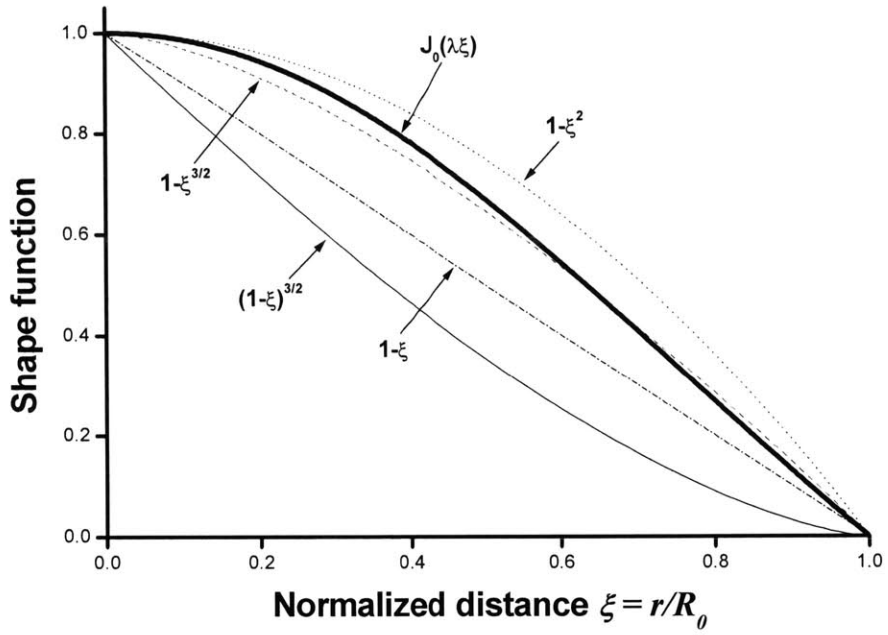

Fig. 7.2 Comparison of shape functions for the evaluation of unknown amplitude a_1

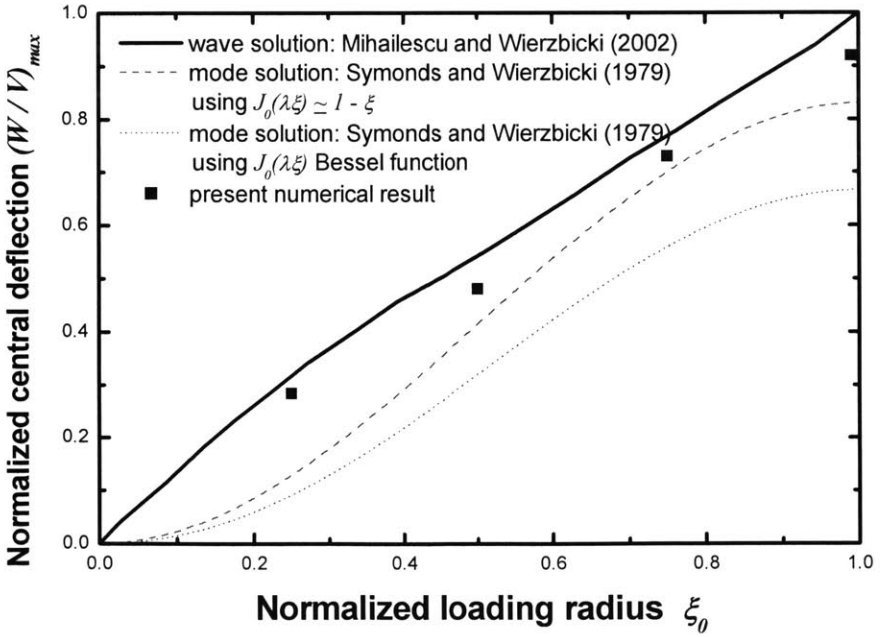

Fig. 7.3 A plot of the dimensionless maximum central deflection of the circular plate as a function of the radius of the uniformly distributed pressure loading

7.2.3.2 Wave solution

A closed form solution for the transverse deflections of thin plates loaded by central impulse loading was recently developed by Mihailescu-Suliciu and Wierzbicki (2002). In the theoretical development, the plate was modeled as a rigid-perfectly plastic circular membrane and then the resulting discontinuous initial boundary problem for the wave equation was solved by complete analysis of all possible shock waves, rarefaction waves, and acceleration waves. Here only the main results of the above solution are summarized. For a complete review, the reader should refer to the above reference.

As a specific example of the solution, the velocity profiles, which is valid until the converging wave initiated from ξ_0 reaches the center $\xi = 0$ of the membrane, are visually shown in Fig. 7.4 and given by

$$v(\xi,\tau)=\begin{Bmatrix} -V, & \xi\in(0,\xi_0-\tau) \\ \dfrac{V(\tau-2\xi_0)}{4\xi_0}, & \xi\in(\xi_0-\tau,\xi_0+\tau) \\ 0, & \tau\in(0,\min(1-\xi_0,\xi_0)) \end{Bmatrix} \tag{7.23}$$

For the complete solution, the final shape of the membrane after all its points have stopped were obtained in terms of the magnitude of the applied impulse and a radius of the centrally loaded area:

For $\xi_0\in(0,\dfrac{1}{2\sqrt{2}})$,

$$W(\xi,\tilde{\tau})=\begin{Bmatrix} 2(\sqrt{2}-1)V\xi_0^2-\dfrac{V}{8\xi_0}(3\xi_0^2+(\xi-3\xi_0^2)), \xi\in(0,2\xi_0) \\ V\xi_0^2\left\{2(\sqrt{2}-1)-\dfrac{1}{\xi}\right\}, \xi\in(2\xi_0,\dfrac{1}{\sqrt{2}}) \\ 2V\xi_0^2(\xi-1), \xi\in(\dfrac{1}{\sqrt{2}},1) \end{Bmatrix} \tag{7.24}$$

For $\xi_0\in(\dfrac{1}{2\sqrt{2}},\dfrac{1}{2})$,

$$W(\xi,\tilde{\tau})=\begin{Bmatrix} -\dfrac{V}{8\xi_0}(\xi-3\xi_0)^2+\dfrac{V}{2\xi_0}\left(\dfrac{\tilde{\tau}^2}{2}+2(2\xi_0-1\tilde{\tau}-4\xi_0^3+\dfrac{34}{4}\xi^2-8\xi_0+2\right), \xi\in(0,\dfrac{1}{\sqrt{2}}) \\ -\dfrac{V}{8\xi_0}\left(3\xi^2-16\xi_0^3\xi+16\xi_0^3-12\xi_0^2-12\xi_0\xi\ln\dfrac{\xi}{2\xi_0}\right), \xi\in(\dfrac{1}{\sqrt{2}},2\xi_0) \\ 2V\xi_0^2(\xi-1), \xi\in(2\xi_0,1) \end{Bmatrix} \tag{7.25}$$

For $\xi_0 = \frac{1}{2}$,

$$W(\xi,\tilde{\tau}) = \begin{Bmatrix} \frac{V}{4}\left(-\xi^2 + 3\xi - 2\tilde{\tau}^2 + 7\tilde{\tau} - 5 - 3(2\tilde{\tau}-3)\ln\frac{3-2\tilde{\tau}}{2}\right), \xi \in (0, \frac{3}{2} - \tilde{\tau}) \\ \frac{V}{4}\left(-3\xi^2 + 2\xi + 1 + 6\xi\ln\xi\right), \xi \in (\frac{3}{2} - \tilde{\tau}, 1) \end{Bmatrix} \tag{7.26}$$

For $\xi_0 = 1$,

$$W(\xi,1) = V(\xi - 1), \xi \in (0,1) \tag{7.27}$$

where the smallest time to permanent deflection $\tilde{\tau}$ is the solution of the following algebraic equation.

$$2\vartheta - 3\ln\vartheta = \frac{3}{2} + 4\xi_0^2, \quad \vartheta = \frac{2 - \tilde{\tau} - \xi_0}{2\xi_0} \in (0,1) \tag{7.28}$$

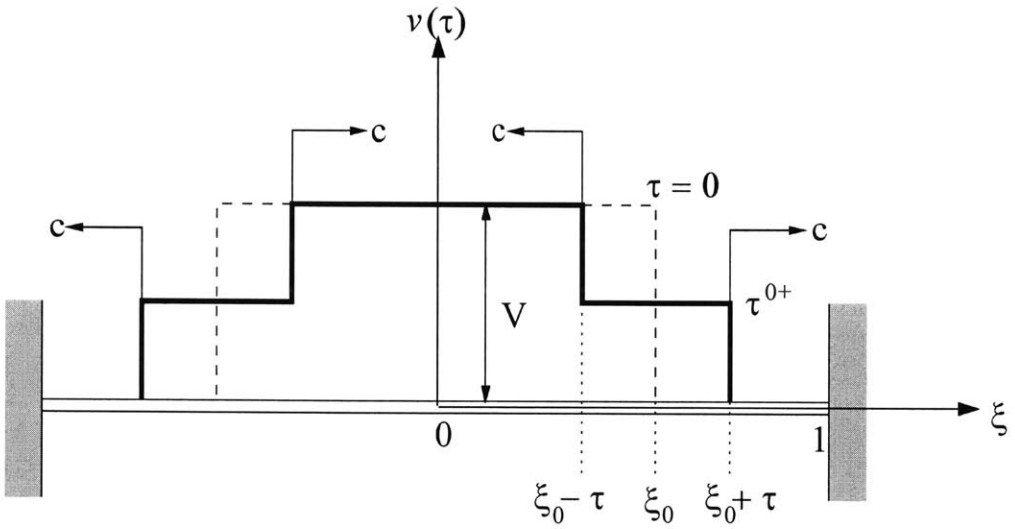

Fig. 7.4 Initial and transient velocity profiles of the wave solution (Mihailescu-Suliciu and Wierzbicki, 2002) up to the point of unloading

7.2.4 Finite Element(FE) solution of the impulsively loaded plate without fracture

Transient responses of clamped thin plates to dynamic loading with various spatial and temporal distributions of pressure were investigated using commercial explicit finite element code, *PAM-CRASH* (2003). The four-node Belytschko-Tsay shell element was employed. Because of the axial symmetry, a quarter model was considered. In the numerical simulation, the displacement and rotation of nodes corresponding to the clamped edges were fixed. The explosive loading was idealized by a rectangular pressure pulse in which the pressure was held constant during a time interval $t_0 > 0$ and then was suddenly removed, Fig. 7.5. In contrast to analytical solutions presented earlier, numerical simulation require a specific value to be assumed for the amplitude of pressure load p_0 and pressure duration t_0. An estimation on those values was made here on the basis of the closed form wave solutions, see Egns. (7.24) ~ (7.27). From that solution, the maximum slope of deflected shape is always constant in the range $\xi_0 \in (0, 1/2)$ and is equal to $\partial w/\partial r = 3V/4$. Using the calculated slope, the constant radial strain, defined by Eq. (7.5) (with u = 0) is

$$(\varepsilon_r)_{\max} = \frac{9}{32}\left(\frac{I_0}{c\rho h}\right)^2 \tag{7.29}$$

The membrane is assumed to fracture when the maximum radial strain reaches a uniaxial strain to fracture ε_f

$$(\varepsilon_r)_{\max} = \varepsilon_f \tag{7.30}$$

Using equations (7.29) and (7.30), the critical impulse to fracture and magnitude of pressure for the uniform rectangular pulse can be respectively written as

$$(I_0)_{cr} = h\sqrt{\frac{32}{9}\sigma_0\rho\varepsilon_f} \tag{7.31}$$

$$V_{cr} = \frac{(I_0)_{cr}}{c\rho h} = \sqrt{\frac{32}{9}\varepsilon_f} \tag{7.32}$$

$$(p_0)_{cr} = \frac{h}{t_0}\sqrt{\frac{32}{9}\sigma_0\rho\varepsilon_f} \tag{7.33}$$

For small magnitudes of the impulse, which is below the critical value defined by Eq. (7.31) or (7.32), the plate undergoes dishing. Section 7.2 of this chapter is concerned with the final deflection profiles and strain distribution of plates for the dishing phase. Therefore, fracture was not taken into account. The prediction of fracture for high intensity of loading will be presented in Section 7.3.

Except for the subsequent Section 7.2.4.1, the magnitude of dimensionless impulse $V = 0.93$, which is 0.75 times the critical impulse $V_{cr} = 1.24$ obtained from Eq. (7.32) for the $\varepsilon_f = 0.43$ of AH36 steel, was used in this Section 7.2.4. By varying the spatial and temporal distribution of pressure with the same amount of I_0, the transverse deflections of thin plates were calculated numerically. The results of the simulation were compared with those of experiment and analytical solution available in the literature.

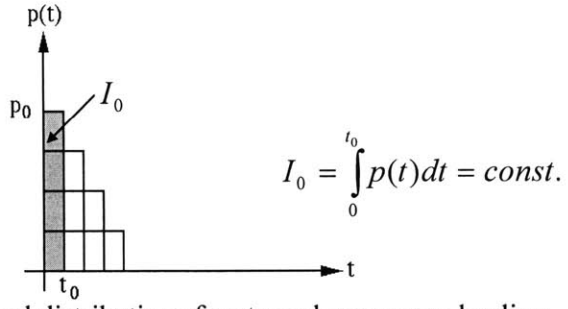

Fig. 7.5 Temporal distribution of rectangular pressure loading

A typical transient responses of plate, characterized by the history of various variables is schematically illustrates in Fig. 7.6. Note that uniform pressure loading was assumed in this case and failure was not included. The kinetic energy of the plate rises steeply to the maximum value at t_0 and then decreases monotonically. All the input energy is absorbed by the plastic deformation of the plate at time t_f. The instantaneous velocity of a mid-point reaches a maximum at t_0 and then stays constant until the certain time when the horizontal shock wave initiated from R_1 arrives to this plate center. Then, it suddenly drops and vanishes. The deflection exhibits an approximately linear increase to a maximum value followed by small elastic vibrations around the permanent value.

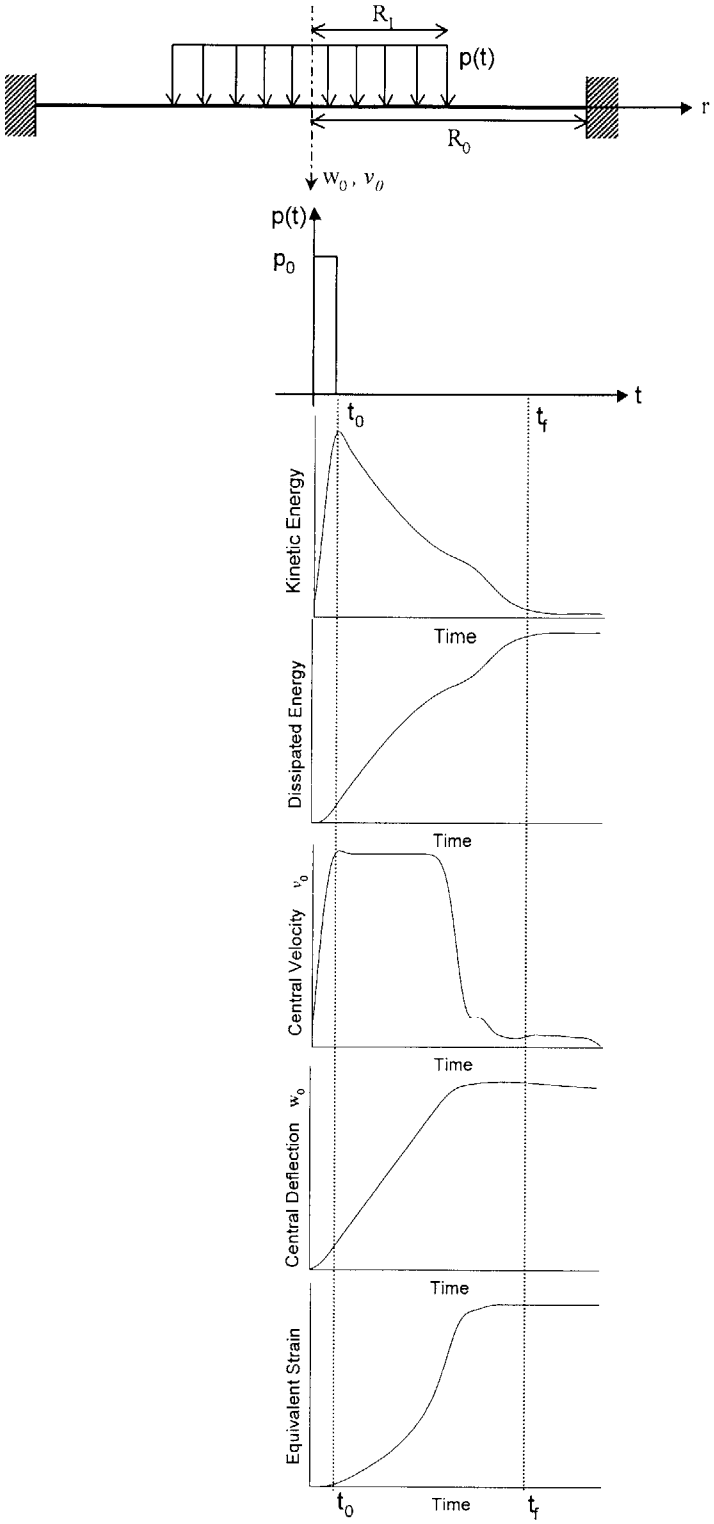

Fig. 7.6 Illustration for the typical transient responses of a clamped thin plate subjected to localized dynamic pressure loading

7.2.4.1 Experimental validation

In this Section 7.2.4.1, the accuracy of FE explicit code, *PAM-CRASH*, in predicting the final deflected shapes and magnitudes of central deflection of plates was confirmed by comparing with published test results. The response of thin circular plates to a localized impulsive load was investigated experimentally and theoretically by Wierzbicki and Nurick (1996). The same plate dimensions and material as the Ref. (Wierzbicki and Nurick, 1996) were used in the numerical simulation. In the above paper, three different loading radii were used (ξ_0 = 0.25, 0.4, and 1.0). Figure 7.7 compares the normalized experimental and numerical permanent deflection profiles for three different values of load radii. The agreement between the experiment and present numerical prediction is quite good.

Teeling-Smith and Nurick (1991) conducted experiments on circular plates uniformly loaded over the entire surface. The plate dimensions and material properties considered in their tests are summarized in Table 7.1. The corresponding stress-strain curve obtained from a series of quasi-static tensile tests for the tested sheets is also shown in Fig. 7.8. Furthermore, according to the Ref. (Teeling-Smith and Nurick, 1991), the Cowper-Symonds relation can be used to take into account the strain rate behavior of the cold-rolled mile steel used in their tests:

$$\sigma_d = \sigma_y \left[1 + \left| \frac{\dot{\varepsilon}}{\dot{\varepsilon}_0} \right|^{1/m} \right] \tag{7.34}$$

where σ_y is the static uniaxial yield stress, σ_d the dynamic yield stress, $\dot{\varepsilon}$ the uniaxial strain rate, while $\dot{\varepsilon}_0$ and m are material constant. $\dot{\varepsilon}_0 = 40s^{-1}$ and $m = 5$ were used. Hence, the same relation (Eq. (7.34)) was also employed in the present numerical simulations of the tests conducted by Teeling-Smith and Nurick (1991). Material Type 103 of *PAM-CRASH* (elastic-plastic *J2* plasticity theory) was used for the plates. This material model allows for the Cowper-Symonds strain rate correction. For the circular plate (a quarter model), approximately 5,000 thin shell elements were used. The mesh size is equal to the thickness of the circular plate. It should be mentioned that no information on fracture for the material used in the explosively loaded plate could be retrieved from that reference. Therefore, the comparison was performed only in the cases of large inelastic deformation without fracture, test no. 210903 and 041001~041008 of Ref. (Teeling-Smith and Nurick, 1991). The comparison of central deflection to thickness ratio obtained from experiment and numerical analysis is shown in Fig. 7.9 with as a function of applied impulse. One can see that present

numerical simulation quite accurately predicts the magnitude of central deflection as well as the deformed profile for a wide range of impulse.

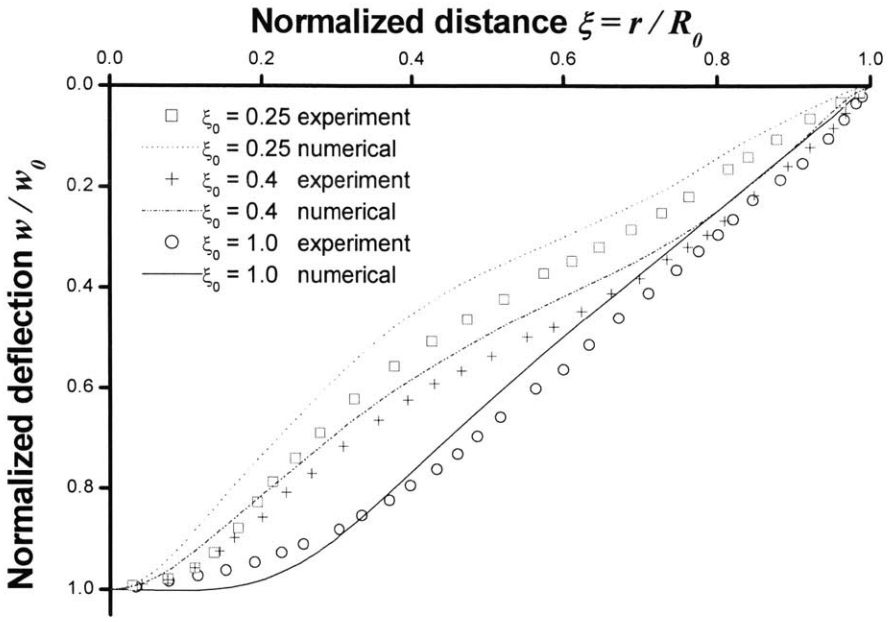

Fig. 7.7 Comparison of experimental and numerical dimensionless deflection profiles of circular plate with different loading radius $\xi_0 = R_1 / R_0$. Note that the experimental data was taken from Wierzbicki and Nurick (1996).

Table 7.1 Geometrical dimensions and material properties used in the experiment of circular plate with loading radius $\xi_0 = 1.0$ (Teeling-Smith and Nurick, 1991). Note that the dimensions and properties shown in this table are only considered for the case of experimental verification of numerical simulation presented in Section 7.2.4.1.

plate thickness h	clamped radius R_0	loaded radius R_1	static yield stress σ_y	average flow stress σ_0 (Eq. (7.1))
1.6mm	50mm	50mm	277MPa	328MPa

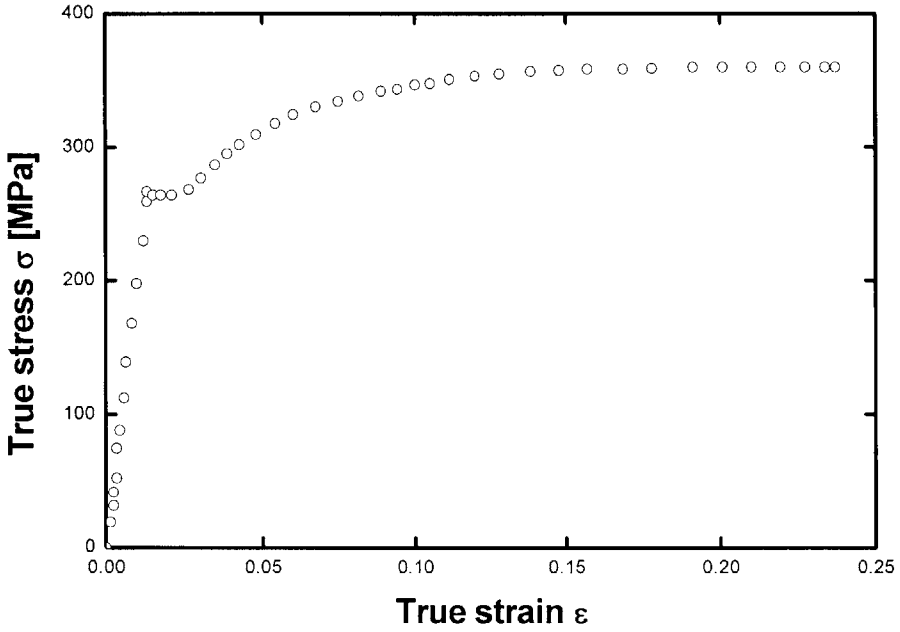

Fig. 7.8 Uni-axial tensile stress-strain curve for the cold-rolled mild steel used in the impulsively loaded plate (Teeling-Smith and Nurick, 1991). Note that the material shown in this figure is only considered for the case of experimental verification presented in Section 7.2.4.1.

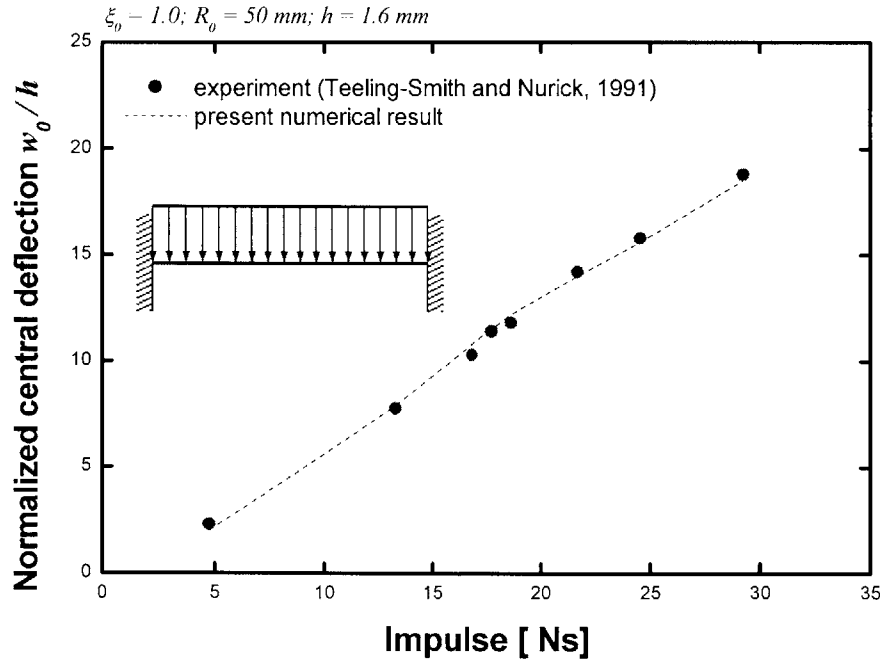

Fig. 7.9 Comparison of experimental and numerical deflection-thickness ratio vs applied impulse of circular plate with loading radius $\xi_0 = 1.0$

7.2.4.2 Comparison of analytical solutions and numerical simulation

The accuracy of the analytical solutions, presented in Section 7.2.3, was further verified by numerical simulation for the specific case of loading radius $\xi_0 = 0.5$. The material used in the comparison was high strength ship steel AH36. The mechanical properties of AH36 steel are the Young's Modulus $E = 210GPa$, the initial yield stress $\sigma_y = 380MPa$, and the tensile stress $\sigma_u = 836MPa$ at the corresponding fracture strain $\varepsilon_f = 0.43$. Moreover, the average plastic flow stress defined by Eq. (7.1) was $\sigma_0 = 690MPa$, as illustrated in Fig. 7.22(c). For detail information on plasticity and fracture for the AH36 steel, the reader should refer to the Section 7.3.2. As an example, we considered here a local segment of ship hull structure, i.e. a circular plate of the radius $R_0 = 5416mm$ and thickness $h = 16mm$. All the results reported in the following are based on the above material and geometry of plate, unless otherwise stated.

According to the wave solution for the case of loading radius $\xi_0 = 0.5$ (Mihailescu-Suliciu and Wierzbicki, 2002), the discontinuity in the second initial condition, Eg. $(7.9)_2$, gives rise at $(\xi_0, 0)$ to two shock waves with constant propagation speeds $d\xi/d\tau = +1$ and $d\xi/d\tau = -1$ respectively, as shown in Fig. 7.10(a). Therefore, ahead of the diverging wave the plate is undisturbed and ahead of the converging wave the dimensionless transverse velocity of plate is constant with the value of V. All plastic deformation are concentrated around the propagating shock wave. In the case of $\xi_0 = 0.5$, the converging and diverging waves reach the center $\xi = 0$ and boundary $\xi = 1$ of the plate simultaneously. Then, the converging wave can not reflect at (0, 0.5), while the diverging wave reflects form fixed boundary at (1, 0.5). The corresponding initial and transient velocity profiles from the wave solution are also illustrated in Fig. 7.10(b).

Figure 7.11 shows the transient profiles for dimensionless velocity and deflection obtained from numerical simulation. It can be seen that the transient velocity profiles from simulation exhibit approximately rectangular shape with two shock waves initiated from $\xi = 0.5$. These two waves respectively reach the center and boundary of plate at time $\tau = 0.55$ which is similar to the theoretically derived wave solution at $\tau = 0.5$. The velocity and deflection profiles corresponding to time $\tau = 0.55$ are marked with thick full line in Fig. 7.11. After $\tau = 0.55$, the reflected wave is also seen to occur at clamped boundary of plate in this figure. Furthermore, the corresponding deflections after this stage display rigid motion with small change in amplitude. The above observations give qualitatively good agreement with the wave solution.

The analytical and numerical deflections at the permanent stage are compared in Fig. 7.12. The deflection was normalized by the middle point deflection. Because the analytical solution was derived for a rigid-perfectly plastic material, an additional run was made to obtain the deflection profile for rigid-plastic material. The corresponding magnitudes of central deflection are summarized in Table 7.2.

Two important conclusions could be drawn from the above comparisons. First, the difference between the final plate shape made of rigid-perfectly plastic and strain hardening material are very small. Secondly, both numerical solutions agree well with the wave solution presented in previous section. The only discrepancy in the deflection profile is near the plate center. This is due to the approximate assumption in the wave solution in which the radial motion and circumferential stress are neglected. Further comparisons will be discussed in later Section 7.2.5.1 where additional parametric study is reported.

Table 7.2 Comparison of normalized magnitude of central deflection(w_0 / R_0) between numerical and analytical predictions (circular plate; $\xi_0 = 0.5$; $R_0 = 5416mm$)

Type of solution (Material)	Wave solution (rigid-plastic $\sigma_0 = 690MPa$)	Mode solution (rigid-plastic $\sigma_0 = 690MPa$)	FE solution (rigid-plastic $\sigma_0 = 690MPa$)	FE solution (strain hardening $\sigma = f(\varepsilon)^{(1)}$)
w_0 / R_0	0.330	0.256	0.293	0.296

Note: (1) The actual stress-strain curve shown in Fig. 7.22(c) was used as a stress-strain relation.

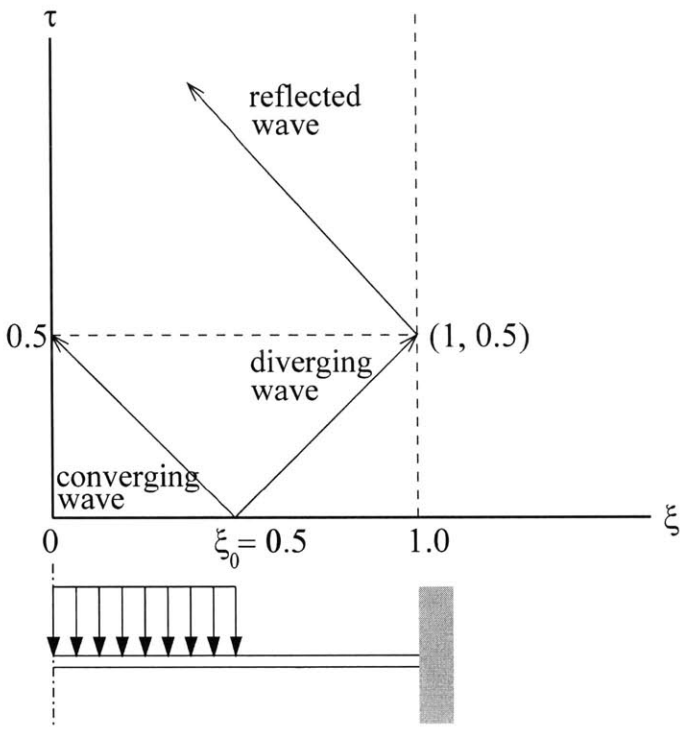

(a)

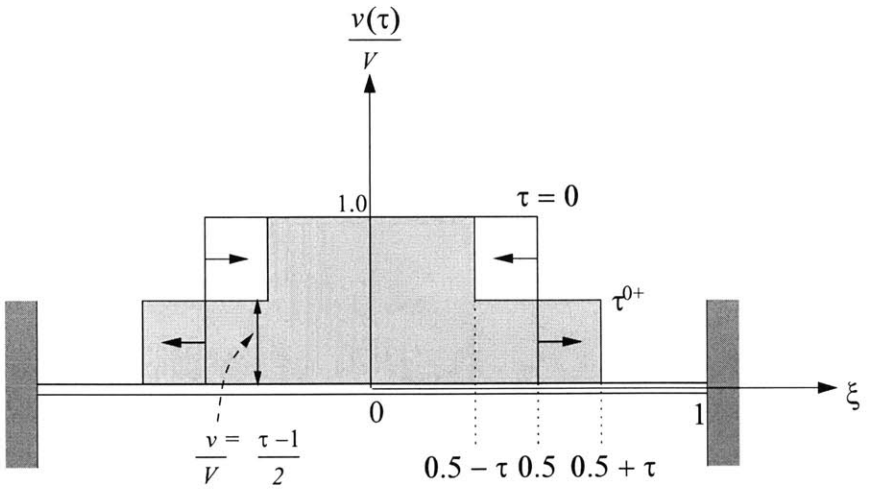

(b)

Fig. 7.10 A phase plane diagram and transient velocity profiles (special case of the wave solution $\xi_0 = 0.5$; Mihailescu-Suliciu and Wierzbicki, 2002); (a) phase plane diagram showing converging and diverging wave initiated from $\xi_0 = 0.5$ and the reflected wave; (b) velocity profiles

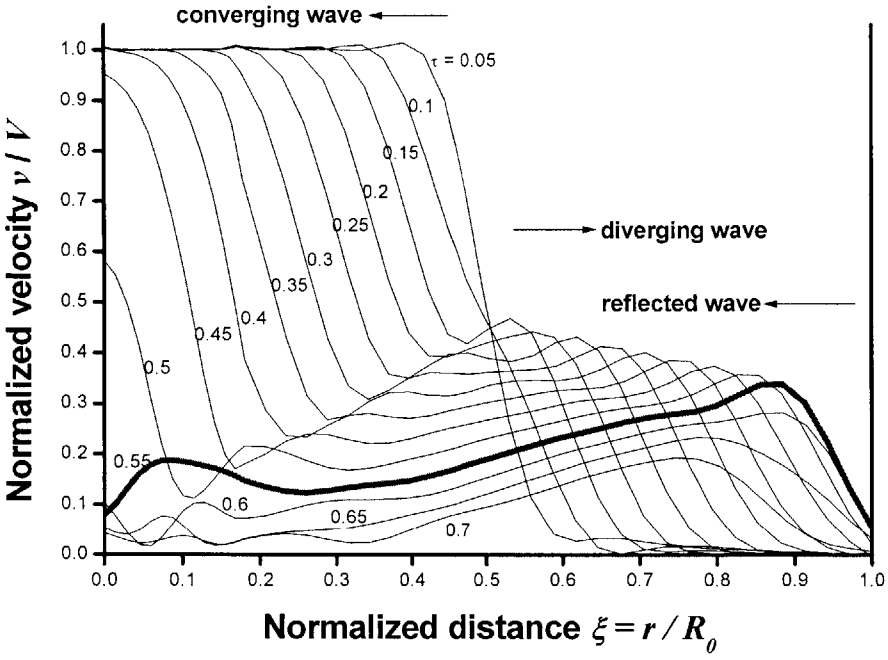

(a)

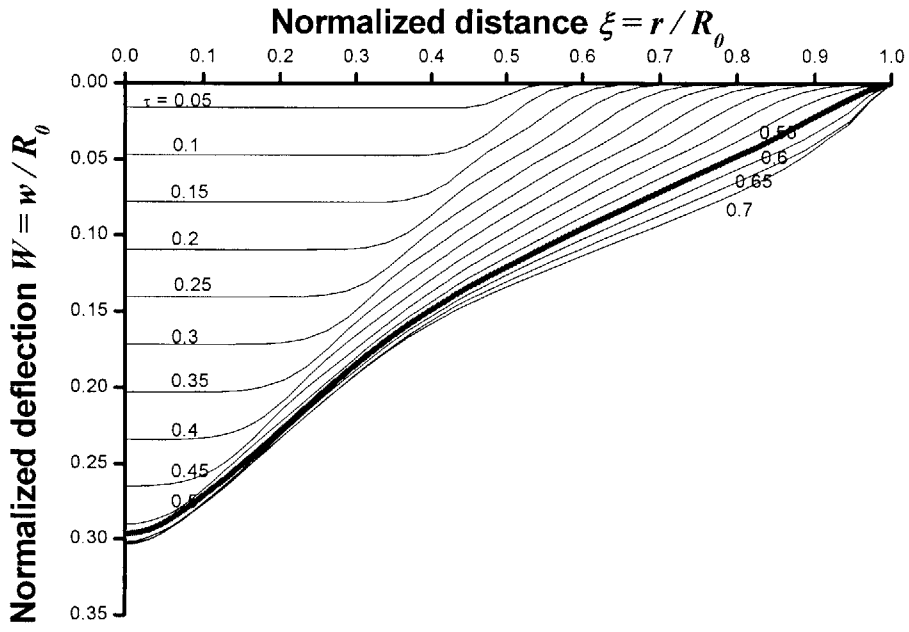

(b)

Fig. 7.11 Numerically obtained transient profiles for normalized velocity and deflection at $\tau = 0.05$ steps (circular plate and $\xi_0 = 0.5$); (a) normalized velocity profiles; (b) normalized deflection profiles

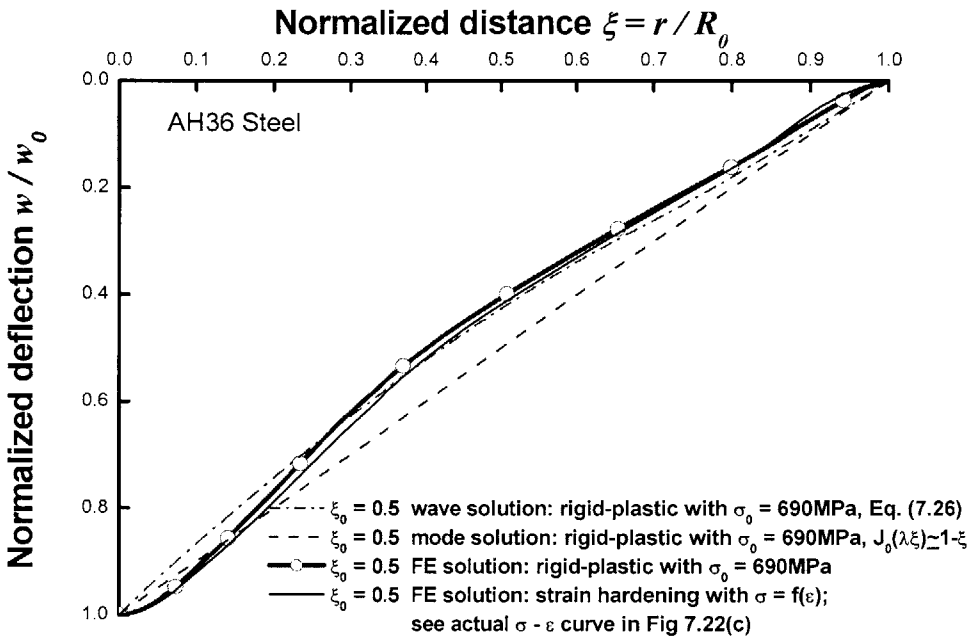

Fig. 7.12 Comparison of normalized final deflection profiles between numerical and analytical predictions (circular plate; $\xi_0 = 0.5$) . Note that the corresponding magnitudes of central deflection (w_0) are separately summarized in Table 7.2.

7.2.4.3 Comparison between solutions for a square and a circular plate

Transient response for plates of different geometry but equal area, thickness, and loading (see Table 7.3) were investigated numerically. The final deflection profiles of square and circular plates are compared in Fig. 7.13 as a function of applied impulse and three different radii of the centrally loaded area. One can see that two plates display quite similar deflection for smaller loading radius $\xi_0 = 0.25$. On the other hand, more distributed loading leads to a difference in the magnitude and shape of deflection. For loading radius $\xi_0 = 0.5$, circular plate shows more localized bulging near the plate center. In the case of $\xi_0 = 1.0$, square plate exhibits constant slope of deflection between the distance $\xi = 0.15$ to 1.0, while circular plate shows change in the slope and more bulging between $\xi = 0.4$ to 0.8. For the case of $\xi_0 = 0.5$, time history plots of central deflection ratio and equivalent strain of two plates are compared in Fig. 7.14. Note that the deflection of middle point is normalized

by the value of circular plate in this figure. The horizontal axis is also expressed as dimensionless time where the current time is normalized with respect to duration of pressure t_0. The time to reach peak deflection and strain is similar between two plates under the equal amount of pressure loading. In contrast, the square plate exhibits a smaller magnitude of peak deflection and strain than the circular plate. The ratios of square to circular peak deflection and equivalent strain are respectively *0.93* and *0.76* at the specific time $t/t_0 = 14$. It should be mentioned that Nurick and Shave (1996) correlate solution for circular and square plate using the area equivalence. While this approach has a lot of merit, it does not capture all the difference between those types of plates.

Unlike the circular plate in which the first failure represents the complete failure due to symmetry of geometry and loading conditions, square and rectangular plates show different failure behavior. Experimental studies (see for example Olson et al., 1993; Nurick and Shave, 1996) show that the tensile tearing of square plate begins at the center of each side and moves towards the corners. As impulse increase, the tearing would occur simultaneously along the central region of each side. Hence, progression of failure is indeed necessary in the analysis of square plate. This will be discussed in next Section 7.2.5.

Table 7.3 Plate dimensions and loading conditions used in the dishing stage

	plate area 10^6 mm^2	clamped plate length R_0/A_0 [1]	plate thickness h	pressure p_0	duration t_0	impulse I_0	V	V/V_{cr}
Circular	92.15	5416mm(R_0)	16mm	34.47MPa	1msec	34.47KPasec	0.93	0.75
Square	92.15	4800mm(A_0)	16mm	34.47MPa	1msec	34.47Kpasec	0.93	0.75

Note: (1) Using the equivalent area between square and circular plates, the half width of square plate $A_0 = 0.88R_0$.

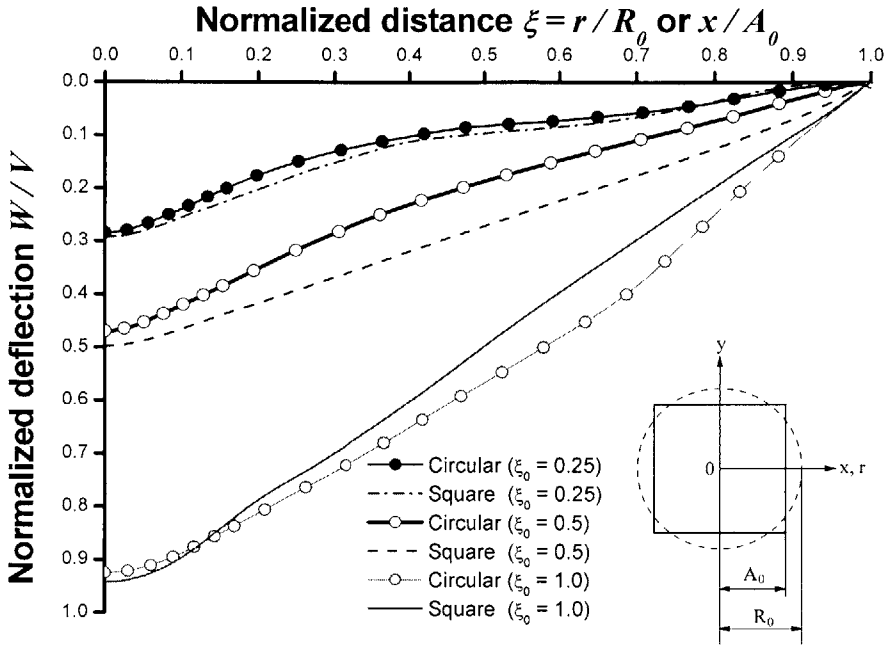

Fig. 7.13 Normalized deflection profiles between square and circular plates with three different values of the ξ_0 (numerical results)

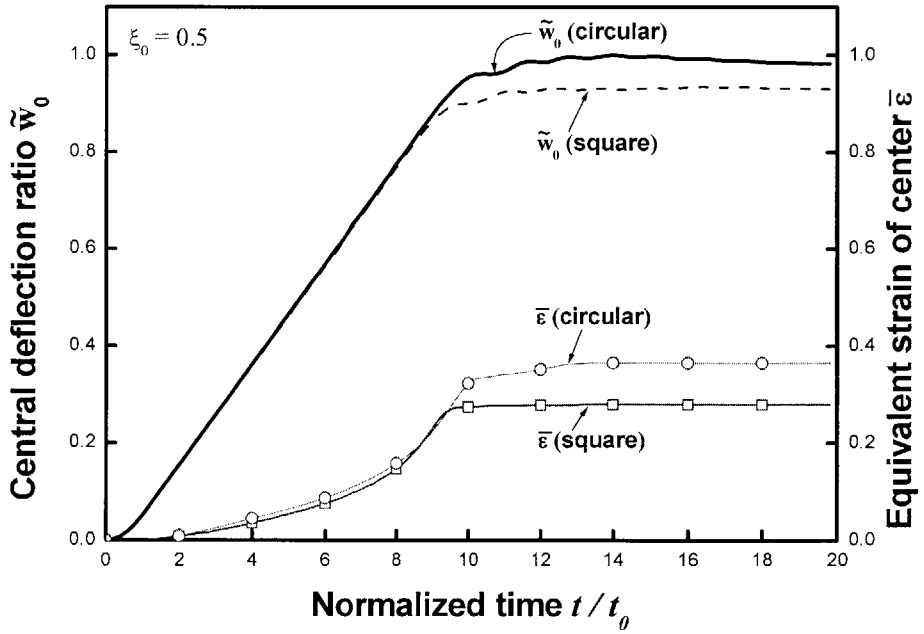

Fig. 7.14 Comparison of central deflection and equivalent strain between circular and square plate ($\xi_0 = 0.5$; numerical results; $\tilde{w}_0 = w_0(square) / w_0(circular)$)

7.2.5 Parametric study of pressure distribution

So far, the transient responses of plate to uniformly distributed pressure loading during the specific time duration have been discussed in this study. The effect of various spatial and temporal distribution of dynamic pressure on the behavior of thin plates will be further investigated and presented in this section. The corresponding pressure and impulse can be rewritten as Eq. (7.35) and also summarized in Table 7.4.

$$p(\mathbf{x},t) = \Phi(\mathbf{x})\mathrm{T}(t), \quad I_0 = \int_0^{t_0} p(\mathbf{x},t)dt, \quad I = \iint_{\partial s} I_0 ds \tag{7.35}$$

where $\Phi(\mathbf{x})$ and $\mathrm{T}(t)$ are the shape and time function of pressure, respectively. I is total impulse imparted to the plate.

Table 7.4 The considered spatial and temporal distribution of dynamic pressure loading

pressure distribution		$\xi_0 = R_1 / R_0$	$\Phi(\mathbf{x})$	$\mathrm{T}(t)$	I
spatial	uniform	0.25, 0.5, 0.75, 1.0	p_0	1, $t \in (0,t_0)$	$I_0 R_1^2$
temporal	rectangle	0.5	$p_0, \frac{1}{2}p_0, \frac{1}{3}p_0, \frac{1}{4}p_0$	1, 2, 3, 4, $t \in (0,t_0)$	$I_0 R_1^2$
	triangle	0.5	p_0	$2(1-\frac{t}{t_0})$, $t \in (0,t_0)$	$I_0 R_1^2$

7.2.5.1 Spatial distribution of pressure

Figure 7.15 shows the effect of three different values of the parameter ξ_0 on the deflected shape of circular plates. For comparison purposes, the results from wave solution (Mihailescu-Suliciu and Wierzbicki, 2002) is included in this figure. It is evident that the deflected shape and magnitude are strongly dependent on the given radius of pressure loading. For small ξ_0, there are more localized deformations around the plate center. The analytically and numerically obtained maximum central amplitudes $(W/V)_{\max}$ are plotted earlier in Fig. 7.3 for the value of the parameter ξ_0. One can see that the above relationship is approximately linear for both cases of the wave solution and simulation. As shown in Fig. 7.15, the wave solution exhibits more sharp deformation than that of

simulation but quite accurately follows its response. In addition, the maximum central amplitude obtained from the wave solution is higher than those of simulation. The above difference can be explained by the fact that the presence of in-plane displacement u, neglected in the wave solution, are retarding the deformation in the central region. Furthermore, as compared to the wave solution, the numerical simulation produced more smooth velocity distribution along the plate. The numerically obtained profiles of in-plane strain components are shown in Fig. 7.16 with two different values of dimensionless impulse V. Note that the critical dimensionless impulse $V_{cr} = 1.24$ was obtained from Eq. (7.32) for the $\varepsilon_f = 0.43$ of AH36 steel, which is needed to initiate the initial circumferential crack (discing). From rotational symmetry, the radial and circumferential strain should be and are equal to each other at the center of plate. It can be seen that the assumption taken in the analytical solution ($u = 0, \varepsilon_\theta = 0$) is clearly not valid near the plate center. However, the neglect of hoop strain does not seem to have much effect on the formation of the circumferential crack (discing). Therefore, considering complex behavior of dynamic problem and assumption used in the theoretical development, it can be concluded that the wave solution gives a good agreement with the numerically obtained results.

As the first step to assess the progression of "damage" as measure by the equivalent plastic strain, Fig. 7.17 shows the equivalent strain history of possible fracture region of the square plate with four different values of ξ_0. Note that a quarter model of square plate and the locations of measurement for equivalent strain are included in Fig. 7.17. For the case of $\xi_0 = 0.25$, the center of the plate (point C) firstly reaches the peak strain approximately at time $t/t_0 = 5.5$ and center of the plate boundary (point A, B) shows almost zero strain during the whole process. For the $\xi_0 = 0.5$, the peak strain firstly occurs at point C ($t/t_0 = 10$) and then occurs at point A, B ($t/t_0 = 12.5$). In contrast, the sequence is reversed in the more distributed loading case $\xi_0 = 0.75$ and 1.0. For the case of $\xi_0 = 1.0$, the center of the plate boundary rapidly reaches the peak strain ($t/t_0 = 2$). The above results indicate that the first failure would occur at the central region of the plate for smaller ξ_0 and larger ξ_0 produce tearing failure at the clamped boundary. This can be clearly confirmed by Fig. 7.18 showing the equivalent strain contour with different values of the parameter ξ_0.

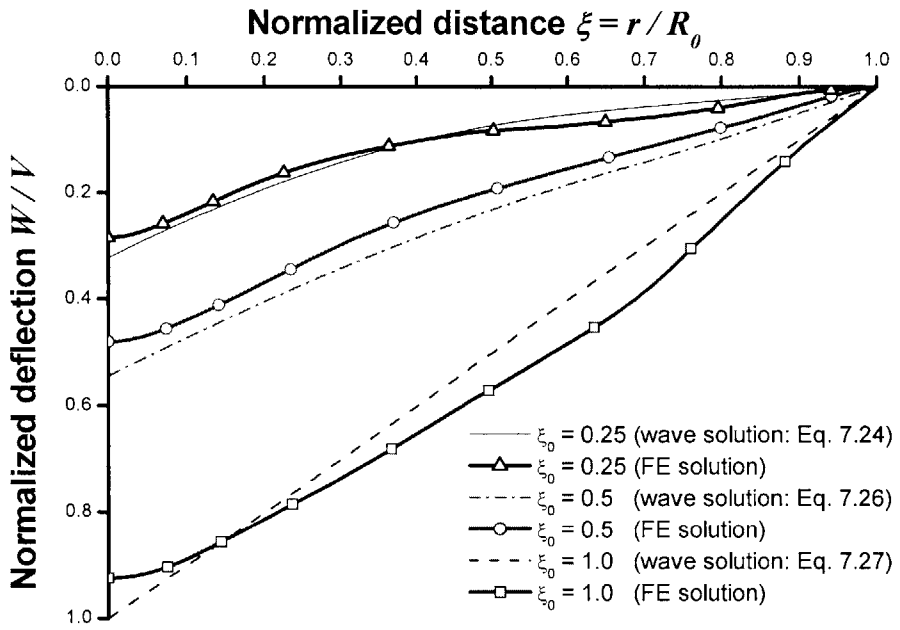

Fig. 7.15 Dimensionless deflection profiles of the circular plate for different values of the radius of the uniformly distributed pressure loading

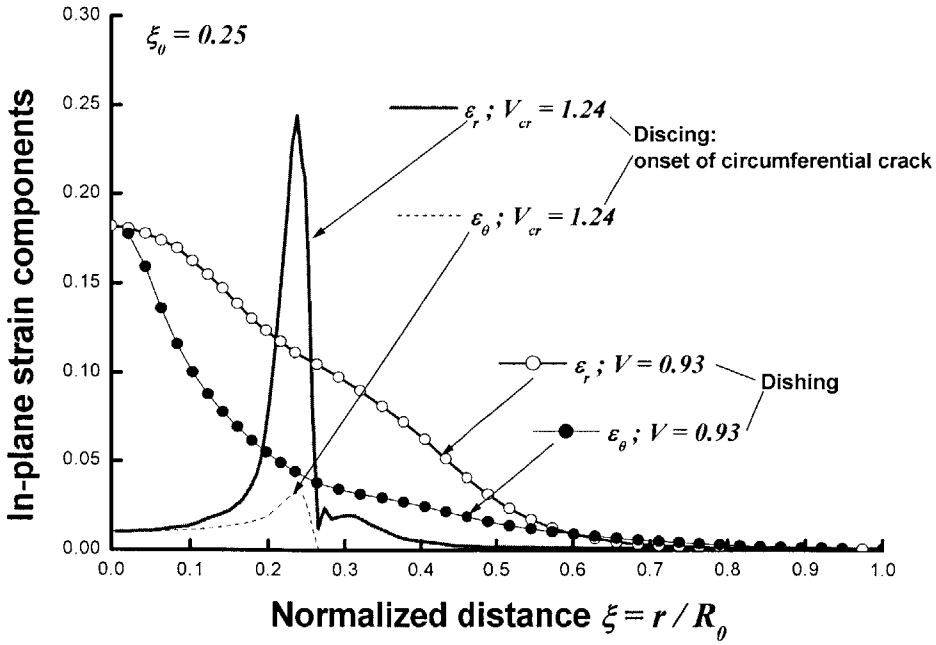

Fig. 7.16 Numerically obtained profiles of in-plane strain components from the center of circular plate to the clamped end at time t = 10msec with two different intensities of applied impulse (ξ_0 = 0.25)

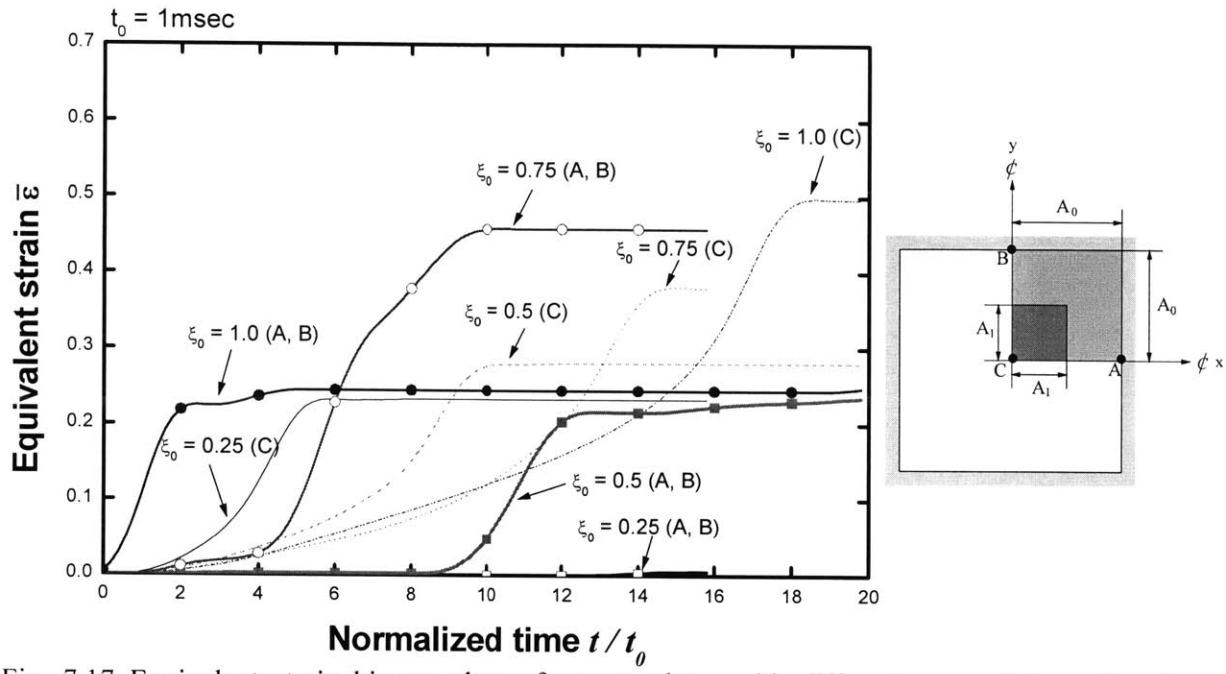

Fig. 7.17 Equivalent strain history plots of square plates with different area of the uniformly distributed pressure loading (numerical results; A_0 = 4800mm; h = 16mm)

7.2.5.2 Temporal distribution of pressure

In order to study the effect of pulse shape, an additional calculation was performed with the pressure time history that was approximated by triangle pressure pulse. With equally loaded area (ξ_0 = *0.5*) and uniform distribution of loading, the deflection profiles of square plate between rectangular and triangular pressure pulse were almost same, as shown in Fig. 7.19. Figure 7.20 shows the time history of central deflection and equivalent strain (see point C in the inserted figure in Fig. 7.17) for the square plates with different time duration of pressure. The total impulse imparted to the plate was same for each case. The numerical values of the deflection and equivalent strain chosen at the specific time (t = 12msec) are summarized in Table 7.5. In addition, the corresponding deflection profiles are also illustrated in Fig. 7.21. From all these results, it is clearly confirmed that the effect of time duration under equal impulse on the deflection shape, amplitude, and strain of the thin plates can be neglected.

The weak effect of the temporal distribution of pressure in short duration pulses is of great significance in practical situations. In many cases of contact explosions or small stand off distance explosions, the precise history is not known. By measuring the total impulse imparted by the blast, the amount of dishing can be found with

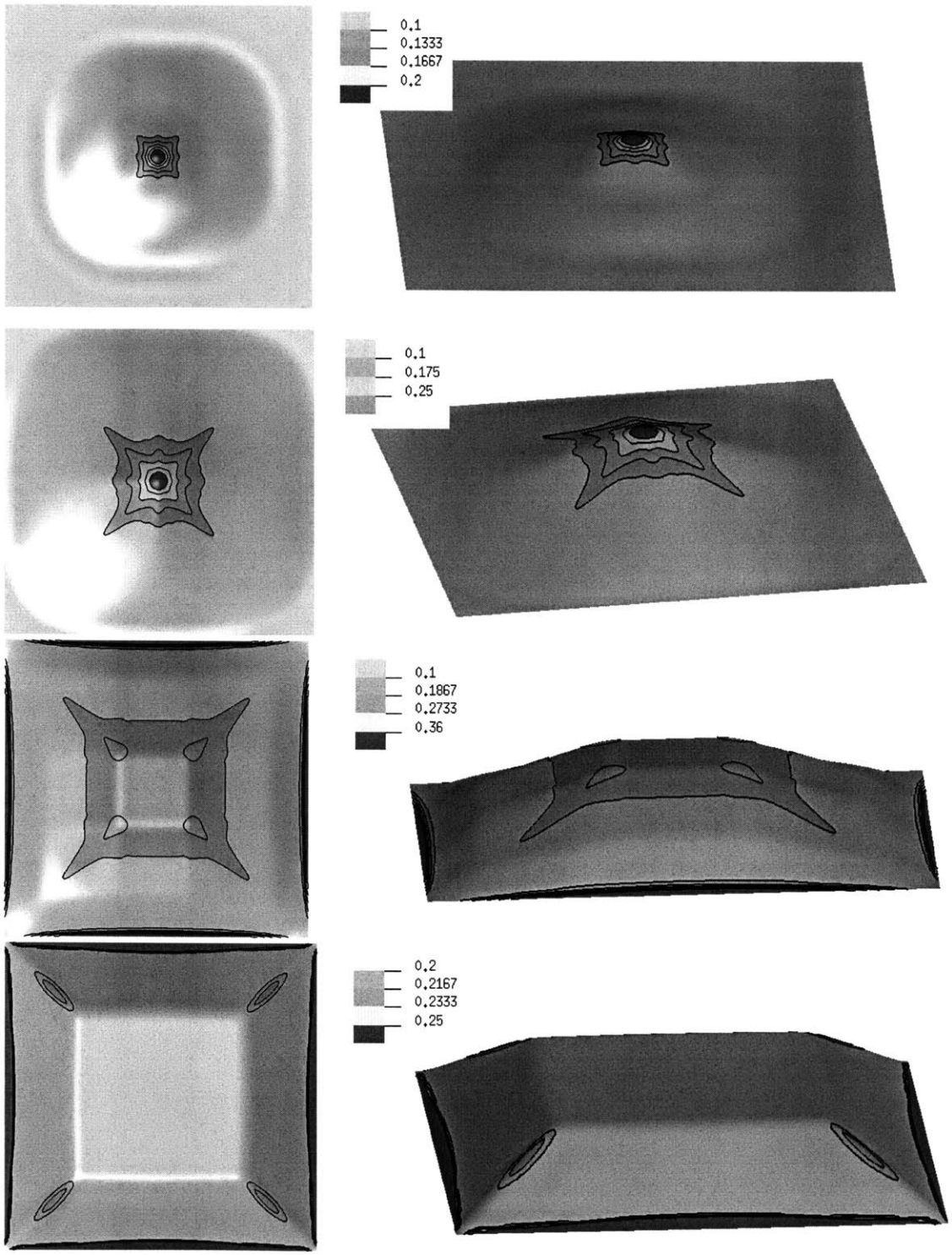

(a) (b)

Fig. 7.18 Equivalent strain contours of square plates with different radius of the uniformly distributed pressure loading, ξ_0 = 0.25, 0.5, 0.75, 1.0 (numerical results of at time t = 10msec); (a) plane views (left); (b) 3-D views (right)

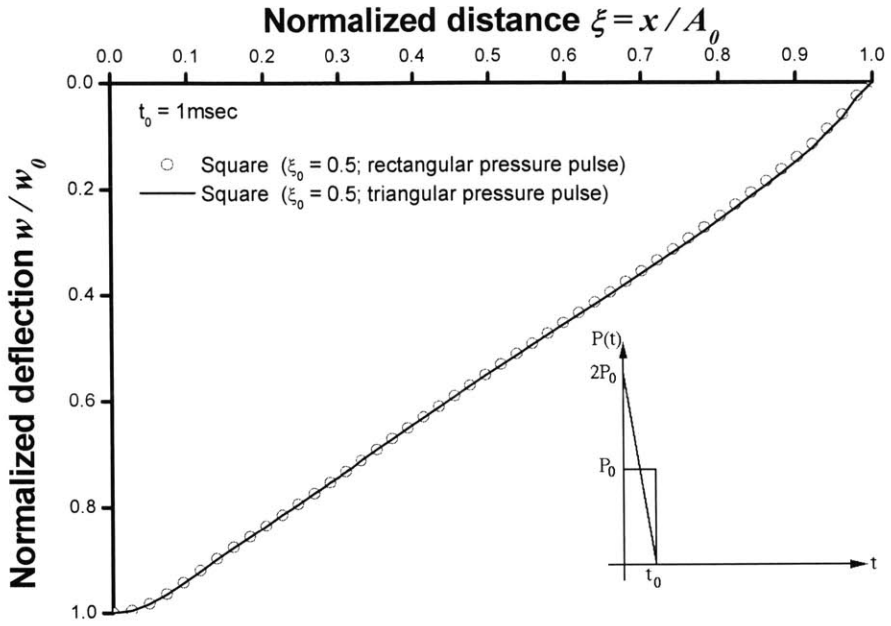

Fig. 7.19 Comparison of deflection profiles for the square plate between rectangular and triangular pressure pulse ($\xi_0 = 0.5$; numerical result)

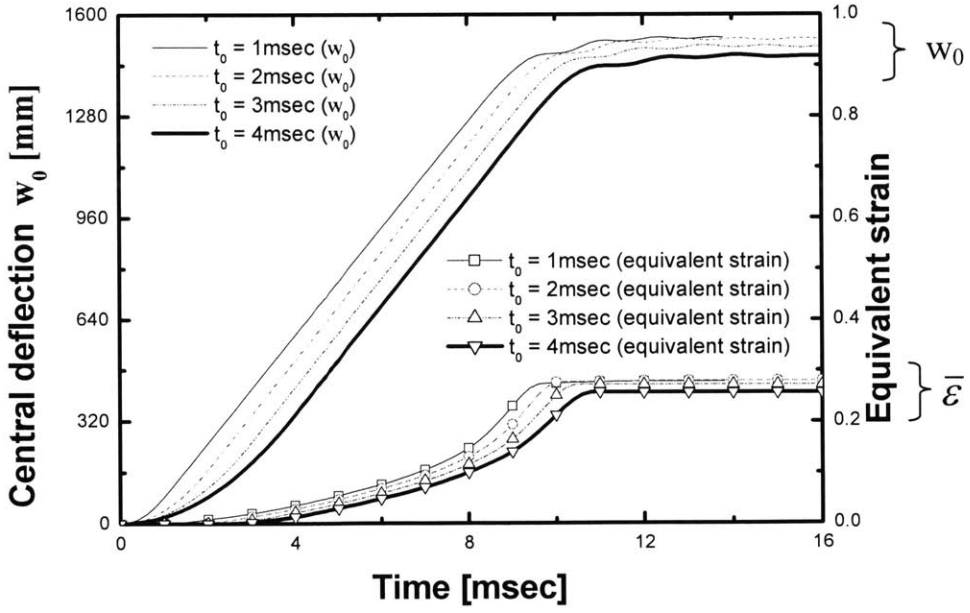

Fig. 7.20 The central deflection and equivalent strain (point C in the inserted figure of Fig. 7.17) of the square plate with different time duration but equal impulse ($\xi_0 = 0.5$; numerical result)

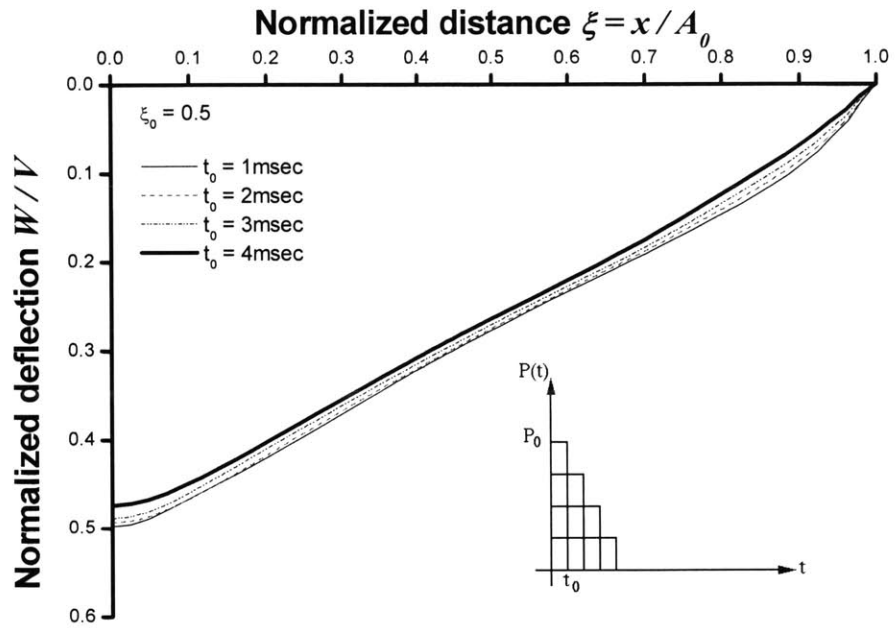

Fig. 7.21 Dimensionless deflection profiles of the square plate with different time duration of pressure loading at t = 12msec ($\xi_0 = 0.5$; numerical result)

Table 7.5 Numerical values of the central deflection ratio and equivalent strain (point C in the inserted figure of Fig. 7.17) for the square plates with different time duration of pressure at t = 12msec (A_0 = 4800mm)

time duration t_0 (msec)	central deflection ratio w_0 / A_0	equivalent strain $\bar{\varepsilon}$	t / t_0
1	0.32	0.28	12
2	0.31	0.28	6
3	0.31	0.27	4
4	0.30	0.26	3

7.2.6 Comparison and conclusion

- Transient response of clamped thin plates under localized dynamic loading with various spatial and temporal distribution of pressure was investigated numerically. As compared to the experimental results published in the literature (Teeling-Smith and Nurick, 1991; Wierzbicki and Nurick, 1996), a good correlation was obtained in terms of profile and magnitude of deflection. The numerical results were further compared to the wave solution developed by Mihailescu-Suliciu and Wierzbicki (2002). It was found that the analytical solution satisfying exactly the wave equation gives good prediction of the final shape and the deflection amplitude of the plate for different radius of the centrally loaded area.
- The responses between square and circular plates were compared for three different loading radii. It was found that difference in the deformation shape is more pronounced in larger loading radii due to the different geometry. Furthermore, it was found that the failure pattern is very different in square and circular plates.
- It was clearly confirmed that the permanent shape of plate is strongly dependent on the spatial distribution of pressure loading, as measured by loaded area. More localized deformation around the plate center was observed for smaller loaded area. A more distributed load led to tearing failure at the clamped boundary. It was also shown that the effect of temporal distribution of pressure on the deflection profiles is weak.

7.3 Discing and petalling

7.3.1 Introduction

Failure by discing and petalling of thin plates can occur under both impact and localized impulsive loading. There has been considerable research on the perforation of thin metallic plates by cylindrical and conical projectiles over the last few decades (Taylor, 1948; Zaid and Paul, 1957, 1958; Thomson, 1951; Johnson et al., 1973). The petalling problem was idealized by simple hole enlargement models in the above studies. The first analytical model taking into account the petalling of the plate and a radial crack propagation process was proposed by Landkof and Goldsmith (1985), where the solution was based on an energy balance and plastic hinge theory. They also performed a thorough experimental study. In a much more recent development, a detailed analysis of petal formation in thin plates by conical and spherical projectiles was presented by Atkins et al. (1998), where the solution was correlated with tests. A closed form solution for the petalling failure mode of circular plates subjected to localized high intensity of impulsive loading was developed by Wierzbicki (1999), where the total energy absorbed by the system and the number of petals as well as the final deformed shape of the plate was determined as a function of plate flow stress, thickness, and parameters of the external loading. The solution proposed by Wierzbicki (1999) was constructed using the concept of the Crack Tip Opening Displacement (CTOD) and it captured the process of curling away the petals from the flat plate with the associated expenditure of bending energy.

The immediate objective of this Section 7.3 is to determine the onset of fracture and subsequent propagation of radial cracks in a class of clamped thin plates with various radii and intensity of applied impulse. The ductile fracture criterion proposed by Bao and Wierzbicki (2004a/b) was introduced in the numerical simulation. In Section 7.3.2, the strain hardening law and critical damage/fracture function are calibrated from tensile test on round specimen of AH36 steel and a parallel numerical simulation. In Section 7.3.3, the closed form solution for the petalling mode proposed by Wierzbicki (1999) is reviewed and the final expression for the normalized crack length is presented. In Section 7.3.4, extensive numerical studies involving discing and petalling failure modes of thin circular plates are discussed. A special attention is paid to the numerical aspect of the selection of a unique number of radial cracks. The evolution of stress, strain, and resulting damage at the critical locations of fracture during crack propagation is presented. Furthermore, the

numerically obtained extent of crack propagation is compared with analytical solution (Wierzbicki, 1999).

7.3.2 Calibration of material and fracture models (AH36 steel)

7.3.2.1 Calibration of material model

The material considered in Chapters 7, 8, and 9 was high strength AH36 steel. Therefore, separate calibration results are presented here for this particular material. Since the range of expected stress triaxiality for the problems considered in those chapters is $1/3 \le \sigma_m / \bar{\sigma} \le 2/3$, which corresponds to branch I in Fig. 2.1(a) or 6.2, it suffices to perform only one calibration test for fracture. The validity of this assumption will be discussed in Section 7.3.5 and also Chapter 9. The critical damage parameters for AH36 steel material are obtained by the conventional calibration method described in Chapter 3.

Smooth round specimen with 6.35 mm diameter, shown in Fig. 7.22(a), was machined from a 25.4 mm thick AH36 steel plate. A load-displacement curve obtained from the quasi-static uniaxial tensile test of the specimen is shown in Fig. 22(b) by circle (Muragishi, 2000). In the numerical simulations of the tensile test, four-node axi-symmetric elements with one point integration and stiffness based hourglass control were used to model smooth round specimen. To study the mesh size sensitivity, two different mesh configurations shown in Fig. 7.23 were used. The specimen was modeled with 10 and 20 elements across the radius, resulting mesh sizes of approximately 0.32 and 0.16 mm in a critical gauge region, respectively.

The numerically obtained load-displacement responses with the initial stress-strain curve and the actual one from the trial-and-error method are shown in Fig. 22(b). The simulation results for two different mesh sizes are also included in Fig. 22(b). Furthermore, the corresponding true stress-strain curves are shown in Fig. 22(c). For the material and specimen considered here, five iterations were performed to obtain the actual stress-strain curve indicated by thick full line in Fig. 22(c). The mechanical properties of AH36 steel are the Young's Modulus $E = 210GPa$, the initial yield stress $\sigma_y = 380MPa$, and the tensile stress $\sigma_u = 836MPa$ at the corresponding fracture strain $\varepsilon_f = 0.43$. Moreover, the average plastic flow stress defined by Eq. (7.1) was $\sigma_o = 690MPa$, see Fig. 22(c).

7.3.2.2 Fracture calibration

The history plots of equivalent strain and stress triaxilaty function at the center of the tensile specimen are shown in Figs. 7.24 and 7.25, respectively. Based on the experimentally determined displacement at the point of fracture ($\delta_f = 5.4mm$), the corresponding magnitude of equivalent strain to fracture can be determined and is $\mathbf{b} = \bar{\varepsilon}_f = 0.43$, as illustrated in Fig. 7.24. In Fig. 7.25, the area under those curves over the range from zero to the point **b** represent the magnitude of calibration constant $D_c = \mathbf{b}(\sigma_m / \bar{\sigma})^0_{av}$, where $\mathbf{b} = \bar{\varepsilon}_f$. The magnitude of the critical damage parameters are summarized in Table 7.6 for two types of meshes. It can be seen from Figs. 7.23 ~ 7.25 and Table 7.6 that the mesh size effect on the calibrated fracture parameters appears to be negligible for this particular AH36 steel.

Table 7.6 Calibrated fracture parameters using two different meshes in the numerical simulation of uniaxial tensile test of AH36 steel; radius of the round specimen in the central gauge region = 3.175mm; gauge length = 25.4mm

Number of elements across the radius	Mesh size/ Radius	$(\sigma_m / \bar{\sigma})^0_{av}$	$\bar{\varepsilon}_f = \mathbf{b}$	$D_c = \mathbf{b}(\sigma_m / \bar{\sigma})^0_{av}$
10	0.025	0.4	0.43	0.172
20	0.0125	0.4	0.43	0.172

(a)

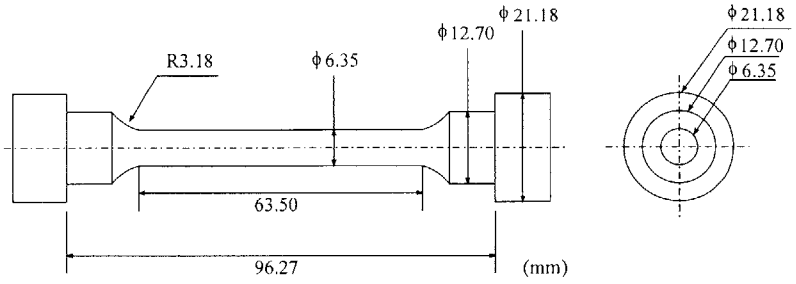

(b)

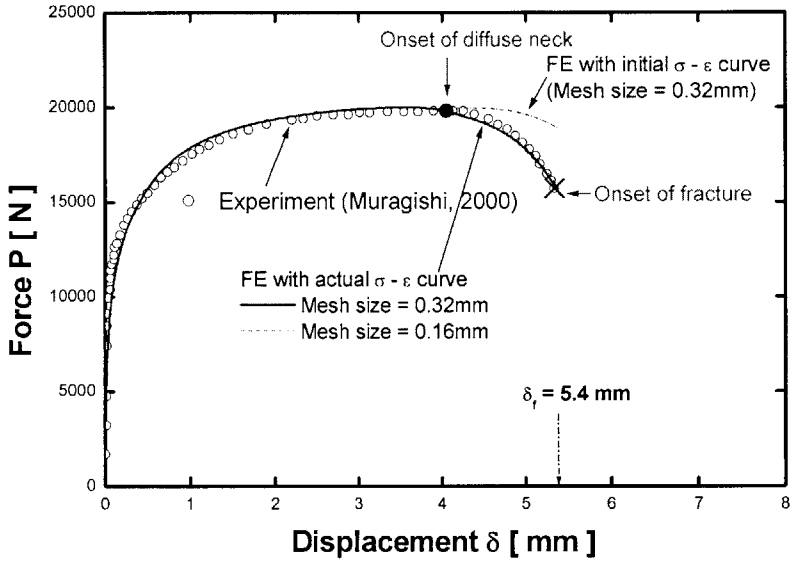

(c)

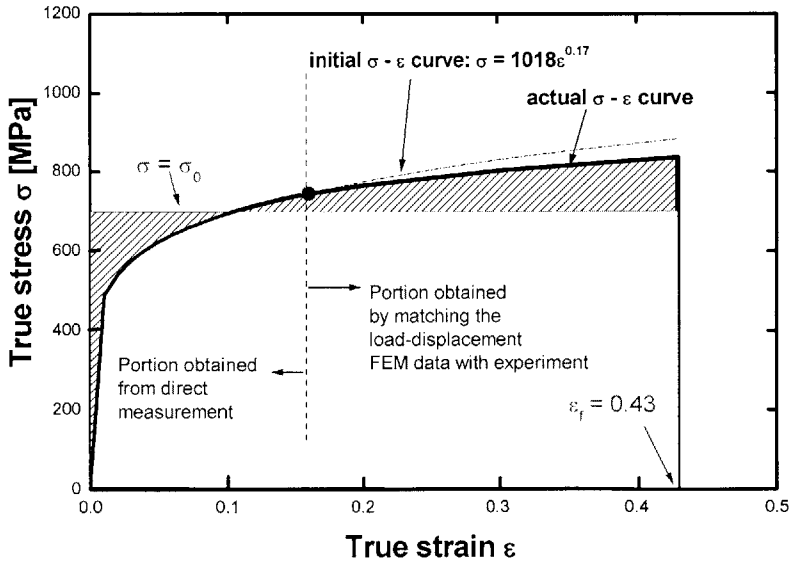

Fig. 7.22 (a) geometry and dimensions of round specimen for uniaxial tensile test of AH36 steel (gauge length = 25.4mm; specimen diameter of gauge region = 6.35mm); (b) load displacement curve for the AH36 steel recorded from tensile test on round specimens; (c) initially assumed and finally obtained true stress-strain curves for AH36 steel

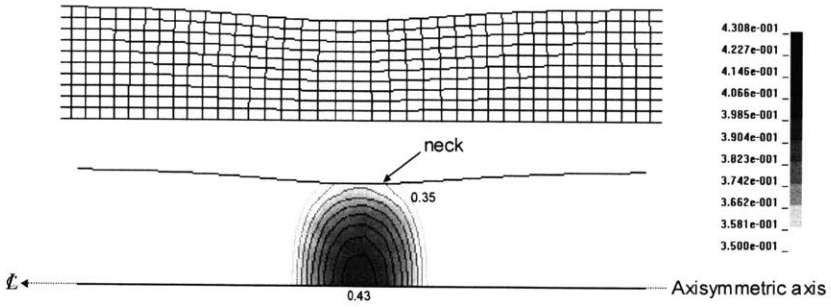

(a)

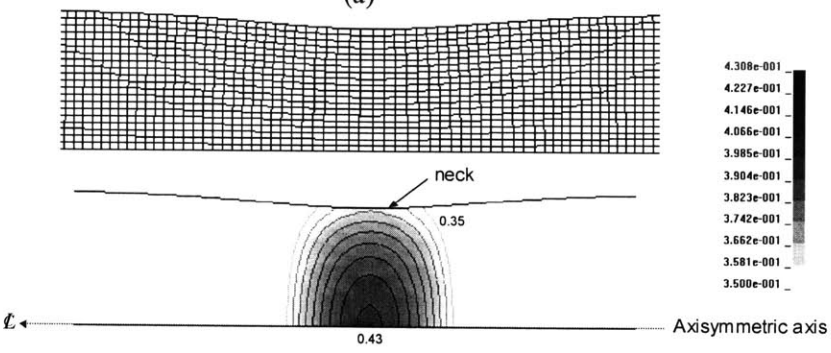

(b)

Fig.7.23 Deformation and equivalent strain contour in the round specimens of AH36 steel with two different mesh sizes of axi-symmetric finite element at the point of fracture; (a) mesh size = 0.32mm; (b) mesh size = 0.16mm

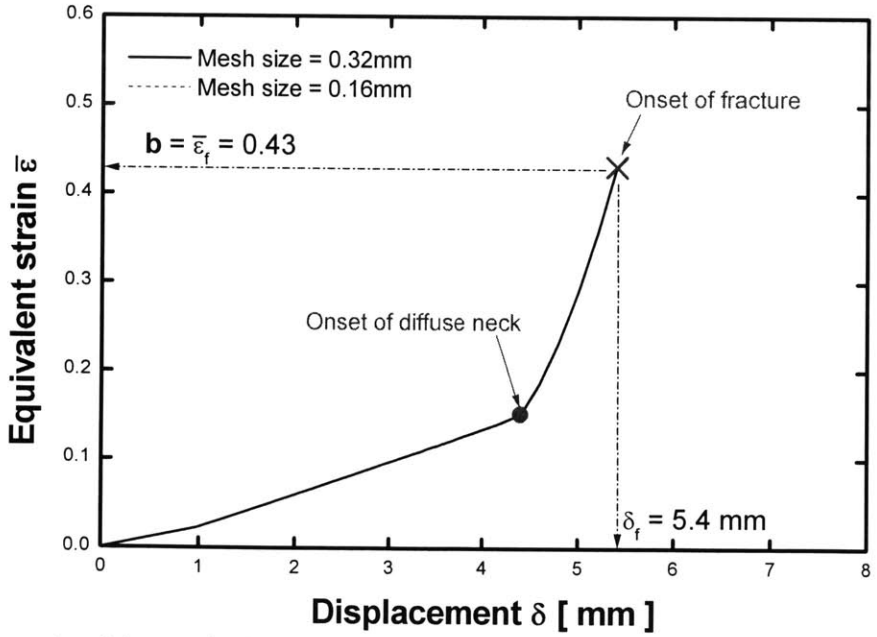

Fig. 7.24 Growth of the equivalent strain at the fracture location using different mesh size (AH36 steel; specimen diameter of gauge region = 6.35mm)

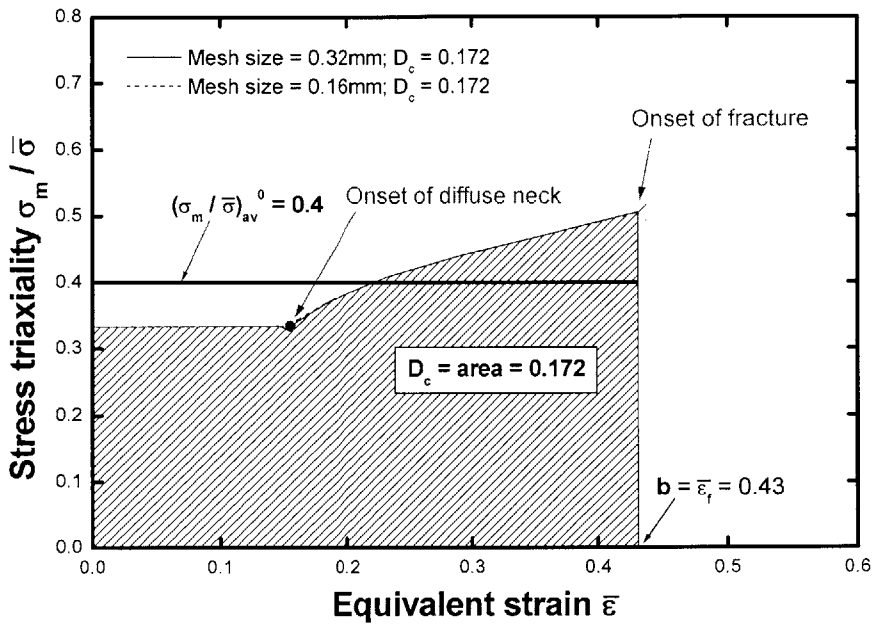

Fig. 7.25 Evolution of stress triaxiality with two different mesh configurations in the case of uniaxial tensile test of round specimen (AH36 steel)

7.3.3 Petalling solution of impulsively loaded plate

The theory used in this section was developed by Wierzbicki (1999). Suppose that a system of n_p radial cracks is formed at a point in an infinite plate dividing it into n_p symmetric petals, Fig. 7.26. The central angle of the petal is denoted by $2\theta_p$ so that

$$\theta_p = \frac{\pi}{n_p} \tag{7.36}$$

and the instantaneous length of crack l_c can be found from

$$l_c = a_c \cos\theta_p \tag{7.37}$$

where a_c is the instantaneous radius of the radial crack. Note that l_c is considered as the process parameter in the present study. The material is assumed to be rigid-plastic with an average flow stress σ_0. The fully plastic bending moment per unit length is $M_0 = (1/4)\sigma_0 h^2$.

The total rate of energy dissipation per n_p petals, normalized with respect to $M_0\dot{l}_c$, derived by Wierzbicki (1999) is

$$\frac{\dot{E}}{M_0\dot{l}_c} = 7.65\pi\left(\frac{l_c}{h}\right)^{0.4}\bar{\delta}^{0.2}\varphi^{0.4}\left[\theta_p(\sin\theta_p)^{0.4}\cos\theta_p\right]^{-1} \tag{7.38}$$

where $\bar{\delta} = \delta_t / h$ is dimensionless crack tip opening displacement parameter (CTOD). The bending moment amplification factor φ, which takes into account a larger bending resistance of a curved plate that is dished before fracture, is defined as

$$\varphi = 1 + 2\sqrt{2\varepsilon_f}\,\theta_p^{\,2}\,\frac{R_1}{h} \tag{7.39}$$

Referring to Eq. (7.38), the total rate of energy is a function of θ_p and it attains a minimum at $\theta_p \cong 40^o$ giving $n_p = 4.5$. Thus, according to the theory, the failure process should produce four or five petals. However, because the minimum rate of energy dissipation is rather weak, a larger number of petals can also be produced. The numerically obtained petals to be presented in following Section 7.3.5 varied between four and eight. Hence, by assuming $\theta_p = 30^o$, which indicates six petals, the minimum normalized rate of energy given by Eq. (7.38) becomes

$$\frac{\dot{E}}{M_0 l_c} = 69.94\left(\frac{l_c\varphi}{h}\right)^{0.4}\bar{\delta}^{0.2} \tag{7.40}$$

For ductile material the dimensionless CTOD parameter $\bar{\delta}$ is of an order of unity. Note that $\bar{\delta}$ is raised to a fractional power 0.2 so that assuming $\bar{\delta}$ different than unity does not practically change the solution. By introducing $\bar{\delta}^{0.2} \cong 1.0$, Eq. (7.40) can be further simplified to

$$\frac{\dot{E}}{M_0 l_c} = 69.94\left(\frac{l_c\varphi}{h}\right)^{0.4} \tag{7.41}$$

For small magnitudes of the impulse the plate undergoes dishing. This problem is fully investigated in Section 7.2. Referring to Eq. (7.32), dishing occurs until tensile fracture takes over at the critical dimensionless impulse

$$V_{cr} = 1.89\sqrt{\varepsilon_f} \tag{7.42}$$

where ε_f is uniaxial fracture strain. For high magnitudes of the impulse above the V_{cr}, the explosion blows out a central cap of the radius R_1 and the remainder of the initial kinetic energy goes into the petalling process. The loss of kinetic energy must thus be equal to the time integral of $\dot{E}$:

$$\frac{1}{2}\pi R_1^2 h\rho c^2 (V^2 - V_{cr}^2) = \int_{t_{cr}}^{t} \dot{E} dt \tag{7.43}$$

where $V = I_0 / c\rho h$ is the normalized impulse, and t_{cr} is critical time for a circumferential crack.

By substituting the expression $\dot{E}$ (Eq. (7.41)) and integrating, one gets

$$\frac{1}{2}\pi R_1^2 h\rho c^2 (V^2 - V_{cr}^2) = 12.49\sigma_0 \varphi^{0.4} h^{1.6} (l_c - R_1)^{1.4} \tag{7.44}$$

Using the definition of plastic wave speed $c^2 = \sigma_0 / \rho$, Eq. (7.44) can be rewritten as

$$V_{cr}^2 \left[\left(\frac{V}{V_{cr}} \right)^2 - 1 \right] = 7.95\varphi^{0.4} \left(\frac{h}{R_1} \right)^{0.6} \left(\frac{l_c}{R_1} - 1 \right)^{1.4} \tag{7.45}$$

By simple arithmetic calculation, the crack length l_c can expressed in terms of plate geometry, bending moment amplification factor, and applied impulse

$$\frac{l_c}{R_1} = 1 + 0.23 \left(\frac{R_1}{h} \right)^{0.43} \frac{V_{cr}^{1.42}}{\varphi^{0.29}} \left[\left(\frac{V}{V_{cr}} \right)^2 - 1 \right]^{0.71} \tag{7.46}$$

By introducing the normalized crack length $\xi_c = l_c / R_0$ and loading radius $\xi_0 = R_1 / R_0$, Eq. (7.46) takes the form which will be used in correlating the present theory with the numerical results. Note that the CTOD parameter does not enter the solution because the dependence on $\overline{\delta}$ is very weak.

$$\xi_c = \xi_0 \left\{ 1 + 0.23 \left(\frac{\xi_0 R_0}{h} \right)^{0.43} \frac{V_{cr}^{1.42}}{\varphi^{0.29}} \left[\left(\frac{V}{V_{cr}} \right)^2 - 1 \right]^{0.71} \right\} \tag{7.47}$$

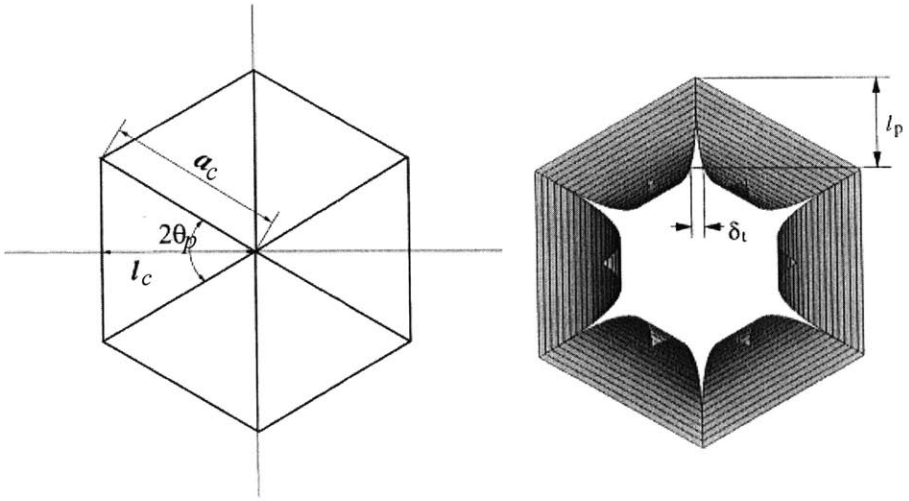

Fig. 7.26 Initial and current geometry of the plate with six radial cracks (after Wierzbicki, 1999)

7.3.4 FE solution with fracture (discing)

7.3.4.1 FE analysis

Numerical results for the petalling failure modes of impulsively loaded, clamped thin circular plates are presented in Sections 7.3.4 and 7.3.5. The considered clamping radius, thickness, and material of circular plate were $R_0 = 5416\ mm$, $h = 16\ mm$, and AH36 steel, respectively. In the present numerical simulation, ductile fracture is assumed to be controlled by Eq. (2.4) or (2.5). When the equivalent strain weighted by stress triaxiality reaches the critical value at all of the integration points in an element, this element is deleted to model crack formation and propagation while its mass is conserved. Since the plate considered in this study was very thin (radius-thickness ratio of 339), the fracture was further assumed to occur instantaneously through the plate thickness. The four-node Belytschko-Tsay shell element with five integration points through thickness was employed. Because the circular plates have the axes of symmetry, a quarter model was considered for the plates with 8 petals. An additional run was carried out using full model to validate the accuracy of the quarter model (see Fig. 7.32(a)). The same loading and boundary conditions were used as defined in Section 7.2.4.

Most of the results were obtained using commercial FE code *PAM-CRASH*. An additional run was also made using *ABAQUS/Explicit* to validate the fracture criterion. In Section 7.3.2, the critical damage value D_c was obtained by the combination of a quasi-static uniaxial tensile test and finite element calculation. Based on the critical value, calculated distributions and histories of stress and strain, the formation and propagation of cracks were predicted by the fracture criterion in a various radii of the centrally loaded area and intensity of pressure. It should be noted that the effect of strain rate and temperature was not taken into account. However, a series of recent papers by Borvik et al. (1999, 2001, 2003) showed that the strain rate has a little effect on the accumulated damage and fracture strain for the Weldox 460E steel, as shown in Fig. 2.13.

7.3.4.2 Onset of fracture (discing)

The numerically obtained profiles of stress triaxiality are shown in Fig. 7.27 with three different values of ξ_0 at the instant point of crack formation. The critical dimensionless impulse V_{cr} = 1.24 calculated from Eq. (7.42) with ε_f = 0.43 for AH36 steel, needed to initiate the initial holing process, was used for all values of ξ_0. It can be seen that the stress state shows the complete biaxial condition around the plate center and plane strain deformation at the clamped end. The stress triaxiality at which fracture occurs, see open circle in Fig. 7.27, is 0.6 for the loading radii $\xi_0 \leq 0.5$ and 0.58 for $\xi_0 = 1.0$. It was found that a peak in radial strain develops and plastic deformation localizes in the circumferential region. The strain localization leads to the development of a circumferential crack which is approximately located at $\xi = \xi_0$. Figure 7.28 shows the corresponding profiles of damage, as defined by Eq. (2.4). It can be clearly seen that the critical distance from the plate center when the accumulated damage first reaches the critical value of D_c = 0.172 increases as ξ_0 increases.

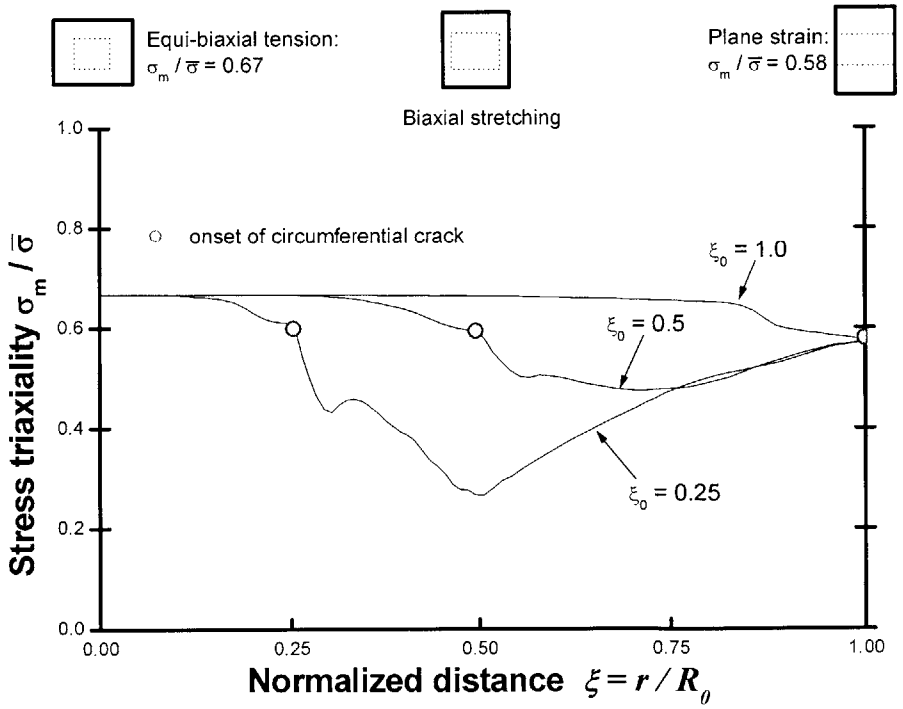

Fig. 7.27 Numerically obtained stress triaxiality profiles of circular plate with three different values of ξ_0 at the point of fracture ($V_{cr} = 1.89\sqrt{\varepsilon_f} = 1.24$)

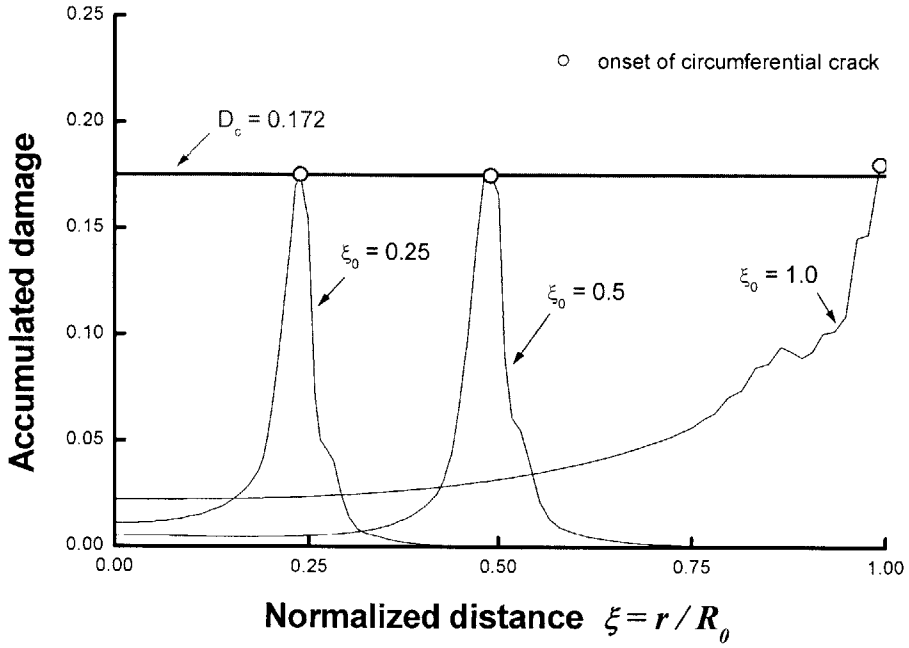

Fig. 7.28 Damage profiles of circular plate at the fracture initiation with three different values of $\xi_0 (V_{cr} = 1.89\sqrt{\varepsilon_f} = 1.24)$

7.3.5 FE solution with fracture (radial crack and petalling)

The sequence of the failure process can be illustrated by examining the deformed shapes of the plate subjected to a high magnitude of impulse above the critical value V_{cr} = 1.24 (see Fig. 7.29). Consider, for example, the dimensionless impulse V = 1.8, which is 1.45 times larger than the critical impulse V_{cr} and loading radius $\xi_0 = 0.25$. Following the initial dishing phase, a circumferential crack forms and a circular cap of the radius ξ_0 is detached in the central region, see Fig. 7.29(b). From this point on, high circumferential strains induced in the plate cause formation of radial cracks, see Fig. 7.29(c), which propagate outward from the center while the subsequent rotation of the plate leads to a number of symmetric petals, see Fig. 7.29(d).

The histories of stress, strain, and resulting damage at the various locations of potential fracture elements (see Fig. 7.30) were explored during the discing and petalling phases. All the results reported in this Section 7.3.5 are obtained from the case of V = *1.8* and $\xi_0 = 0.25$, unless otherwise stated. Note that the fractured elements and the neighboring elements along the radial crack path are denoted by C_i and a_i, respectively.

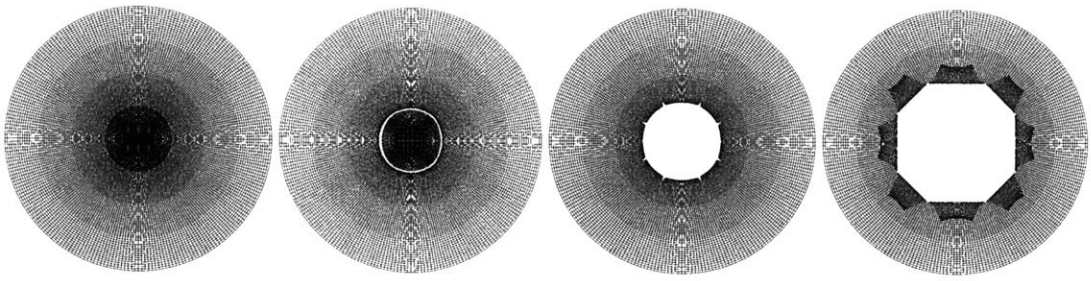

(a) $\tau = 0.0$ (b) $\tau = 0.06$ (c) $\tau = 0.08$ (d) $\tau = 1.3$

Fig. 7.29 Plan views for the sequence of fracture patterns of thin circular plate subjected to localized impulsive loading ($\xi_0 = 0.25, V = 1.8$). Note that the central cap is removed in (c) and (d); The normalized time is denoted by $\tau = ct / R_0$.

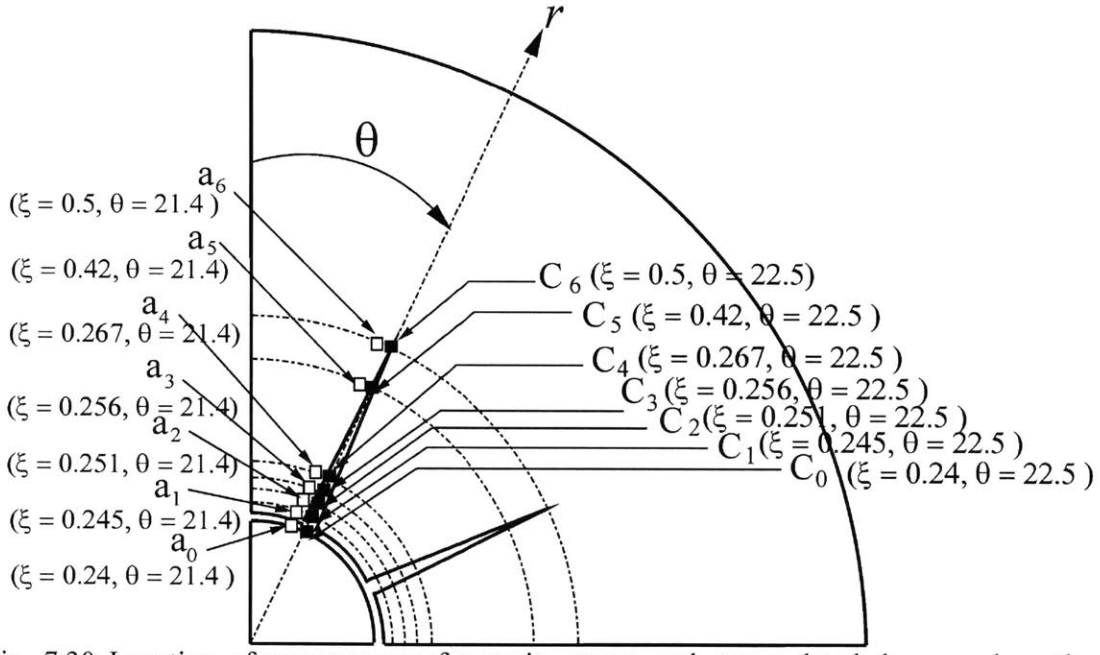

Fig. 7.30 Location of measurement for strain, stress, and accumulated damage along the crack propagation (a quarter model; $\xi_0 = 0.25$). Note that the fractured elements and the neighboring elements along the radial crack path are denoted by $\boldsymbol{C_i}$ and $\boldsymbol{a_i}$, respectively.

7.3.5.1 Formation and number of radial cracks

Figure 7.31 shows the damage distribution along the hoop direction of the plate from the onset of discing ($\tau = 0.0561$) to the final stage ($\tau = 1.3$) of the petalling process. Note that the range of angle shown in Fig. 7.31 is $0^0 \le \theta \le 90^0$, which indicates a quarter model of the circular plate. It is interesting to see that initially many tiny radial cracks initiate from the edge of circular hole. Most of them are short-lived, they are arrested, and only two cracks defining eight petals of the full model

remain active. The sequence of the failure process can be also observed in Fig 7.33 where 3-D views of deformed shapes are presented with color coded contours of stress triaxiality and normalized damage (D/D_C). In Fig. 7.31, the positions at which the two dominant radial cracks occurred are indicated by the symbol (×). The range of angle θ is 20°~26° so that eight radial cracks and later on eight petals are formed. No material or structural imperfections were introduced in the numerical simulation. It would then appear that circumferential periodicity θ_p= 22.5° is an intrinsic property of the solution.

The detail profiles of damage between the onset of discing failure at $\xi = 0.24$ and the initial formation of radial cracks at $\xi = 0.245$ are shown in Fig. 7.32 as functions of angular direction and normalized time. Moreover, the numerical results obtained from full finite element model are included. It is seen that the difference between quarter and full model is almost zero, which means that the local stress, strain, and resulting damage are not influenced by the imposed constraints of quarter model. It can be further observed that the profile of damage exhibits fully axi-symmetry at the point of circumferential crack ($\tau = 0.0561$). Once circumferential cracks develop (discing), the profiles of damage lose their symmetry and show a rather random distribution. On continued deformation, this irregular distribution of damage along the hoop direction changes into the periodic profiles with $\theta_p = 22.5°$, as already shown in Fig. 7.31.

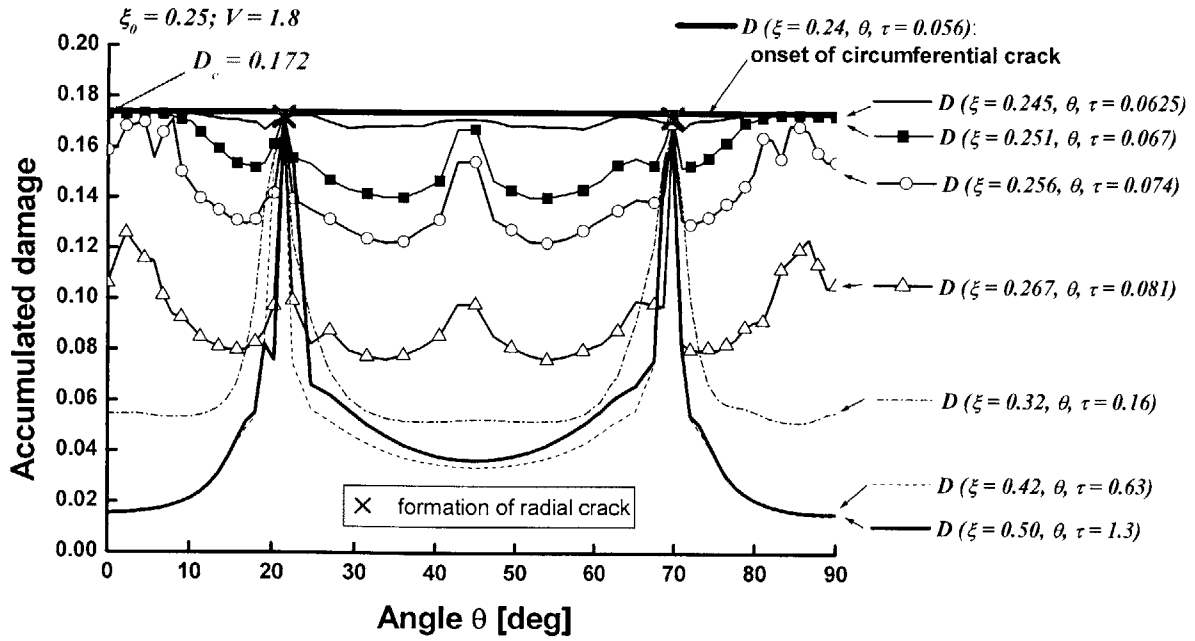

Fig. 7.31 Profiles of accumulated damage along the angular direction as functions of ξ and τ throughout the whole stages of dynamic response (a quarter model; $V = 1.8$; $\xi_0 = 0.25$)

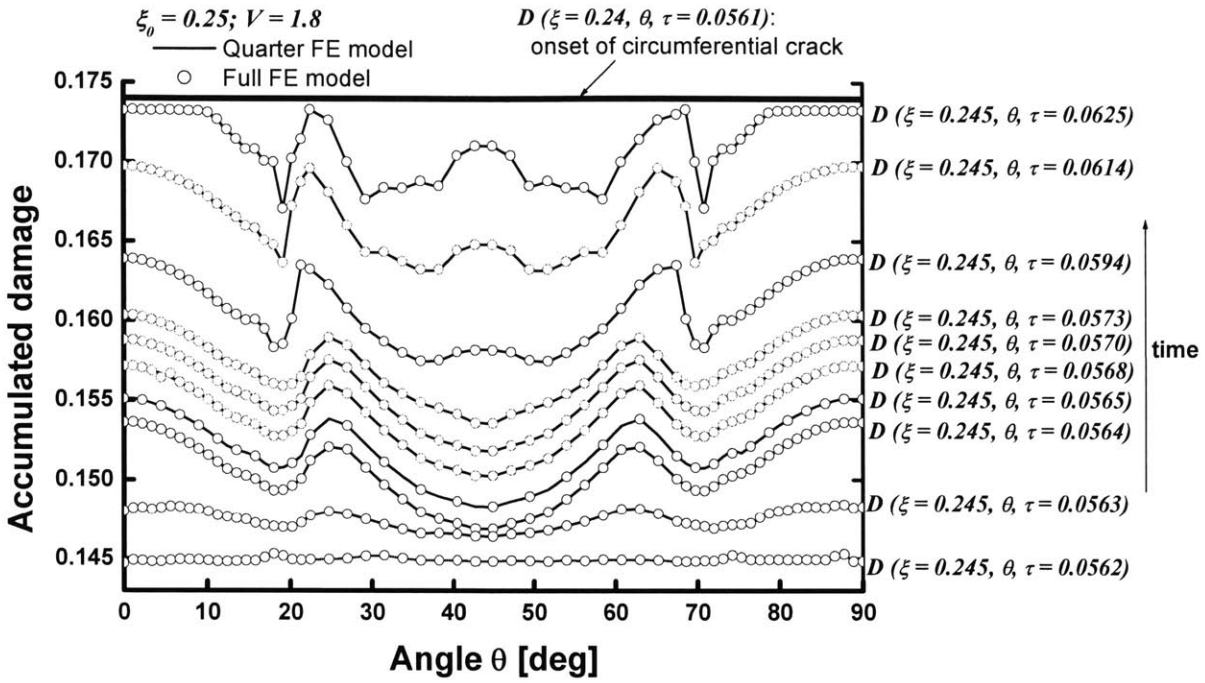

(a)

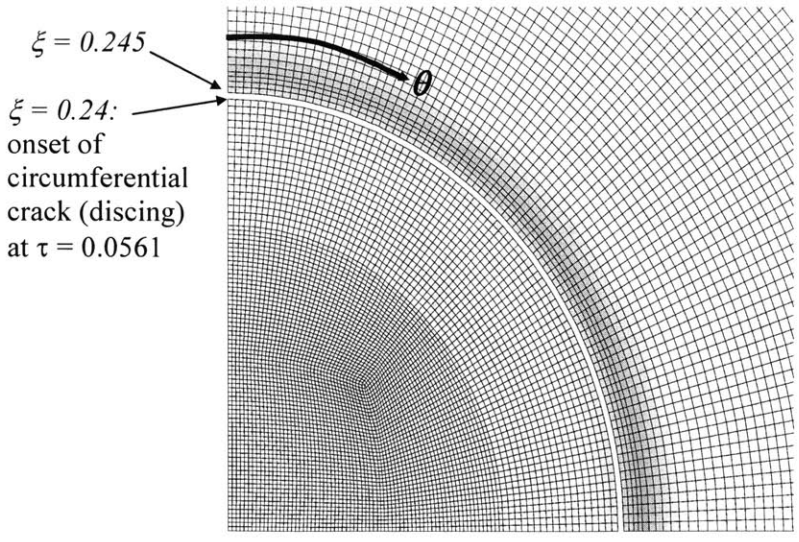

(b)

Fig. 7.32 (a) Close-up of damage profiles along the angular direction right after the discing failure ($\xi = 0.24$, θ, $\tau = 0.0562$) to the point of radial crack formation ($\xi = 0.245$, θ, $\tau = 0.0625$) ; (b) Enlarged view of deformed mesh at $\tau = 0.0563$ ($V = 1.8$; $\xi_0 = 0.25$)

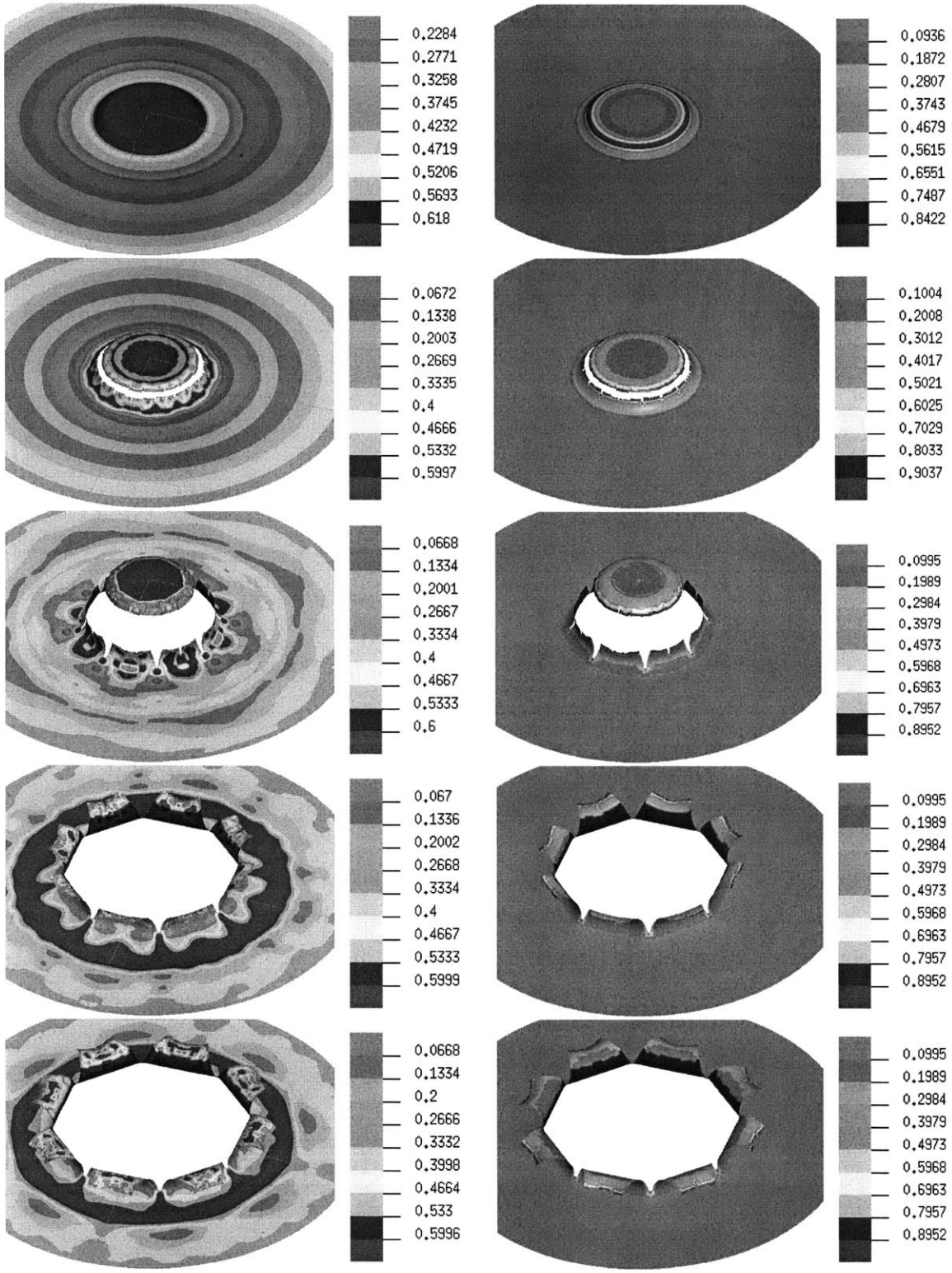

Fig. 7.33 Color coded contours of stress triaxiality (left) and normalized damage, D/D_c, (right) at different values of $\tau = 0.056, 0.081, 0.16, 0.63, 1.1 (V = 1.8; \xi_0 = 0.25)$

7.3.5.2 Evolution of stress and strain fields

In-plane components of strain and stress The history plots of in-plane strain and stress components at the elements ahead of crack path (denoted by C_i in Fig. 7.30) are shown in Fig. 7.34(a) and (b), respectively. The element $\mathbf{C}_0$ corresponds to the formation of circumferential crack and the subsequent radial cracks are indicated by the elements, $\mathbf{C}_1 \sim \mathbf{C}_6$. It is clearly shown that the local stress and strain states are mainly influenced by radial components (marked with open symbols) during the initial dishing phase. After the onset of discing, the radial components of stress and strain cease to increase, while high circumferential components (marked with filled symbols) are developed in the plate. The corresponding strain paths from numerical simulation are shown in Fig. 7.35(a). The axes are the in-plane major and minor principal strains, $\varepsilon_1 = \max(\varepsilon_r, \varepsilon_\theta)$ and $\varepsilon_2 = \max(\varepsilon_r, \varepsilon_\theta)$. The loci of fracture points obtained from the best curve fitting of numerical result and analytically predicted by Eq. (2.25) are, respectively, marked with thin and thick full line in Fig. 7.35(a). One can see that two FFLDs compares well with each other. The in-plane strain paths in the neighboring elements of the crack path (denoted by a_i) are also shown in Fig. 7.35(b). It can be observed that the strain paths in the elements a_i are within the range of fracture locus defined by Eq. (2.25) except for the case of element a_0 (circumferential crack) i.e. radial cracks could not be developed in the subsequent elements, $a_1 \sim a_6$.

Stress triaxiality and equivalent strain The stress triaxiality versus normalized time in the elements C_i and a_i are shown in Figs. 7.36 and 7.37, respectively. The fracture points of each element are marked with symbol (×) in those figures. One can see that stress triaxialities in the elements C_0 and a_0 correspond to the crack formation of uncracked bodies. Therefore, these show smooth variation with the progression of time. On the other hand, once fracture occurs, there are significant variations in stress triaxialities for other elements. This is due to the fact that the first crack formation in the elements C_0 and a_0 introduces redistribution of stresses and large stress gradients around the crack path. Furthermore, the stress triaxialities in the elements ahead of a propagating crack (C_1, C_2, C_3, and C_4) increase right after the onset of fracture (see close-up of the window in Fig. 7.36). This provides a needed stress elevation for the radial crack to growth. By contrast, stress triaxialities in the neighboring elements (a_1, a_2, a_3, and a_4) decrease (see close-up of

the window in Fig. 7.37). However, the above mentioned large variation of stress triaxialities in the elements is restricted to only the small regime of equivalent plastic strain ($\bar{\varepsilon} < 0.05$), as shown in Fig. 7.38, which also includes the average stress triaxiality defined by $\left(\frac{\sigma_m}{\bar{\sigma}}\right)_{av} = \frac{1}{\bar{\varepsilon}_f}\int_0^{\bar{\varepsilon}_f}\frac{\sigma_m}{\bar{\sigma}}d\bar{\varepsilon}$. It is clearly illustrated that the difference in the magnitude of the average stress triaxiality between crack formation (element C_0) and propagation (elements $C_1 \sim C_6$) is small, even though the latter includes a large stress gradient around the crack tip (see Fig. 7.38(a)). The same observations can be also made for the case of elements a_i, as shown in Fig. 7.38(b). In all cases, the average stress triaxiality is of an order of 0.58. This corresponds to neck and fracture formation in plane strain deformation. The above observations are quite consistent with those form the cases of tensile specimen and double hulls under static loading, respectively presented in Chapters 5.3 and 6.2.

Accumulated damage Figure 7.39 presents accumulated damage versus normalized time at the above locations. It is seen that elements C_0 and a_0 first reach the critical damage. Then elements $C_1 \sim C_6$ sequentially reach the critical value with the progression of time, which shows that cracks propagate from the initial circumferential crack to the subsequent radial cracks toward the clamped boundary of the plate. It can be also observed that the cumulated damages of elements $a_1 \sim a_6$ are below the critical value.

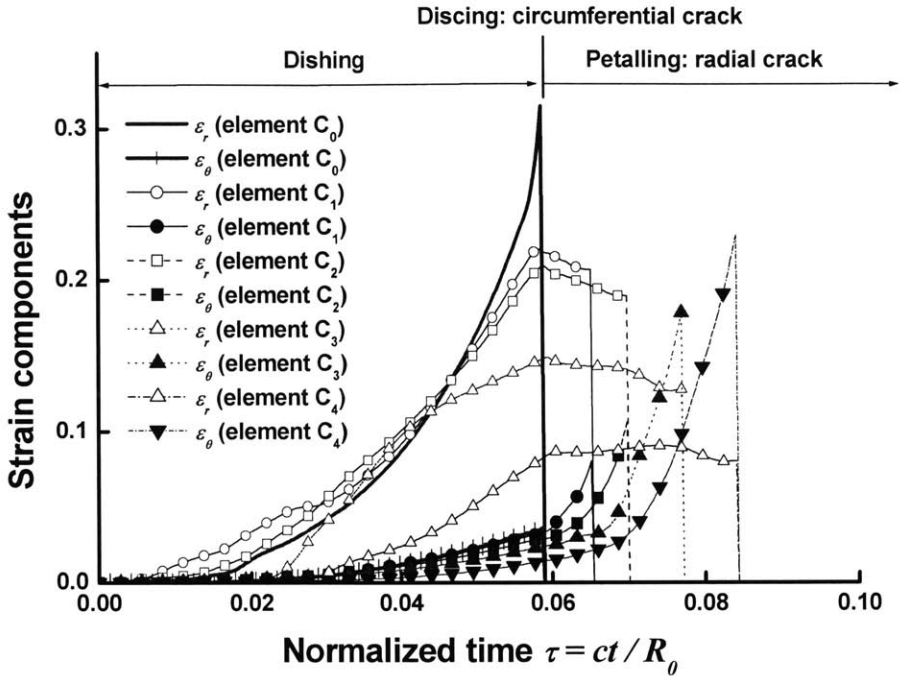

(a)

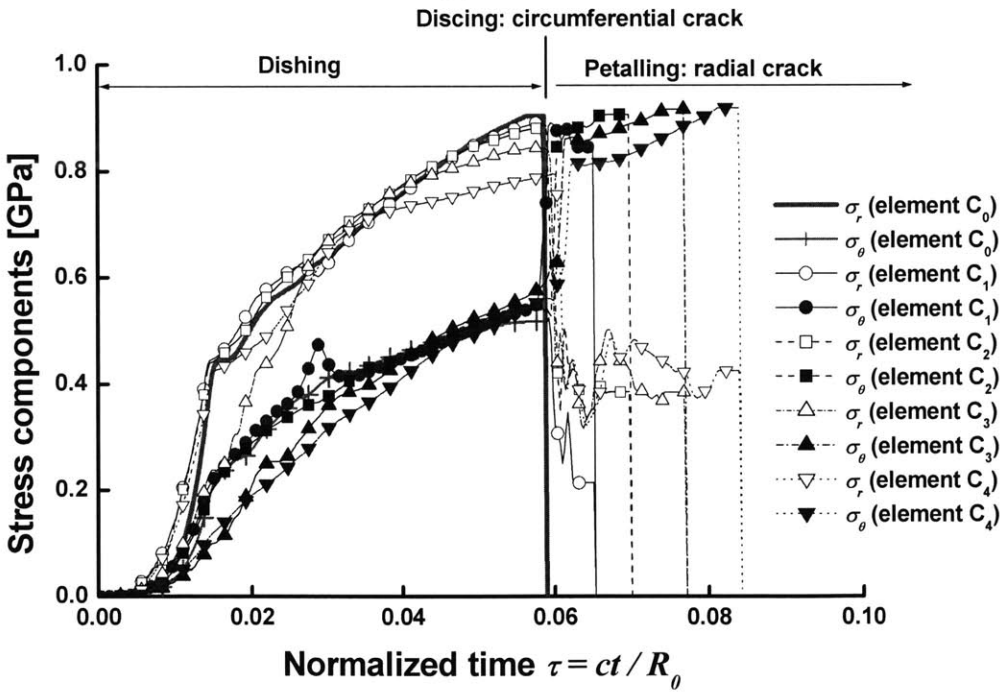

(b)

Fig. 7.34 History plots of in-plane strain and stress components in front of crack path; (a) in-plane strain components; (b) in-plane stress components ($V = 1.8$; $\xi_0 = 0.25$)

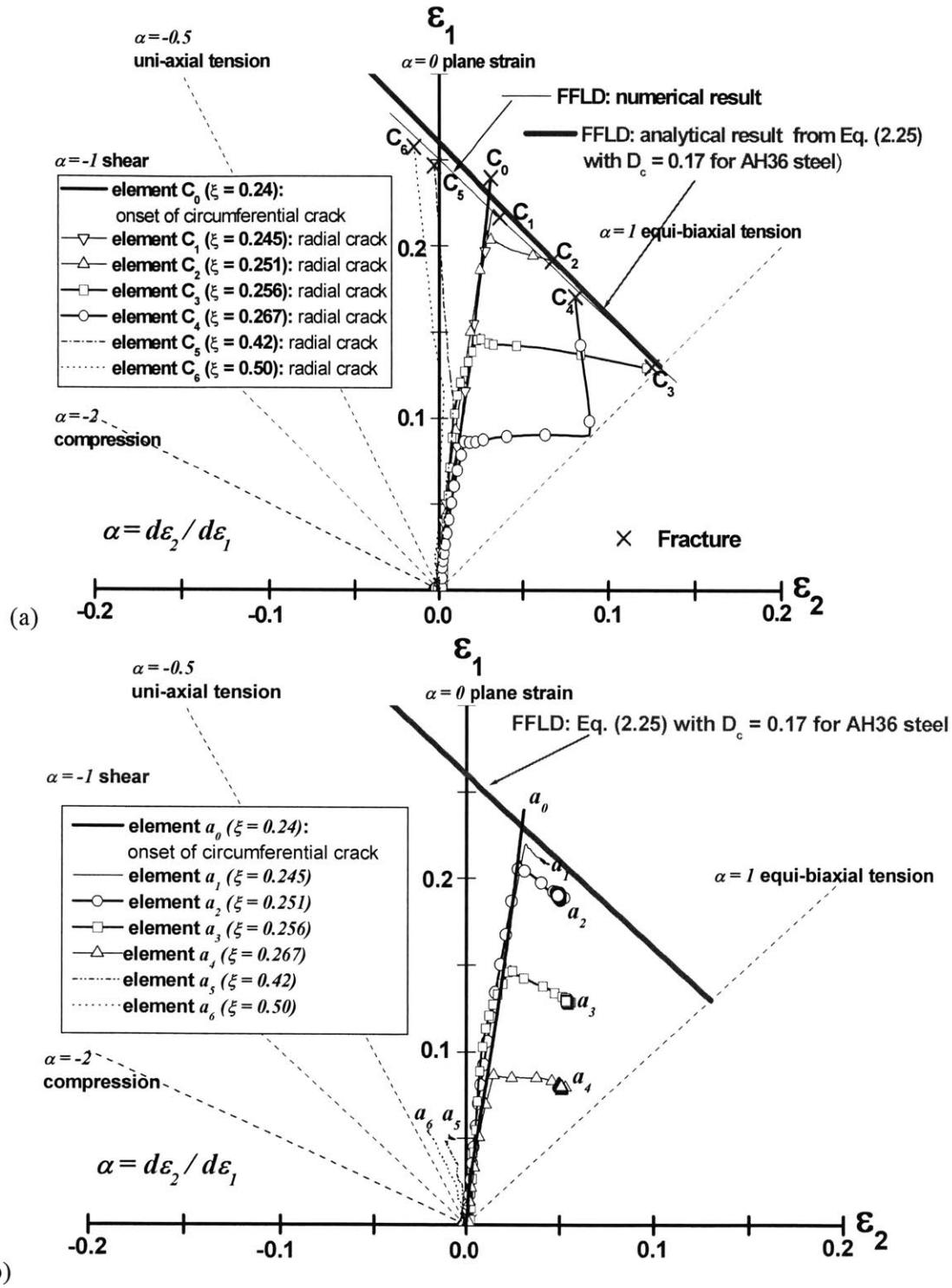

Fig. 7.35 In-plane major and minor principal strain paths at the potential points in front of crack path($V = 1.8; \xi_0 = 0.25$); (a) fractured elements (C_i) along the crack path; (b) neighboring elements (a_i) of the crack path; Note that $\varepsilon_1 = \max(\varepsilon_r, \varepsilon_\theta)$ and $\varepsilon_2 = \min(\varepsilon_r, \varepsilon_\theta)$

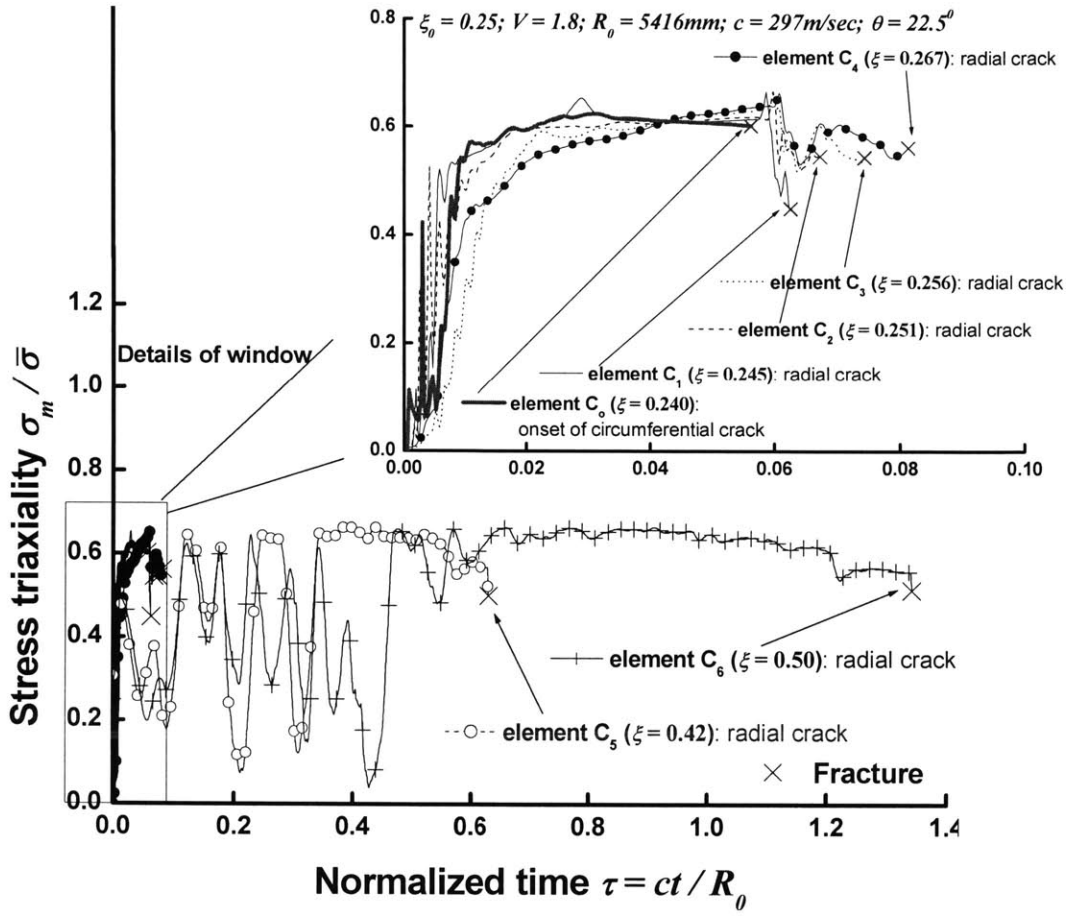

Fig. 7.36 Stress triaxiality versus normalized time at the fractured elements (C_i) along the crack path ($V = 1.8;\ \xi_0 = 0.25$)

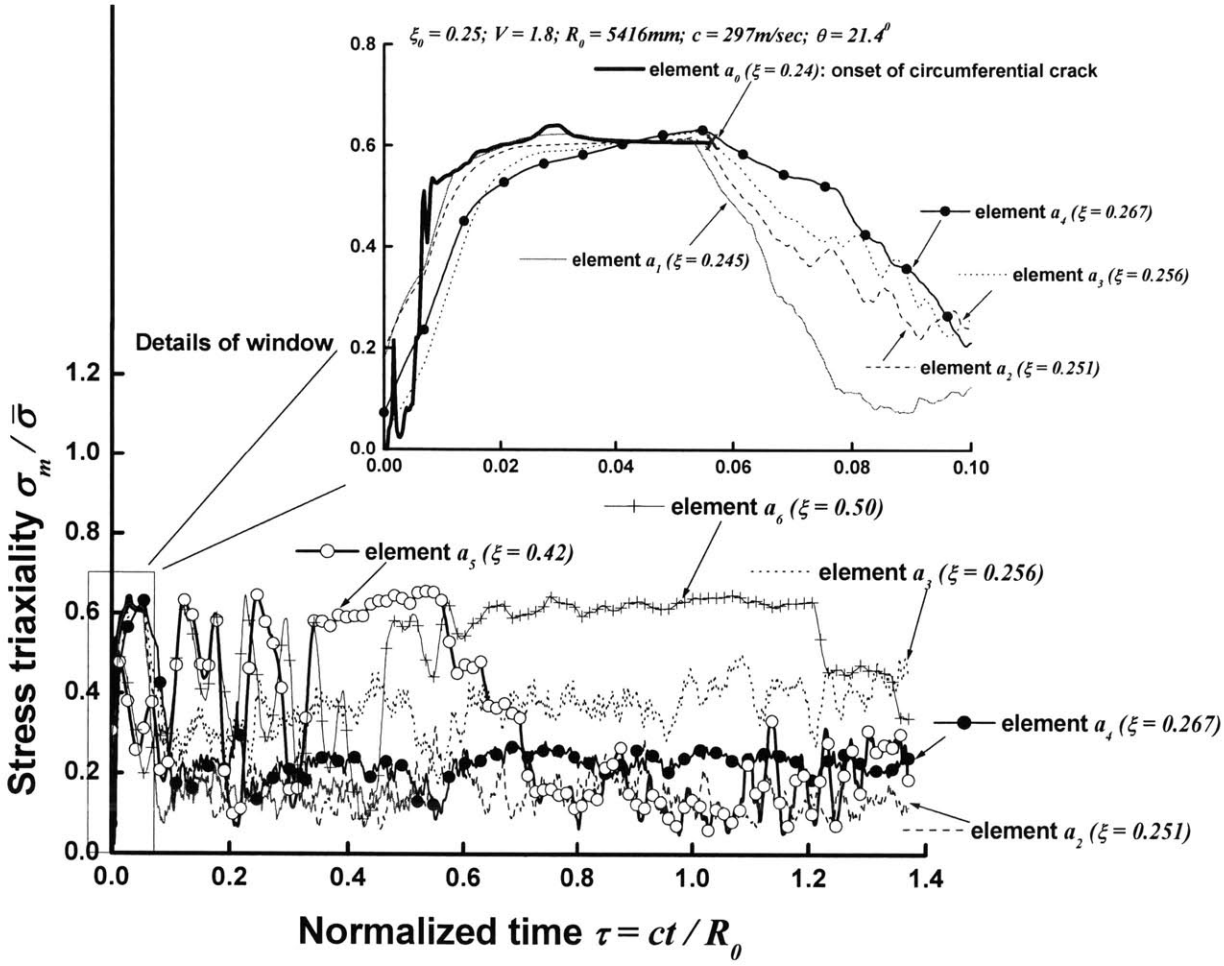

Fig. 7.37 Stress triaxiality versus normalized time at the neighboring elements (a_i) of the crack path ($V = 1.8$; $\xi_0 = 0.25$)

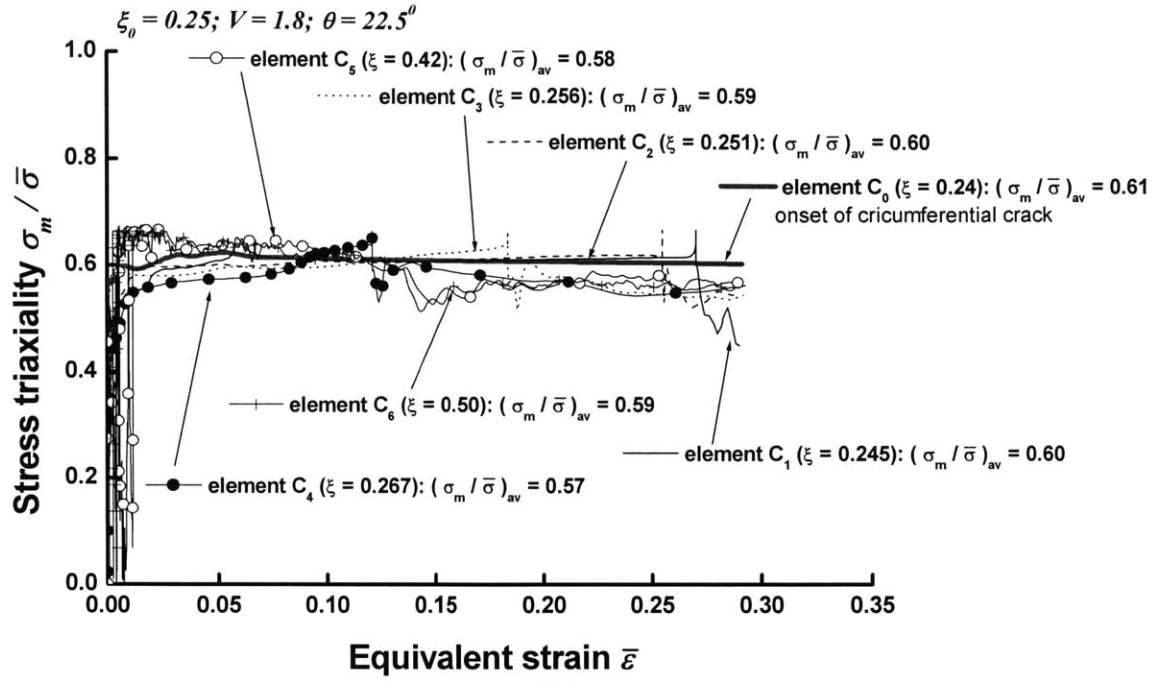

(a)

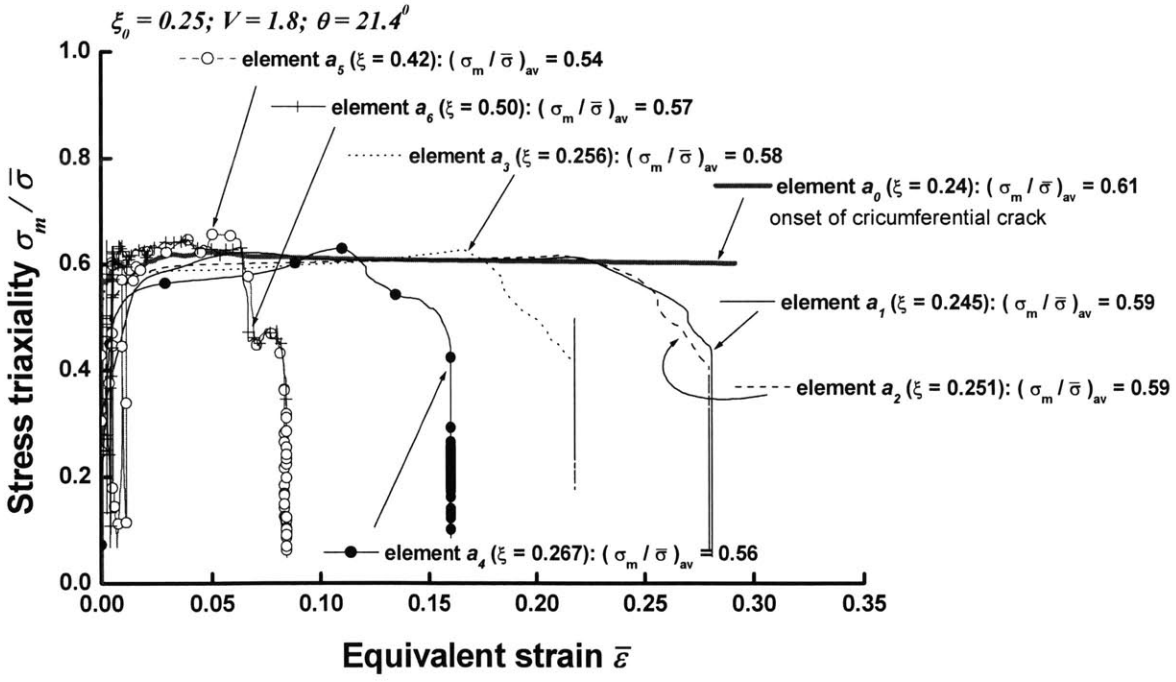

(b)

Fig. 7.38 Stress triaxiality versus equivalent plastic strain at the potential fracture points along the crack path ($V = 1.8$; $\xi_0 = 0.25$) ; (a) elements $\boldsymbol{C_i}$ (radial crack path); (b) elements $\boldsymbol{a_i}$ (vicinity of the radial crack path)

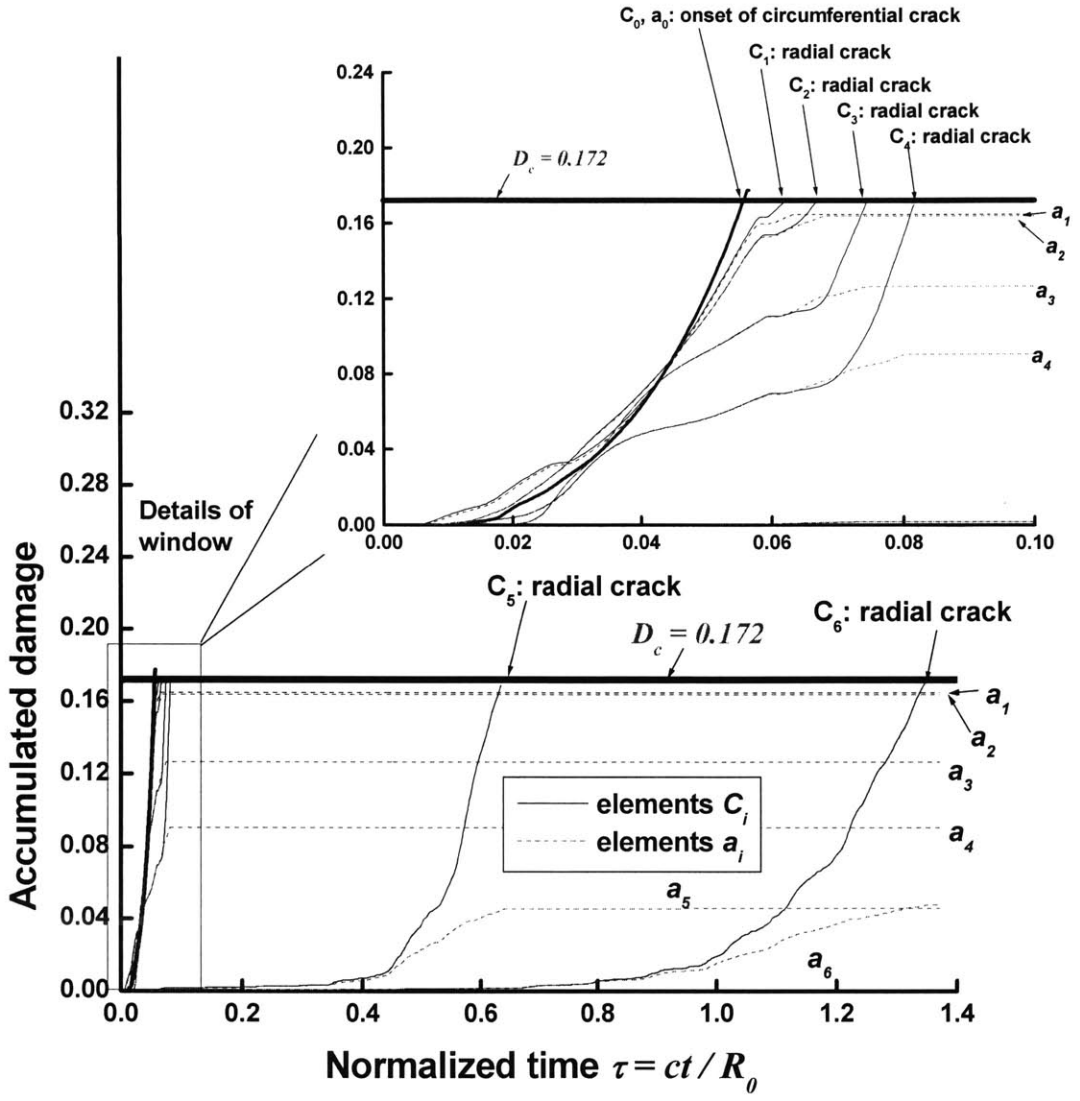

Fig. 7.39 Accumulated damage versus normalized time at the potential fracture points along the crack path ($V = 1.8$; $\xi_0 = 0.25$)

7.3.5.3 Effect of fracture criterion and mesh size on crack propagation

As shown in preceding subsection, the average stress triaxiality in the potential fracture point of the present problem is approximately constant during the petalling process and equal to, $(\sigma_m / \bar{\sigma})_{av} \cong 0.58$. Hence, according to Eq. (7.48) which is an alternative expression for the postulated fracture criterion (Eq. (2.4)) in the branch I, the equivalent strain, if calculated from Eq. (7.48), can be reasonably used to predict fracture and the critical strain to fracture is $\bar{\varepsilon}_f = 0.3$ for the critical damage value $D_c = 0.172$.

$$\bar{\varepsilon}_f = \frac{D_c}{(\sigma_m / \bar{\sigma})_{av}} \tag{7.48}$$

For the finite element predictions using *PAM-CRASH* Version 2G (2003), the elements with an equivalent strain larger than the specified fracture strain ($\bar{\varepsilon}_f = 0.3$) were deleted to predict the formation and propagation of cracks throughout the petalling process. To validate the above equivalent strain modified by the average stress triaxiality, an additional run was performed by *ABAQUS/Explicit* Version 6.4.1 (2003) that has a provision of making the critical fracture strain dependent on stress triaxiality, Eq. (7.49)

$$\bar{\varepsilon}_f = \begin{cases} \infty, & \dfrac{\sigma_m}{\bar{\sigma}} \le -\dfrac{1}{3} \\ \dfrac{0.18}{3 + \dfrac{\sigma_m}{\bar{\sigma}}}, & -\dfrac{1}{3} < \dfrac{\sigma_m}{\bar{\sigma}} \le 0 \\ 1.56\left(\dfrac{\sigma_m}{\bar{\sigma}}\right)^2 + 0.18, & 0 \le \dfrac{\sigma_m}{\bar{\sigma}} \le 0.4 \\ \dfrac{0.172}{\dfrac{\sigma_m}{\bar{\sigma}}}, & 0.4 \le \dfrac{\sigma_m}{\bar{\sigma}} \end{cases} \tag{7.49}$$

where the fracture locus was constructed from the calibration of uniaxial tensile test for AH36 steel in conjunction with the general form of weighting function given by Eq. (2.6). The calibrated parameters, as summarized in Table 7.6, were applied to Eq. (2.6). The relationship between parameters **a** and **b** for AH36 steel calculated was **a** = *0.43***b** for the hardening exponent n = 0.17 of AH36 steel, according to Eq. (3.46). We selected the case with the loading radius $\xi_0 = 0.25$ and normalized impulse $V = 1.8$. Figure 7.40 compares the plastic work between two different fracture

criteria given by Eqns. (7.48) and (7.49). It is seen that the difference between two cases is insignificant. Furthermore, the resulting dimensionless crack length $\xi_c = l_c / R_0$ is almost same between two cases, as shown in Fig. 7.45. Therefore, for the remainder of this chapter, the fracture strain weighted by the average stress triaxiality from Eq. (7.48) was used.

During the petalling process, it is possible that severe distortion of elements near the crack tip may occur. This mesh distortion may potentially produce unreliable results of stress and strain states. One way of handling this deficiency is to use an adaptive mesh technique which can create elements with fine resolution over the region where the crack is assumed to propagate (Tradegard et al., 1998; Borvik et al., 2002) Figure 7.41 compares the deformed shapes of the plate between the adaptive and fixed mesh at the initial dishing and final petalling phases. Note that meshes were refined by factors of two for the region being approached by the crack tip in the adaptive mesh configuration. It should be also pointed out that the fixed mesh configuration has a sufficiently small size of elements across the plate radius. The ratio of average element length to the plate radius was approximately 0.005, which provides 27,000 elements in quarter model. It can be clearly seen that the deformed shapes are almost identical using adaptive mesh or fixed mesh. Moreover, as shown in Fig. 7.45, the difference in normalized crack length between two different mesh configurations is also insignificant. This weak dependence of mesh size on the transient response of dynamic problem is quite consistent with the results of Borvik et al. (2002).

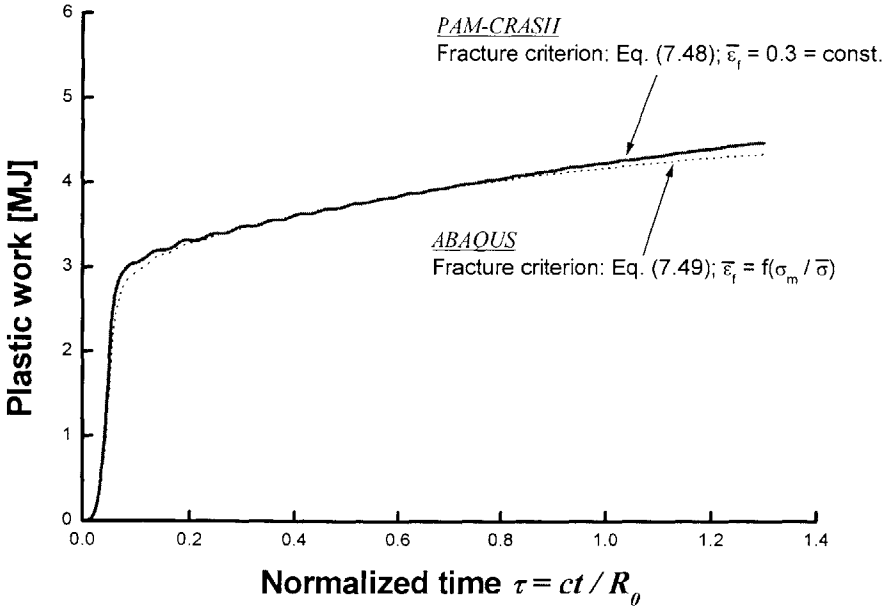

Fig. 7.40 Plastic work of the plate during the petalling process based on two fracture criterion ($\xi_0 = 0.25; V = 1.8$)

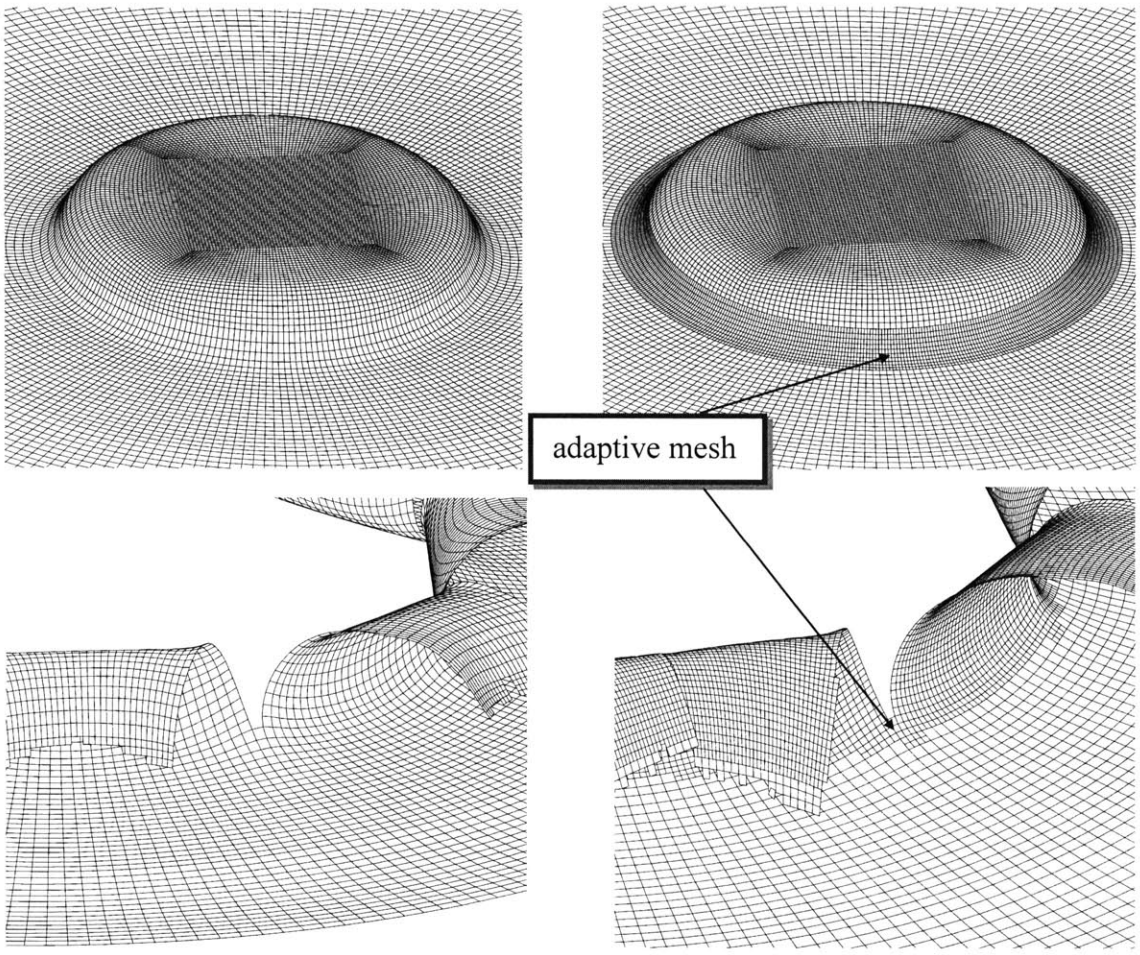

(a) using fixed mesh (b) using adaptive mesh

Fig. 7.41 Enlarged views of the deformed mesh in the potential fracture site at different values $\tau = 0.05,\ 1.3\,(\xi_0 = 0.25, V = 1.8)$

7.3.6 Effect of spatial distribution and intensity of pressure

A 3-D view of the set of deformed shapes from the initial dishing to final stages of petalling process is shown in Fig. 7.42 with two different values of loading radius ξ_0. The set of figures on the left is the plate with $\xi_0 = 0.25$, while those on the right correspond to $\xi_0 = 0.5$. The

corresponding sectional views along the symmetry plane of the petals are also shown in Fig. 7.43. The applied impulse in those two figures was $V = 1.8$. For this amount of impulse, radial cracks initiated from the central hole reached approximately half of the distance to the clamped boundary of the plate in the case of $\xi_0 = 0.25$, while radial cracks almost reached the boundary for $\xi_0 = 0.5$. The above results clearly indicate that the extent of damage is strongly influenced by the spatial distribution of pressure under the same amount of applied impulse.

A sequence of six pictures shown in Fig. 7.44 illustrates the final deformed shapes of the plates with increasing intensity of impulse for two different values of loading radius ξ_0. It is seen that the extent of petalling phases depends on the intensity of impulse. At $V_{cr} = 1.24$, circular caps were initially blown out in the central region for both cases of $\xi_0 = 0.25$ and 0.5. With increasing amounts of impulse, radial cracks propagated outward from the central hole and led to a set of four to eight symmetric petals. The amount of normalized impulse (V) required to have radial cracks reached the outer radius of the plate was approximately 3 and 1.8, respectively for $\xi_0 = 0.25$ and 0.5.

The analytically obtained dimensionless crack length $\xi_c = l_c / R_0$ from Eq. (7.47) is compared with those from numerical simulation in Fig. 7.45 over the various ranges of impulse and two different loading radii. Note that the horizontal axis indicates the ratio of applied impulse to the critical value $V_{cr} = 1.24$. One can see that the correlation between two solutions is excellent for all cases.

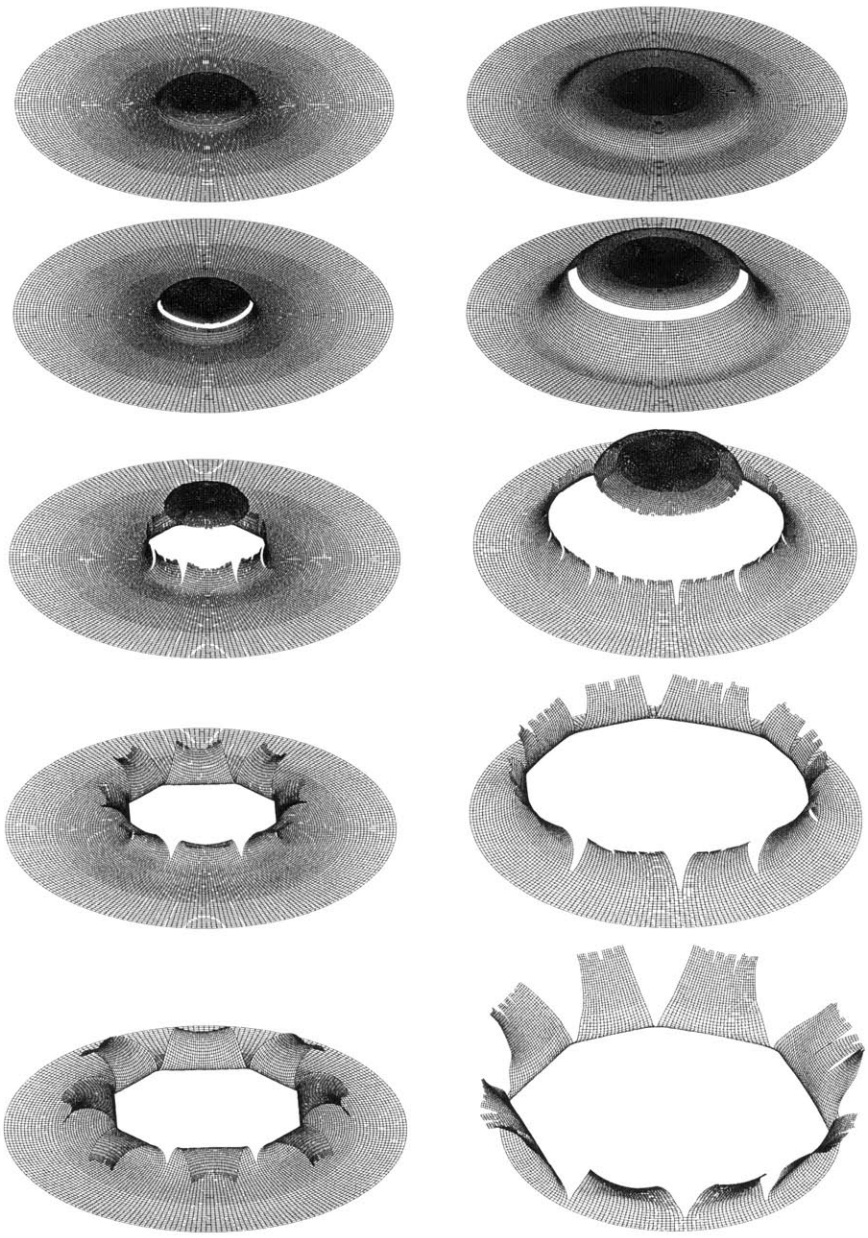

(a) $\xi_0 = 0.25, V = 1.8$ (b) $\xi_0 = 0.5, V = 1.8$

Fig. 7.42 Numerically predicted shape of petals at different values of $\tau = 0.02, 0.06, 0.24, 0.6, 1.3$ using fixed mesh

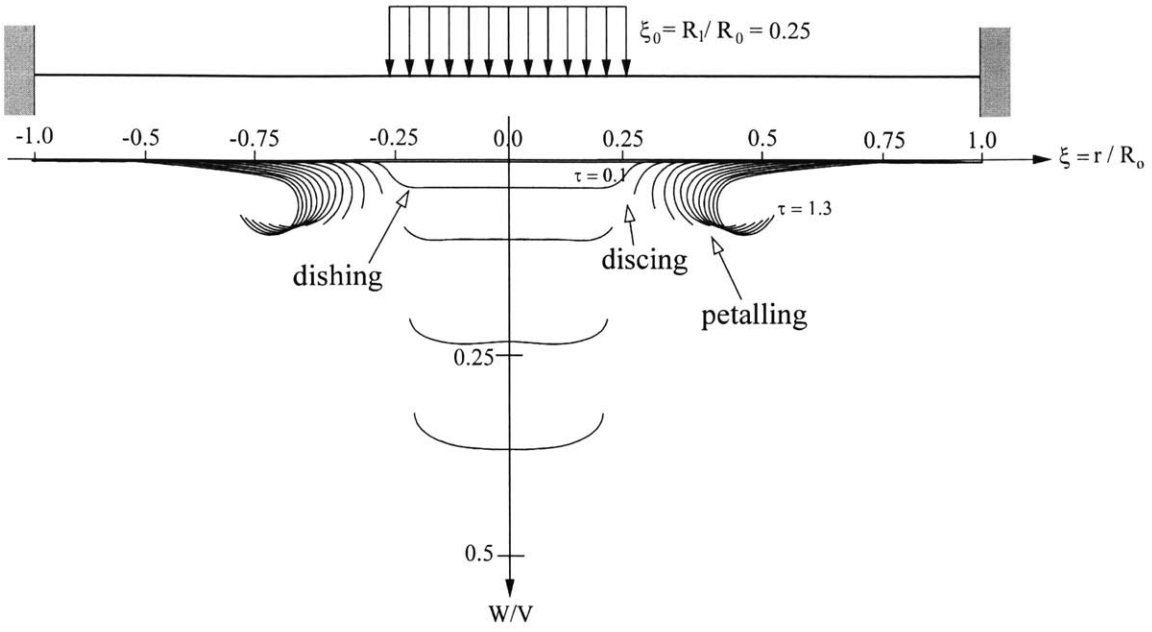

(a) $\xi_0 = 0.25, V = 1.8$

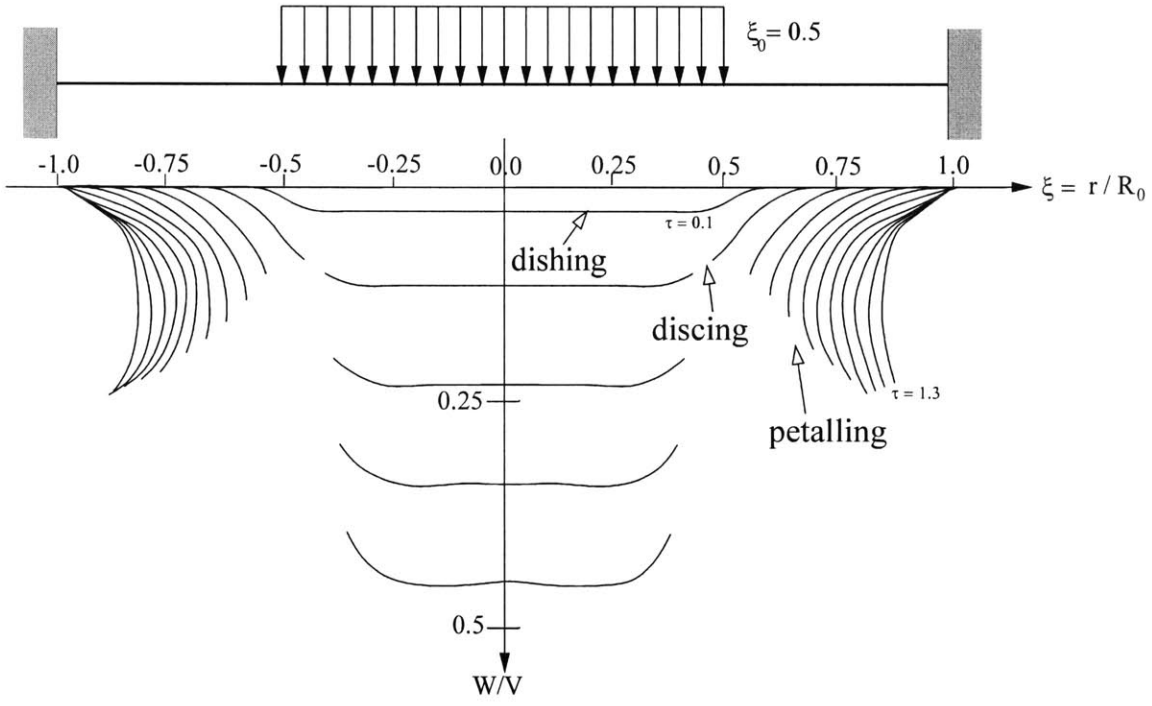

(b) $\xi_0 = 0.5, V = 1.8$

Fig. 7.43 Numerically predicted transient profiles for deflection and petals of circular plate at $\tau = 0.1$ steps ($V = 1.8$)

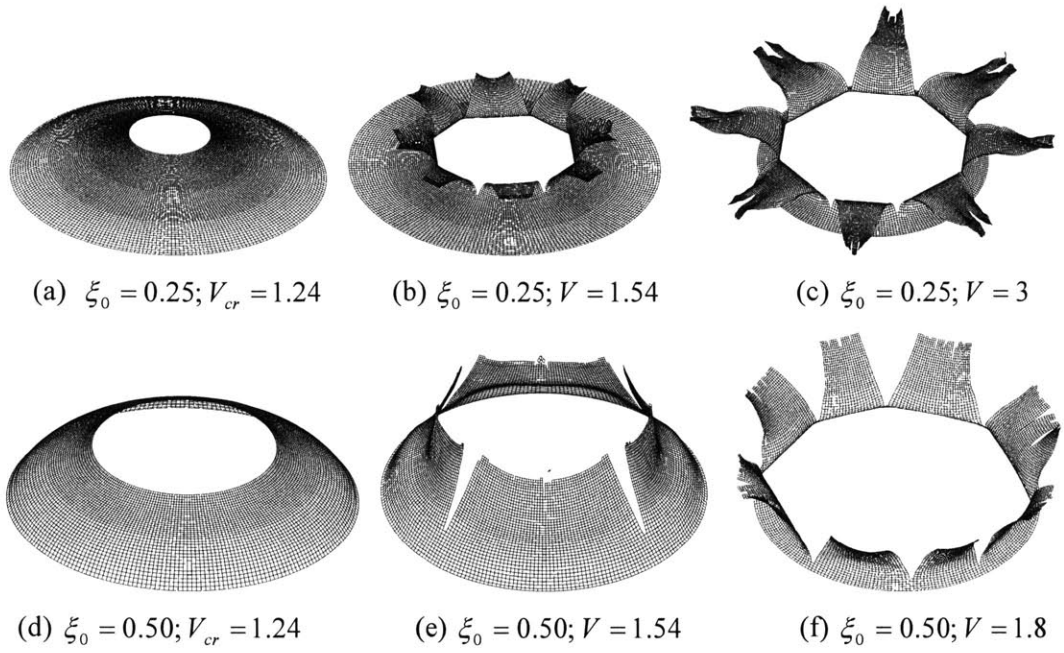

(a) $\xi_0 = 0.25; V_{cr} = 1.24$ (b) $\xi_0 = 0.25; V = 1.54$ (c) $\xi_0 = 0.25; V = 3$

(d) $\xi_0 = 0.50; V_{cr} = 1.24$ (e) $\xi_0 = 0.50; V = 1.54$ (f) $\xi_0 = 0.50; V = 1.8$

Fig. 7.44 Final deformed shapes of circular plates subjected to localized impulsive loading with increasing intensity of impulse (fixed mesh)

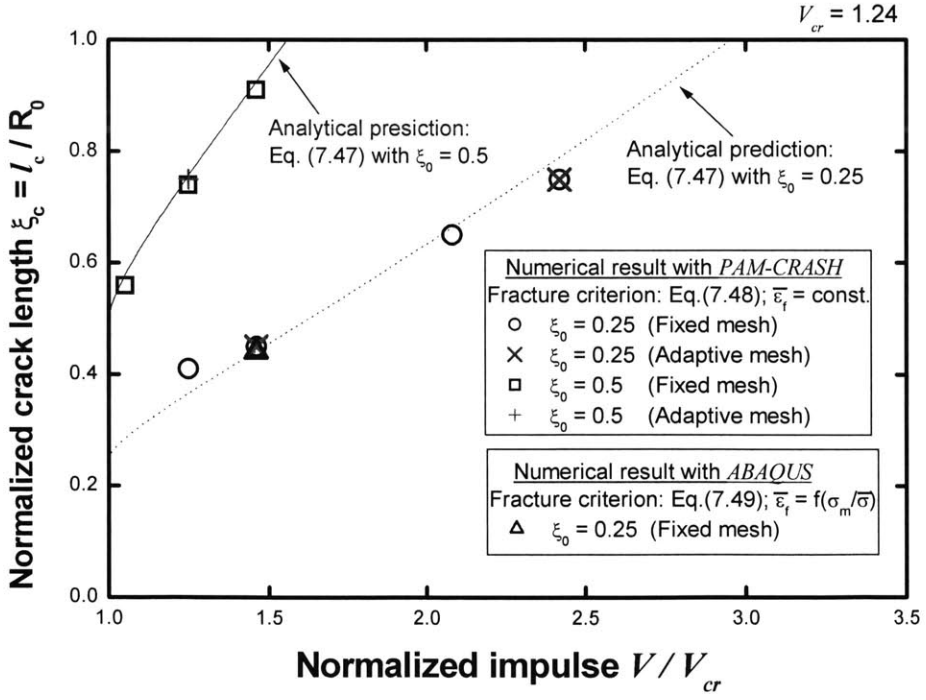

Fig. 7.45 Comparison of normalized crack length ξ_c between numerical and analytical predictions with two different values of ξ_0 and various normalized impulse V / V_{cr}

7.3.7 Conclusion to Chapter 7.3

The onset of fracture and subsequent propagation of radial cracks of thin clamped circular plates under localized impulsive loading were predicted analytically and numerically for discing and petalling stages with increasing intensity of applied impulse and various radii of the loaded area. The equivalent plastic strain to fracture $\bar{\varepsilon}_f$ modified by the stress triaxiality $\sigma_m / \bar{\sigma}$ was shown to be a correct ductile fracture criterion. The present fracture criterion was calibrated by performing finite element calculation of uni-axial tensile test for specimen of the high strength structural AH36 steel. Based on the critical damage value, and calculated distributions and histories of stress and strain, the formation site and extent of fracture were predicted for a range of loading radii and intensity of applied impulse. The main points of present studies are:

- The strain and stress states at the potential fracture points were explored numerically during the petalling process. It was found that the average stress triaxiality at the fracture points is approximately constant, $(\sigma_m / \bar{\sigma})_{av} \cong 0.58$ corresponding to plane strain condition. Hence, the propagation of radial cracks can be reasonably predicted, if the fracture strain is weighted by the average stress triaxiality. Through the comparative study on the propagation of cracks using adaptive and fixed mesh, it was shown that the fracture behavior (the crack length and deformed shape of petals), between two meshes is insignificant, provided the size of elements is sufficiently small in the fixed mesh configuration.
- It was clearly confirmed that the crack length and final deformed shapes of petals are strongly dependent on the loaded area and intensity of applied impulse. Furthermore, the analytical solution for the normalized crack length, developed by Wierzbicki (1999) using the CTOD criterion, was shown to be in good agreement with the numerical solutions over the various range of impulse and two different loading radii.

This page intentionally left blank

Chapter 8

Static and Transient Responses of Double Hulls under Localized Loading

Large scale sandwich panels made of steel offer a great potential of maintaining structural integrity under accidental loads. In the shipbuilding, the concept of a double hull has offered an improved damage protection of oil tankers involved in groundings or collisions. A thorough understanding of the deformation and fracture of the sandwich panels in general and double hulls in particular, subjected to localized explosive loading is essential not only to assess their vulnerability and survivability but also to improve their design. Traditionally, these sandwich panels are composed of two face plates and a quasi-homogeneous core, such as honeycomb, foam, or stainless steel fibers. Larger structures, for example extruded aluminum panels for ICE trains, have a discrete shear web structure. The present thesis is concerned with large scale panels referred in the shipbuilding industry as double hulls. There could be numerous structural arrangements of the interior web system and four such types of discrete structures are considered in this thesis. Much like in the case of thin single plate, a typical failure mode of clamped sandwich panels under dynamic loading condition involves three stages with increasing intensity of applied loading: dishing, discing (capping), and petalling. Chapter 8 deals primarily with the first dishing stage with no fracture. The transient responses including force transmission mechanism, deflection, energy absorption capability, and response time of sandwich structures are numerically investigated. In

Chapter 9, an extensive parametric study on the failure of the sandwich panels with various core arrangements is presented with an emphasis in the latter two stages of deformation involving fracture.

8.1 Formulation of the problem

Consider a fully clamped square double hulls of width $2L_0$ under a localized explosive pressure loading $p(t)$, as defined in Fig. 8.1. As in the case of single, presented in Chapter 7, the explosive loading is idealized by the uniform transversal pressure $p(t)$ applied over a central square region of the plate of width $L_1 \leq L_0$. For the idealized dynamic pressure loading, a notion of the total impulse per unit area $I_0 = \int_0 p(t)dt$ is introduced where t is current time and t_0 is duration of the pressure pulse. In the case of rectangular pressure loading, the magnitude of impulse per unit area is equal to $I_0 = p_0 t_0$ where p_0 is the load intensity.

As shown in Fig. 8.1, the double hulls are comprised of inner and outer hulls connected longitudinally with various arrangements of the core structures. The inner and outer hull act as face plates of a sandwich structure with the addition of longitudinal webs. Four different configurations of the core are considered in the present thesis: Blast Resistant Adaptive Sandwich (hereafter referred to as BRAS), Unidirectionally Stiffened Double Hull (hereafter referred to as USDH), Hat-type corrugated core (hereafter referred to as Navtruss), and Y-type corrugated core (hereafter referred to as Y-web). The new concept of adaptive and reconfigurable sandwich design (i.e. BRAS) that will substantially increase the strength and fracture resistance during dynamic loading event was originally proposed by Wierzbicki (2002). A complete review on the concept of the BRAS is given in Section 8.2. Over the last decade, USDH has been actively developed and used for naval combatants and commercial tankers, see for e.g., Beach (1991), Sikora et al. (1997), Kee et al. (1995), and Paik et al. (1999). Other two types of double hulls are currently available under the commercial name, "Navtruss" and "Y-web", respectively. The concept of "Navtruss" has been around in the Navy for over two decades. The "Y-web" core configuration was recently developed in the Schelde Naval Shipbuilding in Netherlands, Ludolphy (2002).

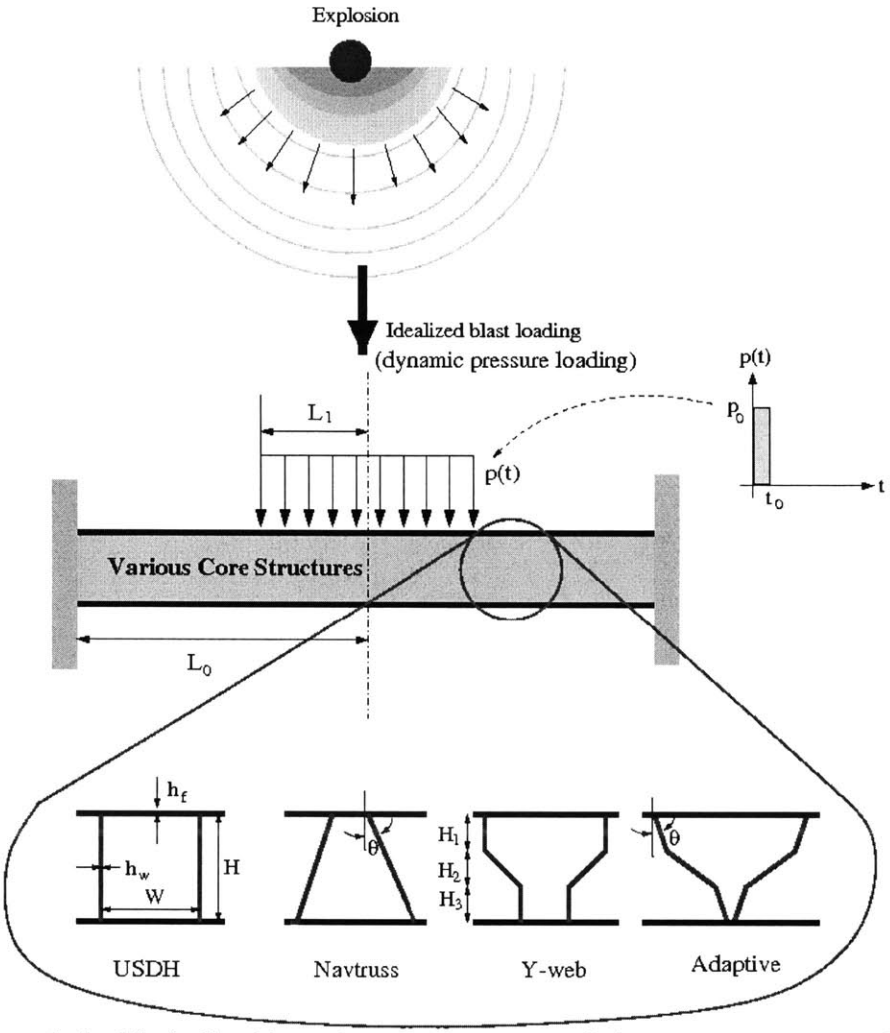

Fig. 8.1 Clamped double hull with various arrangements of the core structure under localized explosive loading

Specification of the core structures Four different geometries of the sandwich panels are defined in Fig. 8.2 where H is the distance between the outer and inner hull (hull separation) and W is the spacing between webs (width of unit cell). The half width L_0 is equal to $L_0 = NW$, where N is the number of cells over the half the plate. In all types of panels considered in the present thesis, the number of cells is fixed ($N = 6$) for simplicity. Note that the close-ups of the periodic units with uniform and non-uniform distribution of thickness over the cross-section are also included in Fig. 8.2 for each type of core structures. The cross-sections on the left for each case indicate the

sandwich panels with uniformly distributed thickness (h_0), while the cross-sections of sandwich panels having different thickness between face sheets (h_f) and web (h_w) are shown on the right. For simplicity, additional restriction was imposed on the thickness distribution, that is, the thickness of the top and bottom face sheets is the same. The inclination angle of transverse webs is denoted by θ. To assess the effect of material distribution on the fracture resistance while maintaining constant cross-sectional area (i.e. constant weight) between the above-mentioned two types of thickness distribution, the dimensionless thickness of a web, $\tilde{h}_w$, and face sheet, $\tilde{h}_f$, normalized by h_0 are introduced:

$$\tilde{h}_w = \frac{h_w}{h_0}, \quad \tilde{h}_f = \frac{h_f}{h_0} \tag{8.1}$$

A constant weight imposes the following relationship between the cross-sectional parameters

$$2Wh_0 + \Omega Hh_0 = 2Wh_f + \Omega Hh_w \tag{8.2}$$

where Ω characterizes different sectional geometries for various types of core structures. In the case of BRAS, Ω is expressed in terms of the input parameters by

$$\Omega = \frac{2}{3\cos\theta} + \frac{1}{3}\sqrt{1+\left(\frac{3W}{H} - 2\tan\theta\right)^2} \tag{8.3}$$

Shown in Eq. (8.8) hull Ω is calculated for all four types of core.

In terms of the dimensionless parameters defined in Eq. (8.1), Eq. (8.2) can be rewritten as

$$\tilde{h}_f = 1 + \Omega\frac{H}{2W}(1-\tilde{h}_w) \tag{8.4}$$

For the case of the sandwich structures with non-uniform distribution of thickness, the mass per unit area, m^*, becomes

$$m^* = 2\rho h_f + \rho\Omega h_w \frac{H}{W} \tag{8.5}$$

where ρ is the density of the material. Note that for the case of single plate $m^* = \rho h$ where h is the thickness of single plate.

Dividing Eq. (8.5) by ρL_0 and introducing dimensionless thickness ratios ($\tilde{h}_w, \tilde{h}_f$), the normalized mass per unit area of the sandwich, $\tilde{m} = m^* / \rho L_0$, takes the form

$$\tilde{m} = 2\tilde{h}_f \frac{h_0}{L_0} + \Omega\tilde{h}_w \frac{h_0}{L_0}\frac{H}{W} \tag{8.6}$$

For given sets of m^*, L_0, and W, the geometry of the BRAS structure shown in Fig. 8.2(a) is uniquely specified by three independent parameters: h_w, θ, and H. As an example, we considered here a local segment of ship hull structure, i.e. half width of the plate $L_0 = 4800mm$ and spacing between periodic webs $W = 800mm$. All the results reported in Chapters 8 and 9 are based on the above geometries. Three respective variables, $\widetilde{h}_w$, θ, and H/W, are considered as geometric parameters in the optimization study of the BRAS presented in Chapter 9. It should be mentioned that the uniform thickness of the plate, h_0, can be obtained by substituting $\widetilde{h}_w = \widetilde{h}_f = 1$ into Eq. (8.6) and is given by

$$\frac{h_0}{L_0} = \frac{\widetilde{m}}{2 + \Omega \dfrac{H}{W}} \tag{8.7}$$

Furthermore, the normalized thickness of the face sheet, $\widetilde{h}_f$, is determined from Eq. (8.4). Note that the Eq. (8.2) and Eqns. (8.4) ~ (8.7) are applicable to other three types of sandwich panels: USDH, Navtruss, and Y-web (see Fig. 8.2(b) ~8.2(d)). As mentioned before, the different sectional geometries of those structures are specified by the parameter Ω for each type of cores, according to

$$\Omega = \begin{Bmatrix} 1, & USDH \\ \sqrt{1+\tan^2\theta}, & Navtruss \\ \dfrac{2}{3} + \dfrac{1}{3}\sqrt{1+\tan^2\theta}, & Y-web \end{Bmatrix} \tag{8.8}$$

As compared to the BRAS, the geometry of USDH is determined by only two independent variables, h_w and H, due to the absence of inclination angle of web θ. Consequently, $\widetilde{h}_w$ and H/W are employed as variables for the optimization study of the USDH, see Chapter 9. Note that the inclination angle of core θ is also related to the normalized core height, i.e. $W_1 / H = \tan\theta$ (Navtruss); $W / H = \tan\theta$ (Y-web), for the cases of Navtruss and Y-web shown in Fig. 8.2(c) and 8.2(d).

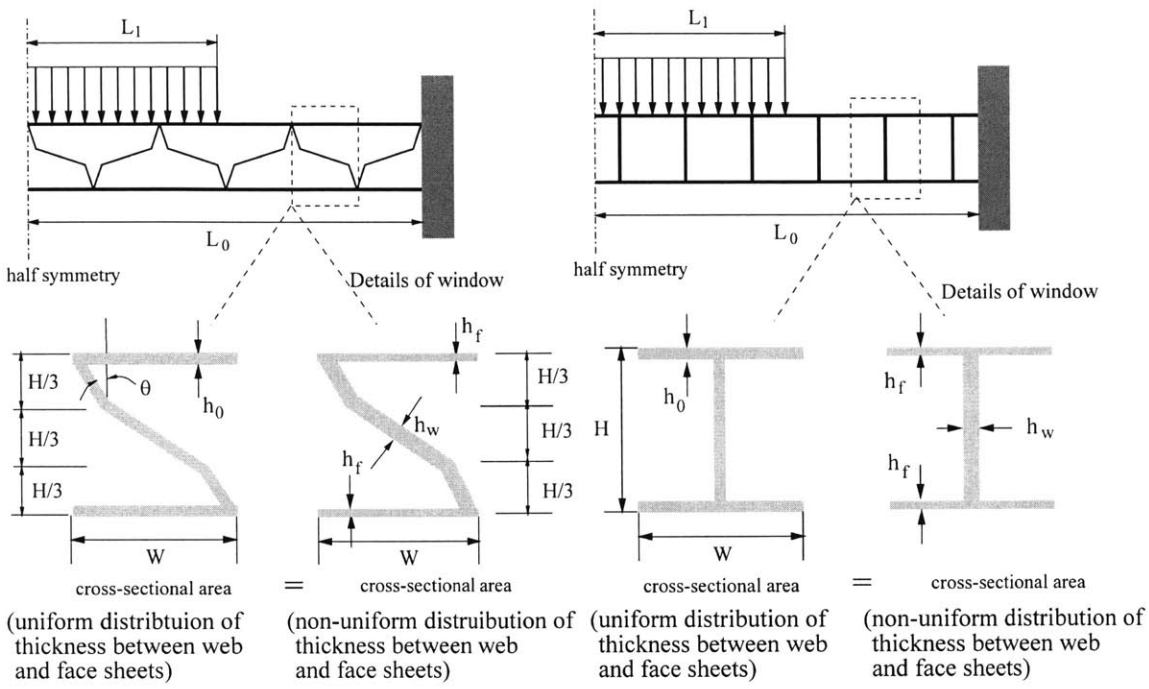

(a) Blast Resistant Adaptive Sandwich (BRAS) (b) Unidirectionally Stiffened Double Hull (USDH)

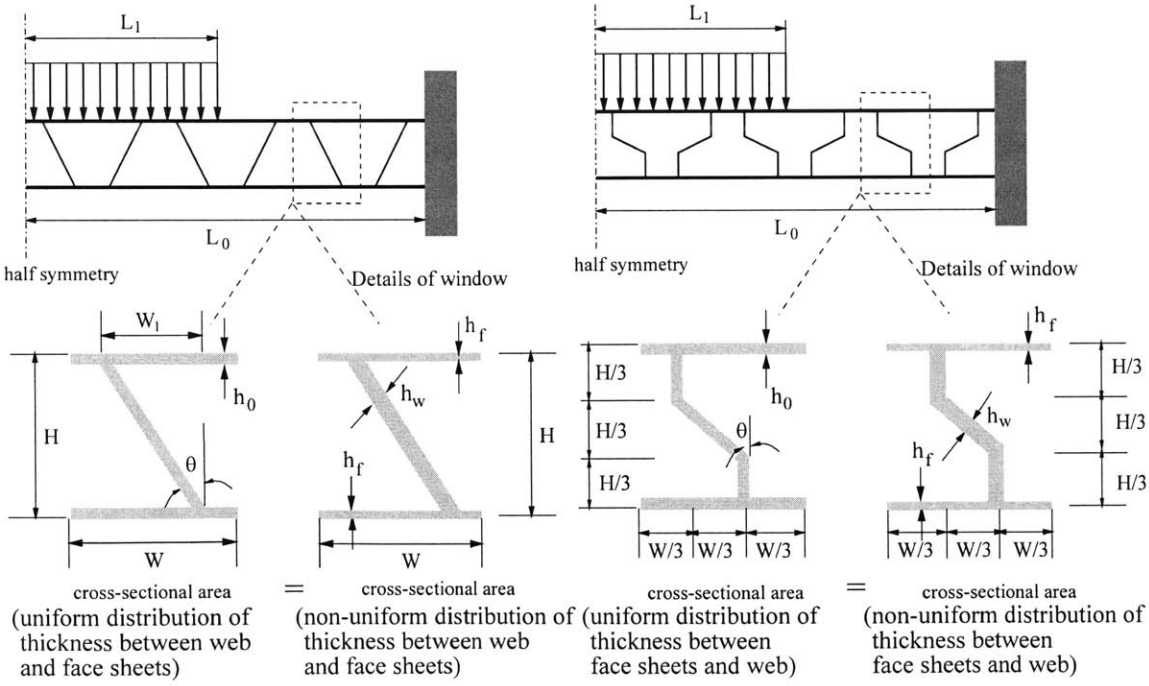

(c) Hat-type corrugated core (Navtruss) (d) Y-type corrugated core (Y-web)

Fig. 8.2 Configurations of double hulls with four different types of core. Note that the half width of plate L_0, the width of applied pressure L_1, and the width of unit cell W are fixed at L_0 = 4800mm, L_1 = 2400mm, and W = 800mm in the present numerical study.

8.2 Concept of Blast Resistant Adaptive Sandwich (BRAS) structure

Partition of energy dissipation and critical dishing energy Figure 8.3 shows the partition of dissipated energy in three major deformation modes of the single circular plate subjected to impulsive loading: dishing, discing, and petalling (Wierzbicki (2001)). Typically, a substantial portion of the energy is dissipated in the dishing mode. Assuming rigid-plastic material with an average flow stress σ_0 defined by Eq. (7.1) and neglecting bending resistance of the plate, the energy of deformation can be approximated as membrane energy dissipation:

$$E_{dish} = \int_0^{2\pi} \int_0^{R_e} \sigma_0 h \varepsilon_r r dr d\theta \tag{8.9}$$

where h and R_e are respectively plate thickness and the extent of deformation zone; ε_r is the radial component of strain tensor. An upper bound for the magnitude of the dishing energy, E_{dish}^{U}, can be found by substituting $\varepsilon_r = \varepsilon_f$ into Eq. (8.9) and takes the form

$$E_{dish}^{U} = \pi R_e^2 \sigma_0 h \varepsilon_f \tag{8.10}$$

where ε_f is the uniaxial strain to fracture. Notwithstanding the approximate character of Eq. (8.10) it identifies all major parameters that control the magnitude of the dishing energy. The presence of the product $\sigma_0 \varepsilon_f$ emphasizes the importance of the proper choice of the material. In a single skin plate, R_e is the distance to the nearest fixed boundary. In sandwich panels, the upper face sheet is continuously supported by the core material. Therefore, the effective deformation radius R_e of sandwich panels can be related to the crushing resistance of core structure.

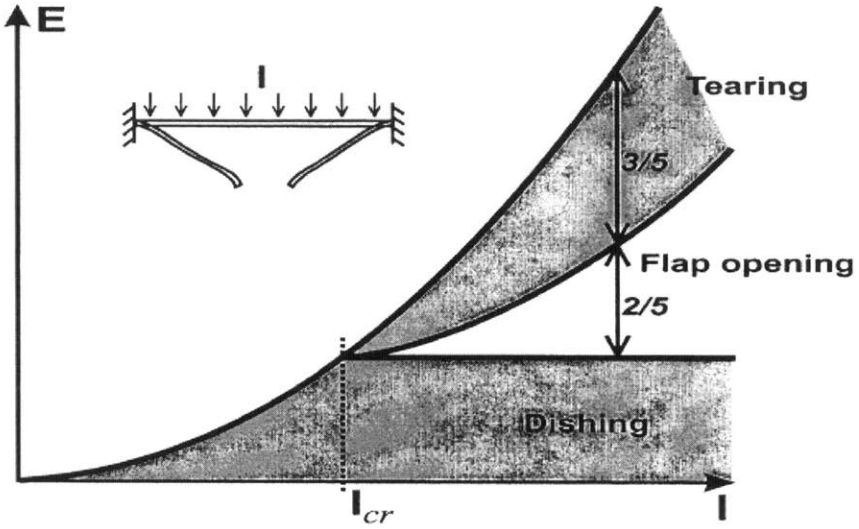

Fig. 8.3 Partition of plastic work between dishing, flap opening (discing), and tearing (petalling) in impulsively loaded circular plate as a function of the applied impulse, I (after Wierzbicki, 2001)

Relation between energy dissipation and crush resistance of core The plastic work dissipated in stretching the face sheets and crushing the core can be found by considering the equivalent plastic work dissipated in static indentation of a membrane bonded to a rigid-plastic foundation, see Fig. 8.4. This problem is solved by Wierzbicki et al. (1995) based on the assumption that top face sheet indentation of the sandwich could be described by the indentation response of a membrane resting on a rigid-plastic foundation. The rigid-plastic foundation force was represented by crushing strength of the core. Moreover, they assumed that impact response of the sandwich panel could be derived from the static indentation response of the panel since the work absorbed in top face sheet indentation was approximately the same in both cases. The solution proposed by Wierzbicki et al. (1995) was extended by Hoo Fatt and Park (2000) where the shear strength of the core is taken into account. Here only the result for the effective deformation radius R_e associated with the crushing strength of core is summarized. For a complete review, the readers are suggested to refer to the above references.

Consider the top face sheet of the sandwich structure statically indented by a circular punch with radius R_1, as show in Fig. 8.4. The thickness of the face sheet is h_f. The indentation force is denoted by P. The corresponding displacement vectors of the face sheet in the z, r, θ directions shown in Fig. 8.4 are denoted by w, u, v, respectively. For a given indentation depth, the extent of plastic

deformation in the radial direction is indicated by R_e (i.e. effective deformation radius). The crushable core is modeled as a rigid-plastic foundation with resistance equal to the average crushing resistance q. Due to rotational symmetry v = 0. The radial displacement vanishes at r = 0 (due to symmetry) and at the outer boundary r = R_e. It is reasonable to assume that u = 0 everywhere in the plate that is securely bonded to the core. The bending resistance of the plate is negligible when compared to its membrane forces since the plate deflections are greater than the plate thickness. Assuming rigid-plastic material, one gets that the radial membrane force reaches a fully plastic yield condition when $N_r = N_0 = \sigma_0 h_f$. Assuming moderately large deflection and using u = v = 0, the components of strain tensor are given by

$$\varepsilon_r = \frac{\partial u}{\partial r} + \frac{1}{2}\left(\frac{\partial w}{\partial r}\right)^2 = \frac{1}{2}\left(\frac{\partial w}{\partial r}\right)^2 \tag{8.11}$$

$$\varepsilon_\theta = \frac{1}{r}\frac{dv}{d\theta} + \frac{u}{r} = 0 \tag{8.12}$$

Vertical equilibrium of the plate outside the punch gives the following differential equation for the vertical deflection w(r):

$$N_0 \frac{\partial}{\partial r}\left(r\frac{\partial w}{\partial r}\right) = qr, \qquad R_1 < r < R_e \tag{8.13}$$

The boundary conditions are

$$2\pi R_1\left(N_0 \frac{\partial w}{\partial r}\right) = -(P - \pi R_1^2 q), \quad r = R_1 \tag{8.14}$$

$$w = 0, \qquad r = R_e \tag{8.15}$$

The left-hand side of Eq. (8.14) represents the total vertical force developed in the face sheet. It must be equilibrated to the difference between the total indentation force P and the crush resistance of the core under the punch.

Integrating Eq. (8.13) twice with respect to the radial coordinate, r, and using boundary conditions in Eqns. (8.14) and (8.15) gives

$$N_0 w = \frac{P}{2\pi}\ln\left(\frac{R_e}{r}\right) - \frac{q}{4}\left(R_e^2 - r^2\right) \tag{8.16}$$

where R_e is an unknown function of the indentation load P.

Applying condition of kinematic continuity to the displacement field given in Eq. (8.16) gives a simple relationship between P and R_e:

$$P = \pi q R_e^2 \tag{8.17}$$

Fracture in a thin face sheet occurs when the maximum radial strain reaches a critical value. Furthermore, Eq. (8.11) implies that the radial strain is largest at $r = R_1$. This gives

$$\frac{\partial w}{\partial r} = \sqrt{2\varepsilon_f}, \quad \text{at } r = R_1 \tag{8.18}$$

The slope can be found from Eqns. (8.16) and (8.17):

$$\frac{\partial w}{\partial r} = \frac{q}{2N_0}\left(r - \frac{R_e^2}{r}\right) \tag{8.19}$$

Applying Eq. (8.19) to (8.18) gives the extent of the deformation zone R_e at which fracture will occur

$$R_e = R_1\sqrt{1 + 2\sqrt{2\varepsilon_f}\,\frac{\sigma_0 h_f}{qR_1}} \tag{8.20}$$

which implies that the effective deformation radius is increasing with the amount of dishing and is proportional to $R_e \approx \sqrt{\frac{\sigma_0}{q}}$ for given punch radius, thickness and material of face sheet. Hence, referring to Eq. (8.10), it is evident that the smaller crushing and shear strengths of the core are, the larger is the spread of plastic deformation and the absorbed energy.

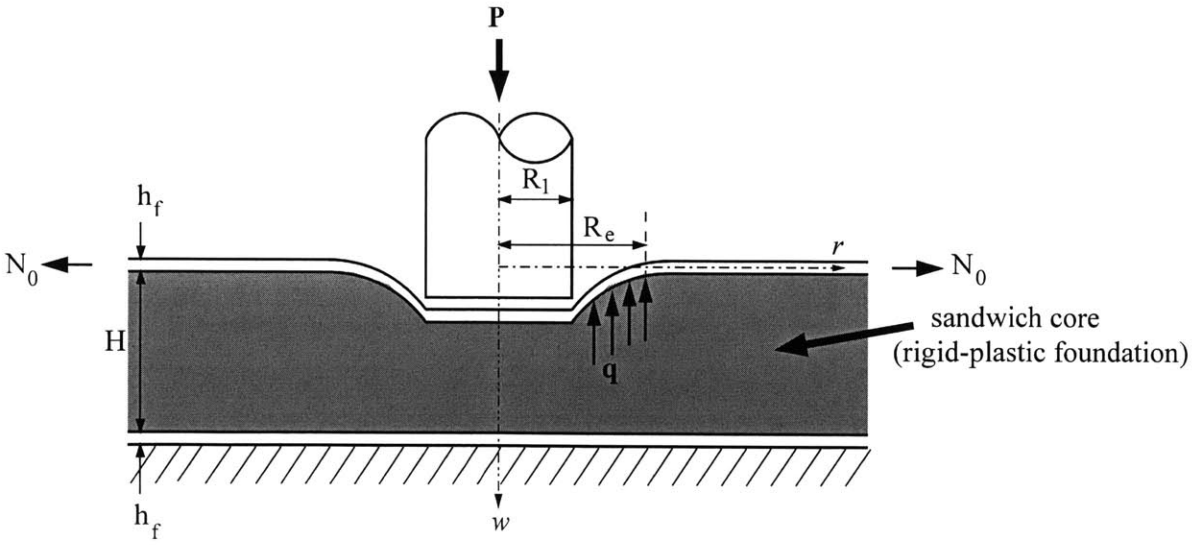

Fig. 8.4 Geometry of the sandwich panel subjected to indentation by a circular punch (after Wierzbicki, 1995)

Blast Resistant Adaptive Sandwich (BRAS) In order to improve the fracture resistance of double hull, inner hull fracture should be minimized while the plastic energy dissipation capacity of the core should be maximized. For the dishing phase, the ideal behavior of sandwich panel is that the top face plate deforms independently from the lower face plate and that the girders are crushed very easily without imposing any deformation to the lower plate. However, the tearing strength and the flap curling resistance of the sandwich panel will be significantly increased if both faceplates are working together. In other words, the sandwich core should be weak in the dishing phase but strong in the petalling phase. To achieve this conflicting demand, Blast Resistance Adaptive Sandwich (BRAS) structure, as schematically shown in Fig. 8.5, has been developed in the present thesis. It should be mentioned that the basic concept of the BRAS was proposed by Wierzbicki (2002). The initial intact and partially damaged configurations of the BRAS are shown on the top of Fig. 8.5. The corresponding variation of crushing strength of the core structure is presented on the bottom of this figure. In next Section 8.3, it will be shown that the static crushing strength of the proposed core after initial collapse is an order of magnitude larger than that of the original intact structure, which is highly beneficial to increase the petalling resistance of the sandwich panel.

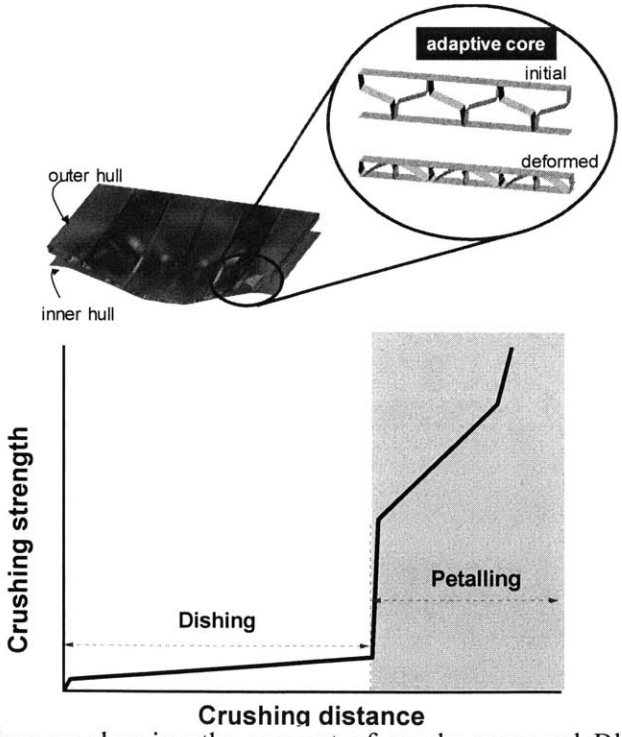

Fig. 8.5 A schematic diagram showing the concept of newly proposed Blast Resistant Adaptive Sandwich (BRAS) structure; original intact and partially damaged configurations of BRAS panel during dynamic pressure loading event (top); desirable variation of core strength for the improvement of fracture resistance of sandwich panel (bottom)

8.3 Static crushing strength of sandwich core structures

Consider unit cell of the width W and the height H of sandwich panels subjected to in-plane transverse load P between two parallel rigid platens, as defined in Fig. 8.6. The geometry of the BRAS is shown in this figure as an example. The explicit non-linear finite element code *PAM CRASH* was employed to calculate the quasi-static process of lateral crush. An element size (16×16mm), which is same as the thickness of face sheet, was used to capture the local bending and folding modes of the crushed webs in realistic manner. For the boundary conditions, the bottom face sheet remained stationary throughout the compression while rigid loading platen was assumed to move with a downward velocity into the upper face sheet. Since the folding location throughout the web is unknown, the self-contact (contact algorithm #36 using "3D bucket" global search algorithm) provided by *PAM-CRASH* was used. This type of contact algorithm could automatically keep the entire mesh from interpenetrating during the analysis. The material considered in Chapters 7, 8 and 9 was high strength AH36 steel and detail information on this material is given in Chapter 7.3.2.

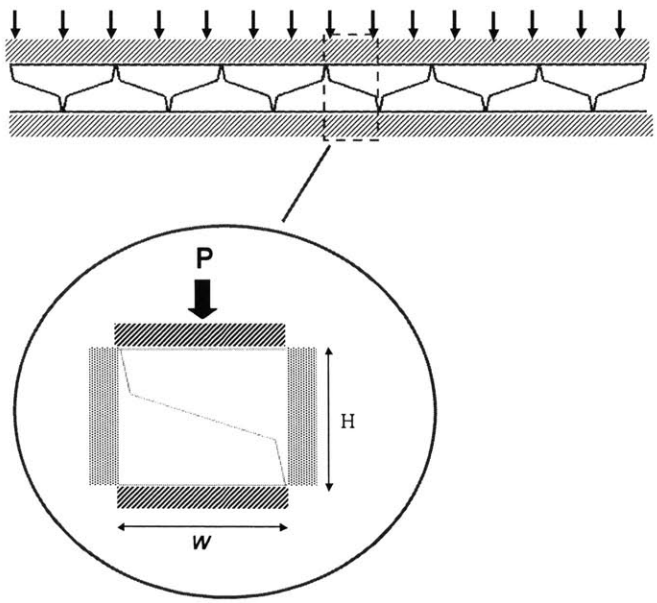

Fig. 8.6 Unit cell of sandwich panel compressed between two rigid platens. Note that all dimensions are in mm (H = W = 800mm; B = 150mm where B is the width of unit cell in longitudinal direction; $h_f = 16mm; h_w = 10mm$)

Instantaneous crushing force and collapse mode Figures 8.7 ~ 8.10 show the instantaneous crushing force response of the sandwich panels with four different core arrangements. In these figures, the instantaneous crushing resistance is denoted by q:

$$q(\delta) = \frac{P(\delta)}{WB} \tag{8.21}$$

where P and δ are respectively instantaneous crushing force and shortening distance; W and B are the width of unit cell in the horizontal and longitudinal direction, respectively. Besides, the associated deformation modes are included in these figures at various stages of the crushing process. One can see that the USDH and the Navtruss develop high initial peak load followed by rapid drop of crush resistance (see Figs. 8.7 and 8.8). On the other hand, the crushing response of the BRAS and the Y-web can be dividend into two stages (see Figs. 8.9 and 8.10). Over the 2/3 of the panel height, the BRAS and the Y-web give a relatively low-level crush resistance. However, the crushing resistance increases by an order of magnitude over the remaining 1/3 of the panel height.

Mean crushing force The above observations can be further confirmed in Fig. 8.11 where the mean crushing strength q_m, defined by Eq. (8.22), is plotted as a function of shortening distance δ.

$$q_m = \frac{1}{\delta_f}\int_0^{\delta_f} \frac{P(\delta)}{WB} d\delta \tag{8.22}$$

The maximum value of δ_f is taken as 0.9H in this calculation. For the cases of the BRAS and the Y-web, the mean crushing strengths corresponding to the two distinct stages are

$$q_m^I = \frac{1}{\delta_c}\int_0^{\delta_c} \frac{P(\delta)}{WB} d\delta, \quad q_m^{II} = \frac{1}{\delta_f - \delta_c}\int_{\delta_c}^{\delta_f} \frac{P(\delta)}{WB} d\delta \tag{8.23}$$

where $\delta_c = 2H/3$ is the critical distance at which sharp increase of crushing force occurs. The numerical values of mean crushing strength are summarized in Table 8.1.

It can be clearly seen that the crushing strength of the BRAS shows a superior increase in the second stage ($q_m^{II}/q_m^I = 40.28$), as compared to the first stage. This increase of crushing resistance comes from multiple internal contacts between transverse web members and face sheets, especially due to the touching between upper/lower segments of web and face sheets. As may be seen in Fig. 8.10, the BRAS gradually collapses to a shape that is stable and much stiffer than the initial shape. As also discussed in previous Section 8.2, this crushing behavior of the BRAS will substantially increase energy dissipation capability and fracture resistance of sandwich panel under impulsive

loading. The much stiffer configuration of BRAS in the second stage will enable the structure to resist the blast pressure and maintain the separation of the face sheets allowing them to undergo further plastic deformation before fracture.

Three additional runs were performed to investigate the effect of inclination angle of web (θ) on the crushing resistance of BRAS, as shown in Fig. 8.12. In this figure, the angle θ ranges from 10^0 to 50^0 and all other parameters are fixed at H = W = 800mm, h_f = 16mm, and h_w = 10mm. It can be observed that the BRAS with $\theta = 10^0$ shows lower crushing resistance in the first stage, while its resistance reveals larger increase than other cases in the remaining second stage. It is interesting to note that the optimum solution for the angle is $\theta = 10^0$ to minimize fracture damage of inner hull of the BRAS structure, according to the optimization study presented in Chapter 9 (see also Fig. 9.18).

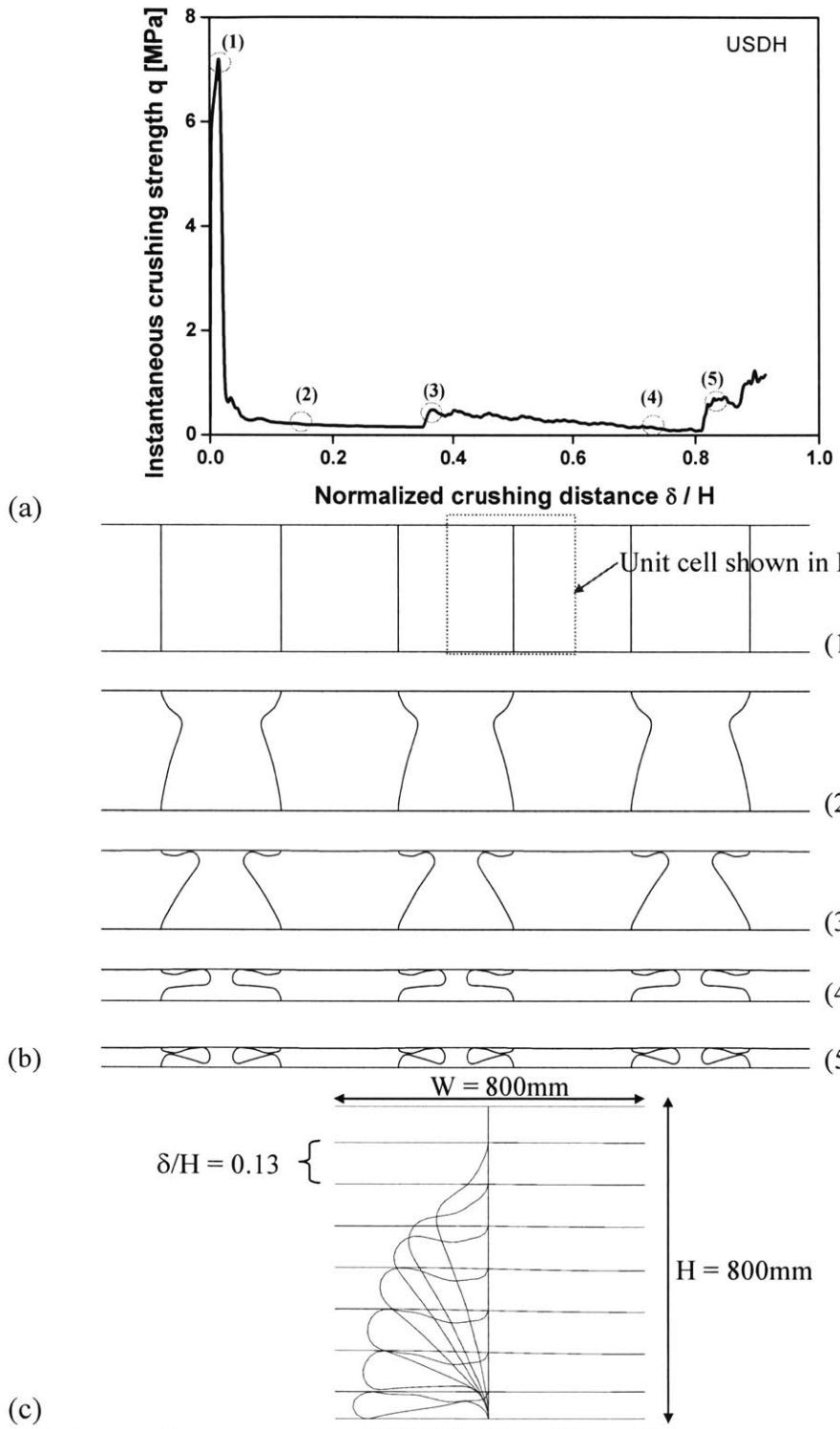

Fig. 8.7 Static crushing responses of USDH (H = W = 800mm; $h_f = 16mm; h_w = 10mm$); (a) instantaneous crushing force versus normalized crushing distance; (b) sequential deformation patterns; (c) overlapped collapse mode of unit cell at δ/H = 0.13 steps

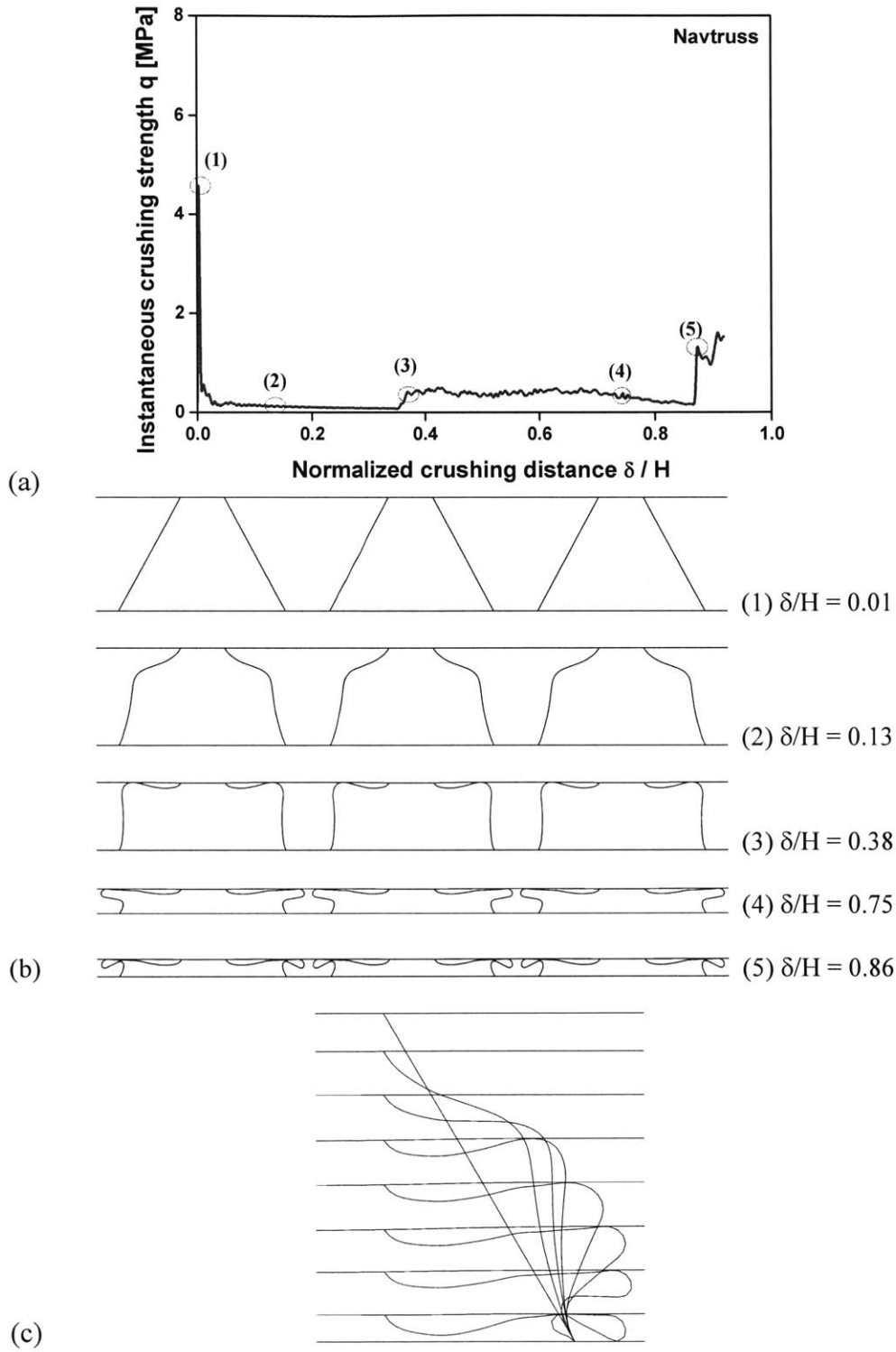

Fig. 8.8 Static crushing responses of Navtruss (H = W = 800mm; $h_f = 16mm; h_w = 10mm$); (a) instantaneous crushing force versus normalized crushing distance; (b) sequential deformation patterns; (c) overlapped collapse mode of unit cell at δ/H = 0.13 steps

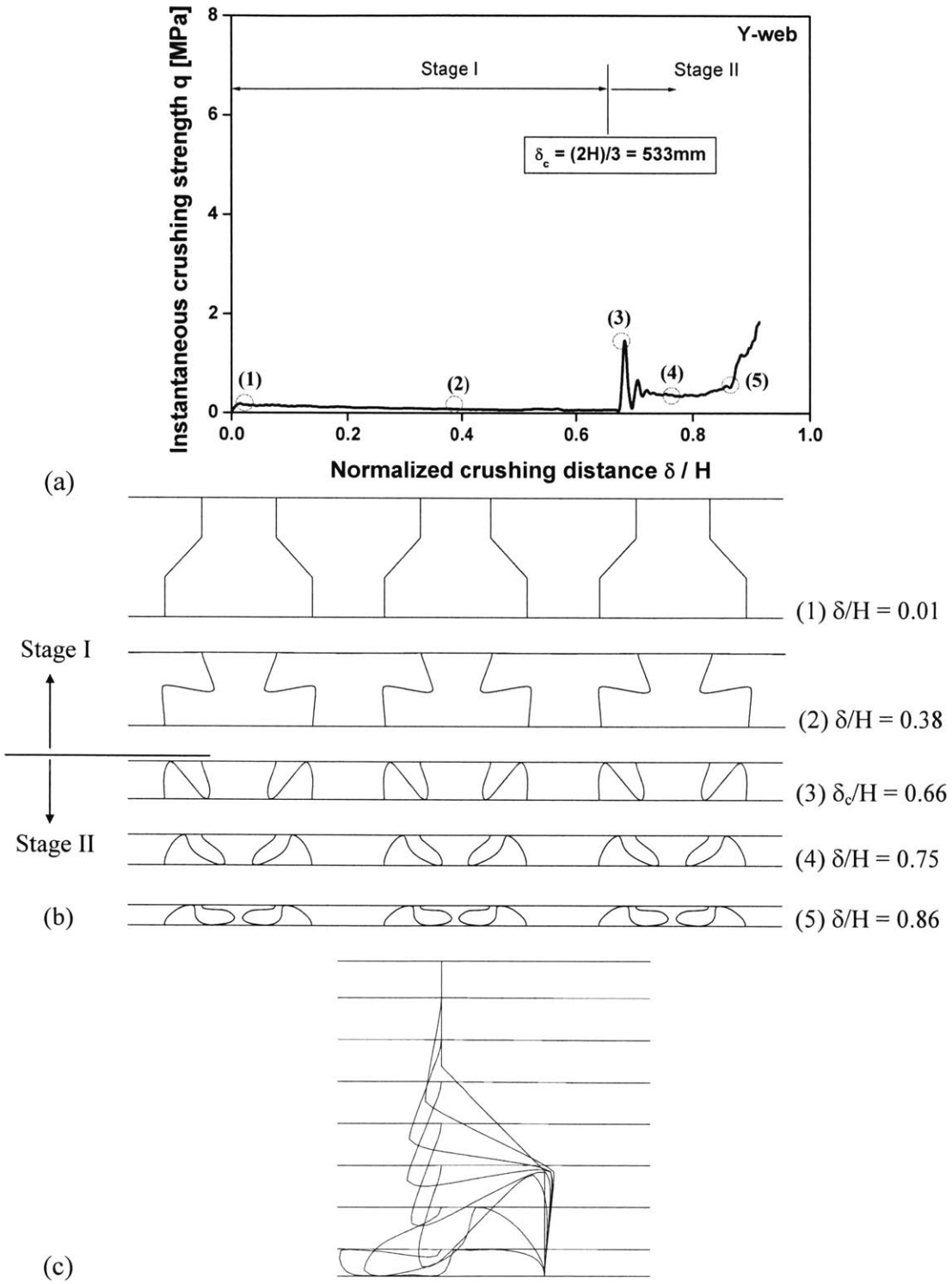

Fig. 8.9 Static crushing responses of Y-web (H = W = 800mm; $h_f = 16mm; h_w = 10mm$); (a) instantaneous crushing force versus normalized crushing distance; (b) sequential deformation patterns; (c) overlapped collapse mode of unit cell at δ/H = 0.13 steps

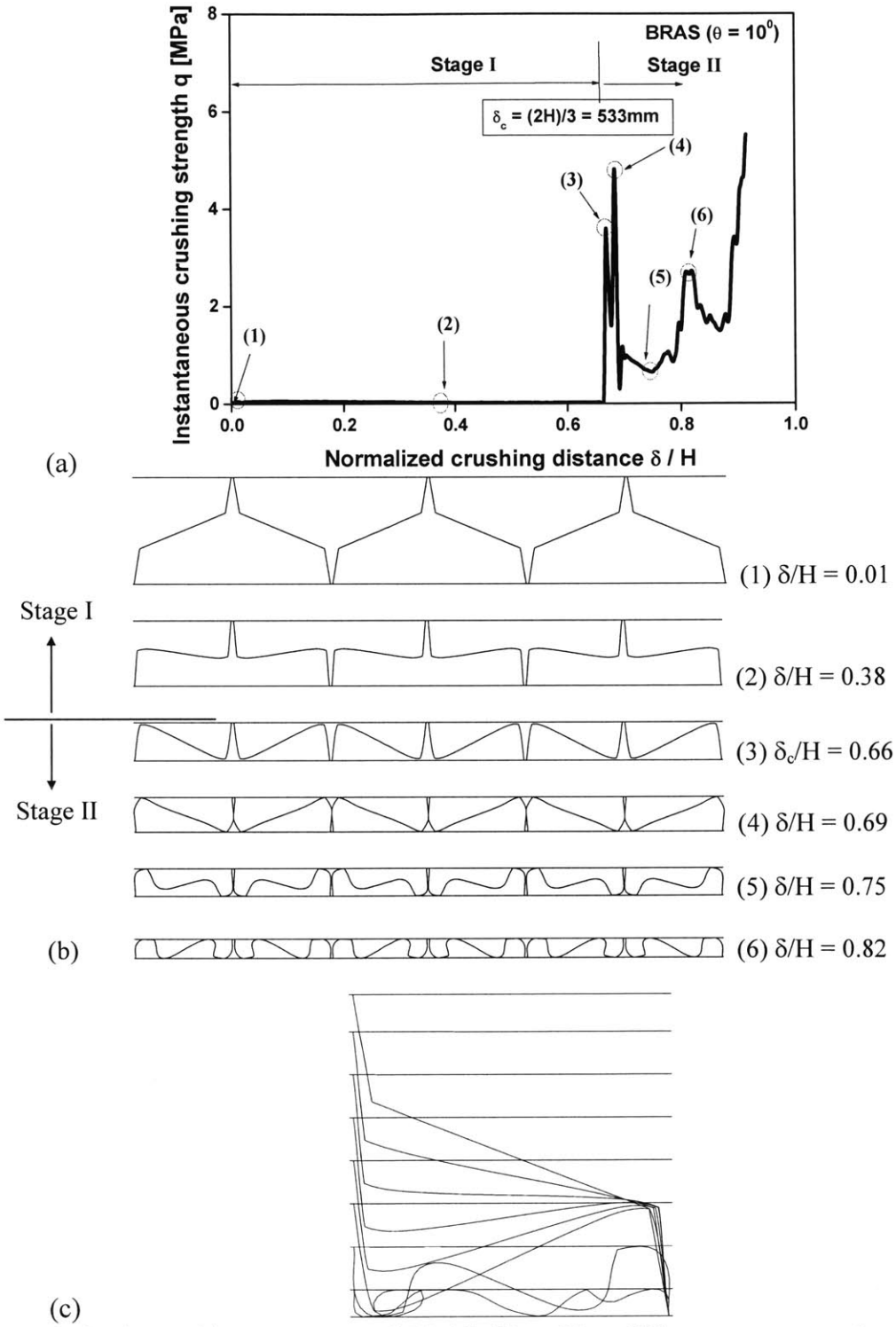

Fig. 8.10 Static crushing responses of BRAS (H = W = 800mm; $h_f = 16mm; h_w = 10mm$); (a) instantaneous crushing force versus normalized crushing distance; (b) sequential deformation patterns; (c) overlapped collapse mode of unit cell at δ/H = 0.13 steps

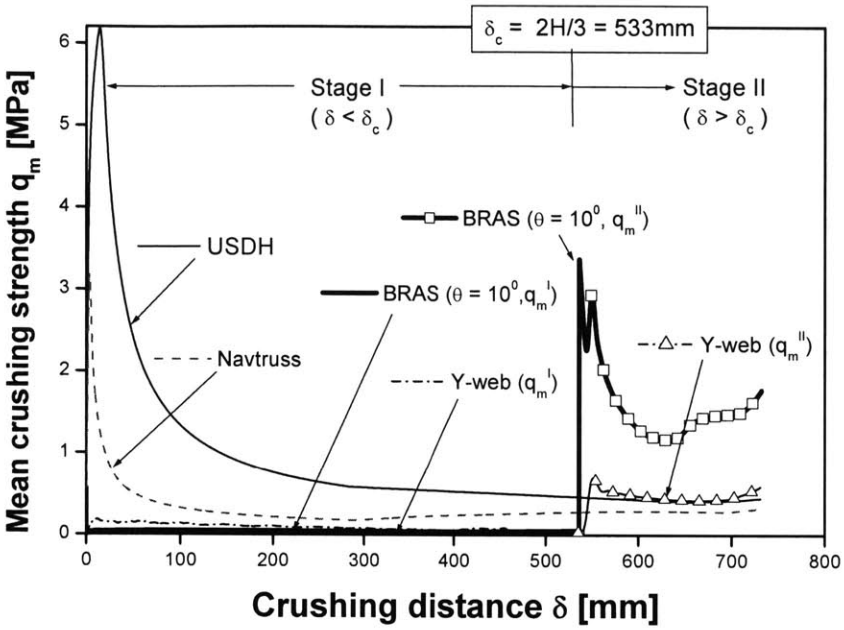

Fig. 8.11 Mean crushing response of sandwich structures with four different core arrangements (H = W = 800mm; $h_f = 16mm$; $h_w = 10mm$)

Table 8.1 Summary of mean crushing strength of unit cell

Type of web	q_m^I (MPa)	q_m^{II} (MPa)	q_m^{II} / q_m^I
USDH	0.048	0.048	1.0
Navtruss	0.027	0.027	1.0
Y-web	0.097	0.049	5.05
BRAS	**0.036**	**1.450**	**40.28**

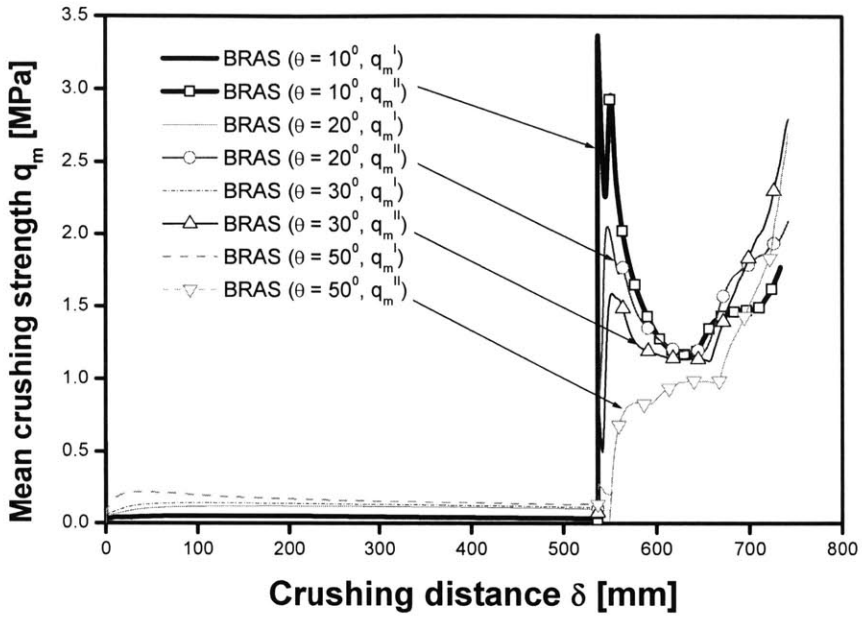

Fig. 8.12 Mean crushing response of the BRAS with four different angles of web, θ (H = W = 800mm; $h_f = 16mm; h_w = 10mm$)

8.4 Transient responses of double hulls under impulsive loading (dishing)

A comprehensive numerical study is presented of the transient responses of clamped sandwich panels to central impulsive loading, shown in Fig. 8.1. A detail description of Finite Element (FE) model and analysis is given in Chapter 9.3.1. Note that fracture is not considered in this Section 8.4 since the range of applied impulse is relatively low ($V < 0.4$), where V is the dimensionless impulse defined by $V = \frac{I_0}{m^* c}$ (see also Eq. (9.4)). Fracture under higher intensity of loading ($V >> 0.4$) is presented in Chapter 9. In all numerical simulations reported in this Section 8.4, the magnitude of applied impulse was I_0 = 35.8 kPasec and the corresponding normalized impulse was V = 0.35 calculated from Eq. (9.4) for the specific value of $\tilde{m} = 0.01$.

In Section 8.4.1, the deformation and energy dissipation characteristics of the BRAS is compared to that of other three core configurations (USDH, Navtruss, Y-web) having the same

weight, see Table 8.2. A parametric study on the dynamically loaded BRAS with various spatial and temporal distributions of dynamic pressure is then carried out in Section 8.4.2. Moreover, a parametric investigation of energy dissipation capabilities and central deflection is conducted for the types of BRAS and USDH with respect to the thickness and angle of web (see Section 8.4.3).

8.4.1 Comparison of four different core arrangements

Plastic energy dissipation and response time The time histories of total plastic energy dissipated in the double hulls are shown in Fig. 8.13 for various types of core structure. Also the corresponding contributions of the face sheets and cores of the double hulls to energy dissipation are shown in Fig. 8.14 together with deformation modes at t = 2msec and 10msec for each of the double hulls. Note that all structures shown in those figures are of the same weight $\widetilde{m} = 0.01$ and are subjected to the same initial impulse $V = I_0 /(c\rho L_0 \widetilde{m}) = 0.35$ with time duration t_0 = 1msec. One can see from Fig. 8.13 that the USDH (thin solid line) and the Navtruss (dashed line) reveal higher energy dissipation up to the time t = 3.5msec than the BRAS and the Y-web. On the other hand, the BRAS (thick full line) shows the highest energy dissipation in the reaming stages of deformation (t > 3.5msec). The above observations can be explained by the deformation modes and the history plots of component energy dissipation shown in Fig. 8.14. It can be seen that both face sheets and cores undergo plastic deformation in the earlier stages of the deformation for the cases of USDH and Navtruss. However, the face sheets and cores of the BRAS and the Y-web deform successively, one after another (i.e. in the sequence of top face sheet, core, and bottom face sheet). Approximately after time t = 3.5msec, a substantially greater fraction of energy is dissipated by the core, especially in the BRAS. Note that a series of deformation modes is shown in Figs. 8.16 ~ 8.19 for each of the sandwich panels.

Figure 8.15 shows the plot of the central deflection versus time of the face plates. One can see that the bottom face sheet of the BRAS starts to deform at t = 4msec, which is 4 times longer than the time duration of blast t_0 = 1msec. In the impulsively loaded double hull, the nature of impulse transfer by the energy absorbing structure such as web to the bottom face sheet is a very important aspect of the response. Here the objective should be to extend the duration of the deformation so that energy absorption is maximized. The extension of the response time in the bottom face sheet (t_{cb}), as defined by Eq. (8.24), indicates that more time is available for dissipation of input energy in the form of plastic deformations and thereby providing an effective blast isolation.

$$\left.\begin{matrix} w_0(\text{bottom}) = 0, & t < t_{cb} \\ w_0(\text{bottom}) \geq 0, & t \geq t_{cb} \end{matrix}\right\} \tag{8.24}$$

where $w_0(\text{bottom})$ denotes the central deflection of the bottom face plate (inner hull). The numerical values of the t_{cb} are summarized in Table 8.3 for each of the double hulls.

Table 8.2 Summary of parameters for the sandwich panels considered in Sections 8.4.1 and 8.4.2 ($H = W = 800$mm)

Parameters	USDH	Navtruss	Y-web	BRAS
$\widetilde{m}$	**0.01**	**0.01**	**0.01**	**0.01**
H/W	1.0	1.0	1.0	1.0
θ	-	30^0	45^0	10^0
Ω	1.0	1.15	1.14	1.62
h_0	16.0mm	15.24mm	15.3mm	13.26mm
$\widetilde{h}_w$	1.0	0.91	0.92	0.75
(h_w)	(16.0mm)	(13.9mm)	(14.0mm)	(10.0mm)
$\widetilde{h}_f$	1.0	1.05	1.05	1.21
(h_f)	(16.0mm)	(16.0mm)	(16.0mm)	(16.0mm)

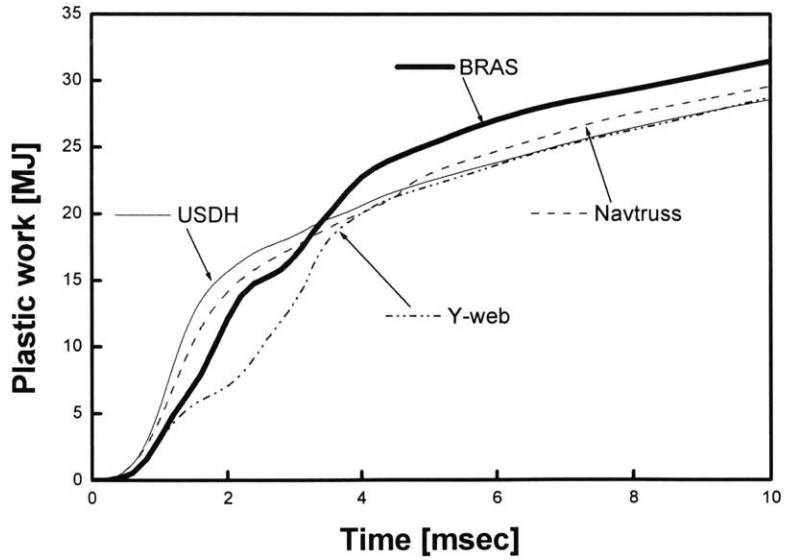

Fig 8.13 The time history of plastic work in sandwich panels with $\widetilde{m} = 0.01$ and subjected to $V = I_0/(c\rho L_0 \widetilde{m}) = 0.35$. Note that normalized loading area $\eta_0 = (L_1/L_0)^2 = 0.25$ and time duration of pressure pulse $t_0 = 1m\sec$. All geometrical dimensions of the sandwich panels are summarized in Table 8.2.

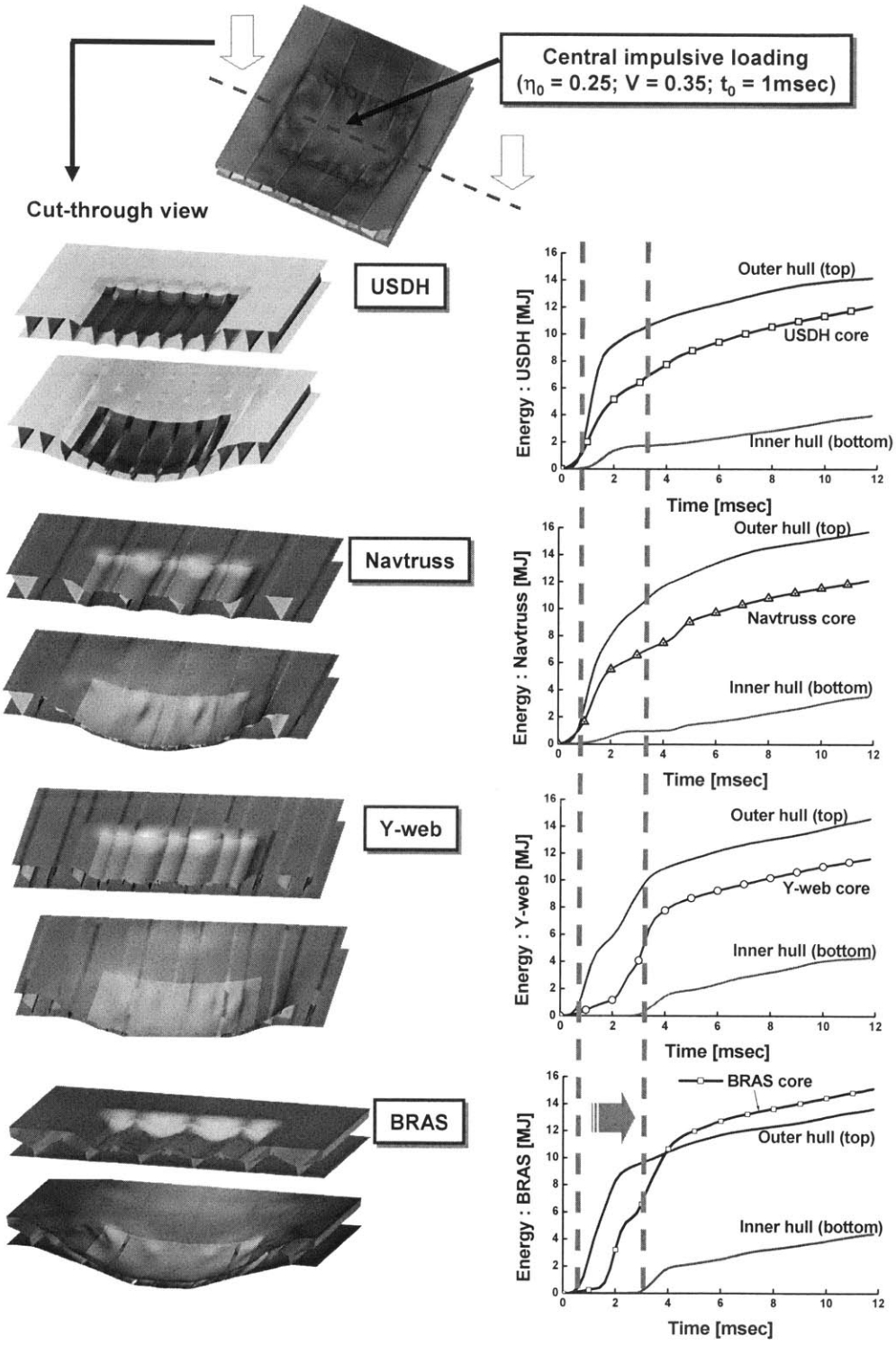

Fig. 8.14 Comparison of the deformed shapes and partition of energy dissipation in double hulls between four different core arrangements. See for geometrical dimensions in Fig. 8.2 and Table 8.2.

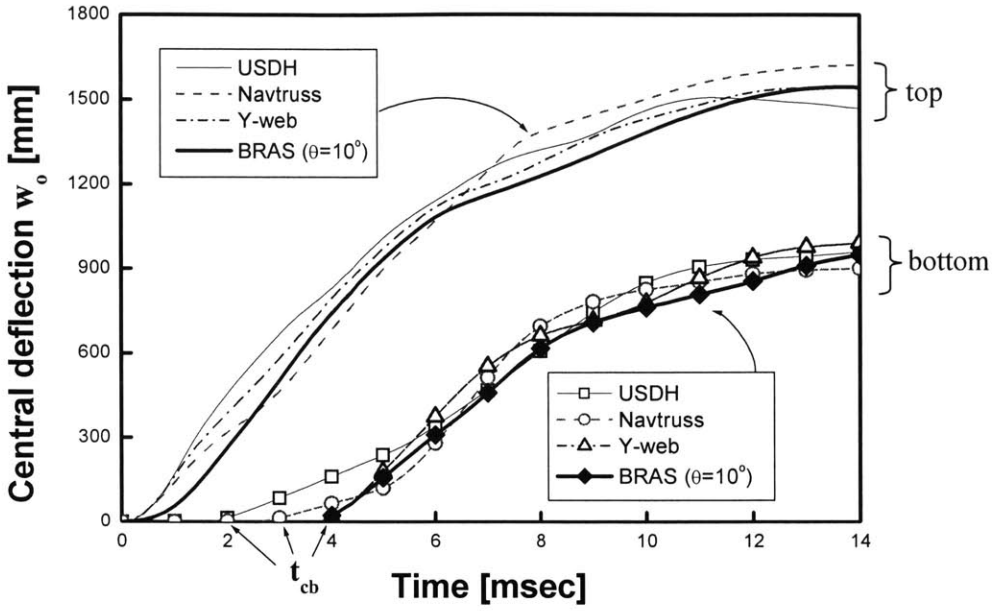

Fig 8.15 The time history of central deflection (w_0) in sandwich panels with $\tilde{m} = 0.01$ and subjected to $V = I_0 /(c\rho L_0 \tilde{m}) = 0.35$. Note that normalized loading area $\eta_0 = (L_1 / L_0)^2 = 0.25$ and time duration of pressure pulse $t_0 = 1 m\sec$. All geometrical dimensions of the sandwich panels are summarized in Table 8.2. The response time of the bottom face sheet is denoted by t_{cb}.

Table 8.3 Comparison of the t_{cb} between four different core structures under dynamic pressure loading

Type of web	Response time t_{cb} (msec)	Duration of pressure t_0 (msec)	t_{cb} / t_0
USDH	2	1	2
Navtruss	3	1	3
Y-web	**4**	**1**	**4**
BRAS	**4**	**1**	**4**

Deformation mode The cross-sectional views of the set of sequential deformation shapes are shown in Figs. 8.16 ~ 8.19 for the sandwich panels with four different core arrangements. Note that two different dimensionless time variables are used in these figures. The first one is t/t_0, where t_0 is duration of pressure pulse. In the present numerical simulations, t_0 = 1msec was used, which is sufficiently short as compared to the duration of motion denoted by t_f, i.e. the time for the plate to reach its maximum deflection (in particular, t_f = 15 ~ 20msec for the considered sandwich structures). In this situation, the blast load pulse has fallen to zero before any significant displacement occurs so that the structure can be described as being subjected to impulsive loading. The second dimensionless time is τ_H where current time is normalized by the traveling time throughout the panel height H wth an initial face velocity, according to

$$\tau_H = \frac{v_{0f} t}{H} \tag{8.25}$$

where v_{0f} is the initial transverse velocity of top face sheet related to the applied impulse I_0 by the momentum conservation

$$v_{0f} = \frac{I_0}{\rho h_f} \tag{8.26}$$

Subsitituting Eqns. (9.4) and (8.6) into Eq. (8.26) leads to an alternative expression of v_{0f}

$$v_{0f} = cV\left(2 + \Omega \frac{h_w}{h_f}\frac{H}{W}\right) \tag{8.27}$$

Applying Eq. (8.27) to (8.25), the normalized time τ_H can be expressed in terms of normalized impulse ($V = I_0 / m^* c$: Eq. (9.4)), tranverse wave speed ($c = \sqrt{\sigma_0 / \rho}$), and sectional geometries of panles

$$\tau_H = cV\left(2 + \Omega \frac{h_w}{h_f}\frac{H}{W}\right)\frac{t}{H} \tag{8.28}$$

Based on the deformation modes and velocity profiles, respectively shown in Figs. 8.16 ~ 8.19 and Figs. 8.21 ~ 8.24, the typical transient response of the impulsively loaded sandwich panels can be divided into two distinct stages:

- Stage I – web core compression phase;
- Stage II – sandwich panel bending and stretching phase.

In Stage I, the impulse per unit area I_0 imparts a transverse velocity v_{0f}, defined by Eq. (8.26), to the top face sheet (outer hull). The outer hull flies into the web subjecting it to compression. The resistance of web decelerates the outer hull and simultaneously accelerates the bottom face sheet (inner hull). At the end of Stage I, the two face sheets are moving with nearly the common velocity. It was observed that the magnitude of common velocity is approximately $0.4\,v_{0f}$ (see solid line with open circle at $t/t_0 = 6$ in Figs. 8.21 and 8.23), possesses 1/3 of initial kinetic energy which remains to be dissipated during subsequent motion. This kinetic energy is dissipated by plastic bending and in-plane stretching of entire sandwich panel in Stage II. For each of the four sandwich panels, almost all plastic energy dissipation has occurred at $\tau_H = 6.0$ (or $t/t_0 = 16$). Subsequently, the panels undergo elastic vibration in the final stage.

Figures 8.16 and 8.17 reveal that in the earlier stage of deformation of USDH and Navtruss, when $\tau_H = 0.39\,(t/t_0 = 1)$, the inner hulls also undergo plastic deformation. This observation indicates that the applied impulse towards the outer hull is transferred to the inner hull without significant reduction by the plastic deformation of webs. On the other hand, for the cases of Y-web and BRAS shown in Figs. 8.18 and 8.19, the inner hulls remain mostly undefromed until the outer hull and transverse web collapse near completely, approximately up to the stage of $\tau_H = 0.94\,(t/t_0 = 3)$, which indicates a substantial reduction in impulse transfer to the inner hull. Furthermore, the BRAS type of core plays a crucial role in Stage II since the bending and membrane resistance of the partially crushed sandwich core is much higher than the original uncrushed core (refer to Figs. 8.10 and 8.11).

Profile of transverse velocity The numerically obtained profiles of transverse velocity, as defined by Fig. 8.20, are shown in Figs. 8.21 ~ 8.24 for the cases of USDH and BRAS. Note that the dimensionless velocity, $\dot{w}/v_{0f}$, is plotted in these figures. It can be cleary observed from Figs. 8.21 and 8.22 that the inner hull of USDH reveals a certain magnitude of velocity in the earlier stage of deformation. In particular, the plate junctions between inner hull and web girder of USDH move with $\dot{w}/v_{0f} \approx 0.2$ when $t/t_0 = 1$. However, in the case of BRAS shown in Figs. 8.23 and 8.24, the magnitude of velocity in the inner hull is almost zero up to $t/t_0 = 3$, which cleary confirm the deformation mode shown in Fig. 8.19.

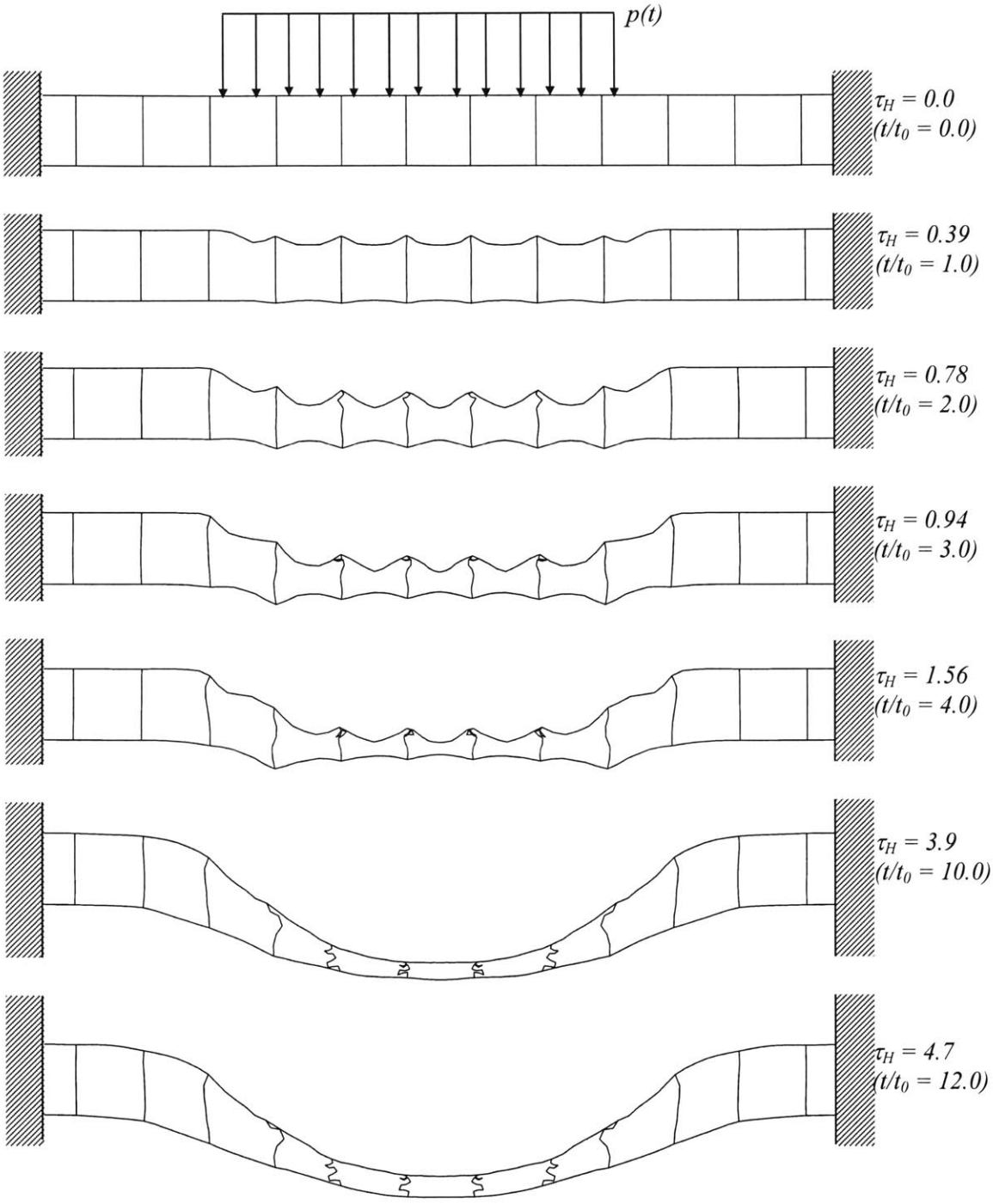

Fig. 8.16 Sequential deformation modes of the USDH with $\widetilde{m} = 0.01$ and subjected to $V = I_0 /(c\rho L_0 \widetilde{m}) = 0.35$. Note: normalized loading area $\eta_0 = (L_1 / L_0)^2 = 0.25$; time duration of pressure pulse $t_0 = 1m\,\text{sec}$; initial velocity of top face plate imposed by applied pressure loading $v_{0f} = 312m/\text{sec}$. See for geometrical dimensions in Fig. 8.2 and Table 8.2.

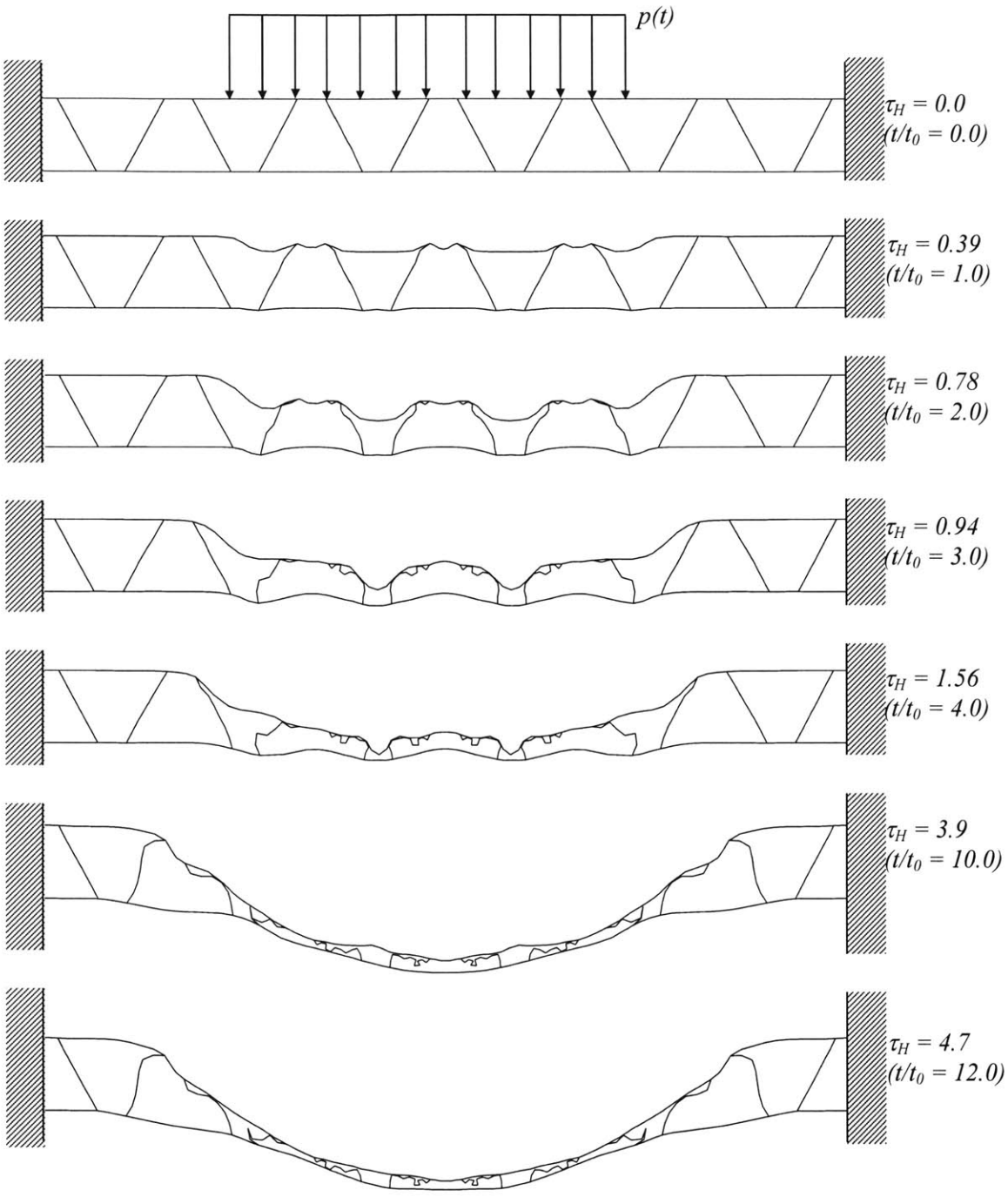

Fig. 8.17 Sequential deformation modes of the Navtruss with $\widetilde{m} = 0.01$ and subjected to $V = I_0 /(c\rho L_0 \widetilde{m}) = 0.35$. Note: normalized loading area $\eta_0 = (L_1 / L_0)^2 = 0.25$; time duration of pressure pulse $t_0 = 1m\sec$; initial velocity of top face plate imposed by applied pressure loading $v_{0f} = 312m/\sec$. See for geometrical dimensions in Fig. 8.2 and Table 8.2.

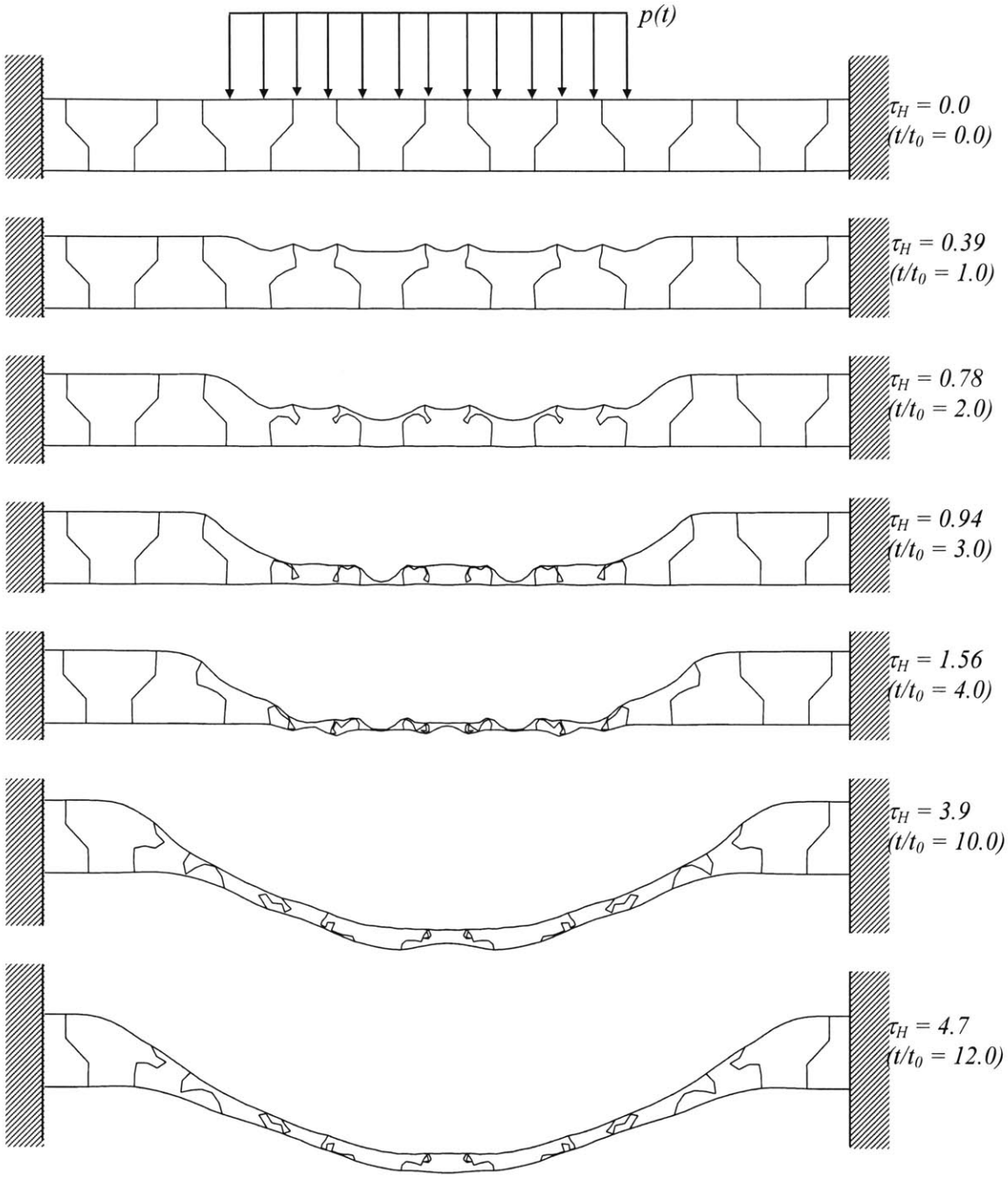

Fig. 8.18 Sequential deformation modes of the Y-web with $\widetilde{m} = 0.01$ and subjected to $V = I_0 /(c\rho L_0 \widetilde{m}) = 0.35$. Note: normalized loading area $\eta_0 = (L_1 / L_0)^2 = 0.25$; time duration of pressure pulse $t_0 = 1m\,\text{sec}$; initial velocity of top face plate imposed by applied pressure loading $v_{0f} = 312m/\text{sec}$. See for geometrical dimensions in Fig. 8.2 and Table 8.2.

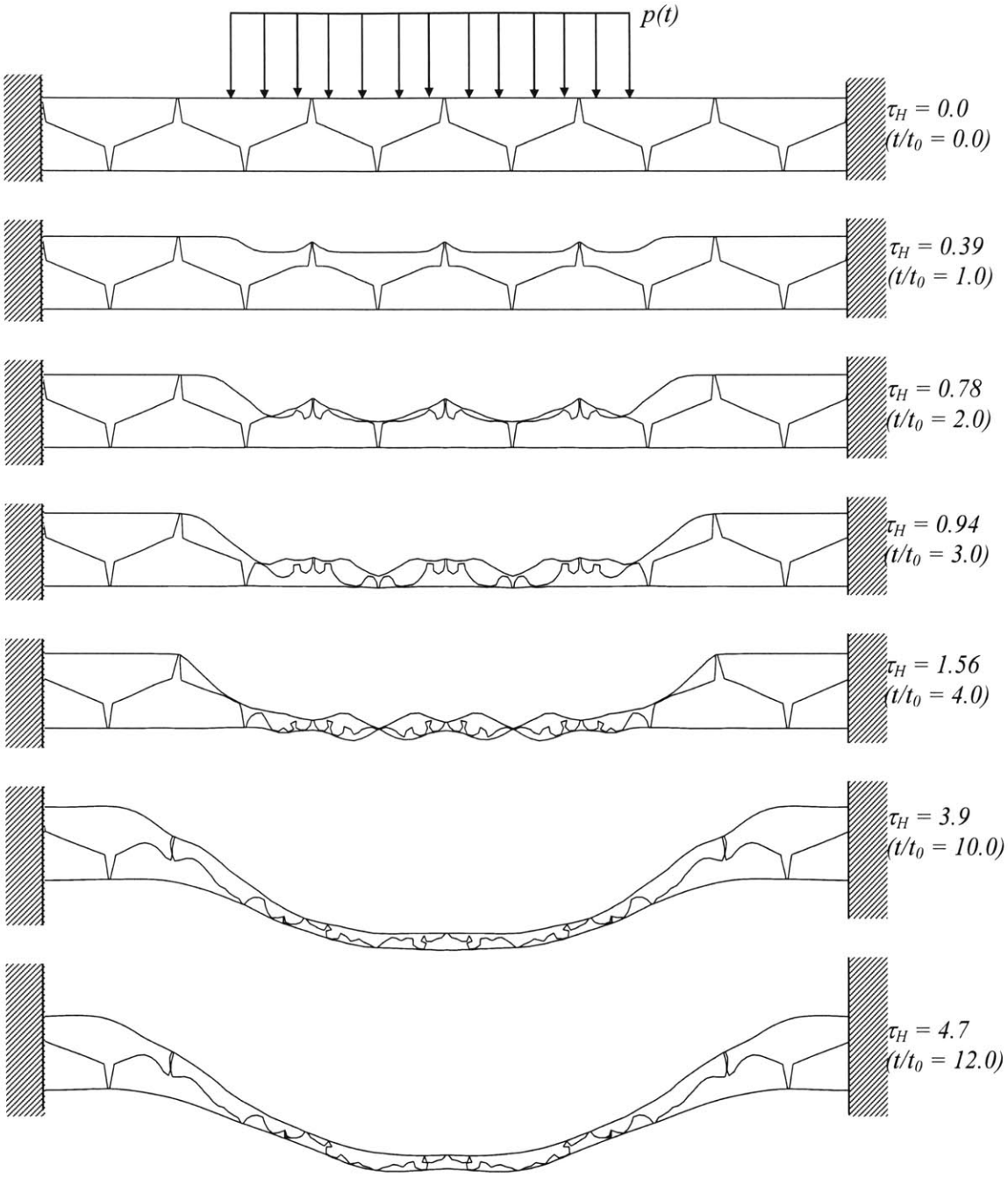

Fig. 8.19 Sequential deformation modes of the BRAS with $\widetilde{m} = 0.01$ and subjected to $V = I_0 /(c\rho L_0 \widetilde{m}) = 0.35$. Note: normalized loading area $\eta_0 = (L_1 / L_0)^2 = 0.25$; time duration of pressure pulse $t_0 = 1m\sec$; initial velocity of top face plate imposed by applied pressure loading $v_{0f} = 312m/\sec$. See for geometrical dimensions in Fig. 8.2 and Table 8.2.

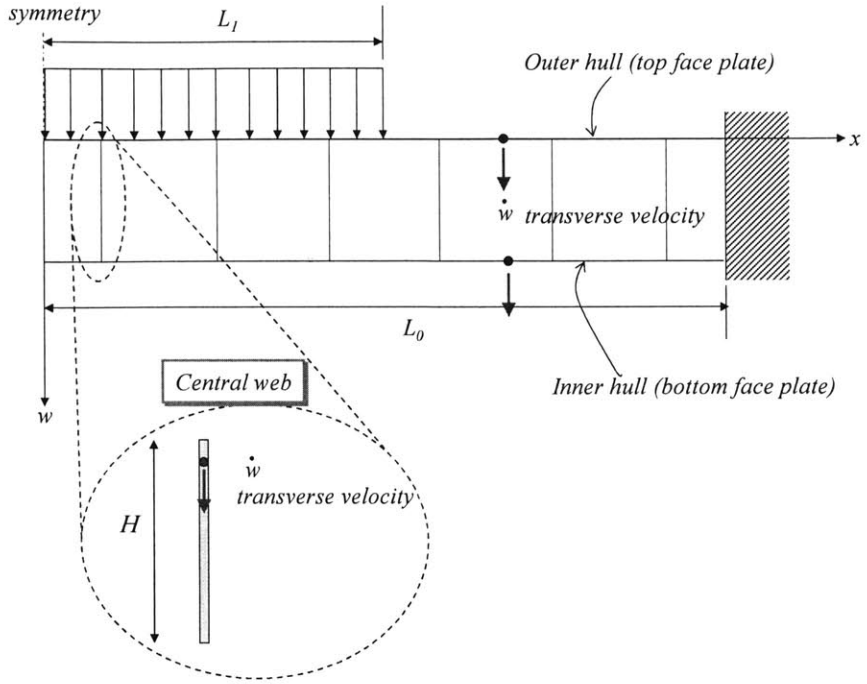

(a) USDH

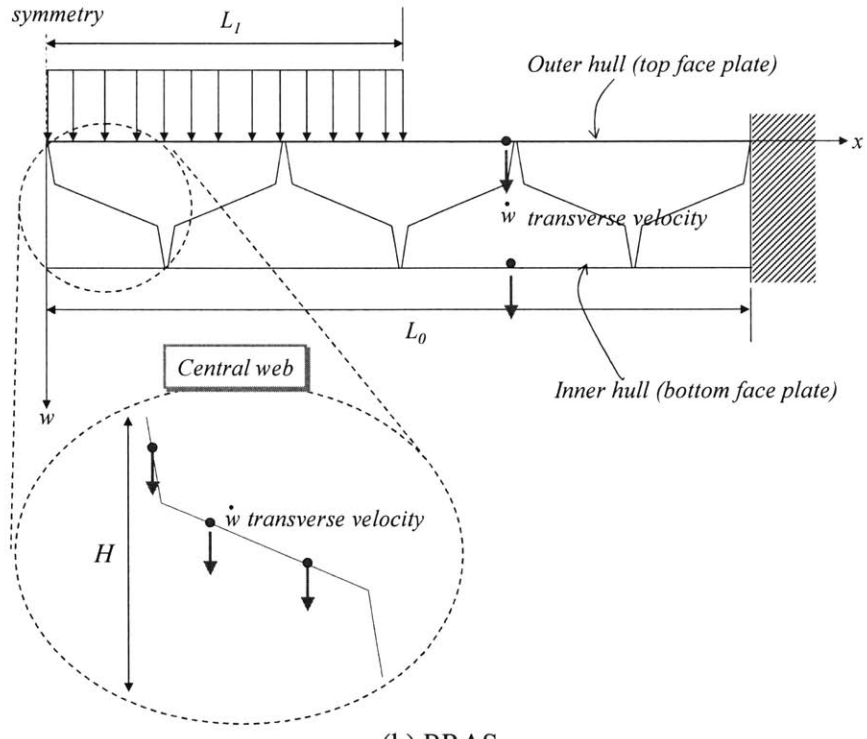

(b) BRAS

Fig. 8.20 Definition of transverse velocity of the sandwich panels due to the applied impulsive loading

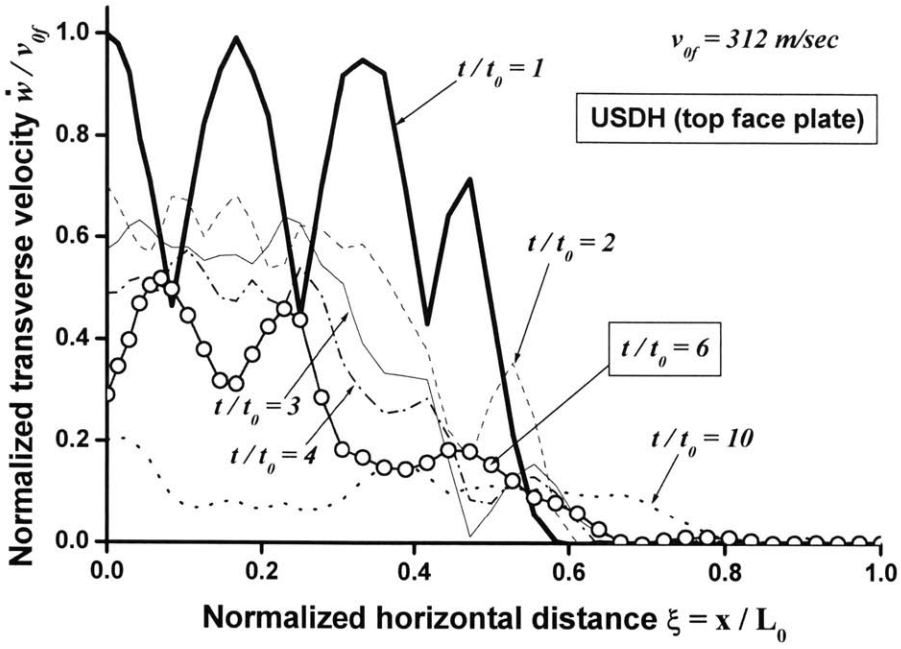

(a) outer hull (top face plate)

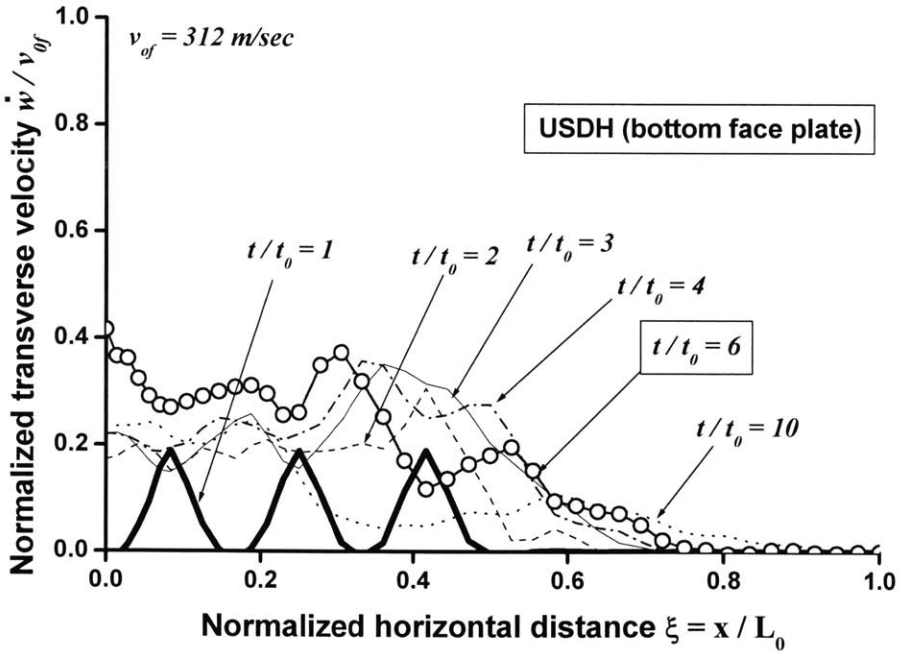

(b) inner hull (bottom face plate)

Fig. 8.21 Numerically obtained transient profiles for normalized transverse velocity along the horizontal directions of two face plates in USDH. Note: normalized loading area $\eta_0 = (L_1 / L_0)^2 = 0.25$; time duration of pressure pulse $t_0 = 1m\,\text{sec}$; initial velocity of top face plate imposed by applied pressure loading $v_{0f} = 312m/\text{sec}$; initial horizontal coordinate (x) is used.

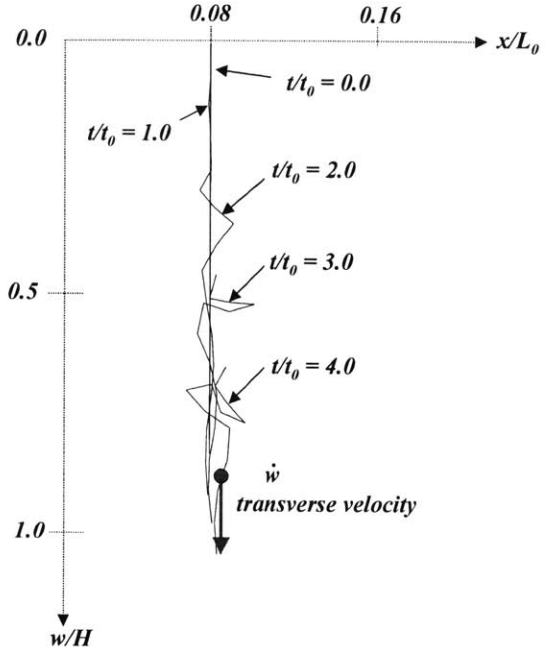

(a) overlapped deformation mode of the central web

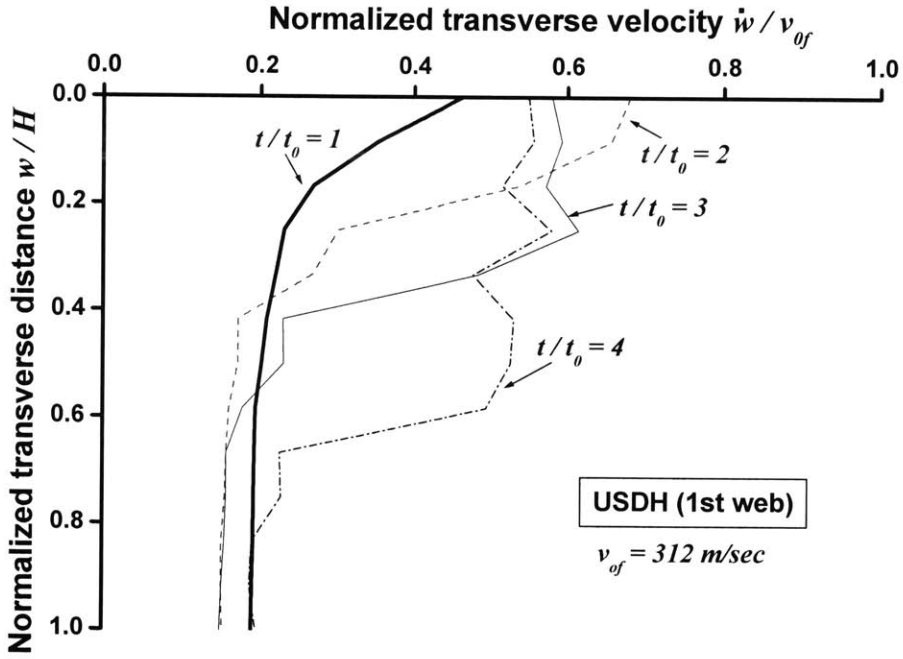

(b) profiles of transverse velocity

Fig. 8.22 Numerically obtained transient profiles for normalized transverse velocity along the central web girder of USDH. Note: normalized loading area $\eta_0 = (L_1 / L_0)^2 = 0.25$; time duration of pressure pulse $t_0 = 1m\,\text{sec}$; initial velocity of top face plate imposed by applied pressure loading $v_{0f} = 312m/\text{sec}$; initial horizontal and transverse coordinate (x, w) is used.

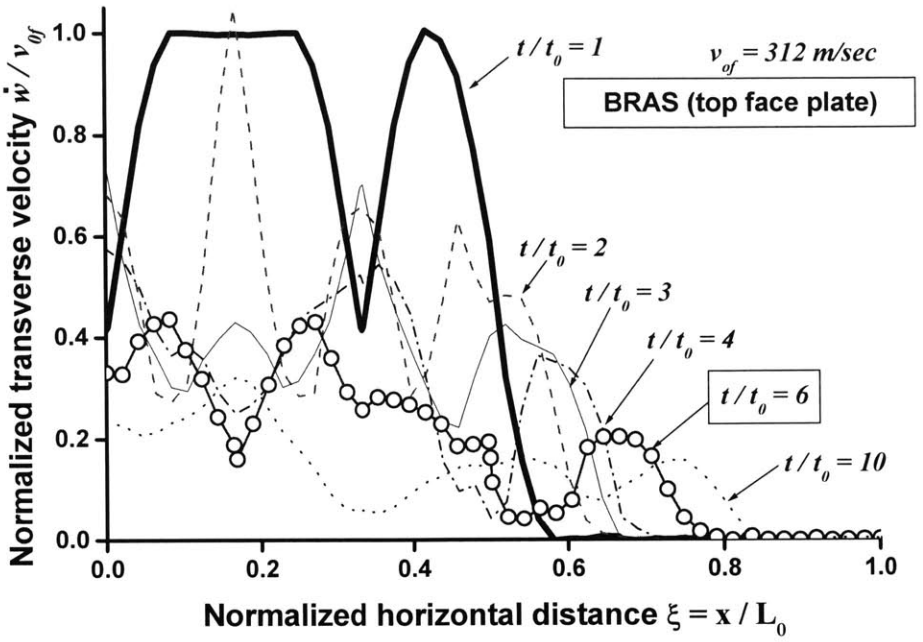

(a) outer hull (top face plate)

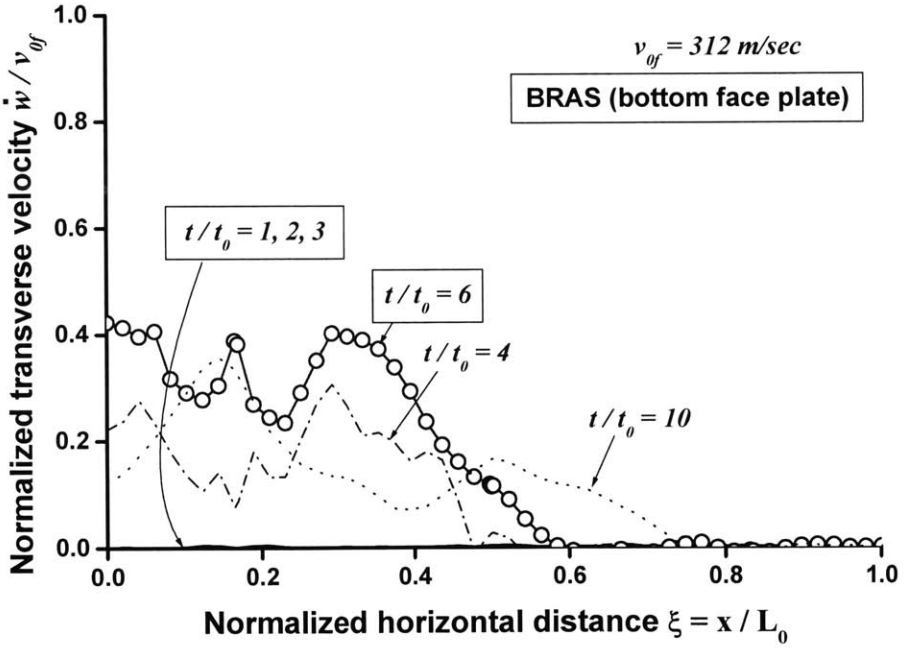

(b) inner hull (bottom face plate)

Fig. 8.23 Numerically obtained transient profiles for normalized transverse velocity along the horizontal directions of two face plates in BRAS. Note: normalized loading area $\eta_0 = (L_1 / L_0)^2 = 0.25$; time duration of pressure pulse $t_0 = 1m\,\text{sec}$; initial velocity of top face plate imposed by applied pressure loading $v_{0f} = 312m / \text{sec}$; initial horizontal coordinate (x) is used.

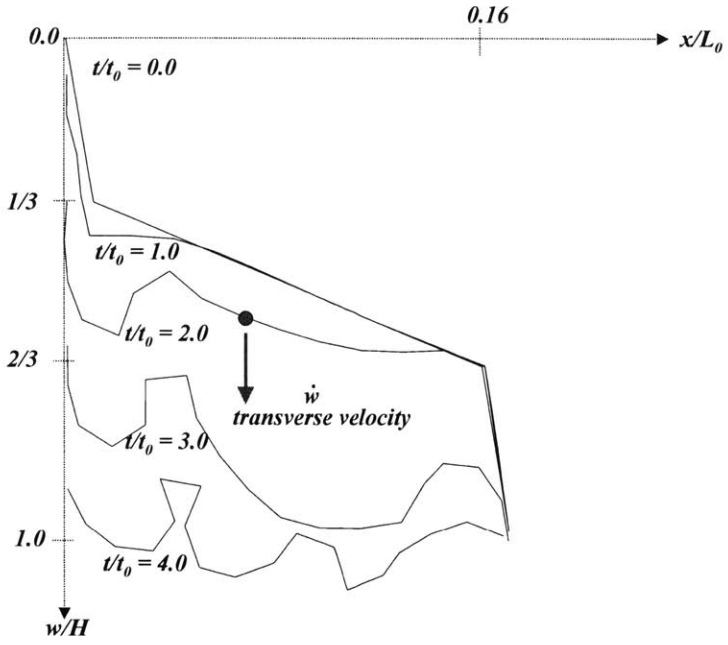

(a) overlapped deformation mode of the central web

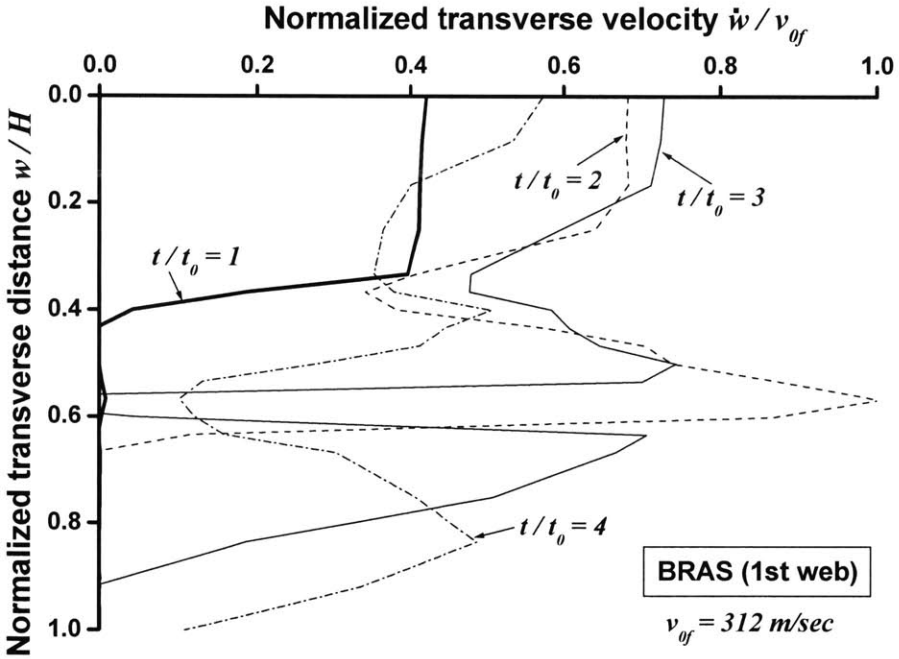

(b) profile of transverse velocity

Fig. 8.24 Numerically obtained transient profiles for normalized transverse velocity along the central web girder of BRAS. Note: normalized loading area $\eta_0 = (L_1 / L_0)^2 = 0.25$; time duration of pressure pulse $t_0 = 1m\,\text{sec}$; initial velocity of top face plate imposed by applied pressure loading $v_{0f} = 312m/\text{sec}$; initial horizontal and transverse coordinate (x, w) is used.

8.4.2 Parametric study of pressure distribution

In Chapter 7, the effect of various spatial and temporal distribution of dynamic pressure on the behavior of thin single plate is investigated. In this Section 8.4.2, the parametric study is further extended into the double hull structure. In particular, the BRAS is considered, see for sectional geometries in Table 8.2.

8.4.2.1 Spatial distribution of pressure

The effect of the normalized loading area $\eta_0 = (L_1 / L_0)^2$ on the final deflected shape and the magnitude of central deflection in the BRAS is shown in Figs. 8.25 and 8.26, respectively. For comparison purposes, the results from single square plate are included in Fig. 8.25. From both two figures, it is clear that the deflected shape is primarily influenced by the loading area. A smaller loading area ($\eta_0 < 0.2$) leads to a more localized bulging near the plate center for both cases of single and double hulls. As can be further seen from Fig. 8.27 where the equivalent plastic strain contours are plotted with four different values of the parameter η_0, a more distributed load produces strain localization which in turn can lead to a premature fracture at the clamped boundary. When compared to the single plate, the deformed shapes of the sandwich panel show more stiff change in the slope at the locations of the plate junction ($\xi = 0.33, 0.66$), see Fig. 8.25. Consequently, highly localized strains are developed along these plate junctions, as can be seen in Fig. 8.27.

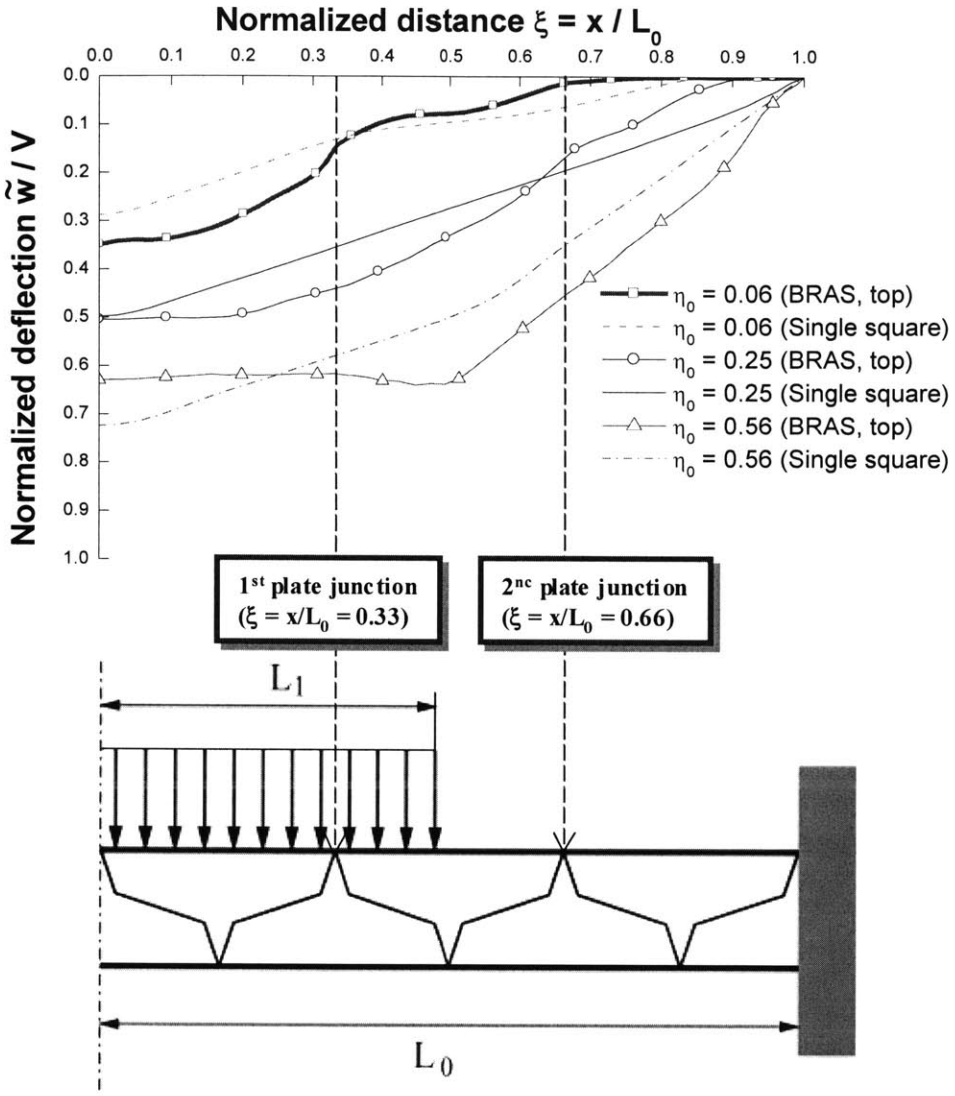

Fig. 8.25 Normalized deflection profiles between the single square plate and the outer hull of BRAS for three different values of normalized loading area $\eta_0 = (L_1 / L_0)^2$. Note that $\widetilde{w} = w / L_0$ and $V = I_0 / cm^*$ respectively denote the dimensionless deflection and impulse.

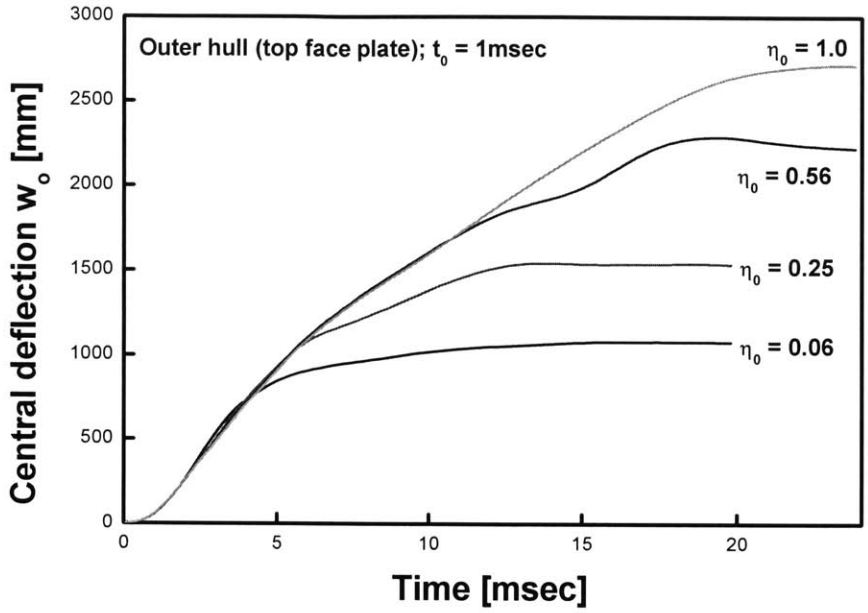

(a) outer hull (top face plate)

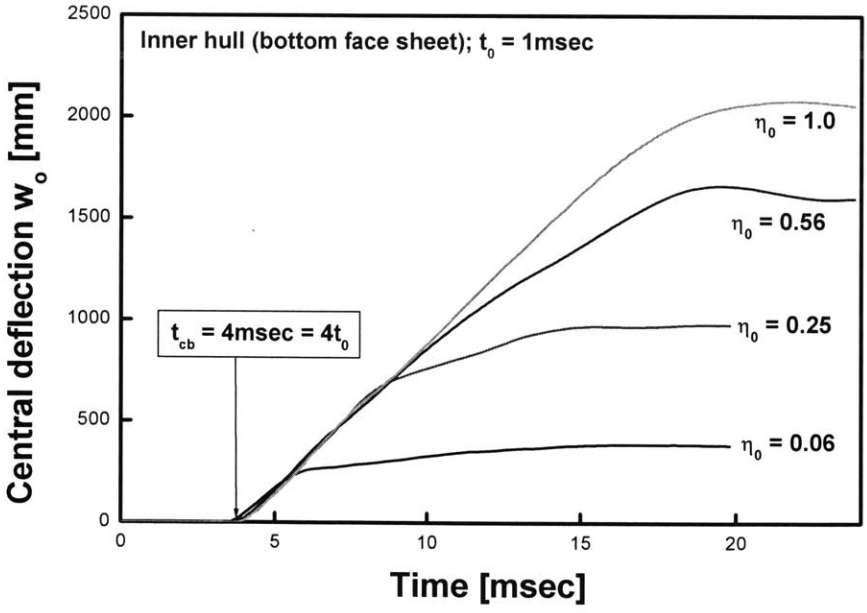

(b) inner hull (bottom face plate)

Fig. 8.26 The time history of central deflection (w_0) in the BRAS subjected to $V = I_0 /(c\rho L_0 \tilde{m}) = 0.35$ for three different values of normalized loading area $\eta_0 = (L_1 / L_0)^2$

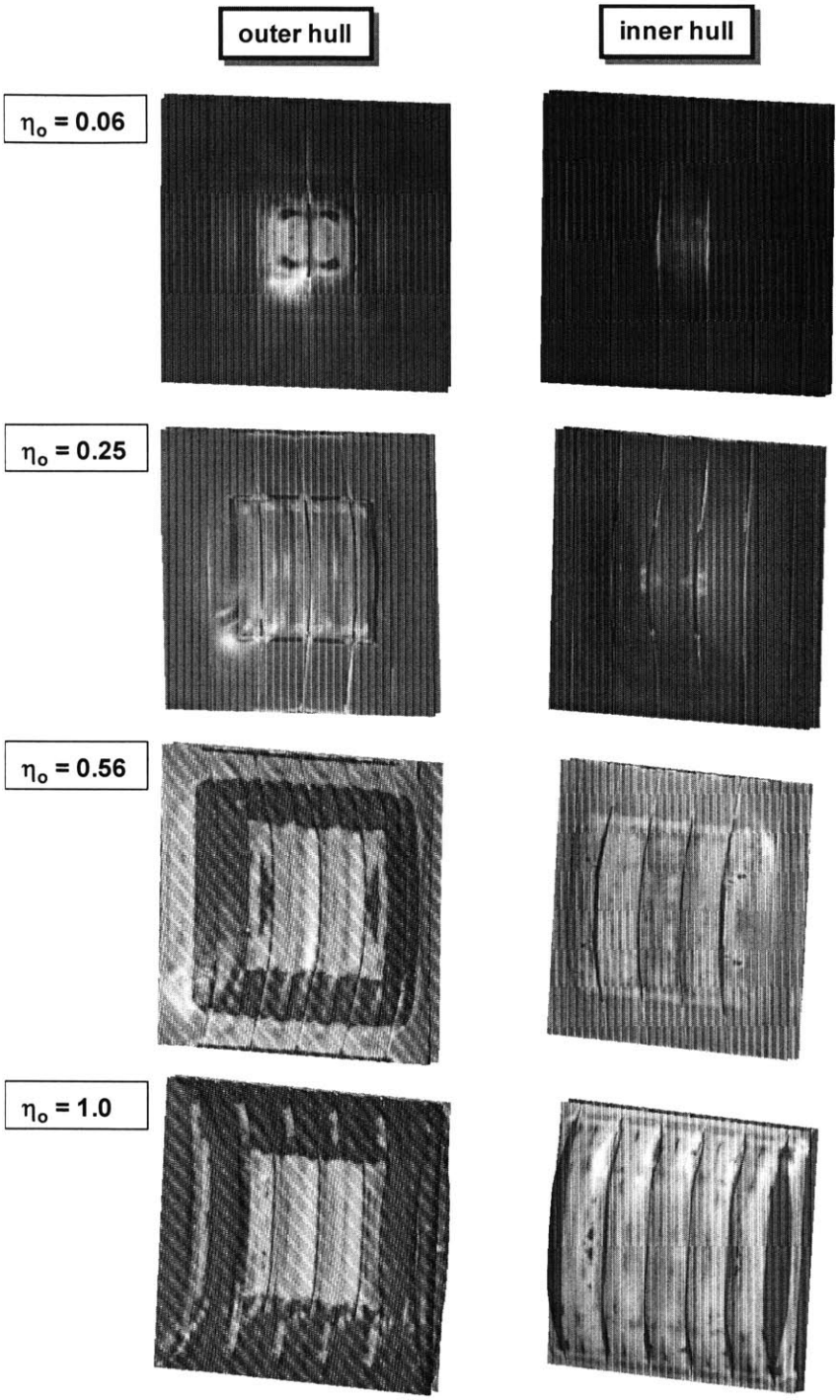

Fig. 8.27 Color coded contours of equivalent plastic strain in the BRAS with four different values of normalized loading area $\eta_0 = (L_1 / L_0)^2$

8.4.2.2 Temporal distribution of pressure

Figure 8.28 shows the time history of central deflection for the BRAS with different time duration of pressure but equal impulse imparted to the top face plate. It can be see that there is not much difference in the magnitude of deflection. In addition, the duration of motion, denoted by t_f, is almost constant and approximately equal to t_f = 15msec for each case. Furthermore, it was found that the deflected shape and strain distributions are not sensitive to the time duration of pressure under equal impulse. All above the observations are quite consistent with those of single plate presented in Chapter 7.

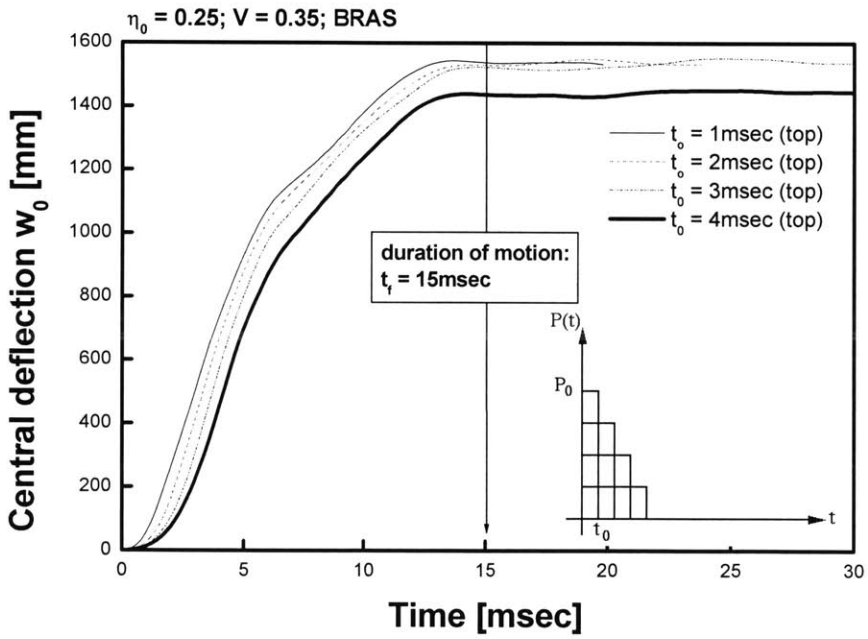

Fig. 8.28 The central deflection of the BRAS with different time duration but equal impulse ($\eta_0 = 0.25; V = 0.35$)

8.4.3 Sensitivity study

In this section, the transient responses involving energy absorption, central deflection, and response time of the USDH and the BRAS are examined by varying the structural design parameters. In this study, thickness and angle of transverse web are taken as potential parameters influencing the transient responses of double hull. For the case of USDH, only thickness of web is considered. Again, no fracture is considered. It should be mentioned that an extensive parametric study to develop an optimal configuration minimizing the fractured area of the inner hull is presented in Chapter 9.

8.4.3.1 Unidirectionally Stiffened Double Hull (USDH)

By fixing the thickness of face sheet at h_f = 16mm, the thickness of web (h_w) of USDH was varied from 5mm to 20mm. Figure 8.29 shows the history plots of central deflection. As can be seen, the USDHs having thicker core experience smaller deflection for both cases of top and bottom face sheets. It is interesting to note that changing the thickness of web does not affect the response time of bottom face sheet (t_{cb}). The response time is almost constant as t_{cb} = 2msec for all cases, see Fig. 8.29(b). By contrast, a significant extension of the t_{cb} is observed in the case of BRAS, as shown in Figs. 8.33 and 8.35. This will be discussed in Section 8.4.3.3.

The history plots of total energy dissipated in the USDH are shown in Fig. 8.30(a) with four different thicknesses of web. The contributions of the components parts of the USDH to total energy dissipation are shown by the time histories of energy absorption in the face sheets and core, respectively in Fig. 8.30(b) and 8.30(c). It can be seen that the USDHs with thicker core reveal higher energy absorption in the earlier stages of deformation (approximately up to t = 4msec), whereas, the highest energy absorption in the remaining stages is achieved by the USDH with thinner core (h_w = 5mm) due to the larger amount of energy dissipation in the web and bottom face sheet. For the cases with thicker core, a greater portion of energy is absorbed in the top face sheet.

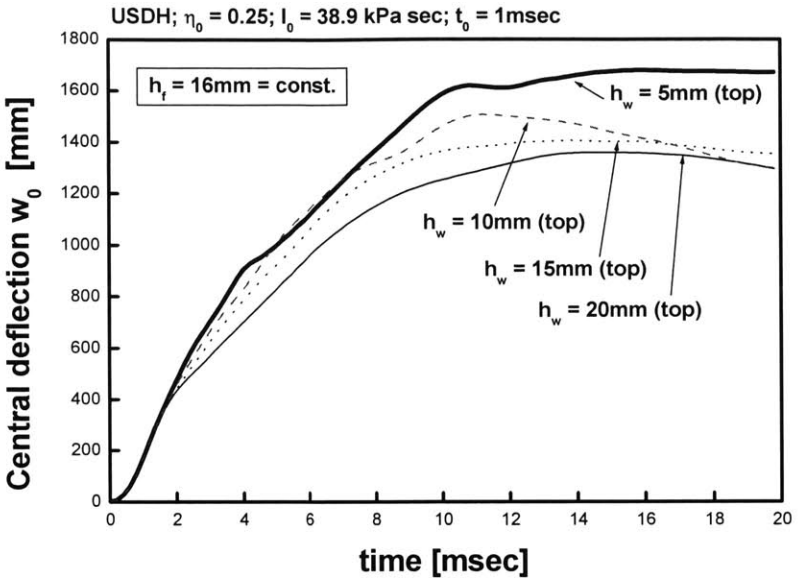

(a) outer hull (top face plate)

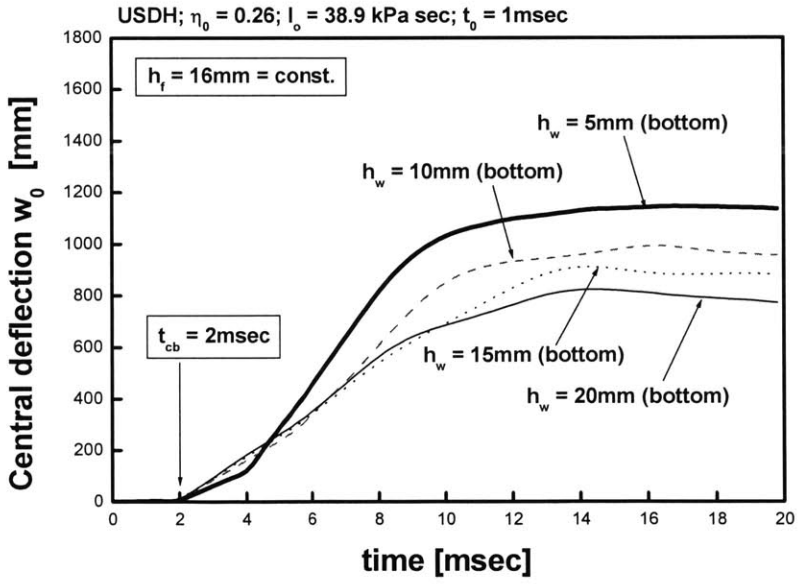

(b) inner hull (bottom face plate)

Fig. 8.29 The time history of the central deflection (w_0) in the USDH subjected to I_0=38.9 kPa sec with four different values of core thickness (h_w). Note that the thickness of face sheet is constant (i.e. $h_f = 16mm$) and the normalized cell height is H/W = 1.0 for all cases shown in this figure.

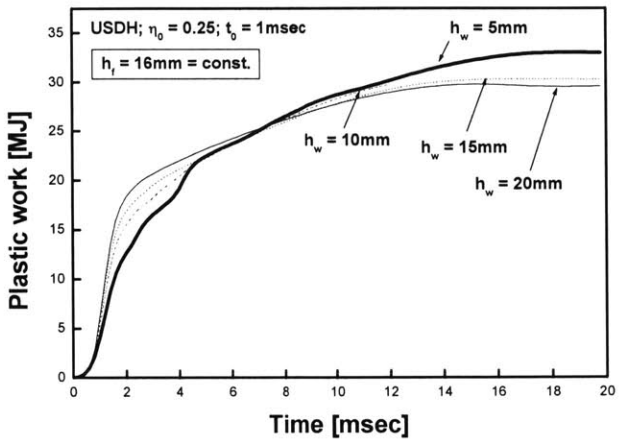

(a)

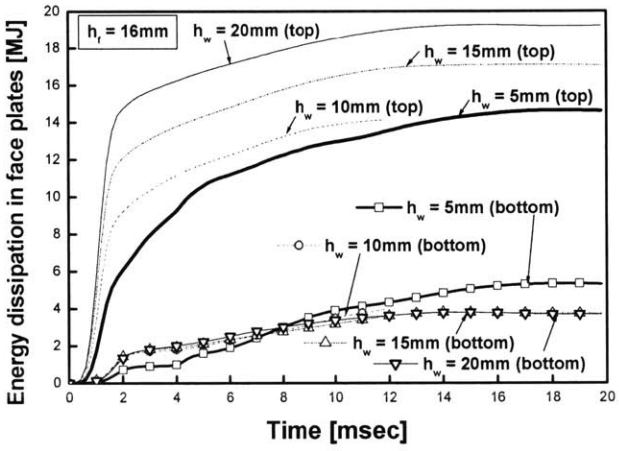

(b)

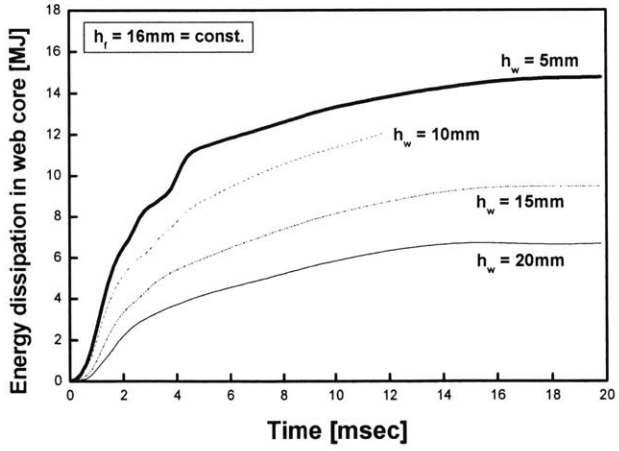

(c)

Fig. 8.30 Partition of energy dissipation in the USDH subjected to I_0=38.9 kPa sec with four different values of core thickness (h_w): (a) total absorbed energy; (b) energy dissipated in the face sheets; (c) energy dissipated in the core. Note that the thickness of face sheet is constant (i.e. $h_f = 16mm$) and the normalized cell height is H/W = 1.0 for all cases shown in this figure.

8.4.3.2 Blast Resistant Adaptive Sandwich (BRAS)

Inclination angle of web θ The variations of the central deflection and the energy absorption of the BRAS against the angle of transverse web are shown in Fig. 8.31 and 8.32, respectively. It is seen that the transient responses are not significantly affected by changing the angle within limits.

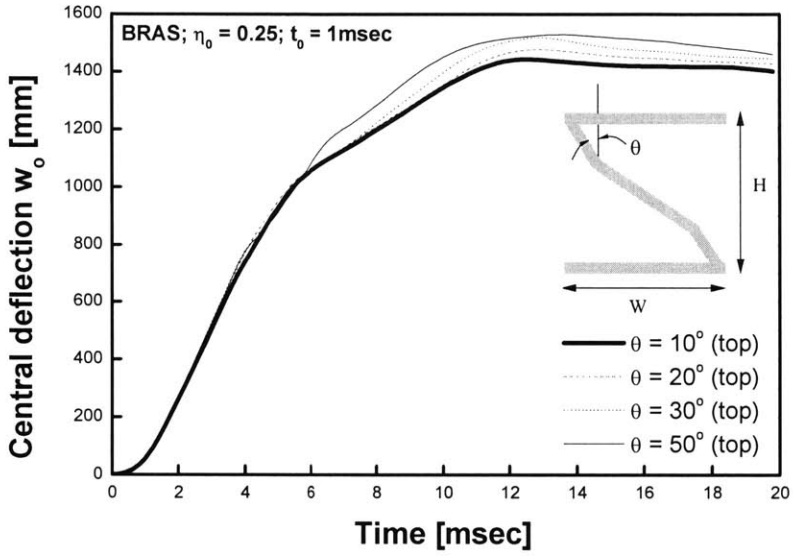

(a) outer hull (top face plate)

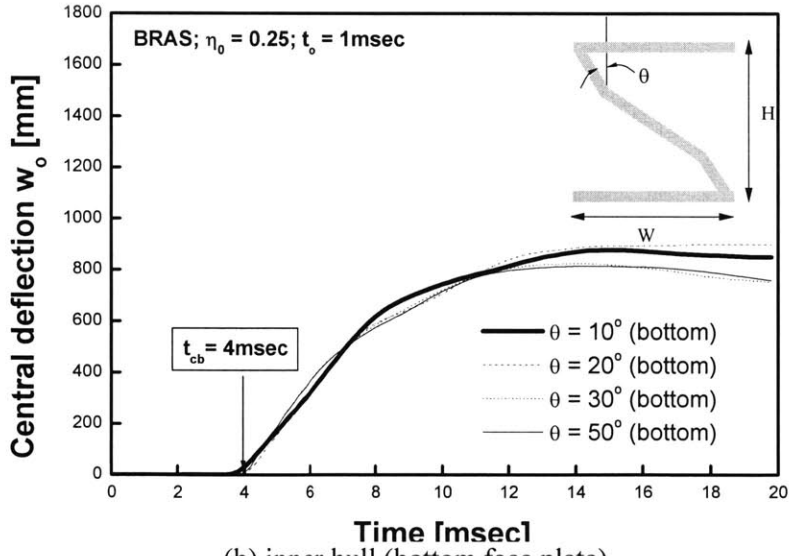

(b) inner hull (bottom face plate)

Fig. 8.31 The time history of the central deflection (w_0) in the BRAS subjected to I_0=38.9 kPa sec with four different angles of web (H/W = 1.0; h_f = 16mm; h_w = 10mm)

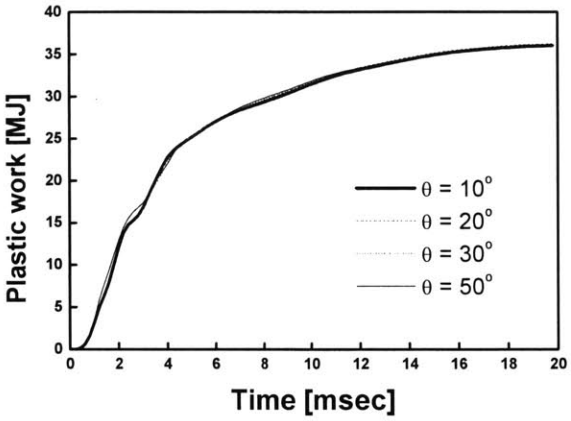

(a) total energy dissipation

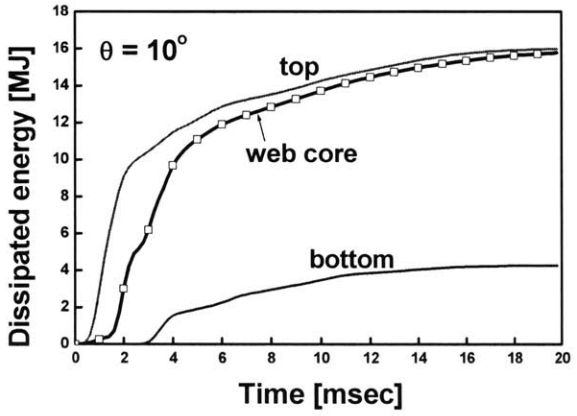

(b) $\theta = 10^o$

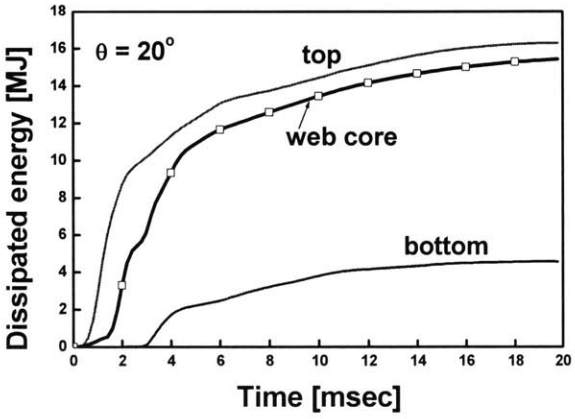

(c) $\theta = 20^o$

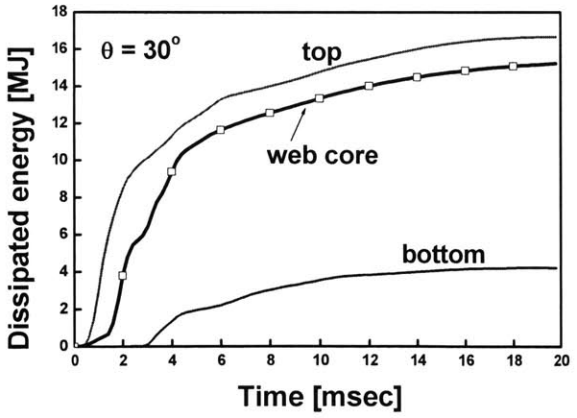

(d) $\theta = 30^o$

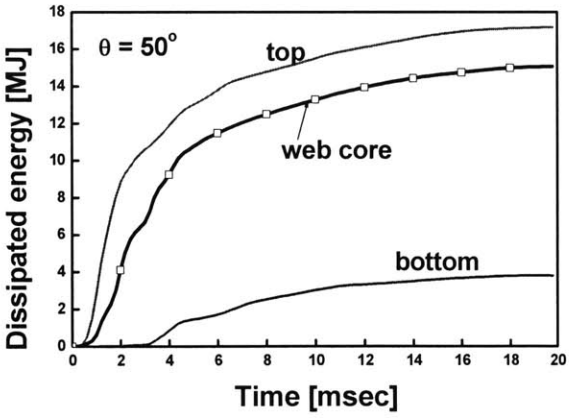

(e) $\theta = 50^o$

Fig. 8.32 Partition of energy dissipation in the BRAS subjected to I_0 =38.9 kPa sec with four different angles of web (H/W = 1.0; h_f = 16mm; h_w = 10mm; t_0 = 1msec)

Thickness of web (h_w) As can be seen from Figs. 8.33 and 8.34, the thickness of web is quite influential parameter for the dynamic behavior of the BRAS. It is important to note that smaller magnitude of deflection and longer response time of the bottom face sheet are obtained by increasing the thickness of web, see Fig. 8.33(b).

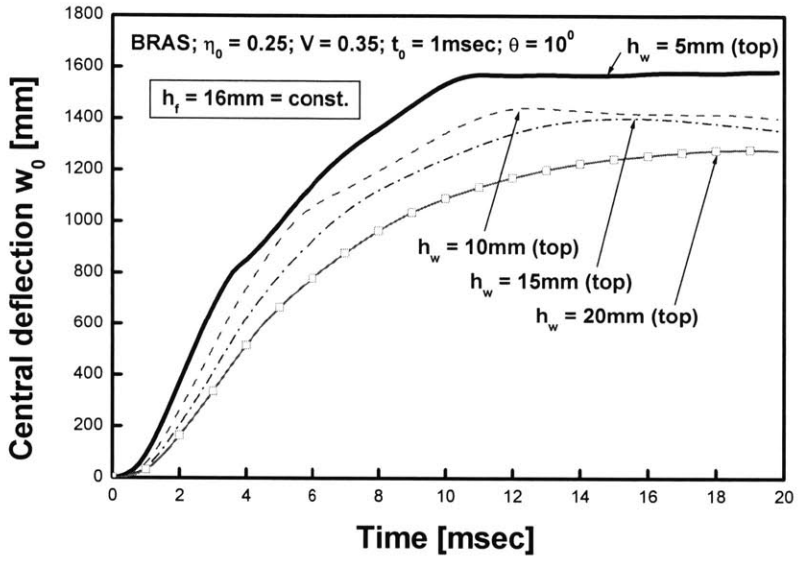

(a) outer hull (top face plate)

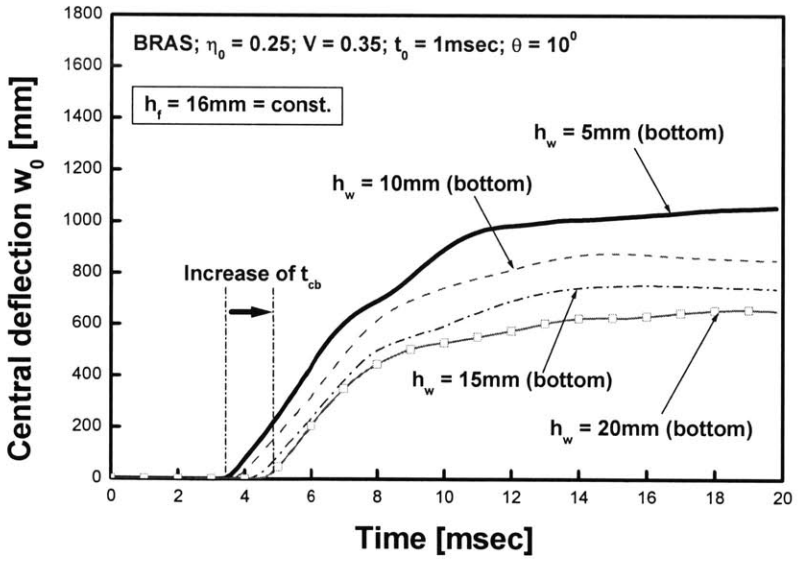

(b) inner hull (bottom face plate)

Fig. 8.33 The time history of the central deflection (w_0) in the BRAS subjected to I_0=38.9 kPa sec with four different values of core thickness. Note that the thickness of face sheet is constant (i.e. $h_f = 16mm$), the angle of web is $\theta = 10^0$, and the normalized cell height is H/W = 1.0 for all cases shown in this figure.

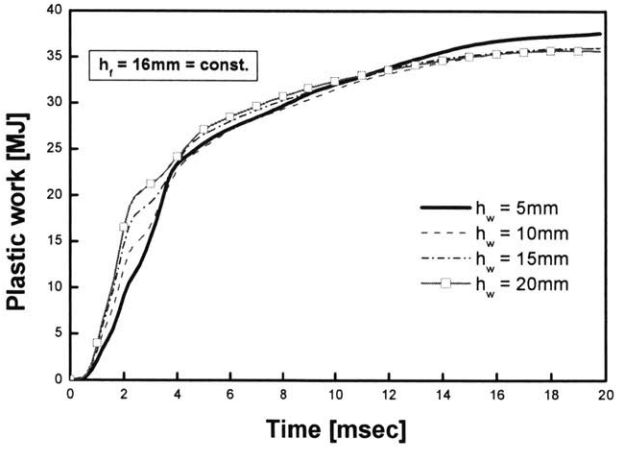

(a)

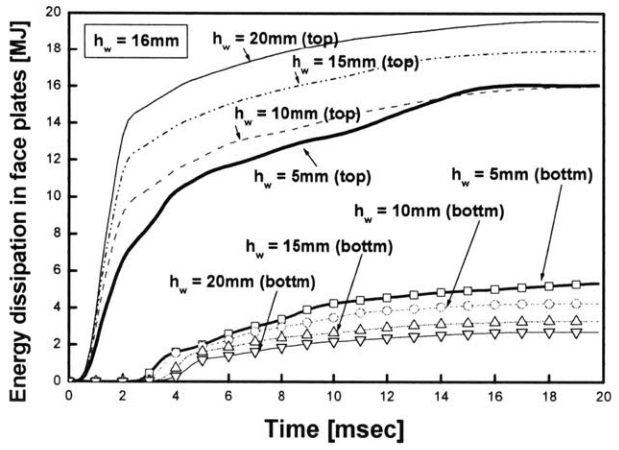

(b)

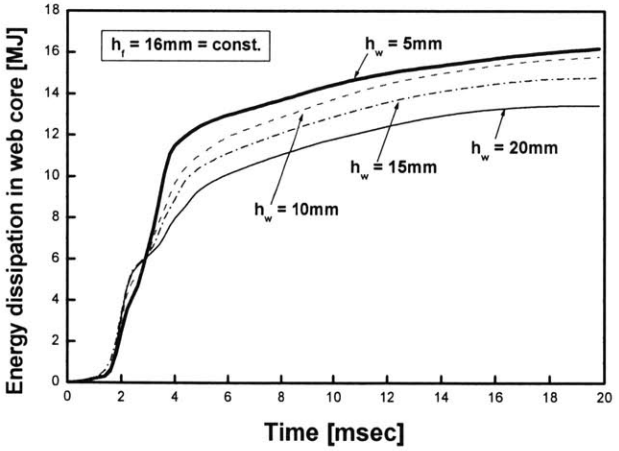

(c)

Fig. 8.34 Partition of energy dissipation in the BRAS subjected to I_0=38.9 kPa sec with four different values of core thickness (h_w): (a) total absorbed energy; (b) energy dissipated in the face sheets; (c) energy dissipated in the core. Note that the thickness of face sheet is constant (i.e. $h_f = 16mm$), the angle of web is $\theta = 10^0$, and the normalized cell height is H/W = 1.0 for all cases shown in this figure.

8.4.3.3 Discussion

In the optimization study presented in Chapter 9, the fractured area of inner hull (bottom face sheet) is considered as a measure of survivability of ships under intense explosive loading. As mentioned earlier in Section 8.4.1, the response time of the bottom sheet (t_{cb}) can be considered as an indicator for the fracture resistance of sandwich structures. The structures should be designed that their collapse time is longer than the duration of blast, thereby providing an effective blast isolation and transferring the least amount of impulse to the inner hull. From the parametric investigation presented in previous sections, it was found that the response time and energy absorption characteristics are significantly affected by the thickness of web. In particular, Fig. 8.35 shows the variation of the t_{cb} as a function of the normalized thickness of web for both cases of the USDH and the BRAS. It can be clearly observed that BRAS provides longer response time than USDH for all variations of thickness considered in this figure. Moreover, the t_{cb} of BRAS is very sensitive to the thickness variation and linearly increased as thickness of web increases. It would thus be of importance to find the optimal variation of thicknesses in the BRAS to increase fracture resistance. This topic is discussed in Chapter 9.

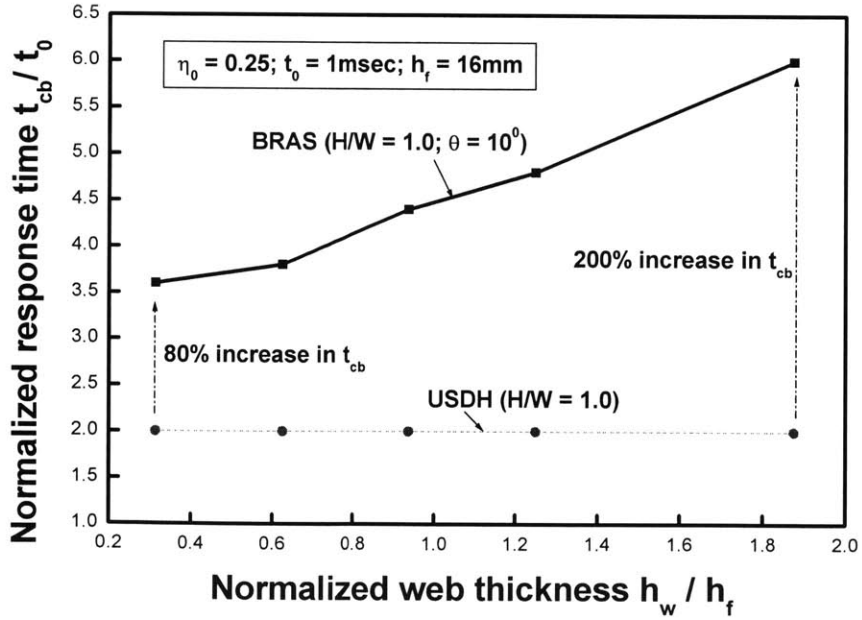

Fig. 8.35 Response time of inner hull (bottom face sheet) between USDH and BRAS subjected to I_0=38.9 kPa sec as a function of core thickness ratio (h_w / h_f; h_f = 16mm)

8.5 Conclusion

- Several parameters and functions characterizing blast response of double hulls with four different core arrangements under large plastic deformations are investigated. Those characteristics are: deformation mode, crush resistance, magnitude of central deflection, energy dissipation, and response time of inner hull. A new concept of adaptive and reconfigurable structural component (BRAS) is introduced that substantially increase the resistance to explosive loading. The key characteristics in the shape of the BRAS is to ensure that during the process of deformation the web folds in a particular manner and absorbs large amount of energy due to intense plastic deformation especially in the petalling stage. It was shown that the static crushing resistance of the partially crushed BRAS core is much higher (approximately 40 times) than the original uncrushed core (refer to Fig. 8.14 and Table 8.1). This behavior of the BRAS will significantly increase the bending and membrane resistance of the structure in the petalling phase, which leads to an increased resistance to fracture. In particular, it is shown in Chapter 9 that the resistance to initial fracture of the optimized BRAS is up to a factor of 1.8 times higher than that of the optimized USDH (see Fig. 9.22).
- Transient responses of the BRAS is compared with that of other three core shapes (USDH, Navtruss, Y-web) having the same weight and subjected to the same intensity of impulsive loading. It was clearly demonstrated that the BRAS shows a sequential collapse pattern. The outer hull facing the impulsive load collapses first. The transverse web starts to deform right after time of impulse duration ($t \approx t_0$). Until the outer hull and web collapse near completely the inner hull remain mostly undeformed, which indicates substantial reduction in impulse transfer to the inner hull.
- It was shown that the double hull exhibits similar behavior as that of single plate under various spatial and temporal distributions of applied loading. For example, the deflected shape of face plate is strongly influenced by the loaded area. More localized deformation around the plate center was observed for smaller loaded area. It was also shown that the effect of temporal distribution of pressure on the deflection is negligible.
- Throughout the sensitivity study on the USDH and BRAS, it was found that the variation of the thickness of web is quite important parameter for the transient responses. It was shown that a

significant extension of the response time (t_{cb}), which is highly beneficial for an effective blast isolation, is achieved by the BRAS with thicker core.

- The above conclusions are valid in the stage of local panel bulging under explosive loading without fracture. The fracture aspect of the response is analyzed next.

Chapter 9

Structural Optimization against Fracture Damage of Double Hulls under Localized Impulsive Loading

9.1 Introduction

Numerous studies using both numerical and experimental methods were published on the transient responses of single stiffened plates subjected to impulsive loading, which was uniformly distributed over the entire plate area. Most of the published work was concerned with the relationship between the intensity of dynamic loading and final permanent deflection of the plates. Tests on stiffened single square plates under uniformly distributed impulses were reported by Nurick et al. (1995). They showed that for the dishing phase there is a general trend of increasing permanent displacement with increasing impulse similar to unstiffened single plates. Other experimental and numerical investigations on the dynamic responses of the single stiffened plates to uniform blast loading were also carried out by Schubak et al. (1993a/b), Louca et al. (1998) and Schleyer et al. (2003). The failure behavior of the clamped edge was studied numerically by Rudrapatna et al. (2000) where an interactive failure criterion accounting for bending, tension and transverse shear was used. The deformation and fracture of stiffened single square plates to

localized impulsive loading has been recently examined by Langdon et al. (2004). They demonstrated that a central localized blast load leads to higher displacements and lower tearing thresholds than those observed during uniformly distributed blast load tests.

In order to seek alternative replacements for a single stiffened plate, a number of studies have been performed on the structural behavior of lightweight metallic sandwich structures. The design criteria on the elastic response and plastic collapse load of Hat-type corrugated core sandwich panels subjected to air blast loading were proposed by Wiernicki et al. (1991). More recently, their design methods were extended by Liang et al. (2001) to study the minimum weight design of the corrugated sandwich panels. A numerical study on the static load capacity and the dynamic response of the Hat-type corrugated core was performed by Boh et al. (2004), where the effect of imperfections, boundary conditions, and modeling assumptions on the analyses was discussed. The transient response of sandwich panel with multi-layered core structure under blast loading was investigated by Guruprasad and Mukherijee (2000a/b), where the deformation mode and energy absorption of the structure were predicted. The optimization study for the sandwich panels with various types of core structure was recently performed by Xue and Hutchinson (2003, 2004). In this paper the effect of core configurations concerning the central deflection of structures was discussed in detail. Most of the above studies were focused on the dishing phase of the sandwich panels subjected to uniform blast loading.

To the best of author's knowledge, rigorous analyses on predicting ductile fracture of double hulls under high intensity and short duration loads are not currently available in the open literature. Previous studies referred to quasi-static loading, such as collision and grounding damage of ship hull structures, for example, Kee et al. (1995), Wierzbicki and Driscoll (1995), Kitamura et al. (2002), Naar et al. (2002), and Wang et al. (2000). In the above studies, a constant and suitably adjusted fracture strain was used without detail information on the critical damage/fracture functions. Furthermore, developing a new structural configuration is imperative to increase the damage tolerance of existing ship hull and other protective structures subjected to explosive loading. An in-depth understanding of the mechanics of energy absorption and fracture of the critical structures is clearly needed.

The primary objective of this chapter is to propose optimal structural configurations to improve the fracture resistance of clamped sandwich panels with various core structures under a wide range of impulsive loading. This is one of the most important contributions of the present thesis since most of the relevant literature was primarily concerned with the dishing phase without fracture for

both cases of single plate and sandwich panels. This chapter is organized in the following way. The problem of structural design optimization to minimize the fractured area of bottom face sheet is formulated in terms of respective geometric parameters and weight in Section 9.2. The considered geometric parameters are thickness distribution over the cross-section, unit cell aspect ratio, and angle of core. The onset and subsequent extent of fracture in the double hulls are numerically predicted using the Bao and Wierzbicki (BW) fracture criterion. In Section 9.3, a special attention is paid to the effect of various types of fracture criteria on the resulting cracked area of double hull. In Section 9.4, the profiles of stress, strain, and accumulated damage at the critical locations of crack formation are discussed together with a sequential failure process for the intensity of impulse V = 0.43 where V is a normalized impulse (as defined by Eq. (9.4)). In Section 9.5, a parametric study involving topology optimization is carried out to minimize the cracked areas of two types of sandwich panels (USDH and BRAS) for two levels of the applied impulse. In Section 9.6, the parametric study is further extended for a wider range of impulse $0.43 < V < 2.5$. Based on the results, optimal configurations that have a consistent deformation and fracture modes for a wide range of intensity of impulsive loading and a specified weight are proposed for the conventional (USDH) and the new (BRAS) types of double hulls. Finally, the performance of the optimized structures is further compared with other types of double hulls (Navtruss and Y-web) that are commercially available.

9.2 Formulation of structural optimization against fracture

Hull girders, in particular, are very important components in ship and offshore structures. They constitute the backbone's of most ship's structure and they are the most vital structural elements in commercial and naval ships. Fracture of hull girders can lead to catastrophic collapse of the whole ship, resulting in gross human and monetary losses. As seen recently in the case of the U.S.S. *Cole* in the Arabian Sea at the port of Aden, Yemen, ship structural integrity is an essential element for survivability. Figure 9.1 shows the 12.2m by 12.2m amidships hole torn in the ship's port side by a waterline explosion (*U.S. Navy website: www.chinfo.navy.mil/navpalib/news/news_stories/cole-shippix.html*). This example highlights the importance of rigorous design of key structural elements such as the hull.

Fig. 9.1 Close-up view of above waterline damage of USS *Cole* (DDG67) after an explosion on October 12, 2000 (U.S. Navy photos)

9.2.1 Evaluation of damaged area (η_{cb})

In this thesis, damaged area of inner hull (bottom face sheet) is considered as a measure of survivability of ships and/or other protective structures under intense dynamic loading. As a specific example, numerically obtained 3-D fracture patterns of the Blast Resistant Adaptive Sandwich (BRAS) are respectively shown in Fig. 9.2(a) and 9.2(b) for two different angles of view. A plan view of the damaged area of bottom face sheet, which is projected crack path into the *x*-*y* plane, is schematically illustrated in Fig. 9.2(c) where dimensionless horizontal and longitudinal coordinates are denoted by $\xi = x / L_0$ and $\zeta = y / L_0$, respectively. The mass and geometry of the BRAS shown in this figure are specified by $\widetilde{m} = 0.01, \widetilde{h}_w = 0.76, \theta = 10^0$, and *H/W* = 1.0; the area of centrally loaded pressure is one quarter of full area ($\eta_0 = (L_1 / L_0)^2 = 0.25$). Note that detail information on the numerical models is presented in Section 9.3. Based on current coordinates of discrete nodal points associated with the crack path (marked by filled circle), the normalized damage area of bottom face sheet, η_{cb} is defined by

$$\eta_{cb} = \frac{1}{2}\sum_{i=1}^{k}(\xi_{i+1} - \xi_i)(\zeta_i + \zeta_{i+1}) \tag{9.1}$$

where k is the number of nodal points within the closed crack path. The above scalar quantity η_{cb} is selected as a measure of fracture resistance for various types of double hulls considered in the present thesis, see Fig. 8.2. Another measure is the initial resistance to the first crack formation at the bottom face sheet.

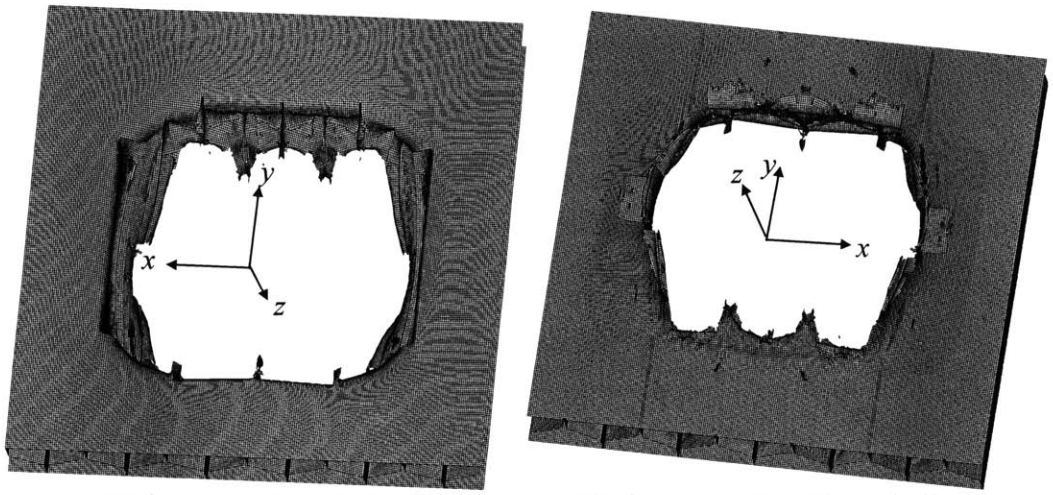

(a) fracture pattern (outer hull) (b) fracture pattern (inner hull)

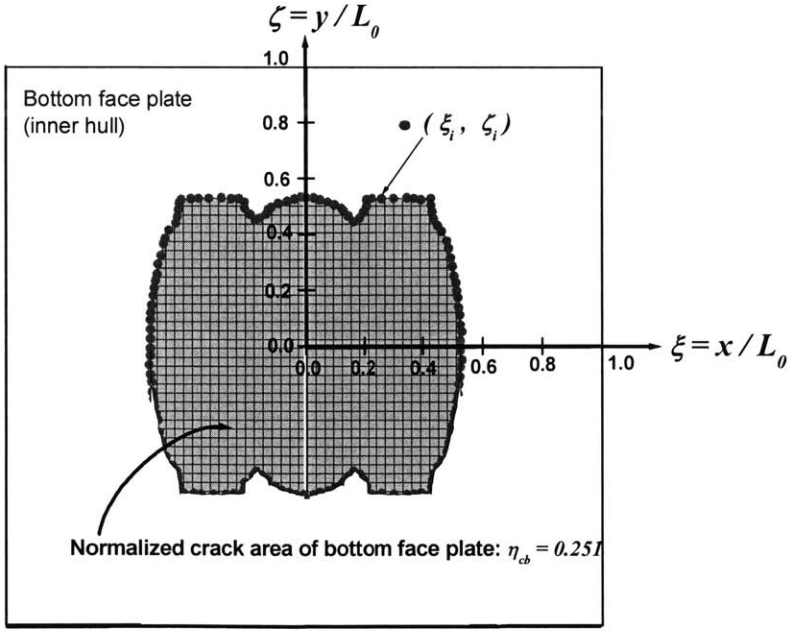

(c) normalized damage area of bottom face plate (inner hull) as a measure of ship survivability

Fig. 9.2 Final fracture patterns and schematic diagram of normalized crack area of double hull. Note that the specific case of BRAS (with $\widetilde{m} = 0.01, \widetilde{h}_w = 0.76, \theta = 10^0$, and H/W = 1.0) under the central impulsive loading (with $\eta_0 = 0.25$ and $V = 0.95$) is shown as an example.

9.2.2 Statement of structural optimization

A major design objective of this Chapter is to minimize the damage area η_{cb} under a prescribed weight of sandwich panels. Therefore, a general problem of structural optimization process for minimum damage can be stated as follows: find the set of design variables, $\mathbf{X}$, that will minimize $\eta_{cb}(\mathbf{X})$ and subject to $C_j(\mathbf{X}) \le 0$ and $X_i^L \le X_i \le X_i^U$. The function $\eta_{cb}(\mathbf{X})$, which is referred to as the objective function, is the damaged area of the sandwich panel. The $C_j(\mathbf{X})$ are referred to as constraints and the domain of the optimum is the limited by the side constraints $X_i^L \le X_I \le X_I^U$.

The geometry and loading configurations of double hulls with four different core arrangements are illustrated in Fig. 8.2 and detail descriptions on the geometrical parameters are also given in Chapter 8.1. For the case of BRAS, three variables are identified: $\widetilde{h}_w$, θ, and H/W, that is,

$$\mathbf{X} = \left\{\widetilde{h}_w, \theta, H/W\right\} \tag{9.2}$$

where the design variables are allowed to vary within prescribed lower (L) and upper (U) limits, see also Table 9.1

$$\begin{aligned} &\widetilde{h}_w{}^L \le \alpha \le \widetilde{h}_w{}^U \\ &\theta^L \le \theta \le \theta^U \\ &\frac{H}{W}^L \le \frac{H}{W} \le \frac{H}{W}^U \end{aligned} \tag{9.3}$$

Since the thickness of web core h_w is determined by $\widetilde{h}_w$ and h_0, the limit of h_0 is also included in Table 9.1 in a normalized form. For the purpose of applicability to real structures, the ranges of thicknesses and cell height are specified based on the sectional dimensions of USDH that is currently available in the open literature (see Table 9.2). A survey of nine different geometries of USDH was made to set up lower and upper bounds on variable geometrical parameters of the double hull. As can be seen from Table 9.2, the bound for the thicknesses of plates normalized by the cell height is $0.0036 \le (h_f, h_w)/H \le 0.027$ and the ratio of cell height to width is $0.88 \le H/W \le 2.33$. It should be noted that the dimensions presented in Table 9.2 are mostly based on data for a standard ship. Hence, they are not directly applicable to an adaptive sandwich type of structural arrangement. For the application to the entire ship, the single skin stiffened construction, which is commonly used in shipbuilding, will be replaced by the sandwich construction with the new adaptive core. Consequently, smaller range of cell height ($300mm \le H \le 1200mm$) should be considered, as

compared to that of standard ship ($2000mm \le H \le 3000mm$). Moreover, a feasible range of thickness is need to be taken due to the manufacturability. Finally, considering the above-mentioned limitations, all the thicknesses of plates taken in the present parametric study are $0.003 \le (h_f, h_w, h_0)/H \le 0.08$ in the normalized form and $3mm \le (h_f, h_w, h_0) \le 45mm$ in magnitude.

We selected the normalized mass $\tilde{m}$ (defined by Eq. (8.6)) as a constraint that provides bounds on various responses quantities. It should be mentioned that additional constraints, such as sectional bending stiffness and buckling strength, could be considered to ensure the global stability for normal loading condition.

The present problem of structural optimization process for BRAS is schematically illustrated in Fig. 9.3. Obviously, this formulation can also be applied to other sandwich panels with different core structures, such as USDH, Navtruss, and Y-web.

Table 9.1 Prescribed ranges of design variables for the present optimization study

h_0/H		$\tilde{h}_w$		H/W		θ	
$(h_0/H)^L$	$(h_0/H)^U$	$\tilde{h}_w^{\ L}$	$\tilde{h}_w^{\ U}$	$(H/W)^L$	$(H/W)^U$	θ^L	θ^U
0.003	0.08	0.1	2.5	0.3	1.8	0^0	50^0

Note: The range of thickness for the face sheet and core is 3mm ~ 45mm.

Table 9.2 Summary of the sectional dimensions of USDH in the literature

Scale	Dimensions in [mm]			Normalized dimensions			References
	h_f	h_w	H	h_f/H	h_w/H	H/W	
1:50	0.75	0.75	41.7	0.018	0.018	1.0	Yahiaoui et al. (1994)
1:1	19.5~23.5	21.0	3000	0.0065~ 0.0008	0.007	-	Zhang (2002)
1:1	18.0~19.0	21.0	2500	0.0072~ 0.0076	0.0084	-	Zhang (2002)
1:6	2.8~3.95	2.8~3.95	350	0.008~ 0.0113	0.008~ 0.0113	1.24~1.49	Paik et al. (1999)
1:1	12.6~22.0	12.6~22.0	2000~ 3500	0.0036~ 0.011	0.0036~ 0.011	1.24~1.49	Paik et al. (1999)
1:10	2.3	2.3	200	0.0115	0.0115	1.0	Wang et al. (2000)
1:1	6.5	5.0	340	0.019	0.015	1.05	Naar et al. (2002)
1:1	12.0~25.0	11.0~21.0	1000~ 2000	0.006~ 0.025	0.0055~ 0.021	0.88~2.33	Sikora et al. (1997)
1:1	15.8~50.8	12.7	1880	0.0084~ 0.027	0.00675	1.5	Kee et al. (1995)

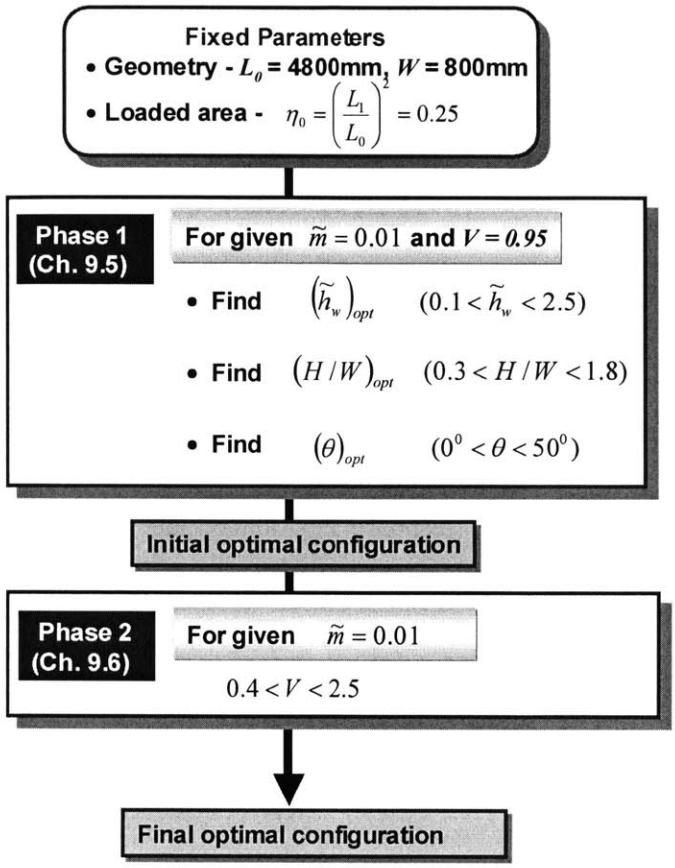

Fig. 9.3 Procedure of present optimization study. Note that $\tilde{m}$ is the normalized mass per unit area (Eq. (8.6)) and $V = I_0 / (c\rho L_0 \tilde{m})$ is the dimensionless magnitude of applied impulse (Eq. (9.4)).

9.3 Development of Finite Element (FE) model

9.3.1 FE analysis of double hulls under impulsive loading

High strength AH36 steel was considered and detail information on plasticity and fracture for this material is presented in Chapter 7.3.2. The finite element models of the double hull panels shown in Fig. 9.4 were created using the mesh generator program, *HyperMesh* Version 6.0. ABAQUS/Explicit Version 6.4.1 (2003) was utilized to simulate the transient responses of double hulls under impulsive loading. The S4R shell element, with five integration points through thickness, one integration point in the element plane, finite membrane strain, arbitrarily large rotation, and

stiffness based hourglass control, was employed. Note that no special elements, such as beam and rigid constraints, were utilized to simulate the presence of weldments between the face sheets and cores. The face sheets and cores were constructed with the shell elements. Because the panels have two axes of symmetry, a quarter model was considered. The ratio of average element length to the plate width L_0 was 0.004, which provides 54,720 elements in the quarter model of BRAS with L_0= 4800mm and H = W = 800mm. The displacement and rotation of nodes corresponding to the clamped edges were fixed. The explosive loading was idealized by a rectangular pressure pulse in which the pressure load (with amplitude of p_0) was held constant during a time interval $t_0 > 0$ and then was suddenly removed. The pressure load was applied only to the outer hull (top face sheet). The duration of pressure pulse used in the numerical simulations was t_0 = 1msec, which is sufficiently short as compared to the response duration of the sandwich structures considered (typically order of 10msec). The intensity of applied impulse can be expressed in terms of the dimensionless initial velocity

$$V = \frac{I_0}{m^* c} \tag{9.4}$$

where $c = \sqrt{\sigma_0 / \rho}$ is the so-called transverse wave speed in the plate, $m^* = \rho L_0 \tilde{m}$ is the mass per unit area, and σ_0 is the average plastic flow stress of the material under quasi-static loading at room temperature (see Eq. (7.1)). The value of c and σ_0 for AH36 steel are 297m/sec and 690MPa, respectively. The pressure amplitude for the uniform rectangular pressure pulse is

$$p_0 = \frac{cm^* V}{t_0} \tag{9.5}$$

The normalized area of the dynamic pressure loading was $\eta_0 = (L_1 / L_0)^2 = 0.25$ for all the results reported in the following.

In the present numerical simulation, ductile fracture was assumed to be controlled by Eq. (7.29). The fracture was simulated with the *SHEAR FAILURE option that has a provision of making the critical strain dependent on stress triaxiality in conjunction with the *PLASTIC option to specify the ductile fracture. When the equivalent strain weighted by stress triaxiality reaches the critical value at all of the integration points in a shell element, this element was deleted to model crack formation and propagation.

All numerical simulations were carried out on a personal computer (2GHz Intel Pentium IV, 2 GBytes RAM). The CPU times for BRAS for the case of H = 800mm and $\theta = 10^0$ were 25 minutes. The CPU times for other three types of structures with H = 800mm were approximately 15 minutes.

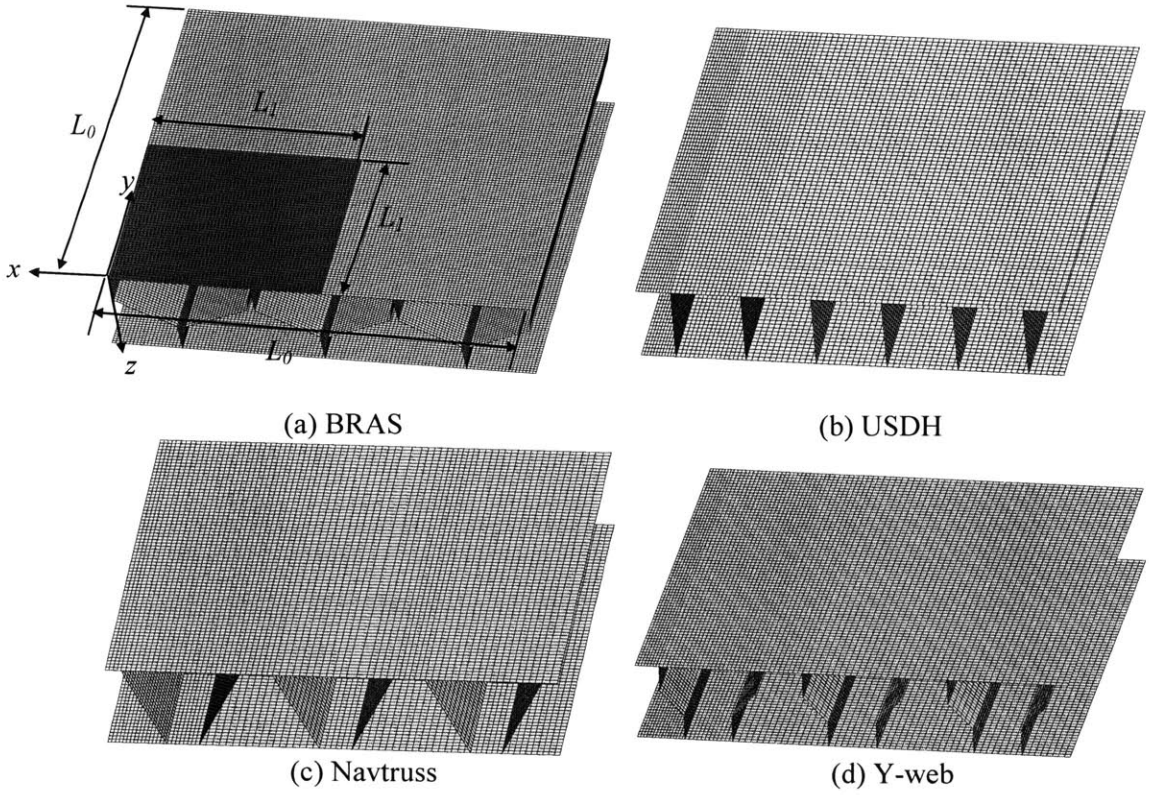

(a) BRAS (b) USDH

(c) Navtruss (d) Y-web

Fig. 9.4 FE models of double hull panels (1/4 model)

9.3.2 Effect of the fracture criterion on the damaged area

In addition to the fracture locus given by Eq. (7.29) under the assumption of **a** = *0.43***b** (see the locus denoted by solid line in Fig. 9.5, $\bar{\varepsilon}_f = f(\sigma_m / \bar{\sigma})$), uniform failure strains (independent of the stress triaxiality) were considered. Calculation were run with three values of the critical equivalent strain 0.43, 0.3, and 0.18. These values correspond to the fracture strains in uniaxial, plane strain tension, and pure shear, respectively. The rationale for using several alternative types of fracture

envelope is that the constant equivalent strain fracture locus is provided in the material library of all commercial FE codes, such as LS-DYNA (2003), PAM-CRASH (2003) etc. However, none of the user's manual of these codes provides any clues on how to determine the fracture parameter.

Two specific cases of double hulls (USDH and BRAS) subjected to the central impulsive loading with the normalized loading area $\eta_0 = 0.25$ and the normalized impulse V = 0.95 were investigated. The plan views of the damaged areas of USDH and BRAS are respectively shown in Figs. 9.6 and 9.7 at time = $10t_0$ where t_0 is the duration of applied pressure pulse. Note that only quarter models are shown and the normalized horizontal (ξ) and longitudinal (ς) axes are used in both figures. It can be seen that the uniform strain based on the condition of plane strain tension ($\bar{\varepsilon}_f = 0.3$) provides similar fracture patterns and damaged area to the case of $\bar{\varepsilon}_f = f(\sigma_m / \bar{\sigma})$. On the other hand, there is noticeable discrepancy in the prediction of the extent of damage using the uniform strains under the condition of uniaxial stress and pure shear ($\bar{\varepsilon}_f = 0.43, 0.18$). Two important conclusions could be drawn from the above comparisons. First, the range of stress triaxiality in the potential fracture point of the present problem is very narrow and can be approximately assumed to be an order of 0.58 (plane strain tension deformation). Second, even though the approach using the uniform strain is used in practice due to its convenience in terms of calibration and implementation in finite element codes, careful attention to the choice of the magnitude $\bar{\varepsilon}_f$ should be given. When using the uniform strain, a suitable constant weighted by the stress triaxiality of the problem should be employed. Note that the fracture locus shown in Fig. 9.5 by solid line ($\bar{\varepsilon}_f = f(\sigma_m / \bar{\sigma})$) was employed as a fracture criterion in all following numerical simulations.

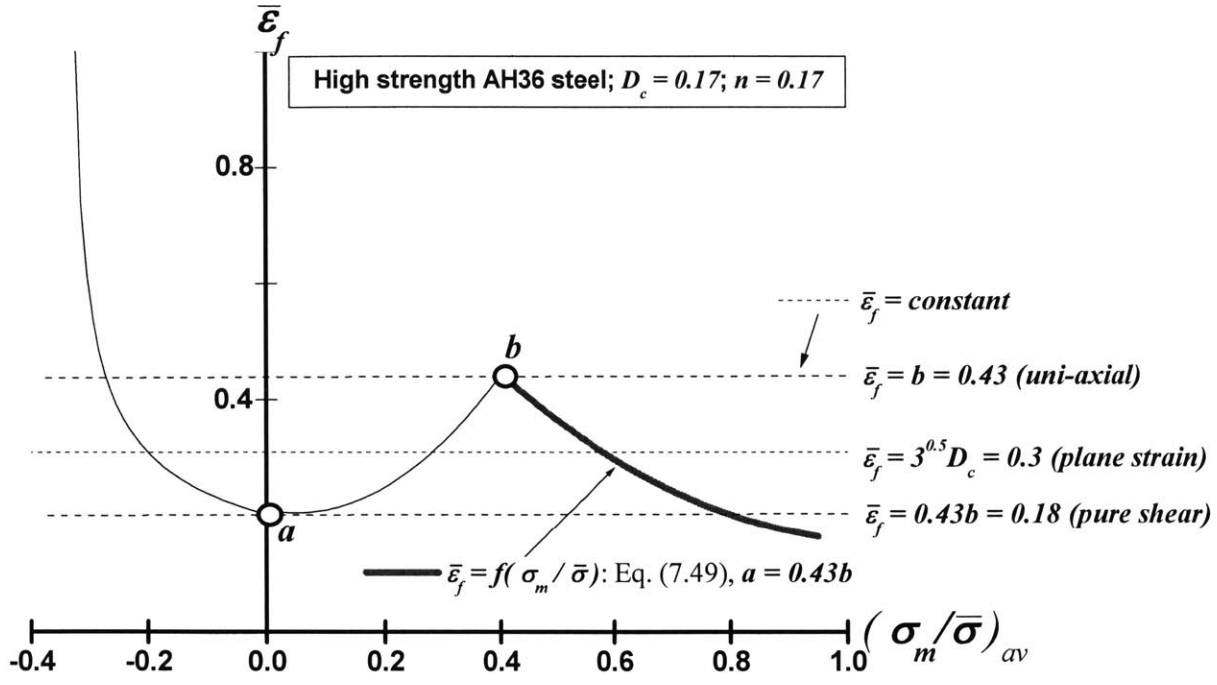

Fig. 9.5 Postulated fracture envelopes for AH36 steel (**a** = 0.18; **b** = 0.43)

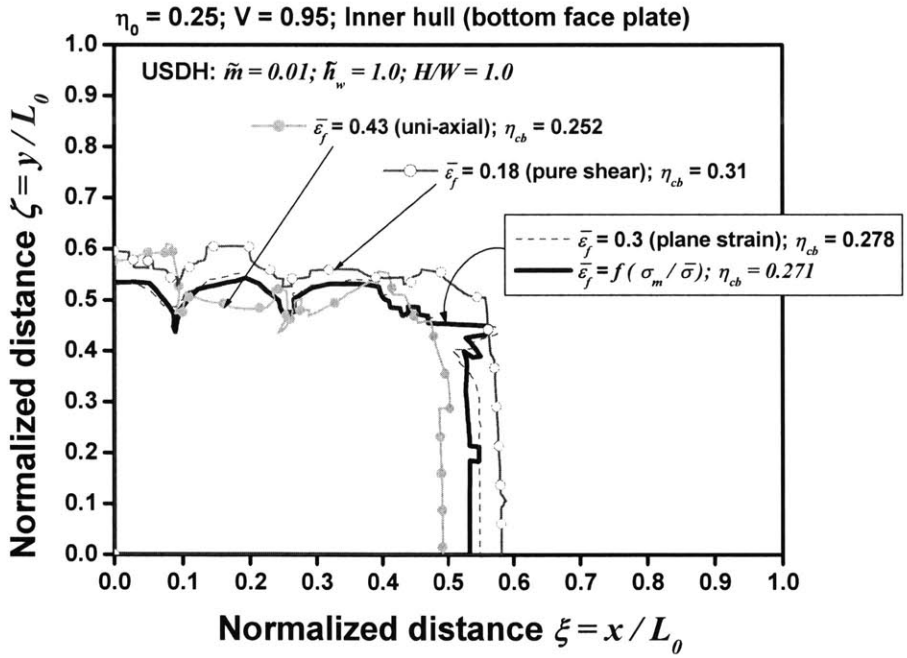

Fig. 9.6 Comparison of the normalized damaged area of bottom face plate (η_{cb}) in USDH obtained from various types of postulated fracture envelopes for AH36 steel. Note that a quarter of full model is shown at time = $10t_0$ (L_0 = 4800mm; W = 800mm).

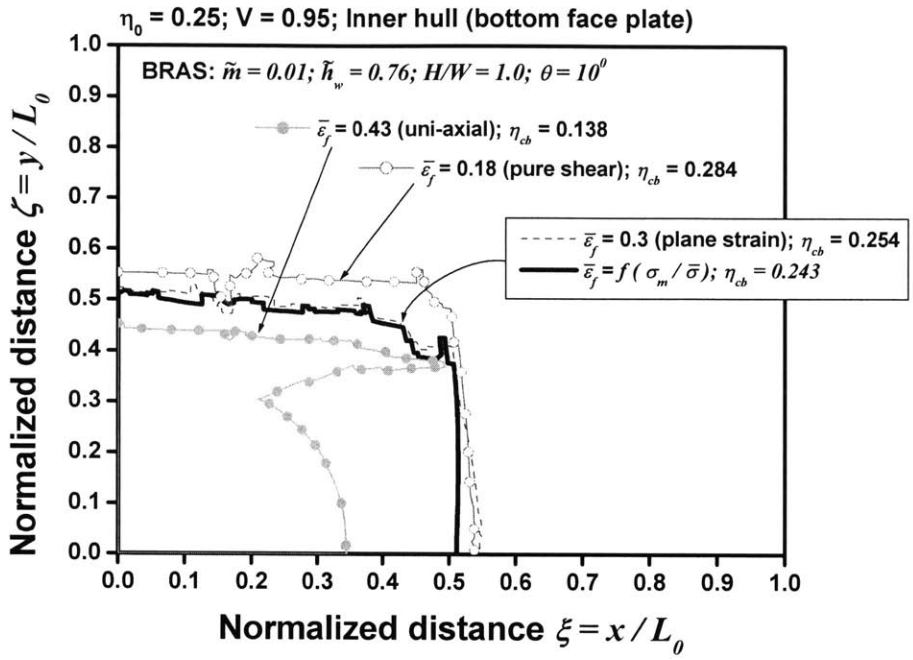

Fig. 9.7 Comparison of the normalized damaged area of bottom face plate (η_{cb}) in BRAS obtained from various types of postulated fracture envelopes for AH36 steel. Note that a quarter of full model is shown at time = $10t_0$ (L_0 = 4800mm; W = 800mm).

9.4. Analysis of formation of cracks in double hulls under impulsive loading

The sequence of the failure process can be illustrated by examining the deformed shapes of the sandwich panels subjected to the localized impulsive loading ($\eta_0 = 0.25$), see Fig. 9.8. The applied magnitude of normalized impulse was V = 0.43, which is 45% smaller than the impulse V = 0.95 being considered in Section 9.5. The set of figures on the left is the USDH ($\tilde{m} = 0.01, \tilde{h}_w = 0.71, H/W = 1.0$), while those on the right correspond to the BRAS ($\tilde{m} = 0.01, \tilde{h}_w = 0.76, H/W = 1.0, \theta = 10^0$). It should be pointed out that the above structures were not yet optimized and only used here as examples of double hulls under impulsive loading. To confirm the symmetric response of the panels, one run with a half model consisting of 109,440 shell elements was made. For both cases of the panels, longitudinal cracks developed initially at the location, $\zeta = 0.475$, of top face sheets (outer hulls). From this point on, the longitudinal cracks followed the connection of the web to the outer hull (weldments) and reached the middle

($\zeta = 0.0$) of the outer hulls. This formation of the longitudinal cracks will be studied in greater details later on by examining the profiles of damage parameters shown in Figs. 9.9 ~ 9.11. With the progress of deformation, cracks were further developed in the horizontal direction of the outer hulls (see the snapshots at $t = 5t_0$ in Fig. 9.8). In the case of USDH, it can be seen that the bottom face sheet (inner hull) deforms from the initial dishing stage. This behavior indicates that the impulse imparted to the outer hull is transferred to the inner hull without further reduction by the plastic deformation of the webs. Consequently, fractures also occurred in the inner hull of USDH (see figures on the left in Fig. 9.8). For the improvement of fracture resistance, inner hull fracture should be minimized while the plastic energy dissipation capacity of the core should be maximized. It is clearly shown that the outer hull of the newly proposed BRAS deforms independently from the inner hull and that adaptive cores are crushed very easily without imposing any deformation to the inner hull approximately up to the stage of $t = 3t_0$. Furthermore, substantial reduction in impulse transfer is observed at the inner hull of the BRAS since large amount of energy is dissipated through intensive plastic deformation of core and fragmentation of outer hull. As a result, fracture can be entirely avoided in the inner hull of the BRAS for this load intensity.

The profiles of important damage parameters - equivalent plastic strain, stress triaxiality, and accumulated damage - were constructed at the point of crack formation in the plate junction of outer hull (see Figs. 9.9 ~ 9.11). Figure 9.9 shows the distributions of equivalent plastic strain along the horizontal and longitudinal directions along with the color-coded contours. All data shown in this figure and also in Figs 9.10 ~ 9.11 was taken from the case of the BRAS at $t = 1.1t_0$. It is seen that peak strain develops and plastic deformation localizes in the plate junction located within the region of applied impulse. Figure 9.10 shows the corresponding profiles of stress triaxiality in the same manner as in Fig. 9.9. It can be seen that the stress state shows the biaxial tension condition ($0.58 < \sigma_m / \bar{\sigma} < 0.67$) around the central region of the plate. The stress triaxiality at which fracture occurs (see filled circle in Fig. 9.10) is 0.58 that corresponds to the plane strain deformation. Figure 9.11 shows the profiles of accumulated damage, as defined by Eq. (2.4). It can be clearly seen that the accumulated damage reaches the critical value of $D_c = 0.172$ (for AH36 steel) at the plate junctions. The above fracture mode "along the plate junction" is quite consistent with the experimental results of Langdon et al. (2004) for the single stiffened plate under localized blast loading. It can be further observed that the sandwich panel exhibits symmetrical behaviors including fracture patterns, stress, and strain fields. Hence, a quarter model was used in all following numerical simulations.

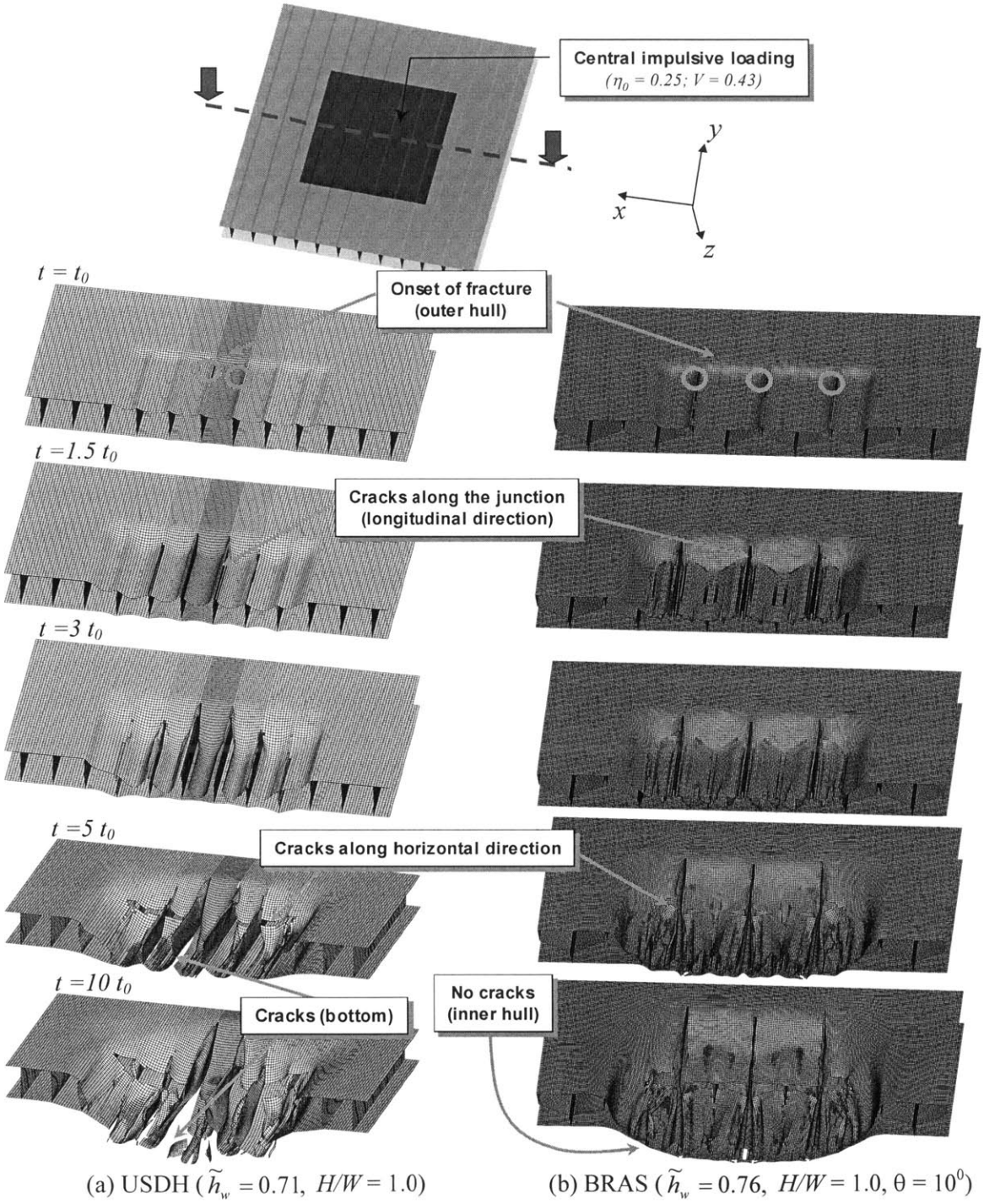

Fig.9.8 Sequence of fracture patterns of the sandwich panels (1/2 model) with $\widetilde{m} = 0.01$ subjected to the central impulsive loading ($\eta_0 = 0.05, V = 0.43$) at different stages of deformation ($t = t_0, 1.5t_0, 3t_0, 5t_0, 10t_0; t_0 = 1m\,\text{sec}$); (a) top view of USDH (left); (b) top view of BRAS (right)

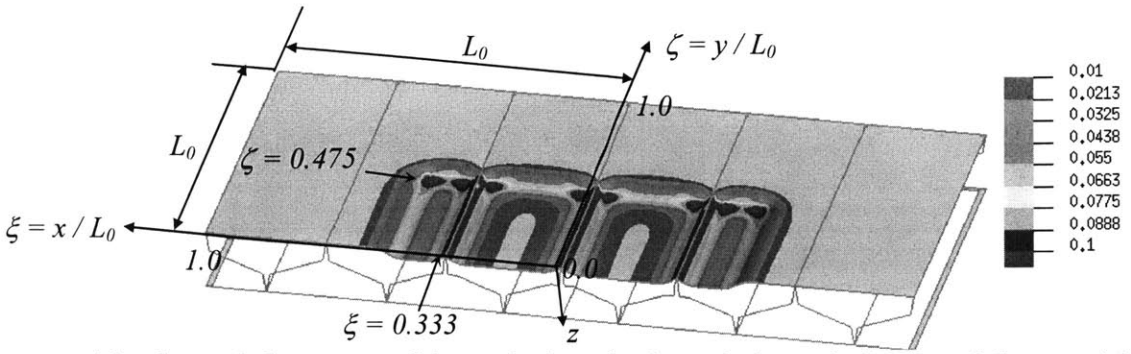

(a) color-coded contours of the equivalent plastic strain (outer hull, 1/2model) at $t = 1.1t_0$

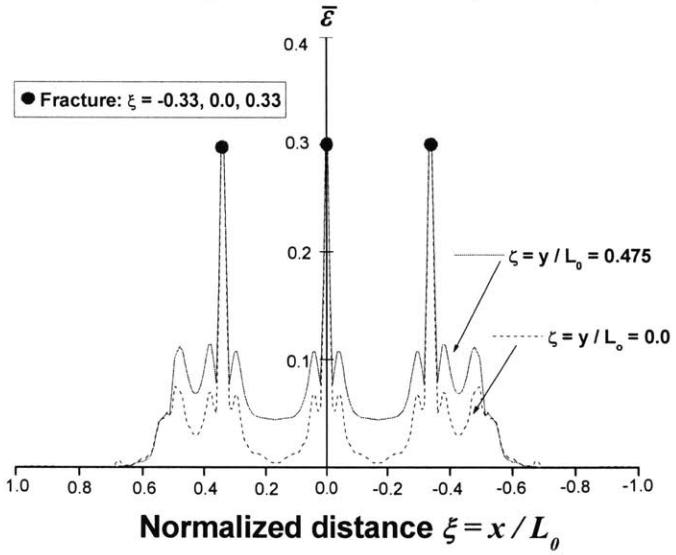

(b) profiles of the equivalent strain along the horizontal direction (x) at $t = 1.1t_0$

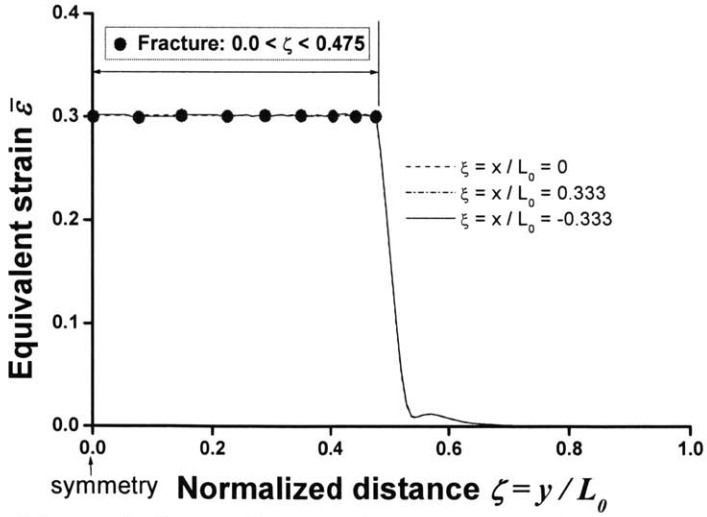

(c) profiles of the equivalent strain along the longitudinal direction (y) at $t = 1.1t_0$

Fig. 9.9 Contours and profiles of the equivalent strain in the top face sheet (outer hull) of the BRAS with $\tilde{m} = 0.01$ subjected to the central impulsive loading ($\eta_0 = 0.25, V = 0.43$). Note that the geometries of the sandwich panel are specified by $H/W = 1.0$, $\theta = 10^0$, $\tilde{h}_w = 0.76$, $L_0 = 4800$mm, and W = 800mm.

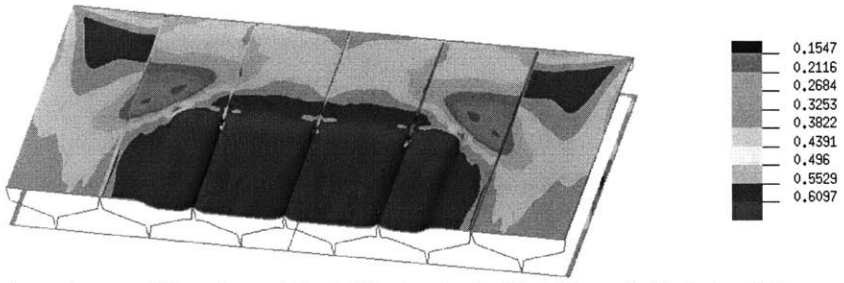

(a) color-coded contours of the stress triaxiality (outer hull, 1/2 model) at $t = 1.1t_0$

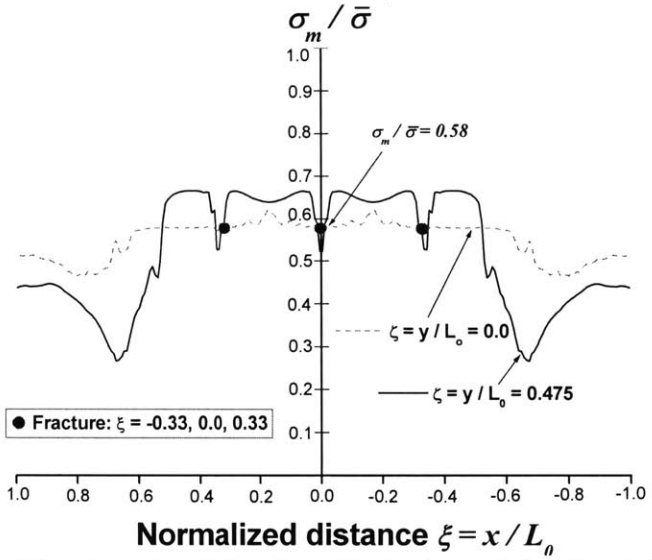

(b) profiles of the stress triaxiality along the horizontal direction (x) at $t = 1.1t_0$

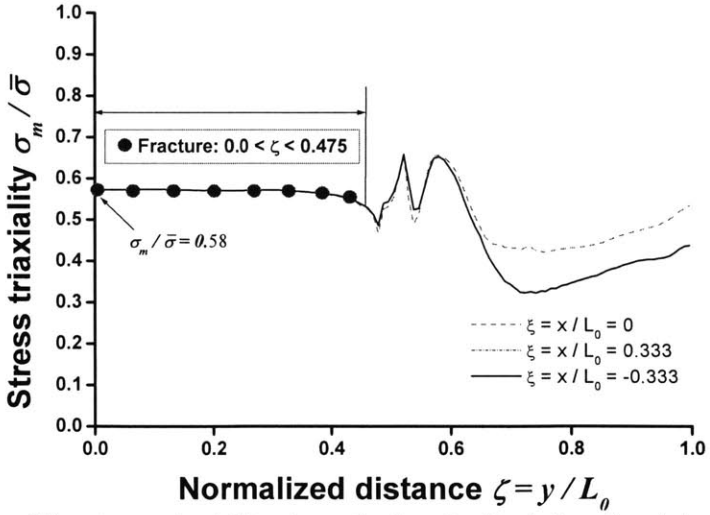

(c) profiles of the stress triaxiality along the longitudinal direction (y) at $t = 1.1t_0$

Fig. 9.10 Contours and profiles of the stress triaxiality in the top face sheet (outer hull) of the BRAS plate with $\tilde{m} = 0.01$ subjected to the central impulsive loading ($\eta_0 = 0.25, V = 0.43$). Note that the geometries of the sandwich panel are specified by $H/W = 1.0$, $\theta = 10^0$, $\tilde{h}_w = 0.76$, $L_0 = 4800$mm, and W = 800mm.

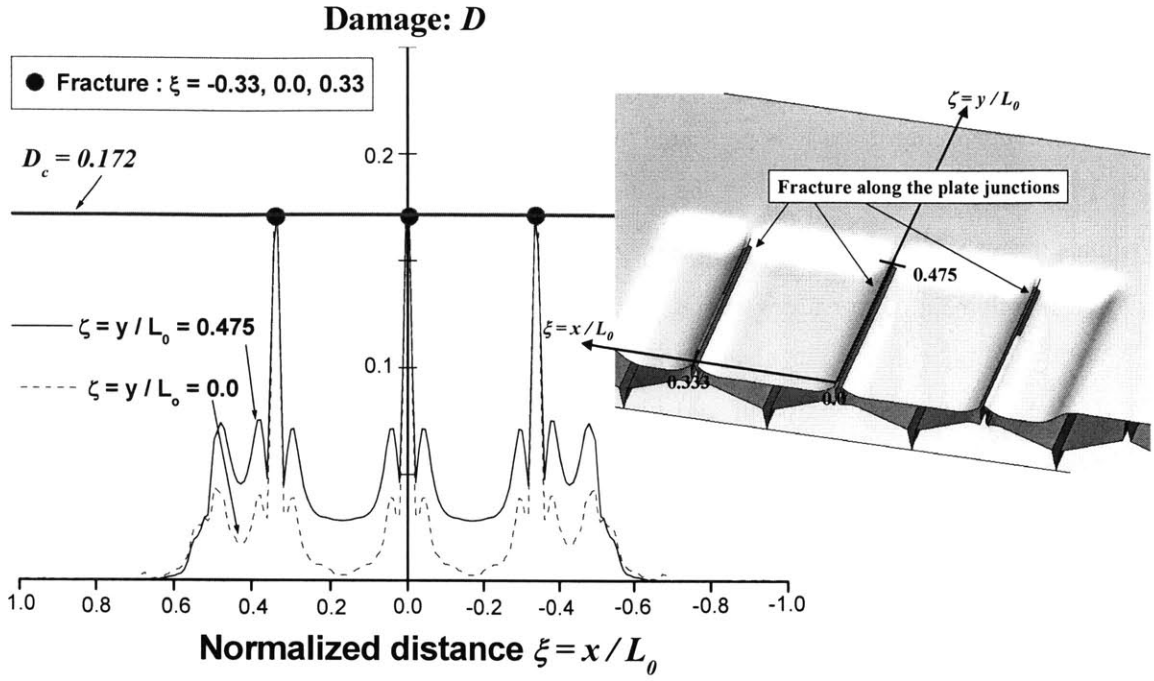

(a) profiles of accumulated damage along the horizontal direction (x) at $t = 1.1t_0$

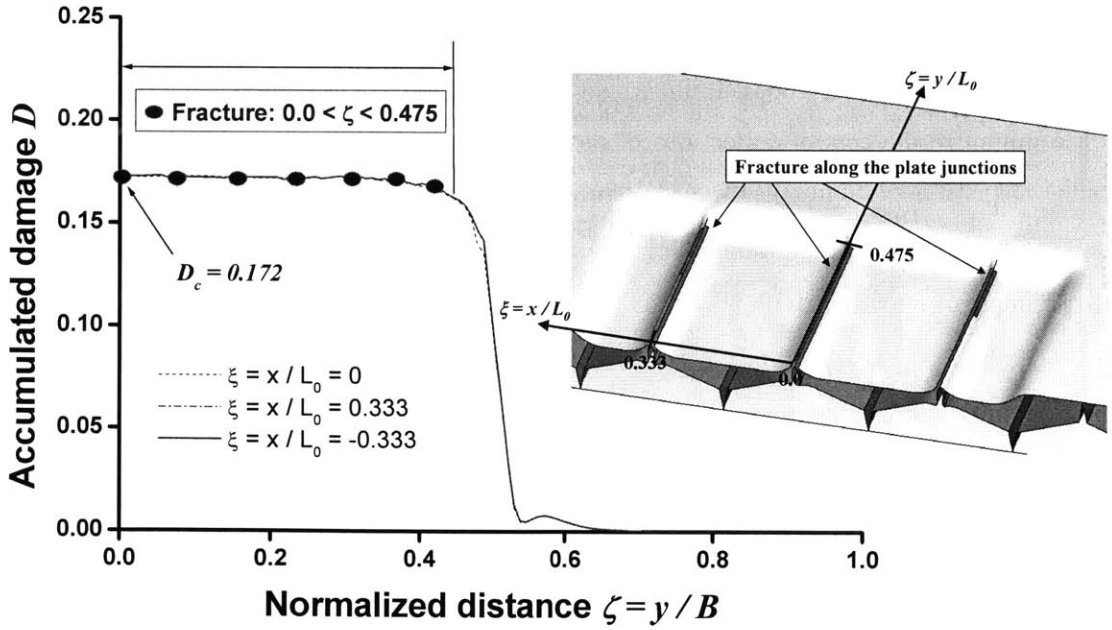

(b) profiles of accumulated damage along the longitudinal direction (y) at $t = 1.1t_0$

Fig. 9.11 Profiles of the accumulated damage in the top face sheet (outer hull) of the BRAS with $\widetilde{m} = 0.01$ subjected to the central impulsive loading ($\eta_0 = 0.25, V = 0.43$). Note that the geometries of the BRAS are specified by $H/W = 1.0$, $\theta = 10^0$, $\widetilde{h}_w = 0.76$, $L_0 = 4800$mm, and W = 800mm.

9.5 Parametric study of double hulls under impulsive loading

An extensive parametric study is presented to determine the optimal configuration of the USDH and the BRAS by seeking to minimize the damaged area for given weight ($\tilde{m}$), plate width (L_0), cell width (W), and impulse (V). The present optimization process is accomplished through the search over the domain of the design variables. No special optimization routine was used. Most of the results were obtained for the given values of $\tilde{m} = 0.01$. Additional runs were also made for $\tilde{m} = 0.014$ to confirm the validity of the optimal paramters. The dimensions of panels were $L_0 = 4800mm$ and $W = 800mm$. The magnitude of applied impulse taken in this Section 9.5 was $I_0 = 105.6KPa\sec$ and the corresponding normalized impulse was $V = 0.95$ from Eq. (9.4) for the specific value of $\tilde{m} = 0.01$. The assumed magnitude of impulse is 2.3 times larger than the critical impulse to fracture for the case of single plate with a standard thickness of hull ($h = 16mm$) for AH36 steel, according to Eq. (7.21).

It should be mentioned that similar optimization study for sandwich plates with pyramidal truss core, triangular-type corrugated core, and square honeycomb core have recently been performed by Xue and Hutchinson (2003, 2004). In their study, the optimal configurations of the three sandwich plates to minimize the central deflections of face sheets were introduced as an objective function. Since the range of applied impulse was relatively low ($V < 0.3$), fracture was not considered in their investigation. They focused on the maximum deflections that the plates sustain. On the other hand, localized impulsive loading with $\eta_0 = 0.25$ and much higher intensity $V >> 0.4$ is considered in the present study. As shown in Figs. 9.19 ~ 9.25, most of structural sandwich panels can not sustain the deformation without fracture for the high intensity of impulse ($V >> 0.4$). Thus, fracture is taken to be the objective function of the present optimum procedure rather than the middle point deflection.

9.5.1 Unidirectionally Stiffened Double Hull (USDH)

9.5.1.1 Effect of thickness distribution ($\tilde{h}_w$)

The normalized damage area of the bottom face sheet (η_{cb}) of the USDH is shown in Fig. 9.12 as a function of relative web core thickness $\tilde{h}_w$. Two different values of the normalized mass were specified ($\tilde{m} = 0.01$ and 0.014). All data in this figure and in all other cases presented in this Chapter 9 was taken at 10ms, which corresponds to 10 times the duration of the pressure pulse ($t_0 = 1$ms). In Fig. 9.12, the dimensionless thickness of core $\tilde{h}_w$ ranges from 0.2 to 2.43 with fixed values of normalized cell height (H/W = 1.0). Accordingly, the dimensionless thickness of face sheet $\tilde{h}_f$ ranges from 1.4 to 0.29, see Eq. (8.4). In view of Eq. (8.7), the uniform thickness of the plate, h_0, generally depends on the parameters: L_0, $\tilde{m}$, Ω, and H/W, that is

$$h_0 = \{L_0, \tilde{m}, \Omega, H/W\} \tag{9.6}$$

In this example shown in Fig. 9.12, the h_0 is only a function of prescribed weight $\tilde{m}$ since other three parameters are set to be constant ($L_0 = 4800mm, \Omega = 1.0, H/W = 1.0$). The numerical values of the sectional parameters considered in Fig. 9.12 are also summarized in the inserted table in the same figure. One can see that in the cases of USDH changing the thickness of the core web ($\tilde{h}_w = 0.2$ or $\tilde{h}_w = 2.4$) is not an efficient way to minimize the damaged area, whereas the USDHs having relatively uniform distribution of thickness ($\tilde{h}_w = 0.9 \sim 1.15$) experience the smallest damaged area. It is further seen that the η_{cb} attains a minimum at $\tilde{h}_w = 1.14$ and 0.95 for the cases of $\tilde{m} = 0.01$ and 0.014, respectively. In the case of $\tilde{m} = 0.01$, the maximum and minimum damaged areas within the prescribed limits of the variables are visually shown in Fig. 9.13 where dimensionless horizontal (ξ) and longitudinal (ς) distances from the center of bottom plate are used. Note that only one quarter of full model is shown in Fig. 9.13. As compared to the maximum area ($\eta_{cb} = 0.38$ obtained from $\tilde{h}_w = 0.2$), 23.7% of the area is reduced by changing the thicknesses of the sandwich panels with $\tilde{h}_w = 1.14$, see shaded area in Fig. 9.13. Based on the above results, it can be concluded that the USDHs with uniformly distributed thickness over the cross-section ($\tilde{h}_w = 0.9 \sim 1.15$) have the smaller damaged area than other types of thickness distribution.

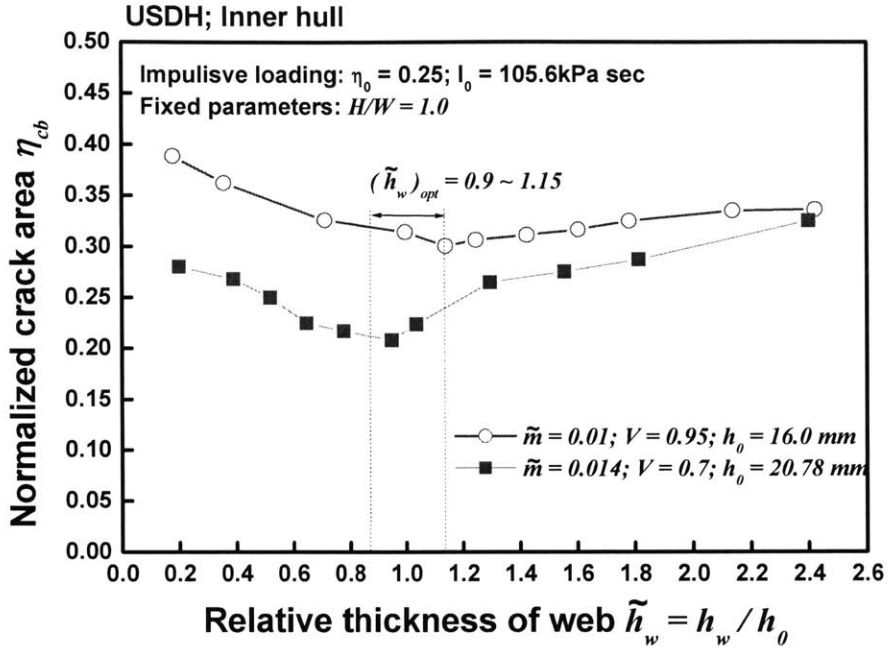

$\tilde{m}$	0.01	0.01	0.01	0.01	0.01	0.01
H/W	1.0	1.0	1.0	1.0	1.0	1.0
Ω	1.0	1.0	1.0	1.0	1.0	1.0
h_0	16.0mm	16.0mm	16.0mm	16.0mm	16.0mm	16.0mm
$\tilde{h}_w$	**0.2**	**0.36**	**0.71**	**1.14**	**2.14**	**2.43**
(h_w)	**(3.2mm)**	**(5.76mm)**	**(11.4mm)**	**(18.2mm)**	**(34.2mm)**	**(38.9mm)**
$\tilde{h}_f$	1.4	1.32	1.1	0.93	0.43	0.29
(h_f)	(22.4mm)	(21.1mm)	(17.6mm)	(14.9mm)	(6.9mm)	(4.6mm)

Fig. 9.12 Normalized damaged area of the bottom fact plate (η_{cb}) of USDH with two different values of $\tilde{m}$ versus relative thickness of web $\tilde{h}_w$ (with $H/W = 1.0$); normalized loading area $\eta_0 = 0.25$; $I_0 = 105.6kPa$ sec; L_0 = 4800mm; W = 800mm

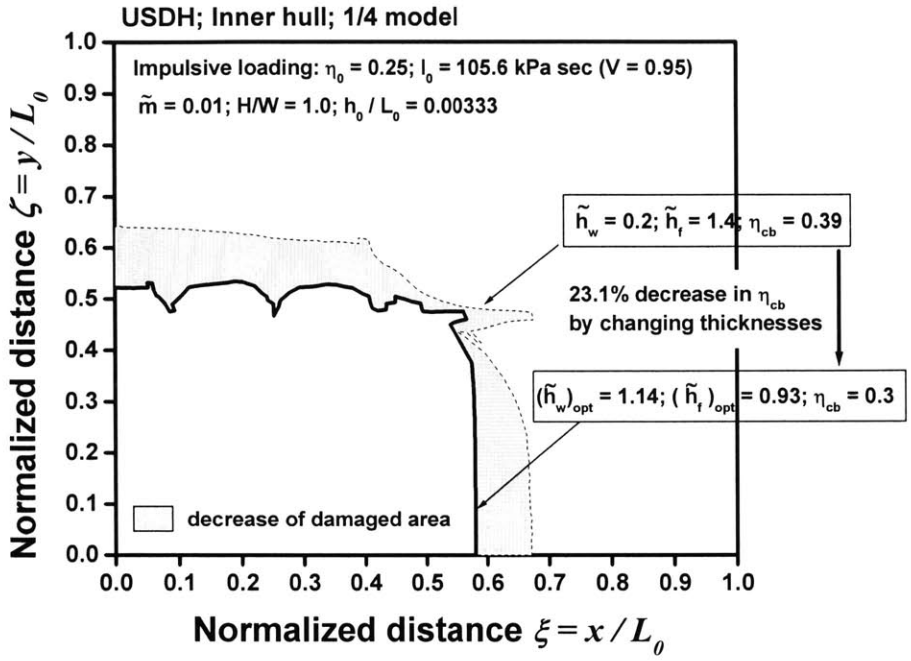

Fig. 9.13 Plan views of the η_{cb} for the two extreme cases of USDH with $\tilde{m} = 0.01$ and characterized by $\tilde{h}_w$ (with $H/W = 1.0$); normalized loading area $\eta_0 = 0.25$; $I_0 = 105.6 kPa$ sec; L_0 = 4800mm; W = 800mm

9.5.1.2 Effect of aspect ratio of unit cell (H/W)

In Fig.9.14, by fixing the parameter at $\tilde{h}_w = 1.14$, the normalized cell height (*H/W*) of USDH was varied from 0.48 to 1.5 for the given weight $\tilde{m} = 0.01$. The uniform thickness (h_0) of the sandwich plates and the relative thickness of face sheet $(\tilde{h}_f)$, respectively, obtained from Eqns. (8.4) and (8.7) decrease with increasing the normalized cell height *H/W*. As can be seen, the crack area of bottom face sheet is affected by the cell height provided *H/W* < 1.0 and it has a minimum at *H/W* = 1.0. Beyond this point (*H/W* > 1.0), there is not much influence of the cell height on the damaged area.

It can be concluded that USDH design does not have much room for reducing the explosive damage. Other core configuration must be looked at.

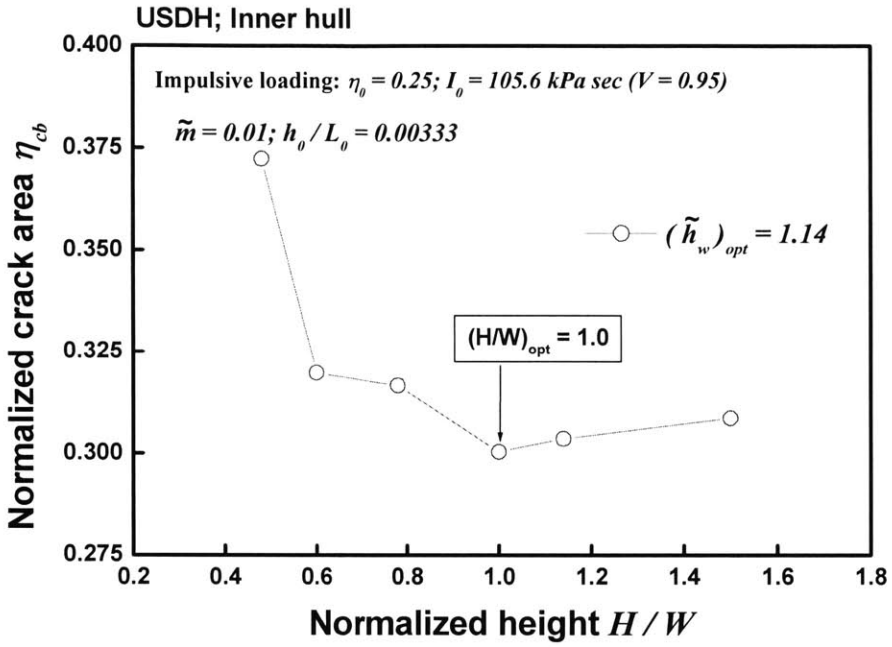

$\tilde{m}$	0.01	0.01	0.01	0.01	0.01	0.01
H/W	**0.48**	**0.6**	**0.78**	**1.0**	**1.14**	**1.5**
Ω	1.0	1.0	1.0	1.0	1.0	1.0
h_0	19.35mm	18.46mm	17.26mm	16.0mm	15.29mm	13.71mm
$\tilde{h}_w$	1.14	1.14	1.14	1.14	1.14	1.14
(h_w)	(22.1mm)	(21.0mm)	(19.7mm)	(18.2mm)	(17.4mm)	(15.6mm)
$\tilde{h}_f$	0.97	0.96	0.95	0.93	0.92	0.90
(h_f)	(18.7mm)	(17.7mm)	(16.3mm)	(14.9mm)	(14.1mm)	(12.3mm)

Fig. 9.14 Normalized damaged area of the bottom fact plate (η_{cb}) of USDH with $\tilde{m} = 0.01$ versus normalized height H / W (with $\tilde{h}_w = 1.14$); normalized loading area $\eta_0 = 0.25$; normalized impulse $V = 0.95$; $L_0 = 4800$mm; W = 800mm

9.5.2 Blast Resistant Adaptive Sandwich Structure (BRAS)

A similar optimization procedure was carried out for the BRAS. As compared to the USDH, an additional parameter, web angle θ, was considered.

9.5.2.1 Effect of thickness distribution ($\widetilde{h}_w$)

In Fig. 9.15, the $\widetilde{h}_w$ ranges from 0.2 to 2.0 with fixed variables of *H/W* = 1.0 and $\theta = 10^0$. One can see that the cracked area in the bottom face sheet (η_{cb}) of BRAS is strongly affected by the thickness distribution between face sheets and core, especially for the case of $\widetilde{m} = 0.014$. A significant reduction of the η_{cb} was achieved by relatively thinner or thicker core ($0.2 < \widetilde{h}_w < 0.3$ or $1.8 < \widetilde{h}_w < 2.0$) for the given magnitudes of impulse $I_0 = 105.6 KPa \sec$. For those ranges of $\widetilde{h}_w$, it was found that the initial kinetic energy imparted to the top face sheet is mostly dissipated by the transverse web and top face sheet of the structures. As clearly shown in Fig. 9.16 where the cracked areas of those two extreme cases are compared, 29% of bottom area was detached from the structure with $\widetilde{m} = 0.01$ and $\widetilde{h}_w = 1.14$. On the other hand, fracture was restricted to only 5% of bottom area in the case of $\widetilde{m} = 0.01$ and $\widetilde{h}_w = 1.9$. The 3-D views of the fracture pattern corresponding to the case ($\widetilde{m} = 0.01$ and $\widetilde{h}_w = 1.9$) are shown in Fig. 9.23(e) and 9.23(k). Furthermore, in order to ensure the validity of the optimum solution of $\widetilde{h}_w$ for a wide range of impulse, additional runs were carried out and the discussion on the results are presented in Section 9.6.1, see also Figs. 9.20 and 9.21.

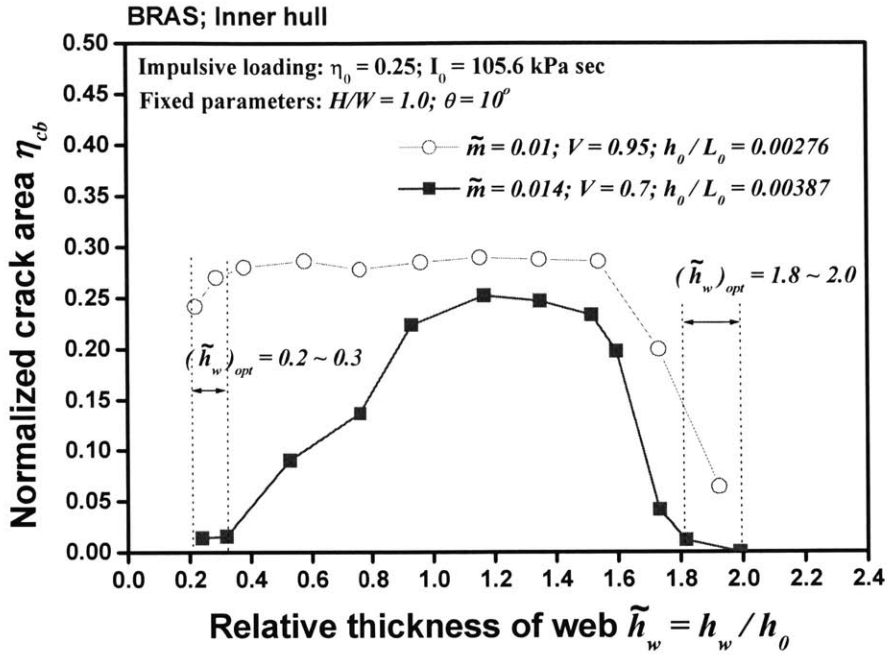

$\tilde{m}$	0.01	0.01	0.01	0.01	0.01	0.01
H/W	1.0	1.0	1.0	1.0	1.0	1.0
θ	10^0	10^0	10^0	10^0	10^0	10^0
Ω	1.62	1.62	1.62	1.62	1.62	1.62
h_0	13.3mm	13.3mm	13.3mm	13.3mm	13.3mm	13.3mm
$\tilde{h}_w$	**0.22**	**0.29**	**0.76**	**1.14**	**1.73**	**1.9**
(h_w)	**(3.0mm)**	**(3.9mm)**	**(10.1mm)**	**(15.1mm)**	**(23.0mm)**	**(25.0mm)**
$\tilde{h}_f$	1.63	1.58	1.19	0.89	0.41	0.27
(h_f)	(21.7mm)	(20.9mm)	(15.9mm)	(11.8mm)	(5.5mm)	(4.0mm)

Fig. 9.15 Normalized damaged area of the bottom fact plate (η_{cb}) of BRAS with two different values of $\tilde{m}$ versus relative thickness of core $\tilde{h}_w$ (with $H/W = 1.0$ and $\theta = 10^0$); normalized loading area $\eta_0 = 0.25$; $I_0 = 105.6 kPa$ sec; L_0 = 4800mm; W = 800mm

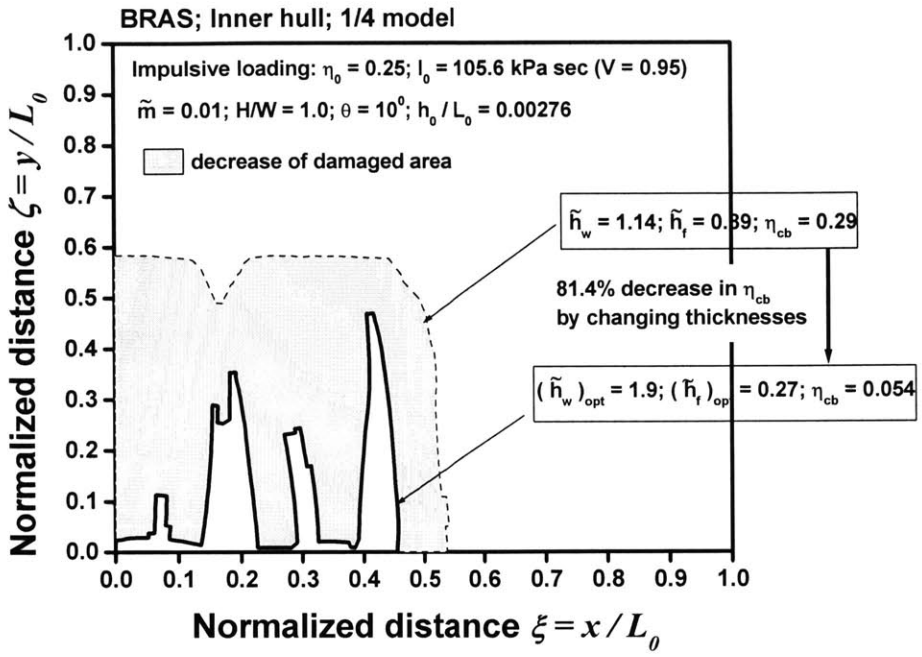

Fig. 9.16 Plan views of the η_{cb} for the two extreme cases of BRAS with $\tilde{m} = 0.01$ and characterized by $\tilde{h}_w$ (with $H/W = 1.0$ and $\theta = 10^0$); normalized loading area $\eta_0 = 0.25$; $I_0 = 105.6 kPa$ sec; L_0 = 4800mm; W = 800mm

9.5.2.2 Effect of aspect ratio of unit cell (H/W)

In Fig. 9.17, the weight is prescribed at $\tilde{m} = 0.01$, the angle of core is fixed at $\theta = 10^0$, and the normalized cell height *H/W* is varied from 0.3 to 1.5 for two different ways of thickness distribution ($\tilde{h}_w = 0.85, 1.9$). In this case, the sectional parameters (Ω, h_0, h_w, h_f) decrease with increasing the normalized cell height *H/W*, see inserted table in Fig. 9.17. As can be seen, the cell height affects the damaged area of the bottom face sheet and the minimum value of the area is obtained at *H/W* = 1.0 for both cases of $\tilde{h}_w = 0.85$ and 1.9. It should be underlined that the effect of the cell height is much weaker than that of thickness distribution. As clearly shown in Fig. 9.17, the BRAS with $\tilde{h}_w = 1.9$ have much smaller damaged area than the case with $\tilde{h}_w = 0.85$ for the entire ranges of cell height considered.

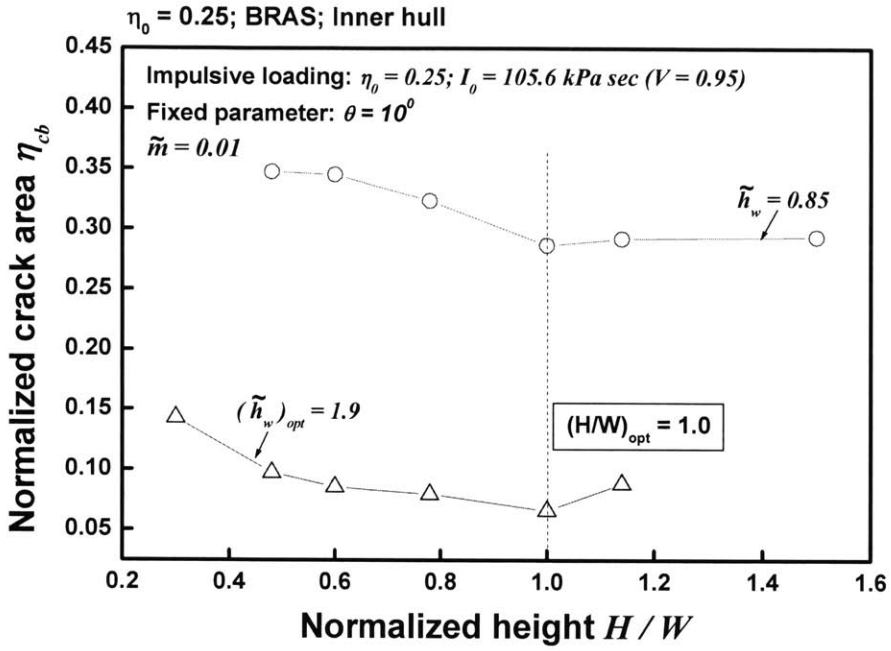

$\tilde{m}$	0.01	0.01	0.01	0.01	0.01	0.01
H/W	**0.3**	**0.48**	**0.6**	**0.78**	**1.0**	**1.14**
θ	10^0	10^0	10^0	10^0	10^0	10^0
Ω	3.89	2.62	2.26	1.89	1.62	1.51
h_0	15.16mm	14.74mm	14.30mm	13.83mm	13.26mm	12.92mm
$\tilde{h}_w$	1.9	1.9	1.9	1.9	1.9	1.9
(h_w)	(28.8mm)	(28.0mm)	(27.2mm)	(26.3mm)	(25.0mm)	(24.5mm)
$\tilde{h}_f$	0.47	0.43	0.39	0.34	0.27	0.23
(h_f)	(7.13mm)	(6.34mm)	(5.58mm)	(4.7mm)	(4.0mm)	(3.0mm)

Fig. 9.17 Normalized damaged area of the bottom fact plate (η_{cb}) of BRAS with $\tilde{m} = 0.01$ versus normalized height H/W (with $\tilde{h}_w = 0.85, 1.9$, and $\theta = 10^0$); normalized loading area $\eta_0 = 0.25$; normalized impulse $V = 0.95$; $L_0 = 4800$mm; W = 800mm

9.5.2.3 Effect of web angle (θ)

In Fig. 9.18, the normalized cell height and mass are fixed at $H/W = 1.0$ and $\widetilde{m} = 0.01$, respectively. The inclination angle of web θ ranges from 5^0 to 40^0. It can be seen that the optimum solution for angle is $\theta = 10^0$ for all three different types of thickness distribution ($\widetilde{h}_w = 0.76, 1.71, 1.9$). Furthermore, the thickness distribution has more influence on the fracture of bottom face sheet than the inclination angle of web. Therefore, it can be concluded that the damaged area of bottom face sheet in the BRAS is primarily dependent on the distribution of thickness ($\widetilde{h}_w$).

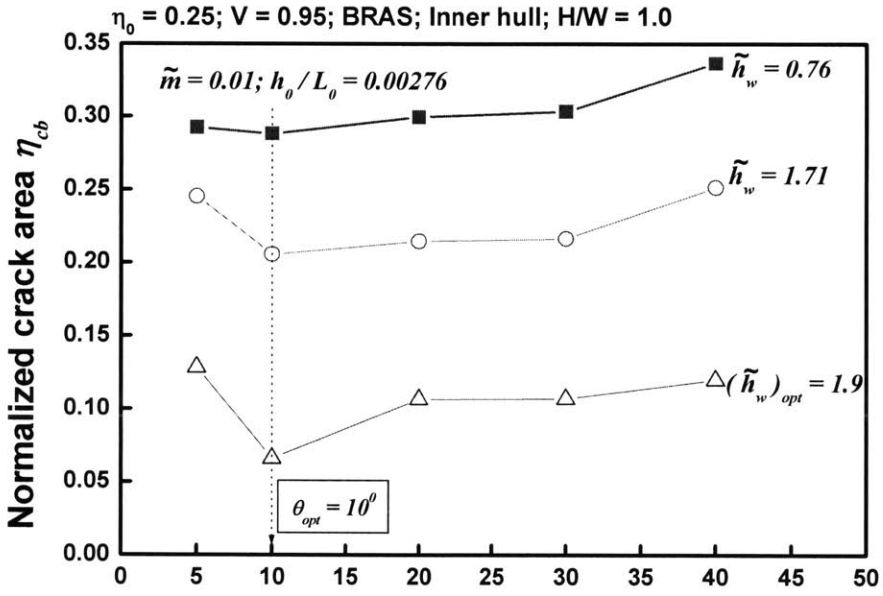

$\widetilde{m}$	0.01	0.01	0.01	0.01	0.01
H/W	1.0	1.0	1.0	1.0	1.0
θ	$\mathbf{5^0}$	$\mathbf{10^0}$	$\mathbf{20^0}$	$\mathbf{30^0}$	$\mathbf{40^0}$
Ω	1.67	1.62	1.54	1.47	1.42
h_0	13.1mm	13.3mm	13.6mm	13.8mm	14.0mm
$\widetilde{h}_w$	1.9	1.9	1.9	1.9	1.9
(h_w)	(24.9mm)	(25.0mm)	(27.2mm)	(26.3mm)	(25.0mm)
$\widetilde{h}_f$	0.25	0.27	0.31	0.34	0.36
(h_f)	(3.3mm)	(4.0mm)	(4.2mm)	(4.7mm)	(5.1mm)

Fig. 9.18 Normalized damaged area of the bottom fact plate (η_{cb}) of BRAS with $\widetilde{m} = 0.01$ versus web angle θ (with $H/W = 1.0$ and three different values of α); normalized loading area $\eta_0 = 0.25$; normalized impulse $V = 0.95$; $L_0 = 4800$mm; W = 800mm

9.6 Performance comparison of double hulls under various intensities of applied impulse

In previous Section 9.5, the optimum solutions for the USDH and BRAS were obtained at the specific magnitude of applied impulse, $I_0 = 105.6kPa\,\text{sec}$, which corresponds to the normalized impulse $V = 0.95$ for $\widetilde{m} = 0.01$ and $V = 0.7$ for $\widetilde{m} = 0.014$. Additional numerical simulations for the USDH and BRAS were performed under a wide range of normalized impulse, $0.4 < V < 2.5$ (see Section 9.6.1). Based on the results, optimal configurations of the two types of sandwich panels was found (see Section 9.6.2). Furthermore, the performances of the above optimized USDH and BRAS were compared with other types of structures, Navtruss and Y-web (see Section 9.6.3).

9.6.1 Seeking the optimal configurations of USDH and BRAS

The normalized crack area η_{cb} of bottom face sheet in the USDH is shown in Fig. 9.19 as a function of normalized impulse V. In this figure, the normalized cell height is fixed at $H/W = 1.0$ and two different distributions of thickness (as specified by $\widetilde{h}_w$) are considered. From the previous results presented in Section 9.5 (see Fig. 9.12), it was found that $\widetilde{h}_w = 1.14$ is the most efficient distribution of thickness for the case of USDH (with $\widetilde{m} = 0.01$) at the level of applied impulse, $V = 0.95$. It is clearly shown in Fig. 9.19 that the USDH with $\widetilde{h}_w = 1.14$ has smaller damaged area for the entire ranges of impulse ($0.4 < V < 2.5$), as compared to one with $\widetilde{h}_w = 0.71$. Therefore, it can be concluded that the optimal geometric parameters of the USDH are the same for all loading intensities and are equal to $\widetilde{h}_w = 1.14$ and $H/W = 1.0$ under the prescribed weight, $\widetilde{m} = 0.01$.

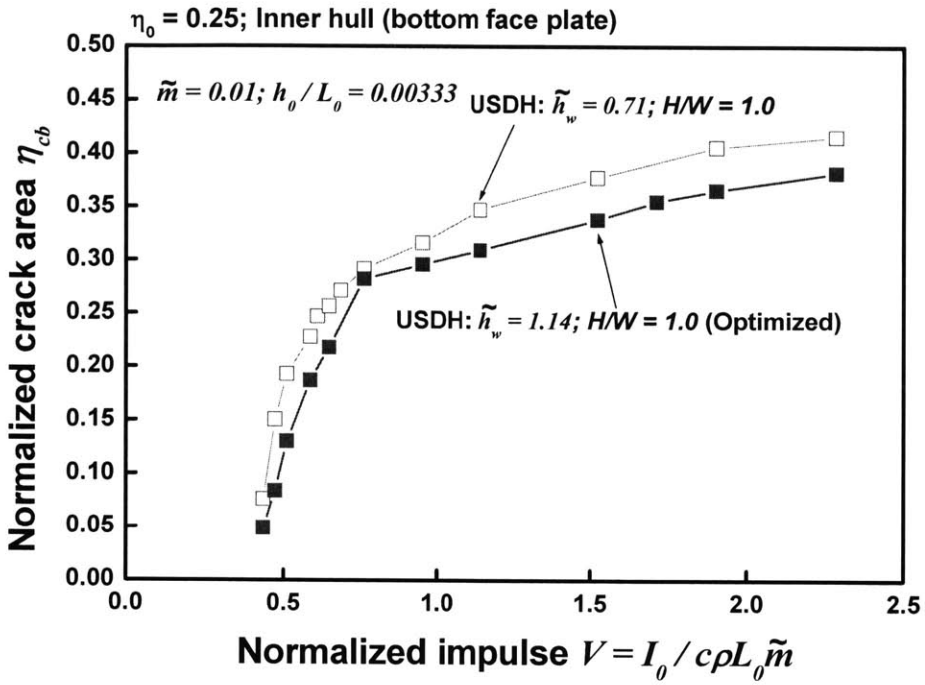

Fig. 9.19 Normalized damaged area of the bottom fact plate (η_{cb}) of the USDHs with two different distribution of thickness over the cross-section ($\tilde{h}_w$ = 1.14 and 0.71) under wide range of normalized impulse $V = I_0 / c\rho L_0 \tilde{m}$. Note that all plates have the same mass $\tilde{m} = 0.01$, normalized loading area $\eta_0 = 0.25$, L_0 = 4800mm, and W = 800mm.

The plots of the η_{cb} in the BRAS versus normalized impulse are shown in Fig. 9.20 for three different types of thickness distribution ($\tilde{h}_w$ = 0.25, 0.76, 1.9). A 3-D view of the deformed shapes of the panels (with $\tilde{h}_w$ = 0.25, 0.76, 1.9) is also shown in Fig. 9.21 with two different levels of impulse, V = 0.76 and 1.8. In Figs. 9.20 and 9.21, the normalized cell height is fixed at H/W = 1.0 and the angle of web is fixed at $\theta = 10^0$. A few observations can be made based on the numerical results present in Figs 9.20 and 9.21:

- The minimum of η_{cb} attains at the relatively thicker core specified by $\tilde{h}_w$ = 1.9 for the entire range of impulse ($0.4 < V < 2.5$). Moreover, it is shown that the plot obtained from the case of $\tilde{h}_w$ = 1.9 and $\tilde{m} = 0.01$ (denoted by the dashed line with ● in Fig. 9.20) is quite close to that of

$\widetilde{h}_w$ = 1.9 and $\widetilde{m} = 0.014$ (denoted by the solid line with ■ in Fig. 9.20). This observation indicates that the relative core thickness, $\widetilde{h}_w$, can be considered as a general parameter providing consistent result for any other value of the specified weight.

- It is interesting to note that the relatively thinner core ($\widetilde{h}_w$ = 0.25) is also be effective in reducing the damaged area within the level of impulse, V < 1.0. However, the damaged area exhibits steep increase beyond this impulse, see solid line with □ in Fig. 9.20. This behavior can be further confirmed by examining the corresponding fracture patterns shown in Fig. 9.21. As can be seen in Figs 9.21(a) and 9.21(d), fracture can be avoided in the bottom face sheet as well as top face sheet in the BRAS ($\widetilde{h}_w$ = 0.25) for the amount of V = 0.76. When the impulse is increased to V = 1.8, approximately 40% of both face sheets are detached and two symmetric petals defining four petals of full model are developed, see Figs 9.21(g) and 9.21(j).
- In the cases of thicker or thinner core ($\widetilde{h}_w$ = 1.9 or 0.25), the critical impulse needed to initiate fracture at the bottom face sheet is $V_{cr}^{b} = 0.73$, which is 1.7 times larger than that of core ($\widetilde{h}_w$ = 0.76), see Fig. 9.20.

Based on the above observation, it can be concluded that the optimal configuration of the BRAS is specified by $\widetilde{h}_w = 1.9$, $H/W = 1.0$, and $\theta = 10^0$ in the wide range of applied impulse.

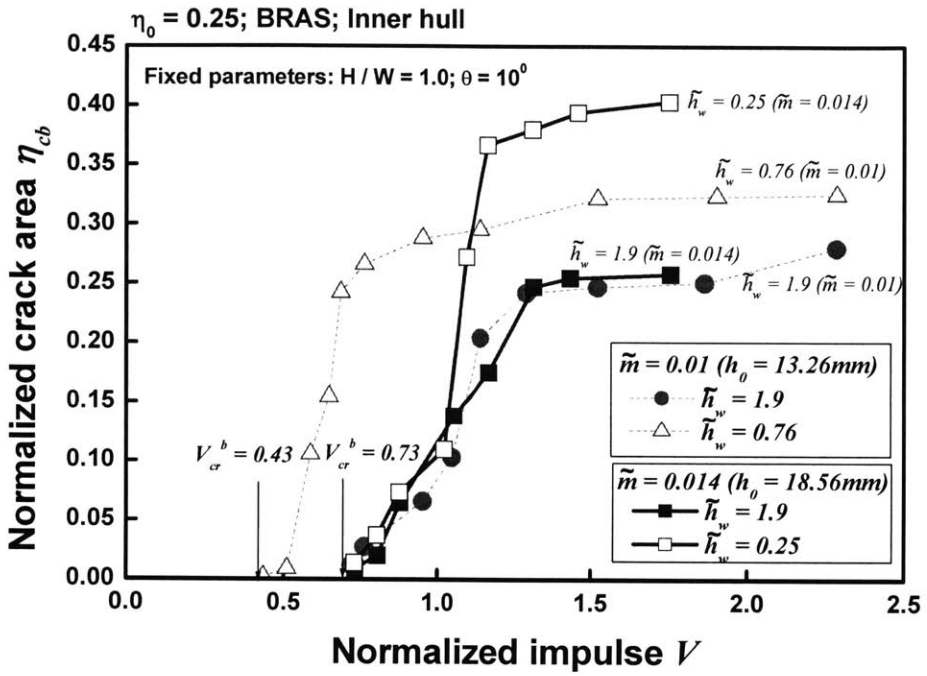

$\tilde{m}$	0.01	0.01	0.014	0.014
H/W	1.0	1.0	1.0	1.0
θ	10^0	10^0	10^0	10^0
Ω	1.62	1.62	1.62	1.62
h_0	13.26mm	3.26mm	18.56mm	18.56mm
$\tilde{h}_w$	0.76	1.9	1.9	0.25
(h_w)	(10.1mm)	(25.0mm)	(35.3mm)	(4.6mm)
$\tilde{h}_f$	1.19	0.27	0.27	1.61
(h_f)	(15.9mm)	(4.0mm)	(5.0mm)	(29.9mm)

Fig. 9.20 Normalized damaged area of the bottom fact plate (η_{cb}) of the BRAS with various distribution of thickness over the cross-section ($\tilde{h}_w = 0.25, 0.76, 1.9$) under wide range of normalized impulse $V = I_0 / c\rho L_0 \tilde{m}$. Note that the critical impulse that needed to initiate fracture in the bottom face sheet is denoted by V_{cr}^b; normalized loading area $\eta_0 = 0.25$; L_0 = 4800mm; W = 800mm.

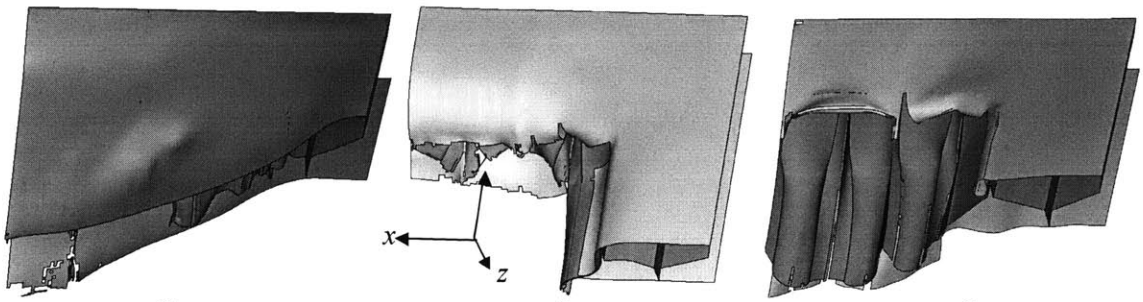

(a) $V = 0.76$; $\widetilde{h}_w = 0.25$ (outer hull) (b) $V = 0.76$; $\widetilde{h}_w = 0.76$ (outer hull) (c) $V = 0.76$; $\widetilde{h}_w = 1.9$ (outer hull)

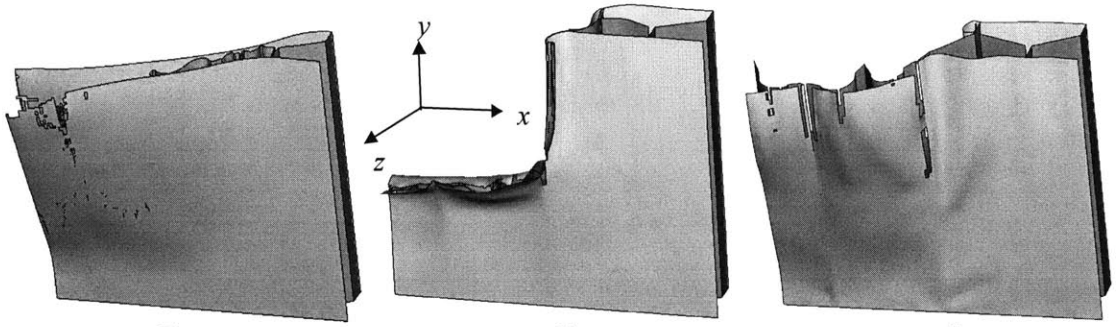

(d) $V = 0.76$; $\widetilde{h}_w = 0.25$ (inner hull) (e) $V = 0.76$; $\widetilde{h}_w = 0.76$ (inner hull) (f) $V = 0.76$; $\widetilde{h}_w = 1.9$ (inner hull)

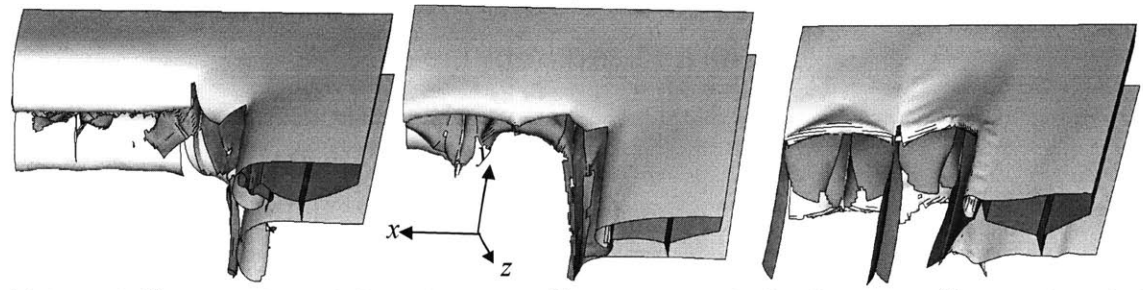

(g) $V = 1.8$; $\widetilde{h}_w = 0.25$ (outer hull) (h) $V = 1.8$; $\widetilde{h}_w = 0.76$ (outer hull) (i) $V = 1.8$; $\widetilde{h}_w = 1.9$ (outer hull)

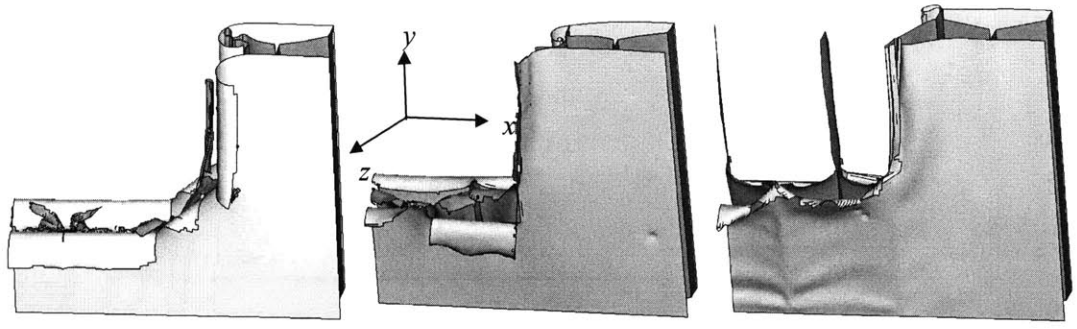

(j) $V = 1.8$; $\widetilde{h}_w = 0.25$ (inner hull) (k) $V = 1.8$; $\widetilde{h}_w = 0.76$ (inner hull) (l) $V = 1.8$; $\widetilde{h}_w = 1.9$ (inner hull)

Fig. 9.21 Comparison of the final fracture patterns (1/4 model) of the BRAS with three different ways of redistributing thickness over the cross-section ($\widetilde{h}_w$ = 0.25, 0.76, 1.9) for the central impulsive loading ($\eta_0 = 0.25; V = 0.76$ and 1.8). The deformation modes are compared in two different directions of views (top and bottom) for each type of case.

9.6.2 Comparison of the optimized configurations

9.6.2.1 Comparison between USDH and BRAS

Figures 9.22 and 9.23, respectively, compare the damaged area η_{cb} and deformed shapes between the optimized USDH and BRAS for various range of impulse. It is clear that a superior performance in terms of the damaged area η_{cb} is achieved by utilizing the adaptive core, especially for $0.5 < V < 1.2$. For instance, the η_{cb} of BRAS is 10 times lower than that of USDH for $V = 0.76$, see Fig. 9.22. Furthermore, as can be seen in Figs. 9.23(g) and 9.23(j) where the fracture patterns in the bottom plates of USDH and BRAS are compared for $V = 0.43$, BRAS provides increased resistance to initial fracture. Consequently, the threshold impulse to initial fracture of the BRAS is $V_{cr}^{b} = 0.73$, which is approximately 1.8 times larger than that of USDH, see also Fig. 9.22. At higher magnitude of impulse ($1.2 < V < 2.5$), approximately 30% of the damaged area of the USDH is also reduced by the BRAS.

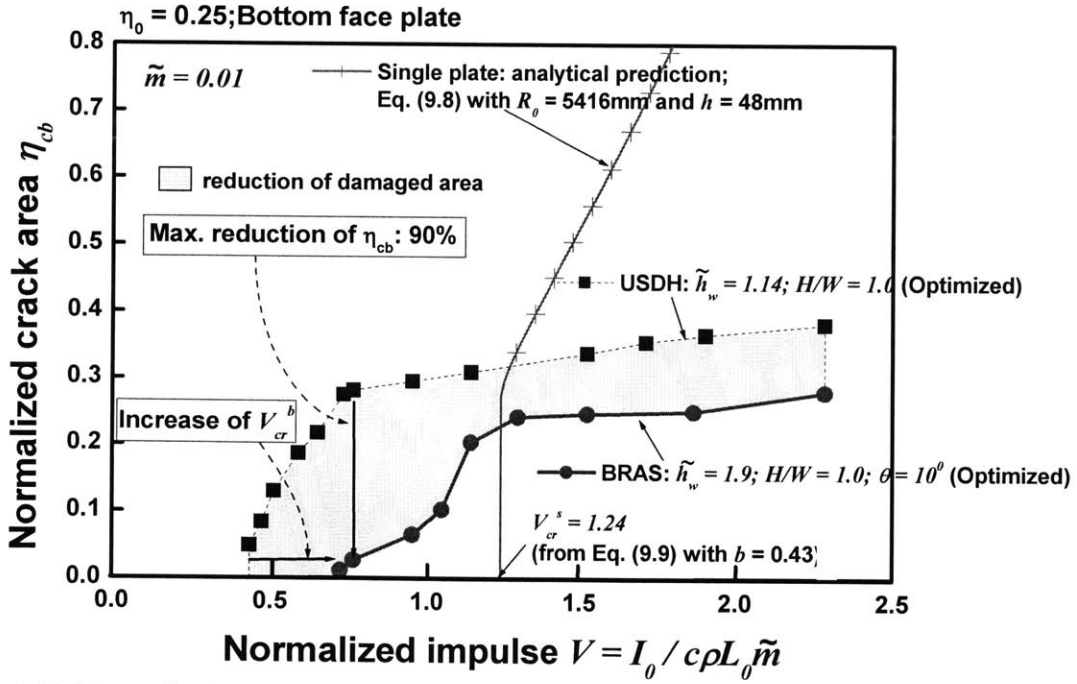

Fig. 9.22 Normalized damaged area of the bottom fact plate (η_{cb}) of optimized USDH and BRAS subjected to wide range of normalized impulse $V = I_0 / c\rho L_0 \tilde{m}$. The analytical results for the single plate of equal mass are also included for comparison. Note that all plates have the same mass $\tilde{m} = 0.01$, normalized loading area $\eta_0 = 0.25$, $L_0 = 4800$mm, and W = 800mm.

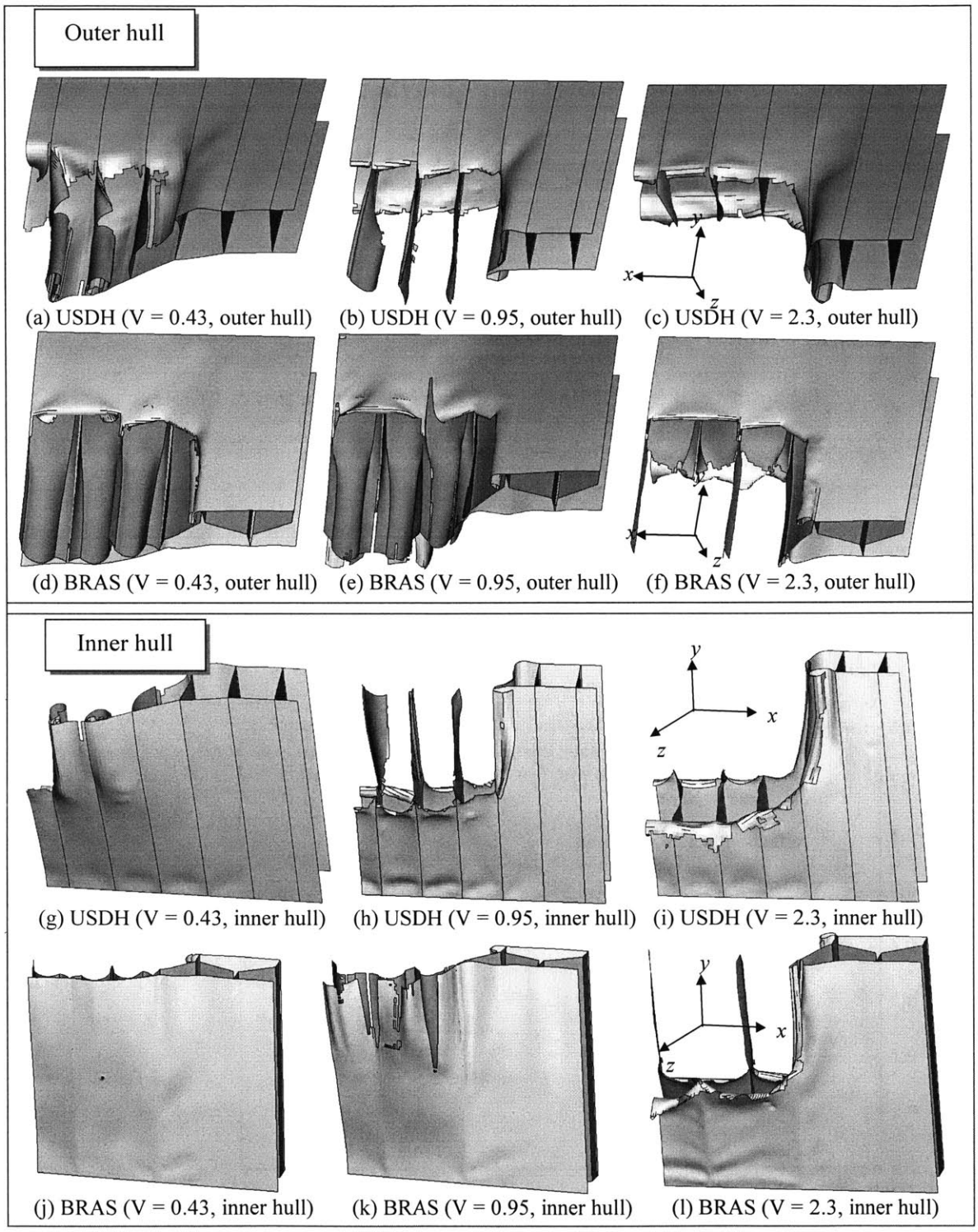

Fig. 9.23 Comparison of the final fracture patterns (1/4 model) of the optimized USDH and BRAS for three different levels of normalized impulse ($V = 0.43, 0.95, 2.3$). The deformation modes are compared in two different directions of views (outer and inner hulls) for each type of case. Note that all plates have the same mass $\tilde{m} = 0.01$, normalized loading area $\eta_0 = 0.25$, L_0 = 4800mm, and W = 800mm.

9.6.2.2 Comparison between double hulls and single hull

In Fig. 9.22, the analytical results for the single circular plate of equal mass are also included for comparison purpose. A closed form solution for the petalling failure mode of single circular plates subjected to localized high intensity of impulsive loading is presented in Chapter 7.3.3, where the normalized crack length was determined as a function of single plate thickness h, uniaxial fracture strain $\mathbf{b} = \varepsilon_f$, and parameters of the external loading, see Eq. (7.47). Based on the assumed geometry of the plate in the above solution shown in Fig. 7.26, the normalized crack area of single circular plate η_{cs} is

$$\eta_{cs} = \frac{6\tan(\pi / n_p)}{\pi}\xi_c^2 \tag{9.7}$$

where n_p is the number of symmetric petals and ξ_c is the normalized crack length given by Eq. (7.47). Substituting $n_p = 6$ and ξ_c into Eq. (9.7), the η_{cs} becomes

$$\eta_{cs} = 1.1\eta_0^2\left\{1 + 0.23\left(\frac{R_0\sqrt{\eta_0}}{h}\right)^{0.43}\frac{(V_{cr}^s)^{1.42}}{\varphi^{0.29}}\left[\left(\frac{V}{V_{cr}^s}\right)^2 - 1\right]^{0.71}\right\}^2 \tag{9.8}$$

where R_0 is the clamped radius of circular plate. Using equivalent area between circular and square plates, $R_0 = (2L_0)/\pi$ is related to the half width of square plate L_0. The bending moment amplification factor φ, which takes into account a larger bending resistance of a curved plate that is dished before fracture, is defined by Eq. (7.39).

For the case of single plate, dishing occurs until tensile fracture takes over at the critical impulse to capping failure V_{cr}^s

$$V_{cr}^s = 1.89\sqrt{\mathbf{b}} \tag{9.9}$$

For higher magnitude of the impulse above the V_{cr}^s, the explosion blows out a central cap of the radius $R_0\sqrt{\eta_0}$ and the remainder of the initial kinetic energy goes into the petalling process. The considered clamping radius and thickness of circular plate were R_0 = 5416mm and h = 48mm. The magnitude of the critical impulse $V_{cr}^s = 1.24$ from Eq. (9.9) for the $\mathbf{b}$ = 0.43 of AH36 steel.

Two observations can be made from the comparison of double hulls and single plate shown in Fig. 9.22. First, in the range of relatively lower impulse ($V << 1.24$), the single plate has advantage

in the sense that it sustains deformation without fracture. This benefit of single plate may be due to the absence of plate junctions that cause high localization of strain in the above range of impulse. On the other hand, a superior performance of double hulls in reducing the damaged area can be clearly seen upon further increase of applied impulse ($V >> 1.24$). For example, in the case of single plate for $V = 2.0$, cracks initiated at the central hole almost reach the clamped boundary, which leads to complete fracture over the entire plate, while the extent of fracture is confined to approximately 40% of full areas in the double hulls under the same amount of impulse $V = 2.0$.

9.6.3 Comparison of four different core structures subjected to the same loading

In Fig. 9.24, the damaged areas (η_{ch}) of the optimized USDH and BRAS are compared with those of other two types of sandwich panels (Navtruss and Y-web) for three different levels of impulse ($V = 0.43$, 0.73, 1.9). The normalized mass of the four structures was taken to be the same and the value was $\widetilde{m} = 0.01$. It should be mentioned that the geometries of the Navtruss and Y-web shown in this figure are not optimized configurations and specified by $H/W = 1.0$ and $\widetilde{h}_w = 1.0$ (see also inserted table in Fig. 9.24). One can see that the optimized BRAS yields less damaged area at all levels of impulse considered in Fig. 9.24. Especially, a significant reduction of the η_{ch} was obtained with the BRAS at $V = 0.73$. For this amount of impulse, the corresponding deformation shapes of the panels with four different core arrangements are shown in Fig. 9.25. The set of figures on the left and right displays the fracture patterns of top and bottom face sheets, respectively. As can be seen in the figures on the left, holes with approximately 25% of full areas were created in the top face sheets of all types of structures. Similar size of holes were also developed at the bottom face sheets of the USDH, Navtruss, and Y-web, see the figures on the right. On the other hand, no distinct fracture was observed at the bottom sheet of the BRAS. This can be explained by the fact that the optimized BRAS absorbs large amount of energy through intense plastic deformation of the adaptive core, allowing bottom face sheet to stretch to large strains before fracture takes place at the sheet.

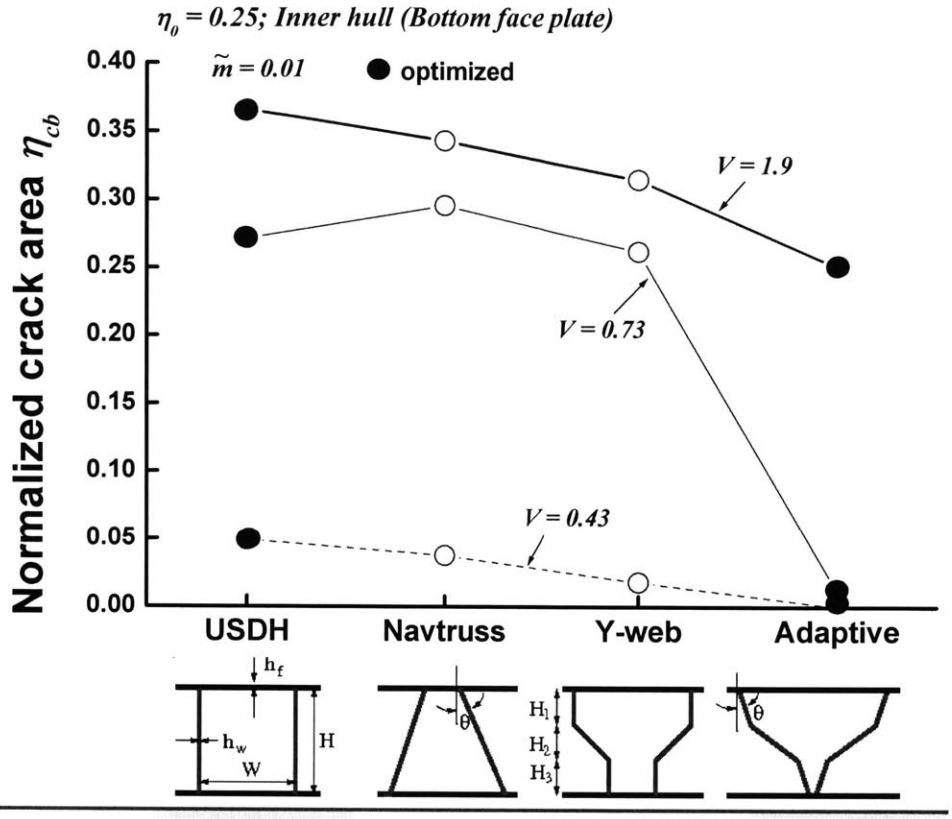

Parameters	USDH (optimized)	Navtruss	Y-web	BRAS (optimized)
$\tilde{m}$	0.01	0.01	0.01	0.01
H/W	1.0	1.0	1.0	1.0
θ	-	30^0	45^0	10^0
Ω	1.0	1.15	1.14	1.62
h_0	16.0mm	15.24mm	15.30mm	13.26mm
$\tilde{h}_w$	1.14	1.0	1.0	1.9
(h_w)	(18.2mm)	(15.24mm)	(15.30mm)	(25.0mm)
$\tilde{h}_f$	0.93	1.0	1.0	0.27
(h_f)	(14.9mm)	(15.24mm)	(15.30mm)	(4.0mm)

Fig. 9.24 Comparison of damaged area between four different core structures. Note that all plates have the same mass $\tilde{m} = 0.01$, normalized loading area $\eta_0 = 0.25$, $L_0 = 4800$mm, and W = 800mm.

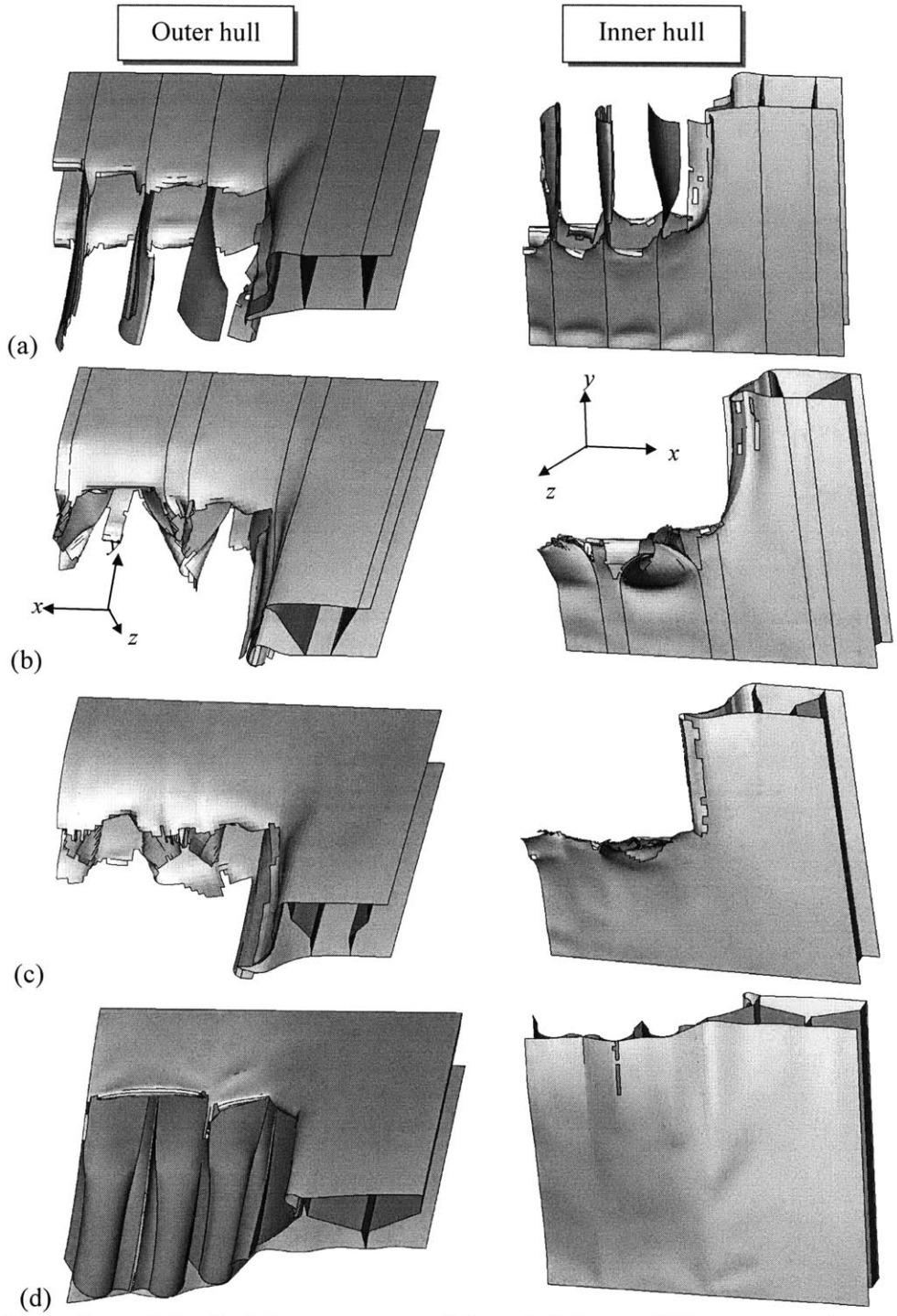

Fig. 9.25 Comparison of the final fracture pattern (1/4 model) in two different views (outer hull on the left, inner hull on the right) of the sandwich panels with four different core arrangements: (a) USDH (optimized, $\widetilde{h}_w$ = 1.14); (b) Navtruss ($\widetilde{h}_w$ =1.0); (c) Y-web ($\widetilde{h}_w$ =1.0); (d) BRAS (optimized, $\widetilde{h}_w$ =1.9). Note that all plates have the same normalized mass ($\widetilde{m} = 0.01$) and loading conditions ($\eta_0 = 0.25, V = 0.73$).

9.7 Conclusion

The purpose of the present chapter is to investigate the fracture behavior of various sandwich panels under localized impulsive loading and perform structural optimization. The main points of the present study can be summarized as follows:

- A study on optimization for minimum damaged area of bottom face sheet (η_{cb}) in the conventional double hull (USDH) and newly developed adaptive sandwich (BRAS) panels was carried out. Over 150 computer runs were made for various amplitudes of loading and geometrical parameters. An effort was made to search for the optimal configurations that have consistent deformation and fracture behaviors for a wide range of applied impulse and prescribed weight. For the case of the USDH, the optimal design variables are $\tilde{h}_w$ = 0.9 ~ 1.15 and H/W = 1.0. For the case of BRAS, it was found that thickness distribution over the cross-section (defined by $\tilde{h}_w$) has more influence on the fracture behavior than other two parameters (H/W and θ). Furthermore, it was shown that fracture can be avoided in both face sheets of the BRAS with relatively thinner core ($\tilde{h}_w$ = 0.2 ~ 0.3) within the range of applied impulse, 0.4 < V < 1.0. However, the high superiority of the thinner core was found to be not valid in the high intensity of impulse (V > 1.0). On the other hand, it was found that the BRAS with thicker core ($\tilde{h}_w$ = 1.8 ~ 2.0) is the most effective in minimizing the damaged area for the entire range of impulse (0.4 < V < 2.5). Finally, the optimal configuration of the BRAS is specified by $\tilde{h}_w$ = 1.8 ~ 2.0, H/W = 1.0, and $\theta = 10^0$.
- Throughout the comparative study on the optimized USDH and BRAS, it was clearly shown that significant reduction of the damaged area can be obtained by the BRAS for various intensities of impulse. The highest reduction of the area was 90% at the level of V = 0.76. Besides, it was found that the threshold impulse to initial fracture (V_{cr}^{b}) of the optimized BRAS is up to a factor of 1.8 times higher than that of the optimized USDH. The great benefit of the BRAS was further confirmed by comparing with other two types of structures (Navtruss and Y-web).
- It was also shown that independent of core structure, double hulls are far more resistant to explosive damage than single hull ships, especially for high intensity of impulse (V > 1.4).

This page intentionally left blank

Chapter 10

Conclusions and Recommendations

10.1 Summary of results and contributions

Extensive numerical, analytical, and experimental studies were carried out on the prediction of ductile crack formation and propagation in a sheet metal structure under localized static and dynamic loading. The major achievement of the present thesis are:

- Using the proposed strain-to-stress mapping procedure, the Bao and Wierzbicki (BW) fracture locus was represented in the space of principal strains and compared with experimental results for various materials.
- A thorough comparative study of the most widely used seven fracture criteria was carried out.
- "Quick calibration" method was developed to simplify the existing calibration procedure and facilitate fracture prediction in many industrial processes.
- Numerical study involving mesh sensitivity on the formation and propagation of cracks in a flat tensile specimen was performed and the results were correlated with tests.
- The applicability of the BW fracture criterion was validated by two component studies in classical punch indentation problems of thin sheets.
- Analytical approximations were developed to predict deformation and fracture in a single plate under static punch indentation. The computational approach to construct the Fracture Forming Limit Diagram (FFLD) was introduced in this problem.

- A connection between crack formation and propagation in ductile sheets was thoroughly investigated by three case studies.
- An in-depth investigation on the deformation and fracture behaviors of clamped thin plates subjected to high intensity and short duration loads was performed.
- A new concept of Blast Resistant Adaptive Sandwich (BRAS) structure was introduced. An extensive parametric study was conducted to optimize the fracture resistance of double hulls against localized explosive loading.

A short summary of each of the above contribution is given below.

Representation of BW fracture locus in the space of principal strains

Based on plane stress von-Mises plasticity, a stain-to-stress space mapping procedure was proposed, which enables the fracture criteria formulated in the strain space to be transformed into the stress space and vice versa. Employing the mapping scheme, the original BW fracture locus, formulated in the space of equivalent strain to fracture and stress triaxiality was transformed into the space of principal strains to fracture, which is understood as Fracture Forming Limit Diagram (FFLD), see thicker line in Fig. 10.1. In addition to the single straight line with $\tan^{-1}(-1)$ that was known earlier as constant through thickness strain to fracture (Eq. (2.25), branch I), two new branches of the fracture locus appeared in the tension-compression quadrant. Until now, the thick full line corresponding the branch I (between uniaxial and equi-biaxial tension) was only recognized as the FFLD in the literature. The above construction of a complete FFLD covering the entire range between compression and equi-biaxial tension of sheet metal is new. In the case of Forming Limit Diagram (FLD), which is a plot of necking strain in principal strain space, the FLD conceptually proposed by Marciniak and Duncan (1992) has been extensively used as an indicator of the regions in which sheet forming can be carried out. This conceptual FLD is also included in Fig. 10.1 for comparison purpose.

So far, the original BW fracture locus (Fig. 2.1 (a)) was constructed only for two materials, 2024-T351 aluminum alloy and A710 steel. The applicability of BW fracture locus to other materials was examined by constructing normalized FFLD of a number of different materials. It was shown that the transformed BW fracture loci (branch I and III) accurately represent experimental fracture points obtained for various materials by different authors.

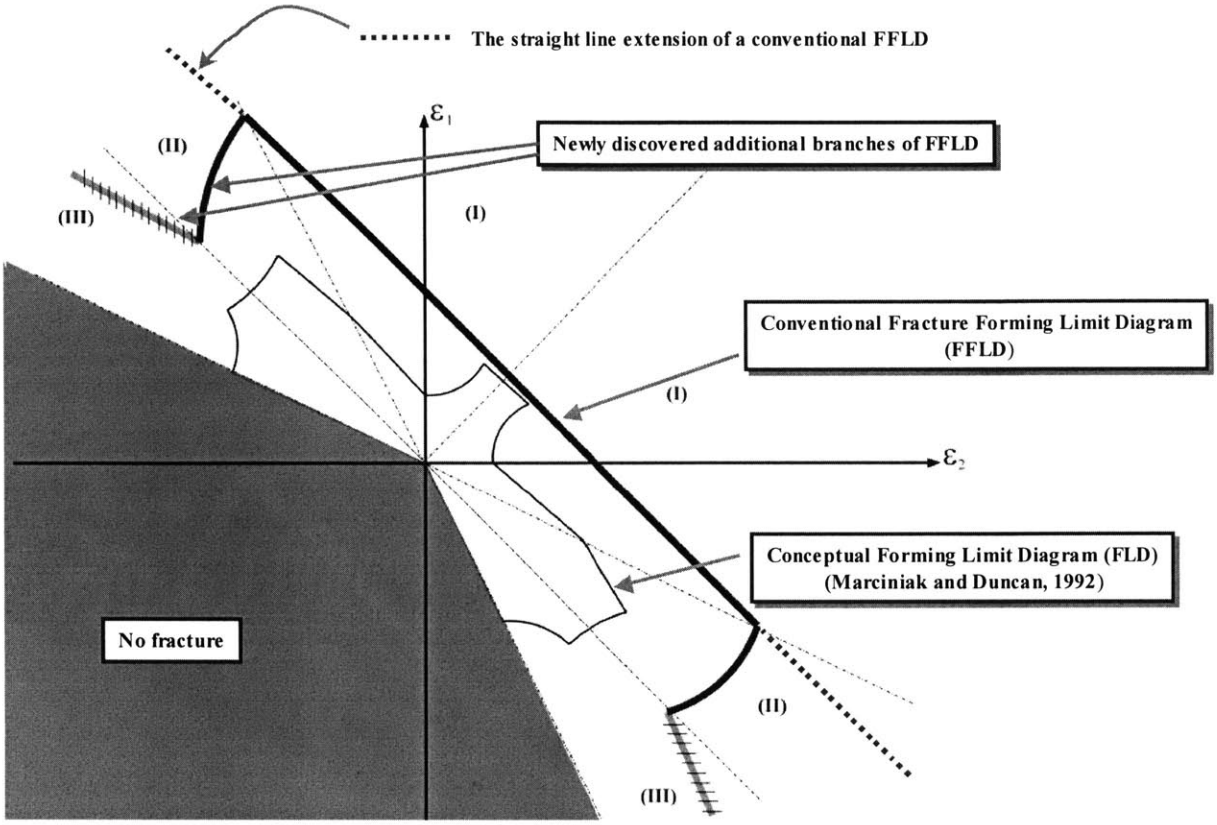

Fig. 10.1 Conceptual Fracture Forming Limit Diagram (FFLD) discovered in the present thesis versus Conceptual Forming Limit Diagram, according to Marciniak and Duncan (1992). Note that the FFLD (thicker line) shown in this figure is identical to the BW fracture locus transformed into the space of principal strains and two additional branches which complete the FFLD in the tension-compression quadrant.

Comparative Study of Seven Fracture Criteria

The accuracy of the local fracture criteria (uncoupled models) that are widely used in engineering applications was assessed. As a reference for the present comparative study, taken was the newly constructed empirical BW fracture criterion. This criterion was compared with the constant equivalent strain criterion, the Wilkins (W) and the Johnson-Cook (J-C) fracture models. Additionally, the maximum shear stress model, the Cockcroft-Latham (C-L), and the conventional FFLD (known as constant thickness strain to fracture defined by Eq. (2.25)) were included in the present evaluation. All criteria were formulated in the general 3-D case for the power law hardening materials and then were specified for the plane stress condition. Using the assumption of

plane stress plasticity and the mapping procedure, fracture loci for all seven cases were constructed in the space of principal stress, principal strain and in the mixed space of the equivalent strain and the stress triaxiality. It was found that in the range of high stress triaxiality ($\sigma_m / \bar{\sigma} > 1/3$) the BW and the conventional FFLD give identical and accurate results. In the intermediate range of stress triaxiality ($0 < \sigma_m / \bar{\sigma} < 1/3$), the BW, the maximum shear stress, and the W fracture loci follow closely experimental points. Finally, in the range of negative stress triaxiality ($\sigma_m / \bar{\sigma} < 0$), the C-L, the W, and the BW fracture envelopes capture best the process of crack formation.

Quick calibration for fracture under monotonic loadings

A simplified calibration method for the BW fracture criterion was proposed to eliminate a need for extensive numerical simulation/test and to determine all relevant fracture parameters in terms of the measurable quantities from a single uniaxial tensile test. Those measurable quantities are hardening exponent and the relative area reduction inside the neck at the instant of fracture. In this new approach, the critical damage parameters i.e. fracture strain in uniaxial tension **b**, average stress triaxiality in uniaxial tension $(\sigma_m / \bar{\sigma})^0_{av}$, and critical damage value D_c, were determined based on approximate closed form solutions for triaxiality in the critical locations as a function of the equivalent strain. Two types of specimens most commonly used in all testing labs were considered: flat and smooth round tensile specimens. In the determination of critical fracture strain in pure shear (i.e. **a**), the hypothesis of the maximum shear stress fracture criterion was used, which uniquely relates the parameter **a** with the **b** and hardening exponent n (Eq. (3.46)). The accuracy of the newly developed calibration method has been verified for five different materials and the agreement between conventional and new methods was always within 10%.

Several important aspects of this new calibration method are summarized in the following: (1) The method is attractive especially for industrial applications since the existing calibration method is a time consuming procedure, which may be difficult to perform in the industrial environments; (2) It provides an alternative way to remove mesh dependence that might compromise the result when using the existing calibration method. In this way a uniqueness of the critical damage parameters is acheivied; (3) It also opens up the possibility for predicting fracture in real structural problems based on standard tensile test without further simulations and tests. For example, using the critical damage parameters obtained from the present quick calibration method and the analytical approximations of the problem, we can predict various features of deformation and

fracture in the clamped single plate under static punch indentation, as schematically illustrated in Fig. 10.2.

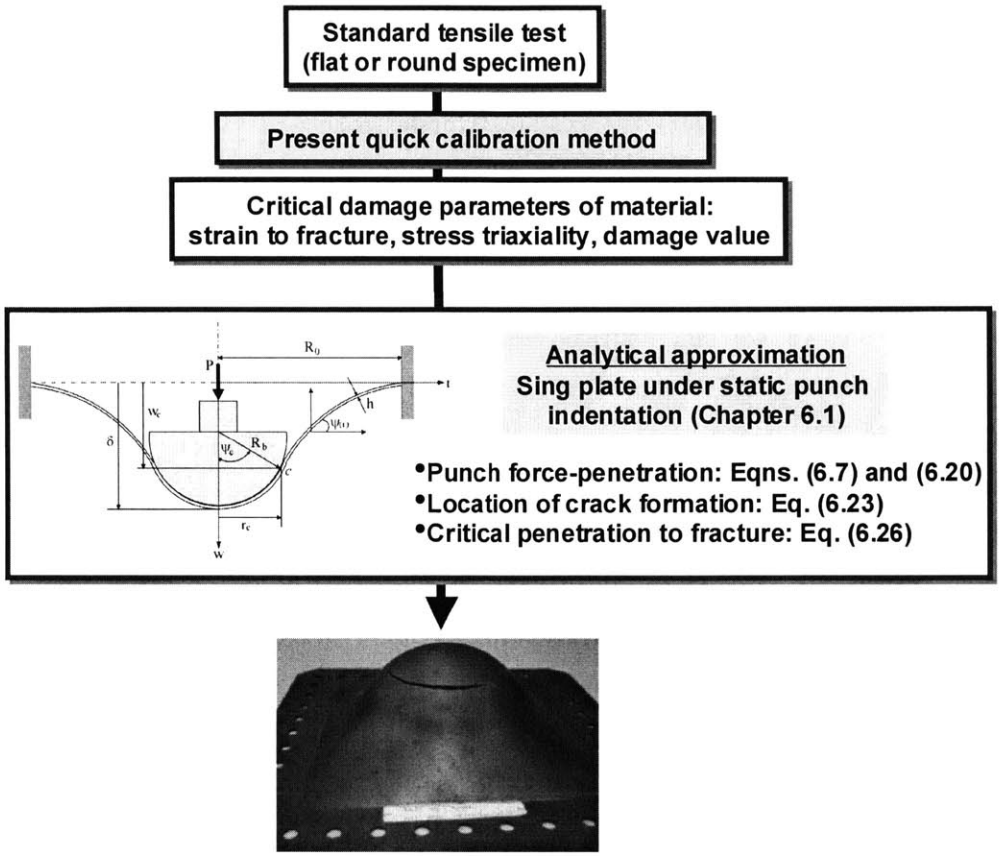

Fig. 10.2 Application example of quick calibration method for the prediction of fracture in structural problems

Effect of mesh size on formation and propagation of cracks in flat tensile specimen

A thorough numerical study, corroborated by experiments, was made to predict all main features of tensile test on a flat specimen from necking to final crack propagation. Most importantly, the effect of mesh size on the formation and propagation of cracks was studied and a strong sensitivity to mesh size was observed for A710 steel material. However, a drop in stress triaxiality coupled with an increase in plastic strain was also observed when using a mesh size as small as 110μm, which indicates a possible convergence of the critical damage functional. Two approaches were proposed to remove the mesh dependence and obtain the reliable results:

(1) Nonlocal approach where the average values of critical damage parameters are calculated over the specified critical volume or representative length in the vicinity of the point of considerations.

(2) The critical parameters are formulated directly as a function of the normalized size of the element i.e. $(\bar{\varepsilon}_f, (\sigma_m / \bar{\sigma})_{av}, D_c) = f$(normalized mesh size).

It was demonstrated that strong mesh dependence of A710 steel can be greatly reduced by the nonlocal approach, leading to result which converges to a unique value at the specified length scale. The nonlocal approach is not new and has been proposed by many authors, e.g. in the porous plasticity model, so-called G-T-N model (see Tvergaard and Needleman, 1997) and the Wilkins model (see Wilkins et al., 1980). However, the effect of material length scale on the average value of fracture parameters was not investigated in their studies. In the present thesis, it was further obserevd that the average value dependents itself on the length scale. In particular, the effect of length scale on the average damage was then quantified (Eq. (5.4)).

In the second approach, a relationship between the critical parameters and the normalized mesh size (Eqns. (5.6) ~ (5.8)) was constructed. Based on this relation, crack propagation of the flat specimen was simulated with various mesh configurations and the results were compared with experimental observations. In the numerical simulation of tensile test, it was found that what primarily depends on the mesh size is the onset of crack formation while the distribution of normalized damage ahead of the crack tip and fracture pattern during the crack propagation are not mesh sensitive provided that the strain-to-fracture, which is function of mesh size in the A710 steel material, is properly defined by Eq. (5.8).

Validation of BW fracture criterion

The present approach to crack formation and propagation, based on the BW fracture model, was validated by two component studies including a thin single plate and stiffened double plates under static punch indentation. It was shown that the numerical simulation incorporating the BW fracture criterion accurately predicts not only crack formation but also crack propagation, which may be understood as a sequence of crack re-initiation, in both punch force-indentation responses and fracture patterns.

Analytical approximations and construction of FFLD in classical punch indentation in thin plates

Based on the approximation of the profiles of the stress ratio and stress triaxiality along the clamped thin plate under static hemi-spherical punch indentation, closed-form solution on transverse deflection, punch force-penetration, location of circumferential crack, and critical penetration to fracture were derived. It was shown that the derived formula are in good agreement with numerical and experimental results. In particular, it was further confirmed that an expression for the critical punch penetration to fracture is more exact than a similar result derived earlier by others (Simonsen and Lauridsen, 2000).

Parallel to analytical study, special attention was paid to the numerical construction of the FFLD by changing friction coefficient between the punch and plate. This computational method can replace the time-consuming typical experimental technique in which the strain path is controlled by applying different blankholder forces or different radii of cut-outs. It is generally known that friction between tool and sheet changes the response of the system. However, except for Ferron and Zeghoul (1993), the variable friction coefficient has not been used as a calibration method to generate FFLD. Moreover, in the simulations done by Ferron and Zeghoul (1993), fracture was assumed to occur according to the criterion of Cockcroft-Latham (C-L), but detail information on the calibration procedure, the effect of friction coefficient on the relevant fracture parameters, and comparison with experimental results was not provided in their study.

Relation between ductile crack formation and propagation in uncracked sheet metals

In the present approach to ductile crack propagation in sheet metals, we follow the hypothesis of Atkins (1986) in which the crack propagation may be considered as a process of continuous re-initiation ahead of crack tip. In addition, from the literature review on computational methods for fracture presented in Chapter 4, it was concluded that no distinction between crack formation and propagation has been made in the computational framework. However, unlike the present thesis, a thorough investigation on evolution of the fracture parameters in the process of crack propagation has not been made by Atkins (1986) and many others.

In the present thesis, the relation between ductile crack formation and subsequent crack propagation was numerically investigated by three case studies with corroboration of experimental observations: flat tensile specimen (Chapter 5.3), clamped double plates under static loading

(Chapter 6.2), and clamped circular plate under impulse loading (Chapter 7.3). From the above three case studies, a consistent observation was made, that is, the difference in fracture parameters between crack formation and propagation is very small. In particular, the entire range of stress triaxiality encountered in the considered problems confined within relatively narrow region between 1/3 (uniaxial tension) and 2/3 (equi-biaxial tension). It was found that the average stress triaxiality i.e. $\left(\frac{\sigma_m}{\bar{\sigma}}\right)_{av} = \frac{1}{\bar{\varepsilon}_f}\int_0^{\bar{\varepsilon}_f}\frac{\sigma_m}{\bar{\sigma}}d\bar{\varepsilon}$ along the crack path is nearly constant. For example, in the problem of the clamped plates under static punch or dynamic pulse loading, the magnitude of average stress triaxiality at the critical locations of fracture involving formation and propagation of cracks was approximately constant and equal to $(\sigma_m/\bar{\sigma})_{av} \approx 1/\sqrt{3}$ corresponding to plane strain tension deformation. This finding provides a reasonable assumption that ductile crack propagation is indeed a sequence of crack formation in the sheet metals under monotonic loadings.

However, it should be mentioned that the above conclusion may not be general since it is based on the limited cases, in which the range of corresponding stress triaxiality is $1/3 < \sigma_m/\bar{\sigma} < 2/3$. Further research is needed for wider ranges of stress triaxilaity and more complex loading situations.

Deformation and fracture of thin single plates under localized impulsive loading (dishing, discing, and petalling)

A comprehensive study covering all the three stages of dynamic response (dishing, discing, petalling) in clamped thin single plates subjected to central impulsive loading was carried out. In the dishing stage, the new contributions of present thesis are: (1) Various types of shape function were introduced into the existing mode solution (Symonds and Wierzbicki, 1979) and the accuracy of those mode shapes in predicting the final deflection of plates was discussed. (2) The final deflected shapes and magnitudes of central deflection of plates obtained numerically were shown to agree well with the wave solution (Mihailescu-Suliciu and Wierzbicki, 2002) and published test results. (3) The responses between circular and square plates were compared for three different loading radii and difference of those plates was quantified. In particular, it was found that difference in the deformation shape is more pronounced in larger loading radii due to different geometry. (4) The effect of various spatial and temporal distribution of dynamic pressure on the behavior of thin plates was investigated. It was observed that the permanent shape of the plate is strongly dependent on the

spatial distribution of pressure loading. Most importantly, the effect of temporal distribution of pressure in short duration pulses was shown to be much weaker, which is great significance in practical situations. This weak effect of temporal distribution was also observed in the case of sandwich structures under same loading conditions.

In the discing and petalling stages, the evolution of stress, strain, and the resulting damage parameter at the critical fracture locations was investigated in great detail. Such an analysis has not been reported in the open literature. For example, by rigorously tracking the damage profiles along the circumferential direction, it was observed that once circumferential cracks occur (discing), the profiles lose their symmetry and show rather a random distribution. However, on continued deformation, this irregular distribution of damage changes into the periodic profiles leading to unique formation of radial cracks. It was clearly demonstrated that the crack length and final deformed shapes of plates are strongly influenced by the spatial distribution and intensity of impulsive loading. Finally, the numerically obtained crack length was shown to agree well with the closed form solution (Wierzbicki, 1999).

Static and transient responses of double hulls with various core arrangements

A new concept of adaptive and reconfigurable structural component, the Blast Resistant Adaptive Sandwich (BRAS) structure, was developed which has led to a substantial improvement of resistance to explosive loading. It was shown that the static crushing resistance of the proposed core after initial collapse is an order of magnitude larger than that of the original intact structure, which is highly beneficial to increase the tearing strength and petalling resistance of the sandwich panel. The transient responses of the BRAS was compared with that of other three core shapes, i.e. Unidirectionally Stiffened Double Hull (USDH); Hat-type corrugated core (Navtruss); Y-type corrugated core (Y-web), having the same weight and subjected to the same intensity of impulsive loading. Many advantages of the BRAS over other structures were observed in terms of energy absorption characteristics, substantial reduction in impulse transfer, and effective blast isolation.

Structural optimization against fracture damage of double hulls

An extensive numerical study was presented for double hulls with four different core arrangements under localized impulsive loading. An optimum design to minimize the fractured area of the inner hull was developed for a given weight. The design variables were the geometrical

parameters: thickness distribution over the cross-section, unit cell aspect ratio, and angle of core. This study is one of the most important aspects of the present thesis since a majority of the relevant literature has been primarily concerned with the plastic deformation without fracture. Rigorous method of predicting fracture of double hulls under high intensity and short duration loads have not been published in the open literature. Based on the extensive parametric study, optimal configurations that have a consistent deformation and fracture modes for a wide range of intensity of impulsive loading and a specified weight were proposed in the cases of the USDH and BRAS. It was clearly shown that significant reduction of the damaged area can be obtained by the BRAS for various intensities of impulse. The highest reduction of the damaged area was 90% at the level of V = 0.76, where V is dimensionless impulse defined by Eq. (9.4). Besides, it was found that the threshold impulse to initial fracture (V_{cr}^{b}) of the optimized BRAS is 1.8 times higher than that of the optimized USDH. These advantages of the BRAS were also valid for other two types of structures (Navtruss and Y-web).

10.2 Future research

Further research should be conducted on the following topics:

- The effect of possible strain rate and temperature dependence of the BW fracture criterion was not considered in this thesis. The assumption that the fracture strain is a unique function of stress triaxiality in the dynamic pressure loading problems is understood as a useful approximation. Further study is needed for various types of materials to establish limit on this simplification.
- In the comparative study of seven fracture criteria, fracture locus of Al 2024-T351 was taken as benchmark results. Therefore, the discussions presented in this study may not be general and different depending on materials. Further comparative study should be performed for a wide range of materials.
- The accuracy of the new "quick" calibration method over a wide range of stress triaxiality, especially in the intermediate and negative stress triaxialities ($-1/3 < \sigma_m / \bar{\sigma} < 1/3$), was

validated by only one material, Al 2024-T351. Further investigation is required for various materials in the above ranges of stress triaxialtiy.

- Other factors besides the element size may influence the prediction of fracture. More work is needed to consider other numerical factors, such as type of element (triangular, quadrilateral, thick shell, thin shell, brick elements, etc.), mesh orientation, number of integration points, etc.
- The discing and petalling behaviors of single circular plate were studied analytically and numerically in the present research. More tests should be conducted to validate quantitatively the analytical and numerical models.
- The deformation and fracture behaviors of double hulls subjected to localized impulsive loading were predicted numerically. Experimental validation is required to ensure the accuracy of numerical simulation.
- The structural optimization of double hulls for damage mitigation was performed with only one specific loading area and several restrictions on the geometrical parameters. More design variables, such as different thickness between inner and outer hulls, different spatial distribution of explosive loading, flexible boundary condition with crushable support, etc., are needed to be considered. The optimization study should be further extended to more particular designs, such as Navtruss, Y-web, traditional stiffened single hulls, and the results should be compared with the present BRAS concept. Besides, more work is required to assess effects of fluid-structure interaction on deformation and fracture of double hulls under impulsive loading.
- Parallel to experimental and numerical studies, closed form solutions for the fracture damage of double hulls (e.g. an expression for the cracked area of inner hull as a function of fracture parameters, geometrical variables of structures, and parameter of the external loading) should be developed. These solutions together with the "quick" calibration method will provide much needed benchmark solution to validate fracture prediction techniques in military and industrial environments.

This page intentionally left blank

Bibliography

[1] Atkins AG, Mai YW. (1985). Crack and craze nucleation. In: *Elastic and plastic fracture*. Chichester: Ellis Horwood, p. 369-431.

[2] Atins AG. (1996a). Fracture in forming. *J Mat Proc Tech*, 56:609-618.

[3] Atkins AG, Arndt S, Muscat-Fenech CM. (1996b). The determination of FFLD from fracture toughness. In: *Proc. of the 4th International Conference on Sheet Metal*, 1:249-260.

[4] ABAQUS/Explicit User's Manual. (2003). Version 6.4.1, Hibbit, Karlsson and Sorensen Inc.

[5] Bridgman PW. (1944). Stress distribution in the neck of a tension specimen. *Trans Amer Soc Metals*, 32:553.

[6] Bridgman, PW (1952). Studies in Large Plastic Flow and Fracture. Harvard University Press, Cambridge, Massachusetts.

[7] Brozzo P, Deluca B, Rendina R. (1972). A new method for the prediction of formability in metal sheet, Sheet Metal Forming and Formability. In: *Proc. of the 7th Biennial Conference of the IDDRG*.

[8] Bodner SR, Symonds PS. (1979). Experiments on viscoplastic response of circular plates to impulsive loading. *J Mech Phys Solds*, 27:91-113.

[9] Beach JE. (1991). Advanced surface ship hull technology – cluster B. *Nav Engrs J*, November:27-37.

[10] Barbuska I, Melenk JM. (1997). The partition of unity method. *Int J Numer Meth Engng*, 40:727-758.

[11] Belytschko T, Lu YY, Gu L. (1994). Element-free Galerkin methods. *Int J Numer Meth Engng*, 37:229-256.

[12] Belytschko T, Organ D, Krongauz Y. (1995a). A coupled finite element-element-free Galerkin method. *Comput Mech*, 17:185-195.

[13] Belytschko T, Lu YY, Gu L, Tabbara M. (1995b). Element-free Galerkin methods for static and dynamic fracture. *Int J Solids Struct*, 32:2547-2570.

[14] Belytschko T, Moes N, Usui S, Parimi C. (2001). Arbitrary discontinuities in finite elements. *Int J Numer Meth Engng*, 50:993-1013.

[15] Borvik T, Langseth M, Hopperstad OS, Malo KA. (1999). Ballistic penetration of steel plates. *Int J Impact Engng*, 22:855-886.

[16] Borvik T, Hopperstad OS, Berstad T, Langseth M. (2001). A computational model of viscoplasticity and ductile damage for impact and penetration. *European J Mech A/Solids*, 20:685-712.

[17] Borvik T, Hopperstad OS, Berstad T, Langseth M. (2002). Perforation of 12mm thick steel plates by 20mm diameter projectiles with flat, hemispherical and conical noses part II: Numerical simulations. *Int J Impact Engng*, 27:37-64.

[18] Borvik T, Hopperstad OS, Berstad T. (2003). On the influence of stress triaxiality and strain rate on the behavior of a structural steel. Part II. Numerical study. *European J Mech A/Solids*, 22:15-32.

[19] Butuc MC, Barata da Rocha A, Gracio JJ, Ferreira Duarte J. (2002). A more general model for forming limit diagrams prediction. *J Mat Pro Tech*, 125-126:213-218.

[20] Besson J, Steglich D, Brocks W. (2003). Modeling of plane strain ductile rupture. *Int J Plastcty*, 19:1517-1541.

[21] Borst R de. (2003). Numerical aspects of cohesive-zone models. *Engng Fract Mech*, 70:1743-1757.

[22] Bao Y. (2003). Prediction of ductile crack formation in uncracked bodies. *Ph D Thesis*, MIT.

[23] Bao Y, Wierzbicki T. (2004a). On fracture locus in the equivalent strain and stress triaxiality space. *Int J Mech Sci*, 46:81-98.

[24] Bao Y, Wierzbicki T. (2004b). A comparative study on various ductile crack formation. *J Engng Mat Tech*, 126:314-324.

[25] Bao Y, Lee YW, Wierzbicki T. (2004c). Evaluation and calibration of seven fracture models. *J Mech Phys Solds*, submitted for publication.

[26] Boh JW, Louca LA, Choo YS. (2004). Numerical assessment of explosion resistant profiles barriers. *Mar Struct* (in press).

[27] Considere M. (1885). *Annales des Points et Chaussees*, 9:574.

[28] Cockcroft, M. G., and Latham, D. J. (1968). Ductility and the workability of metals. *J the Inst of Metals,* 96:33-39.

[29] Chakrabarty J. (1970). A theory of stretch forming over hemispherical punch heads. *Int J Mech Sci*, 12:315-325.

[30] Chakrabarty J. (1999). Stretch forming of sheet metals. In: Applied Plasticity. NewYork:Springer, p. 98-112.

[31] Clausing, DP. (1970). Effect of plastic strain state on ductility and toughness. *Int J Fract Mech,* 6:71-85.

[32] Cheng JH, Kikuchi N. (1986). A mesh rezoning technique for finite element simulations of metal forming processes. *Int J Numer Mech Engng*, 23:219-228.

[33] Cheng JH. (1988). Automatic adaptive remeshing for finite element simulation of forming processes. *Int J Numer Mech Engng*, 26:1-18.

[34] Clift SE, Hartley P, Sturgess CEN, Rowe GW. (1990). Fracture prediction in plastic deformation processes. *Int J Mech Sci*, 32:1-17.

[35] Dydutch M, Habraken AM, Cescotto S. (1992). Automatic adaptive remeshing for numerical simulations of metal forming. *Comput Meth Appl Mech Engng*, 101:283-298.

[36] Dyrli HK. Strain analysis and fracture of crushed aluminum tubes. (1999). Report 30, Impact and Crashworthiness Lab, MIT.

[37] Daux C, Moes N, Dolbow J, Sukumar N, Belytschko T. (2000). Arbitrary branched and intersecting cracks with the extended finite element method. *Int J Numer Meth Engng*, 48:1741-1760.

[38] Embury JD, LeRoy GH. (1977). Failure maps applied to metal deformation processes. In: *Proc. of the ICF-4*, 1:15-42.

[39] Erturk T, Kazazoglu E. (1982). *ASTM STP No. 753*, 19.

[40] Ferron G, Zeghloul A. (1993). Strain localization and fracture in metal sheets. In: Norman Jones and Tomasz Wierzbicki, eds. *Structural Crashworthiness and Failure.* London:Elsevier; p. 131-163.

[41] Goodwin GM. (1968). Application of strain analysis to sheet metal forming problems in the press shop. SAE paper no. 680093.

[42] Ghosh AK, Hecker SS. (1975). Failure in thin sheets stretched over rigid punches. *Metall Trans*, 6A:1065-1074.

[43] Ghosh AK. (1978). Plastic flow properties in relation to localized necking in sheets. In: *Mechanics of sheet metal forming*. Plenum Press: New York-London, p. 287-312.

[44] Gurson AL. (1977). Continuum theory of ductile rupture by void nucleation and growth-I. *Engng Mat Tech*, 99:2-25.

[45] Giovanola JH, Kirkpatrick SW. (1998). Using the local approach to evaluate scaling effects in ductile fracture. *Int J Fract*, 92:101-116.

[46] Gouveia BPPA, Rodrigues JMC, Martins PAF. (2000). Ductile fracture in metal working: experimental and theoretical research. *J Mat Proc Tech*, 101:52-63.

[47] Guruprasad S, Mukherjee A. (2000a). Layered sacrificial claddings under blast loading, Part I – analytical studies. *Int J Impact Engng*, 24:957-973.

[48] Guruprasad S, Mukherjee A. (2000b). Layered sacrificial claddings under blast loading, Part I – analytical studies; Part II – experimental studies. *Int J Impact Engng*, 24:957-984.

[49] Hill R. (1948). The mathematical theory of plasticity. Chap X, Clarendon Press, UK:Oxford.

[50] Hill R. (1952). On discontinuous plastic states, with special reference to localized necking in thin sheets. *J Mech. Phys Solids*, 1:19-30.

[51] Hecker SS. (1975). Simple techniques for determining forming limit curves. *Sheet Metal Indust*, 52:671.

[52] Hancock JW, Mackenzie AC. (1976). On the mechanics of ductile fracture in high-strength steels subjected to multi-axial stress-states. J *Mech Phys Solds*, 24:147-69.

[53] Hoo Fatt MS, Park KS. (2000). Perforation of honeycomb sandwich plates by projectiles. *Composites*, Part A:889-899.

[54] Hopperstad OS, Borvik T, Langseth M, Labibes K, Albertini C. (2003). On the influence of stress triaxiality and strain rate on the behavior of a structural steel. Part I. Experiments. *European J Mech A/Solids*, 22:1-13.

[55] Hagbart SA. (2004). A comparative study on shell element deletion and element splitting. *Master Thesis*, MIT.

[56] Jones N. (1968). Impulsive loading of a simply supported circular rigid-plastic plate. *J Appl Mech*, 35:59-65.

[57] Johnson W, Chitkara NR, Ibrahim AH, Dasgupta AK. (1973). Hole flanging and punching of circular plates with conically headed cylindrical punches, *J Strain Anal*, 8(3):228-41.

[58] Johnson GR, Cook WH. (1985). Fracture characteristics of three metals subjected to various strains, strain rates, temperatures and pressures. *Engng Fract Mech*, 21: 31-48.

[59] Johnson GR, Holmquist TJ. (1989). Test data and computational strength and fracture model contants for 23 materials subjected to large strain, high strain rates, and high temperature. Technical Report LA-11463-MS. Los Alamos National Laboratory.

[60] Jain M, Allin J, Lloyd DJ. (1999). Fracture limit prediction using ductile fracture criteria for forming of an automotive aluminum sheet. *Int J Mech Sci*, 41:1273-1288.

[61] Keeler SP, Backofen WA. (1963). Plastic instability and fracture in sheet stretched over rigid punches. *Trans ASME*, 56:25-48.

[62] Kudo, H., and Aoi, K. (1967). Effect of compression test conditions upon fracturing of medium carbon steel. *J Japan Soc Techn Plasticity* 18:17-27.

[63] Kuhn HA. (1976). Final Report AISI Proj 56-350, University of Pittsburgh.

[64] Keegstra PNR, Head LJ, Turner CE. (1978). A two-dimensional dynamic linear-elastic finite-element program for the analysis of unstable crack propagation and arrest. In: Luxmoore AR and Owen DRJ eds, *Numerical Methods in Fracture Mechanics*. University of College; Swansea, p. 634-647.

[65] Knibloe JR, Wagoner RH. (1989). Experimental investigation and finite element modeling of hemispherically stretched steel sheet. *Metall Trans*, 20A:1509-1521.

[66] Kaminishi K. (1992). Crack initiation and extension under penetration of thin metal sheet. *JSME Internat Jnl*, 35(4):475-481.

[67] Kee A, Matic P, Darby I, Rodd JL. (1995). Finite element analysis of the quarter scale advanced double hull design. *Nav Engrs J*, May:185-196.

[68] Kitamura O. (2002). FEM approach to the simulation of collision and grounding damage. *Marine Struc*, 15:403-428.

[69] LeRoy GH, Embury JD, Edward G, Ashby MF. (1981). A model of ductile fracture based on the nucleation and growth of voids. *Acta Metall,* 29:1509-1522.

[70] Landkof B, Goldsmith W. (1985). Petalling of thin, metallic plates during penetration by cylindro-conical projectiles. *Int J Solds Structs*, 21(3):245-66.

[71] Leblond JB, Perrin G, Devaux J. (1994). Bifurcation effects in ductile metals with damage delocalization. *J Appl Mech*, 61:236-242.

[72] Lee NS, Bathe KJ. (1994). Error indicators and adaptive remeshing in large deformation finite element analysis. *Fin Elem Anal Design*, 16:99-139.

[73] Loca LA, Pan YG, Harding JE. (1998). Response of stiffened and unstiffened plates subjected to blast loading. *Engng Struct*, 20(12);1079-1086.

[74] Lesuer DR. (2000). Experimental investigations of material models for Ti-6Al-4V titanium and 2024-T3 aluminum. Technical Report DOT/FAA/AR-00/25, Lawrence Livermore National Laboratory.

[75] Liang CC, Yang MF, Wu PW. (2001). Optimum design of metallic corrugated core sandwich panels subjected to blast loads. *Ocean Engng*, 28:825-861.

[76] Ludolphy H. (2002). Damage tolerant structures. In: *Proc. of the Workshop on "Blast Resistant Materials and Structures"*. Warrenton, VA, September 3-5.

[77] Lee YW, Wierzbicki T. (2003). Relationship between the Forming and Fracture Limit Diagrams with calibration and applications. In: *Proc. of the AmeriPAM03*. Troy, Michigan, October 21-22.

[78] LS-DYNA User's Manual. (2003). Version 970, Livermore Software Technology Co.

[79] Langdon GS, Yuen Kim SC, Nurick GN. (2004). Experimental and numerical studies on the response of quadrangular stiffened plates. Part II: localized blast loading. *Int J Impact Engng*, 31(1):85-11.

[80] McClintock FA. (1968). A criterion of ductile fracture by the growth of holes. *J Appl Mech*, 35:363-71.

[81] McClintock FA, Zheng ZA. (1993). Ductile fracture in sheets under transverse strain gradients. *Int J Fract*, 64:321-337.

[82] Marciniak Z, Kuczynsky K, Pokora T. (1973). Influence of the plastic properties of a material on the forming limit diagram for sheet metal in tension. *Int J Mech Sci*, 15:789-805.

[83] Marciniak Z. (1978). Sheet metal forming limits. In: *Mechanics of sheet metal forming*. Plenum Press: New York-London, p. 215-235.

[84] Marciniak Z, Duncan JL. (1992). Tensile instability. In: *The mechanics of sheet metal forming*. Edward Arnold, p. 42-67.

[85] Marusich TD, Ortiz M. (1995). Modeling and simulation of high-speed machining. *Int J Numer Meth Engng*, 38:3675-3694.

[86] Mikkelsen LP. (1997). Post-necking behavior modeled by a gradient plasticity theory. *Int J Solds Strucs*, 34:4531-4546.

[87] Mikkelsen LP. (1999). Necking in rectangular tensile bars approximated by a 2-D gradient dependent plasticity model. *Eur J Mech A/Solds*, 18:805-818.

[88] Moes N, Dolbow J, Belytschko. (1999). A finite element method for crack growth without remeshing. *Int J Numer Meth Engng*, 46:131-150.

[89] Moes N, Belytschko. (2002). Extended finite element method for cohesive crack growth. *Engng Fract Mech*, 69:813-833.

[90] Muragishi O. (2000). Premature cleavage of ship plating under reversed bending. *Ph D Thesis*, MIT.

[91] Mihailescu-Suliciu M, Wierzbicki T. (2002). Wave solution for an impulsively loaded rigid-plastic circular membrane. *Arch Mech*, 54:5-6, p. 737-759.

[92] Needleman, A. (1972). A numerical study of necking in circular cylindrical bar. *J Mech Phys Solds*, 20:111-127.

[93] Needleman A. (1988). Material rate dependence and mesh sensitivity in localization problems. *Computs Methods Appl Mech Engng*, 67:69-85.

[94] Needleman A, Tvergarrd V. (1994). Mesh effects in the analysis of dynamic ductile crack growth. *Engng Fract Mech*, 47:75-91.

[95] Norris DM, Reaugh JE, Morgan B, Quinones DF. (1978). A plastic-strain, mean-stress criterion for ductile fracture. *J Engng Mater Tech*, 100:270-286.

[96] Nurick GN, Martin JB. (1989a). Deformation of thin plates subjected to impulsive loading-a review, Part I: theoretical considerations. *Int J Imapct Engng*, 8:159-70.

[97] Nurick GN, Martin JB. (1989b). Deformation of thin plates subjected to impulsive loading-a review, Part II: experimental studies. *Int J Imapct Engng*, 8:171-86.

[98] Nurick GN, Shave GC. (1996). The deformation and tearing of thin square plates subjected to impulsive loads-an experimental study. *Int J Imapct Engng*, 18:99-116.

[99] Nurick GN, Gelman ME, Marshall NS. (1996). Tearing of blast loaded plates with clamped boundary conditions. *Int J Imapct Engng*, 18:803-27.

[100] Nurick GN, Radford AM. (1997). Deformation and tearing of clamped circular plates subjected to localized central blast loads. In: Reddy BD, eds. *Recent developments in computational and applied mechanics*. A volume in honor of John B Martin, p. 276-301.

[101] Naar H, Kujala P, Simonsen BC, Ludolphy H. (2002). Comparison of the crashworthiness of various bottom and side structures. *Marine Struc*, 15:443-460.

[102] Oyane M, Sato T, Okimoto K, Shima S. (1980). Criteria for ductile fracture and their applications. *J Mech Work Tech*, 4:65-81.

[103] Ortiz M, Quigley JJ IV. (1991). Adaptive mesh refinement in strain localization problems. *Comput Meth Appl Mech Engng*, 90:781-804.

[104] Olson MD, Nurick GN, Fagnan JR. (1993). Deformation and rupture of blast loaded square plates-predictions and experiments. *Int J Imapct Engng*, 13:279-291.

[105] Paul B, Zaid M. (1957). Normal perforation of a thin plate by truncated projectiles. *J Franklin Inst*, 264:117-26.

[106] Pijaudier-Cabot G, Bazant ZP. (1987). Nonlocal damage theory. *J Engng Mech ASCE*, 113:1512-1533.

[107] Paik JK, Chung JY, Choe IH, Thayamballi AK, Pedersen PT, Wang G. (1999). On the rational design of double hull tanker structures against collision. *SNAME Annual Meeting*, Baltimore, MD.

[108] PAM-CRASH 2G User's Manual. (2003). Engineering Systems International Group.

[109] Rice JR, Tracey DM. (1969). On the ductile enlargement of voids in triaxial stress fields. *J Mech Phys Solds*, 17:201-17.

[110] Rousselier G. (1987). Ductile fracture models and their potential in local approach of fracture. *Nuclr Engng and Desgn*, 105:97-111.

[111] Rankin CC, Brogan FA, Riks E. (1993). Some computational tools for the analysis of through cracks in stiffened fuselage shells. *Comput Mech*, 13:143-156.

[112] Rashid MM. (1997). A new theory for free-surface formation in solid continua. *Int J Solds Structs*, 34(18):2303-2320.

[113] Rashid MM. (1998). The arbitrary local mesh replacement method: An alternative to remeshing for crack propagation analysis. *Comput Methods Appl Mech Engrg*, 154:133-150.

[114] Rudrapatna NS, Vaziri R, Olson MD. (1999). Deformation and failure of blast-loaded square plates. *Int J Imapct Engng*, 22:449-67.

[115] Rudrapatna NS, Vaziri R, Olson MD. (2000). Deformation and failure of blast loaded stiffened plates. *Int J Impact Engng*, 24:457-474.

[116] Remmers JJC, Borst R de, Needleman A. (2003). A cohesive segments method for the simulation of crack growth. *Comput Mech*, 31:69-77.

[117] Swift HW. (1952). Plastic instability under plane stress. *J of Mech Phys Solds*, 1:1-18.

[118] Stören S, Rice JR. (1975). Localized necking in thin sheets. *J of Mech Phys Solds*, 23:421-441.

[119] Symonds PS, Wierzbicki T. (1979). Membrane mode solution for impulsively loaded circular plates. *J Appl Mech*, 46:58-64.

[120] Schubak RB, Olson MD, Anderson DL. (1993a). Rigid-plastic modelling of blast loaded stiffened plates-Part I: one way stiffened plates. *Int J Mech Sci*, 35(3/4):289-306.

[121] Schubak RB, Olson MD, Anderson DL. (1993b). Rigid-plastic modelling of blast loaded stiffened plates-Part II: partial end fixity, rate effects and two-way stiffened plates. *Int J Mech Sci*, 35(3/4):307-324.

[122] Sikora J, Grassman JM, Sensharma P, Watts J. (1997). Advanced double hull structural design technology. *Nav Engrs J*, May:117-128.

[123] Skallerud B, Zhang ZL. (1999). Effects of finite element mesh on numerical prediction of ductile tearing. *Fatigue and Fracture Mechanics: Twenty Ninth Volume* ASTM STP 1332, 201-214.

[124] Simonsen BC, Lauridsen LP. (2000). Energy absorption and ductile failure in metal sheets under lateral indentation by a sphere. *Int J Imapct Engng*, 24:1017-1039.

[125] Simonsen BC, Törnqvist R. (2004). Experimental and numerical modeling of ductile fracture in large-scale shell structures. *Mar Struct*, 17:1-27.

[126] Stoughton TB. (2000). A general forming limit criterion for sheet metal forming. *Int J Mech Sci*, 42:1-27.

[127] Stoughton TB, Zhu X. (2004). Review of theoretical methods of strain-based FLD and their relevance to the stress-based FLD. *Int J Plastcty* (in press).

[128] Schleyer GK, Hsu SS, White MD, Birch RS. (2003). Pulse pressure loading of clamped mild steel plates. *Int J Impact Engng*, 28(2):223-247.

[129] Taylor GI. (1948). The formation of enlargement of circular holes in thin plastic plates. *Q J Mech Appl Math*, 1:103-24.

[130] Thomson WT. (1951). An approximate theory of armor penetration. *J Appl Physics*, 26:80-3.

[131] Tadros AK, Mellor PB. (1977). An experimental study of the in-plane stretching of sheet metal. *Int J Mech Sci*, 17:203-210.

[132] Tvergaard V, Needleman A. (1984). Analysis of the cup-cone fracture in a round tensile bar. *Acta Metallurgica*, 32:157-169.

[133] Tvergaard V. (1993). Necking in tensile bars with rectangular cross-section. *Comput Methods Appl Mech Engn*, 103:207-290.

[134] Tvergaard V, Needleman A. (1997). Nonlocal effects on localization in a void-sheet. *Int J Solds Struc*, 34:2221-2238.

[135] Teeling-Smith RG, Nurick GN. (1991). The deformation and tearing of thin circular plates subjected to impulsive loads. *Int J Imapct Engng*, 11:77-91.

[136] Thunes R. (1994). Development of analytical models of wedge indentation into unidirectionally stiffened and orthogonally stiffened double hulls. Report 21, *Joint MIT-Industry Program on Tanker Safety*, MIT.

[137] Takuda H, Mori K, Fujimoto H, Hatta N. (1997). Fracture prediction in stretch forming using finite element simulation combined with ductile fracture criterion. *Arch Appl Mech*, 67:143-150.

[138] Tradegard A, Nilsson F, Ostlund S. (1998). FEM-remeshing technique applied to crack growth problems. *Compu Methods Appl Mech Engrg*, 160:115-31.

[139] Takuda H, Mori K, Takakura N, Yamaguchi K. (2000). Finite element analysis of limit strains in biaxial stretching of sheet metals allowing for ductile fracture. *Int J Mech Sci*, 42:785-798.

[140] Tang CY, Chow CL, Shen W, Tai WH. (1999). Development of a damage-based criterion for ductile fracture prediction in sheet metal forming. *J Mater Proc Tech*, 91:270-277.

[141] Wilkins ML, Streit RD, Reaugh JE. (1980). Cumulative strain damage model of ductile fracture: simulation and prediction of engineering fracture tests. UCRL-53058, Lawrence Livermore Laboratory, Livermore.

[142] Wiernicki CJ, Liem F, Woods GD, Furio AJ. (1991). Structural analysis methods for lightweight metallic corrugated core sandwich panels subjected to blast loads. *Nav Engrs J*, May:192-203.

[143] Wierzbicki T, Driscoll JC. (1995). Crushing damage of web girders under localized static loads. *J Constrcut Steel Research*, 33:199-235.

[144] Wierzbicki T, de Lacruz-Alvarez A, Hoo Fatt MS. (1995). Impact energy absorption of sandwich plates with crushable core. In: *Proc. of the ASME/AMD Symposium, Impact Waves, and Fracture*. LosAngeles, CA, 205:391-411.

[145] Wierzbick T, Nurick GN. (1996). Large deformation of thin plates under localized impulsive loading. *Int J Imapct Engng*, 18:899-918.

[146] Wierzbick T. (1999). Petalling of plates under explosive and impact loading. *Int J Impact Engng*, 22:935-54.

[147] Wierzbicki T. (2001). Energy partitioning in the holing process of explosively loaded plates. In: *Proc. of the Workshop on "Blast and Shock Resistant Materials and Structures"*. Naval Research Laboratory, Washington DC.

[148] Wierzbicki T. (2002). Development of blast resistant adaptive sandwich structures. In: *Proposal to the ONR within the MURI 2002 topic #11*, MIT.

[149] Wierzbicki T, Bao Y, Werner H. (2002). Ductile fracture: theory, calibration and applications. In "*EuroPAM 2002*", ESI Group.

[150] Wierzbicki T, Bao Y. (2004). Bridgman revisited: on the history effects on ductile fracture. *J Mech Phys Solds*, submitted for publication.

[151] Wang G, Ohtsubo H, Arita K. (1998). Large deflection analysis of a rigid-plastic circular plate pressed by a sphere. *J Appl Mech*, 65:533-535.

[152] Wang G, Arita K, Liu D. (2000). Behavior of a double hull in a variety of stranding or collision scenarios. *Marine Struc*, 13:147-187.

[153] Wells GN, Sluys LJ. (2001). A new method for modeling cohesive cracks using finite elements. *Int J Numer Meth Engng*, 50:2667-2682.

[154] Woertz JC. (2002). Quasi-static tearing tests of metal plating. *Master Thesis*, MIT.

[155] Yagawa G, Sakai Y, Ando Y. (1977). Analysis of a rapidly propagating crack using finite elements. In: Hahn GT and Kanninen, eds. *Fast Fracture and Crack Arrest*. ASTM STP 627, p. 109-122.

[156] Yahiaoui M, Patrick MB, Trauth KA. (1994). Experimental studies on scale models for grounding. Report 18, *Joint MIT-Industry Program on Tanker Safety*, MIT.

[157] Zaid M, Paul B. (1958). Mechanics of high speed projectile perforation. *J Franklin Inst*, 265:317-35.

[158] Zhu L. (1996). Transient deformation modes of square plates subjected to explosive loadings. *Int J Sol Struct*, 33:301-14.

[159] Zhang ZL, Hauge M, Odegard J, Thaulow C. (1999). Determining material true stress-strain curve from tensile specimens with rectangular cross-section. *Int J Solds Strcut*, 36:3497-3516.

[160] Zhang S. (2002). Plate tearing and bottom damage in ship grounding. *Mar Struct*, 15:101-117.

[161] Zhenyu X, Hutchinson JW. (2003). Preliminary assessment of sandwich plates subject to blast loads. *Int J Mech Sci*, 45:687-705.

[162] Zhenyu X, Hutchinson JW. (2004). A comparative study of impulse-resistant metal sandwich plates. *Int J Impact Engng*, 30(10):1265-1369.

Appendix A

Representation of seven fracture criteria in three different spaces

Criterion I, Bao-Wierzbicki

- $(\sigma_m/\bar{\sigma}, \bar{\varepsilon}_f)$:

$$\bar{\varepsilon}_f = \begin{cases} \dfrac{\mathbf{b}}{3\dfrac{\sigma_m}{\bar{\sigma}}}, & \dfrac{\sigma_m}{\bar{\sigma}} \in (\dfrac{1}{3}, \dfrac{2}{3}) \\ 9(\mathbf{b}-\mathbf{a})(\dfrac{\sigma_m}{\bar{\sigma}})^2 + a, & \dfrac{\sigma_m}{\bar{\sigma}} \in (0, \dfrac{1}{3}) \\ \dfrac{\mathbf{a}}{1+3\dfrac{\sigma_m}{\bar{\sigma}}}, & \dfrac{\sigma_m}{\bar{\sigma}} \in (-\dfrac{1}{3}, 0) \end{cases} \tag{A1}$$

- $(\varepsilon_{2f}, \varepsilon_{1f})$:

$$\varepsilon_{1f} = \begin{cases} \dfrac{\mathbf{b}}{2(1+\alpha)}, & \alpha \in (-\dfrac{1}{2}, 1) \\ \dfrac{9(\mathbf{b}-\mathbf{a})(1+\alpha)^2}{2\sqrt{3}(1+\alpha+\alpha^2)^{3/2}} + \dfrac{\sqrt{3}a}{2\sqrt{1+\alpha+\alpha^2}}, & \alpha \in (-1, -\dfrac{1}{2}) \\ \dfrac{\sqrt{3}\mathbf{a}}{2}\dfrac{1}{\sqrt{3}(1+\alpha)+\sqrt{1+\alpha+\alpha^2}}, & \alpha \in (-2, -1) \end{cases} \tag{A2}$$

- $(\sigma_{2f}, \sigma_{1f})$:

$$\sigma_{1f} = \begin{cases} \sigma_{1f}^{0}\left[\dfrac{\sqrt{1+\alpha+\alpha^2}}{\sqrt{3}(1+\alpha)}\right]^n \dfrac{2+\alpha}{\sqrt{3}\sqrt{1+\alpha+\alpha^2}}, & \alpha \in (-\dfrac{1}{2}, 1) \\ \sigma_{1f}^{0}\left[\dfrac{3(1+\alpha)^2-(a/b)(1+2\alpha)(2+\alpha)}{1+\alpha+\alpha^2}\right]^n \dfrac{2+\alpha}{\sqrt{3}\sqrt{1+\alpha+\alpha^2}}, & \alpha \in (-1, -\dfrac{1}{2}) \\ \dfrac{\sigma_{1f}^{0}}{2}\left[\dfrac{\sqrt{1+\alpha+\alpha^2}}{\sqrt{1+\alpha+\alpha^2}+\sqrt{3}(1+\alpha)}\right]^n \dfrac{2+\alpha}{\sqrt{1+\alpha+\alpha^2}}, & \alpha \in (-2, -1) \end{cases} \tag{A3}$$

Criterion II, Maximum Shear Stress

$$\tau_{\max} = \text{constant} = \sigma_{1f}^{0} \tag{A4}$$

- $(\sigma_m / \bar{\sigma}, \bar{\varepsilon}_f)$:

$$\bar{\varepsilon}_f = \begin{cases} \mathbf{b}\left(\dfrac{\sqrt{3}\sqrt{1+\alpha+\alpha^2}}{2+\alpha}\right)^{\frac{1}{n}}, & \alpha \in (-\dfrac{1}{2}, 1) \text{ or } \dfrac{\sigma_m}{\bar{\sigma}} \in (\dfrac{1}{3}, \dfrac{2}{3}) \\ \mathbf{b}\left(\dfrac{\sqrt{3}\sqrt{1+\alpha+\alpha^2}}{1-\alpha}\right)^{\frac{1}{n}}, & \alpha \in (-1, -\dfrac{1}{2}) \text{ or } \dfrac{\sigma_m}{\bar{\sigma}} \in (0, \dfrac{1}{3}) \\ \mathbf{b}\left(\dfrac{\sqrt{3}\sqrt{1+\alpha+\alpha^2}}{1-\alpha}\right)^{\frac{1}{n}}, & \alpha \in (-2, -1) \text{ or } \dfrac{\sigma_m}{\bar{\sigma}} \in (-\dfrac{1}{3}, 0) \end{cases} \tag{A5}$$

- $(\varepsilon_{2f}, \varepsilon_{1f})$:

$$\varepsilon_{1f} = \begin{cases} \mathbf{b}\left(\dfrac{\sqrt{3}\sqrt{1+\alpha+\alpha^2}}{2+\alpha}\right)^{\frac{1}{n}} \dfrac{\sqrt{3}}{2\sqrt{1+\alpha+\alpha^2}}, & \alpha \in (-\dfrac{1}{2}, 1) \\ \mathbf{b}\left(\dfrac{\sqrt{3}\sqrt{1+\alpha+\alpha^2}}{1-\alpha}\right)^{\frac{1}{n}} \dfrac{\sqrt{3}}{2\sqrt{1+\alpha+\alpha^2}}, & \alpha \in (-1, -\dfrac{1}{2}) \\ \mathbf{b}\left(\dfrac{\sqrt{3}\sqrt{1+\alpha+\alpha^2}}{1-\alpha}\right)^{\frac{1}{n}} \dfrac{\sqrt{3}}{2\sqrt{1+\alpha+\alpha^2}}, & \alpha \in (-2, -1) \end{cases} \tag{A6}$$

- $(\sigma_{2f}, \sigma_{1f})$:

$$\sigma_{1f} = \begin{cases} \sigma_{1f}^{0}, & \alpha \in (-\frac{1}{2}, 1) \\ \sigma_{1f}^{0} \frac{2+\alpha}{1-\alpha}, & \alpha \in (-1, -\frac{1}{2}) \\ \sigma_{1f}^{0} \frac{2+\alpha}{1-\alpha}, & \alpha \in (-2, -1) \end{cases} \tag{A7}$$

Criterion III, Cockcroft-Latham

$$\int_{0}^{\bar{\varepsilon}_f} \sigma_1 d\bar{\varepsilon} = \text{constant} = (W_{cr})_f \text{ (pure shear condition)} \tag{A8}$$

- $(\sigma_m / \bar{\sigma}, \bar{\varepsilon}_f)$:

$$\bar{\varepsilon}_f = \mathbf{a} \left(\frac{\sqrt{1+\alpha+\alpha^2}}{2+\alpha} \right)^{\frac{1}{n+1}} \tag{A9}$$

- $(\varepsilon_{2f}, \varepsilon_{1f})$:

$$\varepsilon_{1f} = \mathbf{a} \left(\frac{\sqrt{1+\alpha+\alpha^2}}{2+\alpha} \right)^{\frac{1}{n+1}} \frac{\sqrt{3}}{2\sqrt{1+\alpha+\alpha^2}} \tag{A10}$$

- $(\sigma_{2f}, \sigma_{1f})$:

$$\sigma_{1f} = \frac{\sigma_{1f}^{0}}{2} \left(\frac{2+\alpha}{\sqrt{1+\alpha+\alpha^2}} \right)^{\frac{1}{n+1}} \tag{A11}$$

Criterion IV, W model

- $(\sigma_m/\bar{\sigma}, \bar{\varepsilon}_f)$:

$$\bar{\varepsilon}_f = \mathbf{b}\left(\frac{9}{7}\right)^{\lambda_w}\left(1-\frac{2}{3}\frac{\sigma_m}{\bar{\sigma}}\right)^{\lambda_w}\left(2-A_w\right)^{-\mu_w} \tag{A12}$$

where $\lambda_w = 2.15$ and $\mu_w = 2.18$ for the case of Al2024-T351. Then, Eq. (A12) can be rewritten as

$$\bar{\varepsilon}_f = \begin{cases} \dfrac{\mathbf{b}}{0.58}\left(1-\dfrac{2}{3}\dfrac{\sigma_m}{\bar{\sigma}}\right)^{2.15}(2-\alpha)^{-2.18}, & \alpha\in(0,1) \\ \dfrac{\mathbf{b}}{0.58}\left(1-\dfrac{2}{3}\dfrac{\sigma_m}{\bar{\sigma}}\right)^{2.15}\left(\dfrac{2+3\alpha}{1+\alpha}\right)^{-2.18}, & \alpha\in(-\dfrac{1}{2},0) \\ \dfrac{\mathbf{b}}{0.58}\left(1-\dfrac{2}{3}\dfrac{\sigma_m}{\bar{\sigma}}\right)^{2.15}\left(\dfrac{3\alpha+1}{\alpha}\right)^{-2.18}, & \alpha\in(-1,-\dfrac{1}{2}) \\ \dfrac{\mathbf{b}}{0.58}\left(1-\dfrac{2}{3}\dfrac{\sigma_m}{\bar{\sigma}}\right)^{2.15}(3+\alpha)^{-2.18}, & \alpha\in(-2,-1) \end{cases} \tag{A13}$$

- $(\varepsilon_{2f}, \varepsilon_{1f})$:

$$\varepsilon_{1f} = \begin{cases} \dfrac{1.49\mathbf{b}}{\sqrt{1+\alpha+\alpha^2}}\left(1-0.381\dfrac{1+\alpha}{\sqrt{1+\alpha+\alpha^2}}\right)^{2.15}(2-\alpha)^{-2.18}, & \alpha\in(0,1) \\ \dfrac{1.49\mathbf{b}}{\sqrt{1+\alpha+\alpha^2}}\left(1-0.381\dfrac{1+\alpha}{\sqrt{1+\alpha+\alpha^2}}\right)^{2.15}\left(\dfrac{2+3\alpha}{1+\alpha}\right)^{-2.18}, & \alpha\in(-\dfrac{1}{2},0) \\ \dfrac{1.49\mathbf{b}}{\sqrt{1+\alpha+\alpha^2}}\left(1-0.381\dfrac{1+\alpha}{\sqrt{1+\alpha+\alpha^2}}\right)^{2.15}\left(\dfrac{3\alpha+1}{\alpha}\right)^{2.18}, & \alpha\in(-1,-\dfrac{1}{2}) \\ \dfrac{1.49\mathbf{b}}{\sqrt{1+\alpha+\alpha^2}}\left(1-0.381\dfrac{1+\alpha}{\sqrt{1+\alpha+\alpha^2}}\right)^{2.15}(3+\alpha)^{-2.18}, & \alpha\in(-2,-1) \end{cases} \tag{A14}$$

- $(\sigma_{2f}, \sigma_{1f})$:

$$\sigma_{1f} = \begin{cases} \sigma_{1f}^{0}\left[1.722\left(1-0.381\dfrac{1+\alpha}{\sqrt{1+\alpha+\alpha^2}}\right)^{2.15}(2-\alpha)^{-2.18}\right]^{n}\dfrac{2+\alpha}{\sqrt{3}\sqrt{1+\alpha+\alpha^2}}, & \alpha\in(0,1) \\ \sigma_{1f}^{0}\left[1.722\left(1-0.381\dfrac{1+\alpha}{\sqrt{1+\alpha+\alpha^2}}\right)^{2.15}\left(\dfrac{2+3\alpha}{1+\alpha}\right)^{-2.18}\right]^{n}\dfrac{2+\alpha}{\sqrt{3}\sqrt{1+\alpha+\alpha^2}}, & \alpha\in(-\dfrac{1}{2},0) \\ \sigma_{1f}^{0}\left[1.722\left(1-0.381\dfrac{1+\alpha}{\sqrt{1+\alpha+\alpha^2}}\right)^{2.15}\left(\dfrac{3\alpha+1}{\alpha}\right)^{-2.18}\right]^{n}\dfrac{2+\alpha}{\sqrt{3}\sqrt{1+\alpha+\alpha^2}}, & \alpha\in(-1,-\dfrac{1}{2}) \\ \sigma_{1f}^{0}\left[1.722\left(1-0.381\dfrac{1+\alpha}{\sqrt{1+\alpha+\alpha^2}}\right)^{2.15}(3+\alpha)^{-2.18}\right]^{n}\dfrac{2+\alpha}{\sqrt{3}\sqrt{1+\alpha+\alpha^2}}, & \alpha\in(-2,-1) \end{cases} \quad \text{(A15)}$$

Criterion V, Johnson-Cook Fracture Criterion

- $(\sigma_m/\bar{\sigma}, \bar{\varepsilon}_f)$:

$$\bar{\varepsilon}_f = C_1 + C_2\exp\left(C_3\frac{\sigma_m}{\bar{\sigma}}\right) \quad \text{(A16)}$$

- $(\varepsilon_{2f}, \varepsilon_{1f})$:

$$\varepsilon_{1f} = \frac{\sqrt{3}}{2\sqrt{1+\alpha+\alpha^2}}\left[C_1 + C_2\exp\left(C_3\frac{1}{\sqrt{3}}\frac{1+\alpha}{\sqrt{1+\alpha+\alpha^2}}\right)\right] \quad \text{(A17)}$$

- $(\sigma_{2f}, \sigma_{1f})$:

$$\sigma_{1f} = \sigma_{1f}^{0}\left[\frac{1}{\mathbf{b}}\left\{C_1 + C_2\exp\left(C_3\frac{1}{\sqrt{3}}\frac{1+\alpha}{\sqrt{1+\alpha+\alpha^2}}\right)\right\}\right]^{n}\frac{2+\alpha}{\sqrt{3}\sqrt{1+\alpha+\alpha^2}} \quad \text{(A18)}$$

Criterion VI, Critical Equivalent Strain

$$\bar{\varepsilon}_f = \text{constant (plane strain tension)} \tag{A19}$$

- $(\sigma_m/\bar{\sigma}, \bar{\varepsilon}_f)$:

$$\bar{\varepsilon}_f = \frac{\mathbf{b}}{\sqrt{3}} \tag{A20}$$

- $(\varepsilon_{2f}, \varepsilon_{1f})$:

$$\varepsilon_{1f} = \frac{\mathbf{b}}{2\sqrt{1+\alpha+\alpha^2}} \tag{A21}$$

- $(\sigma_{2f}, \sigma_{1f})$:

$$\sigma_{1f} = \sigma_{1f}^0 \left(\frac{1}{\sqrt{3}}\right)^n \frac{2+\alpha}{\sqrt{3}\sqrt{1+\alpha+\alpha^2}} \tag{A22}$$

Criterion VII, Localized Necking (FLD) and conventional Fracture Forming Limit Diagram (FFLD)

- $(\sigma_m/\bar{\sigma}, \bar{\varepsilon}_n)$:

$$\bar{\varepsilon}_n = \begin{cases} \dfrac{2n}{3\dfrac{\sigma_m}{\bar{\sigma}}}, & \alpha \in (-\frac{1}{2}, 0) \text{ or } \dfrac{\sigma_m}{\bar{\sigma}} \in (\frac{1}{3}, \frac{1}{\sqrt{3}}); \text{ Hill} \\ \dfrac{3\alpha^2 + n(2+\alpha)^2}{\sqrt{3}(2+\alpha)\sqrt{1+\alpha+\alpha^2}}, & \alpha \in (0,1) \text{ or } \dfrac{\sigma_m}{\bar{\sigma}} \in (\frac{1}{\sqrt{3}}, \frac{2}{3}); \text{ Storen and Rice} \end{cases} \tag{A23}$$

- $(\varepsilon_{2n}, \varepsilon_{1n})$:

$$\varepsilon_{1n} = \begin{cases} \dfrac{n}{1+\alpha}, & \alpha \in (-\frac{1}{2}, 0); \text{ Hill(1952)} \\ \dfrac{3\alpha^2 + n(2+\alpha)^2}{2(2+\alpha)(1+\alpha+\alpha^2)}, & \alpha \in (0,1); \text{ Storen and Rice(1975)} \end{cases} \tag{A24}$$

- $(\sigma_{2n}, \sigma_{1n})$:

$$\sigma_{1n} = \begin{cases} \sigma_{1f}^{0}\left(\frac{2n}{\mathbf{b}}\right)^{n}\left[\frac{\sqrt{1+\alpha+\alpha^2}}{\sqrt{3}(1+\alpha)}\right]^{n}\frac{2+\alpha}{\sqrt{3}\sqrt{1+\alpha+\alpha^2}}, & \alpha \in (-\frac{1}{2}, 0); \text{ Hill} \\ \sigma_{1f}^{0}\left(\frac{2n}{\mathbf{b}}\right)^{n}\left[\frac{3\alpha^2+n(2+\alpha)^2}{2\sqrt{3}(2+\alpha)\sqrt{1+\alpha+\alpha^2}}\right]^{n}\frac{2+\alpha}{\sqrt{3}\sqrt{1+\alpha+\alpha^2}}, & \alpha \in (0, 1); \text{ Storen and Rice} \end{cases} \tag{A25}$$

Note that the conventional FFLD corresponds to one branch of BW criterion for stress triaxialities larger than 1/3 (see top of Eqns. (A1), (A2), and (A3)).

This page intentionally left blank

Appendix B

Referred journal publications by Y-W Lee related to this thesis

- Lee YW, Woertz JC, Wierzbicki T. Fracture prediction of thin plates under hemispherical punch with calibration and experimental verification. *Internal Journal Mechanical Science*, 46:751-781, 2004.
- Lee YW, Wierzbicki T. Fracture prediction of thin plates under localized impulsive loading, Part I: dishing. *International Journal Impact Engineering*, In press.
- Lee YW, Wierzbicki T. Fracture prediction of thin plates under localized impulsive loading, Part II: discing and petalling. *International Journal Impact Engineering*, In press.
- Lee YW, Wierzbicki T. Structural optimization against fracture damage of double hulls under localized impulsive loading. *Marine Structures*, In press.
- Bao Y, Lee YW, Wierzbicki T. Evaluation and calibration of seven fracture models. *Internal Journal Mechanical Science*, submitted for publication.
- Lee YW, Wierzbicki T, Bao Y. Effect of mesh size on initiation and propagation of crack in flat tensile specimens. *Mechanics of Materials*, submitted for publication.
- Lee YW, Wierzbicki T. Quick fracture calibration for industrial use. *Engineering Fracture Mechanics*, submitted for publication.